

Iron and Carbon Speciation in
Non-Buoyant Hydrothermal Plumes
along the East Pacific Rise:

A Chemistry Love Story

A DISSERTATION
SUBMITTED TO THE FACULTY OF
UNIVERSITY OF MINNESOTA
BY

Colleen Lynn Hoffman

IN PARTIAL FULFILLMENT OF THE REQUIREMENTS
FOR THE DEGREE OF
DOCTOR OF PHILOSOPHY

Advisor: Brandy M. Toner, PhD

September 2018

© Colleen Lynn Hoffman 2018

Acknowledgements

First and foremost, I would like to thank my advisor, Dr. Brandy Toner, for all the mentorship and support over the last 5 years. Your confidence in my abilities always helped me achieve goals I did not think possible. Thank you for letting me run wild with crazy aspirations before reining me in for more realistic objectives. Through all the personal and professional ups and downs, the Toner lab was a wonderful lab to grow, collaborate, and build the foundation of my scientific career.

Next, I would also like to thank Dr. Sarah Nicholas for collection of my samples at sea. Without your willingness to put your dissertation on hold, my dissertation would have never happened. Additionally, Dr. Nicholas, Dr. Brandi Cron Kamermans, Rebecca Sims, and Caroline Pierce, all need to be thanked for their they help over multiple beamline data collections and synchrotron trips. You all were integral in me becoming better spectroscopist and making sure I kept my sanity at beamtime.

I want to thank past and current committee members. Special thanks to Dr. William Seyfried, and Dr. Katsumi Matsumoto for lively discussions and mentorship over the years that was vital in my development as a scientist and enhanced my understanding of hydrothermal systems and oceanographic processes.

I would also like to give a special thanks to Dr. Phoebe Lam, Dr. Jessica Fitzsimmons, Dr. Chris German, and Dr. Rob Sherrell for letting a geochemist feel welcomed in the oceanography world. Your collaborations were integral to my development as a scientist and enhanced this dissertation.

I would like to thank the captain and crew of R/V Thomas G. Thompson and Co-Chief Scientists Dr. James Moffett and Dr. Chris German for supporting our research during the GEOTRACES GP16 cruise.

I also thank Sirine Fakra and Matthew Marcus, beamline scientists at the Advanced Light Source (ALS) 10.3.2, and David Kilcoyne, beamline scientist at ALS 5.3.2.2 for their mentorship, patience, and guidance in STXM and X-ray microprobe. Dr. Mahalingam Balasubramanian, beamline scientist at the Advance Photon Source (APS) 20-BM-B, for his mentorship, and patience in bulk EXAFS measurements. Adam Gillespie, Tom Regier, and James Dynes, beamline scientists at the Canadian Light Source (CLS) SGM, and Yongfeng Hu, Aimee MacLennan, and Qunfeng Xiao, beamline

scientists at the CLS SXRMB for their mentorship, patience, and guidance in bulk XANES measurements.

A big thank you must be given to all the amazing Undergraduate Researchers I worked with throughout the years. Aubrey Dunshee, for help with iron mineral synthesis and put up with long days in the lab testing both of our sanity. Ayele Ekue, who was amazing at learning new techniques and being flexible as we developed new methods. Collin Schladweiler, whose mastery of the SEM, is the reason I have beautiful SEM images, and Haleigh Ziebol, for help with quickly compiling and organizing large datasets.

At this point, would like to thank Andy Scobbie, Thor Sellie, Dr. Brandi Cron Kamermans, Rebecca Sims, Michael Ottman, Dr. Sofia Oufqir, and Reba VanBusekom for cruise preparation support; Dr. James Brandes for sharing carbon XANES standard spectra for carbonate minerals; Xiang Wang for mentorship and discussions about Gaussian curve fitting; and Dr. Nick Seaton for training and support in using the SEM at the UMN Characterization Facility.

I would like to give a big thank you to all the funding sources that supported this dissertation. First, there is the National Science Foundations and GEOTRACE community that supported my initial stipend and the cost of the cruise (OCE-1232986). Without their support this dissertation would be just an idea. Next, I would like to thank University of Minnesota for supporting me with a Doctoral Dissertation Fellowship for my final year and conference travel, and Thesis Travel Grant to travel to beamtime. The University of Minnesota-College of Earth Sciences for the Frances Gibson Fellowship to support my research development my first year. The University of Minnesota-College of Biological Sciences for the Moos Graduate Fellowship for Aquatic Biology that supported me for fourth summer and aided in method development. The University of Minnesota-Council of Graduate Students Community Development Grant for support my partial travel expenses to the first GEOTRACES Summer School. The Geological Society of America Graduate Student Research Grant for supporting my last few experiments of my dissertation. And lastly, to the Midwest branch of the America Federation of Mineralogical Societies scholarship to supplement my research when needed.

I want to thank all the facilities that allowed me to use (or one of my colleagues) their facilities: The Advanced Light Source is supported by the Director, Office of Science, Office of Basic Energy Sciences, of the U.S. Department of Energy under Contract No. DE-AC02-05CH11231; This research used resources of the Advanced Photon Source, a U.S. Department of Energy (DOE) Office of Science User Facility operated for the DOE Office of Science by Argonne National Laboratory under Contract No. DE-AC02-06CH11357; Research described in this dissertation was performed at the Canadian Light Source, which is supported by the Canada Foundation for Innovation, Natural Sciences and Engineering Research Council of Canada, the University of Saskatchewan, the Government of Saskatchewan, Western Economic Diversification Canada, the National Research Council Canada, and the Canadian Institutes of Health Research; and parts of this work were carried out in the Characterization Facility, University of Minnesota, a member of the NSF-funded Materials Research Facilities Network (www.mrfn.org) via the MRSEC program.

And finally, a very special thanks to my mom, brother, family, Captain Scott Perry, Dr. Brian Leung, author C.E. Clayton, Jennifer Leung, April Nunn M.S.W., Lizzy Wierenga, Dieuwertje Kast M.Sc. and MAT, Elisa Finan, Dr. Cynthia Joseph, Amanda Bailor J.D., Dr. Brandi Cron Kamermans, Rebecca Sims M.Sc., Dr. Megan Korchinski, Morgan Monz, Aubrey Dunshee, Ley Hartley, Bri Beltran R.N., and Katie Rau for being an amazing support network. Your encouragement and support (and sometime last-minute editing help) kept me going when I did not think I could continue.

Dedication

I dedicate this dissertation to my mother, Carol Hoffman and late father Gregory Hoffman, who always supported my dreams, instilled the importance of critical thinking, and inspired me to be curious about the natural world. My younger brother, Brett Hoffman, for always being there from the day he was born. My friends, both near and far, and new and old, who were always there to offer their encouragement over wine, video chats, and/or food. My significant other, Scott Perry, for being my confidant and reminding me to always make time for sunset drives along the Mississippi. To Dr. Sarah Bennett and the late Dr. Katrina Edwards, who took a chance on a lost, junior chemistry major, and Dieuwertje Kast who convinced me that marine biogeochemistry was a real field of study. To all the teachers, professors, peers, and family who inspired and believed in me. And finally, to my both alive and deceased fish, Squishy, Snape, David Bowie, T, L, C, Thing 1, Thing 2, Mr. T, Vader, and the Jets, who unwillingly came on this journey with me when I rescued them from the pet store.

Table of Contents

List of Tables.....	viii
List of Figures.....	ix
CHAPTER 1	1
1.1 Overview	2
1.2 The Unique Characteristics of a Mid-Oceanic Ridge (MOR) Hydrothermal systems.....	3
1.3 The “Leaky” East Pacific Rise.....	5
1.3.1 Integrating hydrothermal vent research along the Northern EPR.....	6
1.3.2 The discovery and significance of hydrothermal venting along the Southern EPR	8
1.4 The Importance of Particle Size for the Transport of Hydrothermally Derived Iron	11
1.5 Challenges in Analyzing Chemical Speciation of Elements in Plume Particles	13
1.6 Objectives and Hypotheses	14
1.7 Approach	15
CHAPTER 2	17
2.1 Overview	18
2.2 Introduction	19
2.3 Methods.....	22
2.3.1 Sample Collection.....	22
2.3.2 X-ray Absorption Spectroscopy.....	24
2.4 Results	27
2.4.1 Bulk Chemistry of Plume Particles.....	27
2.4.2 Bulk Chemistry of Station 20 Sediment Fluff	35
2.4.3 Particle-by-Particle Chemistry of Plume	35
2.5 Discussion	45
2.5.1 Plume Particle Morphology and Chemistry.....	45
2.5.2 Sources of Particulate Organic Carbon to the Plume.....	47
2.5.3 Evidence for a Sulfur-Depleted Plume	49
2.5.4 Characteristics of Settling Plume Material	50
2.5.5 Particle Formation and Transport Characteristics.....	51
2.6 Conclusions	53

CHAPTER 3	55
3.1 Overview	56
3.2 Introduction	56
3.3 Methods	59
3.3.1 Sample Collection	59
3.3.2 Scanning Transmission Microscopy (SEM)	60
3.3.3 X-ray absorption spectroscopy	61
3.4 Results	65
3.4.1 Morphology of marine particles in the SEPR hydrothermal plume	66
3.4.2 X-ray Microscopy	69
3.4.3 X-ray absorption spectroscopy	76
3.5 Discussion	80
3.5.1 Distal plume zones	80
3.5.2 Distal plume particle morphology and carbon chemistry	81
3.5.3 Iron(III)-oxyhydroxides dominate particulate iron speciation	84
3.5.4 Iron and carbon speciation of settling plume material	87
3.6 Conclusion	88
CHAPTER 4	90
4.1 Overview	91
4.2 Introduction	91
4.3 Methods	94
4.3.1 Sample Collection	94
4.3.2 Bulk X-ray absorption spectroscopy	94
4.4 Results	95
4.4.1 Bulk X-ray Absorption Near Edge Structure (XANES) Spectroscopy	95
4.4.2 Carbon 1s X-ray Absorption Near Edge Structure (XANES) Spectroscopy	96
4.4.3 Nitrogen 1s X-ray Absorption Near Edge Structure (XANES) Spectroscopy	104
4.4.4 Oxygen 1s X-ray Absorption Near Edge Structure (XANES) Spectroscopy	104
4.5 Discussion	105
4.5.1 Characteristics of particulate organic materials in settling plume material	105
4.5.2 Properties of natural organic matter	109

4.6	Conclusion.....	110
CHAPTER 5		112
5.1	Summary	113
5.2	Future Directions.....	114
REFERENCES		117
APPENDIX 1 - Chapter 2 Supplementary Information		137
APPENDIX 2 - Chapter 3 Supplemental Information		149
Appendix 2.1	Scanning Transmission X-ray Microscopy	149
Appendix 2.2	Particulate aluminum (pAl) bulk chemistry	154
Appendix 2.3	Scanning Transmission X-ray Microscopy Images and Spectra.....	155
Appendix 2.4	Carbon 1s XANES Gaussian fitting within <i>Athena</i>	160
Appendix 2.5	Fe 1s XANES linear least square fitting data with <i>Mr Fitty</i>	172
Appendix 2.6	Fe 1s EXAFS linear combinations fitting results and unaltered spectra 274	
APPENDIX 3 - Chapter 4 Supplemental Information		276
Appendix 3.1	Carbon 1s XANES Gaussian fitting within <i>Athena</i>	276
Appendix 3.2	Nitrogen 1s XANES Gaussian fits within <i>Athena</i>	293
Appendix 3.3	Oxygen 1s XANES Gaussian fitting in <i>Athena</i>	305

List of Tables

Table 1.1 East Pacific Rise Spreading Centers and Rates	6
Table 2.1 GEOTRACES-EPZT samples analyzed.....	36
Table 2.2 Significant C 1s XANES peaks (eV) within analyzed GP16 hydrothermal plume samples.....	39
Table 2.3 Important Carbon 1s peaks (eV), bonds, and orbitals.....	40
Table 2.4 Iron 1s μ XANES.....	44
Table 3.1 Approximate energy ranges for primary peaks for C 1s XANES	70
Table 3.2 Percentage of carbon functional groups present in the mid-plume GP16 marine particles.....	72
Table 3.3 Percentage of carbon functional groups present in the fluff layer	73
Table 4.1 Approximate energy ranges for primary absorption peaks for C 1s, N 1s, and O 1s.....	95
Table 4.2 C 1s XANES Gaussian Curve Fitting.....	99
Table 4.3 N 1s XANES Gaussian Curve Fittings.....	100
Table 4.4 O 1s XANES Gaussian Curve Fitting.....	102

List of Figures

Figure 1.1 Global Distribution of Hydrothermal Venting..	3
Figure 1.2 Generic ridge vent system dynamics.	5
Figure 1.3 Hydrothermal Anomalies along the East Pacific Rise..	6
Figure 1.4 SEPR particulate Fe hydrothermal plume	9
Figure 1.5 He and particulate Fe plumes along the GEOTRACES (GP16) transect.....	10
Figure 1.6 Schematic of Different Sample Collection Techniques	11
Figure 1.7 Size fractions of Fe particles	12
Figure 2.1 Bulk Chemistry Profiles.	28
Figure 2.2 Bulk XANES of Station 20 fluff layer.	29
Figure 2.3 Station 18 Elemental Maps and C 1s XANES	36
Figure 2.4 Station 20 Elemental Maps and C 1s XANES.	38
Figure 2.5 Near-field Fe 2p XANES	41
Figure 2.6 Near-field Fe 1s μ XANES.	43
Figure 3.1 Figure 3.1 SEM Images for mid-plume particles collected on GP16.....	65
Figure 3.2 Total POC and PIC concentration along the GP16 transect.....	67
Figure 3.3 Total particulate Fe and Mn (pFe and pMn) concentrations along the GP16 transect.	68
Figure 3.4 SEM images of organic coatings and EPS at Station 25	69
Figure 3.5 Carbon 1s XANES for GP16 plume and fluff layer samples	71
Figure 3.6 Iron 2p XANES in the GP16 mid plume samples	75
Figure 3.7 Iron 1s XANES speciation of GP16 mid-plume particles	76
Figure 3.8 Iron EXAFS from the GP16 hydrothermal plume, fluff layer, and sediments.	78
Figure 4.1 Gaussian Curve Fitting of aquatic NOM in settling hydrothermal plume particles	98

CHAPTER 1

Introduction

1.1 Overview

In the ocean, iron (Fe) is an important micronutrient for phytoplankton growth. Phytoplankton play a vital role in the global carbon (C) cycle, accounting for 50% of the total photosynthesis on the planet (Field et al. 1998; Moore et al. 2013; Fitzsimmons et al. 2014). When they die, phytoplankton sink and can become buried in the sediments of the deep ocean, removing C from the atmosphere and surface water. While Fe is an abundant element overall in the Earth's crust (Edwards et al. 2004), it is extremely diluted in the surface ocean. Iron-poor surface waters limit phytoplankton growth (Vraspir and Butler 2009) and their ability to remove C from the atmosphere and surface ocean. Over the past few decades, research has focused on constraining the global Fe cycle and its impacts on the global C cycle (Tagliabue et al. 2010). Hydrothermal vents have become a highly debated potential source of Fe to the surface ocean. Initially, the hypothesis stated that hydrothermal Fe would all be oxidized and deposited locally upon being expelled from the vent. Therefore, hydrothermal vent would have a negligible effect on global biogeochemical cycles (Elderfield and Schultz 1996). However, as a variety of new sampling techniques were developed to preserve reduction-oxidation (redox) states and increase the ability to collect trace-metal clean samples (Johnson et al. 1997; Johnson et al. 2007; Breier et al. 2009), it was discovered that hydrothermal Fe could be protected from oxidation and removal to the sediments and be a potential source of Fe to the deep ocean and surface waters in some locations (Toner et al. 2009a; Toner et al. 2012a). With the amount of Fe released through hydrothermal venting to the ocean per year being similar in magnitude to that delivered by global riverine run-off (Elderfield and Schultz 1996), hydrothermal vents could be an unrecognized nutrient source to the surface ocean and play a role in global C cycling. Two main mechanisms, nanoparticles with slow settling rates, and complexation reactions with organic functional moieties, have been hypothesized to transport solid and aqueous phase Fe over long distances (Bennett et al. 2008; Toner et al. 2009a; Yücel et al. 2011). During the time interval of this dissertation, studies have investigated a large hydrothermal Fe source emanating from the East Pacific Rise (EPR; Resing et al. 2015; Fitzsimmons et al. 2017; Lee et al. 2018). This has informed current working geochemical models about the complexity of reaction pathways and transport mechanisms active in hydrothermal plumes with implications for

basin-scale transport and bioavailability of hydrothermal Fe (Tagliabue and Resing 2016; Tagliabue et al. 2017). This dissertation will focus on investigating the chemical speciation and transport mechanisms of Fe in non-buoyant plume particles along the East Pacific Rise. Therefore, further informing the global impact of hydrothermal venting within ocean basins.

1.2 The Unique Characteristics of a Mid-Oceanic Ridge (MOR) Hydrothermal systems

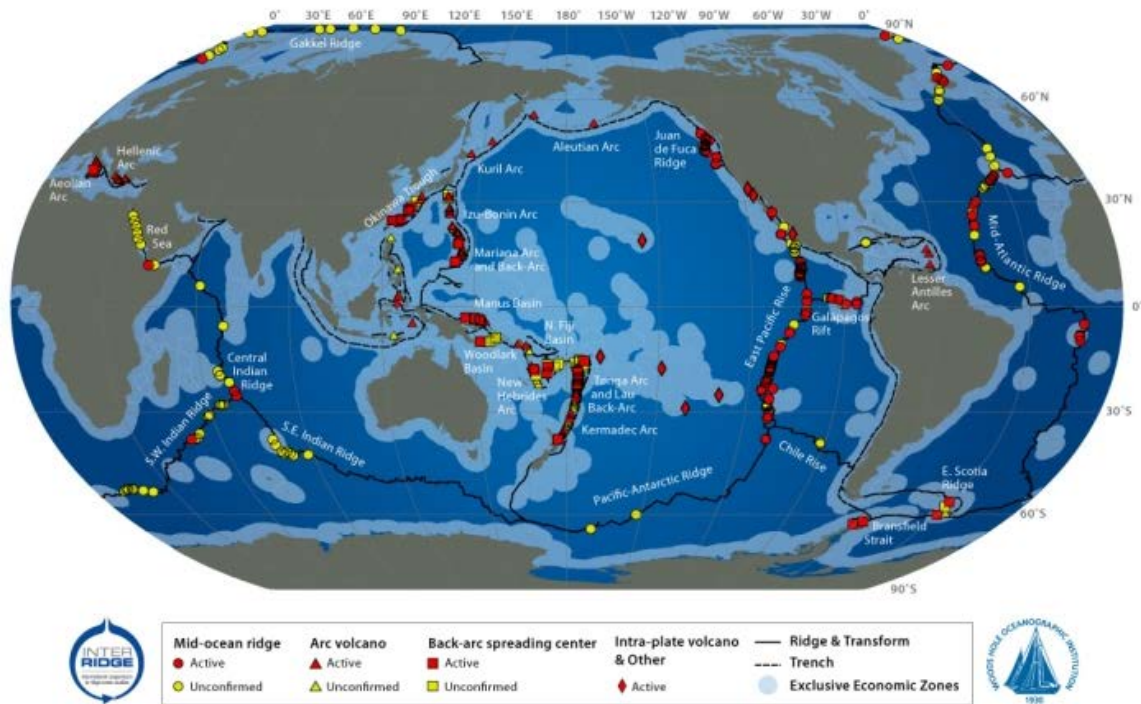


Figure 1.1 Global Distribution of Hydrothermal Venting. Hydrothermal vents are found globally along Mid-Oceanic Ridge spreading system. Red symbols are active vents that have been found with yellow symbols signifying suspected vents from detected vent fluids characterizes in the overlying water column. The InterRidge database keeps a continually updated version of this map online. Reproduced from German and Seyfried 2014.

Hydrothermal vents are found in every ocean basin on Earth and are located along the global mid-ocean ridge (MOR) spreading system where new seafloor is created through tectonic activity (Figure 1.1; Tivey 2007; German and Seyfried 2014). Hydrothermal vent fluids, at MOR spreading centers, are generated by the circulation of seawater through the ocean crust and water-rock reactions at high temperatures. Briefly, fluids penetrate the crust, undergo low-temperature reactions to remove magnesium and calcium from the seawater. In the recharge zone, trace-metals are leached from the

surrounding rock into the acidic, anoxic, magnesium-poor fluids. As the fluids exceed the temperature and pressure of the boiling curve of seawater, the vent fluids separate into a low salinity-vapor phase and brine phase, preferentially selecting specific elements and volatiles into each phase (Figure 1.2; Tivey 2007). These hot, buoyant fluids then rise to the seafloor inducing chemical reactions and precipitation/dissolution of sulfide mineral deposits, creating chimneys that focus the less dense (hotter, 350-400°C) vent fluids into underwater geysers called hydrothermal plumes (Janecky and Seyfried 1984).

Hydrothermal plumes are characterized by vigorous mixing of vent fluids with deep-sea waters. Continuous and eruptive venting produces nutrient-rich plume(s) when mixed with surrounding seawater. The initially hot, buoyant plume undergoes dilution (ca. 10,000:1) as it rises into the deep-sea (Lupton et al. 1985; German and Seyfried 2014). As the plume continues to mix with cold seawater, it becomes neutrally buoyant and increasing dilute until matching the density of the cooler surrounding seawater (German and Seyfried 2014).

The strong chemical gradients between vent fluids and surrounding seawater are the basis of hydrothermal vent ecosystems. Within these gradients, elements can exist in different redox states. Iron has three redox states in which it can exist; Fe(0), Fe(II), and Fe(III). Iron(II) and Fe(III) are commonly found in hydrothermal plumes and can be found in both dissolved and particulate forms (Feely et al. 1996; Toner et al. 2009a; Toner et al. 2012a; Breier et al. 2012; Li et al. 2014). The speciation of Fe—aqueous phase, solid phase, valence state, local coordination environmental—determines whether it can be transported long distances and be utilized as a nutrient by phytoplankton.

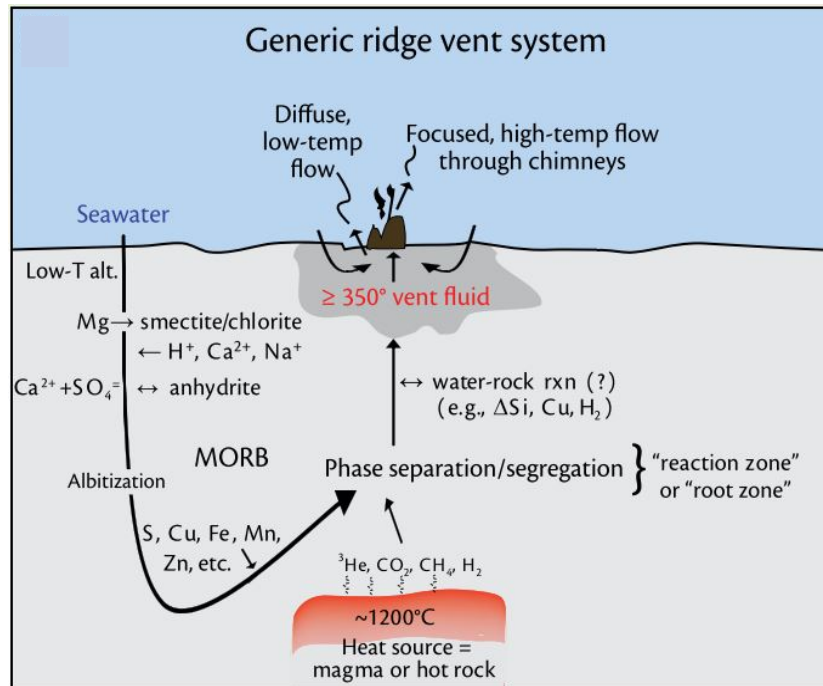


Figure 1.2 Generic ridge vent system dynamics. Mid-oceanic ridge hydrothermal fluids are created through circulation and alteration of seawater in the ocean crust. Water-rock reactions enrich the vent fluids with trace-metal that are late expelled at the seafloor. Reproduced from Tivey 2007.

1.3 The “Leaky” East Pacific Rise

One of the largest known instances of hydrothermal venting is found along the East Pacific Rise (EPR, Figure 1.3). The EPR is a divergent plate boundary, made up of the Pacific, Cocos, Rivera, North American, Antarctic and Nazca plates, that extends from the Gulf of California to Antarctica (Charlou et al. 1996). Due to its size, the EPR has been found to contain slow spreading ridges and fast spreading ridges in the north, with an ultra-fast spreading ridge in the south (Table 1). Many of the vents found along the EPR are basalt-hosted and chemically reducing in nature (Von Damm et al. 1985; Tivey 2007; Bennett et al. 2008; Toner et al. 2009a). Multiple vents located along the EPR have been observed to be Fe rich and a potential source of Fe into the ocean interior (Toner et al. 2009a; Tagliabue et al. 2010; Fitzsimmons et al. 2014; Li et al. 2014; Resing et al. 2015; Tagliabue and Resing 2016; Fitzsimmons et al. 2017; Homoky 2017; Tagliabue et al. 2017).

Table 1.1 East Pacific Rise Spreading Centers and Rates

Spreading Ridge Type	Spreading Rate (mm/yr)	Ridge Location	Example	Sources
Slow	~60	North	Guaymas Basin	Von Damm et al. 1985
Fast	110	North	EPR 9-10°N	Gartman et al. 2014
Ultra-fast	~141-162	South	EPR 13-18°S	Charlou et al. 1996

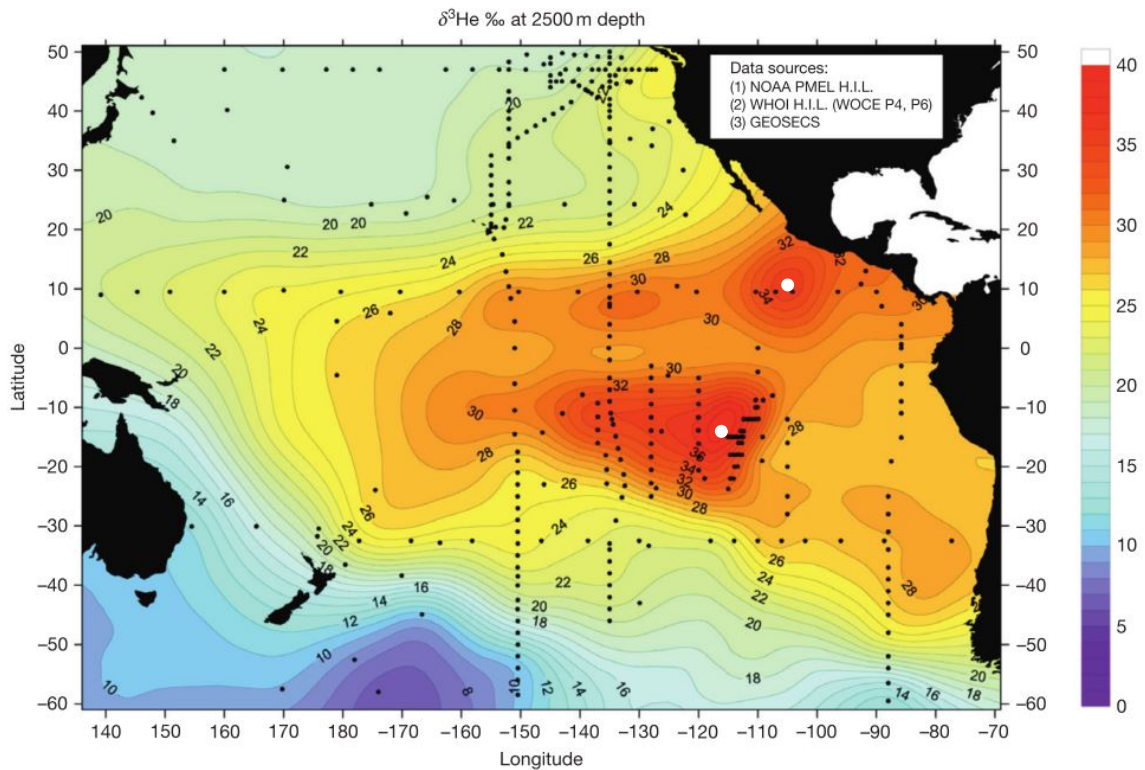


Figure 1.3 Hydrothermal Anomalies along the East Pacific Rise. The $\delta^3\text{He}$ anomalies indicate where mantle fluids are seeping into the ocean at 2500 m depth along the East Pacific Rise and into the ocean interior. High areas of concentration are in red with low areas of concentrations in blue. The two main hot spots along the ridge (white circles) will be discussed in this dissertation. Reproduced from German and Seyfried 2014.

1.3.1 Integrating hydrothermal vent research along the Northern EPR

A few decades after the first discovery of hydrothermal system along the Galapagos rift spreading center in 1977 (Weiss et al. 1977), the National Science Foundation designed the Ridge2000 program to integrate the geological, biological, chemical, physical, and oceanographic research currently being conducted at vent sites along the northern EPR

(NEPR). The Ridge2000 program provided researchers the opportunity to set up observatories and revisit vents sites to test interdisciplinary working hypotheses. The success of the Ridge2000 program aided in our current understanding of the dynamics of a MOR hydrothermal venting system, and showed the importance of conducting interdisciplinary research in designated *in-situ* ocean observatories. This program has inspired other experimental observatories, such as cabled observatories at Axial Seamount and Endeavor Segment along the Juan de Fuca Ridge, to monitor the dynamics and behaviors of distinct MOR spreading centers (Kelley et al. 2014).

1.3.1.1 Transport mechanisms of hydrothermal plume material

One of the big discoveries of the Ridge2000 program was how particulate organic C (Corg) interacted with hydrothermal Fe within hydrothermal plumes (Toner et al. 2009a). Specifically, plume particles were observed to be composites of Corg with Fe in various forms, including Fe oxyhydroxides, Fe sulfides, and organic matter enriched in Fe(II) despite the oxic conditions. Within plumes, Corg is produced from abiotic reactions within vent fluids, entrainment of near vent biological material, the production of cell material and ligands, and entrainment of dissolved Corg (Bennett et al. 2008; Toner et al. 2009a; Sander and Koschinsky 2011; Lam et al. 2018). Organic C has been observed to be associated with minerals within the buoyant plume. These associations form Corg-mineral composites that appear to change the reactivity of Fe particles, trace elements, and other redox species in the rising and non-buoyant hydrothermal plume (Toner et al. 2009a; Bennett et al. 2011b; Toner et al. 2012a; Breier et al. 2012). In some cases, sulfur-rich organic material has also been proposed to slow the oxidation of Fe(II) through strong complexes between sulfhydryl groups and Fe(II) (Toner et al. 2009a). Organic C composites can also influence the oxidation and longevities of nanoparticles (e.g. nanoparticulate pyrite) within the water column (Gartman et al. 2014). Yet, the degree to which abiotic oxidation or biotic oxidation controls the reactivity and longevity of nanoparticulate and particulate Fe within the hydrothermal plumes are still largely unknown.

Before this discovery, particulate Fe was largely thought to precipitate as minerals and settle to sediments around the vent field site: not having an effect on global geochemical

cycles (Elderfield and Schultz 1996). However, modeling minerals encased in carbon rich matrices shows a reduction in the sinking velocity due increasing the transport potential of Fe away from the ridge increased (Breier et al. 2012). Furthermore, nanoparticles are hypothesized to be additional mechanism in the longevity and transport of Fe into the ocean interior. Nanoparticles (<100 nm) have a slower settling velocity and experience chemical alteration through mixing and/or biological processes (Yücel et al. 2011; Breier et al. 2012; Gartman et al. 2014). Samples collected in the NEPR and globally at other spreading centers indicate that nanoparticulate pyrite has the ability to potentially travel 9,000-27,000 km before 99% of the Fe becomes oxidize, and may account for 10% of our current dissolved Fe fraction (Yücel et al. 2011; Gartman et al. 2014). The above models and the observations suggest two viable mechanisms for transporting hydrothermal Fe into the oceans interior. Understanding this interplay between the chemical and physical aspects of transporting hydrothermal Fe will provide insight into the impact of hydrothermal venting on global geochemical cycles.

1.3.2 The discovery and significance of hydrothermal venting along the Southern EPR

In 1972, the Southern Tow expedition by Scripps Institute for Oceanography discovered a large ^3He plume around EPR 15°S that extended over 2000 km westward (Lupton and Craig 1981). In 1993, the Southern EPR (SEPR) plume was revisited to investigate endmember fluids between 17-19°S and trace metal concentrations between 13-19°S (Charlou et al. 1996; Feely et al. 1996). Over the next decade, research was limited in the area until geochemical modeling in the late 2000s suggested that hydrothermal venting along the SEPR could be important for primary production in the Southern Ocean (Tagliabue et al. 2010; Tagliabue et al. 2017). This ignited a new-found interest in understanding role of hydrothermal venting in global geochemical cycling and the impact of the SEPR. Three recent expeditions along the SEPR have been exploring the physical and geochemical mechanisms of hydrothermal Fe using our most trace-metal clean techniques (Fitzsimmons et al. 2014; Resing et al. 2015; Fitzsimmons et al. 2017; Moffett and German 2018; Peters et al. 2018).

1.3.2.1 Hydrothermal Fe and the important role of the Southern EPR

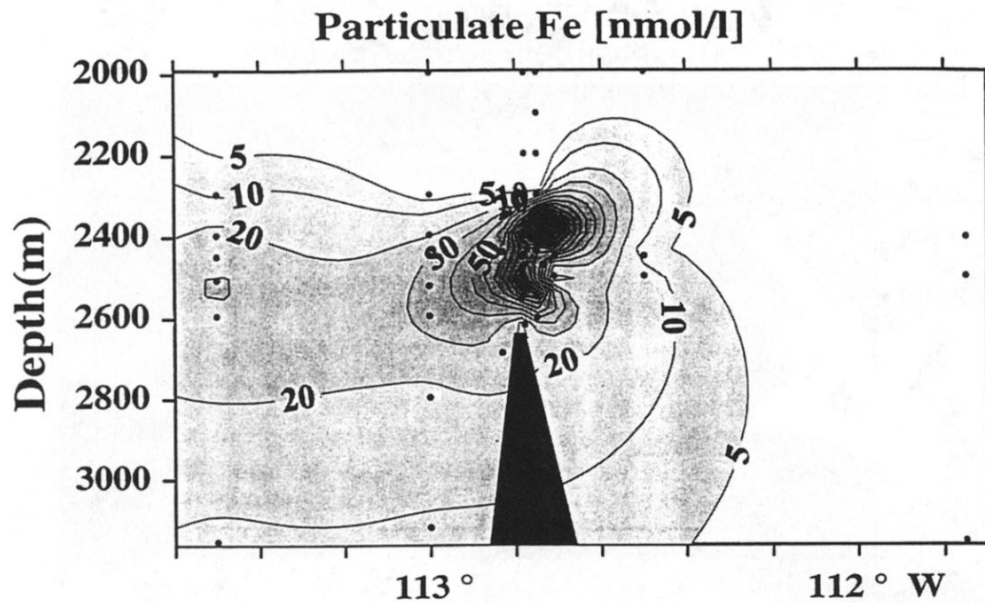


Figure 1.4 SEPR particulate Fe hydrothermal plume. The first discovery of a particulate Fe plume in the SEPR was estimated to travel ~80 km from the ridge axis. The highest concentration of particulate Fe was found around 15°S. Most of the aggregates were found to be iron oxyhydroxides. Reproduced from Feely et al. 1996.

The first SEPR particulate Fe plume was observed in the 1990s. The plume was most concentrated around EPR 15°S, the same location as ³He anomaly reported by Lupton and Craig 1981. Iron oxyhydroxide aggregates were observed to travel 80 km away from the ridge axis (Figure 1.4; Feely et al. 1996). The lack of sulfides detected was attributed to the vent fluids either having recently experienced an eruption, or producing S-enriched biogenic particles and elemental sulfur within the buoyant plume. Vent sites below 17°20'S that were observed to be gas and sulfur rich, suggesting two different types of venting along the SEPR (Charlou et al. 1996; Feely et al. 1996). These vents sites along the SEPR largely went unstudied for the next decade.

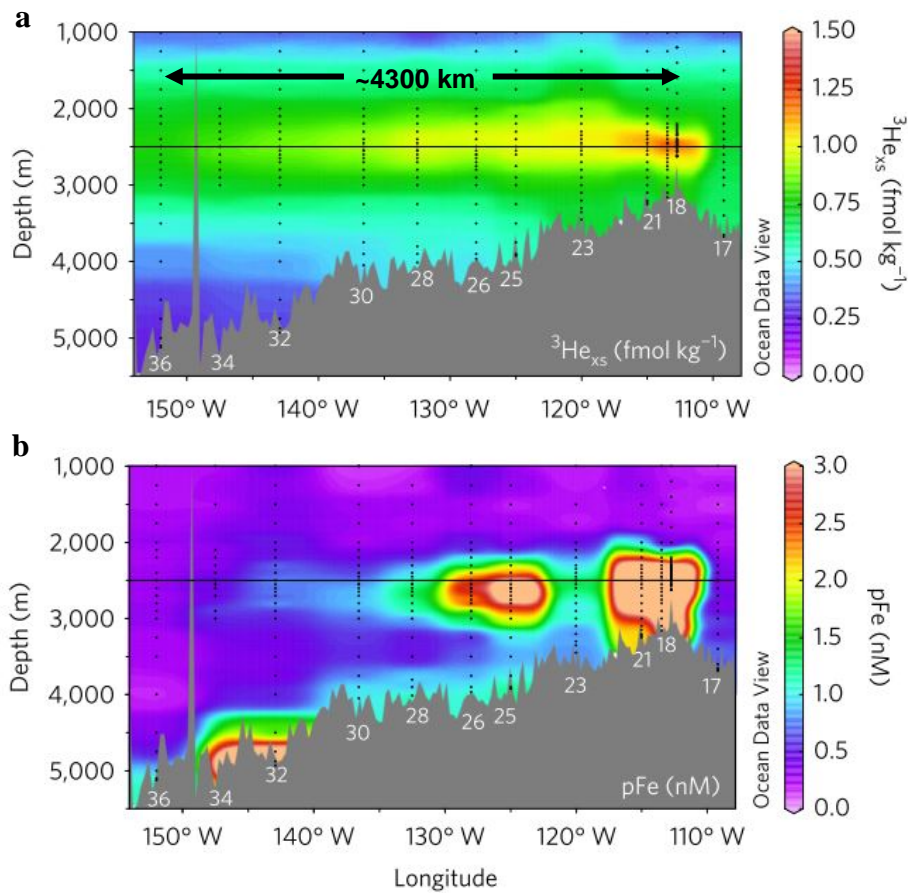


Figure 1.5 He and particulate Fe plumes along the GEOTRACES (GP16) transect. During the 2013 GP16 cruise (a) the He and (b) particulate Fe plumes were observed to travel westward for ~4300 km and ~3300 km, respectively. This was the first time hydrothermal Fe was observed travel hundreds of kilometers into the ocean interior. Reproduced from Fitzsimmons et al. 2017.

In the late 2000s, biogeochemical models suggested hydrothermal venting along SEPR could be an important nutrient source for primary production in the Southern Ocean (Tagliabue et al. 2010). This sparked a new interest and debate about the role of the SEPR in global nutrients cycles. In 2013, the NSF funded GEOTRACES-East Pacific Zonal Transect cruise, set out to investigate the role of trace elements within SEPR hydrothermal plume. Through that expedition, a ~ 4300 km $^3\text{He}_{xs}$ plume and ~ 3300 km particulate Fe plume were discovered (Figure 1.5; Resing et al. 2015; Fitzsimmons et al. 2017). Both were observed to extend west of the ridge axis. The ^3He plume was more than twice the size than previous observations and 40 times larger for the previously reported particulate Fe plume (Lupton and Craig 1981; Feely et al. 1996). Due to its sheer

size, multiple vents are thought to contribute to the SEPR hydrothermal plume, with potentially a second, younger source contributing material around 125°W (Kipp et al. 2018). However, the mechanisms for Fe transport within hydrothermal plume are still poorly understood and have mainly be focused on near-field or buoyant plume samples.

1.4 The Importance of Particle Size for the Transport of Hydrothermally Derived Iron

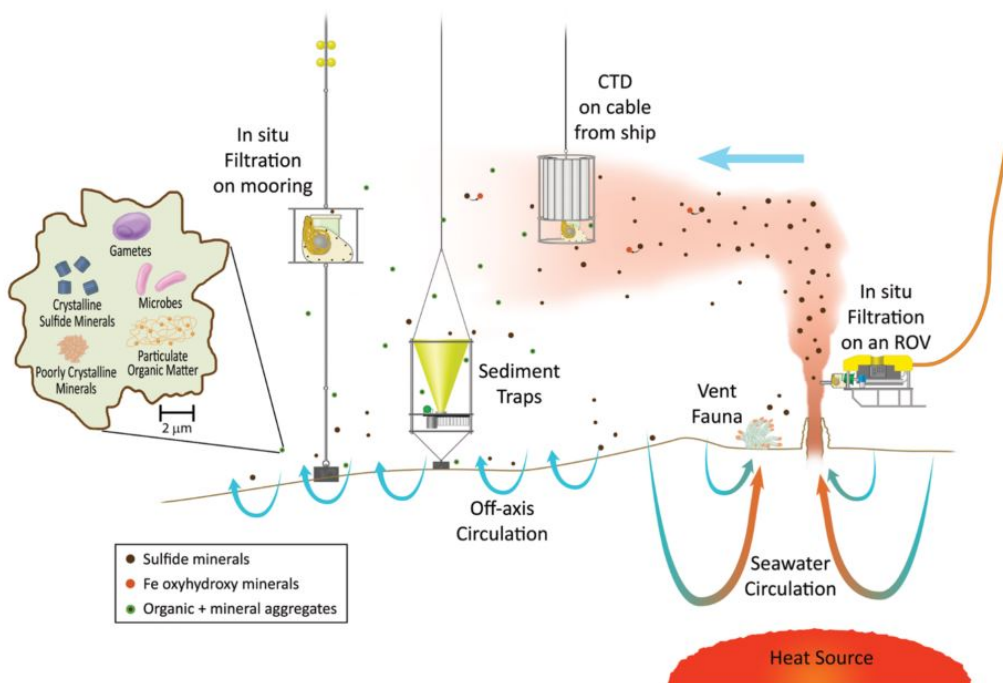


Figure 1.6 Schematic of Different Sample Collection Techniques. Hydrothermal plume particles can be collected using different instrument and devices that are deployed in the water column or seafloor. Reproduced from Toner et al. 2016.

To evaluate the chemical speciation and transport mechanism of hydrothermal plume particles, sample collection, filtration and filter properties, and particle size class must be considered when designing experiments. Currently, two filtration methods, (1) shipboard and (2) *in-situ*, and four collection methods, (1) remotely operated vehicles (ROV) or submersibles, (2) sediment traps, (3) Conductivity-Temperature-Depth (CTD) rosettes, and (4) mooring (e.g. McClane pumps), are widely used at vent sites (Figure 1.6; Toner et al. 2016). Using *in-situ* filtration is currently considered the best way to protect particles from redox reactions. However, using preservatives within sediment trap bottles

or collecting discrete water samples, and filtering shipboard in an anoxic glove bag are both viable alternatives to preserve the redox state of particles. For further sample preservation, samples can be rinsed with nitrogen-sparged double distilled water, sealed in mylar, and frozen to further inhibit additional biogeochemical reactions. Instituting all or a combination of these techniques will aid in reducing geochemical artifacts due to sample handling.

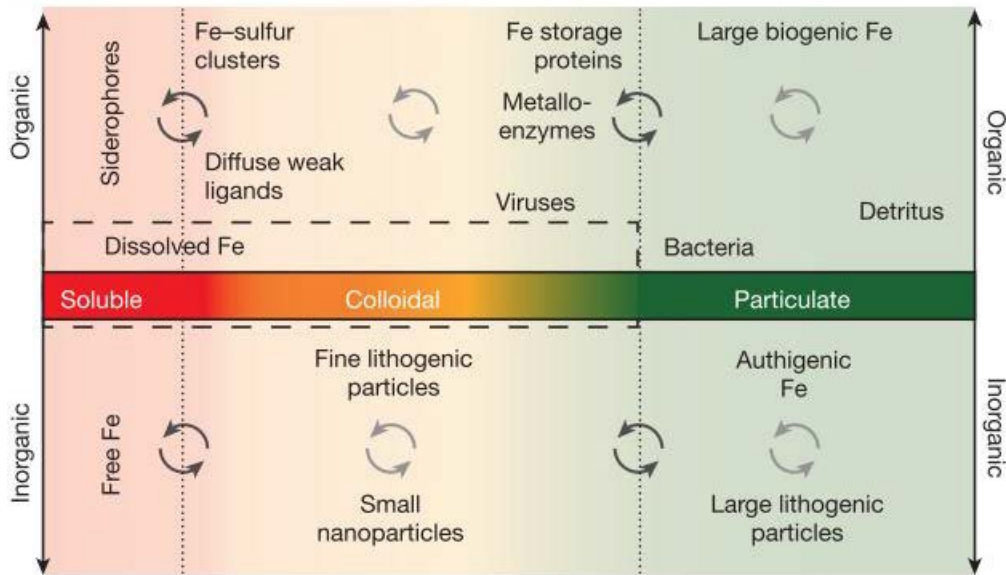


Figure 1.7-Size fractions of Fe particles. Iron particles exist within three operationally defined size fractions: particulate ($> 0.2 \mu\text{m}$), colloidal ($0.02\text{-}0.2 \mu\text{m}$), and soluble ($<0.02 \mu\text{m}$). Biological material (i.e. bacterial and viruses) can also be separated into these operationally defined groups. The colloidal and soluble size fractions are commonly combined and referred to as the dissolve fraction. Example of Fe particles with similar behaviors and characteristics are provided above. Defining the particle size fraction will provide insight into the reactivity and transport of the Fe particles in a hydrothermal plume. Reproduced from Tagliabue et al. 2017.

When filtering, filter size will affect the particle size fraction that is collected. Within the discipline of oceanography, particle size is operationally defined by the filter pore size; therefore, providing a common language among scientist to discuss groups of like fractions (Fitzsimmons and Boyle 2014; Tagliabue et al. 2017). Researchers are then able to investigate how different behaviors within each fraction impact the transportation of hydrothermal particles away from the ridge axis into ocean basins. The three main particle size fractions are soluble, colloid, and particulate (Figure 1.7). Within oceanography, particles captured on a $0.2 \mu\text{m}$ filter or larger are considered the

particulate fraction. The particulate fraction, particles can be separated into the large size fraction (LSF; $> 51 \mu\text{m}$) and small size fraction (SSF; $0.8\text{--}51 \mu\text{m}$) which gives us further insight into reactivity and behavior of particles (Lam et al. 2018; Lee et al. 2018). Particles collected between $0.02\text{--}0.2 \mu\text{m}$ are considered the colloidal fraction (Fitzsimmons et al. 2014; Fitzsimmons and Boyle 2014). While the significance of colloids has been explored previously within different oceanographic regimes (Wells and Goldberg 1993; Chen and Wang 2010), the importance of colloids within hydrothermal plumes is a new area of investigation (Fitzsimmons et al. 2014; Fitzsimmons et al. 2017). Lastly, anything passing through a $0.02 \mu\text{m}$ filter is considered soluble or “truly dissolved” (Fitzsimmons and Boyle 2014). In the literature, a fourth more broad size fraction, called dissolved, is used to represent both the colloidal and soluble fractions (Figure 1.7). However, by one estimate around 10% of the dissolved Fe within hydrothermal plumes could be solids in the colloidal size fraction (Yücel et al. 2011; Fitzsimmons et al. 2014). Investigating the properties and characteristics of each size fraction could provide important insights into linking reaction and transport pathways of Fe from the soluble to particulate phases within hydrothermal plumes.

1.5 Challenges in Analyzing Chemical Speciation of Elements in Plume Particles

One of the challenges in collecting hydrothermal plume material is the variability in filter loading of marine particles. As the plume becomes more dilute with distance from the ridge axis, variability in particle concentration, quality, and size distribution affect the particle fraction that is able to be collected and analyzed (Breier et al. 2009). Moreover, natural particles are heterogeneous mixtures of different mineral aggregates in organic matter matrices (e.g. Toner et al. 2009; Breier et al. 2012). Gold standard solid-state analytical tools, such as X-ray tube sourced powder X-ray Diffraction (XRD) and Energy Dispersive X-ray Spectroscopy (EDS), are not well equipped to deal with limited amount of sample, variation in chemical speciation of multiple elements, overall micro- and nano-meter scale variations in composition of natural particles. Additionally, most of the bulk chemistry and imaging techniques require damaging or destroying the sample which inhibits revisiting the sample for multiple analyses (Lam et al. 2015). To successfully analyze natural particles, analytical methods need to have a low noise to signal ratio, and

be able to switch rapidly between elements of interest. Synchrotron radiation provides a non-destructive, high intensity light source that can be tuned from soft (C, O) to hard (Fe, Mn) X-ray energies to evaluate co-location, chemical speciation, and mineralogy of multiple elements on the same sample and aggregate (Toner et al. 2009a; Chan et al. 2011; Toner et al. 2012a; Toner et al. 2014b; Toner et al. 2016). Using X-ray microprobe, bulk, and microscopy techniques in concert with each other will provide a more complete examination of the chemistry within and between natural particles. Therefore, informing current geochemical models about particle dynamics within an environmental system.

1.6 Objectives and Hypotheses

MOR hydrothermal vents generate micronutrient-rich fluids that support a vast array of microbial and planktonic life (Reed et al. 2015). However, there is limited understanding regarding the mechanisms that allow for long distance transport of hydrothermally derived micronutrients, such as Fe, from vents to be utilized in High Nutrient-Low Chlorophyll zones (i.e. the Southern Ocean; Moore et al. 2013; Tagliabue et al. 2017). The goal of this dissertation is to provide direct observations of chemical speciation and gain insights into chemical mechanisms affecting the transport potential of hydrothermal Fe from vents to the ocean. The research has the potential to improve models of Fe budgets and cycling within the ocean.

The two main objectives for this dissertation are to:

- (1) investigate the chemical speciation of particulate Fe within a non-buoyant plume. Fe(II) sulfide minerals (such as pyrite) have been observed to dominate particles near the vent while Fe(III) oxyhydroxide minerals dominate particles in the neutrally buoyant plume (German and Seyfried 2014).
- (2) understand how the type (e.g. lipids, proteins, etc.) of Corg influences the longevity of particulate Fe into the ocean interior. Previous research also supports the hypothesis that Corg forms chemical associations with hydrothermally derived Fe in buoyant plumes

(Toner et al. 2009a). However, it is still unclear how different types of C and/or particles size impact the accessibility and redox state of Fe over basin-scale transport.

Therefore, keeping the above objectives in mind, my hypotheses are:

- H1: Particulate Fe will be transported within the non-buoyant plume beyond the distance calculated using Stokes settling for pure Fe-bearing minerals of a particular particle size class.
- H2: The proportion of chemically oxidized particulate Fe will increase within the non-buoyant plume the further the distance is from the ridge axis.
- H3: Intra-particle associations between Corg and Fe will be present in all pFe transported away from the ridge axis.

1.7 Approach

To investigate these hypotheses, marine particles were collected on two research cruises using two collection methods described below:

1. On the 2013 U.S. GEOTRACES-East Pacific Zonal cruise (GP 16), marine particles were collected over an ~8000 km transect that includes the ~4300km SEPR hydrothermal plume. Marine particles were collected by *in-situ* filtration at discrete depths throughout the water column. Once shipboard marine particles were handled in a nitrogen filled anaerobic chamber with a HEPA bubble. To remove sea salts, filters were washed with nitrogen-sparged MilliQ, and then, sealed in mylar to preserve the redox state of the marine particles. Filters were then frozen at -20°C to further inhibit the kinetics of chemical oxidation.
2. On the 2006 RESET/LADDER 1 cruise descending particles were collected from the non-buoyant hydrothermal plume near Bio 9 (9°50.291'N; 104°17.488'W) and Ty-Io (9°50.099'N; 104°17.509'W) vents using a 21-position time-series sediment traps that were deployed ~5 m above the seafloor (~2500 m). Samples were collected every 6 days continuously from July 1 to November 4, 2006 (“LADDER 1” trap R1 and R2). Trap R1 was located ~30 m southwest of the Bio9 vent complex

within the axial summit (Rouxel et al. 2008; Rouxel et al. 2016). Trap R2 was located outside the axial summit caldera, 115 m southwest of Ty-Io black smoker vents (Rouxel et al. 2016). Before the deployment, the 250 ml polyethylene sample cups were filled with a 20% dimethyl sulphoxide (DMSO) and 4% NaCl solution buffered to pH 9.0 ± 0.5 to stop all biological activity within the samples, retaining sample integrity for mineralogical, geochemical and molecular microbiological investigations. Upon trap recovery, each sample cup was capped and refrigerated at 4°C.

All samples were analyzed using non-destructive, high intensity synchrotron light sources to characterize the Fe and C speciation in marine particles on the micro- and nanometer scale (Toner et al. 2016). Three techniques used in this dissertation to understand and evaluate chemical speciation of Fe and C are as follows:

1. Particle-by particle X-ray microscopy. This technique is used to visualize individual particles and investigate the Fe-Corg particle relationship.
2. Particle-by-particle chemical speciation of Fe and C using X-ray Absorption Near Edge Structure (XANES). This technique aids in understanding the chemical speciation of Fe and C in particles.
3. Detailed structure and coordination chemistry using Extended X-ray Absorption Fine Structure (EXAFS). This technique is able to differentiate between different groups of Fe mineral classes that are not well defined in the XANES region (e.g. Fe(III) oxyhydroxides and Fe (III) phyllosilicates). This aids in understanding the reactivity of particulate Fe within samples.

The results from this dissertation will advance our understanding of how hydrothermal vents influence the global Fe cycle, and impact phytoplankton growth in the surface waters. Phytoplankton growth acts as a sink in global carbon models; removing the greenhouse gas carbon dioxide from the surface ocean and atmosphere. Therefore, an unrecognized mechanism to increase Fe in the surface ocean could impact current global climate models.

CHAPTER 2

Near-field iron and carbon chemistry of non-buoyant hydrothermal plume particles, Southern East Pacific Rise 15°S

This chapter was modified from the following published article:

Hoffman, C.L., Nicholas, S.L., Ohnemus, D.C., Fitzsimmons, J.N., Sherrell, R.M., German, C.R., Heller, M.I., Lee, J. mi, Lam, P.J., Toner, B.M., 2018. Near-field iron and carbon chemistry of non-buoyant hydrothermal plume particles, Southern East Pacific Rise 15°S. *Mar. Chem.* 201, 183–197. doi:10.1016/j.marchem.2018.01.011

2.1 Overview

Iron (Fe)-poor surface waters limit phytoplankton growth and their ability to remove carbon (C) from the atmosphere and surface ocean. Over the past few decades, research has focused on constraining the global Fe cycle and its impacts on the global C cycle. Hydrothermal vents have become a highly debated potential source of Fe to the surface ocean. Two main mechanisms for transport of Fe over long distances have been proposed: Fe-bearing nanoparticles and organic C complexation with Fe in the dissolved (dFe) and particulate (pFe) pools. However, the ubiquity and importance of these processes is unknown at present, and very few vents have been investigated for Fe-Corg interactions or the transport of such materials away from the vent. Here we describe the near-field contributions (first ~100 km from ridge) of pFe and Corg to the Southern East Pacific Rise (SEPR) plume, one of the largest known hydrothermal plume features in the global ocean. Plume particles ($> 0.2 \mu\text{m}$) were collected as part of the U.S. GEOTRACES Eastern Pacific Zonal Transect cruise (GP16) by *in-situ* filtration. Sediment cores were also collected to investigate the properties of settling particles. In this study, X-ray absorption near edge structure (XANES) spectroscopy was used in two complementary X-ray synchrotron approaches, scanning transmission X-ray microscopy (STXM) and X-ray microprobe, to investigate the Fe and C speciation of particles within the near-field non-buoyant SEPR plume. When used in concert, STXM and X-ray microprobe provide fine-scale and representative information on particle morphology, elemental co-location, and chemical speciation. Bulk chemistry depth profiles for particulate Corg (POC), particulate manganese (pMn), and pFe indicated that the source of these materials to the non-buoyant plume is hydrothermal in origin. The plume particles at stations within the first ~100 km down-stream of the ridge were composites of mineral (oxidized Fe) and biological materials (organic C, Corg). Iron chemistry in the plume and in the core-top suspended sediment fluff layer were both dominated by Fe(III) phases, such as Fe(III) oxyhydroxides and Fe(III) phyllosilicates. Particulate sulfur (pS) was a rare component of our plume and sediment samples. When pS was detected, it was in the form of an Fe sulfide mineral phase, composing $\leq 0.4\%$ of the Fe on a per atom basis. The resuspended sediment fluff layer contained a mixture of inorganic (coccolith fragments) and Corg bearing (lipid-rich biofilm-like) materials. The particle morphology and co-location of C

and Fe in the sediment was different from that in plume particles. This indicates that if the Fe-Corg composite particles settle rapidly to the sediments, then they experience strong alteration during settling and/or within the sediments. Overall, our observations indicate that the particles within the first ~ 100 km of the laterally advected plume are S-depleted, Fe(III)-Corg composites indicative of a chemically oxidizing plume with strong biological modification. These findings confirm that the Fe-Corg relationships observed for non-buoyant plume particles within ~ 100 m of the vent site are representative of particles within this region of the non-buoyant plume (~100 km). These findings also point to dynamic alteration of Fe-Corg bearing particles during transport and settling. The specific biogeochemical processes at play, and the implications for nutrient cycling in the ocean are currently unknown and represent an area of future investigation.

2.2 Introduction

Chemically altered fluids are created by the circulation of seawater through the ocean crust at seafloor spreading centers (German and Seyfried 2014). These vent fluids have physical and chemical characteristics different from those of the original seawater. When circulating fluids re-enter the deep ocean through hydrothermal vents they create hydrologic features called plumes that possess gradients in temperature and chemical composition. From a global perspective, the characteristics of vent fluids are variable among the 285 verified vent sites (InterRidge Vents Database 4.3); however, a few general themes emerge. Relative to deep ocean water, vent fluids have high temperature, low oxidation-reduction (redox) potential, and high dissolved metal and/or sulfur (S) concentrations. In vent fluids, redox active elements are present in chemically reduced and water soluble forms (e.g. iron ($\text{Fe}^{2+}_{(\text{aq})}$), manganese ($\text{Mn}^{2+}_{(\text{aq})}$), copper ($\text{Cu}^{+}_{(\text{aq})}$), and hydrogen sulfide ($\text{H}_2\text{S}_{(\text{aq})}$, $\text{HS}^{-}_{(\text{aq})}$). In close proximity to vents, the supply of reduced chemical species to an otherwise oxic deep ocean allows chemosynthetic microorganisms to serve as the foundation of vent primary productivity (e.g. Van Dover 2000; Luther et al. 2001; Fisher et al. 2007; Dick and Tebo 2010; Dick et al. 2013; Li et al. 2014).

Transport of plume particles from sites of venting to the greater ocean requires materials to stay suspended in seawater on a time-scale that is comparable to basin-scale advection. In near-vent settings, several mechanisms for transport of hydrothermal Fe to

the open ocean have been proposed: (1) nanoparticulate or colloidal solids having slow settling rates due to small size (Hsu-Kim et al. 2008; Yücel et al. 2011; Kadar et al. 2012; Sands et al. 2012); (2) uptake and dispersal by water-column microorganisms (Dick and Tebo 2010; Li et al. 2014); (3) complexes with dissolved organic C (DOC) or ligands (Sander et al. 2007; Bennett et al. 2008; Sander and Koschinsky 2011; Hawkes et al. 2013); and (4) adsorption to and aggregation with particulate organic C (POC) (Toner et al. 2009a; Breier et al. 2012). It is well understood that materials sourced from vents can travel 100s to 1000s of km off-axis (Boström et al. 1969; Lyle 1986; Feely et al. 1990; Wu et al. 2011; Nishioka et al. 2013; Saito et al. 2013; Fitzsimmons et al. 2014; Resing et al. 2015; Fitzsimmons et al. 2017). Recently, long distance transport of plume particles—solids captured by 0.2 μm filtration—has been demonstrated for composites of Fe and organic C (Corg) (Fitzsimmons et al. 2017). The idea that the mobility and reactivity of Fe in the ocean is dependent on organic C has deep roots in the marine chemistry literature (e.g. Lewis et al. 1995; Rue and Bruland 1995). As a community, we are now discovering that the strong biogeochemical tether between aqueous phase Fe and Corg also extends to solid phase Fe and Corg in the deep ocean (German et al. 2015; Toner et al. 2016). However, the specific interactions between Fe and Corg in plume particles have been investigated for very few vent sites globally (e.g. East Pacific Rise 9-10°N; Toner et al. 2009a; Breier et al. 2012). The implications of those interactions for the bioavailability of Fe to marine organisms are completely unknown at present.

At locations of high temperature venting, there are three major zones of particle formation that generally correlate with the residence time of materials within plumes: (1) the fresh buoyant plume has a residence time of seconds and a spatial scale of less than approximately one vertical meter; (2) the aged buoyant plume has a resident time of minutes to hours and a spatial scale up to 100s of vertical meters; and (3) the non-buoyant plume has a residence time of days to years and a spatial scale of 100s of meters to 1000s of horizontal kilometers (German and Seyfried 2014). Within each of these zones, different physical, chemical, and biological processes dominate (Feely et al. 1987; Lilley et al. 1995; Dick et al. 2013; Reed et al. 2015). In the first zone, particle formation is caused primarily by the abrupt change in temperature experienced by the vent fluids upon contact with cold (ca. 2-3°C) deep ocean water. The solubility of minerals such as

chalcopyrite (CuFeS_2), pyrite (FeS_2), and sphalerite (ZnS_2) are temperature dependent and mineral precipitation can be rapid in the first meter of the buoyant plume (Tivey and McDuff 1990; Tivey 2007). Biological activity is not thought to be an important factor in zone one due to the short residence time and in some cases high temperatures of the vent fluids. It is important to note that this general framework does not preclude seafloor particle formation. In the second zone, physical processes are dominated by the entrainment of deep ocean water, turbulent mixing of vent fluids and seawater, and rapid dilution of vent fluids (Jiang and Breier 2014). Particle formation in zone two is caused by aggregation of near-vent (organic and inorganic) debris with minerals from zone one, chemical alteration of entrained debris (e.g. via reactions with hydrogen sulfide), and continued mineral precipitation based on the solubility and oxidation kinetics of metals such as Fe(III) (e.g. Dymond and Roth 1988; Tivey and McDuff 1990; Field and Sherrell 2000; Adams et al. 2011; Bennett et al. 2011b; Bennett et al. 2011a; Holden et al. 2012). The degree to which active, *in-situ* biological processes influence particle formation in zone two is not well understood; however, there is evidence that microbial cells do respond to plume conditions within this zone at some locations (Bennett et al. 2013; Sheik et al. 2015). The third zone is characterized by dilute particle concentrations, gradual chemical gradients of demonstrable hydrothermal origin, long distance transport of hydrothermally derived solutes and particles, and residence times relevant for *in-situ* biological activity (Cowen and Bruland 1985; Dick et al. 2009; Reed et al. 2015; Resing et al. 2015; Fitzsimmons et al. 2017).

In this chapter, we describe the chemistry of hydrothermally derived particles ($> 0.2 \mu\text{m}$) within the first $\sim 100 \text{ km}$ of a non-buoyant plume sourced from the Southern East Pacific Rise (SEPR) at 15°S and points further south (Shimmield and Price 1988). Particles were collected during the GEOTRACES Eastern Pacific Zonal Transect (EPZT, GP16) using *in-situ* filtration above the plume, within the plume, and below the plume at two sites: on-axis (Station 18) and 83 km off-axis (Station 20). A seafloor sediment sample was also collected at Station 20. Particulate Fe and C speciation were measured using two complementary X-ray synchrotron approaches: (1) scanning transmission X-ray microscopy (STXM) for imaging and C 1s and Fe 2p X-ray absorption near edge structure (XANES) spectroscopy, and (2) X-ray microprobe for X-ray fluorescence

(XRF) mapping for S, Fe, and other elements, and Fe 1s XANES. The particle-specific Fe and C chemistry is complemented by depth profiles of POC, pFe, and pMn concentrations, as well as bulk C 1s, Mn 1s, and Fe 1s bulk XANES spectra for the Station 20 sediment fluff layer.

Previous investigations of plume characteristics along-axis at the SEPR observed plumes of varying Fe:S, Fe oxyhydroxide-rich plumes north of 17°20'S, and plumes with maximum Fe concentrations observed at 15°S (Feely et al. 1996). At this time, the distribution and characteristics of vents and endmember fluids along the 13°S - 17°S SEPR are unknown as previous studies have focused mainly on characterizing vent fluids between 17°S - 19°S (Charlou et al. 1996; Feely et al. 1996). There is evidence that the plume detected on-axis at 15°S (Station 18) is not the sole contributor of material to Stations 20 and all points west (Shimmield and Price 1988; Resing et al. 2015; Fitzsimmons et al. 2017). The plume detected at Station 20 may well be an integration of hydrothermal fluxes from points as far south as 20°S. Specifically, the hydrothermal materials contributing to the plume at Station 20 may hail from a deep gyre flowing north from approximately 30°S, steered by the EPR topography, which then turns west close to 15°S (Shimmield and Price 1988). Therefore, the observations provided here describe the particle inputs into the SEPR 4000+ km plume at the 15°S ridge axis (Station 18) as well as the integrated hydrothermal signal at Station 20.

2.3 Methods

2.3.1 Sample Collection

2.3.1.1 *In-situ Filtration and Sample Preservation*

As part of the US GEOTRACES-Eastern Pacific Zonal Transect cruise (GP16), marine particles were collected by *in-situ* filtration along a ~8000 km transect that includes greater than 4000 km of hydrothermally influenced waters. Samples from Station 18 (the ridge axis) and Station 20 (83 km west of the ridge axis) were filtered using a custom manifold attached to the deployed dual-flow McLane pumps. The overall *in-situ* pump program is described by Ohnemus and Lam 2015; Heller et al. 2017; Lam et al. 2018; Lee et al. 2018. The filter manifold was used to collect up to four 25 mm filters simultaneously on a third, un-metered flowpath of the McLane pumps: two 0.2 μm

polycarbonate filters for analysis by STXM and two 0.2 μm polyethersulfone (PES) filters for X-ray Microprobe. Shipboard, the filter manifold was opened in an anaerobic chamber (Coy Labs) to prevent exposure of the sample to ambient oxygen, and all sample processing occurred under a nitrogen-hydrogen (95% N_2 , 5% H_2) atmosphere (the anaerobic chamber was vented within a self-built shipboard High Efficiency Particulate Arresting (HEPA) chamber). Filters were rinsed using N_2 -sparged 18.2 $\text{M}\Omega\cdot\text{cm}$ purified double distilled water (MilliQ) via vacuum pump to remove seasalts (the pump was located outside of the HEPA bubble with a line plumbed to the anaerobic chamber). Replicate filters were: (1) placed in acid-washed PetriSlides for X-ray microprobe analysis and archiving, and (2) placed in acid-washed microfuge tubes with 0.5 mL N_2 -sparged MilliQ for STXM preparation. Prior to leaving the anaerobic chamber, all samples were sealed in mylar bags with an oxygen-free atmosphere. Sample packs were then frozen at -20°C to reduce the kinetics of chemical oxidation.

2.3.1.2 Particulate Organic C (POC), Inorganic C (PIC), Mn (pMn), and Fe (pFe) Analyses

Size fractionated (1-51 μm ; >51 μm) samples for bulk POC, PIC, pMn, and pFe analyses were collected on 142 mm filters connected to the two main, metered flowpaths of the McLane *in-situ* pumps. Sampling and analytical details are described in Lam et al. 2018. Briefly, POC was determined from combustion in elemental analyzers, PIC was measured directly by coulometry, which is the measurement of CO_2 upon addition of weak acid. Particulate Mn and pFe were measured by high resolution inductively coupled plasma mass spectrometry (HR-ICP-MS) following a two-step total digestion in a strongly oxidizing solution followed by a strong mineral acid mixture on a hotplate. Bulk compositions are reported as the sum of the two size fractions, and represent particulate concentrations > 1 μm .

2.3.1.3 Sediment Core Collection

At Station 20, a sediment core was collected using a Royal Netherlands Institute for Sea Research (NIOZ) mono-corer, specifically designed to collect surface sediment samples with minimal disturbance of the sediment-water interface which was suspended from the

ODF (Ocean Data Facility) CTD (conductivity, temperature, depth)-rosette for the final deep cast conducted at that station. In a shipboard cold room (4°C), the overlying seawater was syphoned off, down to ~0.5 cm above the 1-2 cm thick visible fluff layer. Then, the fluff layer was syphoned off, being careful not to resuspend the consolidated sediment, and solids were separated by centrifugation within hour of sediment core recovery. The pellet of fluff material was then frozen in the tip of the 50 mL polypropylene centrifuge tubes. Shore-based splitting of the fluff layer sample was accomplished by thawing the pellet and resuspending in pH purified water (Milli-Q water with a small volume of ultraclean NH₄OH), then removing representative sub-samples with a pipet while vortex mixing to maintain a homogeneous suspension.” Prior to XANES analysis, fluff layer materials were separated from aqueous solution by 0.2 µm filtration. Sediment coring was not possible at Station 18 due to the very thin sediment cover at the site, so only data from Station 20 is reported here.

2.3.2 *X-ray Absorption Spectroscopy*

2.3.2.1 *Scanning Transmission X-ray Microscopy*

Water column samples from Station 18 and 20 were prepared in an anaerobic chamber for STXM analysis by defrosting and gently shaking the PC filter (stored in 0.5 mL of N₂-sparged MilliQ). Approximately 1 µL of the suspension was deposited onto a silicon nitride membrane (Silson Ltd.) and allowed to dry at ambient temperature in the glove bag. Imaging and C 1s and Fe 2p XANES spectroscopy were conducted at beamline 5.3.2.2, Advanced Light Source (ALS), Lawrence Berkeley National Laboratory, Berkeley, CA, USA (Kilcoyne et al. 2003). Samples were analyzed in a helium flushed microscope chamber. The transfer of the sample from the mylar packaging to the instrument resulted in approximately 30 s of exposure to ambient conditions. For Station 18 and 20 samples, we collected three different types of data: (1) transmission images covering sample areas from 1 mm² to 10 µm², (2) elemental maps for C and Fe, (3) C 1s and Fe 2p XANES spectra in point-scans, line-scans, or three dimensional “stacks” (a series of 2D images at different incident energies spanning the C and Fe absorption edges such that full XANES spectra can be extracted from each pixel of the composite stack of images) (e.g. Barber et al., 2017; Brandes et al., 2004; Chan et al., 2011; Chen et al.,

2014; Toner et al., 2016, 2009a). Elemental maps reveal particle morphology and the location of C and Fe within particles. Carbon 1s XANES distinguishes between Corg and inorganic C (Cinorg), while Fe 2p XANES differentiates between reduced or oxidized Fe species. Data processing included principle component analysis for the selection of groups of pixels having related spectral properties, pre-edge subtraction, post-edge normalization, and elemental optical density maps using the software *axis2000* (Hitchcock 2016). Normalized spectra were compared to our C 1s and Fe 2p reference databases and literature for identification. Reference materials for C 1s and Fe 2p are published elsewhere (Fenter et al. 2002; Urquhart and Ade 2002; Stöhr 2003; Brandes et al. 2004; Toner et al. 2009a; Brandes et al. 2010; Chan et al. 2011; Sedlmair et al. 2012).

2.3.2.2 X-ray Microprobe

The speciation of Fe in plume particles was measured using micro-focused XRF and Fe 1s μ XANES spectroscopy at beamline 10.3.2 of the ALS with previously developed methods for marine particles (Marcus et al. 2004; Toner et al. 2012a; Lam et al. 2012a; Breier et al. 2012; Toner et al. 2014a; Toner et al. 2016). All particles were analyzed on original polyethersulfone (PES; trademark SUPOR) filters and all sample preparation was conducted within positive pressure (N₂ or Ar) glove bags. The final step in sample preparation included application of a layer of sulfur-free mylar film (Premier Lab Supply TF-125-255) to limit exposure of the sample to ambient oxygen during analysis using the method established by Zeng et al., (2013). The monochromator was calibrated using an Fe foil XANES scan with the inflection point set to 7110.75 eV (Kraft et al. 1996). Micro-XRF and μ XANES data were collected using a Canberra 7-element Ge solid-state fluorescence detector. Micro-XANES data were collected from 7012 to 7417 eV in quick-XANES mode with a single sweep of the monochromator lasting 30 s.

Data collection occurred in the following manner for each filter: (1) a large μ XRF “survey” map with an area of approximately $1000 \times 3000 \mu\text{m}^2$, pixels of $6 \times 6 \mu\text{m}^2$, and incident energy of 10 keV was collected to measure the distribution of particles and elements on the filter; (2) “fine” μ XRF sub-maps of approximately $100 \times 100 \mu\text{m}^2$, pixels of $3 \times 3 \mu\text{m}^2$, and incident energies spanning the Fe 1s absorption edge; and (3) Fe 1s point-XANES spectra.

Data processing for XRF maps included deadtime correction and plotting with beamline 10.3.2 software (Marcus et al. 2004). Data processing for the XANES spectra included deadtime correction, energy calibration, pre-edge subtraction, post-edge normalization, and linear least-squares fitting with a reference database using beamline 10.3.2., *Athena*, and *SixPack* softwares (Marcus et al. 2004; Ravel and Newville 2005; Webb 2005; Marcus et al. 2008).

2.3.2.3 Bulk X-ray Absorption Spectroscopy

For fine particles associated with the fluff layer, bulk C, Mn, and Fe 1s XANES spectra were collected at the Canadian Light Source (CLS) in Saskatoon, Saskatchewan, Canada.

The bulk C 1s XANES were collected at the CLS High Resolution Spherical Grating Monochromator (SGM) beamline. The sediment was applied to gold-coated silicon-chips as an aqueous droplet under ambient temperature and atmosphere, allowed to dry, and placed in the SGM vacuum sample-chamber. Sample analysis parameters were chosen to: (1) prevent photon-damage to the sample, (2) collect data representative of the sample, and (3) improve signal-to-noise through a series of fast (30-60 s) and non-overlapping point scans (Gillespie et al. 2015). All experimental spectra were collected in fluorescence mode using an Amptek silicon-drift detector positioned at 45 degrees. The incident beam, I_0 signal, was collected as scattered beam from a blank gold-coated sample holder using a second Amptek detector positioned at 90 degrees. Individual spectra were curated, averaged, and normalized to I_0 using a custom script prepared by Adam Gillespie in Igor Pro (Gillespie et al. 2014). Energy calibration, pre-edge subtraction, and post-edge normalization were accomplished using *Athena* software (Ravel and Newville 2005). Spectra were compared to 13 carbonate mineral reference spectra provided by Jay Brandes (Brandes et al. 2010).

The bulk Mn and Fe 1s XANES spectra were collected at the CLS Soft X-ray Microcharacterization Beamline (SXRMB). The sediment was applied as a dry powder to double-sided C tape and adhered to a copper sample plate under ambient temperature and atmosphere, and placed in the SXRMB vacuum sample-chamber. The monochromator was calibrated using an Fe foil XANES scan with the inflection point set to 7110.75 eV

(Kraft et al. 1996). All experimental spectra were collected in fluorescence mode using an Amptek silicon-drift detector positioned at 45 degrees, with I_0 collected simultaneously in an ion chamber. Data processing for the XANES spectra consisted of I_0 normalization, energy calibration, pre-edge subtraction, post-edge normalization, and linear least-squares fitting with a reference database using beamline 10.3.2., *Athena*, and *SixPack* softwares (Marcus et al. 2004; Ravel and Newville 2005; Webb 2005; Marcus et al. 2008). Linear combination fitting of Mn 1s XANES with reference spectra in the energy range of 6500-6650 eV was accomplished using laboratory synthesized standards: birnessite (KMnO_2), δ - MnO_2 , manganite (γ - MnOOH), Mn_2O_3 (bixbyite), and Mn_3O_4 (hausmannite) (Bargar et al. 2000; Villalobos et al. 2003). The Fe 1s XANES spectrum was fit using linear combinations of 70 reference spectra in the energy range of 7110-7400 eV (Marcus et al. 2008).

2.4 Results

2.4.1 Bulk Chemistry of Plume Particles

Concentration profiles for total ($> 1 \mu\text{m}$) POC, PIC, pFe, and pMn from Stations 17, 18, and 20 are shown in Figure 2.1. Station 17 is upstream of the ridge, Station 18 is at the ridge crest, and Station 20 is downstream from the ridge.

There is an increase in pFe and pMn concentrations at Station 18 and 20 compared to Station 17 at mid-plume depth, and compared to the water column above (above plume background). The enriched particulate metal concentrations, centered at ~ 2500 m water depth, coincide with the SEPR hydrothermal plume (Fitzsimmons et al. 2017; Lam et al. 2018; Lee et al. 2018). At Station 18, the above plume background pFe and pMn concentrations are 0.56 nM and 0.11 nM, respectively (2200 m water depth). At the mid-plume depth of Station 18 (2450 m water depth), the pFe and pMn concentrations are two orders of magnitude higher 44.2 nM and 5.2 nM, respectively. At Station 20, the pFe and pMn concentrations are lower but still quite high at the mid-plume (2550 m; 28.9 nM pFe and 6.38 nM pMn) are also enriched over the above plume background (2200 m; 0.76 nM pFe and 0.12 nM pMn). The low Station 17 pFe and pMn concentrations at mid-plume depth (2500m; 0.307 nM pFe and 0.075 nM pMn) suggest the increase is not from lateral advection from stations east of the plume.

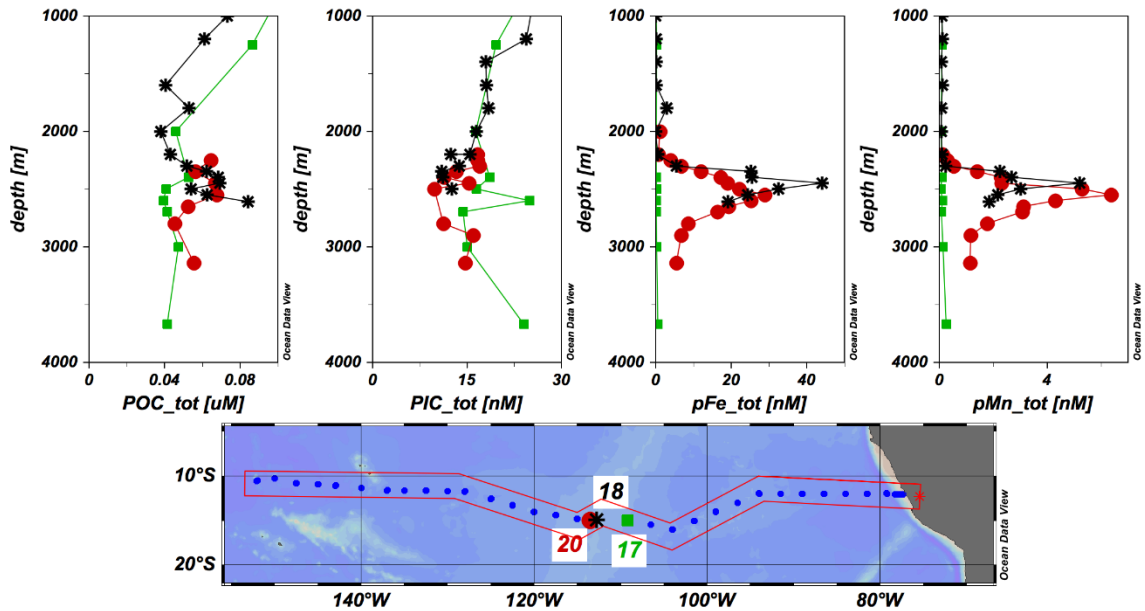


Figure 2.1 Bulk Chemistry Profiles. Depth distribution of total particulate organic carbon (POC_{tot}), total particulate inorganic carbon (TIC_{tot}), total particulate Fe (pFe_{tot}), and total particulate Mn (pMn_{tot}) for Station 17 (up-current from the ridge axis), Station 18 (over ridge axis), and Station 20 (83 km down-current from the ridge axis).

At the mid-plume depth of Station 18, there is a measurable increase in total POC concentration over background (above plume background and mid-plume depth of Station 17) concentrations that is consistent with plume-generated POC or sorption of dissolved OC (DOC) onto mineral surfaces (Lam et al. 2018). A small decrease in total PIC concentration in the plume (Station 18 and 20) is likely due to enhanced aggregation and removal in the plume (Lam et al. 2018). The bulk chemistry is further discussed in (Lam et al. 2018; Lee et al. 2018).

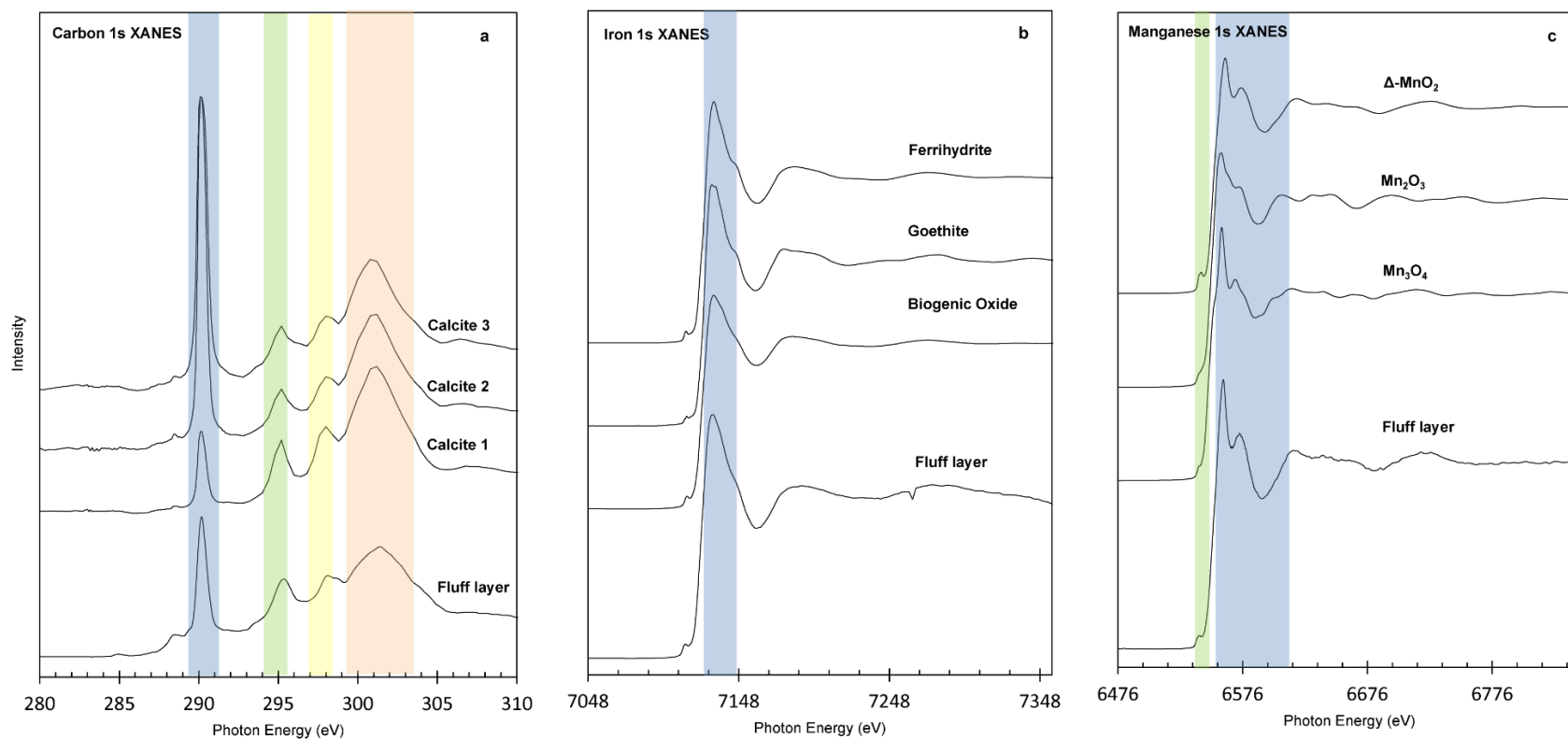


Figure 2.2 Bulk XANES of Station 20 fluff layer. (a) Carbon 1s XANES spectrum plotted with three calcite reference spectra having different crystal orientations (Brandes et al. 2010). (b) Iron 1s XANES spectrum plotted with three Fe(III) oxyhydroxide standards (Toner et al. 2009b). (c) Manganese 1s XANES spectrum plotted with three Mn oxide standards (Bargar et al. 2000; Villalobos et al. 2003). Identifying features and peaks are highlighted.

2.4.2 Bulk Chemistry of Station 20 Sediment Fluff

Sub-samples of the fine fluff layer materials from Station 20 were examined by bulk C 1s, Mn 1s, and Fe 1s XANES.

The bulk C 1s XANES spectrum (Figure 2.2a) was compared to that 13 carbonate minerals and was most consistent with calcite (Brandes et al. 2010). Brandes et al., (2010) reports that the intensity of the main peak for the carbonate minerals varies due to crystal orientation (Brandes et al., 2010; see Figure 2.2a for a calcite example). Our fluff sample is composed of randomly oriented crystals (whole mount, drop coat preparation), so the main peak height has intermediate intensity relative to the standards. Although calcite spectra are very similar to aragonite, from our STXM and XRF maps (Appendix 1.1-1.2), we know that coccoliths and foraminifera are common in this sample, and therefore, the phase identification is calcite (de Vargas et al. 2007).

The bulk Fe 1s XANES spectrum (Figure 2.2b) was fit using linear combinations of 70 reference spectra in the energy range of 7110-7400 eV (Marcus et al. 2008). The best fit to the data was a three-component fit composed of 70 atom % marine Fe(III) oxyhydroxide (“biogenic iron oxyhydroxide”; Toner et al., 2009b), 15 atom % augite (inosilicate), and 15 atom % roedderite (cyclosilicate).

The bulk Mn 1s XANES spectrum (Figure 2.2c) was fit using linear combinations of reference spectra in the energy range of 6500-6650 eV: birnessite (KMnO_2), $\delta\text{-MnO}_2$, manganite ($\gamma\text{-MnOOH}$), Mn_2O_3 (bixbyite), and Mn_3O_4 (hausmannite) (Bargar et al. 2000; Villalobos et al. 2003). The best fit was a one-component fit with $\delta\text{-MnO}_2$. The $\delta\text{-MnO}_2$ standard is a synthetic layer-type Mn oxide with hexagonal-in-sheet symmetry and an average oxidation number of 4.02 ± 0.02 (Villalobos et al. 2003).

2.4.3 Particle-by-Particle Chemistry of Plume

Samples from above (above plume background), within (top, middle, and bottom), and below (near bottom background) the well-defined plume (Jenkins et al. 2018), as well as fluff layer, were analyzed by STXM and the X-ray microprobe (Table 2.1). STXM was used to visualize particle morphology and intra-particle texture, as well as C and Fe chemistry through C 1s and Fe 2p XANES. The X-ray microprobe was used to collect Fe

1s XANES. Together, these two techniques allow us to visualize intra- and inter-particle characteristics, and to measure Fe and C chemistry.

Table 2.1 GEOTRACES-EPZT samples analyzed

GT#	St. #	Depth (m)	Location	STXM*	X-ray Microprobe [§]	# of Fe 1s μ XANES
8564	18	1000	Above Plume Background	Yes	Yes	7
8439	18	2350	Plume Top	No	Yes	12
8436	18	2500	Plume Middle	Yes	Yes	14
8434	18	2610	Plume Bottom	Yes	Yes	19
8707	20	2350	Plume Top	Yes	No	
8705	20	2550	Plume Middle	Yes	Yes	16
8737	20	2600	Plume Bottom	Yes	No	
8702	20	3140	Near Bottom Background	Yes	Yes	17
8767	20	3178	Fluff layer	Yes	Yes [†]	13

*Polycarbonate filters were used for STXM analysis

§PES SUPOR Filters were used for X-ray Microprobe analysis

† Bulk XANES analyses

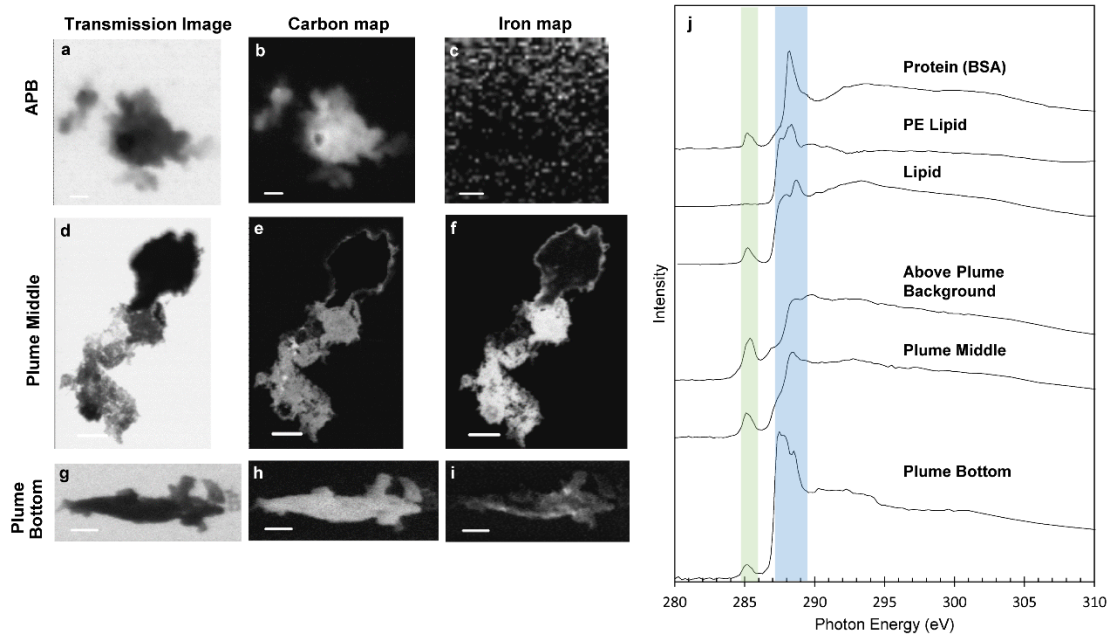


Figure 2.3 Station 18 Elemental Maps and C 1s XANES. Transmission images were collected at 290 eV (a,d, g). Total carbon optical density ranges from 1.12 (b), 1.35 (e), and 0.994 (h). Total iron optical density ranges from 0.0595 (c), 2.83 (f), and 0.584 (i). Scale bars for a-b 500nm, c is 200 nm, d-f are 5 μ m, and g-i are 1 μ m. Carbon 1s XANES spectra from the above plume background, plume middle, and plume bottom are compared to standards protein (BSA), phosphatidylethanolamine (PE) lipid, and lipid (j) (Chan et al.

2011). The green bar highlights the ~285 eV peak corresponding to the $1s-\pi^*_{C=C}$ transition. The blue bar highlights the unique signatures of organic carbon.

2.4.3.1 Carbon 1s and Fe 2p Scanning Transmission X-ray Microscopy and X-ray Absorption Near Edge Structure Spectroscopy

Images, total C maps, and total Fe maps for particles collected above, within, and below the hydrothermal plume at Stations 18 and 20, as well as the fluff layer from Station 20, are displayed in Figures 2.3 and 2.4 (additional data in Appendix 1, Appendix 1.3-1.10).

Carbon 1s spectra were collected on particles from above, within, and below the hydrothermal plume at Stations 18 and 20, as well as sediments from Station 20 (Figures 2.3j, 2.4p, Appendix 1.3n, 1.4u, 1.5r, 1.6k, 1.7v, 1.8l, 1.9l, 1.10j). Spectra were collected from sample areas thin enough to have good X-ray transmitting properties. Principal component analysis (PCA) of the spectral datasets generated by STXM was used to investigate intra-particle C chemistry. Often, the PCA components were composed of spectra having similar chemistry but with different degrees of saturation based on variations in sample thickness. When particles had uniform C chemistry, a single representative spectrum was chosen for analysis and display.

Tables 2.2 and 2.3 report the initial, primary, and secondary peak positions and C bonding information for representative C 1s XANES spectra for each Station. Specific peaks and spectral shapes are used as a fingerprint to identify C compounds in each sample:

1. Within the plume at Station 18 and 20, the C chemistry of samples was most consistent with aliphatic chained compounds that contained alkene or aromatic features (Brandes et al. 2004). Occasionally, carbonyl or organic acid features were observed. These characteristics are observed in many organic molecules, such as ligands, as well as DOC and POC (Golchin et al. 1994; Weishaar et al. 2003; Boiteau et al. 2016).

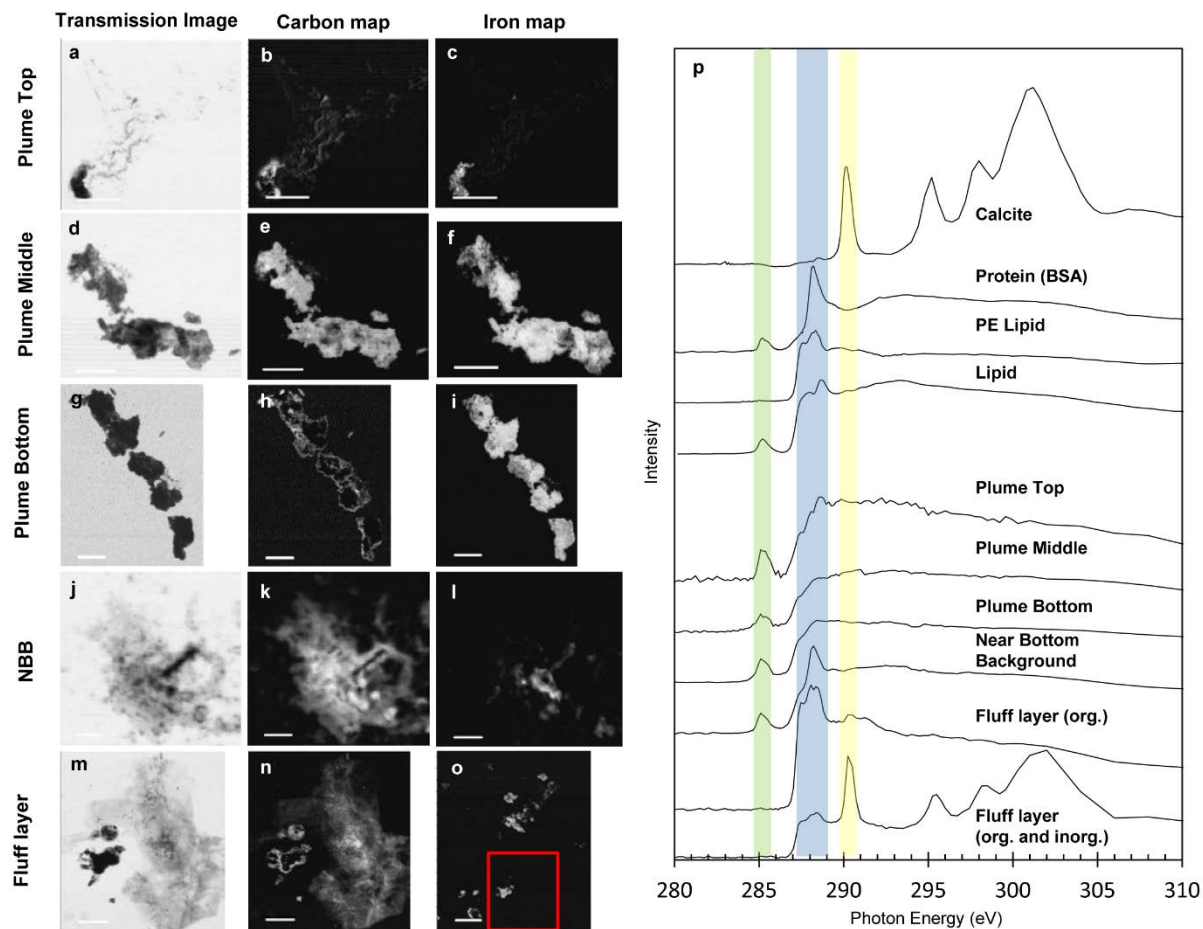


Figure 2.4 Station 20 Elemental Maps and C 1s XANES. Transmission images were collected at 290 eV (a, d, g, j, and m). Total carbon optical density ranges from 1.10 (b), 1.50 (e), 0.0.853 (h), 1.36 (k), and 0.927 (n). Total iron optical density ranges from 1.69 (c), 2.57 (f), 2.85 (i), 0.961 (l), and 2.61 (o). Scale bars for (a-i, m, and n) are 5 μ m, (j-l) are 2 μ m, and (o) is 10 μ m. Carbon 1s XANES spectra from the plume top, plume middle, plume bottom, near bottom background, and benthic fluff layer are compared to standards protein (BSA), PE lipid, lipid, and calcite (p) (Brandes et al. 2010; Chan et al. 2011). The green bar highlights the ~285 eV peak corresponding to the $1s-\pi^*_{C=C}$ transition. The blue bar highlights the unique signatures of organic carbon, while the yellow bar corresponds to distinct peaks associated with inorganic carbon. With the benthic fluff layer data, we are able to identify both organic and inorganic signatures.

Table 2.2 Significant C 1s XANES peaks (eV) within analyzed GP16 hydrothermal plume samples

GT#	Location	Initial Peak	Primary Peak	Secondary Peak(s)	Carbon Compound
8564	Above plume bkgrd	285.3	288.6	289.9	Unsaturated (w/organic acids and alcohol moieties)
8436	Middle	285.1	288.4	n/a	Aliphatic (w/aromatic or alkenes and organic acids)
8434	Bottom	285.1	287.8	n/a	Carbonyl (w/aromatic or alkenes)
8707	Top	285.2	288.7	n/a	Aliphatic (w/aromatic or alkenes)
8705	Middle	285.1	288.0	n/a	Aliphatic (w/aromatic or alkenes)
8737	Bottom	285.1	288.5	n/a	Aliphatic (w/aromatic or alkenes)
8702	Near bottom bkgrd	285.1	288.2	n/a	Protein (BSA)
8767	Fluff	n/a	288.1	n/a	Carbonyl (no aromatic, PE lipid)
8767	Fluff	288.4	290.2	295.5, 298.5, 302.0	Carbonate (aragonite), Carbonyl (no aromatic, PE lipid)

Sources: Brandes et al., 2010, 2004; Chan et al., 2011; Fenter et al., 2002; Stöhr, 2003; Toner et al., 2009a; Urquhart and Ade, 2002

Table 2.3 Important Carbon 1s peaks (eV), bonds, and orbitals

Name	Bond	Peak(s)	Antibonding Orbital	Characteristics
Double bond	C=C	~285	π^*	Alkene or Aromatic
Carbonate	CO	289.9-290.3	π^*	
Alcohol	C-OH	~289	σ^*	
Carbonyl	C=O	287.7-288.6	π^*	Carboxyl, ketone, etc.
Amide-linked Carbonyl	N-C=O	288.2	π^*	Aromatic amino acid

π^* and σ^* refer to the antibonding orbitals a molecule. STXM measures the energy associated with exciting an electron into these orbitals. Peak ranges correlates to peak shifting observed within complex environmental molecules.

Sources: Brandes et al., 2010, 2004; Fenter et al., 2002; Stöhr, 2003

- At Station 18, the above plume background particles typically yielded spectra with alkene/ring, carbonyl, and alcohol moieties (Figure 2.3a, j; Fenter et al. 2002; Brandes et al. 2004a; Sedlmair et al. 2012). These characteristics are consistent with fatty acids, commonly found in cell membranes/walls. Unlike the plume samples, the above plume background initial peak has higher intensity relative to particles located within the plume and does not return to the baseline before increasing to the primary peak (Figure 2.3j; Table 2.2).
- At Station 20, the near bottom background particles typically yielded spectra most consistent with proteinaceous material when compared to our reference spectra and the literature (Brandes et al. 2004; Chan et al. 2011). The spectra are consistent with aromatic/olefinic bonds in amino acids and amide-linked carbonyl groups (Brandes et al. 2004). These spectra and associated images indicate that the near bottom background particles are rich in microbial biomass, including intact, free-living cells.
- The fluff layer at Station 20 contains two distinct spectral signatures. The first is a Corg signal associated with a carbonyl moiety and is consistent with the lipid standard from our reference database (Chan et al. 2011). The second C signature contains a combined Corg and Cinorg signals, with the Cinorg signal contributed by calcite (CaCO_3 ; Brandes et al., 2010). The Cinorg is observed in coccolith fragments that have settled out of the upper water column (de Vargas et al., 2007; Figures 2.4m,n, Appendix 1.10). The biofilm-like, lipid-rich materials observed in the fluff

layer appear to be unique to the benthic region, when compared with near bottom background, plume, and above plume background samples.

Iron 2p XANES spectra for particles within the hydrothermal plume at Stations 18 and 20 are displayed in Figure 2.5, and are consistent with Fe(III) oxyhydroxides, which have one distinctive peak at 709.6 eV. While the Fe 2p XANES are sensitive to Fe(II) versus Fe(III), and Fe(II)-bearing silicates versus Fe-sulfides, it is rather insensitive to the different Fe(III) oxyhydroxide forms (Toner et al. 2009b; von der Heyden et al. 2012). These Station 18 and 20 spectra are consistent with an oxidized plume dominated by Fe(III)-bearing particles, and no instances of fine grained Fe-sulfides were observed by STXM.

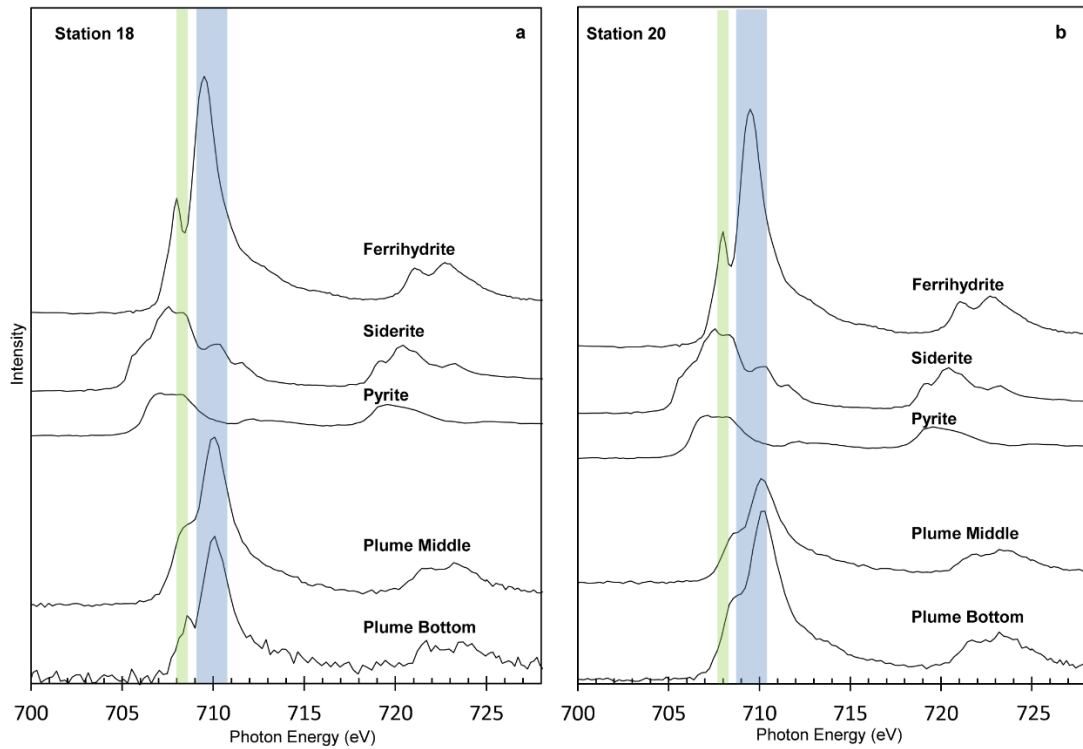


Figure 2.5 Near-field Fe 2p XANES. Iron 2p XANES spectra from the plume middle and plume bottom at Station 18 (a) and Station 20 (b) are compared to standards pyrite, siderite, ferrihydrate and goethite. Peaks from both Station 18 and 20 are most similar with those of ferrihydrate (Toner et al. 2009a). Identifying features and peaks are highlighted.

2.4.3.2 *Microprobe Iron 1s X-ray Absorption Near Edge Structure Spectroscopy*

Particulate Fe speciation, as described by Fe 1s μ XANES, is reported in Figure 2.6 for Station 18 and 20. Approximately 10-20 Fe 1s μ XANES spots were examined for each sample from within the near-field hydrothermal plume (Table 2.1). As described for bulk Fe 1s XANES, the data were fit using linear combinations of reference materials. Those fit results were binned post-fitting into the following broad categories based on the chemistry of Fe, the geologic setting, and the relative sensitivities of Fe 1s μ XANES into different Fe-bearing phases: (1) Fe(III)-oxyhydroxides and -organics; (2) Fe(III) phyllosilicates; (3) Fe(II) oxides, salts, and glasses; (4) Fe sulfides; (5) silicates; and (6) native Fe. While any of these particle types could be transported from elsewhere (allochthonous), several of these categories represent materials that can readily form within plumes (autochthonous). The two separate categories for silicate minerals, “Fe(III) phyllosilicates” and “silicates”, were chosen to represent the fact that phyllosilicates may form within the plume while nesosilicates, inosilicates, tectosilicates, cyclosilicates (hereafter “silicates”) are unlikely to form within the plume. “Native” Fe is an Fe(0) or metallic form which, in general, is considered to be a ship/surface ocean contaminant.

Compared to background, plume particles from Stations 18 and 20 had 60 % or greater, on a per atom basis, Fe(III) oxyhydroxide materials, with ferrihydrite-like phases being the most common best-fit to the data (Table 2.4 and Appendix 1.11). Iron(III)-bearing phyllosilicates contributed an additional ~ 5 - 30 % of the particulate Fe(III). The high percentage of Fe(III) detected with microprobe Fe 1s μ XANES is consistent with the STXM-generated Fe 2p and bulk Fe 1s XANES results (Figures 2.5 and 2.6). Non-sulfide, Fe(II)-bearing phases contributed ~ 5 - 20% of the Fe, while silicates represented minor contributors of Fe to the plume. Iron-bearing sulfides were present in trace quantities in the plume and were detected in two of our samples at 0.1 % and 0.4 % Fe (per atom basis). No measurable difference in particulate Fe speciation between Station 18 and 20 at plume depths was observed.

The near bottom background and fluff layer at Station 20 share overall Fe speciation characteristics: high Fe(III) oxyhydroxides (> 80 %) with phyllosilicates, silicates, and Fe(II) in the range of ~ 1 – 14 % each (Figure 2.6; Table 2.4). However, the near bottom

background have trace quantities of Fe sulfide (0.3 %), while no Fe sulfides were detected within the fluff layer at Station 20. The pFe speciation in the near-field, near bottom background, and fluff layer were quite similar to but more oxidized than the overlying plume (i.e. more Fe(III) and less Fe(II)).

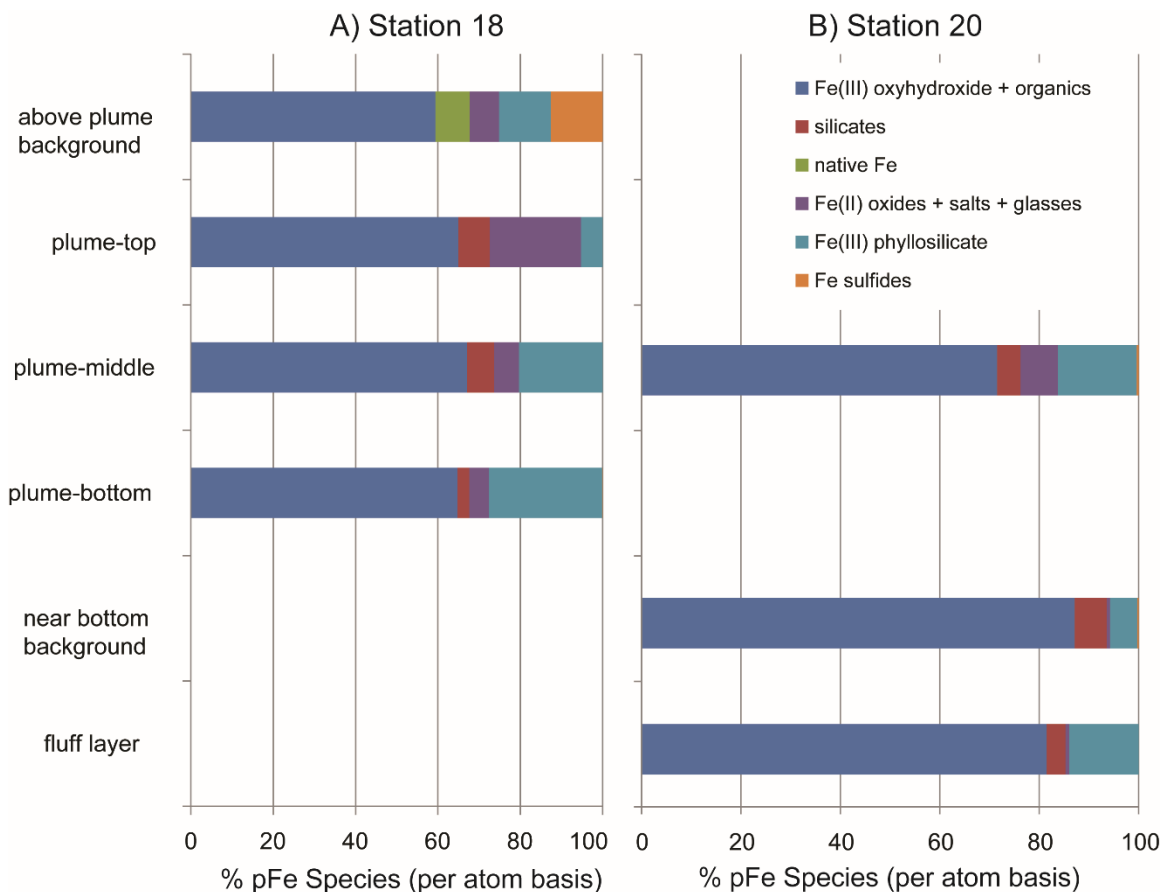


Figure 2.6 Near-field Fe 1s μ XANES. Particulate Fe speciation profiles for Station 18 and 20. All values were generated by linear least-squares fitting of point-XANES data (Fe 1s absorption edge) and post-analysis binning into broad Fe species groups. GEOTRACES numbers, water depth and other characteristics are in Table 2.1. A) Samples for above plume background and plume top, middle, and bottom were analyzed for Station 18. B) Samples for plume middle, near bottom background, and benthic fluff layer were analyzed for Station 20. C) Percent Fe species on per atom basis for all Station 18 and 20 samples are summarized. These values are sums of Fe species observed divided by the total number of observations; no statistical model applied. The error estimate for each species bin is less than 5 atom % (Welter et al. 1999; O'day et al. 2004; Bargar et al. 2005; Nicholas et al. 2017). See section 3.3.2 for discussion of the native Fe and sulfide components of the above plume background sample.

Table 2.4 Iron 1s μ XANES

	pFe Species Bins	fluff layer	near bottom background	plume-bottom	plume-middle	plume-top	above plume background
Station 18	Fe(III) oxyhydroxide + organics	-	-	64.7	67.1	64.9	59.4
	silicates	-	-	2.9	6.5	7.7	0.0
	native Fe	-	-	0.0	0.0	0.0	8.4
	Fe(II) oxides + salts + glasses	-	-	4.8	6.1	22.1	7.1
	Fe(III) phyllosilicate	-	-	27.5	20.3	5.2	12.6
	Fe sulfides	-	-	0.1	0.0	0.0	12.6
Station 20	Fe(III) oxyhydroxide + organics	81.5	87.2	-	71.5	-	-
	silicates	3.8	6.5	-	4.7	-	-
	native Fe	0.0	0.0	-	0.0	-	-
	Fe(II) oxides + salts + glasses	0.8	0.7	-	7.6	-	-
	Fe(III) phyllosilicate	13.9	5.5	-	15.8	-	-
	Fe sulfides	0.0	0.3	-	0.4	-	-

The above plume background sample exhibited the greatest diversity of pFe speciation with ~ 60 % Fe(III) oxyhydroxide and ~ 10 % each of Fe(III) phyllosilicates, Fe sulfide, native Fe, and Fe(II). Native Fe is considered to be a contaminant from the ship, while Fe sulfides could be attributed to the production of reduced sulfur compounds created by plankton in the upper water column (Durham et al. 2015; Ksionzek et al. 2016; Ohnemus et al. 2016). Recently, Ohnemus et al. 2016 observed acid volatile sulfide (AVS) concentrations in the euphotic zone overlaying the SEPR hydrothermal plume which they attributed to the phytoplankton production of reduced sulfur. Unlike the plume, near bottom background, and fluff layer, no silicates were detected in the above plume background at this depth. While the diversity of Fe phases was greater in the above plume background than the plume, the overall pFe concentrations in the above plume background were ~ 60 times lower than the plume (Figure 2.3).

2.5 Discussion

2.5.1 Plume Particle Morphology and Chemistry

Overall, there is much diversity in particle morphology and chemistry in the near-field SEPR hydrothermal plume. However, several trends are observed from samples collected above-plume, within-plume (top, middle, and bottom), below-plume, and at the fluff layer. In general, materials collected within the plume are characterized by strong C- and Fe-enrichment, a high degree of co-location between the two elements, and organic-rich materials (as previously observed for plumes of the EPR 9-10°N area; Toner et al., 2009a) (Figures 2.3d-i, 2.4a-i, Appendix 1.4-1.8). For all water column samples (above plume background, within-plume, and near bottom background), the C chemistry is most consistent with Corg compounds, while the fluff layer at Station 20 is a mixture of Corg and Cinorg.

The plume-top particles from Station 20 are an exception to the overall morphology trends within the plume. Particle morphologies at this location indicate a mixture of plume derived materials and sinking POC from the overlying water column (Figure 2.4a-c, Appendix 1.6). Cell wall remnants and diatoms have been reported to preserve POC through the water column and contain distinct branching or patterned morphologies (Brandes et al. 2004; Abramson et al. 2009), which can be seen in Figure Appendix 1.6i-

j. Particles also contain C-rich matrices that have been observed previously in hydrothermal plumes (Toner et al. 2009a). However, while the plume-top particles are C-rich, Fe element maps indicate particles are either depleted in or Fe-poor. These observations suggest that the plume-top particles are a combination of above plume background and in-plume materials.

The in-plume particles are distinct from the marine particles sampled above and below the plume in terms of relative Fe:C, particle morphology, and degree of co-location of Fe and C in particles. The above plume background sample from Station 18 is enriched in C and depleted in Fe relative to the in-plume particles (Figure 2.3a-c, Appendix 1.3). Samples from the near bottom background, the water depth below the well-defined ^3He plume (Jenkins et al. 2018), are Fe-rich particles coated by organics and are distinct from plume samples with regards to morphology and chemistry (Figure 2.4j-l, Appendix 1.9). For example, in some cases, the near bottom background particles are microbial cells (Figures 2.4k, Appendix 1.9b, e, and g). In the Station 20 fluff layer, C and Fe are both detected. However, the pattern of co-location of these elements is different from that observed in the plume (Figures 2.4m, n, o, Appendix 1.10). Iron is concentrated in coccolith fragments (Cinorg), while Corg is dominated by lipid-rich material. The lipid-like materials are potentially produced by microbial processing of hydrothermal and/or upper water column inputs to the sediments. These specific elemental correlations, and particle morphologies and chemistries are unique to the fluff layer and not observed in any of the water column samples.

The C chemistry within the plume is distinct from that of the above plume background and near bottom background. Within the plume at Station 18 and 20, the C 1s XANES spectra are characterized by plume particles containing aliphatic chains or carbonyl groups (Table 2.2). All spectra contained an initial peak at ~285 eV; associated with either an unsaturated chain or aromatic ring. A primary peak between 287.7-288.6 eV was observed and is consistent with a carbonyl moiety (Brandes et al. 2004). At Station 20, there was increasing aliphatic character in the in-plume material. All spectra at Station 20 contain carbonyl moieties, with the top of the plume containing the strongest signal of that type (Figure 2.4p; Table 2.2) (Brandes et al. 2004).

2.5.2 Sources of Particulate Organic Carbon to the Plume

Sources of POC to the non-buoyant plume could include: (1) upstream contributions from laterally advecting deep ocean water and settling particles from the upper water column; (2) sub-seafloor processes such as microbial activity and abiotic synthesis; (3) mixing with deep ocean water during dispersion; (4) entrainment into the buoyant plume of materials from vent biota, sediments, and deep ocean waters; (5) biological activity within the plume; and (6) transfer of DOC to POC within the plume via adsorption (to solids). Source 1 contributes to background POC at plume depth but does not account for the POC profile observed at Station 18 (Figure 2.1; upstream POC concentrations at Station 17 are low at plume depth). Due to dilution in the buoyant plume (ca. 1:10,000 vent fluid:seawater), sub-seafloor contributions to the POC in the non-buoyant plume (i.e. Source 2) at Stations 18 and 20 should be negligible. The particle characteristics and morphologies of the plume-top particles at Station 20 provide evidence for some mixing with overlying water (i.e. Source 3), but the POC profile indicates that the waters above the plume are lower in POC than the plume so are not expected to be a major source of POC to the plume (Figure 2.1). These observations are supported by POC profiles (Figure 2.1) that show clear enhancements of POC concentrations at plume depths relative to above plume background, near bottom background, and Station 17 (up current of the ridge) values and are discussed in detail in Lam et al. 2018. Overall, our data are most consistent with sources 4-6, and these are discussed below.

With sub-seafloor, and advected/settling sources of POC to the plume rejected as major contributors of plume Corg, the main sources must be entrainment of near-vent material, biological activity within the plume and/or DOC sorption. Entrainment of POC into the buoyant plume (Bennett et al. 2011b; Breier et al. 2012; Bennett et al. 2013; Dick et al. 2013; Jiang and Breier 2014; Bennett et al. 2015; Olins et al. 2017) and the production of POC within non-buoyant plumes (Bennett et al. 2011b; Bennett et al. 2011a; Bennett et al. 2013; Bennett et al. 2015) have been identified as major processes active at vent fields. High POC concentrations have been reported at EPR 9°50'N for the dispersing plume, similar to the features we observe for Stations 18 and 20 at SEPR (Figure 2.1; Bennett et al. 2011b).

Within the plume at Stations 18 and 20, we observe that the dominant pFe species is Fe(III) oxyhydroxides (Figure 2.6). Given a conservative surface area for Fe(III) oxyhydroxides ($100\text{m}^2/\text{g}$) and a Corg sorption ratio of 0.76 mg/m^2 , we would predict approximately 27 nM of DOC could be predicted adsorbed to plume particles (Keil et al. 1993; Lam et al. 2018). This sorption of DOC to mineral surfaces could result in the enrichment in the total POC observed within the plume, and would be an additional explanation of the feature observed in Figure 2.1.

We observe that Corg- and Fe(III)-rich particles at Stations 18 and 20 have similar morphologies, textures, C distribution, Fe distribution and mineralogy in the plume (Figures 2.3, 2.4, 2.6, Appendix 1.4, Appendix 1.7). While transport of vent-derived material off-axis on this length scale is in agreement with prior work at this site (Feely et al. 1996), the SEPR non-buoyant plume is likely a coalescence of materials from many vents in the vicinity of our sampling locations. Therefore, a conceptual model comprising only *de novo* plume particle formation at Station 18 and advection of those materials to Station 20 may be an over-simplification. However, estimates of plume ages using short- and medium-lived radium (Ra) isotopes indicate that materials are progressively older downstream in the plume: at Stations 18 and 20, the in-plume materials were ~1 month and 2.4 - 5.5 years old, respectively (Kipp et al. 2018). This suggests that some of the plume particles at Station 20 are the result of 80+ km of transport from Station 18 and vent sites further south.

Using the conceptual model of in-plume transport of POC from Station 18 to 20, we can further evaluate POC entrainment into or production within the SEPR plume through a comparison of particle morphology and C chemistry of other near-vent systems along the EPR. The SEPR mid-plume POC at Stations 18 and 20 bears morphological resemblance to particles collected within ~ 250 m of EPR 9-10°N (Breier et al. 2009; Toner et al. 2009a; Toner et al. 2012a; Breier et al. 2012). However, the plume POC and Fe chemistries are different between the two sites. Specifically, non-buoyant plume and settling plume particles are both rich in proteinaceous material at EPR 9-10°N, which is taken as evidence for fresh vent biomass inputs (Toner et al. 2009a; Breier et al. 2012). At Station 18, some proteinaceous signatures are also observed (Figure 2.3j) but they are less common at Station 20 (Figures Appendix 1.6-1.10). This suggests that near-vent

Corg inputs could be important for the SEPR, but that certain POC pools are lost during transport through biogeochemical alteration and/or differential settling. Whether the mechanisms of alteration are biological, chemical, physical, or some combination, the trend of particle alteration within the plume appears to continue past Station 20.

Fitzsimmons et al. 2017 recently reported that plume particle morphology and chemistry continue to change between Stations 20 and 21 of the EPZT.

2.5.3 Evidence for a Sulfur-Depleted Plume

Past work at the SEPR revealed variable pS ($> 0.4 \mu\text{m}$) concentrations in non-buoyant plume particles from $13^{\circ}33'$ to $18^{\circ}40'S$ (Feely et al. 1996): the mean Fe:S and mean pS concentration were reported as $13.72 \pm 19.96 \text{ nM}$ ($0.44 \pm 0.64 \mu\text{g} / \text{L}$) and $1375 \pm 873.2 \text{ nM}$ ($44.1 \pm 38 \mu\text{g} / \text{L}$), respectively. Feely et al. 1996 used pFe and pS concentrations, nephelometer data, and transmission electron microscopy to conclude that the plumes were Fe-rich and S-depleted north of $17^{\circ}20' S$. Overall, the bulk Fe 1s, microprobe Fe 1s, and STXM-Fe 2p XANES data sets presented in this contribution are consistent with a near-field environment that is dominated by oxidizing conditions and depleted in Fe-S bearing minerals. The depleted S status of the plume could reflect several different properties of the vent and plume at this location:

1. The vented fluids at SEPR near $15^{\circ}S$ could have low pS concentration. This would be consistent with the work of Feely et al. 1996. At this time, the vent fields and vent fluid characteristics for this region of the SEPR are not known, so the Fe:S in fluids contributing to the plume cannot be assessed directly at this time.
2. The particle size of S-bearing materials could be less than the $0.2 \mu\text{m}$ filter used in this study, and be part of the nano-particulate or colloidal pool (e.g. Yücel et al. 2011). However, this is unlikely given the isotopically heavy values observed in the SERP dFe plume (Fitzsimmons et al. 2017). When Fe-sulfides precipitate in the plume, they carry an isotopically light signature, regardless of the particulate size fraction (nano or macro).

3. The pS could be preferentially removed from the plume by oxidation or settling processes during the ~ 1 month in-plume residence time of particles at Station 18 and 2.4-5.5 years at Station 20 (Kipp et al. 2018).

2.5.4 *Characteristics of Settling Plume Material*

For the Station 20 fluff layer, the STXM results indicate that both Corg (POC) and Cinorg (PIC) bearing phases are present (Figure 2.4, Appendix 1.10). The bulk C 1s XANES spectrum confirms the STXM observations and shows a Cinorg:Corg of approximately 10:1 based on normalized absorption intensity. The inputs of materials to the sediments at Station 20 are from the upper water column and overlying hydrothermal plume. The PIC:POC at the mid-plume (depth of 2500 m) is approximately 0.25 (Figure 2.1), so the plume is enriched in Corg (relative to Cinorg) in comparison to the fluff layer. The mean photic zone PIC:POC in the small size fraction (SSF; 1-51 μm) is 0.04 ± 0.02 , while the large size fraction (LSF; > 51 μm) is 0.14 ± 0.29 (Lam et al. 2018), so the water column is greatly enriched in Corg. The PIC:POC is known to generally increase with water depth as POC remineralizes faster than PIC dissolves in the water column. The PIC:POC in sediments reflects the tendency of POC to be respired while PIC tends to be preserved (i.e. the sediments and entire water column at Station 20 are above the calcite saturation horizon). Overall, the particle morphology and C chemistry (as measured by XANES) of the fluff layer is different from the above plume background, plume, and near bottom background measured for this study. These findings are consistent with the bulk PIC-POC values in that the Corg inputs to the fluff layer appear to be extensively remineralized and altered (Sayles et al. 2001; Ziervogel and Forster 2005).

The STXM, microprobe, and bulk XANES results are consistent with chemically oxidizing conditions in the fluff layer at Station 20. The Fe and Mn mineralogy is dominated by Fe(III) oxyhydroxides and Mn(IV) oxides (Figure 2.2). While the microprobe Fe 1s XANES analysis did detect Fe-sulfide particles in the near bottom background and two plume samples, no Fe-sulfides were detected in the fluff layer by any of our methods (Figure 2.6).

2.5.5 Particle Formation and Transport Characteristics

Within the plume at Station 18, the spatial correlation of Fe, Mn, and Ca in particles is not strong. For example, in the plume at Station 18, we observe particles rich in only Fe, rich in only Mn, rich in only Ca, as well as binary and tertiary combinations of the three elements (red, green, blue, yellow, and white particles in XRF maps, Appendix 1.12). However, if a comparison of Station 18 and 20 is made at mid-plume, it appears that a separate population of Mn-rich particles is emerging (green particles in XRF maps, Appendix 1.13). Fitzsimmons et al. 2017, Lam et al. 2018, and Lee et al. 2018 also report different behavior for pMn and pFe in the SEPR plume. Lee et al. 2018 noted the sinking of LSF aggregates from the plume for both pFe and pMn at Station 18 and 20. However, pFe was observed to partition preferentially into the SSF while pMn was distributed equally between the LSF and SSF at Station 18 and 20. This would imply different oxidation, precipitation, and/or aggregation dynamics for these two elements in the near field. Fitzsimmons et al. 2017 noted that both pFe and pMn removal were consistent with first order kinetics from Station 20 westward. However, the pMn and $^3\text{He}_{\text{xs}}$ plumes did not settle gravitationally in their westward extension while the pFe (and dFe) plume did. Fitzsimmons et al. 2017 hypothesized that the far-field pMn behavior might be caused by Mn-oxidizing bacteria within the SEPR plume.

Recent research has mainly focused on exploring possible transport mechanisms for pFe in hydrothermal plumes (Butler 2005; Bennett et al. 2008; Toner et al. 2009a; Sander and Koschinsky 2011; Yücel et al. 2011; Bennett et al. 2011a; Fitzsimmons et al. 2014; Fitzsimmons et al. 2017). However, many aspects of those proposed mechanisms for Fe should also apply to Mn. Iron and Mn are both redox active transition metals whose reduced divalent states (Fe^{2+} , Mn^{2+}) are soluble in seawater (Emerson 2000; Tebo et al. 2004). These elements also share a tendency for the oxidized trivalent states (Fe^{3+} , Mn^{3+}) to form strong complexes with organic ligands and precipitate to form sparingly soluble oxides, hydroxides, and oxyhydroxide minerals (Hem and Lind 1983; Kostka et al. 1995; Wu and Luther 1995; Post 1999; Cornell and Schwertmann 2003; Trouwborst et al. 2006; Sander and Koschinsky 2011). Manganese has an additional 4+ state that is common in Earth surface environments as sparingly soluble Mn(IV) oxides (Post 1999). The Fe- and Mn-bearing minerals formed in aqueous/soil/sediment systems tend to be finely grained,

often nanoparticulate, with high (bio)geochemical reactivity (e.g. Brown et al., 1999; Emerson et al., 2010; Navrotsky et al., 2008; Nealson et al., 1989). These two elements also have an essential difference that bears strongly on their behavior in oxygenated seawater: abiotic Fe^{2+} oxidation by dissolved oxygen is rapid, while Mn^{2+} oxidation is slow without a catalyst (such as microbes or mineral surfaces; e.g. Nealson et al. 1989; Field and Sherrell 2000). While we can expect certain particle properties to affect pFe and pMn transport similarly (size, density), microbial activity and surface catalysis could have a larger role in pMn transport characteristics.

Microbial oxidation of Mn that leads to the production of pMn in hydrothermal vent systems is well established, especially for the Guaymas Basin and Juan de Fuca Ridge. The evidence ranges from transmission electron microscopy, to shipboard kinetic experiments, to meta-transcriptomic tracking of Mn(II) oxidation genes during entrainment of microbial populations in the Guaymas Basin plumes (Cowen et al. 1986; Kadko et al. 1990; Mandernack and Tebo 1993; Dick et al. 2006; Dick and Tebo 2010). Based on all that is known about Mn chemistry in natural systems, we expect that homogeneous Mn oxidation will proceed more slowly than Fe oxidation unless microbial or surface catalyzed oxidation processes are occurring. Microbial oxidation places the solid-phase Mn(III, IV) products of that reaction in close proximity to cells and cellular exudates. It has been demonstrated through microscopy that Mn oxidation in the laboratory and in nature for a wide variety of microorganisms creates microbe-mineral composite particles (e.g. Cowen et al., 1986; Santelli et al., 2011; Tebo et al., 2004; Toner et al., 2005). Therefore, it is reasonable to assume that pMn in the EPZT plume has this composite character.

We have demonstrated through direct observation that the pFe of the EPZT plume also consists of organic-inorganic composites (this contribution; Fitzsimmons et al., 2017). Why then do we observe different settling behaviors between pFe and pMn over short and long transport distances? We propose that the main difference in settling is based on the timing and in-plume location of the interactions between the metal and Corg. These differences in particle formation are created by the changes in rate and mechanism of oxidation for Fe and Mn. Therefore, in our low-S SEPR plume, Fe oxidizes rapidly to form Fe(III)oxyhydroxides. This process occurs within the buoyant and early non-

buoyant plume and is likely complete within hours-days (Field and Sherrell 2000a). The composite nature of the pFe we observe suggests physical aggregation of Fe(III)oxyhydroxides with entrained Corg. Particles with those characteristics persist in the non-buoyant plume for 80+ km. However, we do have evidence that the particles change with greater transport time so the pFe must be subject to physical, chemical, or biological alteration (Fitzsimmons et al. 2017). These alteration processes may ultimately lead to particles with a size and density that allows a gradually settling pFe plume on a time scales of decades (Fitzsimmons et al. 2017).

In contrast to Fe, homogeneous Mn oxidation and particle formation should be slow in seawater. In the near-field, where dMn concentrations are high, microbial oxidation may cause initial oxidation and precipitation events through entrainment of active Mn-oxidizer populations (Kessick and Morgan 1975; Hem 1981; Hem and Lind 1983; Campbell et al. 1988; Tebo et al. 2004; Bargar et al. 2005; Webb et al. 2005; Dick et al. 2006; Johnson et al. 2016). However, at high dMn concentrations, abiotic auto-oxidation/autocatalysis of Mn(II) by Mn(III, IV) phases could be a more important contributor to near-field particle growth (Kessick and Morgan 1975; Hem 1981). In this scenario, the particles could grow quickly, be combinations of Mn(II), Mn(III), and Mn(IV) reflecting a variety of possible reaction pathways (Hem and Lind 1983; Webb et al. 2005; Johnson et al. 2016), and partition into the rapidly settling LSF as observed by Lee et al. 2018. While we might expect the resulting pMn in the far-field plume to suffer the same fate as pFe (i.e. alteration and settling) the dilute conditions of the far-field plume may favor microbial Mn oxidation (Bargar et al. 2005). Any alteration of pMn that occurs within the far-field plume does not appear to change the overall neutral buoyancy of the pMn particle population (Fitzsimmons et al. 2017; Lee et al. 2018): perhaps because neutral buoyancy is a selective advantage to the Mn oxidizing microorganisms (e.g. dispersal, optimal dMn concentration). This is an area ripe for further investigation.

2.6 Conclusions

In this study, we have explored the hypothesis that Corg contributes to the export of hydrothermally sourced pFe over long distances into the interior of ocean basins (Toner et al. 2009a; Fitzsimmons et al. 2014; German et al. 2015; Fitzsimmons et al. 2017).

Through a suite of synchrotron X-ray microscopy, microprobe, and spectroscopy techniques, we have observed that in the non-buoyant hydrothermal plume at 15°S on the EPR, near-field plume particles are composites of mineral and biological materials that are dominated by Fe(III)-bearing oxyhydroxide phases but are also rich in Corg. The profiles for pFe and POC at background Station 17 (upstream of the ridge axis), and at Stations 18 (ridge axis) and 20 (83 km down-plume away from the ridge axis) all indicate that the inputs of both Fe and Corg to the dispersing plume are dominated by hydrothermally derived materials. The Fe is contributed by vent fluids directly, while the Corg is entrained from the near-vent ecosystems, sorbed to hydrothermal particles within the plume, or due to *in-situ* production associated with microbial activity within the plume. The particulate Fe(III)-Corg associations we observed in the non-buoyant plume extending out to 100 km off-axis from the ridge crest at SEPR are consistent submersible-based observations made previously in the near-field, no greater than 100 m from sites of active venting at the 9°N EPR site (Toner et al. 2009a; Breier et al. 2012). The commonality of processes revealed in this contribution demonstrates the export of hydrothermal pFe to the ocean interior is indeed facilitated through an association with Corg in dispersing non-buoyant plumes.

CHAPTER 3

Hydrothermally derived iron oxyhydroxides are short-range ordered phases over ~4300 km of ocean transport

This chapter is modified from the following manuscript:

Hoffman, C.L., Nicholas, S.L., Schladweiler, C., Fitzsimmons, J.N., Sherrell, R.M., German, C.R., Heller, M.I., Lee, J. mi, Lam, P.J., Toner, B.M. Hydrothermally derived iron oxyhydroxides are short-range ordered phases over ~4300 km of ocean transport". in prep.

3.1 Overview

In the surface ocean, iron (Fe) is a growth limiting nutrient for microscopic marine life, which impacts their ability to remove carbon (C) from the atmosphere and surface waters. While there are several sources of Fe in the ocean, hydrothermal vents are the most disputed. Recent geochemical studies have demonstrated multiple mechanisms that allow hydrothermally derived Fe to be protected and transported within the buoyant and non-buoyant plume. Hydrothermal vents impact on the global Fe budget has been difficult to constrain, as mechanisms for the sources and sinks of hydrothermal Fe are still poorly understood. Marine particles and sediments were collected over ~8000 km GP16 cruise transect, which included the ~4300 km Southern East Pacific Rise (SEPR) hydrothermal plume. In this study, we measured particle chemistry in the mid and far-field SEPR hydrothermal plume. Iron and C speciation and morphology were measured using the Scanning Transmission X-ray Microscope (STXM) and X-ray Microprobe. Additionally, Extended X-ray Absorption Fine Structure (EXAFS) was used to evaluate differences between Fe(III) oxyhydroxide mineral phases. In the near-field (~200 km) and mid-field (~200-2700 km), particle morphology is dominated by nanoparticulate Fe:C aggregates. Carbon speciation was mostly comprised of organic carbon (Corg) rich moieties that were abundant in carbonyl groups. Unlike the Fe:C co-location seen near-field SEPR hydrothermal plume particles, the mid-plume Fe particles were encased in C-rich matrices that slowed the development of more stable structural formations in Fe(III) oxyhydroxide mineral phases. Iron(III) oxyhydroxides were the dominant Fe-bearing mineral group throughout the plume and sediments. Fe-sulfides were only detected >3200 km from the ridge and were not expected to be of hydrothermal origin. These findings suggest that Corg is important in the distal transport and longevity of non-buoyant hydrothermal Fe.

3.2 Introduction

Iron (Fe) is an essential micronutrient for phytoplankton growth. However, within the modern ocean, Fe concentrations are on the order of picomolar and decreases with depth. Phytoplankton account for 50% of total photosynthesis on the planet and are integral to the global carbon (C) cycle (Field et al. 1998; Moore et al. 2013; Fitzsimmons et al.

2014). Within High Nutrient Low Chlorophyll (HNLC) regions of the ocean, such as the Southern Ocean, certain micronutrients required for photosynthesis are depleted and phytoplankton growth limited (Moore et al. 2013). For example, phytoplankton growth, and conversion of inorganic C to biomass, was observed to increase when Fe was added to samples collected from HNLC regions (Anderson and Morel 1982; Brand et al. 1983). If these controlled experiments could be scaled up, it would provide an additional mechanism to remove C from the atmosphere and surface ocean in Fe-limited regions of the ocean.

Iron has multiple sources to the global ocean. Sources include dust, glaciers, rivers, sinking organic matter from the surface waters, upwelling of margin sediments, and (highly debated) hydrothermal plume (Tagliabue et al. 2017). Initially, it was believed that dust and upwelling of margin sediments were the main sources that supplied Fe and spurred phytoplankton growth in the surface waters. However, key areas in the global ocean (e.g. the Southern Ocean) were shown to be underproductive due to Fe limitation (Moore et al. 2013). This limited the productivity of the ocean to capture and bury C. Around a decade ago, it was discovered that hydrothermal Fe could be protected from oxidation and be a potential source of Fe to the Southern Ocean (Toner et al. 2009a; Tagliabue et al. 2010; Sander and Koschinsky 2011). Previous studies suggested that Fe is immediately oxidized and deposited locally around the vent site, having little impact on global geochemical cycles. Recent data from the Southern East Pacific Rise (SEPR) further shows that hydrothermal Fe can in fact travel great distances from the venting source and be a source of Fe to the ocean interior (Resing et al. 2015; Fitzsimmons et al. 2017; Hoffman et al. 2018; Lam et al. 2018; Lee et al. 2018). Yet, the mechanisms for basin-scale transport of hydrothermal Fe are still widely debated (Bennett et al. 2008; Toner et al. 2009a; Yücel et al. 2011; Gartman et al. 2014). Proposed mechanisms are nanoparticles and organic C (Corg) matrices in the buoyant plume that preserve Fe(II) over longer distances (Toner et al. 2009a; Bennett et al. 2011b; Sander and Koschinsky 2011; Yücel et al. 2011; Gartman et al. 2014; Hoffman et al. 2018). These mechanisms produce slower settling velocities of particulate Fe and are hypothesized to transport Fe 100s to 1000s km from the ridge axis (Yücel et al. 2011; Holden et al. 2012; Gartman et

al. 2014). These findings suggest hydrothermal vents could be an unrecognized source of Fe to the ocean interior and surface waters.

Hydrothermal vents are located globally along Mid-Oceanic Ridge (MOR) spreading center and supply as much Fe to the ocean as river run off (Elderfield and Schultz 1996). Cold oxygen-rich seawater circulates through heated and fractured rock where it undergoes alterations through water-rock reactions (Seewald and Seyfried 1990; von Damm 1990; German and Seyfried 2014). Here, sulfur and trace metals (e.g. Fe, Mn, Cu, etc.) are leached from surrounding rocks, reduced, and undergo phase separation when the boiling curve is reached (Seyfried and Ding 1993; Tivey 2007). These hot (>350 C), acidic, altered fluids become buoyant and create hydrothermal plumes when mixed with seawater at the seafloor (Weiss et al. 1977; von Damm 1990; Tivey 2007). Oxidation-reduction (redox) disequilibrium occurs as cold ocean water is entrained into the buoyant plume, quickly producing Fe-sulfides and other mineral precipitates that are deposited locally or carried into the neutrally buoyant plume (von Damm 1990; Elderfield and Schultz 1996; German and Seyfried 2014). Within hydrothermal vent fluids and plumes, Fe can exit in two different redox states: reduced Fe(II) and oxidized Fe(III). Iron sulfides, such as pyrite, FeS, and pyrrhotite, are commonly produced minerals near the vent (Feely et al. 1992; German and Seyfried 2014). Ultimately, as the plume reaches neutrally buoyancy and disperses hydrothermally derived materials on currents (Adams et al. 2011; German and Seyfried 2014; Fitzsimmons et al. 2017), Fe becomes increasingly oxidized producing Fe(III) oxyhydroxides as the dominant mineral phase.

However, very little is currently known about Fe oxidation states and transport mechanisms within non-buoyant plumes that extend over a few hundred kilometers. A few early plume studies observed bacterial scavenging or elevated concentrations of Fe and other trace elements 10-100 km from the ridge axis (Trefry et al. 1985; Cowen et al. 1986; Feely et al. 1996). Of these early studies, only one investigated Fe redox states of hydrothermal particles (Feely et al. 1996). At the time, most studies were focused on characterization of hydrothermal fluids and the buoyant plume (von Damm 1990; Tivey 2007; German and Seyfried 2014). The recent discovery of a ~4300 km ³He_{xs} plume and ~3300 km dissolved and particulate Fe plume along the SEPR (Resing et al. 2015; Fitzsimmons et al. 2017; Jenkins et al. 2018; Lam et al. 2018; Lee et al. 2018) further

raises two questions: 1. How is hydrothermal Fe being transported 1000s km into the ocean interior? and 2. How does the redox state of Fe changed over those long distances? In this study/chapter, the objectives are to identify the chemical speciation of particulate Fe and particulate C over the ~4300 km SEPR hydrothermal plume to gain further insight into basin-scale transport of hydrothermal Fe.

3.3 Methods

3.3.1 Sample Collection

3.3.1.1 Marine Particles Collections

As part of the US GEOTRACES-Eastern Pacific Zonal Transect cruise (GP16), marine particles were collected by *in situ* filtration along a ~8000 km transect that includes a ~4300 km hydrothermal plume. Samples from Station 18 (~ridge axis) thru 36 (~4300 km off axis) were filtered using a custom accessory manifold attached to the deployed dual-flow McLane pumps. The overall *in situ* pump program included 142 mm diameter 0.8 μm polyethersulfone (PES) filters downstream of a prefilter and is described in detail by Ohnemus and Lam 2015; Heller et al. 2017; Lam et al. 2018; Lee et al. 2018. The accessory manifold was used to collect up to four 25 mm filters simultaneously on a third, un-metered flowpath of the McLane pumps: two 0.2 μm polycarbonate filters for analysis by Scanning Transmission X-ray Microscopy (STXM) and two 0.2 μm polyethersulfone (PES) filters for X-ray Microprobe. Additionally, the 142 mm-diameter 0.8 μm PES filters were used for analysis by Extended X-ray Absorption Fine Structure (EXAFS).

The 25 mm PC and PES filters were opened in an anaerobic chamber (Coy Labs) to prevent exposure of the sample to ambient oxygen. Sample processing occurred under a nitrogen hydrogen (95% N₂, 5% H₂) atmosphere (the anaerobic chamber was located within a self-built shipboard High Efficiency Particulate Arresting (HEPA) chamber). Filters were rinsed using N₂-sparged 18.2 M Ω ·cm purified double distilled water (MilliQ) via vacuum pump to remove seasalts (the pump was located outside of the HEPA bubble with a line plumbed to the anaerobic chamber). The 25 mm diameter filters and filter replicates were: (1) placed in acid-washed petri-slides for X-ray microprobe and archiving, and (2) placed in acid-washed microfuge tubes with 0.5 mL N₂-sparged

MilliQ for STXM preparation. Prior to leaving the anaerobic chamber, all samples were sealed in mylar bags within an oxygen-free atmosphere. Sample packs were then frozen at -20°C to reduce the kinetics of chemical oxidation.

Upon recovery, the 142 mm PES filters were rinsed, and split into 1/8 or 1/16 wedges using a ceramic rotary blade within a clean bubble created on the ship. One of the PES filter wedges was placed in an acid-washed petri-slide for bulk EXAFS analysis. The sample wedges were then placed in the anaerobic chamber, sealed in mylar bags, and frozen at -20°C .

3.3.1.2 Sediment Core Collection

At Stations 20, 23, 25, 26, 28, 30, 32, 32, and 36, sediment cores were collected using a gravity corer suspended beneath the ODF (Ocean Data Facility) CTD (conductivity, temperature, depth) rosette during the final deep cast at that station. In a shipboard cold room (4°C), the overlying fluids were syphoned off, including a surficial fluff layer that was removed from the consolidated sediments and separated out by centrifugation within hours of sediment core collection. Shipboard, fluff material was frozen in 50 mL polypropylene tubes. Shore-based splitting of fluff layer sample was accomplished by re-suspension in pH 8.0 purified water buffered by NH_4OH . Prior to microprobe and bulk EXAFS analysis, fluff layer materials were separated from aqueous solution by $0.2\ \mu\text{m}$ filtration. Cores were later split into 1 cm segments. The fluff and 0-1 cm sediment layers are discussed in this chapter.

3.3.2 Scanning Transmission Microscopy (SEM)

Scanning electron microscopy was used to characterize (size, shape, etc.) and visualize marine particles. Images were collected using the JEOL 6500 Scanning Electron Microscope (SEM) at the UMN Characterization Facility.

A small wedge of the $0.45\ \mu\text{m}$ PES SUPOR filter wedges for Station 18-30 were cut in a glove bag (Cole-Parmer Captair Pyramid Glove Bag) under N_2 -positive pressure and sealed in a cleaned plastic case. In a laminar flow hood, filters were adhered to the SEM sample holder by carbon tape. The samples underwent carbon coating at the level of 50\AA . Samples were then loaded onto a holder and inserted into the SEM. Imaging of the filter

wedge were taken at random points throughout the view screen to investigate particle diversity. At each point of interest, images were taken at low magnification ($\sim \times 5,000$) and high magnifications ($\sim \times 25,000$ - $35,000$) without moving the toggle or center point. All images were uploaded to WinSCP and then converted to JPEGs or TIFFs.

3.3.3 *X-ray absorption spectroscopy*

3.3.3.1 *Scanning Transmission X-ray Microscopy (STXM)*

Marine particles were collected for the entire GP 16 SEPR hydrothermal plume (Stations 18-36) and fluff layers (Stations 20, 23, 25, 26, 28, 30, 32, 32, and 36). However, due to STXM beamtime being limited, far-field marine particles from Station 21-30 in the SEPR hydrothermal plume and Station 23, 26, and 30 were selected at the top priority based on bulk chemistry data (Fitzsimmons et al. 2017; Lam et al. 2018; Lee et al. 2018). Marine particles for the SEPR hydrothermal plume filters were prepared in an anaerobic chamber. Due to low particle concentration on far-field PC filters, filters from the top, middle, and bottom at each station were defrosted, rinsed with N_2 -sparged Milli-Q, and pooled into one aliquot. Sediment fluff layer suspensions were initially prepared in dilute aqueous solutions buffered to seawater pH using NH_4^+ these suspensions were subsequently diluted 1:10 with MilliQ under ambient conditions. Approximately $1\mu L$ of the aliquot of particle suspensions was deposited onto a silicon nitride window (Silson Ltd.) and air-dried in a glove bag. Imaging and C 1s and Fe 2p X-ray absorption near edge structure (XANES) spectroscopy were conducted at beamline 5.3.2.2, Advanced Light Source (ALS), Lawrence Berkeley National Laboratory, Berkeley, CA, USA (Kilcoyne et al. 2003). Samples were transferred to the STXM instrument with ~ 30 s of exposure to ambient atmosphere and analyzed in a helium flushed microscope chamber.

A global image of each silicon nitride sample holder was collected and surveyed to ensure an accurate representation of particles diversity within each sample. For each sample, three different types of data were collected: (1) transmission images covering sample areas from 1 mm^2 to $10\text{ }\mu\text{m}^2$, (2) elemental maps for C and Fe, (3) C 1s and Fe 2p XANES spectra in point-scans, line-scans, or three dimensional “stacks” (a series of 2D images at different incident energies spanning the C and Fe absorption edges such that

full XANES spectra can be extracted from each pixel of the composite stack of images) (e.g. Brandes et al. 2004; Toner et al. 2009; Chan et al. 2011; Chen et al. 2014; Toner et al. 2016; Barber et al. 2017). STXM data processing included: (1) elemental optical density maps, (2) principal component analysis of spectral features, (3) selection of XANES spectra and subsequent pre-edge subtraction, post-edge normalization using *aXis2000* (Hitchcock, 2016). Images show the particle dimensions and textures. The elemental maps reveal particle morphology and the location of C and Fe within particles. Carbon 1s XANES distinguishes between Corg and inorganic C (Cinorg) and provides bond specific composition of Corg. Iron 2p XANES primarily differentiates between reduced and oxidized Fe species. Normalized spectra were compared to our C 1s and Fe 2p reference databases and literature for identification. Reference materials for C 1s and Fe 2p are published in (Fenter et al. 2002; Urquhart and Ade 2002; Stöhr 2003; Brandes et al. 2004; Toner et al. 2009a; Brandes et al. 2010; Chan et al. 2011).

Functional group peak identification and Gaussian curve fitting in *Athena* was used when no reference material matched experimental spectra (Ravel and Newville 2005; Webb 2005; Nico et al. 2017). Using previously published methods, 7 curves were identified (1 arctangent and 6 gaussian curves; Lehmann et al. 2009; Nico et al. 2017). The arctangent parameters were defined and fixed for all spectra within this dataset. Initial guesses were placed into the model, but final height and widths for the gaussian curves were determined by *Athena*. Percentages of the identified functionals were calculated based on the area under the curve. Best fits were determined by the minimization of χ^2 and R-factor (Appendix Table 2.2.1 and 2.2.2). Additional details regarding initial guesses and model setup are provided in Appendix Section 2.3.

3.3.3.2 X-ray Microprobe

Using previously established methods, micro-focused X-ray fluorescence mapping (μ XRF) and Fe 1s μ XANES, at beamline 10.3.2 of the ALS was used to investigate Fe speciation of marine particles from Station 21-36 (Marcus et al. 2004; Lam et al. 2012b; Toner et al. 2012b; Breier et al. 2012; Toner et al. 2014a; Toner et al. 2016). Additionally, micro Extended X-ray Absorption Fine Structure (μ EXAFS) spectroscopy was used to analyze particles at Station 18-30. All particles were analyzed on 25 mm 0.2

um polyethersulfone (PES; trademark SUPOR) filters and all sample preparation was conducted within positive pressure (N₂ or Ar) glove bags. The final step in sample preparation included application of a layer of sulfur-free mylar film (Premier Lab Supply TF-125-255) to limit exposure of the sample to ambient oxygen during analysis using the method established by Zeng et al. 2013. The monochromator was calibrated using an Fe foil XANES scan with the inflection point set to 7110.75 eV (Kraft et al. 1996). Micro-XRF, μ XANES, and μ EXAFS data were collected using a Canberra 7-element Ge solid-state fluorescence detector. Micro-XANES data were collected from 7012 to 7417 eV in quick-XANES mode with a single sweep of the monochromator lasting 30 s. Micro-EXAFS data were collected from 7000 to 8000 eV in quick-EXAFS mode.

Data collection for each filter included: (1) a large μ XRF “survey” map with an area of approximately $1000 \times 3000 \mu\text{m}^2$, pixels of $6 \times 6 \mu\text{m}^2$, and incident energy of 10 keV was collected to measure the distribution of particles and elements on the filter; (2) “fine” μ XRF sub-maps of approximately $100 \times 100 \mu\text{m}^2$, pixels of $3 \times 3 \mu\text{m}^2$, and incident energies spanning the Fe 1s absorption edge; (3) Fe 1s point-XANES spectra; and (4) selection of Fe 1s point-EXAFS spectra of interest.

Data processing for XRF maps included deadtime correction and plotting with beamline 10.3.2 LabView software (Marcus et al. 2004). Data processing for the XANES and EXAFS spectra included: (1) deadtime correction and energy calibration (beamline 10.3.2 custom LabView software), (2) pre-edge subtraction and post-edge normalization (*Athena*; Ravel and Newville 2005; Webb 2005). Linear least-squares fitting of XANES data with a reference database (Marcus et al. 2008) was done using a custom *mrfitty* python widget (Nicholas et al. 2017) using previously published reference spectra (Toner et al. 2009b).

3.3.3.3 Bulk X-ray Absorption Spectroscopy

Bulk Fe 1s EXAFS spectra for Stations 20, 21, and 25 were collected at the Canadian Light Source (CLS) Soft X-ray Microcharacterization Beamline (SXRMB). The fluff layer was applied as a dry powder to double-sided C tape and adhered to a copper sample plate under ambient temperature and atmosphere and placed in the SXRMB vacuum sample-chamber. The monochromator was calibrated using an Fe foil XANES scan with

the inflection point set to 7110.75 eV (Kraft et al. 1996). All experimental spectra were collected in fluorescence mode using an Amptek silicon-drift detector positioned at 45 degrees, with I0 collected simultaneously in an ion chamber. Data processing for the EXAFS spectra consisted of I0 normalization, energy calibration, pre-edge subtraction, post-edge normalization, and linear least-squares fitting with a reference database using *Athena* and *mrfit* python widget (Ravel and Newville 2005; Webb 2005; Nicholas et al. 2017). The Fe 1s EXAFS spectrum was fit using linear combinations of 33 reference spectra (Toner et al. 2009b).

Additionally, bulk Fe 1s EXAFS spectra of mid-plume marine particles from Stations 18, 20, 21, and 25 and 0-1 cm sediments from 17, 20, and 26 were collected at the Advanced Photon Source (APS) at Argonne National Labs in Lemont, IL. The bulk Fe 1s EXAFS were collected on beamline 20-BM-B. Filter (wedges of PES 142 mm) samples from the mid-plume were prepared by cutting the filter into small squares. Two to three layers of the sample were applied to a piece of Kapton X-ray tape. A second layer of adhesive was applied on top of the filters to hold the stacked filter pieces in place. For the sediment samples, two different sample preparation methods were used depending on the total Fe concentration and its elemental matrix. The first method comprised of grinding a calculated (*Hephaestus* module of the *IFEFFIT* software package) amount of cellulose and sediment mixture together to create a pellet for transmission mode detection. Mixtures were ground for ~ 20 minutes with a mortar and pestle to homogenize the cellulose and sediment mixture. A predetermined amount of the mixture was then weighed (~150 mg) and placed in between a 13 mm die set. Pressure was added incrementally at 1660 lbs. for 30 seconds until a total of ~5000 lbs. of pressure was reached. The pellet was then removed and sealed between two layers of Kapton adhesive. The second method required depositing a small amount of sediment in the center hole of a plastic washer for fluorescence mode detection. Plastic washers were cleaned with deionized water and attached to a piece of Kapton adhesive prior to packing in the sediment powder. Sediment samples were slowly added to the center hole of the water and pressed onto the adhesive. A second layer of Kapton adhesive was then placed to the top side of the plastic washer, covering the washed and sediment sample. All samples were placed on the sample stage in an ambient-air hutch.

Iron 1s EXAFS spectra were collected both in transmission and fluorescence mode. Fluorescence data was collected using a Canberra 7-element fluorescence detector positioned at 45 degrees relative to the sample surface. The incident beam (I_0), transmitted beam (I_t), and reference foil (I_{ref}) were collected in ion chambers simultaneously for each EXAFS scan. Data processing of individual spectra included averaging, energy calibration, pre-edge subtraction, and post-edge normalization using *Athena* (Ravel and Newville 2005; Webb 2005). Linear combination fitting of bulk EXAFS was conducted using *mrfit* python widget (Nicholas et al. 2017) with the same reference database described above.

3.4 Results

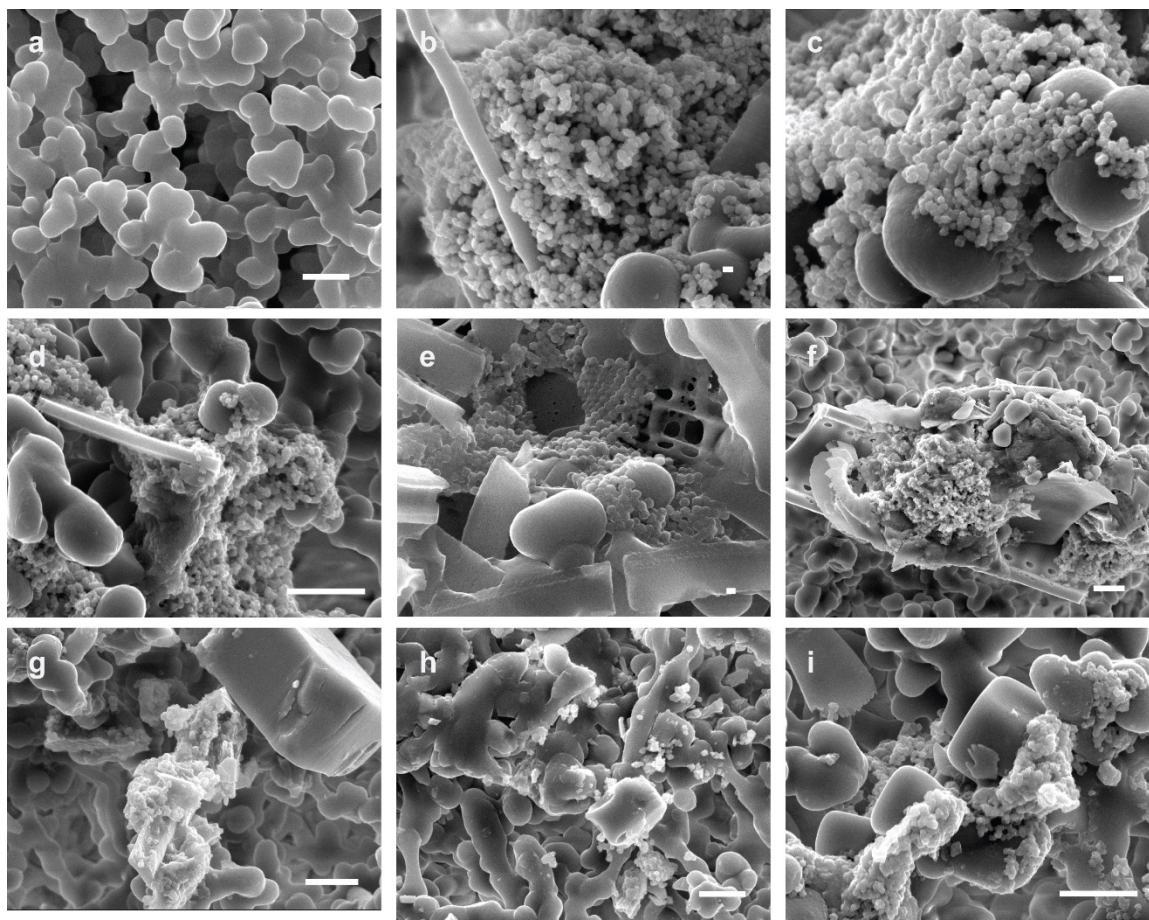


Figure 3.1 SEM Images for mid-plume particles collected on GP16. Particles were analyzed at the following stations: (a) blank control PES filter, (b) Station 18, (c) Station 20, (d) Station 21, (e) Station 23, (f) Station 25, (g) Station 26, (h) Station 28, and (i) Station 30. Nanoparticle aggregates are observed into the far-field. Scales bars for a, b, and e are 100 nm. All other scale bars are 1 μm .

3.4.1 Morphology of marine particles in the SEPR hydrothermal plume

Scanning electron microscopy (SEM) images of marine particles (greater than 0.2 μm) show that nanoparticulate aggregates are observed in the mid-plume up to 2000 km away from the ridge axis (Figure 3.1b-d). Individual nanoparticles were observed to be between 100-200 nm in diameter. The density of marine particles on filters was greatest at Station 18 and 20 (Figure 3.1b,c, Appendix 2.1.1-2.2.2). Station 21 (~200 km) was observed to occasionally contain rod shaped particles of ~ 2 μm in length intermixed with nanoparticulate aggregates (Figure 3.1d, Appendix 2.1.3). At Station 23 (~800 km) there was a decrease in particle loading on the filter consistent with dilution of the plume observed in the bulk data (Lam et al. 2018; Lee et al. 2018; Figures 3.2, 3.3, and Appendix 2.2.1). Nanoparticles are still observed but less abundant than in the first ~200 km from the ridge axis (Figure 3.1e, Appendix 2.1.4). At Stations 25-30 (~1350-2700 km), an increase in particle loading was seen on the filter consistent with the bulk pFe concentrations (Figure 3.3b). Nanoparticles were observed throughout filters from these Stations, but overall particle density decreased further from the ridge axis. Stations 25-30 also contain a higher observable abundance of settling material from the surface ocean (e.g. plankton, diatoms) (Figure 1f-i, Appendix 2.1.5-2.1.8). At Station 25 (~1350 km) there were observable organic matrices that provide a surface for nanoparticles and other micro/macroparticles to bind together (Figure 3.1f, Figure 3.4a-c, Appendix 2.1.5). The range of morphological diversity for each Station can be seen in Appendix 2.1.

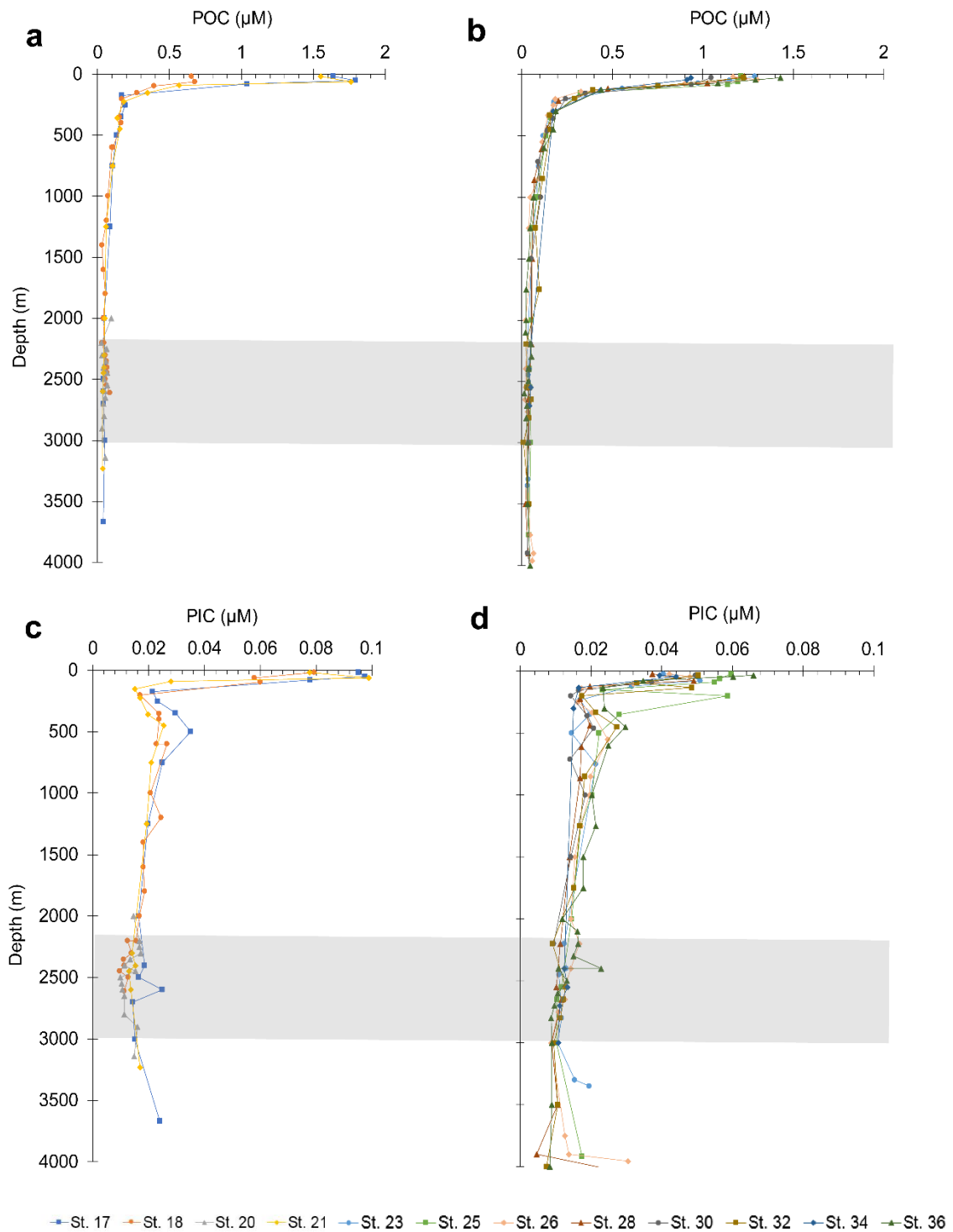


Figure 3.2 Total POC and PIC concentration along the GP16 transect. Depth distribution of total particulate organic carbon (POC) and total particulate inorganic carbon (PIC) for (a, c) Station 17 (up-current of the ridge axis), the near-field (Station 18-21), and (b, d) the mid and far-field hydrothermal plume (Stations 23-36) in the SEPR hydrothermal plume (Lam et al. 2018). The mid-plume depth is highlighted in grey.

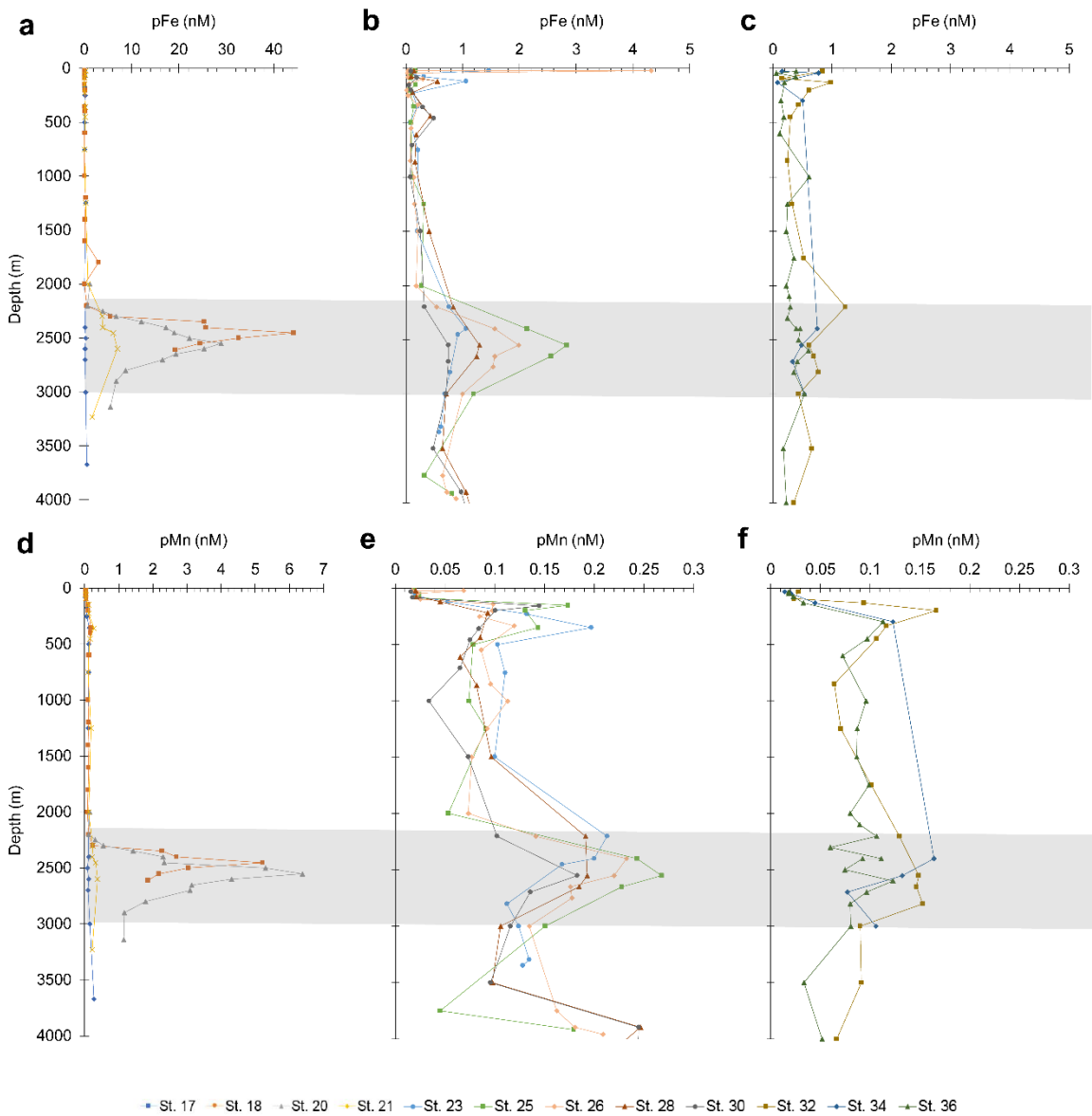


Figure 3.3 Total particulate Fe and Mn (pFe and pMn) concentrations along the GP16 transect. Depth distribution of total particulate iron (pFe) and total particulate manganese (pMn) for (a, d) Station 17 (up-current of the ridge axis), the near-field (Station 18-21), (b, e) the mid-field (Stations 23-30), and (c, f) the far-field hydrothermal plume (Stations 32-36) in the SEPR hydrothermal plume (Lee et al. 2018). The mid-plume depth is highlighted in grey.

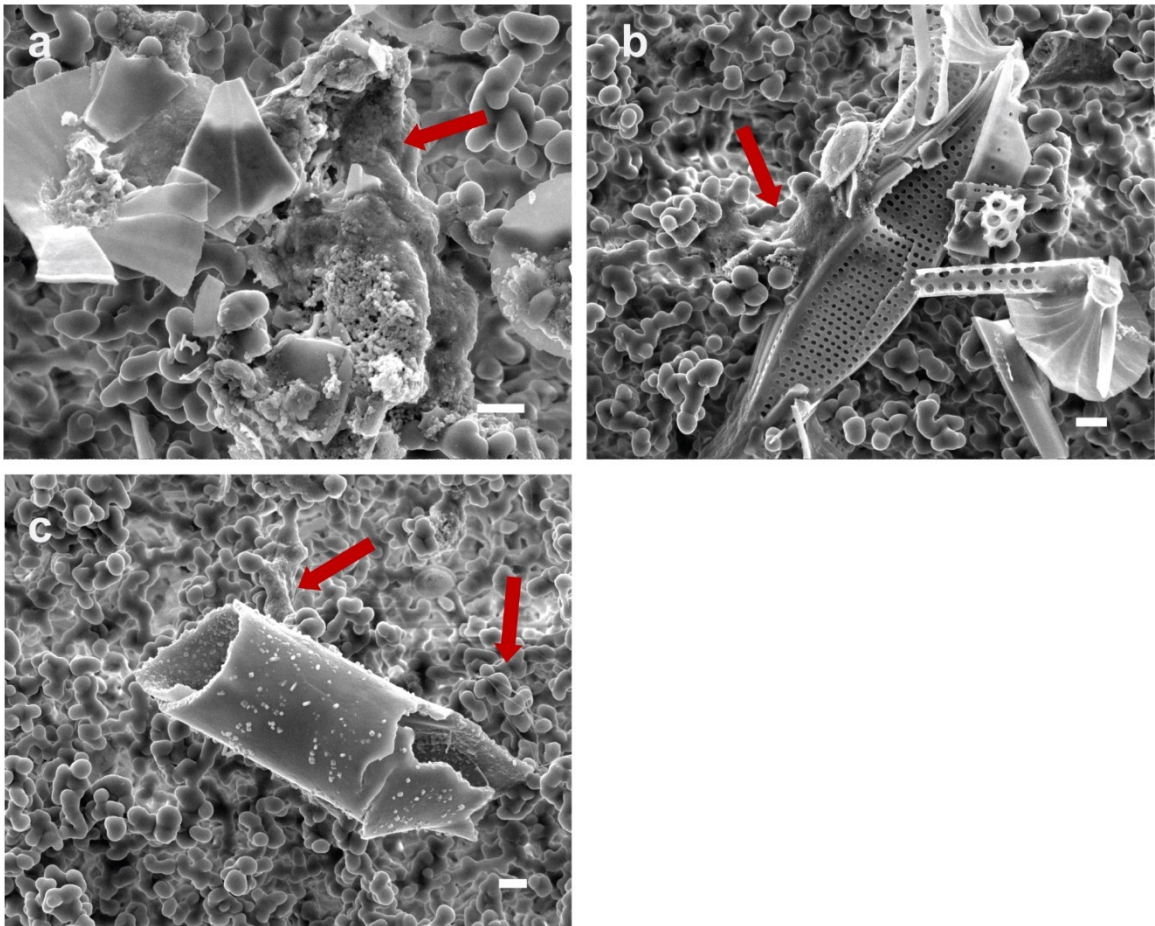


Figure 3.4 SEM images of organic coatings and EPS at Station 25. (a, b) Organic matrices were observed in SEM images at Station 25 (~1350 km from the ridge axis). In some cases, (c) strings of organics that were reminiscent of extracellular polymeric substances were also seen. The red arrows highlight where and how these organic substances appear under SEM. All scale bars are 1 μm .

3.4.2 X-ray Microscopy

Images, total C maps, and total Fe maps for particles collected from Station 21-30, as well as the fluff layer from Station 23, 26, and 30, are displayed in Appendix 2.3, Figures Appendix 2.3.1-2.3.9. Plume particles for Station 18 and 20, and Station 20 fluff layer are previously discussed in Chapter 2 (Hoffman et al. 2018). Overall, particles within the far-field plume, contained Fe particles within C matrices (Appendix 2.3.1-2.3.6). This is distinct from the Fe and C co-location observed within the near-field (Hoffman et al. 2018), and previous buoyant plume observations at EPR 9-10°N (Toner et al. 2009a). At Station 21, rod shaped Fe particles were observed throughout all sample areas investigated (Appendix 2.3.1). This was the only station where that particle morphology was observed. At Stations 23-30, Fe particles decreased in abundance and were

increasingly less associated with C the further from the ridge axis they progressed (Appendix 2.3.2-2.3.6). At Station 30, only one area was able to be investigated and may not fully represent the particle diversity of this station.

Within the sediment fluff layer, Fe particles were observed to be both associated and not associated with POC. A larger abundance of coccolithophores were observed throughout the sediment fluff samples (Appendix 2.3.7-2.3.9). Particle morphology was distinct from that observed in the plume.

3.4.2.1 C 1s and Fe 2p X-ray Absorption Near Edge Structure Spectroscopy

Table 3.1 Approximate energy ranges for primary peaks for C 1s XANES

Name	Bond	Transition	Peak(s) (eV)
Aromatic, quinone	C=O	1s- π^*	283.0–284.5
Alkenes, Aromatic	C=C	1s- π^*	284.9-285.5
Aromatic w/chain and N-substituted aromatic	C–OH C=O R–(C=O)–R' C=N, C–N	1s- π^*	286.0–287.4
Carbonate	CO	1s- π^*	289.9-290.3
Alcohol	C-OH	1s- σ^*	289.3-289.5
Carbonyl	C=O	1s- π^*	287.7-288.6
Aliphatic	C-H	3s- σ^*	287.1-287.4

Sources: Brandes et al., 2004; Lehmann et al., 2009; Nico et al., 2017; Plashkevych et al., 1998.

Carbon 1s XANES were collected on particles from Stations 21-30, as well as sediment fluff layers from Station 23, 26, and 30 (Figure 3.5, Appendix 2.3). Near-field (Station 18 and 20) mid-plume and fluff layers were previously discussed in Chapter 2 (Hoffman et al. 2018) but have been displayed in Figure 3.4 to show spectral diversity through the plume and fluff layers. Spectra were collected from sample areas thin enough to have good X-ray transmitting properties. Principal component analysis (PCA) of the spectral datasets generated by STXM was used to investigate intra-particle C chemistry. Often, the PCA components were composed of spectra having similar chemistry but with different degrees of saturation based on variations in sample thickness. When particles had uniform C chemistry, a single representative spectrum was chosen for analysis and display.

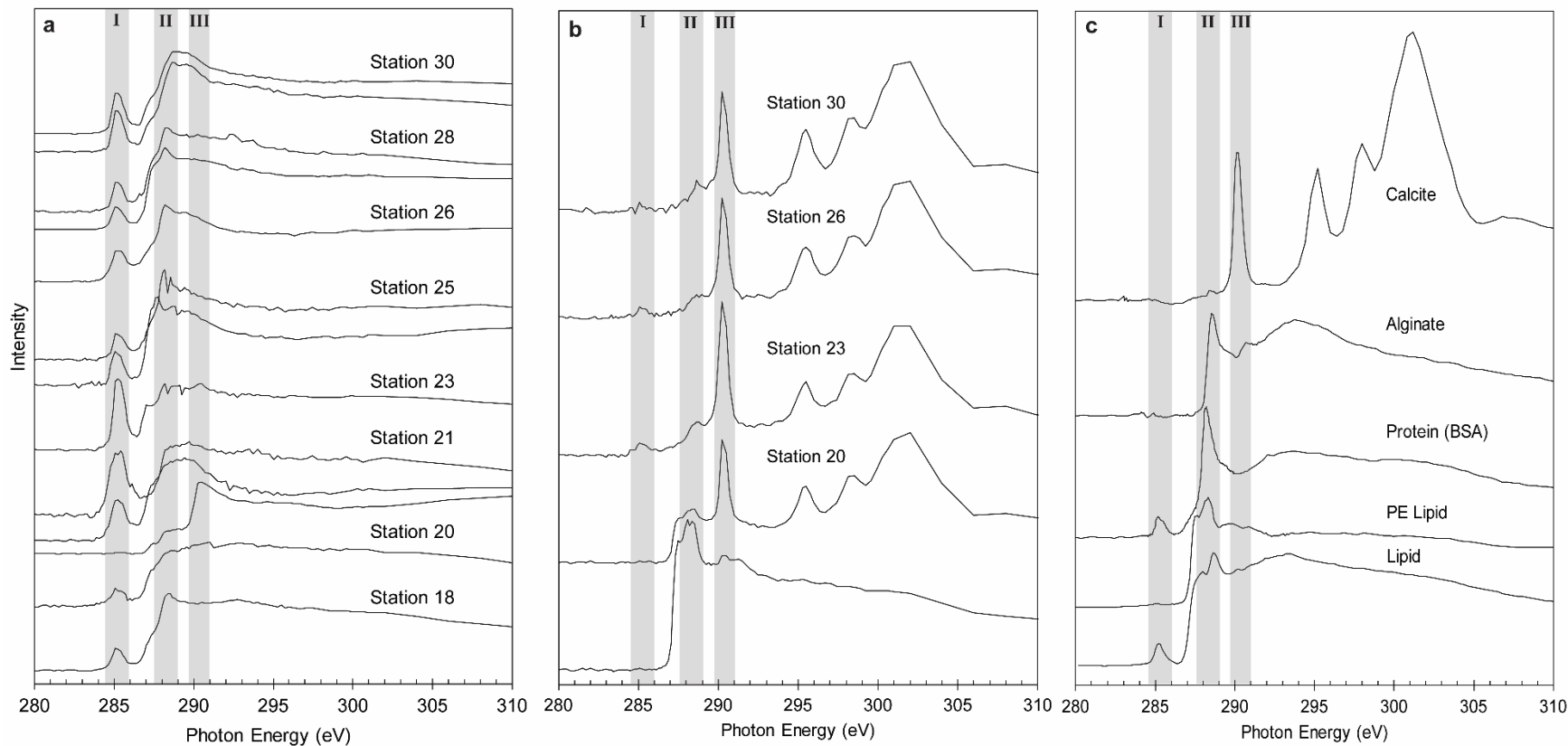


Figure 3.5 Carbon 1s XANES for GP16 plume and fluff layer samples. (a) Carbon 1s XANES spectra from mid-plume particles at Station 18-30 (b) and fluff layer particles at Station 20, 23, 26, and 30 are compared to (c) standards protein (BSA), PE lipid, lipid, alginate, and calcite (Brandes et al. 2010; Chan et al. 2011). The grey bars highlight the ~ 285 eV peak corresponding to the $1s-\pi^*_{C=C}$ transition (I), the region associated with carbonyl functional groups (II), and the 290.0 eV peak associated with carbonate. The plume particles were mostly comprised of organic C, while the fluff layer contained both organic and inorganic C signatures.

Table 3.2 Percentage of carbon functional groups present in the mid-plume GP16 marine particles

Sample Name	Station	GT #	aromatic, quinone (%)	unsaturated, aromatic, alkene (%)	N-substituted aromatic (%)	Aliphatic (%)	Carbonyl (%)	Alcohol (%)	Carbonate (%)	unidentified (%)
Cs069 (cluster 3)	18	8436		1.94			11.85	5.23		80.99
Cs034 (cluster 2)	20	8705	0.44	1.81			15.04		12.94	69.76
Cs016 (cluster 2)	21	8882					4.19		13.41	82.39
Cs042 a3	21	8882		6.33			11.49	1.54		57.44
Cs080 a2	21	8882		9.64	1.13		1.18	17.48		70.56
Cs012 a3	23	9065		7.72		0.96	3.20	29.28		58.84
Cs040 a1	25	9255		2.87		2.44	6.19	25.49		63.01
Cs 043 a3	25	9255		2.13			17.78			80.10
Cs 011 a1	26	9346		3.88		6.67	2.54	13.71		73.20
Cs 150 (cluster 2)	28	9595		1.67		3.30	13.13		25.70	56.20
Cs 150 (cluster 3)	28	9595		2.42			14.85		7.90	74.84
Cs 049 (cluster 2)	30	9838		3.70			17.91		15.28	63.11
Cs 049 (cluster 3)	30	9838		4.14		0.34	15.16	18.62		61.74

- : no XANES data

blank: functional group not present

unidentified refers to broad peaks beyond 290 eV

Table 3.3 Percentage of carbon functional groups present in the fluff layer

Sample Name	Station	GT #	unsaturated, aromatic, alkene (%)	N-substituted aromatic (%)	Aliphatic (%)	Carbonyl (%)	Alcohol (%)	Carbonate (%)	unidentified, secondary peaks* (%)
Cs030 (cluster 3)	20	8767			2.92	15.43		21.92	59.73
Cs030 (cluster 4)	20	8767			0.62	6.23		4.43	88.72
Cs075 (cluster 2)	23	9097	0.76	0.31		3.21		5.88	89.83
Cs111 (cluster 2)	26	9485	0.43		0.46	1.48		4.05	93.59
Cs090 (cluster 3)	30	9867	0.12			0.19	2.37	2.78	94.53

- : no XANES data

blank: functional group not present

unidentified and secondary peaks refers to broad peaks beyond 290 eV. Secondary peaks is specifically referring to carbonate secondary peaks (Brandes et al. 2010).

Table 3.1 reports functional groups and associated peak ranges observed throughout the mid-plume and sediment fluff layers. Specific peaks and spectral shapes are used as a fingerprint to identify C compounds in each sample. Gaussian curve fitting was used to determine changes in functional group moieties within and between Stations (Appendix 2.4). Tables 3.2 and 3.3 show percentages of functional groups that were identified within the mid-plume and sediment fluff layer. Quality of the fits were determined by reduced χ^2 and R-factor values ≤ 0.01 (Appendix Table 2.4.1). Within the sediment fluff layer reduced χ^2 and R-factor values ≤ 0.02 (Appendix Table 2.4.2) were considered a good fit because of the complexity of fitting the secondary peaks of carbonate mineral peaks located within the broad sigma (~ 291 - 305 eV) region of the spectra. The sigma region is needed in order to produce the broad features observed in this region but is rarely able to be interpreted due to the variety of sigma bonds they represent (Nico et al. 2017). These features are notated under the column “unidentified” within Tables 3.2 and 3.3.

Within the plume, carbon speciation varied between and within Stations (Figure 3.5a). However, even with that variability, a few similarities emerged. All Stations contained carbonyl groups (~ 288 eV; 4-18%) which are associated with chemical moieties such as ketones and carboxylic acids. All but one spectrum at Station 21 contain aromatic/alkene groups (~ 285 eV; 1.6-10%). These two features are some of the main components found in proteins, lipids, and polysaccharides (Figure 3.5c). At Station 18, 21-26, and 30, alcohol moieties range from 1.5-30% of the spectra. Carbonate features (~ 290 eV; 7-26%) also appear in Station 20, 21, 28, and 30. Aliphatic carbon, nitrogen-substituted aromatic, aromatic/quinone features all have minor contributions at specific stations through the mid plume.

The C speciation of the sediment fluff layer was more uniform between and within Stations when compared to the mid plume. All Stations contained carbonyl groups (0.2-15%) with carbonate peaks (3-22%). Station 20 contained distinct organic (284 eV-290 eV) and inorganic signatures (290 eV). The organic spectra contain a broad carbonate peak compared to the sharp narrow peaks distinct in the inorganic spectra and all other Stations. The broad carbonate feature could be indicative of a less crystalline phase of carbonate or alteration. At all Stations a combined inorganic-organic carbon signature was seen. Station 23, 26, and 30 additionally contained small inputs of aromatic and

alkene bonds observed around ~285 eV (0.1-0.8%). The organic C signatures seen throughout the fluff layer were similar our lipid and protein standards (Toner et al. 2009a; Chan et al. 2011). All inorganic C signatures were comparable to calcite (Brandes et al. 2010)

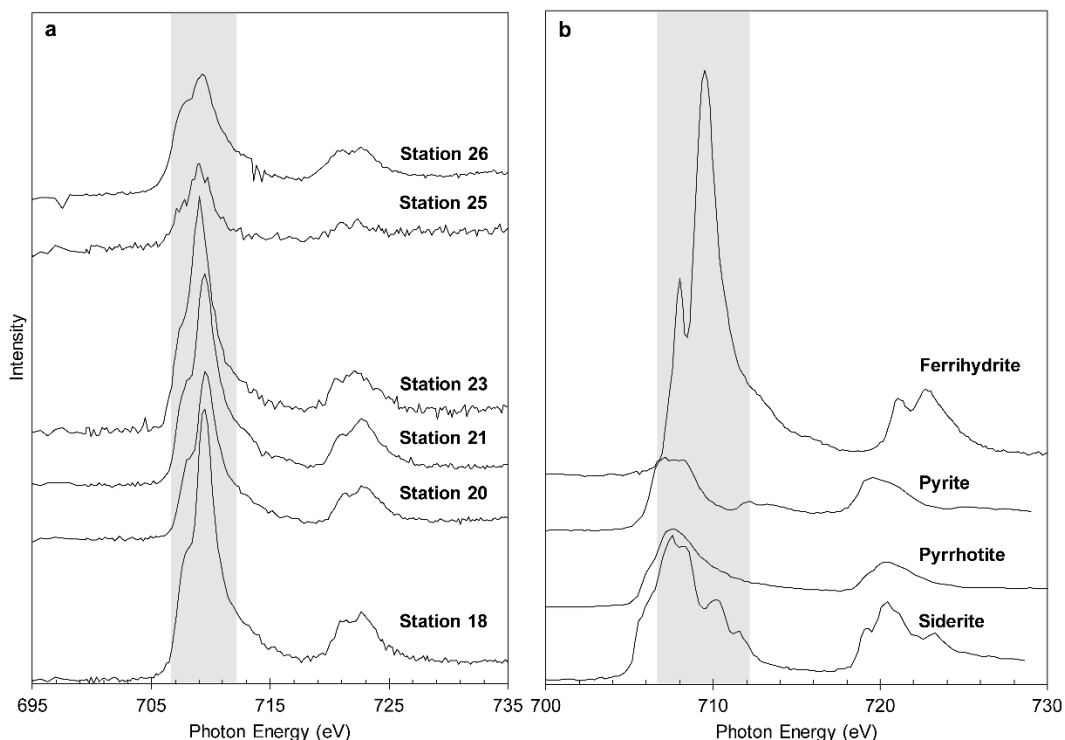


Figure 3.6 Iron 2p XANES in the GP16 mid plume samples. Iron 2p XANES spectra from the mid-plume at Station 18-26 (a) are compared to standards pyrite, siderite, ferrihydrate and goethite. Iron 2p spectra throughout the GP16 plume are most similar to ferrihydrate (Toner et al. 2009a). Identifying features and peaks are highlighted. No Fe 2p spectra were collected for Stations 28 and 30.

Iron 2p XANES spectra for the far-field SEPR hydrothermal plume at Stations 21-28 are displayed in Figure 3.6. Due to a limitation of instrument time, an Fe spectrum was unable to be obtained from Station 30. All spectra have one distinctive peak at 709.6 eV that is consistent with Fe(III)-oxyhydroxides (e.g. Ferrihydrate, Goethite, etc.). Fe 2p XANES are sensitive differences in Fe speciation, but are insensitive to the different in similar mineral groups (e.g. Ferrihydrate vs. Goethite; Toner et al. 2009b; von der Heyden et al. 2012). The results from Station 21-28 are consistent with an oxidized plume dominated by Fe(III)-bearing particles, and no instances of nanoparticulate Fe-sulfides.

3.4.3 X-ray absorption spectroscopy

3.3.1 Particulate Fe speciation through the SEPR hydrothermal plume (Fe 1s XANES, point and bulk EXAFS)

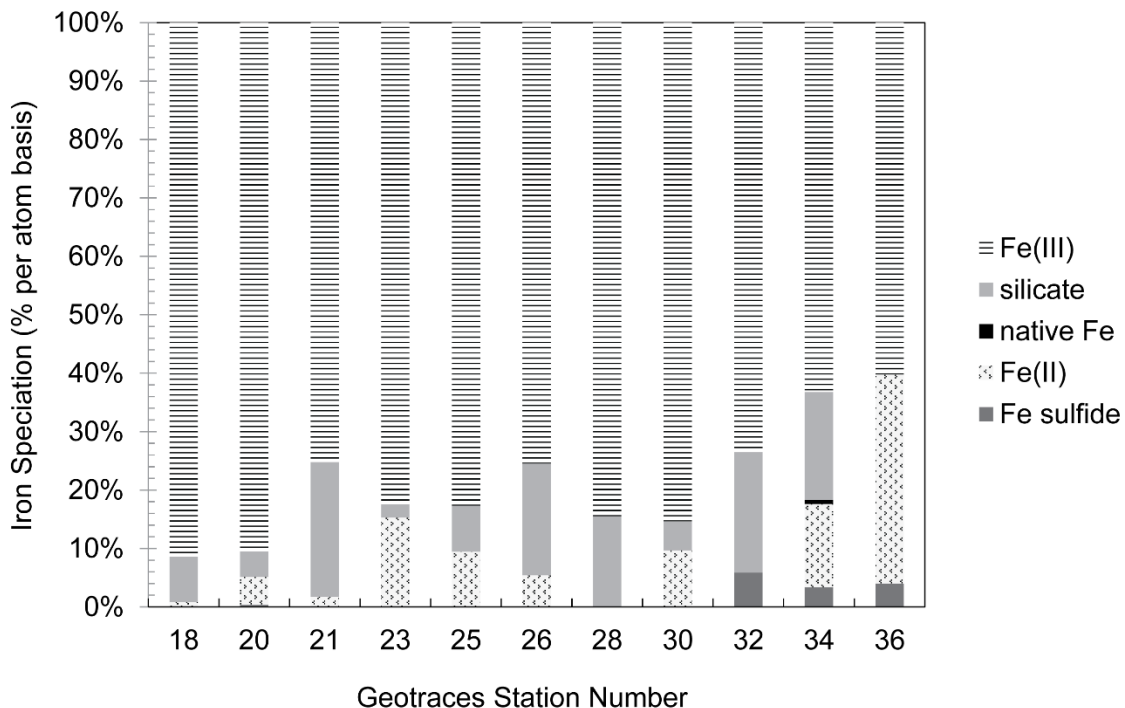


Figure 3.7 Iron 1s XANES speciation of GP16 mid-plume particles. Particulate Fe speciation profiles for mid-plume Stations 18-30. All values were generated by linear least-squares fitting of point-XANES data (Fe 1s absorption edge) and post-analysis binning into broad Fe species groups. These values are sums of Fe species observed divided by the total number of observations; no statistical model applied. Throughout the plume, Fe(III) particles consisted of 60-90% (Appendix Table 2.5.2).

Particulate Fe speciation for Stations 18-36 was determined using Fe 1s XANES, point EXAFS, and bulk EXAFS data (Figure 3.7 and Figure 3.8a). Point and bulk EXAFS were used to define the local coordination environment within samples with a large abundance of poorly-ordered crystalline minerals; such as Fe(III) oxyhydroxides (Newville 2004). Iron 1s XANES is not sensitive to these small variances in mineral structure and is unable to tell them apart. Using these three methods in concert provides the ability to define the mineralogy in samples with a large abundance of similar Fe species (i.e. all Fe(III)). Due to limited time on the instruments, point EXAFS data was only collected at Station 18-30, while bulk EXAFS data was only collected at Station 18, 20, 21, and 25 (Figure 3.8a and Appendix 2.6.1).

Both Fe 1s XANES and EXAFS data were fit using linear combinations of reference materials. For Fe 1s XANES those fit results were binned post-fitting into the following broad categories based on the chemistry of Fe, the geologic setting, and the relative sensitivities of Fe 1s μ XANES into different Fe-bearing phases: (1) Fe(III); (2) Fe(II); (3) Fe sulfides; (4) silicates; and (5) native Fe (Appendix Table 2.5.1). Both Fe(III) oxyhydroxides and Fe(III) phyllosilicates were binned into the Fe(III) category. The categories Fe(II) and Fe sulfides were created to distinguish between Fe(II) oxides, salts, and glasses (hereafter referred to as “Fe(II)”) versus minerals such as pyrite, pyrrhotite, mackinawite, trolite and FeS (hereafter referred to as “Fe sulfides”). “Native” Fe is considered to be a ship/surface ocean contaminant.

Overall, Fe 1s XANES suggests a hydrothermal plume that is oxidized and comprised mostly of Fe(III) oxyhydroxides and Fe(III) phyllosilicates (Appendix Table 2.5.2, Figure 3.7). The near-field (Stations 18 and 20) are dominated by particles that are ~90-92% Fe(III) with only a small percentage of Fe sulfides being detected (<1%) at Station 20. This is in agreement with what has been previously reported in the bulk and particle chemistry of this region of the SEPR hydrothermal plume (Hoffman et al. 2018; Lam et al. 2018; Lee et al. 2018).

Progressing down-plume away from the ridge (Stations 21-36), particles are still dominantly Fe(III) (~60-75%; Figure 3.7, Appendix Table 2.5.2). An increase in percentages of silicates (~2-23%) and Fe(II) bearing particles (~2-36%) from the near-field. Overall, there does not seem to be a distinct pattern or trend represented by the data for these two particle groups between down-plume Stations. Yet, within a down-plume Station, these two particle classes seem to be inverses of each other (i.e. when silicates increase in abundance there is a decrease in Fe(II) bearing minerals phases and vice versa). No sulfides were detected for down-plume Stations 21-30. Iron sulfides were between 4-6% at Station 32-36. The increase in Fe sulfides this far away from the active ridge suggests these are settling reduced sulfur compounds produced by plankton in the upper water column (Durham et al. 2015; Ksionzek et al. 2016; Ohnemus et al. 2016). Bulk chemistry and isotope data from Station 32-36 suggests these regions are expected to be comprised of mostly of background seawater and ligand stabilized dissolved Fe (Fitzsimmons et al. 2017).

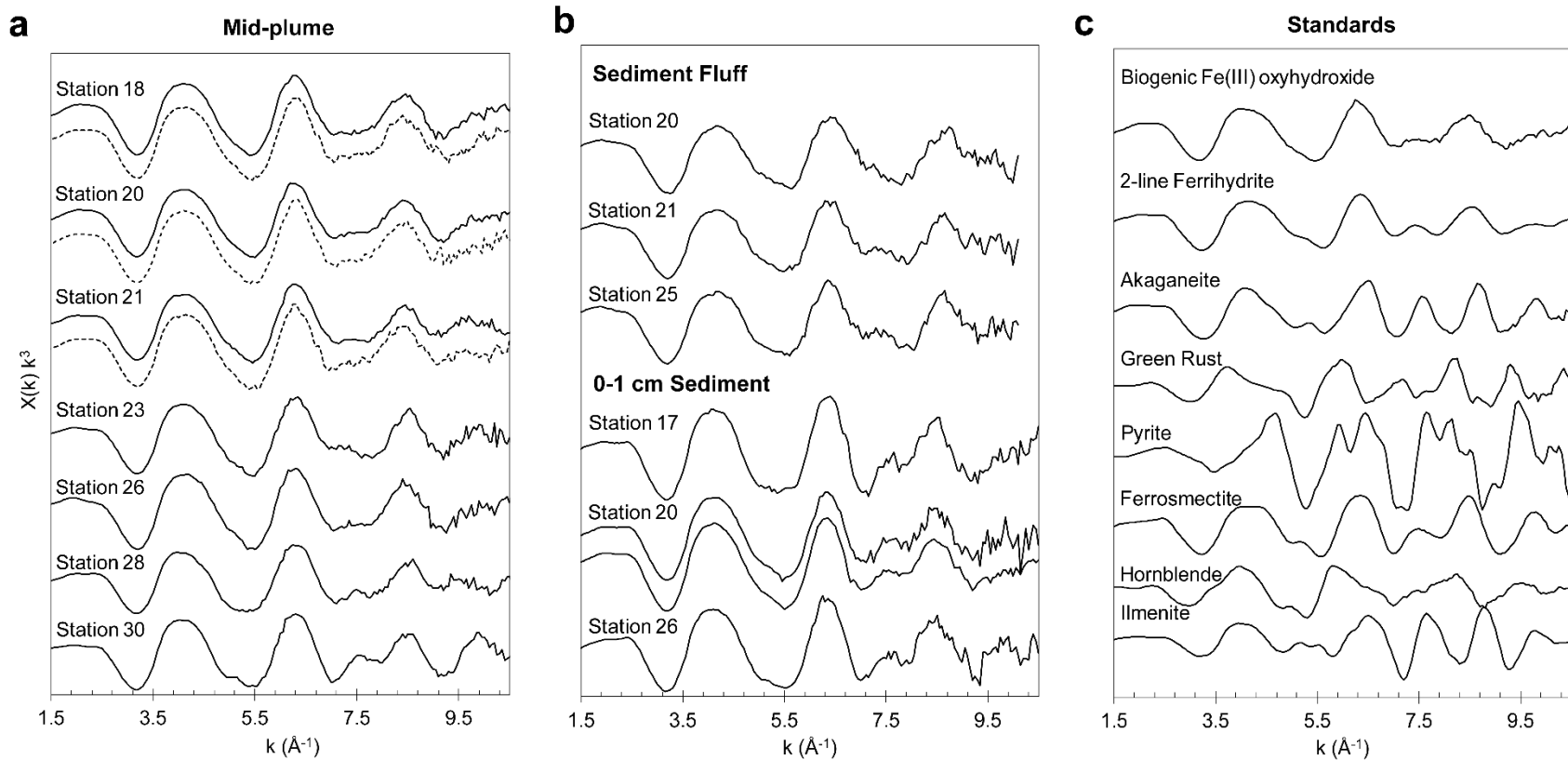


Figure 3.8 Iron EXAFS from the GP16 hydrothermal plume, fluff layer, and sediments. Iron mineralogy was investigated in (a) the mid-plume, (b) fluff layer and 0-1 cm sediments along the GP16 transect. Samples were all fit using linear combination fitting using known (c) standards (Toner et al. 2009b). Plume particles were found to be mostly comprised of biogenic Fe(III) oxyhydroxides, while the fluff layer were mainly 2-line Ferrihydrite and other Fe(III) oxyhydroxides.

For both bulk and point Fe 1s EXAFS the fit results were binned post-fitting into (1) Fe(III)-oxyhydroxide, (2) Fe(III) phyllosilicate, (3) Fe(II, III) hydroxide/oxide, (4) Ti Fe oxide, (5) mica, (6) amphibole, (7) Fe(III) oxide, (8) Fe(II) sulfide, (9) Fe(II) carbonate, and (10) Fe(II) phosphate (Appendix Table 2.6.1). Within Figure 8c, the specific spectra called within these bins are plotted. Where bulk and point EXAFS were both collected at the same Station, there was a high degree of agreement between the fits (Figure 3.8a).

The mineralogy of plume particles at Station 18-26 were ~90% short range ordered Fe oxyhydroxides (e.g. biogenic Fe oxyhydroxide from Toner et al. 2009b). Beyond Station 26, an increase in mineral diversity is seen. Station 28 is predominantly a blend of 2-line ferrihydrite and hornblende (amphibole aka a “silicate”), while Station 30 is a combination of montmorillonite (Fe(III) phyllosilicate), ilmenite (Ti Fe oxide), and green rust (Fe(II, III) hydroxide). In some cases, akaganeite was added in low abundances (<<1%) as an additional Fe(III) oxyhydroxide that was present.

3.4.3.1 Particulate Fe mineralogy of the SEPR Sediment fluff layer and 0-1 cm sediments (Fe 1s bulk EXAFS)

Particulate Fe mineralogy for the sediment fluff layers at Station 20, 21, and 25 and 0-1 cm sediments for Station 17, 20, and 26 was determined using bulk Fe 1s EXAFS (Figure 3.8b). Similar to the plume samples, the fluff layer and sediment samples were fit using linear combination fitting. The bins were similarly binned into the same EXAFS categories as the plume samples (Appendix Table 2.6.1).

All sediment fluff layer samples are dominated by 2-line ferrihydrite (~85-92%). No additional mineral categories were observed within these samples. For the 0-1 cm sediment samples, Station 17 was a mixture of short range ordered (>80%) and crystalline Fe(III) oxyhydroxides (~12%), which suggest settling of plume-like material. Station 20 was a mixture of biogenic Fe oxyhydroxide (~65-80%), 2-line ferrihydrite (~33%), and akaganeite (2-15%), which was slightly more crystalline than the material observed in the plume. Station 26 sediments were comparable to plume samples at Station 28 and 30; a mixture of 2-line ferrihydrite (~80%), hornblende (~21%), and akaganeite (~7%).

3.5 Discussion

3.5.1 *Distal plume zones*

The SEPR hydrothermal plume is one of the largest hydrothermal plumes currently recorded, extending over 4300 km west of the EPR ridge (Resing et al. 2015; Jenkins et al. 2018; Moffett and German 2018). Based upon radioisotopes, bulk chemistry, and our data, the SEPR hydrothermal plume can be broken into three distinct parts. First, we have the near-field hydrothermal plume which consists of Stations 18-21 (0-200 km from the ridge). Residence times for the near-field vary between a month at Station 18 to 5.2-11.1 years at Station 21 (Kipp et al. 2018). Bulk chemistry for this region is dominated by the high concentrations of both particulate and dissolved trace metals commonly found in hydrothermal plumes and fluids (Resing et al. 2015; Fitzsimmons et al. 2017; Lam et al. 2018; Lee et al. 2018). Within this region, over 90% of particulate Fe was lost, while dissolved Fe remained conservative within the plume (Resing et al. 2015; Fitzsimmons et al. 2017).

Next, we have the mid-field hydrothermal plume that consists of Station 23-30 (~800-2700 km from the ridge). Based on the residence times, and the bulk particulate and dissolved Fe (Fitzsimmons et al. 2017; Kipp et al. 2018; Lee et al. 2018), the mid-field region can be further separated into two distinct groups: Station 23 (~800 km) and Stations 25-30 (~1350-2700 km). At Station 23 a dilution in plume material is observed within the particulate and dissolved Fe (Resing et al. 2015; Fitzsimmons et al. 2017; Lee et al. 2018). It is hypothesized to be caused anticyclonic recirculation of plume material (Faure and Speer 2012; Fitzsimmons et al. 2017). A slight dilution is seen with the helium isotope ($^3\text{He}_{xs}$) data, as well, but it is not nearly as distinct at the particulate and dissolved Fe bulk chemistry signatures (Resing et al. 2015; Jenkins et al. 2018). Residence time for Station 23 is around 5.5- >30 years old (Kipp et al. 2018). At Station 25-30 particulate and dissolved Fe increase in concentration, compared to Station 23 (Resing et al. 2015; Fitzsimmons et al. 2017; Lee et al. 2018). Similar to the near-field particulate Fe is exponentially lost versus dissolved Fe being conserved over the 1350 km range between Station 25-30 (Resing et al. 2015; Fitzsimmons et al. 2017). Residence time for varies between 2.7-5.4 years old at Station 25 to 4.2-13.6 years old at Station 28, suggesting input of a younger hydrothermal source (Kipp et al. 2018). Rates for deep

ocean currents and $^3\text{He}_{\text{xs}}$ contractions for this region suggests that plume material could comprised of material from vents further south of EPR 15°S (Resing et al. 2015; Kipp et al. 2018). Radium data was not collected from beyond Station 28, and therefore, individual residence times will not be able to be reported for Station 30 or the fair-field hydrothermal plume.

Lastly, we have the far-field plume which consists of Station 32-36 (~3300-4300 km). Iron isotope data and Fe speciation discussed below (Section 3.3) suggests this region is mostly made up background seawater and ligand complexed dissolved Fe (Fitzsimmons et al. 2017). Overall, plume resistance time from the ridge axis (Station 18) to Station 36 is expected to be between 20-70 years (Fitzsimmons et al. 2017; Moffett and German 2018).

3.5.2 *Distal plume particle morphology and carbon chemistry*

Within the near-field non-buoyant plume, nanoparticle aggregates were the most abundant particle form observed. At Station 18 and 20, plume particles were dominated by aggregates with a high degree of Fe-C co-location (Hoffman et al. 2018). This was similar to previous investigation of Fe:C speciation of hydrothermal plume particles at EPR 9-10°N (Toner et al. 2009a). Yet, at Station 21, a distinct change in particle morphology was observed. Elemental maps and SEM images showed mixtures of nanoparticle aggregates and rod-shaped particles (Figure 3.1d; Appendix 2.1.1-2.1.3, 2.3.1). This indicates a transition point in physiochemical form of particulate Fe from nanoparticle spheres to rods within the SERP hydrothermal plume (Fitzsimmons et al. 2017). It should be noted that Station 21 was the only location throughout the SEPR hydrothermal plume to observe rod shaped, Fe-rich minerals (Figure 3.1d; Appendix 2.3.1). Alteration through STXM sample preparation and analysis as well as increase particle crystallinity in SEPR plume material are both potential sources for the morphological changes observed. However, given no beam damage was detected and the rod-shaped minerals were also observed on the SEM imaged PES filters (Figure 3.1d), it is unlikely the STXM preparation and analysis influence morphological changes at Station 21. Moreover, unlike particles at Station 18 and 20, Fe particles at Station 21 were encased in C-rich matrices (Appendix 2.3.1). These Corg embedded Fe particles

would be expected to have an overall low specific gravity, allowing them to persist in the non-buoyant plume for 100-1000s of kilometers (Fitzsimmons et al. 2017). These matrices were comprised multiple Corg signatures (Figure 3.5a) different from those observed at Station 18 and 20 (Hoffman et al. 2018). While the spectral signature within and between Station 18 and 20, and Station 21 were distinct from each other, the same types of functional groups were routinely observed at all three Stations. This implies a high affinity for molecules with those functional groups to bond with plume material.

In the mid-field SERP hydrothermal plume, nanoparticle aggregates similar to Station 18 and 20 were observed at Station 25-30 (Appendix 2.1.1-2.1.3, Appendix 2.1.5-2.1.8), but not at Station 23. The distinct carbon spectral signatures (rich in aromatic carbon) and particle morphologies present at Station 23 (Appendix 2.1.4, 2.3.2, Figure 3.5a) suggest these particles are unique from other places in the plume. Station 23 is where there is an observed dilution in the SEPR hydrothermal plume potentially caused by anticyclonic currents (Resing et al. 2015; Fitzsimmons et al. 2017; Lee et al. 2018). At Station 25-30 the nanoparticle aggregates become less abundant in micrographs and are diluted with other particle types (e.g. diatoms and other sinking upper water column material) as samples increase in distance from the ridge axis (Figure 3.1). Particle morphologies from Station 25-30 indicate a mixtures of plume derived materials and sinking POC from the overlying water column (Appendix 2.1.5-2.1.8). Diatoms and other decaying biological materials contain distinct morphologies from plume material and have been observed at other hydrothermal field sites (Brandes et al. 2004; Abramson et al. 2009; Toner et al. 2009a; Hoffman et al. 2018). This is consistent with radium isotope data suggesting the age of plume material at Station 25 is comparable to Station 20 and is sourced from a hydrothermal venting further south (Kipp et al. 2018). Additionally, material looking similar to extracellular polymeric substances (EPS) and biofilms is observed throughout Station 25 (Figure 3.4). EPS is associated with active biological communities and is comprised of a variety of different biomolecules (e.g. polysaccharides, proteins, nucleic acids, etc.; Lawrence et al. 2003). Given the distance from the ridge (~1350 km) and depth of the plume (~2500 km), entrainment of surrounding microbial communities from deep ocean water would be expected to be one of the dominant source of this material at Station 25. Unlike buoyant or near-field non-buoyant plumes entrainment of biological

material from active vent fauna would not be expected this far away (~1350 km) from the vent ridge (Toner et al. 2009a; Breier et al. 2012; Dick et al. 2013; Hoffman et al. 2018). Carbon spectra signatures at Station 25 do show lipid-like compounds present (Figure 3.5a,c). But due to some peak shifting and widening features within the spectra are not expected to be pure samples. This suggests either degraded lipid compound or a mixtures with other organic compounds. Progressing down plume to Station 26-30, decreases in particle size and Fe-C associations (Appendix 2.3.4-2.3.6) suggest physiochemical changes (e.g. surface charge, sorption capacity, etc.; Essington 2004) and settling of larger aggregates at known Stokesian settling rates within the plume (Breier et al. 2012; Fitzsimmons et al. 2017). Similar to Station 25, carbon spectra signatures for Station 26-30 suggest mixtures of lipid-like compounds and other organics (Figure 3.5a,c).

Carbon chemistry within all near-field and mid- plume particles is most consistent with Corg. Carbonyl groups and aromatic C are two of the most commonly detected Corg functional groups (Table 3.1) within particles in the near-field (Hoffman et al. 2018) and mid-plume SEPR hydrothermal plume (Table 3.2). Carbonyl groups and aromatic rings are found in many different biological and chemical compounds (e.g. ketones, phenols, amides, carboxylic acids, proteins, polysaccharides, etc.) that make up POC (Lehmann et al. 2009; Toner et al. 2009a; Bennett et al. 2011b). Within organic matter, proteins are a special group of compounds called an amphiphile. An amphiphile is a compound that contains both polar and nonpolar region and can electrostatically bond with minerals through organic amides and other charged functional groups to protect minerals from biological alterations and uptake over long time periods (Wershaw 1993; Kleber et al. 2007). The abundance of carbonyls and aromatic structures observed throughout Station 18-30 indicate these are important functional groups for POC-mineral interactions and transport throughout the SEPR hydrothermal plume (Table 3.2, Appendix 2.4.1-2.4.12). However, in complex environmental mixture like our samples, C XANES is not sensitive enough in determining the exact compound chemical compound present. We mostly likely, have mixtures of biological materials, organic acids, and ligands which have all been observed at hydrothermal vents (Toner et al. 2009a; Dick et al. 2013; Li et al. 2014; McDermott et al. 2015; Buck et al. 2018). Further investigations in the chemical composition (i.e. nitrogen and oxygen speciation) of these materials will provide

important insight into which materials the abundance and diversity of certain compounds with POC in hydrothermal plumes.

Inorganic C was occasionally detected in plumes samples from Station 20, 28, and 30. This would suggest entrainment of underlying sediments or settling biological material from the surface ocean. While both are possible for Station 20, entrainments of underlying sediments are highly unlikely for the Station 28 and 30 given the depth of the plume and bulk chemistry (Fitzsimmons et al. 2017; Lam et al. 2018; Lee et al. 2018). Additionally, unlike the sharp peaks for the sediment fluff samples, the inorganic C peak ~290 eV was broad for all the plume samples. This indicates inorganic C is either a small component or that the complexity of this bonding environment represents multiple bonds that were not captured through Gaussian curve fitting (Lehmann et al. 2009; Nico et al. 2017).

3.5.3 *Iron(III)-oxyhydroxides dominate particulate iron speciation*

The particulate Fe in the SEPR hydrothermal plume is comprised of mostly oxidized Fe(III) (Appendix Table 2.5.2). Particulate Fe speciation in the SEPR hydrothermal plume is predominately short-range ordered Fe(III) oxyhydroxides (Figure 3.8a,c), similar to the biogenic Fe oxyhydroxides observed at Juan de Fuca (Toner et al. 2009b).

Iron(III) oxyhydroxides are a mineral group that contains a wide variety of crystallinity. On a spectrum, ferrihydrite is on one extreme and is generally considered thermodynamically unstable and poorly ordered under standard conditions. On the other end would be goethite which is thermodynamically stable and crystalline under standard conditions (Cornell and Schwertmann 2003; Kukkadapu et al. 2003). The crystal strength of the Fe(III) oxyhydroxide mineral structure is determined by the specific arrangements of Fe and oxygen (O) bond (Essington 2004; Toner et al. 2009b). Multiple configurations are possible depending on the rate and how the Fe oxyhydroxide mineral is precipitated as well as sorption of organic and inorganic ligands present within the solution (Cornell and Schwertmann 2003; Kukkadapu et al. 2003; Toner et al. 2009b). In controlled laboratory experiments the aging of 2-line ferrihydrite to an Fe oxide is conducted by decreasing the surface area and increasing Fe-O-Fe bonds through consolidations of the hydroxylated bonded sites (Kukkadapu et al. 2003).

Biogenic Fe oxyhydroxide mineral crystal structure consists of edge sharing octahedrals in a two-dimensional structure, which is even more poorly ordered than 2-line ferrihydrite and other members of the Fe(III) oxyhydroxide mineral family (Toner et al. 2009b). The less structural order therefore corresponds to less crystallinity than other Fe oxyhydroxides (Toner et al. 2009b). Under standard conditions, this is not a stable phase for Fe to thermodynamically persist in for a few minutes, let alone 1000 of kms in hydrothermal plumes (Cornell and Schwertmann 2003; Navrotsky et al. 2008). However, organic or inorganic ligands have been shown decrease the rate of more stable structural features in aqueous solutions (Toner et al. 2009b), which aid in transporting hydrothermal Fe over long distances.

Sources for organic and inorganic ligands within plumes included (1) entrainment microbial communities, sediments and vent biota, (2) production of biological compounds by *in-situ* microbial communities, (3) mixing of deep ocean water and sinking POC from the surface waters, and (4) abiotic synthesis (Bennett et al. 2011b; Dick et al. 2013; German and Seyfried 2014; Li et al. 2014; McDermott et al. 2015). As hydrothermal fluids undergo the kinetically rapid mineral formation, dilution (1000:1) and cooling in the buoyant plume, entrainment of biologically rich diffuse flow fluids and organics from hydrothermal chimney walls have been observed to be intimately associated with the speciation of Fe in the plume (Toner et al. 2009a; German and Seyfried 2014; Baker et al. 2016). Moreover, POC-mineral complexes and ligands produced by microbial communities have been shown to be associated with Fe within the non-buoyant plume (Sander et al. 2007; Bennett et al. 2011b; Li et al. 2014). From these observations along with frequency of Fe:C associations in the distal plume elemental maps (Appendix 2.3.1-A2.3.6), it is reasonable to assume organics within the SEPR hydrothermal plume are inhibiting the formation of crystalline Fe(III) oxyhydroxides over 1000s km (Figure 3.8).

Beyond Station 26, increased crystallinity and mineralogical diversity is observed. Mixtures of Fe silicates, Fe(III) phyllosilicates, Fe(II) hydroxides and Fe(III) oxyhydroxides are present both at Station 28 and 30 (Figure 3.8). Iron and C elemental maps (Appendix 2.3.4-2.3.6), as well as, SEM images (Figure 3.1g-i, Appendix 2.1.6-2.1.8) indicate less association with Corg and decreases in Fe particle size. Bulk

chemistry data suggests, particles at these Stations are predominantly partitioned into the small size fraction (SSF, 0.8–51 μm) versus the large size fraction (LSF, >51 μm) observed at Station 18 and 20 (Lee et al. 2018). Smaller Fe particles will aid particulate Fe's ability to travel 1000s of kms into the ocean interior (Yücel et al. 2011; Gartman et al. 2014).

While small particle size could be advantageous to the longevity of particulate Fe within hydrothermal plumes (Yücel et al. 2011; Gartman et al. 2014), the decrease in Fe:C associations have seemed to have also increase the alterations experienced by Fe in the mid-field SEPR hydrothermal plume. As stated above, Fe(III) oxyhydroxides are thermodynamically unstable when compared to mineral phases such as goethite at neutral pH and oxic conditions (Cornell and Schwertmann 2003; Kukkadapu et al. 2003; Brandt et al. 2012). At Station 18-26, the presence of Corg matrices seems to have slowed the formation of more stable Fe oxyhydroxide crystal structures within the SEPR hydrothermal plume. However, at Station 28 and 30, Fe oxyhydroxides begin to experience recrystallization of O-Fe-O bonds into more stable Fe phases and decreasing the surface area for Corg to sorb. Iron isotope data from the SEPR hydrothermal plume suggests Fe oxyhydroxides in the near and mid-plume diminish and mix with the dissolved Fe phase, releasing organically bound Fe(III) into the dissolved Fe pool through reversible dissolved-particle exchange (Fitzsimmons et al. 2017). This process could account for the increased structural order and alterations observed in Fe oxyhydroxide mineral phases at Station 28 and 30.

Iron-sulfides were only detected at Station 20 (Hoffman et al. 2018) and far-field Stations 32-36 (~3200-4300 km). Bulk chemistry and isotope data from Station 32-36 suggests particles from these Stations are expected to be comprised of mostly of background seawater and ligand stabilized dissolved Fe (Fitzsimmons et al. 2017). Given the lack of sulfides detected elsewhere in the plume and distance from the venting ridge, the sulfides are most likely reduced sulfur compounds settling from the surface waters (Durham et al. 2015; Ksionzek et al. 2016; Ohnemus et al. 2016). As for the lack of sulfides closer to ridge, previous studies also found that plume particles above 17°20'S were Fe-rich and sulfur poor (Feely et al. 1996). Particulate sulfur was variable in these regions meaning the vent could be comprised of low particulate sulfur fluids (Feely et al.

1996; Hoffman et al. 2018). Additionally, particle size ($> 0.2 \mu\text{m}$), or preferentially removal through oxidation and settling processes before the SEPR hydrothermal plume reached Station 18 could have also contributed to sulfides not being detected (Hoffman et al. 2018). Due to the isotopically heavy dissolved Fe observed through the plume, colloidal Fe sulfides are not expected to be present within the plume (Fitzsimmons et al. 2017) suggesting particle size has little impact on the lack of Fe sulfur detected. On the other hand, radium isotopes indicate the plume is around a month old at the Station 18 and 2.4-5.5 years old at Station 20 (Kipp et al. 2018). When compared to plume samples collected at buoyant hydrothermal plumes that are hours to days old, a month is enough time for Fe-sulfide particles to settle out of the plume and undergo oxidation processes (Gartman and Luther III 2014). Studies investigating endmember fluids of vents along EPR 15°S will aid in evaluating current processes observed in the non-buoyant plume.

3.5.4 Iron and carbon speciation of settling plume material

Similar to the fluff layer at Station 20 (Hoffman et al. 2018), the distal plume sediment fluff layers (Stations 23, 26, and 30) were a mixture of Corg (POC) and inorganic C (PIC). The plume samples were enriched in Corg compared to the sediment fluff layer. Carbonyl groups were again one of the most common detected functional groups observed, suggesting mixtures of biological material and carbonate settling from the overlying water column (Table 3.3). PIC:POC ratios increased with depth in both the SSF and LSF along the SEPR hydrothermal plume, indicating the shorter time scales for remineralization of POC compared to PIC (Hoffman et al. 2018). Besides the slight enrichment of POC at Station 18 and 20, no increase of POC was observed mid-plume at Stations 21-36 (Hoffman et al. 2018; Lam et al. 2018). Similarly to the near field, all sediment fluff layers are above the calcite saturation horizon, meaning the PIC:POC ratios will increase due to respiration of POC. Morphologically, the sediment fluff layer samples for Station 23, 26, and 30 are all very similar to each other, but distinct from the particles seen in the plume (Appendix 2.3). They all contain coccolithophores and other settling particles from the upper water column (de Vargas et al. 2007). These morphologies were also observed at Station 20 (Hoffman et al. 2018).

Both Fe 1s XANES and EXAFS results for the sediment fluff layer and 0-1 cm sediments are consistent with chemically oxidized Fe(III) minerals. The Fe mineralogy in all the fluff samples are dominated by 2-line ferrihydrite, a more crystalline form of biogenic Fe oxyhydroxide then seen within the plume. This suggests settling Fe particle undergo recrystallization of the O-Fe-O bonds within the fluff layer before settling and becoming buried in the sediments.

The 0-1 cm sediments underlying the plume contain Fe mineral mixtures reminiscent of overlying plume material. At Station 20, particles were mixtures of biogenic and Fe(III) oxyhydroxides, while at Station 26 Fe(III) oxyhydroxides (i.e. 2-line ferrihydrite) and hornblende were abundant. At Station 26-28 there is slight particulate benthic nepheloid layer with higher concentrations of particulate Fe (Fitzsimmons et al. 2017). Given the mineralogy of Station 26 is more similar to plume particle at Station 28 and 30, it is possible that these materials were resuspended, altered, and resettled by seafloor eddies (Adams et al. 2011; Zhang et al. 2014). Therefore, it is possible the underlying sediments do not represent particles directly settled from the overlying water column, but in fact, particles from a within a specific range of settled material. No sulfides were detected in our fluff layer of 0-1 cm samples.

3.6 Conclusion

We have investigated the speciation of Fe and C within the ~4300 km long SEPR hydrothermal plume and underlying sediments. This is the first time hydrothermally influenced particulate Fe has been observed and characterized this far away from a venting ridge. Within the plume, particulate Fe was mainly comprised of short-range ordered Fe oxyhydroxides and Corg mineral aggregates. The Corg is sourced from entrained of deep ocean water, settling POC from the overlying water column, and/or produced of biochemical molecules by *in-situ* microbial communities. In the near and mid-field plumes, these Corg associations with Fe were observed to slow the settling rates and structural growth of Fe oxyhydroxide mineral, potentially through reversible exchange with organically bound dissolved Fe. Conversely, in the far-field plume (>2700 km from the ridge axis) and underlying sediments, Fe was less association with Corg which lead to an increase in structural order and diversity of particulate Fe mineral

phases. If the results here are representative of global hydrothermal systems, Corg plays an integral role in the transport and longevity of non-buoyant hydrothermal Fe into the ocean interior. Future long-range non-buoyant plume studies at additional hydrothermal vent sites and development of models to the proposed mechanisms between the dissolved-particulate Fe phases will enable us to evaluate the impact of hydrothermal vents on the global Fe cycle.

CHAPTER 4

Characterizing aquatic NOM in settling plume material at East Pacific Rise 9°50'N

This chapter is modified from the following manuscript:

Hoffman, C.L., Sims, R., Rouxel, O., German, C.; Dynes, J.; Reginer, T., Gillespie, A., Toner, B.M. Characterizing aquatic NOM in settling plume material at East Pacific Rise 9°50'N. in prep.

4.1 Overview

Natural organic matter (NOM) aids in the transport and uptake of essential micronutrients in both marine and terrestrial environments. At hydrothermal vents, aquatic NOM was observed to increase transport and longevity of iron (Fe) into the ocean interior. This is important given Fe is a growth limiting nutrient for microscopic life, but most of the ocean is Fe poor. Increased transport of hydrothermal Fe could lead to an increase in ocean primary production and a carbon sink. However, characterization and mechanisms for aquatic NOM-mineral interactions are still highly debated and poorly understood. Here, we describe the organic chemical composition of settling hydrothermal plume material in order to enhance our understanding of the role of aquatic NOM in transporting hydrothermal Fe. Descending plume particles were collected using sediment traps at two vents, Bio9 and Ty-10, along the East Pacific Rise (EPR) 9-10 N. Bulk carbon, nitrogen, and oxygen X-ray absorption near edge spectroscopy (XANES) was used to investigate the chemical composition of aquatic NOM within plume particles. The aquatic NOM of descending plume material was mostly comprised of amphiphilic-rich compounds, such as amino acids and carbonyl groups. When interacting with minerals in soil, amphiphiles have been shown to create membrane-like coatings that protect minerals from degradation and oxidation processes. Thus, amphiphilic-rich aquatic NOM could play a significant role in protecting the oxidation state of hydrothermal Fe as it is carried away from the venting ridge into the ocean interior.

4.2 Introduction

Natural organic matter (NOM) affects the physical and (bio)chemical properties of marine and terrestrial environments (Hedges et al. 2000; Essington 2004; Hansell et al. 2009; Schmidt et al. 2011). NOM is comprised of three distinct pools of organic compounds mainly made up of carbon (C), nitrogen (N), and oxygen (O). The first, biomass, is comprised of living organisms, their metabolic byproducts, and organic compounds (e.g. ligands, enzymes, etc.) used to uptake nutrients (Essington 2004; Kleber et al. 2007). Additionally, cell death and lysis can also release biochemical compounds into the extracellular environment (Essington 2004). Secondly, humic and non-humic substances affect the buffering capacity, sorption of organic compounds, and

stability of particles. Humic substances, such as fulvic acid and humic acid have been shown to be vital in protecting and impacting the bioavailability of minerals in aquatic and soil environments (Wershaw 1986; Zhou et al. 1994; Repeta et al. 2002; Sutton and Sposito 2005; Gledhill and Buck 2012). The final group is comprised of organic residues. Organic residues are undecayed or partially decayed organic materials (e.g. phytoplankton, etc.; Essington 2004). Individually each of these pools contains distinct chemical compounds and structures (Essington 2004). While no one comprehensive structure currently exists for NOM, these known structures of organic compounds have and continue to inform researches about the chemical signature and elemental abundances detected in the composition of NOM (Schulten and Schnitzer 1997; Leenheer et al. 1998; Kubicki and Aplitz 1999; Hedges et al. 2000; Kujawinski et al. 2002; Repeta et al. 2002; Gledhill and Buck 2012). Furthermore, it is also important to consider environmental conditions (e.g. pH, temperature, etc) of the system. Temperature, pH, and other physical characteristics can alter the distribution of functional groups present in NOM and the reactivity with mineral surfaces (Oades 1984; Oades 1988; Curtin et al. 1998; Leenheer et al. 1998; Essington 2004). Characterization of the structure of NOM across different environments is still a very active area of research.

Over the years, researchers have discovered key trends that describe NOM characteristics and its ability to impact transport of minerals (Wershaw 1993; Knicker and Hatcher 1997; Kleber et al. 2007). The first is that the large quantities of NOM molecules are amphiphilic, have a non-polar and polar region, or have amphiphilic tendencies (Wershaw 1986; Wershaw 1993; Essington 2004; Kleber et al. 2007). Secondly, these organic compounds seem to have an affinity to self-assemble, allowing the NOM to shield the hydrophobic region from water within the environment and leave the charged outer layer to interact with cations, mineral surfaces or other organics (Kleber et al. 2007). There are three zones that have been proposed when NOM interacts with a mineral surface (Wershaw 1993; Kleber et al. 2007). These zones are the contact zone, zone of hydrophobic interactions, and kinetic zone. Each varies in thickness depending on the mineral it is bonding with (Kleber et al. 2007). The contact zone is where the NOM interacts with a mineral surface. Here, the outer layer of NOM binds to minerals through electrostatic interactions (i.e. a positive mineral surface would interact with negatively

charge NOM). The hydrophobic zone is believed to have freedom of motion and shields the hydrophobic portions of the organic molecules (Wershaw 1993; Kleber et al. 2007). The kinetic zone is the area where the bonded NOM can further interact with its surrounding environment. These are all important features that aquatic NOM could utilize to aid in transporting hydrothermal particles in the ocean interior and protect them from oxidation processes.

Multiple studies within the past decade have shown the important role of aquatic NOM in transporting hydrothermal particles and sequestering C to the seafloor (Toner et al. 2009a; Holden et al. 2012; Breier et al. 2012; German et al. 2015; Fitzsimmons et al. 2017; Hoffman et al. 2018). Moreover, aquatic NOM has also been shown to play a vital role in the bioavailability and uptake of key nutrients, such as iron (Fe), for biological growth (Gledhill and Buck 2012; Li et al. 2014). Given that Fe is an essential micronutrient to support life and the majority of the ocean is Fe poor, aquatic NOM could be essential in transporting nutrients to otherwise depleted locations (Gledhill and Buck 2012; Moore et al. 2013; Fitzsimmons et al. 2014; Tagliabue et al. 2017). However, only a few studies have examined the mechanisms and chemical composition of aquatic NOM in marine environments (Hedges and Keil 1995; Hedges and Oades 1997; Hedges et al. 2000; Repeta et al. 2002; Aufdenkampe et al. 2009). At East Pacific Rise (EPR) 9-10°N, aquatic NOM has been observed to protect Fe minerals from oxidation (Toner et al. 2009a). Aquatic NOM-mineral aggregates, rich in aromatic, and carbonyl moieties, have also been observed along the EPR (Toner et al. 2009a; Hoffman et al. 2018). These aquatic NOM-mineral aggregates are generally seen as less dense and can be carried over long distances, which aids in the transport of reduced Fe into the ocean interior and potentially be utilized by microorganisms and/or planktonic life (Breier et al. 2012; Tagliabue et al. 2017). This begs the question: What are the most abundant organic compounds in aquatic NOM and how does that impact its ability to protect and transport Fe in hydrothermal plumes? In this chapter, we investigated the C, N, and O speciation of settling hydrothermally-influenced aquatic NOM to gain insight into the essential organic compounds integral in transporting hydrothermal particle.

4.3 Methods

4.3.1 Sample Collection

Descending particles were collected from the non-buoyant hydrothermal plume near Bio 9 (9°50.291'N; 104°17.488'W) and Ty-Io (9°50.099'N; 104°17.509'W) vents using a 21-position time-series sediment traps deployed ~ 5 m above the seafloor (~2500 m). Samples were collected every 6 days continuously from July 1 to November 4, 2006 (“LADDER 1” series, Traps R1 and R2). Trap R1 was located ~ 30 m southwest of the Bio9 vent complex within the axial summit (Rouxel et al. 2008; Rouxel et al. 2016). Trap R2 was located outside the axial summit caldera, 115 m southwest of Ty-Io black smoker vents (Rouxel et al. 2016). Before the deployment, the 250 ml polyethylene sample cups were filled with a 20% dimethyl sulphoxide (DMSO) and 4% NaCl solution buffered to pH 9.0 ± 0.5 to stop all biological activity within the samples, retaining sample integrity for mineralogical, geochemical and molecular microbiological investigations. Upon trap recovery, each sample cup was capped and refrigerated at 4°C. Oxygen was present during sample collection, storage, processing, and analysis. Dissolved oxygen concentrations were inferred to be between saturation and the EPR ambient concentration of $\sim 100 \mu\text{mol kg}^{-1}$ (Field and Sherrell 2000b; Toner et al. 2009a). For X-ray absorption near edge structure (XANES) spectroscopy analysis, 10 ml subsamples were drawn from each trap bottle under sterile conditions. The 10 ml subsamples were rinsed of DMSO and NaCl using a glass filtration apparatus fitted with 25 mm 0.2 μm polycarbonate filters. The subsamples were introduced to the filtration apparatus, filtered using either laboratory or hand-pump vacuum, and rinsed with approximately 10 μl of purified water. Rinsed subsamples were stored as 1 mL suspensions for XANES analyses. Subsequently, all remaining sediment trap sample processing was conducted using standard methods established for sediment trap analyses (Honjo et al. 1995).

4.3.2 Bulk X-ray absorption spectroscopy

Bulk carbon (C), nitrogen (N), and oxygen (O) 1s XANES spectra were collected at the Canadian Light Source (CLS) for fine particles associated with the sediment traps at Bio9 and Ty-Io vents. The bulk C, N, and O 1s XANES were collected at the CLS High Resolution Spherical Grating Monochromator (SGM) beamline. The sample suspensions

were applied to gold-coated silicon-chips as an aqueous droplet under ambient temperature and atmosphere, allowed to dry, and placed in the SGM vacuum chamber. Sample analysis parameters were chosen to: (1) prevent photon-damage to the sample, (2) collect data representative of the sample, and (3) improve signal-to-noise through a series of fast (30-60 s) and non-overlapping point scans (Gillespie et al. 2015).

All experimental spectra were collected in fluorescence mode using an Amptek silicon-drift detector positioned at 45 degrees relative to the sample. The incident beam, I₀ signal, was collected as scattered beam from a blank gold-coated sample holder using a second Amptek detector positioned at 90 degrees relative to the sample. Individual spectra were curated, averaged, and normalized to I₀ using a custom script prepared by Adam Gillespie in Igor Pro (Gillespie et al. 2014). Energy calibration, pre-edge subtraction, post-edge normalization, and Gaussian fitting was accomplished using *IFFET Athena* software (Ravel and Newville 2005). The Gaussian fitting followed procedures prepared by Marco Keiluweit and Nico et al. 2017. For Gaussian fitting, no more than 7 curves were identified for each spectrum (1 arctangent and 6 gaussian curves; Nico et al. 2017). For each element, the arctangent was well defined and held constant through the data set. Gaussian curves were identified based on peak features within the spectrum, and iteratively determined in *Athena*. Best fits were based upon the minimization of χ^2 and R-factor. Those values are reported in the Appendix Tables 3.1.1, 3.2.1, and 3.3.1.

4.4 Results

4.4.1 Bulk X-ray Absorption Near Edge Structure (XANES) Spectroscopy

Table 4.1 Approximate energy ranges for primate absorption peaks for C 1s, N 1s, and O 1s

Element	Name	Bond	Transition	Peak(s) (eV)
Carbon	Alkenes, Aromatic	C=C	1s- π^*	284.9-285.5
	Carbonate	CO	1s- π^*	289.9-290.3
	Alcohol	C-OH	1s- σ^*	289.3-289.5
	Carbonyl	C=O	1s- π^*	287.7-288.6
	Aliphatic	C-H	3s- σ^*	287.1-287.4
Nitrogen	Nitrile	C \equiv N	1s- π^*	399.4-399.9
	Amide, Amine,			
	Pyrrole	N-C	1s- π^*	400.7-403.2

	Nitro compounds	R-NO ₂	1s-π*	403.8-404.8
	Amino compounds		1s-σ*	405.5-409.7
Oxygen	Metal oxide	M-O _x		528-529.8
	Ketones, aldehydes	C=O; HC=O	2s-π*	530.6-531.3
	Carboxylic acids, carbox-amides	COOH; CONH	2s-π*	532.0-532.7
	Carboxylic group	COO ⁻	1s-π*	~533
	Alcohol	R-OH	1s-σ*	534.1
	Ethers	C-O-C, O-C-N	1s-σ*	535.4-535.6
	Water	H ₂ O	1s-σ*	535, 537-542

Sources: Brandes et al., 2004; de Groot et al., 1989; Lehmann et al., 2009; Plashkevych et al., 1998; Tanaka et al., 2001.

Table 4.1 reports functional groups and associated peaks observed within the settling marine particulates from sediment Traps R1 and R2. Previous research noted that a jellyfish had become lodged in the opening samples 11-21 Trap R2 (Sylvan et al. 2012; Rouxel et al. 2016) that could affect the particle flux and biological communities present. This was taken into consideration when interpreting results from samples 13-21 from Trap R2.

One bulk spectrum was collected for each sediment trap sample investigated. In general, specific peaks and spectral shapes can be used as a fingerprint to identify C, N, and O compounds through comparisons with reference standards. Gaussian curve fitting was also used to determine changes in functional group moieties in samples (Figure 4.1). Tables 4.2-4.4 show percentages of functional groups that were identified for each element at each time point, while Figure 4.1 shows a represented sample from both Trap R1 and R2. The goodness of the fit parameters are reported in (Appendix Tables 3.1.1, 3.2.1, and 3.3.1). The broad sigma bond (C: ~291-305 eV, N: 405-415 eV, O: 534-542 eV) regions of the spectra are needed to fit each spectrum, but are rarely interpreted as specific functional moieties due to the wide variety of sigma bonds they represent (Nico et al. 2017). These features are notated under the column “unidentified” within Tables 4.2-4.4.

4.4.2 Carbon 1s X-ray Absorption Near Edge Structure (XANES) Spectroscopy

Carbon 1s XANES were collected on marine particles from Trap R1 (Bio 9) and Trap R2 (Ty-Io; Table 4.2). Marine particles from Trap R1 all contained aromatic/alkene C

(0.7-2.5%), aliphatic C (1-13%), carbonyl C (3-35%), and carbonate (2-28%). Samples 2, 14, 17-19 from Trap R1 also contained between 6-15% of alcohol moieties.

Aromatic/alkene, aliphatic, carbonyl, and alcohols are all considered to be signatures of organic C within a sample. Excluding the unidentified sigma bonds, samples at Trap R1 are mainly comprised of organic C with a carbonate peak indicative of calcite (~290 eV; Brandes et al. 2010). Bulk particulate organic C (POC) and particulate inorganic C (PIC) values also suggest particles rich in organic C with a small inorganic component (Table 4.2; Rouxel et al. 2016).

For Trap R2, all samples contained aromatic/alkene (0.7-3%) and carbonyl C (3-27%). All but one sample (Trap R2-20) contained carbonate moieties (1-29%), and all but two samples (Trap R2-2 and Trap R2-20) contained aliphatic C (0.5-5.5%). Similar to Trap R1, only 4 samples (Trap R2-1, R2-2, R2-7, and R2-17) contained alcohol moieties (0.7-20%). Bulk POC and PIC were not calculated for this site. There was more variability in organic C signatures present among samples at Trap R2 than observed at Trap R1. However, overall samples at Trap R2 were also organic C rich with a carbonate peak indicative of calcite (~290 eV; Brandes et al. 2010).

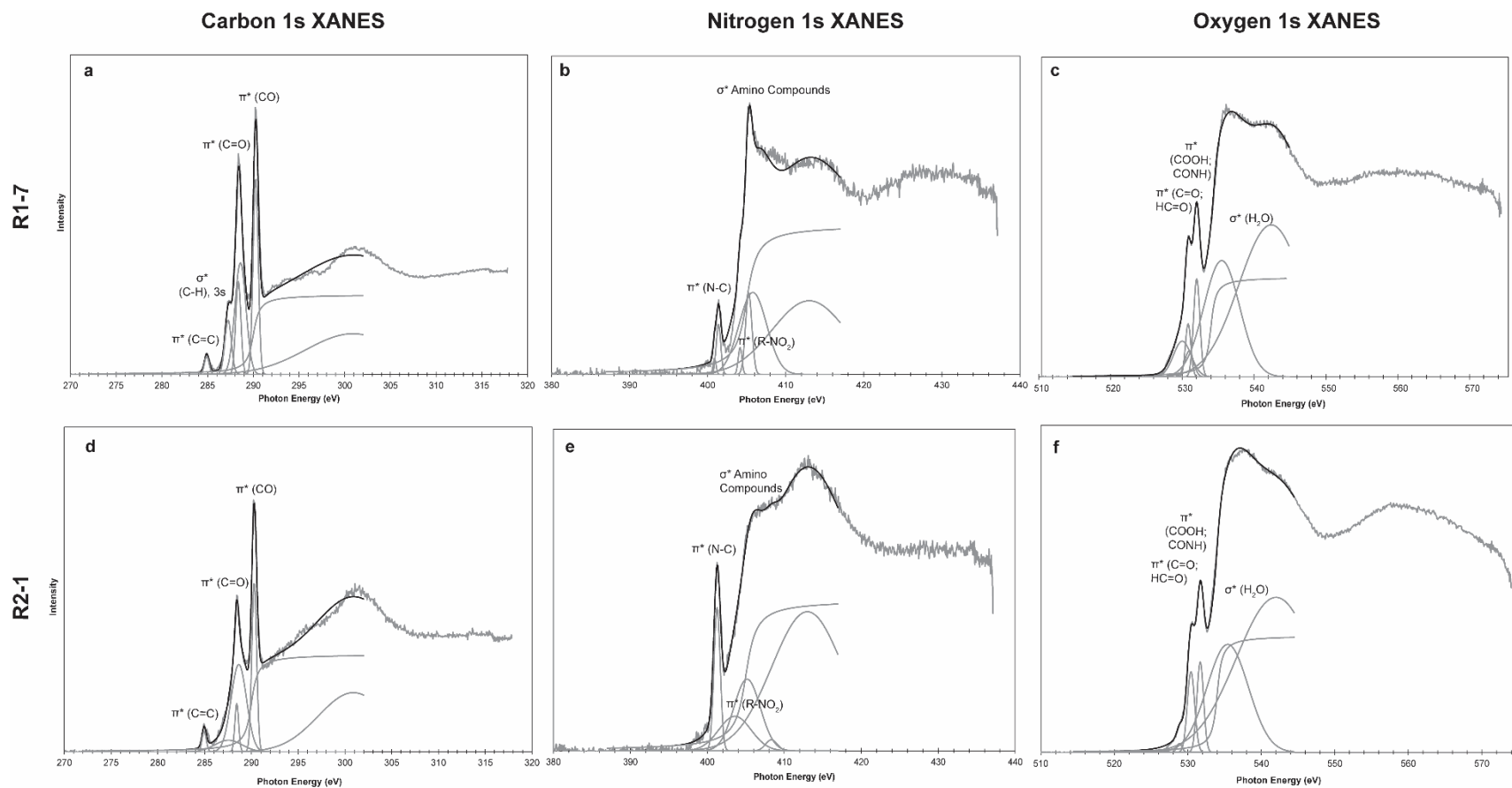


Figure 4.1 Gaussian Curve Fitting of aquatic NOM in settling hydrothermal plume particles. Carbon (C), nitrogen (N), and oxygen (O) 1s XANES were used in concert to understand the chemical composition aquatic NOM in settling hydrothermal plume material at two locations, Bio 9 (Trap R1) and Ty-Io (Trap R2). Representative spectra for C, N, and O of typical aquatic NOM signatures for (a-c) Bio9 and (d-f) are plotted above. The grey lines underneath the spectra correspond to the gaussian curves that produced to the best fits (solid black line) for each spectrum. Commonly, found functional groups are noted in parentheses.

Table 4.2 C 1s XANES Gaussian Curve Fitting

Sample	Location	unsaturated/		Carbonyl	Alcohol	Carbonate	unidentified	POC *	PIC*
		Aromatic/Alkene	Aliphatic						
		(%)	(%)	(%)	(%)	(%)	(%)	(wt.%)	(wt.%)
R1-1	Bio 9	0.70	1.12	21.12		28.27	48.80	1.24	2.24
R1-2	Bio 9	1.45	4.53	10.77	13.95	22.24	47.07	2.06	0.31
R1-4	Bio 9	1.49	2.82	27.37		11.11	57.22	4.84	0.41
R1-5	Bio 9	1.05	3.13	32.27		17.23	46.32	8.12	0.36
R1-6	Bio 9	0.99	1.35	32.98		24.49	40.19	3.95	0.55
R1-7	Bio 9	1.20	5.11	24.50		14.45	54.76	3.77	0.73
R1-8	Bio 9	2.47	2.47	21.60		2.27	71.19	3.62	1.35
R1-14	Bio 9	1.66	4.82	8.16	14.72	11.61	59.03	6.61	1.18
R1-16	Bio 9	1.16	2.83	35.36		8.74	52.01	6.75	0.94
R1-17	Bio 9	1.17	4.22	11.85	6.16	5.17	71.42	9.39	2.05
R1-18	Bio 9	1.71	6.54	7.63	14.10	7.93	62.09	9.03	1.88
R1-19	Bio 9	1.97	12.73	2.72	6.49	1.70	74.39	7.26	0.80
R1-20	Bio 9	1.70	5.01	23.77		9.75	59.78	4.89	0.86
R2-1	Ty-lo	1.28	4.55	2.70	19.56	11.84	60.08	<i>n.d.</i>	<i>n.d.</i>
R2-2	Ty-lo	2.03		24.97	0.68	12.93	59.39	<i>n.d.</i>	<i>n.d.</i>
R2-4	Ty-lo	2.61	1.89	25.15		4.30	66.06	<i>n.d.</i>	<i>n.d.</i>
R2-6	Ty-lo	1.27	2.14	22.99		18.80	54.80	<i>n.d.</i>	<i>n.d.</i>
R2-7	Ty-lo	1.41	0.00	20.59	5.57	3.27	69.22	<i>n.d.</i>	<i>n.d.</i>
R2-8	Ty-lo	1.67	0.46	26.57		8.37	62.91	<i>n.d.</i>	<i>n.d.</i>
R2-13	Ty-lo	0.85	1.59	23.23		4.46	69.88	<i>n.d.</i>	<i>n.d.</i>
R2-14	Ty-lo	0.75	3.60	22.27		9.23	64.15	<i>n.d.</i>	<i>n.d.</i>
R2-15	Ty-lo	0.76	5.49	22.05		5.92	68.78	<i>n.d.</i>	<i>n.d.</i>
R2-16	Ty-lo	1.93	3.81	19.04		15.95	57.27	<i>n.d.</i>	<i>n.d.</i>
R2-17	Ty-lo	1.39	4.00	16.91	4.21	29.03	44.47	<i>n.d.</i>	<i>n.d.</i>

R2-18	Ty-lo	0.77	4.13	24.28	17.35	53.47	<i>n.d.</i>	<i>n.d.</i>
R2-19	Ty-lo	0.70	0.90	22.90	1.11	74.39	<i>n.d.</i>	<i>n.d.</i>
R2-20	Ty-lo	0.83		22.11		76.34	<i>n.d.</i>	<i>n.d.</i>
R2-21	Ty-lo	1.85	2.05	21.26	4.53	70.30	<i>n.d.</i>	<i>n.d.</i>

n.d.: not determined

blank: functional group not present

*values are the total combined values of >1 mm and <1 mm from Rouxel et al. 2016

Table 4.3 N 1s XANES Gaussian Curve Fittings

Sample	Location	Nitrile (%)	Amide/amine/ Pyrrole (%)	Nitro compounds (%)	Amino compounds (%)	unidentified (%)	TN* (wt.%)
R1-1	Bio 9	-	-	-	-	-	0.38
R1-2	Bio 9	-	-	-	-	-	0.35
R1-4	Bio 9		8.14	1.09	19.03	71.74	0.87
R1-5	Bio 9		3.22		51.57	45.21	1.68
R1-6	Bio 9		6.96	5.12	33.72	54.20	0.66
R1-7	Bio 9		3.20	1.17	32.40	63.25	0.66
R1-8	Bio 9		6.11	25.96	3.88	64.05	0.59
R1-14	Bio 9	-	-	-	-	-	1.03
R1-16	Bio 9		5.04		33.93	61.04	1.30
R1-17	Bio 9		8.03	4.70	30.67	56.60	1.38
R1-18	Bio 9	-	-	-	-	-	1.42
R1-19	Bio 9		5.55	21.58	16.49	56.38	1.08
R1-20	Bio 9	-	-	-	-	-	0.72
R2-1	Ty-lo		6.48	8.05	14.49	70.98	<i>n.d.</i>
R2-2	Ty-lo		6.11	21.20	3.92	68.77	<i>n.d.</i>

R2-4	Ty-lo		7.27	12.47	27.62	52.64	<i>n.d.</i>
R2-6	Ty-lo	-	-	-	-	-	<i>n.d.</i>
R2-7	Ty-lo	-	-	-	-	-	<i>n.d.</i>
R2-8	Ty-lo		6.16	25.74	3.59	64.51	<i>n.d.</i>
R2-13	Ty-lo		5.72	20.50	4.15	69.62	<i>n.d.</i>
R2-14	Ty-lo		9.90	4.01	21.26	64.82	<i>n.d.</i>
R2-15	Ty-lo	1.53	9.18	8.97	6.72	73.61	<i>n.d.</i>
R2-16	Ty-lo	2.37	8.07		9.42	79.71	<i>n.d.</i>
R2-17	Ty-lo	4.96	15.32	1.79	6.41	71.53	<i>n.d.</i>
R2-18	Ty-lo	-	-	-	-	-	<i>n.d.</i>
R2-19	Ty-lo	-	-	-	-	-	<i>n.d.</i>
R2-20	Ty-lo	-	-	-	-	-	<i>n.d.</i>
R2-21	Ty-lo		1.71	2.67	64.31	31.30	<i>n.d.</i>

- : no XANES data

n.d.: not determined

blank: functional group not present

*values are the total combined values of >1 mm and <1 mm from Rouxel et al. 2016

Table 4.4 O 1s XANES Gaussian Curve Fitting

Sample	Location	Metal-Oxides (%)	Ketones/ aldehydes (%)	Carboxylic acids/ carbox-amides (%)	Carboxylic group (%)	Alcohol (%)	Ethers (%)	unidentified (%)	Particle Flux* (mg/m ² /d)	Fe* (wt. %)
R1-1	Bio 9	-	-	-	-	-	-	-	114.30	22.92
R1-2	Bio 9	-	-	-	-	-	-	-	142.60	29.26
R1-4	Bio 9	1.08	8.56					90.36	53.76	21.22
R1-5	Bio 9		13.15	1.64			33.58	51.62	74.21	20.63
R1-6	Bio 9		10.68	3.74			27.71	63.86	32.78	28.55
R1-7	Bio 9	4.01	3.28	3.91				88.8	50.68	42.84
R1-8	Bio 9	3.77	2.65	0.38				92.5	59.80	37.88
R1-14	Bio 9	-	-	-	-	-	-	-	81.67	28.76
R1-16	Bio 9	0.5	5.15	2.83		25.41		66.1	37.23	17.59
R1-17	Bio 9	1.34	3.35	1.22			32.52	61.56	42.77	21.21
R1-18	Bio 9	-	-	-	-	-	-	-	100.12	29.32
R1-19	Bio 9	2.12	3.28	1.27				93.32	115.86	36.70
R1-20	Bio 9	-	-	-	-	-	-	-	86.69	34.45
R2-1	Ty-lo	0.26	3.40	3.36			24.76	68.33	16.61	4.23
R2-2	Ty-lo	0.32	2.59	5.37			23.84	67.87	35.80	4.52
R2-4	Ty-lo	0.36	4.83	2.18			26.67	65.96	20.72	4.24
R2-6	Ty-lo	-	-	-	-	-	-	-	31.89	3.54
R2-7	Ty-lo	-	-	-	-	-	-	-	<i>n.d.</i>	<i>n.d.</i>
R2-8	Ty-lo	1.10	1.62	0.52				96.75	<i>n.d.</i>	<i>n.d.</i>
R2-13	Ty-lo		5.66	3.77			39.71	50.86	<i>n.d.</i>	<i>n.d.</i>
R2-14	Ty-lo		10.79	4.21	0.85		34.85	49.94	<i>n.d.</i>	<i>n.d.</i>
R2-15	Ty-lo	0.72	0.82	8.52			27.65	62.27	<i>n.d.</i>	<i>n.d.</i>
R2-16	Ty-lo		5.11	1.53	0.57		35.27	57.52	<i>n.d.</i>	<i>n.d.</i>
R2-17	Ty-lo	0.71	4.13	6.33			37.26	51.57	<i>n.d.</i>	<i>n.d.</i>

R2-18	Ty-lo	-	-	-	-	-	-	-	<i>n.d.</i>	<i>n.d.</i>
R2-19	Ty-lo	-	-	-	-	-	-	-	<i>n.d.</i>	<i>n.d.</i>
R2-20	Ty-lo	-	-	-	-	-	-	-	<i>n.d.</i>	<i>n.d.</i>
R2-21	Ty-lo	0.23	2.65	0.80	4.03		34.06	58.22	<i>n.d.</i>	<i>n.d.</i>

- : no XANES data

n.d.: not determined

blank: functional group not present

*values are the total combined values of >1 mm and <1 mm from Rouxel et al. 2016

4.4.3 Nitrogen 1s X-ray Absorption Near Edge Structure (XANES) Spectroscopy

Functional group observations for N 1s XANES collected on marine particles from Traps R1 (Bio 9) and R2 (Ty-Io) are in Table 4.3. All samples from Trap R1, contained amide/amine/pyrrole N groups (3-8%) and amino N compounds (4-52%). All but two samples (Traps R1-5 and R1-16) contained nitro N compounds (1-26%).

At Trap R2, similar functional group characteristics were observed. All samples contained amide/amine/pyrrole N groups (2-15%) and amino N compounds (4-28%). All but one sample (Trap R2-16) contained nitro N compounds (2-26%). Trap R2 samples 15-17 also contained a small percentage of nitrile N compounds (1.5-5%).

All N signatures observed at Traps R1 and R2 are the building blocks of amino compounds, such as alanine and histidine (Leinweber et al. 2007; Lehmann et al. 2009). However, these functional groups can also be present in polysaccharides, sugars, and weak acids (i.e. carboxylic acid). When compared to published pure amino acids (Leinweber et al. 2007), the spectra observed throughout the Traps R1 and R2 deployments suggest either samples with a mixture of different N compounds or degraded amino acids based on the broad or missing peaks seen throughout the spectra. Additionally, few spectra display a pure amino acid or N compound signatures when compared to standards in the literature (Leinweber et al. 2007; Lehmann et al. 2009).

4.4.4 Oxygen 1s X-ray Absorption Near Edge Structure (XANES) Spectroscopy

Oxygen 1s XANES was collected from samples of Traps R1 (Bio 9) and R2 (Ty-Io; Table 4.4). Oxygen can be found in most inorganic and organic compounds. This makes assigning unique peak functional group categories difficult. For example, the broad sigma region (~534-542 eV) of O 1s XANES can be comprised of water bonds, sigma bonds of metal oxides, or a mixture of both. Even within the $1s \rightarrow \pi^*$ range of the spectra different O-bearing groups have overlapping peaks which can cause a broadening effect versus crisp peak features. Keeping this in mind, the results presented here focus mainly on the organic peak functional groups classification for oxygen. The small peak between 528-529 eV was reported as metal oxyhydr(oxides) based on the bulk elemental composition, as well as spectroscopic data for these samples (Table 4.4; de Groot et al. 1989; Toner et al. 2009; Chan et al. 2011; Rouxel et al. 2016). The main peaks of the metal

oxyhydr(oxides) were similar to organic O peaks, which creates difficulty in identifying mixtures. Even with this difficulty, O 1s XANES can corroborate the C 1s and N 1s XANES data and provided a glimpse into the inorganic environments of samples at Traps R1 and R2.

Oxygen 1s XANES spectra collected for samples from Trap R1 all contained ketone and aldehyde moieties (3-13%). All but one sample (Trap R1-4) contained carboxylic acids and carboxamide moieties (0.4-4%). Samples 5, 6, and 17 from Trap R1 contain ester moieties (28-34%). For C, all of these functional groups would be a part of the carbonyl functional group and undisguisable from each other in mixtures. Trap R1-16 was the only sample to contain an alcohol moiety, and it accounted for 25% of O 1s functional group signature for that sample. Samples 4, 7, 8, 16, 17, and 19 from Trap R1 displayed a peak between ~528-529 eV that is typically assigned uniquely to metal oxides (de Groot et al. 1989). Bulk elemental composition data indicates that iron and other metals were present within samples (Table 4.4; Rouxel et al. 2016). Therefore, it is plausible metal oxides were collected.

At Trap R2, samples all contain ketone/aldehyde (0.8-11%) and carboxylic acids/carboxamide (0.5-8.5%) moieties. All but one sample (Trap R2-8) contain esters moieties (24-40%). Samples from Trap R2-14, -16, and -21 also contain carboxylic groups (0.6-4%). Similar to Trap R1, within the C 1s XANES, all of the above discussed functional groups would be a part of the carbonyl group and are undisguisable from each other in mixtures. When compared to Trap R1, more samples within Trap R2 contained the small metal oxides peak (de Groot et al. 1989). Within the 7 samples it was observed in, it accounted for 0.2-1% of the observed functional groups.

4.5 Discussion

4.5.1 Characteristics of particulate organic materials in settling plume material

Our results suggest Cinorg and Corg mixtures in all but one sample at Trap R2. At each location, samples were consistent in their Cinorg and Corg components, while between locations there was some variability in functional groups present. The Cinorg signatures observed are most consistent with calcite rich particles (Brandes et al. 2010). Overall, the organics within each sample consists mainly of aliphatic, aromatic-rich moieties with

carbonyl groups (Table 4.2-4.4). The carbonyl groups are comprised of ketones, carboxyl-amides, and carboxylic acids which have been observed to be abundant within marine and soil particles (Table 4.4; Brandes et al. 2004; Lehmann et al. 2005; Lehmann et al. 2009; Solomon et al. 2009; Sedlmair et al. 2012; Hoffman et al. 2018). From a bulk chemistry perspective Trap R1 and R2 were seen as identical, receiving the same contribution of organic and inorganic carbon over the duration of sample collection (Rouxel et al. 2016). The slight functional group variability observed between locations, could be due to the differences in the distance each trap was placed from the active vent field (Trap R1 was 30 m from Bio9 while Trap R2 was 115 m from Ty-Io). Particle chemistry and particle flux have been shown to be directly impacted by distance from the venting ridge (German et al. 2002; Toner et al. 2009a; Hoffman et al. 2018). It should also be noted that a jellyfish was caught in the mouth of the sediment Trap R2 for collection bottles 11-21 which has directly impacted the abundance of particles we were able to collect and analyze. Moreover, seasonal mesoscale eddies around EPR 9-10°N also have the potential to influence settling of organic and inorganic particle flux away from the hydrothermal vent (Adams et al. 2011). Mesoscale eddies are formed when currents interact with the ridge or anticyclonic eddy (Adams et al. 2011). These variabilities allow for the transport of basin-scale transport of trace metals, biological material, larva, and heat from both high and low temperature venting around EPR 9-10°N (Adams et al. 2011).

Carbonyl groups are defined as an -C=O , which can be the foundation for many different chemical compounds (e.g. ketones, phenols, amides, carboxylic acids, etc.) found in natural organic matter (NOM). Within sediment trap particle collected at Trap R1 and R2, carbonyls were one of the most abundant functional groups observed. Using C and O XANES in concert, distinctions between the abundance of ketones/aldehydes and carboxylic acids/carbox amides were able to be determined at each sample. All Trap R1 samples contained over twice the amount of ketones/aldehydes versus carboxylic acids/carbox amides, while Trap R2 showed no distinct patterns over the course of sample collection (Table 4.4). At Trap R2, samples were equally distributed between the two functional groups, while others contain one more of one or the other (Table 4.4), showing no trends in preferring one carbonyl functional group over the other. Therefore,

this suggests that the aquatic NOM at Trap R1 and R2 are chemically distinct from one another.

Carbonyl groups are also present within many proteins and amino acids (Kirtley et al. 1992; Leinweber et al. 2007). Amino acids are the building blocks for proteins in biological life. High abundance of proteinaceous materials within settling plume material suggests entrainment of microbially rich deep waters, sediments, vent fauna, or organically rich diffuse flow into the vent fluids (Bennett et al. 2011b; Dick et al. 2013; Baker et al. 2016). Moreover, within NOM, proteins have been shown to be a special group of amphiphilic (contain both polar and nonpolar regions) molecules that can electrostatically bond with minerals through organic amides and other charged functional groups (Kleber et al. 2007). Organic amides are a nitrogen group that is bonded to a carbonyl group. They are commonly found in many amino acid structures (Leinweber et al. 2007) and can provide protection from oxidation or biological uptake of minerals over long period of time (Kleber et al. 2007).

While no pure protein or amino acids signatures were observed, N XANES suggest there are either mixtures or degraded amino compounds within most samples at both Trap R1 and R2 (Appendix 3.1-3.3). Nitrogen is one of the key identifying element found in proteinaceous material. When used in concert with C and O XANES, a more complete picture of the chemical structure can be determined in environmental samples. However, other techniques such as NMR and mass spectrometry would be needed to determine the complete chemical structure. At Trap R1, samples containing amino compounds consistently were around 10 times higher in abundance of amino acids than samples collected at Trap R2 (Table 4.3). Due to the shorter distance from the vent field, Trap R1 would be expected to have organics entrained from local vent fauna and surrounding microbial communities using the vent fluids as food source (Dick et al. 2013; German and Seyfried 2014). While no data is provided about for vent fauna during this deployment, both sites were found to contain distinct microbial communities due the distinct vent fluid chemistries at Bio9 (Trap R1) and Ty-Io (Trap R2; Sylvan et al. 2012; Rouxel et al. 2016). A rich and active microbial community is potentially the reason for the abundance of amino compounds observed at both Trap R1 and R2 (Table 4.3).

Aquatic NOM (also known as particulate Corg) has multiple input sources in hydrothermal plumes. Hydrothermal plumes have three distinct regions: the seafloor/endmember fluids, the buoyant plume, and the non-buoyant plume (German and Seyfried 2014). Sources of aquatic NOM to these regions include entrainment of seafloor biological material (vent biota and sediments) and diffuse flow, microbial activity in the rising and non-buoyant plume, mixing of deep ocean water, settling particles from the upper water column, and shifts in Corg size fraction pool due to sorption onto Corg onto minerals (Bennett et al. 2011b; Holden et al. 2012; Bennett et al. 2013; Dick et al. 2013; Jiang and Breier 2014; Bennett et al. 2015; Olins et al. 2017; Hoffman et al. 2018). High concentrations of aquatic NOM have both been observed in the rising/buoyant plume and non-buoyant plume at EPR 9-10°N (Bennett et al. 2011b; Rouxel et al. 2016). Within the buoyant plume, entrainment of diffuse flow and microbial communities were found to be the most plausible explanations for the increase of aquatic NOM over background (Bennett et al. 2011b). Studies of diffuse flow hydrothermal fluids have observed higher fluxes of organic ligands and bioactive chemicals compared with adjacent high temperature fluids (Sander et al. 2007; Sander and Koschinsky 2011; Baker et al. 2016). Entrainment of these organically rich diffuse fluids into the rising plume can aid and feed in transport metals to otherwise depleted locations (Toner et al. 2009a; Sander and Koschinsky 2011; Baker et al. 2016; Hoffman et al. 2018).

Within the non-buoyant plume, the increases in aquatic NOM at EPR 9-10°N were attributed to scavenging of Corg onto minerals and microbial activity (Bennett et al. 2011b). Active microbial communities entrained into the non-buoyant plume have been shown to have the ability to switch on and off the produce of different organic compounds (e.g. ligands, enzymes, etc.) to increase their ability to access metals/nutrients within in the dispersing plume material (Cowen et al. 1986; Dick et al. 2013; Li et al. 2014). The combination of cell death, and active organics being produced for uptake of nutrients but the two distinct microbial communities were observed at Trap R1 and R2 (Sylvan et al. 2012), would influence the organic signatures capture in our settling aquatic NOM. Additionally, given the further distance of Trap R2, higher concentrations of sinking aquatic NOM from the surface waters would be expected to be observed than at Trap R1 as the plume becomes increasingly dilute. These dynamics, along with the

organics excreted from the jellyfish at Trap R2-13-R2-21, could account for the slight variability in functional groups percentages capture between both locations.

4.5.2 *Properties of natural organic matter*

NOM is seen as an essential component of the environment, aiding in buffering capacity, metal binding capacity, sorption of minerals and other organics, and stabilizing of aggregates with in soils and sediments (Bennett et al. 2011b). These are all important features that aquatic NOM could utilize to aid in transporting hydrothermal particles in the ocean interior and protect them from oxidation processes. Within the last few decades, the soil science community has proposed a bi-layer model for NOM-mineral interactions (Wershaw 1986; Wershaw 1993; Kleber et al. 2007) Briefly, the model suggests heterogenous mixtures that have amphiphilic surface properties that can either sorb or create organic layers on mineral surfaces. These amphiphiles coatings have been observed to contain carboxyl end groups that can bond to a positively charged mineral surface (Wershaw 1993). The middle layer between the charged NOM surfaces layers would be comprised of hydrophobic compounds that would be shielded in an aqueous environment. Degradation of proteins, amino acids, humics, and mixtures of other biological material (e.g. polysaccharides and carbohydrates) can also create these bonding environments ideal for NOM-mineral interactions. The high abundance of carbonyl and amino compounds observed in our samples suggest this is potential mechanism for aquatic NOM to adhere to hydrothermal-derived mineral surfaces.

Adding the complexity of these dynamics, is the proposed idea that there is a range of amphiphilicity within NOM (Kleber et al. 2007). Nonpolar molecules occupy one extreme, comprising mostly of alkyl and aromatic functional groups that are hydrophobic. For the mid-range and amphiphilic-rich compounds, alcohols, ethers, carboxyls, and amides are the dominate functional groups. For amphiphilic dominate NOM, the pH of the environment can affect the chemical properties and the bonding capacity of the OM present (Kleber et al. 2007). This can create different bonding environments for OM when interacting with minerals.

At Trap R1 and R2, amino compounds, ethers, and carboxylic acids were all abundant. This is not super surprising given entrainment the presence of organically-rich fluids

around EPR 9-10°N and that microbial communities were observed at both Trap R1 and R2 (Sylvan et al. 2012; Baker et al. 2016). Many of these organic compounds are commonly found in cells and biochemical compounds excreted by microorganisms (Madigan et al. 2012), as well as humic substances (Essington 2004; Sutton and Sposito 2005). However, the amphiphilic nature of aquatic NOM observed in settling hydrothermal plume material could be an essential clue in understanding mechanisms for how aquatic NOM bonds to hydrothermal particles. For example, amphiphilic-rich NOM in soils has been hypothesized to self-assemble and sorb to mineral surfaces, creating hydrophobic and hydrophilic layers that will affect the final sorptive capacity of the NOM (Kleber et al. 2007). A high sorptive capacity could protect minerals from oxidation and degradation from biological organisms. Such mechanisms could be used to transport and protect hydrothermal Fe into the ocean interior. Further investigations would be needed to understand mechanisms for aquatic NOM-mineral formation.

4.6 Conclusion

Carbon, N, and O XANES were used in concert to understand the chemical properties of settling hydrothermal material at EPR 9-10°N. Previous spectroscopic and model studies showed that Corg-mineral aggregates were important in both protecting the oxidation state and transporting hydrothermal (Toner et al. 2009a; Toner et al. 2012a; Breier et al. 2012). Overall, settling particles were mixtures of organic and inorganic compounds. While there was much diversity in the organic compounds present, all inorganics were calcite. The aquatic NOM was found to be mostly comprised of amino compounds, ethers, and carboxylic acids. These compounds are commonly found in biochemical molecules in diffuse flow and from local microbial communities (Von Damm and Lilley 2004; Madigan et al. 2012). The high abundance of these molecules suggests amphiphiles are an important component of vent derived or influenced aquatic NOM. As the soil science community has shown, amphiphiles can self-assemble and create membrane-like coating on minerals (Wershaw 1993; Kleber et al. 2007). One model suggests amphiphilic fragments sorb and accumulate on the charged mineral surfaces, arranging with the hydrophobic portion inward and a charged outer layer that can interact with additional NOM or cations (Wershaw 1993; Kleber et al. 2007). Yet,

little is known about these mechanisms or behaviors in aquatic NOM (Hedges and Keil 1995). Additional studies would be needed to investigate the mechanisms and structures of aquatic NOM within settling plume material, as well as understand its role in transporting trace metals, like Fe, into the ocean interior.

CHAPTER 5

Conclusions

5.1 Summary

This dissertation has examined the chemical speciation and chemical mechanism affecting the transport of hydrothermal iron (Fe) in non-buoyant plumes. Two main questions have been addressed:

1. What is the chemical speciation of particulate Fe within non-buoyant hydrothermal plumes and how does it change over 100-1000s of kilometers from the ridge axis?
2. How does the speciation of organic carbon (Corg) affect the of hydrothermally derived particulate Fe?

Over the last decade, hydrothermal vents have become a highly debated source of Fe to the ocean interior. Currently, nanoparticles and Corg matrices have been proposed as two potential mechanisms for aiding in basin-scale transport of hydrothermal Fe. In the southern East Pacific Rise (SEPR), Corg:Fe aggregates were detected over 2700 km from the ridge and mainly comprised of Fe(III) oxyhydroxides. Similarly, in the northern East Pacific Rise (NEPR), high abundances of Corg and Fe were seen in settling hydrothermal material 30-100 m from active hydrothermal venting.

At both locations, Corg contained high abundances of carbonyl groups. Carbonyl groups are commonly found in many organic compounds, such as amino acids, proteins, and polysaccharides. Within hydrothermal plumes, these compounds can be sourced from in-situ production from microbial communities, settling of organic matter from the upper water column, and entrainment of biological material, organically rich diffuse flow, or/and deep ocean water. In the NEPR, high abundances of amino compounds were also identified, suggesting in-situ production or entrainment organically rich diffuse flow of biological material.

Moreover, many of these compounds contain polar and nonpolar regions and are referred to as amphiphiles. Amphiphiles contain a charged outer layer that has been shown to create membrane-like coatings on mineral surfaces. In the SEPR, these coatings were observed to prevent the formation of increased structural order within detected Fe(III) oxyhydroxide mineral phases and decrease the settling rate of hydrothermal

particulate Fe. If these studies are representative of global hydrothermal systems, Corg plays in critical role in transporting hydrothermal Fe into the ocean interior.

5.2 Future Directions

This dissertation is the first to explore particulate Fe and C speciation of non-buoyant hydrothermal particles 1000s of kilometers from the ridge axis. Previous studies have mainly focused on investigating buoyant and non-buoyant plume dynamics (~100 m) close to the ridge axis. This is because hydrothermal particles were thought to settle locally around the vents field and have little impact on global geochemical cycles. In this study, it has been shown that Corg can increase the longevity and transport of particulate Fe over 1000s of kilometers, which can impact global geochemical cycles.

However, this work has raised a few questions that require further investigation. First, the lack of Fe sulfides detected in the SEPR hydrothermal plume raise the question about where the sulfur is the sulfur, and where is it going once it is expelled. The SEPR is a basalt-host hydrothermal system and is expected to have high hydrogen sulfide concentrations near the venting ridge based on expected water-rock reactions (Tivey 2007). Hydrothermal fluids surveying further south of where the GP16 cruise crossed the EPR ridge (EPR 15°S) have shown fluids rich in both hydrogen sulfide and trace metals (Charlou et al. 1996). When mixed with cold seawater, these fluids produce plumes rich in Fe sulfides that have been hypothesized to travel 1000s km down plume (Yücel et al. 2011; Gartman et al. 2014). However, for EPR 15°S, where the GP16 cruise crossed the ridge, no information about endmember fluids or surveys of the ridge axis have been conducted. Based on the ³He signatures (Figure 1.3), surveying the Southern East Pacific Rise (SEPR) from 0-17°S will provide vital information about vent location and end member fluids that are contributing the ~4300 km SEPR hydrothermal plume. Previous studies have used various techniques to study the hydrothermal plume material and water chemistry of this area (Lupton and Craig 1981; Feely et al. 1996; Hoffman et al. 2018) but have never surveyed the chemistry of the hydrothermal fluids along EPR 0-17°S. Endmember fluids are important in understanding unaltered hydrothermal fluids before they mixed with seawater. This enables a time zero point that can allow for modeling and

calculations about reaction transport rates for particulate and dissolved species within the SEPR hydrothermal plume.

Moreover, recent research at EPR 9°N has shown the importance of axial low-temperature diffuse flow in delivering stabilized Fe into the ocean interior (Baker et al. 2016), which could be a key component of the SEPR hydrothermal plume. Low-temperature diffuse flow has generally been overlooked due to lack of detection using established techniques for high-temperature vent fluids (Baker et al. 2016), and the assumption that these low-temperature fluids are entrained and contribute to the high-temperature plumes. Surveying the SEPR along 0-17°S will enable scientists to interrogate the contribution of high vs. low temperature fluids as well as locate where active and inactive venting is taking place along the SEPR. This along with previous studies conducted along EPR 17-20°S (Charlou et al. 1996), could help in understanding dynamics of the SEPR hydrothermal plume and inform reactive transport geochemical models about basin-scale movements of trace metals from hydrothermal plumes.

Secondly, the organic geochemistries and mechanisms of natural organic matter (NOM) are still poorly constrained in marine and hydrothermal systems. Further characterization of aquatic natural organic matter (NOM) in other hydrothermal fluids will aid in understanding the relationship of Fe and C within hydrothermal plumes. Aquatic NOM has been shown to be an important component in transporting hydrothermally-derived Fe into the ocean interior (Toner et al. 2009a; Bennett et al. 2011b; Hoffman et al. 2018). However, the mechanisms are still highly debated within the scientific community (Wershaw 1993; Hedges and Oades 1997; Kleber et al. 2007). We would invite the scientific community to further interrogate these mechanisms using other methods, such as NMR, mass spectrometry, and surface area, to understand aquatic NOM-mineral interactions of settling hydrothermally-derived material.

Lastly, synchrotrons provide a non-destructive way to analyze the chemical speciation of complex environmental samples, like hydrothermal plume particles. Unlike current bulk chemistry techniques that require destructive sample methods, the synchrotron provides the opportunity to revisit the same sample multiple times. Yet, interpretation of spectra signatures can be complex and take years of running standards to responsibly comprehend. Developing new statistical tools to aid in interpretation of complex

environment spectra will enhance our understanding of the dynamics within environmental systems. In this dissertation, Gaussian curve fitting and linear combination fitting were used a method to constrain and interpret spectra collected on hydrothermal particles. Both of these methods have been around for some time and are important tools in for interpreting and analyzing spectra but do have limitations. For example, it was only recently Gaussian curve fitting was shown as a way to analyze and interpret complex organic mixtures in environmental samples, such as marine and soil particles (Lehmann et al. 2009; Nico et al. 2017). Yet, there is still much discussion within the community as the best method contain the Gaussian curves when fitting spectra. Further development of methods to quantify synchrotron spectra and related data to bulk chemistries for environmental samples will enhance interpretations and provide new insights about dynamics within environmental systems.

REFERENCES

- Abramson L, Wirick S, Lee C, et al (2009) The use of soft X-ray spectromicroscopy to investigate the distribution and composition of organic matter in a diatom frustule and a biomimetic analog. *Deep Res Part II Top Stud Oceanogr* 56:1369–1380. doi: 10.1016/j.dsr2.2008.11.031
- Adams DK, Mcgillicuddy Jr DJ, Zamudio L, et al (2011) Surface-Generated Mesoscale Eddies. *Science* (80-) 332:580–583. doi: 10.1126/science.1201066
- Anderson MA, Morel FMM (1982) The influence of aqueous iron chemistry on the uptake of iron by the coastal diatom *Thalassiosira weissflogii*. *Limnol Oceanogr* 27:789–813. doi: 10.4319/lo.1982.27.5.0789
- Aufdenkampe AK, Hedges JI, Richey JE, et al (2009) Sorptive Fractionation of Dissolved Organic Nitrogen and Amino Acids onto Fine Sediments within the Amazon Basin Sorptive fractionation of dissolved organic nitrogen and amino acids onto fine sediments within the Amazon Basin. *Limnology* 46:1921–1935.
- Baker ET, Resing JA, Haymon RM, et al (2016) How many vent fields? New estimates of vent field populations on ocean ridges from precise mapping of hydrothermal discharge locations. *Earth Planet Sci Lett* 449:186–196. doi: 10.1016/j.epsl.2016.05.031
- Barber A, Brandes J, Leri A, et al (2017) Preservation of organic matter in marine sediments by inner-sphere interactions with reactive iron. *Sci Rep* 7:366. doi: 10.1038/s41598-017-00494-0
- Bargar JR, Tebo BM, Bergmann U, et al (2005) Biotic and abiotic products of Mn(II) oxidation by spores of the marine *Bacillus* sp. strain SG-1. *Am Mineral* 90:143–154. doi: 10.2138/am.2005.1557
- Bargar JR, Tebo BM, Villinski JE (2000) In situ characterization of Mn(II) oxidation by spores of the marine *Bacillus* sp. strain SG-1. *Geochim Cosmochim Acta* 64:2775–2778. doi: 10.1016/S0016-7037(00)00368-9
- Bennett S a., Achterberg EP, Connelly DP, et al (2008) The distribution and stabilisation of dissolved Fe in deep-sea hydrothermal plumes. *Earth Planet Sci Lett* 270:157–

167. doi: 10.1016/j.epsl.2008.01.048
- Bennett SA, Coleman M, Huber JA, et al (2013) Trophic regions of a hydrothermal plume dispersing away from an ultramafic-hosted vent-system: Von Damm vent-site, Mid-Cayman Rise. *Geochemistry, Geophys Geosystems* 14:317–327. doi: 10.1002/ggge.20063
- Bennett SA, Dover C Van, Breier JA, Coleman M (2015) Effect of depth and vent fluid composition on the carbon sources at two neighboring deep-sea hydrothermal vent fields (Mid-Cayman Rise). *Deep Res Part I Oceanogr Res Pap* 104:122–133. doi: 10.1016/j.dsr.2015.06.005
- Bennett SA, Hansman RL, Sessions AL, et al (2011a) Tracing iron-fueled microbial carbon production within the hydrothermal plume at the Loihi seamount. *Geochim Cosmochim Acta* 75:5526–5539. doi: 10.1016/j.gca.2011.06.039
- Bennett SA, Statham PJ, Green DRH, et al (2011b) Dissolved and particulate organic carbon in hydrothermal plumes from the East Pacific Rise, 9°50'N. *Deep Sea Res I* 58:922–931. doi: 10.1016/j.dsr.2011.06.010
- Boiteau RM, Mende DR, Hawco NJ, et al (2016) Siderophore-based microbial adaptations to iron scarcity across the eastern Pacific Ocean. *Proc Natl Acad Sci* 113:14237–14242. doi: 10.1073/pnas.1608594113
- Boström K, Peterson MNA, Joensuu O, Fisher DE (1969) Aluminum-poor ferromanganous sediments on active oceanic ridges. *J Geophys Res* 74:3261–3270. doi: 10.1029/JB074i012p03261
- Brand LE, Sunda WG, Guillard RRL (1983) Limitation of marine phytoplankton reproductive rates by zinc, manganese, and iron. *Limnol Oceanogr* 28:1182–1198. doi: 10.4319/lo.1983.28.6.1182
- Brandes JA, Lee C, Wakeham S, et al (2004) Examining marine particulate organic matter at sub-micron scales using scanning transmission X-ray microscopy and carbon X-ray absorption near edge structure spectroscopy. *Mar Chem* 92:107–121. doi: 10.1016/j.marchem.2004.06.020
- Brandes JA, Wirrick S, Jacobsen C (2010) Carbon K-edge spectra of carbonate minerals. *J Synchrotron Radiat* 17:676–682. doi: 10.1107/S0909049510020029
- Brandt F, Schäfer T, Claret F, Bosbach D (2012) Heterogeneous formation of ferric oxide

- nanoparticles on chlorite surfaces studied by x-ray absorption spectromicroscopy (STXM). *Chem Geol* 329:42–52. doi: 10.1016/j.chemgeo.2011.08.016
- Breier J a., Rauch CG, McCartney K, et al (2009) A suspended-particle rosette multi-sampler for discrete biogeochemical sampling in low-particle-density waters. *Deep Res Part I Oceanogr Res Pap* 56:1579–1589. doi: 10.1016/j.dsr.2009.04.005
- Breier J a., Toner BM, Fakra SC, et al (2012) Sulfur, sulfides, oxides and organic matter aggregated in submarine hydrothermal plumes at 9°50'N East Pacific Rise. *Geochim Cosmochim Acta* 88:216–236. doi: 10.1016/j.gca.2012.04.003
- Brown GE, Henrich VE, Casey WH, et al (1999) Metal Oxide Surfaces and Their Interactions with Aqueous Solutions and Microbial Organisms *Microbial Organisms*. *Chem Rev* 99:77–174. doi: 10.1021/cr980011z
- Buck KN, Sedwick PN, Sohst B, Carlson CA (2018) Organic complexation of iron in the eastern tropical South Pacific: Results from US GEOTRACES Eastern Pacific Zonal Transect (GEOTRACES cruise GP16). *Mar Chem* 201:229–241. doi: 10.1016/j.marchem.2017.11.007
- Butler A (2005) Marine siderophores and microbial iron mobilization. *Biometals* 18:369–374. doi: 10.1007/s10534-005-3711-0
- Campbell AC, Gieskes JM, Lupton JE, Lonsdale PF (1988) Manganese geochemistry in the Guaymas Basin , Gulf of California. *Methods* 52:345–357.
- Chan CS, Fakra SC, Emerson D, et al (2011) Lithotrophic iron-oxidizing bacteria produce organic stalks to control mineral growth: implications for biosignature formation. *ISME J* 5:717–727. doi: 10.1038/ismej.2010.173
- Charlou L, Jean-baptiste P, Stievenard M (1996) Mineral and gas chemistry of hydrothermal fluids of an ultra fast spreading ridge : East Pacific Rise , 17° to 19°S (Naudur cruise , 1993) phase separation processes controlled by volcanic and tectonic activity members show large variations between the. *J Geophys Res* 101:15,899-15,919.
- Chen C, Dynes JJ, Wang J, et al (2014) Soft X-ray spectromicroscopy study of mineral-organic matter associations in pasture soil clay fractions. *Environ Sci Technol* 48:6678–6686. doi: 10.1021/es405485a
- Chen M, Wang W (2010) Bioavailability of natural colloid-bound iron to manne

- plankton : Influences of colloidal size and aging Min Chen and Wen-Xiong.
46:1956–1967.
- Cornell RM, Schwertmann U (2003) The iron oxides: structure, properties, reactions, occurrences and uses. John Wiley and Sons, Darmstadt, Germany, Germany
- Cowen JP, Bruland KW (1985) Metal deposits associated with bacteria: implications for Fe and Mn marine biogeochemistry. *Deep Sea Res Part A Oceanogr Res Pap* 32:253–272. doi: 10.1016/0198-0149(85)90078-0
- Cowen JP, Massoth GJ, Baker ET (1986) Bacterial scavenging of Mn and Fe in a mid- to far-field hydrothermal particle plume. *Nature* 322:169–171. doi: 10.1038/322169a0
- Curtin D, Campbell CA, Jalil A (1998) Effects of acidity on mineralization: pH-dependence of organic matter mineralization in weakly acidic soils. *Soil Biol Biochem* 30:57–64. doi: 10.1016/S0038-0717(97)00094-1
- de Groot FMF, Grioni M, Fuggle JC, et al (1989) Oxygen 1s x-ray-absorption edges of transition-metal oxides. *Phys Rev B* 40:5715–5723.
- de Vargas C, Aubrey MP, Probert I, Young J (2007) Origin and Evolution of Coccolithophores. In: Falkowski PG, Knoll AH (eds). Elsevier, Boston, pp 251–285
- Dick GJ, Anantharaman K, Baker BJ, et al (2013) The microbiology of deep-sea hydrothermal vent plumes: Ecological and biogeographic linkages to seafloor and water column habitats. *Front Microbiol* 4:1–16. doi: 10.3389/fmicb.2013.00124
- Dick GJ, Clement BG, Webb SM, et al (2009) Enzymatic microbial Mn(II) oxidation and Mn biooxide production in the Guaymas Basin deep-sea hydrothermal plume. *Geochim Cosmochim Acta* 73:6517–6530. doi: 10.1016/j.gca.2009.07.039
- Dick GJ, Lee YE, Tebo BM (2006) Manganese(II)-Oxidizing Bacillus Spores in Guaymas Basin Hydrothermal Sediments and Plumes. *Appl Environ Microbiol* 72:3184–3190. doi: 10.1128/AEM.72.5.3184–3190.2006
- Dick GJ, Tebo BM (2010) Microbial diversity and biogeochemistry of the Guaymas Basin deep-sea hydrothermal plume. *Environ Microbiol* 12:1334–1347. doi: 10.1111/j.1462-2920.2010.02177.x
- Durham BP, Sharma S, Luo H, et al (2015) Cryptic carbon and sulfur cycling between surface ocean plankton. *Proc Natl Acad Sci* 112:453–457. doi: 10.1073/pnas.1413137112

- Dymond J, Roth S (1988) Plume dispersed hydrothermal particles: A time-series record of settling flux from the Endeavour Ridge using moored sensors. *Geochim Cosmochim Acta* 52:2525–2536. doi: 10.1016/0016-7037(88)90310-9
- Edwards KJ, Bach W, McCollom TM, Rogers DR (2004) Neutrophilic Iron-Oxidizing Bacteria in the Ocean: Their Habitats, Diversity, and Roles in Mineral Deposition, Rock Alteration, and Biomass Production in the Deep-Sea. *Geomicrobiol J* 21:393–404. doi: 10.1080/01490450490485863
- Elderfield H, Schultz a. (1996) Mid-Ocean Ridge Hydrothermal Fluxes and the Chemical Composition of the Ocean. *Annu Rev Earth Planet Sci* 24:191–224. doi: 10.1146/annurev.earth.24.1.191
- Emerson D (2000) Microbial oxidation of Fe(II) and Mn(II) at circumneutral pH. In: *Environmental Microbe-Metal Interactions*. ASM Press, Washington D. C., pp 31–52
- Emerson D, Fleming EJ, McBeth JM (2010) Iron-oxidizing bacteria: an environmental and genomic perspective. *Annu Rev Microbiol* 64:561–83. doi: 10.1146/annurev.micro.112408.134208
- Essington ME (2004) *Soil and Water Chemistry*. CRC Press LLC, Boca Raton
- Faure V, Speer K (2012) Deep Circulation in the Eastern South Pacific Ocean. *J Mar Res.* doi: 10.1357/002224012806290714
- Feely R a., Baker ET, Marumo K, et al (1996) Hydrothermal plume particles and dissolved phosphate over the superfast-spreading southern East Pacific Rise. *Geochim Cosmochim Acta* 60:2297–2323. doi: 10.1016/0016-7037(96)00099-3
- Feely RA, Lewison M, Massoth GJ, et al (1987) Composition and dissolution of black smoker particulates from active vents on the Juan de Fuca Ridge. *J Geophys Res Solid Earth* 92:11347–11363. doi: 10.1029/JB092iB11p11347
- Feely RA, Massoth GJ, Baker ET, et al (1990) The effect of hydrothermal processes on midwater phosphorus distributions in the northeast Pacific. *Earth Planet Sci Lett* 96:305–318. doi: 10.1016/0012-821X(90)90009-M
- Feely RA, Massoth GJ, Baker ET, et al (1992) Tracking the Dispersal of Hydrothermal Plumes from the Juan de Fuca Ridge Using Suspended Matter Compositions. *J Geophys Res* 97:6–9.

- Fenter PA, Rivers ML, Sturchio NC, Sutton SR (2002) Reviews in Mineralogy and Geochemistry Volume 49: Applications of Synchrotron Radiation in Low-Temperature Geochemistry and Environmental Science. Geochemical Society, Chicago, Illinois, USA
- Field CB, Behrenfeld MJ, Randerson JT, Falkowski P (1998) Primary Production of the Biosphere: Integrating Terrestrial and Oceanic Components. *Science* (80-) 281:237–240. doi: 10.1126/science.281.5374.237
- Field MP, Sherrell RM (2000a) Dissolved and particulate Fe in a hydrothermal plume at 9°45'N, East Pacific Rise: Slow Fe(II) oxidation kinetics in Pacific plumes. *Geochim Cosmochim Acta* 64:619–628. doi: 10.1016/S0016-7037(99)00333-6
- Field MP, Sherrell RM (2000b) Dissolved and particulate Fe in a hydrothermal plume at 9°45'N, East Pacific Rise: *Geochim Cosmochim Acta* 64:619–628. doi: 10.1016/S0016-7037(99)00333-6
- Fisher C, Takai K, Le Bris N (2007) Hydrothermal Vent Ecosystems. *Oceanography* 20:14–23. doi: 10.5670/oceanog.2007.75
- Fitzsimmons JN, Boyle E a., Jenkins WJ (2014) Distal transport of dissolved hydrothermal iron in the deep South Pacific Ocean. *Proc Natl Acad Sci* 111:16654–16661. doi: 10.1073/pnas.1418778111
- Fitzsimmons JN, Boyle EA (2014) Assessment and comparison of Anopore and cross flow filtration methods for the determination of dissolved iron size fractionation into soluble and colloidal phases in seawater. *Limnol Oceanogr Methods* 12:246–263. doi: 10.4319/lom.2014.12.246
- Fitzsimmons JN, John SG, Marsay CM, et al (2017) Iron persistence in a distal hydrothermal plume supported by dissolved-particulate exchange. *Nat Geosci*. doi: 10.1038/ngeo2900
- Gartman A, Findlay AJ, Luther GW (2014) Nanoparticulate pyrite and other nanoparticles are a widespread component of hydrothermal vent black smoker emissions. *Chem Geol* 366:32–41. doi: 10.1016/j.chemgeo.2013.12.013
- Gartman A, Luther III GW (2014) Oxidation of synthesized sub-micron pyrite (FeS₂) in seawater. *Geochim Cosmochim Acta* 144:96–108. doi: 10.1016/j.gca.2014.08.022
- German C, Seyfried WE (2014) *Hydrothermal Processes*, 2nd edn. Elsevier Ltd.

- German CR, Colley S, Palmer MR, et al (2002) Hydrothermal plume-particle fluxes at 13 degrees N on the East Pacific Rise. *Deep Res Part I-Oceanographic Res Pap* 49:1921–1940. doi: 10.1016/S0967-0637(02)00086-9
- German CR, Legendre LL, Sander SG, et al (2015) Hydrothermal Fe cycling and deep ocean organic carbon scavenging: Model-based evidence for significant POC supply to seafloor sediments. *Earth Planet Sci Lett* 419:143–153. doi: 10.1016/j.epsl.2015.03.012
- Gillespie AW, Phillips CL, Dynes JJ, et al (2015) *Advances in Using Soft X-Ray Spectroscopy for Measurement of Soil Biogeochemical Processes*. Elsevier Ltd
- Gillespie AW, Sanei H, Diochon A, et al (2014) Perennially and annually frozen soil carbon differ in their susceptibility to decomposition: Analysis of Subarctic earth hummocks by bioassay, XANES and pyrolysis. *Soil Biol Biochem* 68:106–116. doi: 10.1016/j.soilbio.2013.09.021
- Gledhill M, Buck KN (2012) The organic complexation of iron in the marine environment: A review. *Front Microbiol* 3:1–17. doi: 10.3389/fmicb.2012.00069
- Golchin A, Oades JM, Skjemstad JO, Clarke P (1994) Study of Free and Occluded Particulate Organic Matter in Soils by Solid state ¹³C CP/MAS\NMR Spectroscopy and Scanning Electron Microscopy. *Aust J Soil Res* 32:285–309. doi: 10.1071/SR9940285
- Hansell D, Carlson CA, Repeta DJ, Schlitzer R (2009) Dissolved Organic Matter in the Ocean. *Oceanography* 22:202–11. doi: 10.5670/oceanog.2009.109
- Hawkes JA, Connelly DP, Gledhill M, Achterberg EP (2013) The stabilisation and transportation of dissolved iron from high temperature hydrothermal vent systems. *Earth Planet Sci Lett* 375:280–290. doi: 10.1016/j.epsl.2013.05.047
- Hedges JJ, Eglinton G, Hatcher PG, et al (2000) The molecularly uncharacterized component of nonliving organic matter in natural environments. *Org Geochem* 31:945–958. doi: [http://dx.doi.org/10.1016/S0146-6380\(00\)00096-6](http://dx.doi.org/10.1016/S0146-6380(00)00096-6)
- Hedges JJ, Keil RG (1995) Sedimentary organic matter preservation: an assessment and speculative synthesis. *Mar Chem* 49:81–115. doi: 10.1016/0304-4203(95)00008-F
- Hedges JJ, Oades JM (1997) Comparative organic geochemistries of soils and marine sediments. *Org Geochem* 27:319–361. doi: 10.1016/S0146-6380(97)00056-9

- Heller MI, Lam PJ, Moffett JW, et al (2017) Accumulation of Fe oxides in the Peruvian oxygen deficient zone implies non-oxygen dependent Fe oxidation. *Geochim Cosmochim Acta* Submitted. doi: 10.1016/j.gca.2017.05.019
- Hem JD (1981) Rates of manganese oxidation in aqueous systems *Wwtl. Geochim Cosmochim Acta* 45:1369–1374.
- Hem JD, Lind CJ (1983) Nonequilibrium models for predicting forms of precipitated manganese oxides. *Geochim Cosmochim Acta* 47:2037–2046. doi: 10.1016/0016-7037(83)90219-3
- Hitchcock AP (2016) aXis 2000- Analysis of X-ray Images and Spectra. <http://unicorn.mcmaster.ca/aXis2000.html>.
- Hoffman CL, Nicholas SL, Ohnemus DC, et al (2018) Near-field iron and carbon chemistry of non-buoyant hydrothermal plume particles, Southern East Pacific Rise 15°S. *Mar Chem* 201:183–197. doi: 10.1016/j.marchem.2018.01.011
- Holden J, Breier J, Rogers K, et al (2012) Biogeochemical processes at hydrothermal vents: microbes and minerals, bioenergetics, and carbon fluxes. *Oceanography* 25:196–208. doi: <http://dx.doi.org/10.5670/oceanog.2012.18>
- Homoky WB (2017) Deep ocean iron balance. *Nat Geosci* 1–2. doi: 10.1038/ngeo2908
- Honjo S, Dymond J, Collier R, Manganini SJ (1995) Export production of particles to the interior of the equatorial Pacific Ocean during the 1992 EqPac experiment. *Deep Res Part II* 42:831–870. doi: 10.1016/0967-0645(95)00034-N
- Hsu-Kim H, Mullaugh KM, Tsang JJ, et al (2008) Formation of Zn- and Fe-sulfides near hydrothermal vents at the Eastern Lau Spreading Center: implications for sulfide bioavailability to chemoautotrophs. *Geochem Trans* 9:6. doi: 10.1186/1467-4866-9-6
- Janecky DR, Seyfried WE (1984) Formation of massive sulfide deposits on oceanic ridge crests: Incremental reaction models for mixing between hydrothermal solutions and seawater. *Geochim Cosmochim Acta* 48:2723–2738. doi: 10.1016/0016-7037(84)90319-3
- Jenkins WJ, Lott DE, German CR, et al (2018) The deep distributions of helium isotopes, radiocarbon, and noble gases along the U.S. GEOTRACES East Pacific Zonal Transect (GP16). *Mar Chem* 201:167–182. doi: 10.1016/j.marchem.2017.03.009

- Jiang H, Breier JA (2014) Physical controls on mixing and transport within rising submarine hydrothermal plumes: A numerical simulation study. *Deep Res Part I Oceanogr Res Pap* 92:41–55. doi: 10.1016/j.dsr.2014.06.006
- Johnson JE, Savalia P, Davis R, et al (2016) Real-Time Manganese Phase Dynamics during Biological and Abiotic Manganese Oxide Reduction. *Environ Sci Technol* 50:4248–4258. doi: 10.1021/acs.est.5b04834
- Johnson KS, Boyle E, Bruland K, et al (2007) Developing standards for dissolved iron in seawater. *Eos (Washington DC)* 88:131–132. doi: 10.1029/2007EO110003
- Johnson KS, Michael Gordon R, Coale KH (1997) What controls dissolved iron concentrations in the world ocean? *Mar Chem* 57:137–161. doi: 10.1016/S0304-4203(97)00043-1
- Kadar E, Fisher A, Stolpe B, et al (2012) Metallic nanoparticle enrichment at low temperature, shallow CO₂ seeps in Southern Italy. *Mar Chem* 140–141:24–32. doi: 10.1016/j.marchem.2012.07.001
- Kadko DC, Rosenberg ND, Lupton JE, et al (1990) Chemical reaction rates and entrainment within the Endeavor Ridge hydrothermal plume. *Earth Planet Sci Lett* 99:315–335.
- Keil RG, Tsamakis E, Bor Fuh C, et al (1993) Mineralogic controls on the concentration and elemental composition of organic-matter in marine sediments: Hydrodynamic separation using Splitt-fractionation. *58:879–893*.
- Kelley DS, Delaney JR, Juniper SK (2014) Establishing a new era of submarine volcanic observatories: Cabling Axial Seamount and the Endeavour Segment of the Juan de Fuca Ridge. *Mar Geol* 352:426–450. doi: 10.1016/j.margeo.2014.03.010
- Kessick MA, Morgan JJ (1975) Mechanism of autooxidation of manganese in aqueous solution. *Environ Sci Technol* 9:157–159.
- Kilcoyne a LD, Tyliszczak T, Steele WF, et al (2003) Interferometer-controlled scanning transmission X-ray microscopes at the Advanced Light Source. *J Synchrotron Radiat* 10:125–36.
- Kipp LE, Sanial V, Henderson PB, et al (2018) Radium isotopes as tracers of hydrothermal inputs and neutrally buoyant plume dynamics in the deep ocean. *Mar Chem* 201:51–65. doi: 10.1016/j.marchem.2017.06.011

- Kirtley SM, Mullins OC, Chen J, et al (1992) Nitrogen chemical structure in DNA and related molecules by X-ray absorption spectroscopy. *Biochim Biophys Acta* 1132:249–254. doi: 10.1016/0167-4781(92)90157-U
- Kleber M, Sollins P, Sutton R (2007) A conceptual model of organo-mineral interactions in soils: Self-assembly of organic molecular fragments into zonal structures on mineral surfaces. *Biogeochemistry* 85:9–24. doi: 10.1007/s10533-007-9103-5
- Knicker H, Hatcher PG (1997) Survival of protein in an organic-rich sediment: Possible protection by encapsulation in organic matter. *Naturwissenschaften* 84:231–234. doi: 10.1007/s001140050384
- Kostka J, Luther III GW, Nealson KH (1995) Chemical and biological reduction of Mn(III)-pyrophosphate complexes: Potential importance of dissolved Mn(III) as an environmental oxidant. *Geochim Cosmochim Acta* 59:885–894. doi: 10.1016/00167-0379(50)00070-
- Kraft S, Stümpel J, Becker P, Kuetsgens U (1996) High resolution x-ray absorption spectroscopy with absolute energy Calibration for the determination of absorption edge energies. *Rev Sci Instrum* 67:681–687. doi: 10.1063/1.1146657
- Ksionzek KB, Schmitt-Kopplin P, Koch BP (2016) Dissolved organic sulfur in the ocean-Biogeochemistry of a petagram inventory. *Science* (80-) 354:456–459.
- Kubicki JD, Apitz SE (1999) Models of natural organic matter and interactions with organic contaminants. *Org Geochem* 30:911–927. doi: 10.1016/S0146-6380(99)00075-3
- Kujawinski EB, Freitas MA, Zang X, et al (2002) The application of electrospray ionization mass spectrometry (ESI MS) to the structural characterization of natural organic matter. *Org Geochem* 33:171–180. doi: 10.1016/S0146-6380(01)00149-8
- Kukkadapu RK, Zachara JM, Fredrickson JK, et al (2003) Transformation of 2-line ferrihydrite to 6-line ferrihydrite under oxic and anoxic conditions. *Am Mineral* 88:1903–1914.
- Lam PJ, Lee JM, Heller MI, et al (2018) Size-fractionated distributions of suspended particle concentration and major phase composition from the U.S. GEOTRACES Eastern Pacific Zonal Transect (GP16). *Mar Chem* 201:90–107. doi: 10.1016/j.marchem.2017.08.013

- Lam PJ, Ohnemus DC, Marcus M a. (2012a) The speciation of marine particulate iron adjacent to active and passive continental margins. *Geochim Cosmochim Acta* 80:108–124. doi: 10.1016/j.gca.2011.11.044
- Lam PJ, Ohnemus DC, Marcus M a. (2012b) The speciation of marine particulate iron adjacent to active and passive continental margins. *Geochim Cosmochim Acta* 80:108–124. doi: 10.1016/j.gca.2011.11.044
- Lam PJ, Twining BS, Jeandel C, et al (2015) Methods for analyzing the concentration and speciation of major and trace elements in marine particles. *Prog Oceanogr* 133:32–42. doi: 10.1016/j.pocean.2015.01.005
- Lawrence J, Swerhone G, Leppard G, et al (2003) Scanning transmission X-ray, laser scanning , and transmission electron microscopy mapping of the exopolymeric matrix of microbial biofilms. *Appl Environ Microbiol* 69:5543–5554. doi: 10.1128/AEM.69.9.5543
- Lee JM, Heller MI, Lam PJ (2018) Size distribution of particulate trace elements in the U.S. GEOTRACES Eastern Pacific Zonal Transect (GP16). *Mar Chem* 201:108–123. doi: 10.1016/j.marchem.2017.09.006
- Leenheer JA, Brown GK, Maccarthy P, Cabaniss SE (1998) Models of metal binding structures in fulvic acid from the Suwannee River, Georgia. *Environ Sci Technol* 32:2410–2416. doi: 10.1021/es9708979
- Lehmann J, Liang B, Solomon D, et al (2005) Near-edge X-ray absorption fine structure (NEXAFS) spectroscopy for mapping nano-scale distribution of organic carbon forms in soil: Application to black carbon particles. *Global Biogeochem Cycles* 19:1–12. doi: 10.1029/2004GB002435
- Lehmann J, Solomon D, Brandes J, et al (2009) Synchrotron-Based Near-Edge X-Ray Spectroscopy of Natural Organic Matter in Soils and Sediments. In: Senesi N, Xiag B, Huang PM (eds) *Biophysico-Chemical Processes Involving Natural Nonliving Organic Matter in Environmental Systems*. John Wiley and Sons, pp 729–781
- Leinweber P, Kruse J, Walley FL, et al (2007) Nitrogen K-edge XANES - An overview of reference compounds used to identify “unknown” organic nitrogen in environmental samples. *J Synchrotron Radiat* 14:500–511. doi: 10.1107/S0909049507042513

- Lewis BL, Holt PD, Taylor SW, et al (1995) Voltammetric estimation of iron (III) thermodynamic stability constants for catecholate siderophores isolated from marine bacteria and cyanobacteria. *Mar Chem* 50:179–188.
- Li M, Toner BM, Baker BJ, et al (2014) Microbial iron uptake as a mechanism for dispersing iron from deep-sea hydrothermal vents. *Nat Commun* 5:3192. doi: 10.1038/ncomms4192
- Lilley MD, Feely RA, Trefry JH (1995) Chemical and Biochemical Transformations in Hydrothermal Plumes. In: Humphris SE, Zierenberg RA, Mullineaux LS, Thomson RE (eds) *Seafloor Hydrothermal Systems: Physical, Chemical, Biological, and Geological Interactions* (. American Geophysical Union, Washington D. C.,
- Lupton JE, Craig H (1981) A Major Helium-3 Source at 15S on the East Pacific Rise. *214*:13–18.
- Lupton JE, Delaney JR, Johnson HP, Tivey MK (1985) Entrainment and vertical transport of deep-ocean water by buoyant hydrothermal plumes. *Nature* 316:621–623. doi: 10.1038/316621a0
- Luther GW, Rozan TF, Taillefert M, et al (2001) Chemical speciation drives hydrothermal vent ecology. *Nature* 410:813–816. doi: 10.1038/35071069
- Lyle MW (1986) Major element composition of leg-92 sediments. *Initial Reports of the Deep Sea Drilling Project* 92. 355–370.
- Madigan MT, Martinko JM, Stahl DA, Clark DP (2012) *Brock Biology of Microorganisms*, 13th edn. Benjamin Cummings, Boston
- Mandernack KW, Tebo BM (1993) Manganese scavenging and oxidation at hydrothermal vents and in vent plumes. *Geochim Cosmochim Acta* 57:3907–3923. doi: 10.1016/0016-7037(93)90343-U
- Marcus M a, MacDowell A a, Celestre R, et al (2004) Beamline 10.3.2 at ALS: a hard X-ray microprobe for environmental and materials sciences. *J Synchrotron Radiat* 11:239–47. doi: 10.1107/S0909049504005837
- Marcus MA, Westphal AJ, Fakra SC (2008) Classification of Fe-bearing species from K-edge XANES data using two-parameter correlation plots. *J Synchrotron Radiat* 15:463–468. doi: 10.1107/S0909049508018293
- McDermott JM, Seewald JS, German CR, Sylva SP (2015) Pathways for abiotic organic

- synthesis at submarine hydrothermal fields. *Proc Natl Acad Sci U S A* 112:7668–72. doi: 10.1073/pnas.1506295112
- Moffett JW, German CR (2018) The U.S.GEOTRACES Eastern Tropical Pacific Transect (GP16). *Mar Chem* 201:1–5. doi: 10.1016/j.marchem.2017.12.001
- Moore CM, Mills MM, Arrigo KR, et al (2013) Processes and patterns of oceanic nutrient limitation. *Nat Geosci* 6:701–710. doi: 10.1038/ngeo1765
- Navrotsky A, Mazeina L, Majzlan J (2008) Size-driven structural and thermodynamic complexity in iron oxides. *Science* (80-) 319:1635–1638. doi: 10.1126/science.1148614
- Nealson KH, Rosson RA, Myers CR (1989) Mechanisms of oxidation and reduction of manganese. In: *Metal Ions and Bacteria*. John Wiley and Sons, New York,
- Newville M (2004) Fundamentals of XAFS. *ReVision* 43. doi: 10.2138/rmg.2014.78.2
- Nicholas SL, Erickson ML, Woodruff LG, et al (2017) Solid-phase arsenic speciation in aquifer sediments: A micro-X-ray absorption spectroscopy approach for quantifying trace-level speciation. *Geochim Cosmochim Acta* 211:228–255. doi: 10.1016/j.gca.2017.05.018
- Nico PS, Regier TZ, Gillespie AW (2017) Carbon near-edge absorption fine structure as a tool for understanding chemical differences in biochars. In: Singh B, Camps-Arbestain M, Lehmann J (eds) *Biochar: A Guide to Analytical Methods*. CSIRO Publishing, Clayton South, Australia, pp 214–228
- Nishioka J, Obata H, Tsumune D (2013) Evidence of an extensive spread of hydrothermal dissolved iron in the Indian Ocean. *Earth Planet Sci Lett* 361:26–33. doi: 10.1016/j.epsl.2012.11.040
- O’day PA, Rivera Jr. N, Root R, Carroll SA (2004) X-ray absorption spectroscopic study of Fe reference compounds for the analysis of natural sediments.pdf. *Am Mineral* 89:572–585.
- Oades JM (1984) Soil organic matter and structural stability: mechanisms and implications for management. *Plant Soil* 76:319–337. doi: 10.1007/BF02205590
- Oades JM (1988) The retention of organic matter in soils. *Biogeochemistry* 5:35–70. doi: 10.1007/BF02180317
- Ohnemus DC, Lam PJ (2015) Cycling of lithogenic marine particles in the US

- GEOTRACES North Atlantic transect. *Deep Res Part II Top Stud Oceanogr* 116:283–302. doi: 10.1016/j.dsr2.2014.11.019
- Ohnemus DC, Rauschenberg S, Cutter GA, et al (2016) Elevated trace metal content of prokaryotic communities associated with marine oxygen deficient zones. *Limnol Oceanogr* 62:3–25. doi: 10.1002/lno.10363
- Olins HC, Rogers DR, Preston C, Iii WU (2017) Co-registered Geochemistry and Metatranscriptomics Reveal Unexpected Distributions of Microbial Activity within a Hydrothermal Vent Field. *Front Microbiol* 8:1–18. doi: 10.3389/fmicb.2017.01042
- Peters BD, Jenkins WJ, Swift JH, et al (2018) Water mass analysis of the 2013 US GEOTRACES eastern Pacific zonal transect (GP16). *Mar Chem* 201:6–19. doi: 10.1016/j.marchem.2017.09.007
- Plashkevych O, Carravetta V, Vahtras O, Ågren H (1998) Theoretical study of X-ray circular dichroism of amino acids. *Chem Phys* 232:49–62. doi: 10.1016/S0301-0104(98)00055-X
- Post JE (1999) Manganese oxide minerals : Crystal structures and economic and. *Proc Natl Acad Sci* 96:3447–3454.
- Ravel B, Newville M (2005) ATHENA, ARTEMIS, HEPHAESTUS: Data analysis for X-ray absorption spectroscopy using IFEFFIT. *J Synchrotron Radiat* 12:537–541. doi: 10.1107/S0909049505012719
- Reed DC, Breier J a, Jiang H, et al (2015) Predicting the response of the deep-ocean microbiome to geochemical perturbations by hydrothermal vents. *ISME J* 1–13. doi: 10.1038/ismej.2015.4
- Repeta DJ, Quan TM, Aluwihare LI, Accardi A (2002) Chemical characterization of high molecular weight dissolved organic matter in fresh and marine waters. *Geochim Cosmochim Acta* 66:955–962. doi: 10.1016/S0016-7037(01)00830-4
- Resing J a., Sedwick PN, German CR, et al (2015) Basin-scale transport of hydrothermal dissolved metals across the South Pacific Ocean. *Nature* 523:200–203. doi: 10.1038/nature14577
- Rouxel O, Shanks WC, Bach W, Edwards KJ (2008) Integrated Fe- and S-isotope study of seafloor hydrothermal vents at East Pacific Rise 9-10°N. *Chem Geol* 252:214–227. doi: 10.1016/j.chemgeo.2008.03.009

- Rouxel O, Toner BM, Manganini SJ, German CR (2016) Geochemistry and iron isotope systematics of hydrothermal plume fall-out at East Pacific Rise 9°50'N. *Chem Geol* 441:212–234. doi: 10.1016/j.chemgeo.2016.08.027
- Rue EL, Bruland KW (1995) Complexation of iron(III) by natural organic ligands in the Central North Pacific as determined by a new competitive ligand equilibration/adsorptive cathodic stripping voltammetric method. *Mar Chem* 50:117–138. doi: 10.1016/0304-4203(95)00031-L
- Saito MA, Noble AE, Tagliabue A, et al (2013) Slow-spreading submarine ridges in the South Atlantic as a significant oceanic iron source. *Nat Geosci* 6:775–779. doi: 10.1038/ngeo1893
- Sander SG, Koschinsky A (2011) Metal flux from hydrothermal vents increased by organic complexation. *Nat Geosci* 4:145–150. doi: 10.1038/ngeo1088
- Sander SG, Koschinsky A, Massoth G, et al (2007) Organic complexation of copper in deep-sea hydrothermal vent systems. *Environ Chem* 4:81–89. doi: 10.1071/EN06086
- Sands CM, Connelly DP, Statham PJ, German CR (2012) Size fractionation of trace metals in the Edmond hydrothermal plume, Central Indian Ocean. *Earth Planet Sci Lett* 319–320:15–22. doi: 10.1016/j.epsl.2011.12.031
- Santelli CM, Webb SM, Dohnalkova AC, Hansel CM (2011) Diversity of Mn oxides produced by Mn(II)-oxidizing fungi. *Geochim Cosmochim Acta* 75:2762–2776. doi: 10.1016/j.gca.2011.02.022
- Sayles FL, Martin WR, Chase Z, Anderson RF (2001) Benthic remineralization and burial of biogenic SiO₂, CaCO₃, organic carbon, and detrital material in the Southern Ocean along a transect at 170° West. *Deep Res Part II Top Stud Oceanogr* 48:4323–4383. doi: 10.1016/S0967-0645(01)00091-1
- Schmidt MWI, Torn MS, Abiven S, et al (2011) Persistence of soil organic matter as an ecosystem property. *Nature* 478:49–56. doi: 10.1038/nature10386
- Schulten H-R, Schnitzer M (1997) Chemical Model Structures for Soil Organic Matter and Soils. *Soil Sci* 162:115–130. doi: 10.1097/00010694-199702000-00005
- Sedlmair J, Gleber SC, Peth C, et al (2012) Characterization of refractory organic substances by NEXAFS using a compact X-ray source. *J Soils Sediments* 12:24–34.

doi: 10.1007/s11368-011-0385-9

- Seewald JS, Seyfried WE (1990) The effect of temperature on metal mobility in subseafloor hydrothermal systems: constraints from basalt alteration experiments. *Earth Planet Sci Lett* 101:388–403. doi: 10.1016/0012-821X(90)90168-W
- Seyfried WE, Ding K (1993) The effect of redox on the relative solubilities of copper and iron in Cl-bearing aqueous fluids at elevated temperatures and pressures: An experimental study with application to subseafloor hydrothermal systems. *Geochim Cosmochim Acta* 57:1905–1917. doi: 10.1016/0016-7037(93)90083-9
- Sheik CS, Anantharaman K, Breier JA, et al (2015) Spatially resolved sampling reveals dynamic microbial communities in rising hydrothermal plumes across a back-arc basin. *ISME J* 9:1434–45. doi: 10.1038/ismej.2014.228
- Shimmield B, Price NB (1988) The scavenging of U, ²³⁰Th and ²³¹Pa during pulsed hydrothermal activity at 20S, East Pacific Rise. *Geochim Cosmochim Acta* 52:669–677. doi: 10.1016/0016-7037(88)90329-8
- Solomon D, Lehmann J, Kinyangi J, et al (2009) Carbon (1s) NEXAFS spectroscopy of biogeochemically relevant reference organic compounds. *Soil Sci Soc Am J* 73:1817. doi: 10.2136/sssaj2008.0228
- Stöhr J (2003) *NEXAFS Spectroscopy, Second*. Springer, Heidelberg, Germany
- Sutton R, Sposito G (2005) Critical Review Molecular Structure in Soil Humic Substances : The New View. *Environ Sci Technol* 39:9009–9015. doi: 10.1021/es050778q
- Sylvan JB, Pyenson BC, Rouxel O, et al (2012) Time-series analysis of two hydrothermal plumes at 9°50'N East Pacific Rise reveals distinct, heterogeneous bacterial populations. *Geobiology* 10:178–192. doi: 10.1111/j.1472-4669.2011.00315.x
- Tagliabue A, Bopp L, Dutay J-C, et al (2010) Hydrothermal contribution to the oceanic dissolved iron inventory. *Nat Geosci* 3:252–256. doi: 10.1038/ngeo818
- Tagliabue A, Bowie AR, Boyd PW, et al (2017) The integral role of iron in ocean biogeochemistry. *Nature* 543:51–59. doi: 10.1038/nature21058
- Tagliabue A, Resing JA (2016) Impact of hydrothermalism on the ocean iron cycle. *Philos Trans A in Press*. doi: 10.1098/rsta.2015.0291
- Tanaka M, Nakagawa K, Koketsu T, et al (2001) Oxygen K-edge X-ray absorption near

- edge structures (XANES) of sublimated films of amino acids. *J Synchrotron Radiat* 8:1009–1011. doi: 10.1107/S0909049500017829
- Tebo BM, Bargar JR, Clement BG, et al (2004) BIOGENIC MANGANESE OXIDES: Properties and Mechanisms of Formation. *Annu Rev Earth Planet Sci* 32:287–328. doi: 10.1146/annurev.earth.32.101802.120213
- Tivey M (2007) Generation of Seafloor Hydrothermal Vent Fluids and Associated Mineral Deposits. *Oceanography* 20:50–65. doi: 10.5670/oceanog.2007.80
- Tivey MK, McDuff RE (1990) Mineral precipitation in the walls of black smoker chimneys: A quantitative model of transport and chemical reaction. *J Geophys Res* 95:12617. doi: 10.1029/JB095iB08p12617
- Toner B, Fakra S, Villalobos M, et al (2005) Spatially Resolved Characterization of Biogenic Manganese Oxide Production within a Bacterial Biofilm. *Appl Environ Microbiol* 71:1300–1310. doi: 10.1128/AEM.71.3.1300
- Toner B, Marcus M, Edwards K, et al (2012a) Measuring the form of iron in hydrothermal plume particles. *Oceanography* 25:209–212. doi: <http://dx.doi.org/10.5670/oceanog.2012.19>
- Toner BM, Berquó TS, Michel FM, et al (2012b) Mineralogy of iron microbial mats from Loihi seamount. *Front Microbiol* 3:118. doi: 10.3389/fmicb.2012.00118
- Toner BM, Fakra SC, Manganini SJ, et al (2009a) Preservation of iron(II) by carbon-rich matrices in a hydrothermal plume. *Nat Geosci* 2:197–201. doi: 10.1038/ngeo433
- Toner BM, German CR, Dick GJ, Breier JA (2016) Deciphering the Complex Chemistry of Deep-Ocean Particles Using Complementary Synchrotron X-ray Microscope and Microprobe Instruments. *Acc Chem Res* 49:128–137. doi: 10.1021/acs.accounts.5b00282
- Toner BM, Nicholas SL, Coleman Wasik JK (2014a) Scaling up : fulfilling the promise of X-ray microprobe for biogeochemical research. *Environ Chem*. doi: <http://dx.doi.org/10.1071/EN13162>
- Toner BM, Nicholas SL, Wasik JKC (2014b) Scaling up: Fulfilling the promise of X-ray microprobe for biogeochemical research. *Environ Chem* 11:4–9. doi: 10.1071/EN13162
- Toner BM, Santelli CM, Marcus M a., et al (2009b) Biogenic iron oxyhydroxide

- formation at mid-ocean ridge hydrothermal vents: Juan de Fuca Ridge. *Geochim Cosmochim Acta* 73:388–403. doi: 10.1016/j.gca.2008.09.035
- Trefry JH, Trocine RP, Klinkhammer GP (1985) Iron and Copper Enrichment of Suspended Particles in Dispersed Hydrothermal Plumes Along the Mid-Atlantic Ridge. *Science* 228:506–509.
- Trouwborst RE, Clement BG, Tebo BM, et al (2006) Soluble Mn (III) in suboxic zones. *Science* (80-) 312:1955–1957. doi: 10.1126/science.1132876
- Urquhart SG, Ade H (2002) Trends in the Carbonyl Core (C 1s, O 1s) @p*C=O Transition in the Near Edge X-ray Absorption Fine Structure Spectra of Organic Molecules. *J Phys Chem B* 106:8531–8538.
- Van Dover CL (2000) *The ecology of deep-sea hydrothermal vents*. Princeton University Press, Princeton, NJ
- Villalobos M, Toner B, Bargar J, Sposito G (2003) Characterization of the manganese oxide produced by *Pseudomonas putida* strain MnB1. *Geochim Cosmochim Acta* 67:2649–2662. doi: 10.1016/S0016-7037(03)00217-5
- von Damm KL (1990) Seafloor hydrothermal activity: Black Smoker chemistry and chimneys. *Annu Rev Earth Planet Sci* 18:173–204.
- Von Damm KL, Edmond JM, Measures CI, Grant B (1985) Chemistry of submarine hydrothermal solutions at Guaymas Basin , Gulf of California. *Geochim Cosmochim Acta* 49:2221–2237.
- Von Damm KL, Lilley MD (2004) Diffuse Flow Hydrothermal Fluids from 9°50'N East Pacific Rise: Origin, Evolution and Biogeochemical Controls. *Subsurf Biosph Mid-Ocean Ridges AGU Monogr*:243–266.
- von der Heyden BP, Roychoudhury AN, Mtshali TN, et al (2012) Chemically and Geographically Distinct Solid-Phase Iron Pools in the Southern Ocean. *Science* (80-) 338:1199–1201. doi: 10.2960/J.v42.m652
- Vraspir JM, Butler A (2009) Chemistry of marine ligands and siderophores. *Ann Rev Mar Sci* 1:43–63. doi: 10.1146/annurev.marine.010908.163712
- Webb SM (2005) SIXPack a Graphical User Interface for XAS Analysis Using IFEFFIT. *Phys Scr T115*:1011–1014. doi: 10.1238/Physica.Topical.115a01011
- Webb SM, Dick GJ, Bargar JR, Tebo BM (2005) Evidence for the presence of Mn(III)

- intermediates in the bacterial oxidation of Mn(II). *Proc Natl Acad Sci U S A* 102:5558–63. doi: 10.1073/pnas.0409119102
- Weishaar JL, Aiken GR, Bergamaschi BA, et al (2003) Evaluation of specific ultraviolet absorbance as an indicator of the chemical composition and reactivity of dissolved organic carbon. *Environ Sci Technol* 37:4702–4708. doi: 10.1021/es030360x
- Weiss RF, Longsdale P, Lupton JE, et al (1977) Hydrothermal plumes in the Galapagos Rift. *Nature* 267:192–193.
- Wells ML, Goldberg ED (1993) Colloid aggregation in seawater. *Mar Chem* 41:353–358. doi: 10.1016/0304-4203(93)90267-R
- Welter E, Calmano W, Mangold S, Tröger L (1999) Chemical speciation of heavy metals in soils by use of XAFS spectroscopy and electron microscopical techniques. *Fresenius J Anal Chem* 364:238–244. doi: 10.1007/s002160051330
- Wershaw RL (1993) Model for Humus: In *Soils and Sediments*. *Environ Sci Technol* 27:814–816. doi: 10.1021/es00042a603
- Wershaw RL (1986) A new model for humic materials and their interactions with hydrophobic organic chemicals in soil-water or sediment-water systems. *J Contam Hydrol* 1:29–45. doi: 10.1016/0169-7722(86)90005-7
- Wu J, Luther GW (1995) Complexation of Fe (III) by natural organic ligands in the Northwest Atlantic Ocean by a competitive ligand equilibration method and a kinetic approach. *Mar Chem* 50:159–177.
- Wu J, Wells ML, Rember R (2011) Dissolved iron anomaly in the deep tropical-subtropical Pacific: Evidence for long-range transport of hydrothermal iron. *Geochim Cosmochim Acta* 75:460–468. doi: 10.1016/j.gca.2010.10.024
- Yücel M, Gartman A, Chan CS, Luther GW (2011) Hydrothermal vents as a kinetically stable source of iron-sulphide-bearing nanoparticles to the ocean. *Nat Geosci* 4:367–371. doi: 10.1038/ngeo1148
- Zeng T, Arnold WA, Toner BM (2013) Microscale characterization of sulfur speciation in lake sediments. *Environ Sci Technol* 47:1287–1296. doi: 10.1021/es303914q
- Zhang Y, Liu Z, Zhao Y, et al (2014) Mesoscale eddies transport deep-sea sediments. *Sci Rep* 4:1–7. doi: 10.1038/srep05937
- Zhou JL, Rowland S, Fauzi R, et al (1994) The formation of humic coatings on mineral

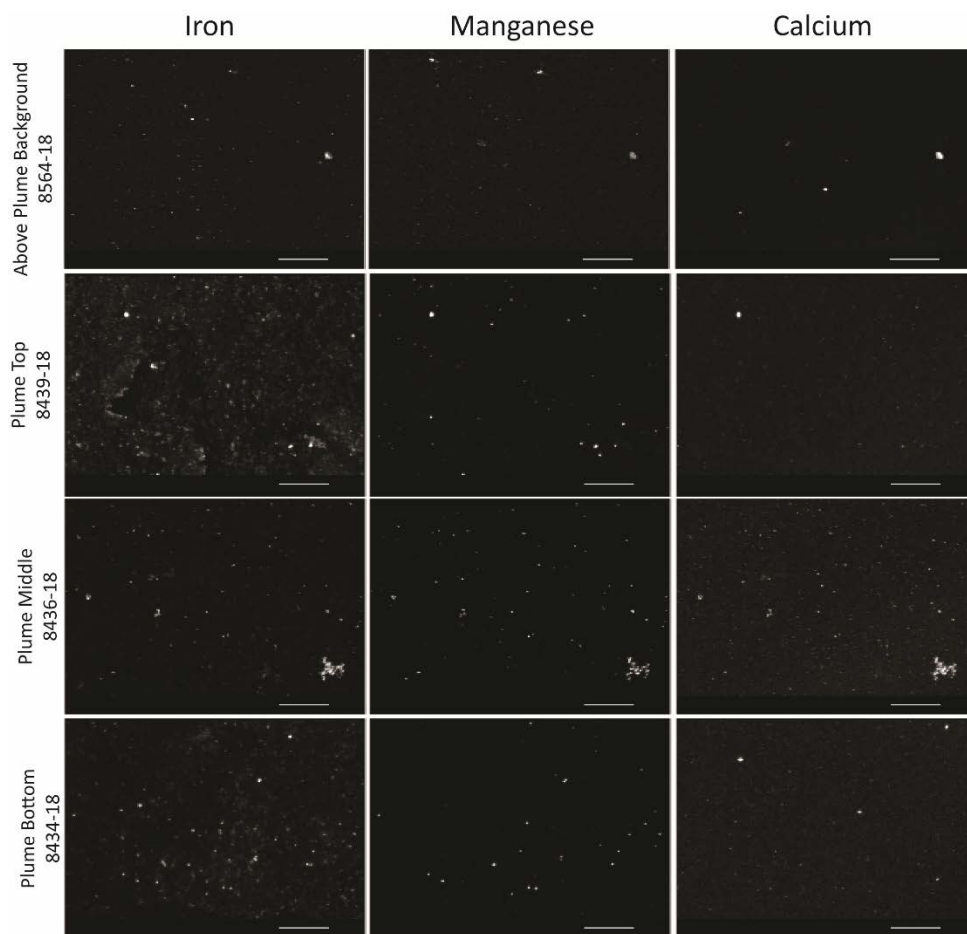
particles under simulated estuarine conditions-A mechanistic study. *Water Res* 28:571–579. doi: 10.1016/0043-1354(94)90008-6

Ziervogel K, Forster S (2005) Aggregation and sinking behaviour of resuspended fluffy layer material. *Cont Shelf Res* 25:1853–1863. doi: 10.1016/j.csr.2005.06.008

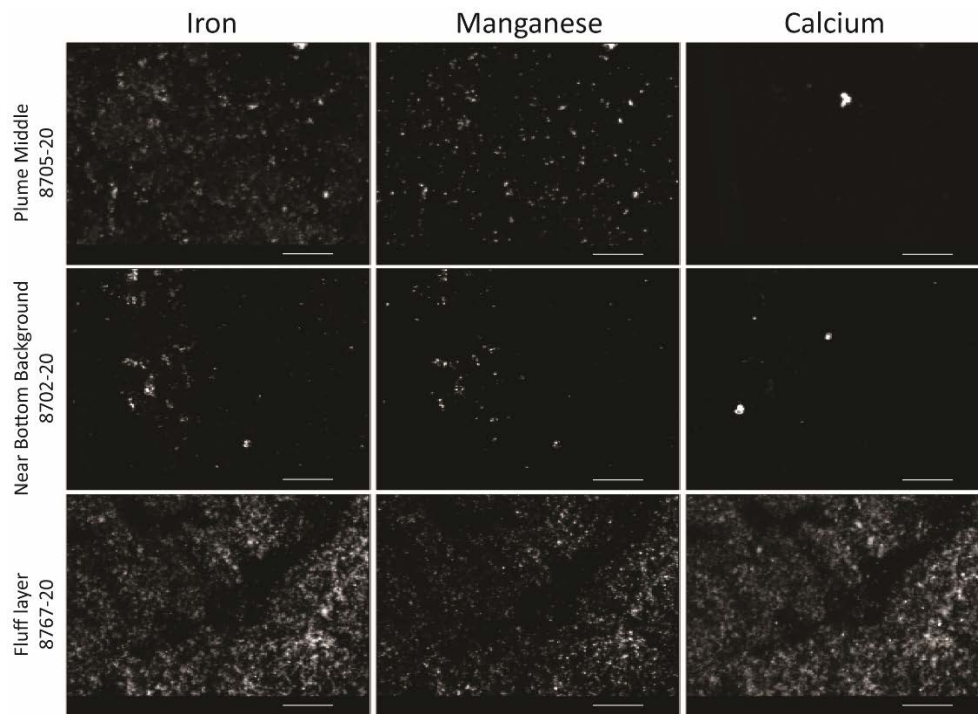
APPENDIX 1 - Chapter 2

Supplementary Information

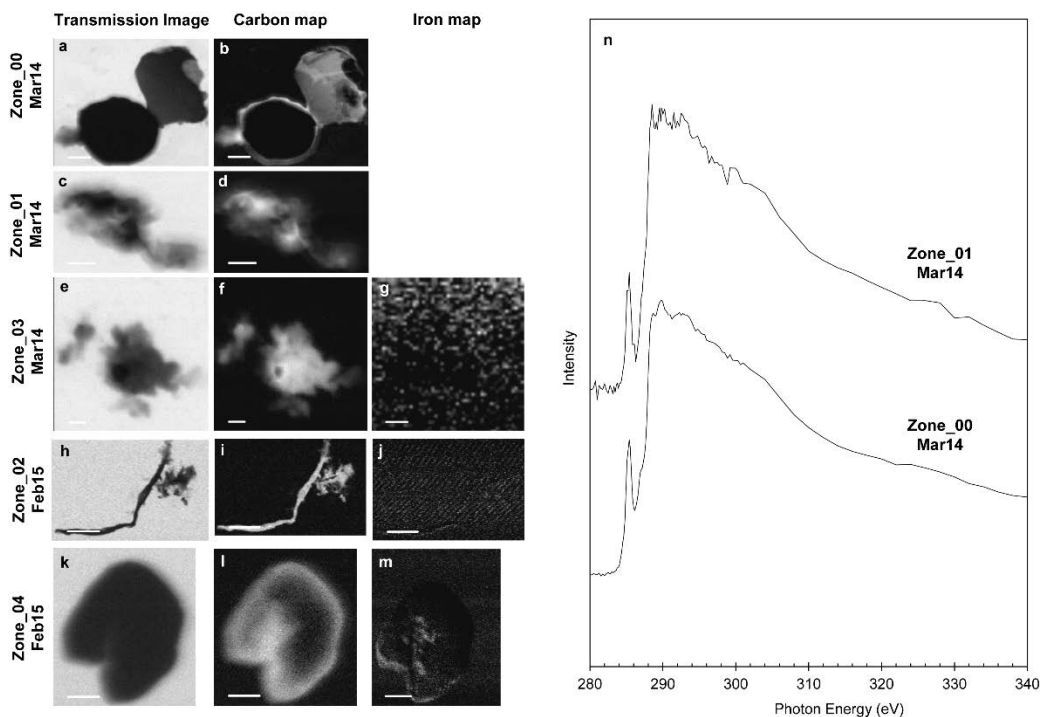
The figures and tables below correspond to supplement materials for Chapter 2 “Near-field iron and carbon chemistry of non-buoyant hydrothermal plume particles, Southern East Pacific Rise 15°S”. Please refer for to Chapter 2 for further explanations and significance of the data provided below.



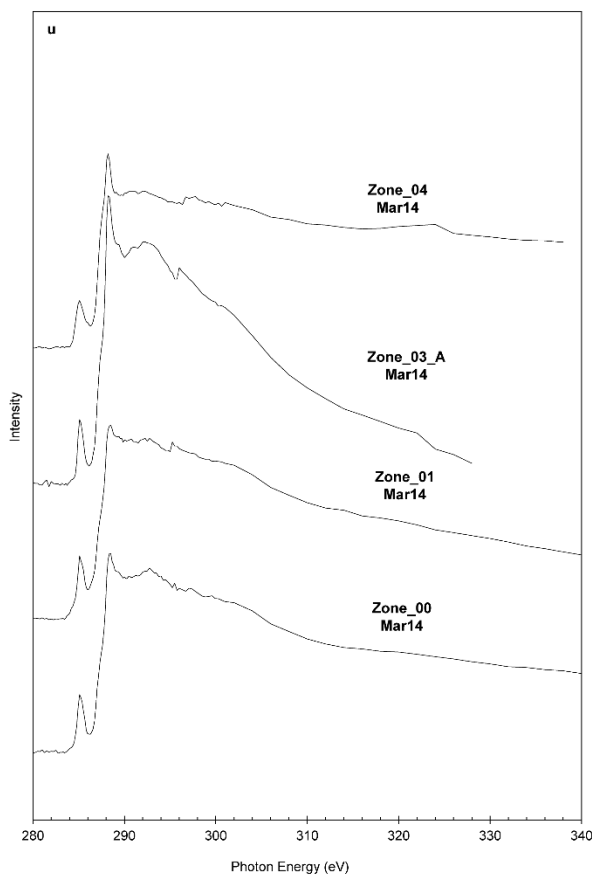
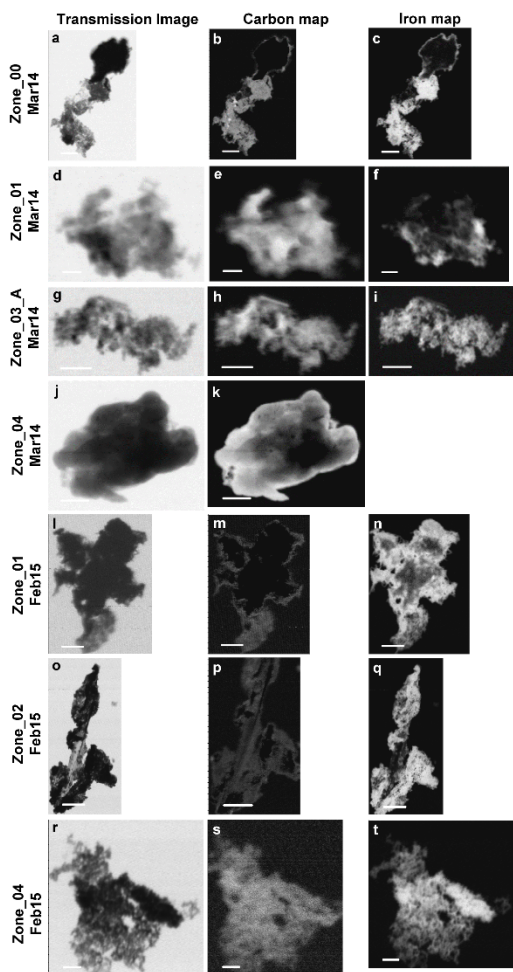
Appendix 1.1 X-ray fluorescence (XRF) maps of total iron, total manganese, and total calcium for the above plume background and top, middle, and bottom plume samples at Station 18. All scale bars 200 micron.



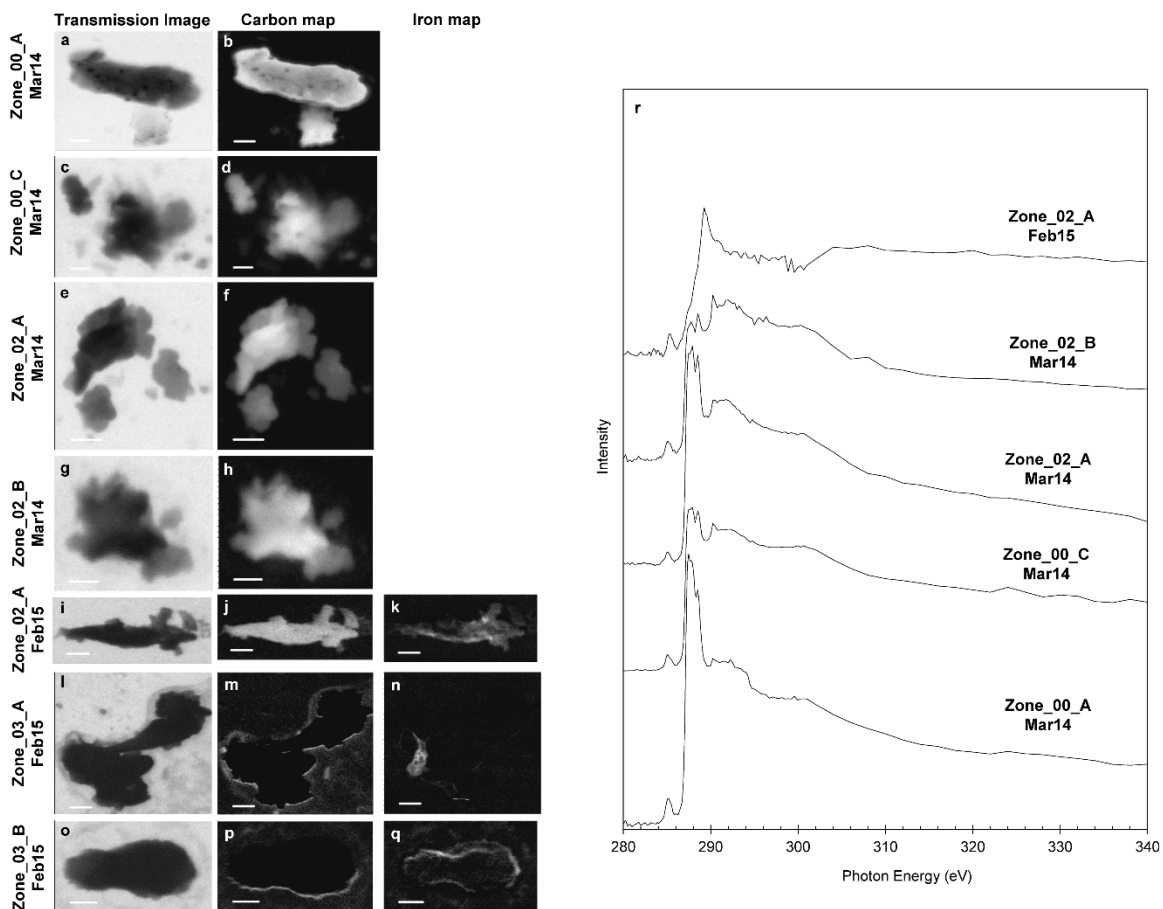
Appendix 1.2 X-ray fluorescence (XRF) maps of total iron, total manganese, and total calcium for the plume middle, near bottom background, and benthic fluff layer samples at Station 20. All scale bars 200 micron.



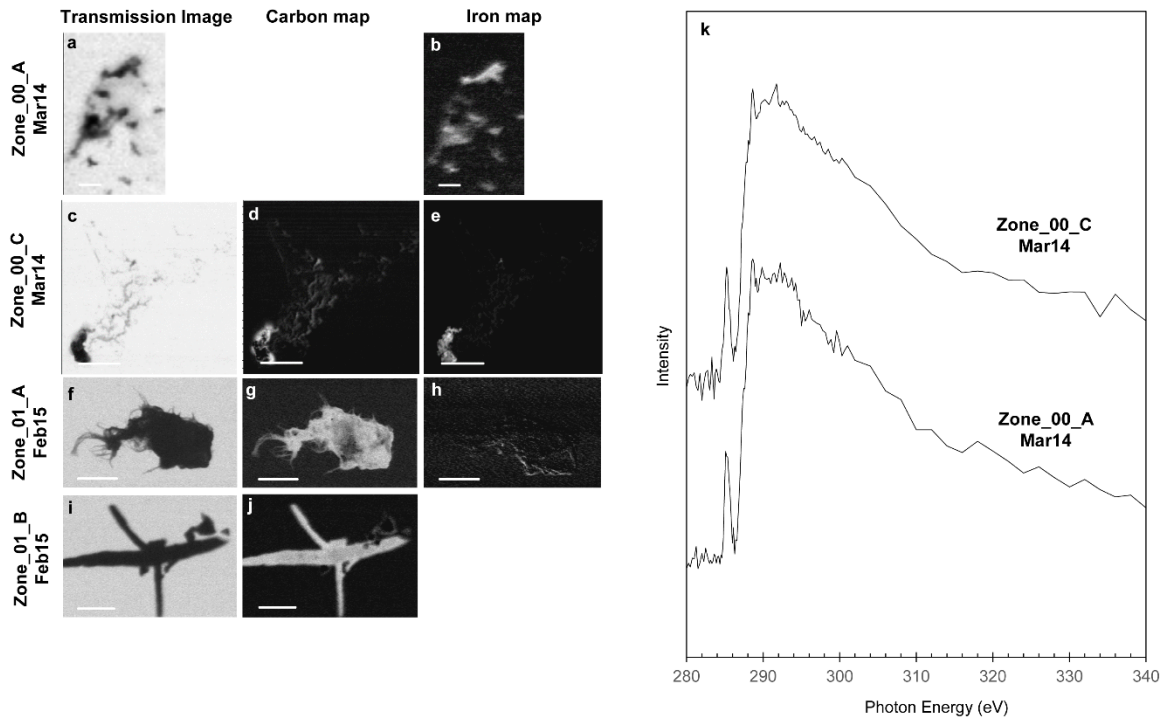
Appendix 1.3 Station 18 STXM elemental maps of the above plume background. All marine particles analyzed at the above plume background (1600 m). Transmission images were collected at 290 eV (a, c, e, h, and k). Total carbon optical density ranges from 1.44 (b), 1.07 (d), 1.12 (f), 1.04 (i), and 0.990 (l). Total iron optical density ranges from 0.0595 (g), 1.86 (f), and 0.302 (i). In some case, and iron map was not run due to no iron being detected in those samples. Scale bars for a-d are 2 μ m, e and f are 500nm, g is 200nm, h-j are 5 μ m, and all others are 1 μ m. Carbon 1s XANES spectra from the above plume background (n).



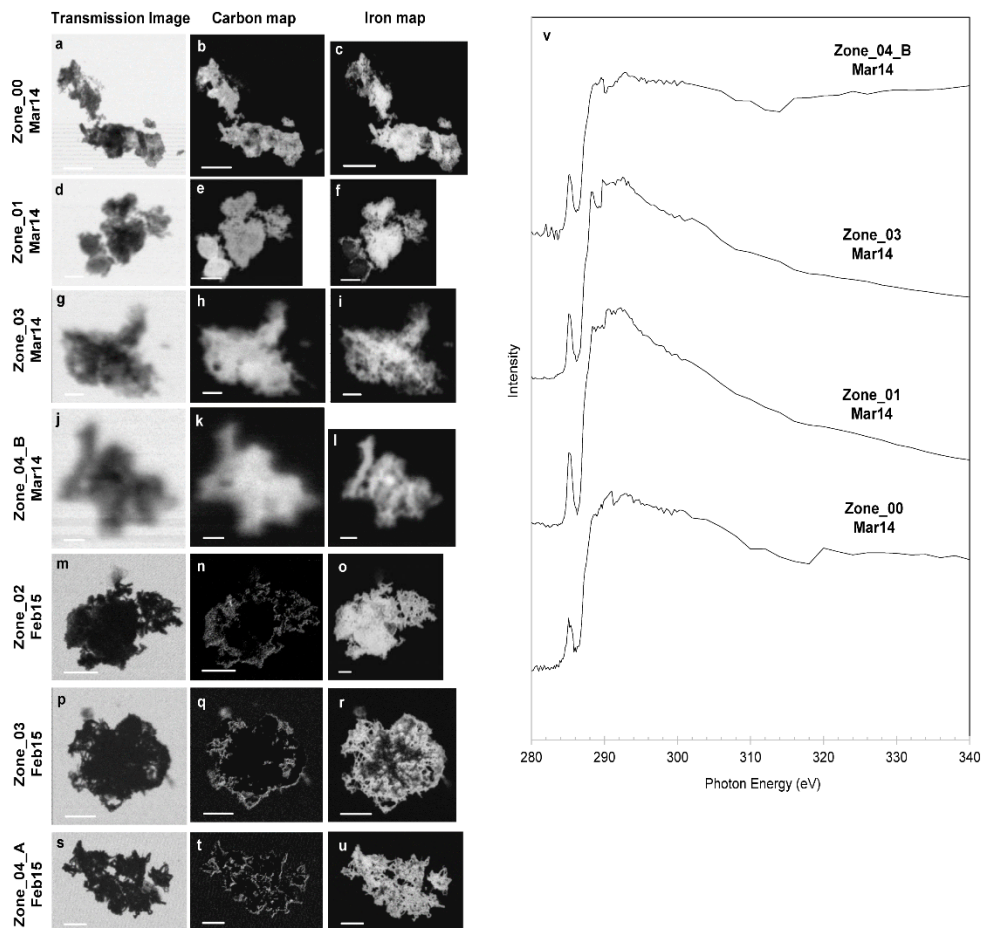
Appendix 1.4 Station 18 STXM elemental maps of the middle of the plume. All marine particles analyzed in the middle of the plume at Station 18 (2500 m). Transmission images were collected at 290 eV (a, d, g, j, l, o, and r). Total carbon optical density ranges from 1.35 (b), 1.59 (e), 1.01 (h), 1.87 (k), 1.25 (m), 1.82 (p), and 0.713 (s). Total iron optical density ranges from 2.83 (c), 1.67 (f), 2.27 (i), 2.26 (n), 2.91 (q), and 2.44 (t). For Zone_04 Mar14 an iron elemental map was not collected. Scale bars for a-c, o-q are 5 μ m, g-n are 2 μ m, and all others are 1 μ m. Carbon 1s XANES spectra from the middle of the plume at station 18 (u).



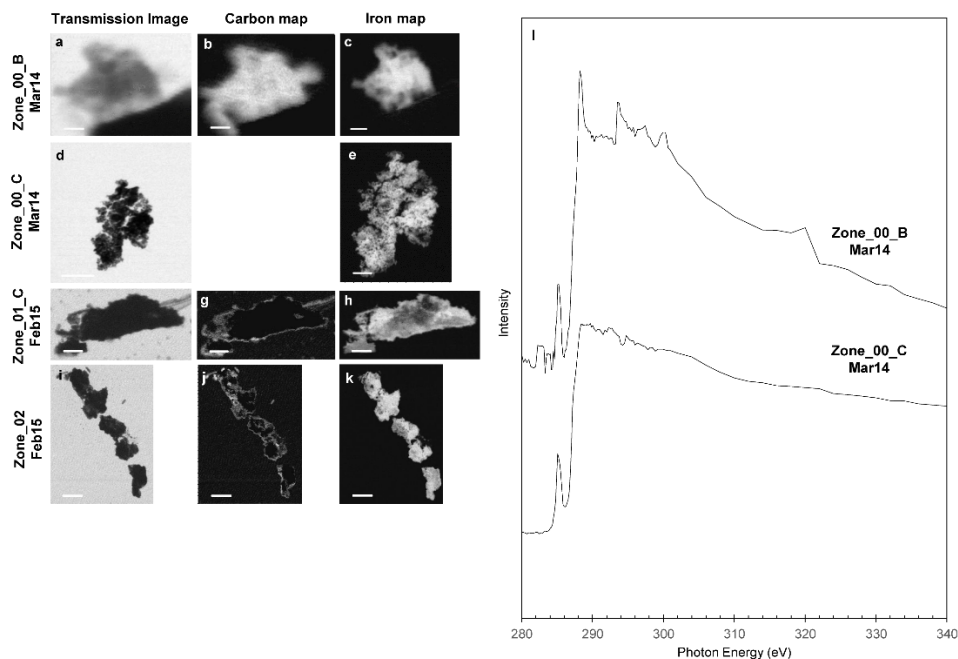
Appendix 1.5 Station 18 STXM elemental maps of the bottom of the plume. All marine particles analyzed at the bottom of Station 18 (2610 m). Transmission images were collected at 290 eV (a, c, e, g, i, l, and o). Total carbon optical density ranges from 1.90 (b), 1.51 (d), 1.60 (f), 0.670 (h), 0.994 (j), 0.606 (m), and 0.580 (p). Total iron optical density ranges from 0.584 (k), 0.854 (n), and 0.472 (q). For particles collect in March 2014, iron elemental maps were not collected. Scale bars a, b, j-n are 2 μ m, c-d, g-h are 500nm, and all others are 1 μ m. Carbon 1s XANES spectra from the bottom of the plume at station 18 (u).



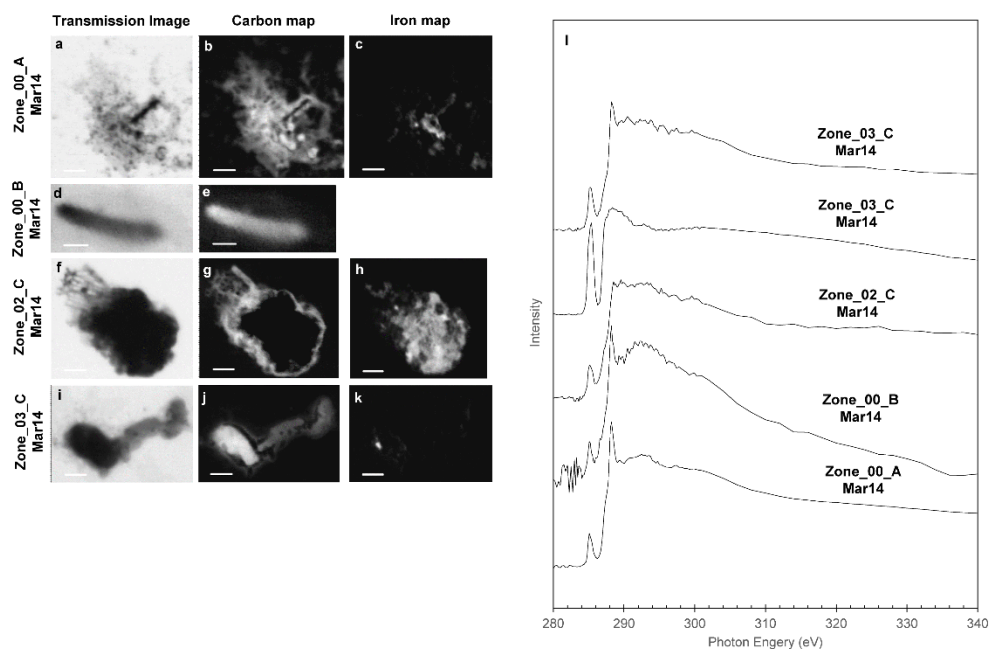
Appendix 1.6 Station 20 STXM elemental maps of the top of the plume. All marine particles analyzed the top of the plume at Station 20 (2350 m). Transmission images were collected at 290 eV (a, c, f, and i). Total carbon optical density ranges from 1.10 (d), 1.20 (g), and 1.28 (j). Total iron optical density ranges from 0.244 (b), 1.69 (e), and 0.411 (h). The carbon elemental map was corrupted for zone_00_A Mar14 and no iron map was collected for Zone_01_B Feb15. Scale bars for a-b are 2 μ m, and all others are 5 μ m. Carbon 1s XANES spectra from the top of the plume at station 20 (k).



Appendix 1.7 Station 20 STXM elemental maps of the middle of the plume. All marine particles analyzed in the middle of the plume at Station 20 (2550 m). Transmission images were collected at 290 eV (a, d, g, j, m, p, and s). Total carbon optical density ranges from 1.50 (b), 1.81 (e), 1.53 (h), 1.20 (k), 0.628 (n), 0.688 (q), and 0.689 (t). Total iron optical density ranges from 2.57 (c), 2.55 (f), 2.27 (i), 1.73 (l), 3.02 (o), 2.67 (r), and 2.82 (u). Scale bars for a-c, m-u are 5 μ m, d-f are 2 μ m, g-j are 1 μ m, and j-l are 500nm. Zone_01 Mar14 was previously published in Fitzsimmons et al., 2017. Carbon 1s XANES spectra from the middle of the plume at station 20 (v).

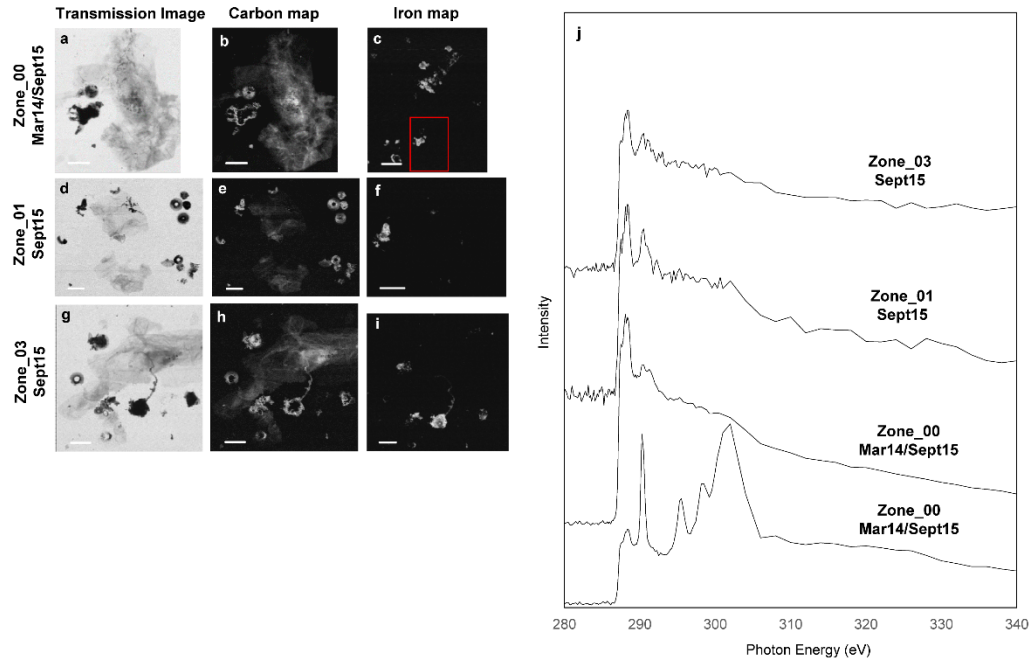


Appendix 1.8 Station 20 STXM elemental maps of the bottom of the plume. All marine particles analyzed at the bottom of the plume at station 20 (2600 m). Transmission images were collected at 290 eV (a, d, f, and i). Total carbon optical density ranges from 1.25 (b), 0.754 (g), and 0.853 (j). Total iron optical density ranges from 1.82 (c), 2.33 (e), 2.54 (h), and 2.85 (k). Scale bars for a-c are 500nm, d, i-k are 5 μ m, and e, f-h are 2 μ m. Carbon 1s XANES spectra from the bottom of the plume at station 20 (l).



Appendix 1.9 Station 20 STXM elemental maps of the near bottom background. All marine particles analyzed at the near bottom background at Station 20 (3140 m). Transmission images were collected at 290 eV (a,d,f, and i). Total carbon optical density ranges from 1.36 (b), 0.535 (e), 1.25 (g), and 1.88 (j). Total iron optical density ranges from 0.961 (c), 1.67 (h), and 1.88 (k). An iron elemental map was not collected

at zone_00_B Mar14. Scale bars for (a-c) are 2 μ m, (d-e) are 500nm, and all others are 1 μ m. Rod-shaped (d-e, g) and spherical cells (b) were commonly observed throughout this sample. Carbon 1s XANES spectra from the near bottom background (l).

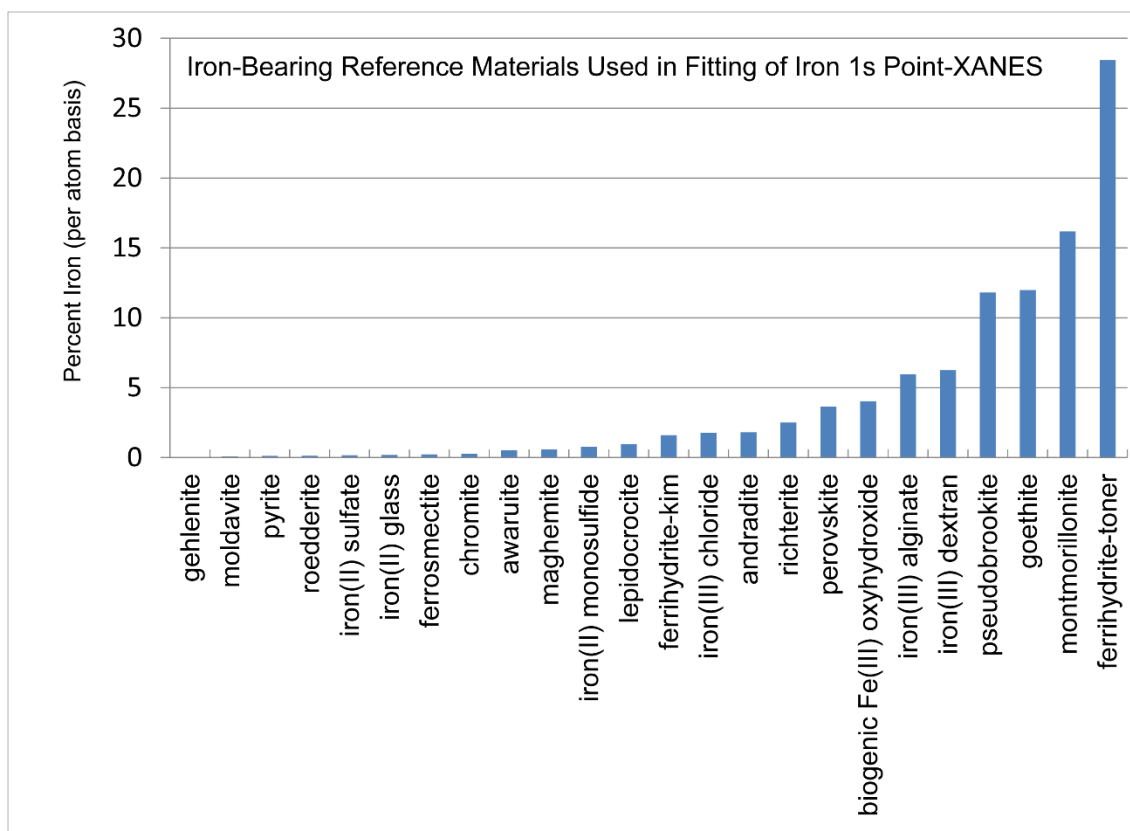


Appendix 1.10 Station 20 STXM elemental maps of the fluff layer. All marine particles analyzed by STXM at the station 20 fluff layer (3178 m). Transmission images were collected at 290 eV (a, d, and g). Total carbon optical density ranges from 2.61 (b), 2.21 (e), and 2.31 (h). Total iron optical density ranges from 0.927 (c), 1.23 (f), and 1.28 (i). The red rectangle in Zone 00 (c) refers to the area mapped in (a) and (b). The scale bar for c is 10 μ m. All other scale bars are 5 μ m. Carbon 1s XAS spectra from the fluff layer at station 20 (j).

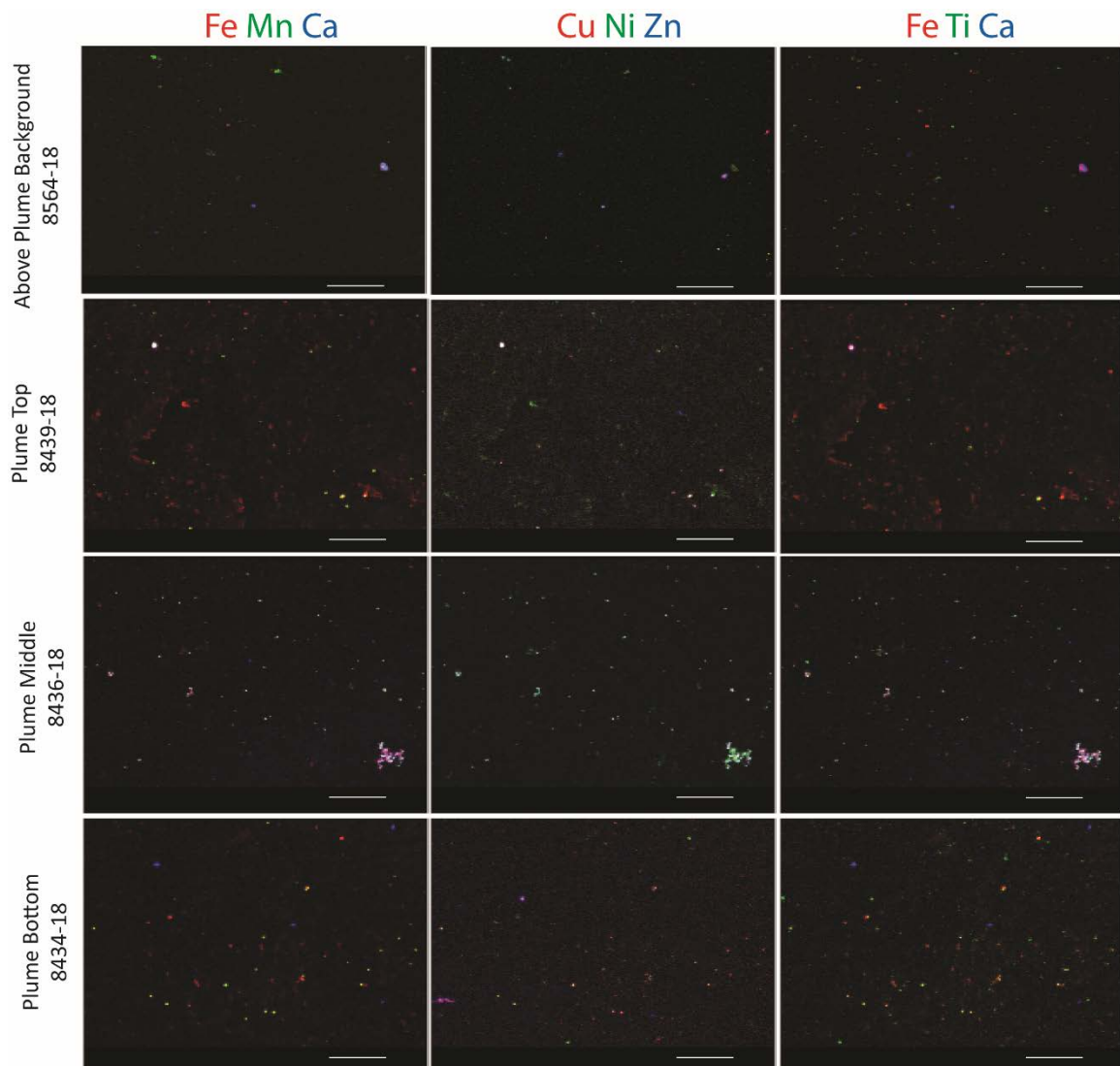
Appendix Table 1.1 Fe 1s μ XANES mineral classifications of post-fit fittings

standard nickname	standard full name	post-fit bins
gehlenite	gehlenite	silicate
moldavite	moldavite	Fe(II)
pyrite	pyrite	Fe sulfide
roedderite	roedderite	silicate
feso4	iron(II) sulfate	Fe(II)
basaltNKT	iron(II) glass	Fe(II)
clayFS	ferrosmeectite	Fe(III)phyllosilicate
chromite	chromite	Fe(II)oxide
awaruite	awaruite	native Fe
maghemite	maghemite	Fe(III)oxide
fes	iron(II) monosulfide	Fe sulfide
lep	lepidocrocite	Fe(III)oxyhydroxide and organics
fhKIM	ferrihydrite-kim	Fe(III)oxyhydroxide and organics

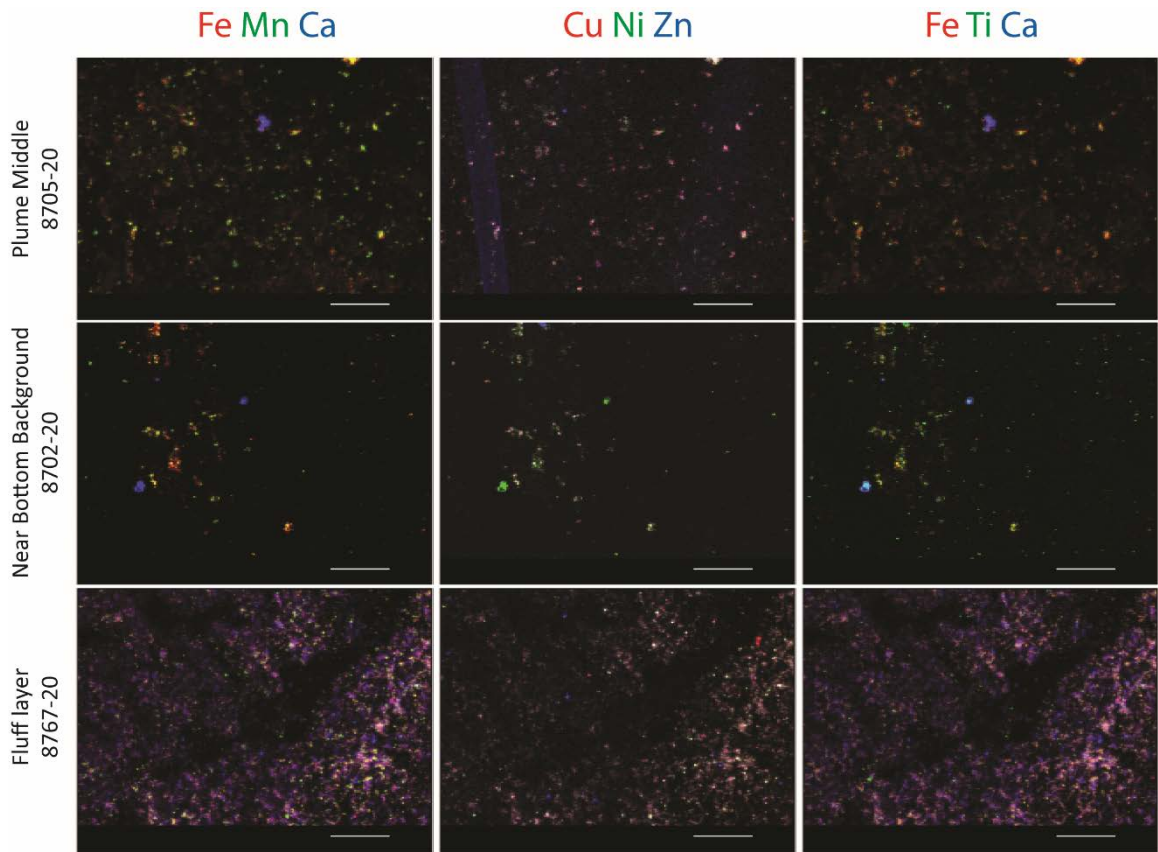
fecl3	iron(III) chloride	Fe(III)oxyhydroxide and organics
andradite	andradite	silicate
richterite	richterite	silicate
perovskite	perovskite	Fe(II)oxide
bio	biogenic Fe(III) oxyhydroxide	Fe(III)oxyhydroxide and organics
alginate	iron(III) alginate	Fe(III)oxyhydroxide and organics
dextran	iron(III) dextran	Fe(III)oxyhydroxide and organics
pseudobrookite	pseudobrookite	Fe(III)oxide
goe	goethite	Fe(III)oxyhydroxide and organics
claySTX	montmorillonite	Fe(III)phyllosilicate
fh	ferrihydrate-toner	Fe(III)oxyhydroxide and organics



Appendix 1.11 Frequency distribution of Fe-bearing standards in linear combination fitting of microprobe Fe 1s XANES data.



Appendix 1.12 X-ray fluorescence (XRF) tricolor maps for above plume background and top, middle, and bottom plume samples at Station 18. Column left (FeMnCa), center (CuNiZn), and right (FeTiCa) are shown in red, green, blue. All scale bars 200 micron.



Appendix 1.13 X-ray fluorescence (XRF) tricolor maps for the plume middle, near bottom background, and benthic fluff layer samples at Station 20. Column left (FeMnCa), center (CuNiZn), and right (FeTiCa) are shown in red, green, blue. All scale bars 200 micron.

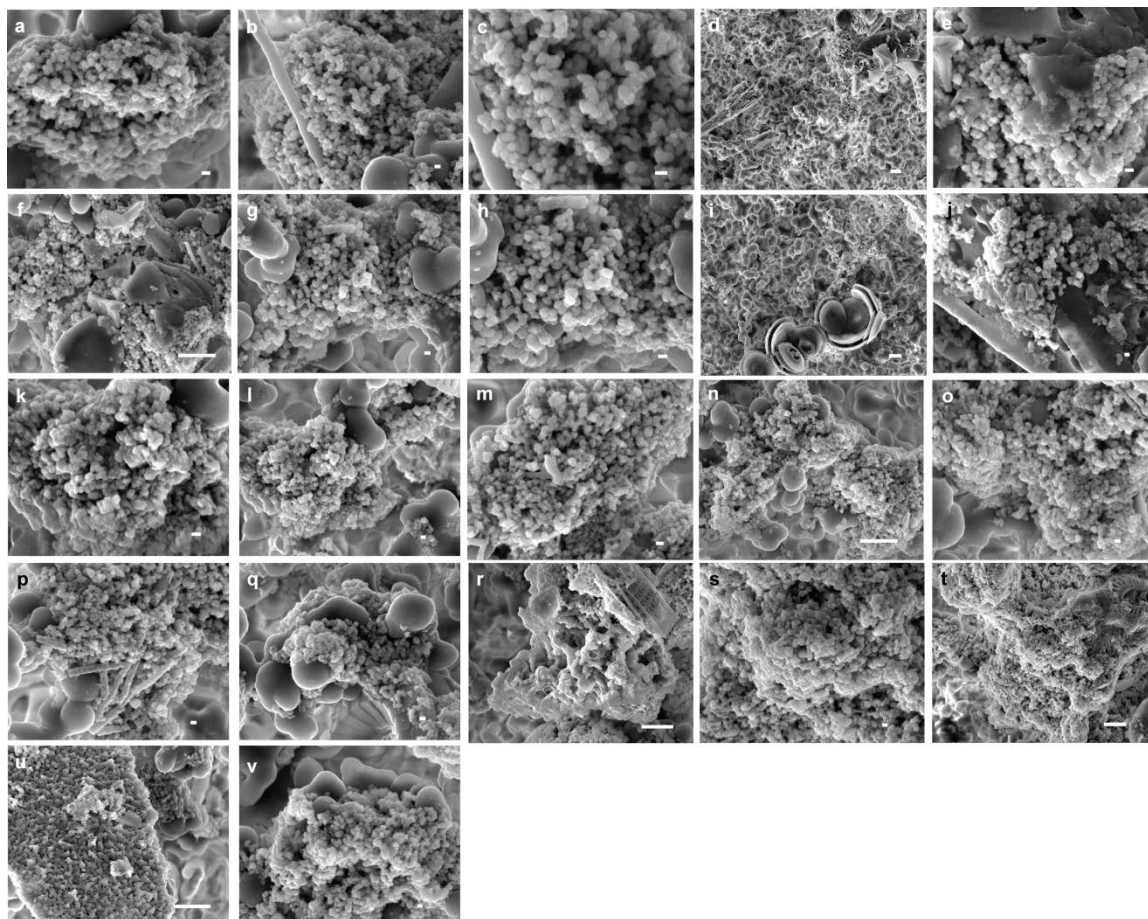
APPENDIX 2 - Chapter 3

Supplemental Information

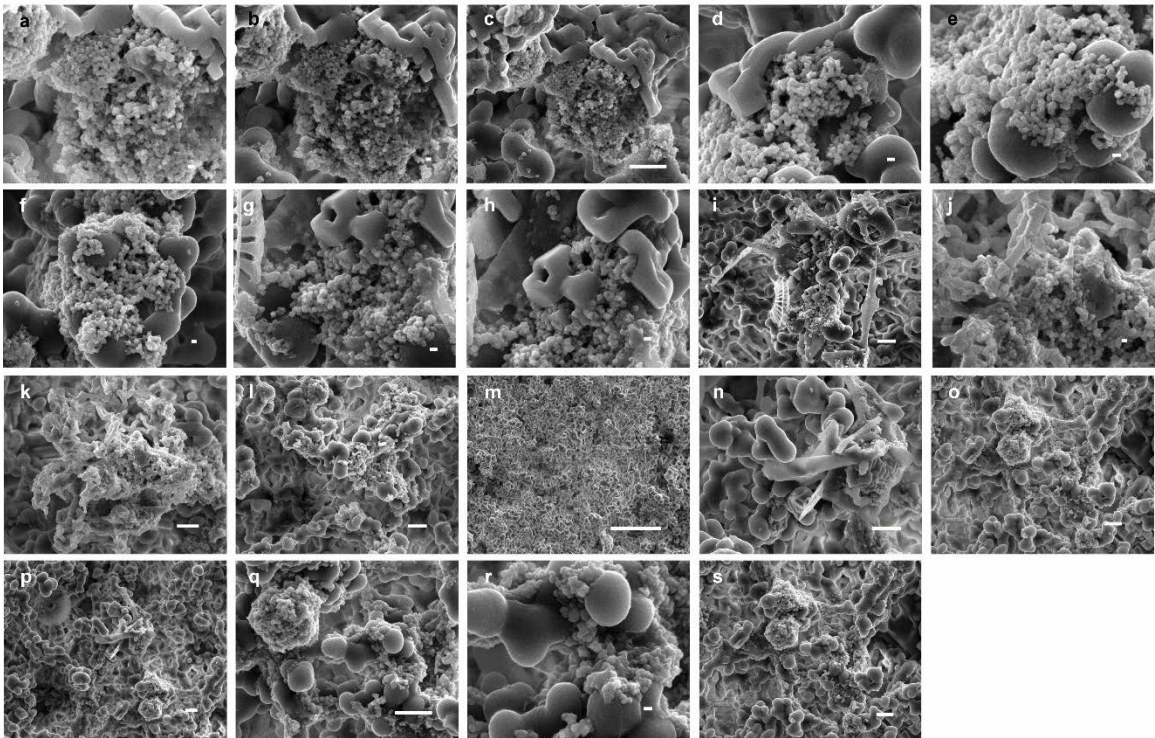
The figures and tables below correspond to supplement materials for Chapter 3 Hydrothermally derived iron oxyhydroxides are short-range ordered phases over ~ 4300 km of oceanic transport”. Please refer for to Chapter 3 for further explanations and significance of the data provided below.

Appendix 2.1 Scanning Transmission X-ray Microscopy

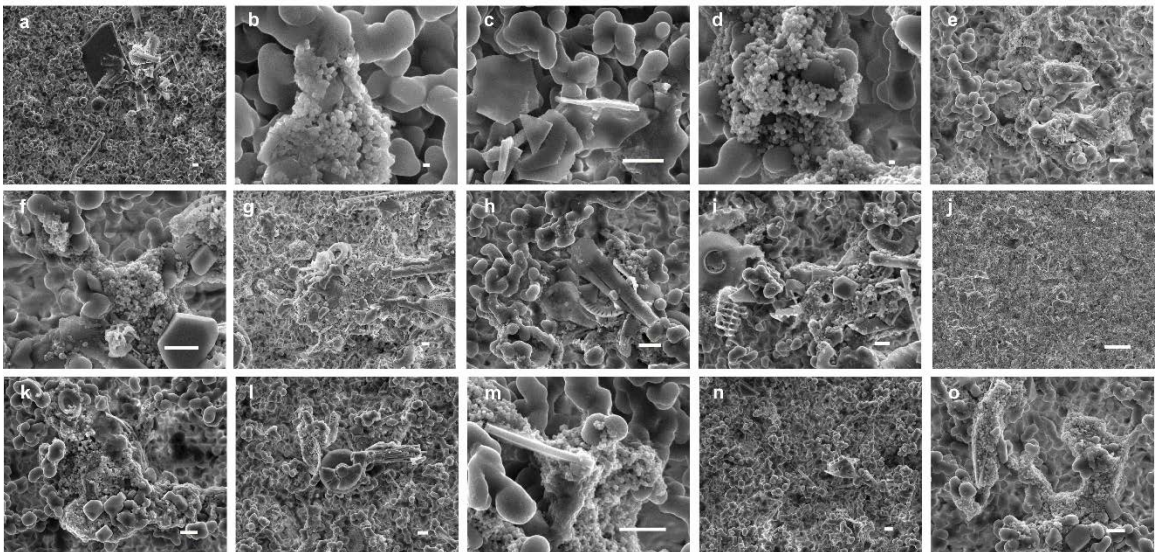
For Stations 18-30 SEM images were collected. These images provided high resolution images of particle morphology. Additionally, visual differences can be seen in particle loading and density at each station.



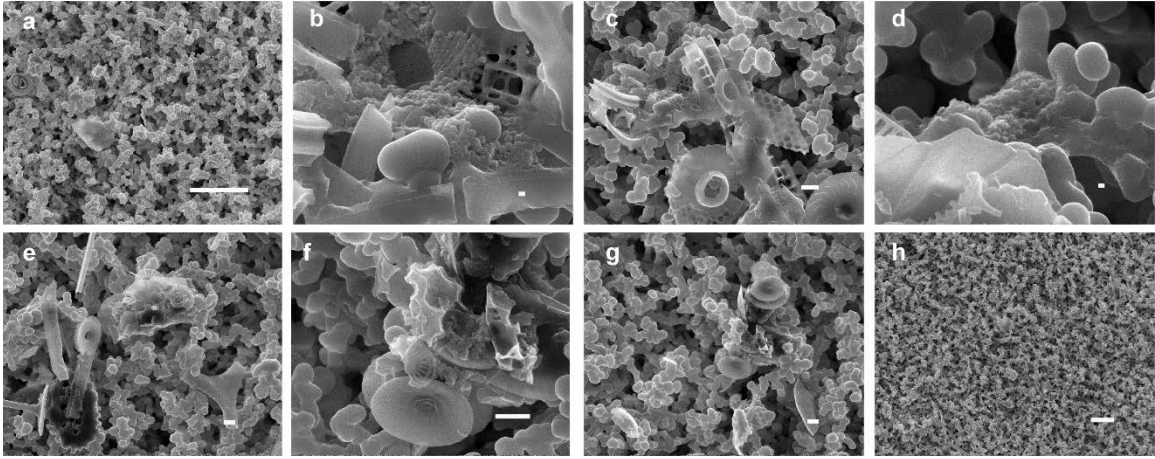
Appendix 2.1.1 SEM particle diversity at Station 18. Scale bars for images d, f, i, n, r, and u are 1 μm . All other scale bars are 100 nm.



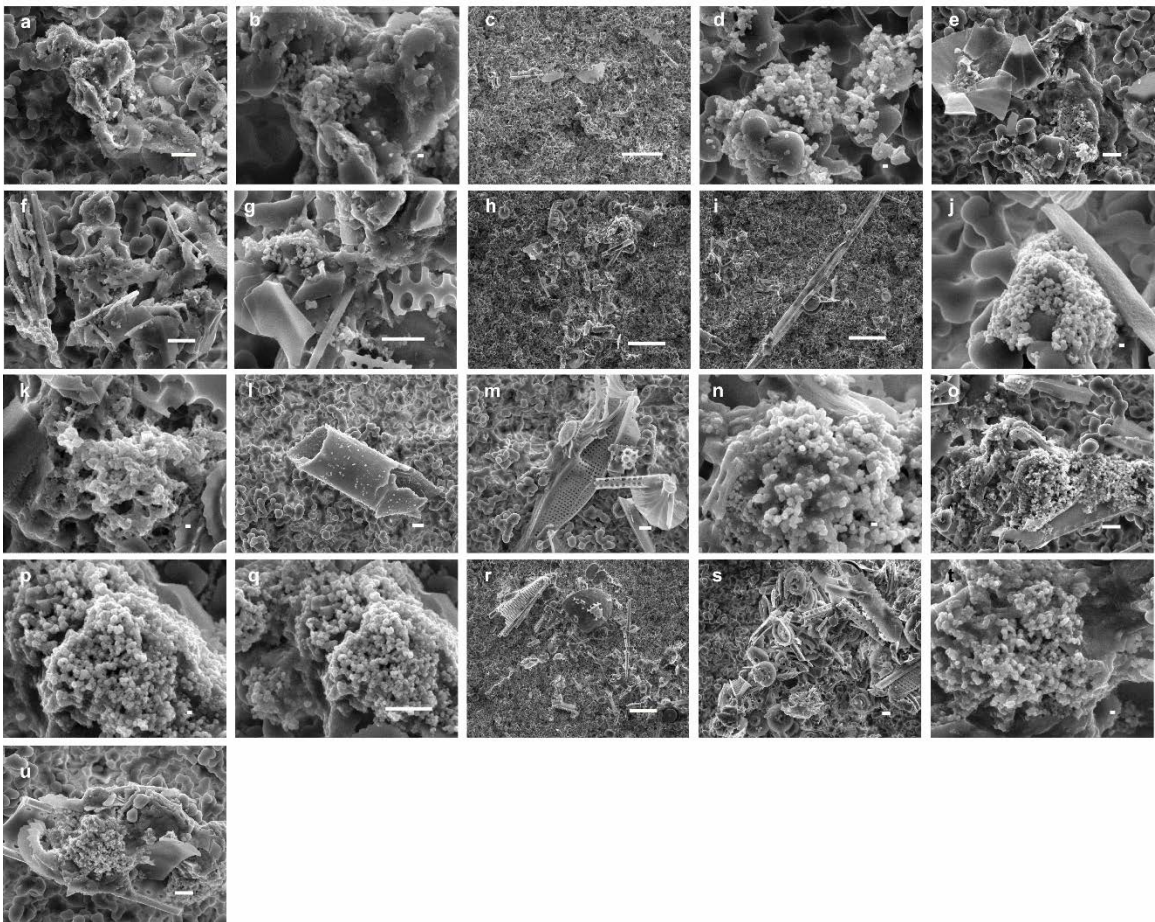
Appendix 2.1.2 SEM particle diversity at Station 20. The scale bar for image m is 10 μm . Scale bars for images c, i, k, l, n-q and s are 1 μm . All other scale bars are 100 nm.



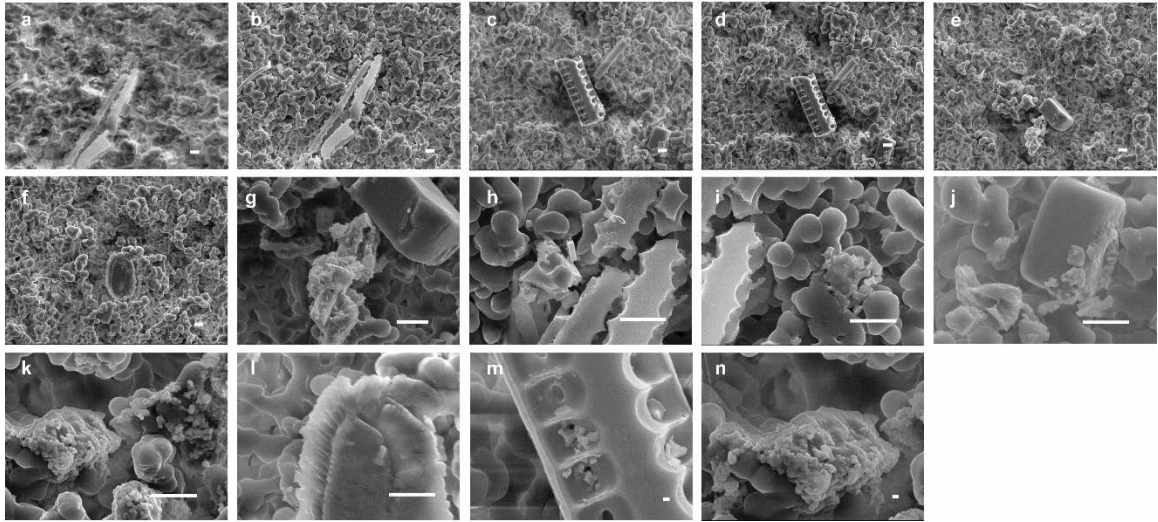
Appendix 2.1.3 SEM particle diversity at Station 21. Scale bars for images b and d are 100 nm. The scale bar for image j is 10 μm . All other scale bars are 1 μm .



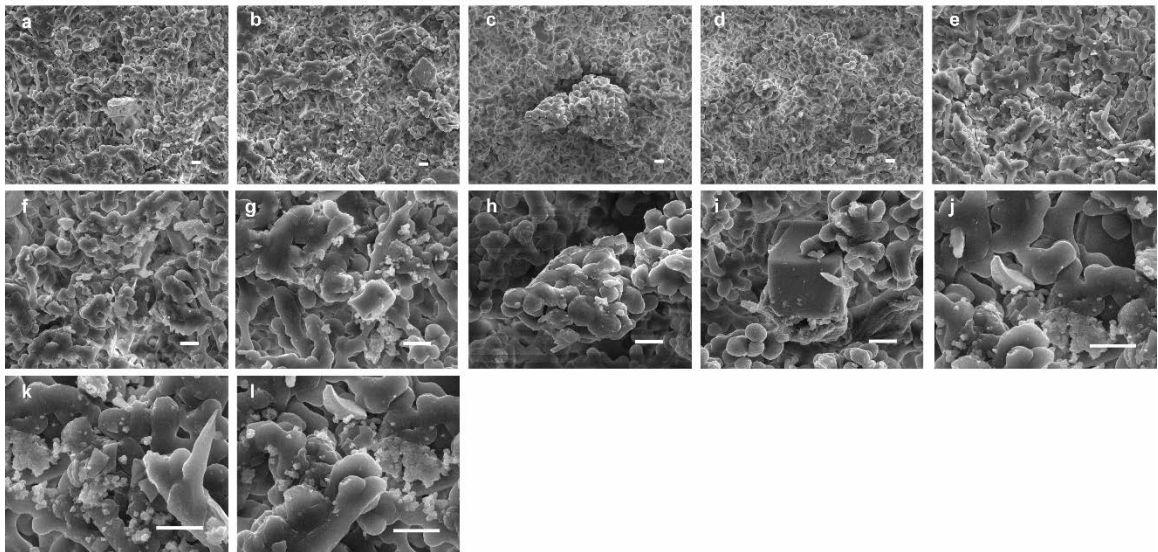
Appendix 2.1.4 SEM particle diversity at Station 23. Scale bars for images a and h are 10 μm . Scale bars for images b and d are 100 nm. All other scale bars are 1 μm .



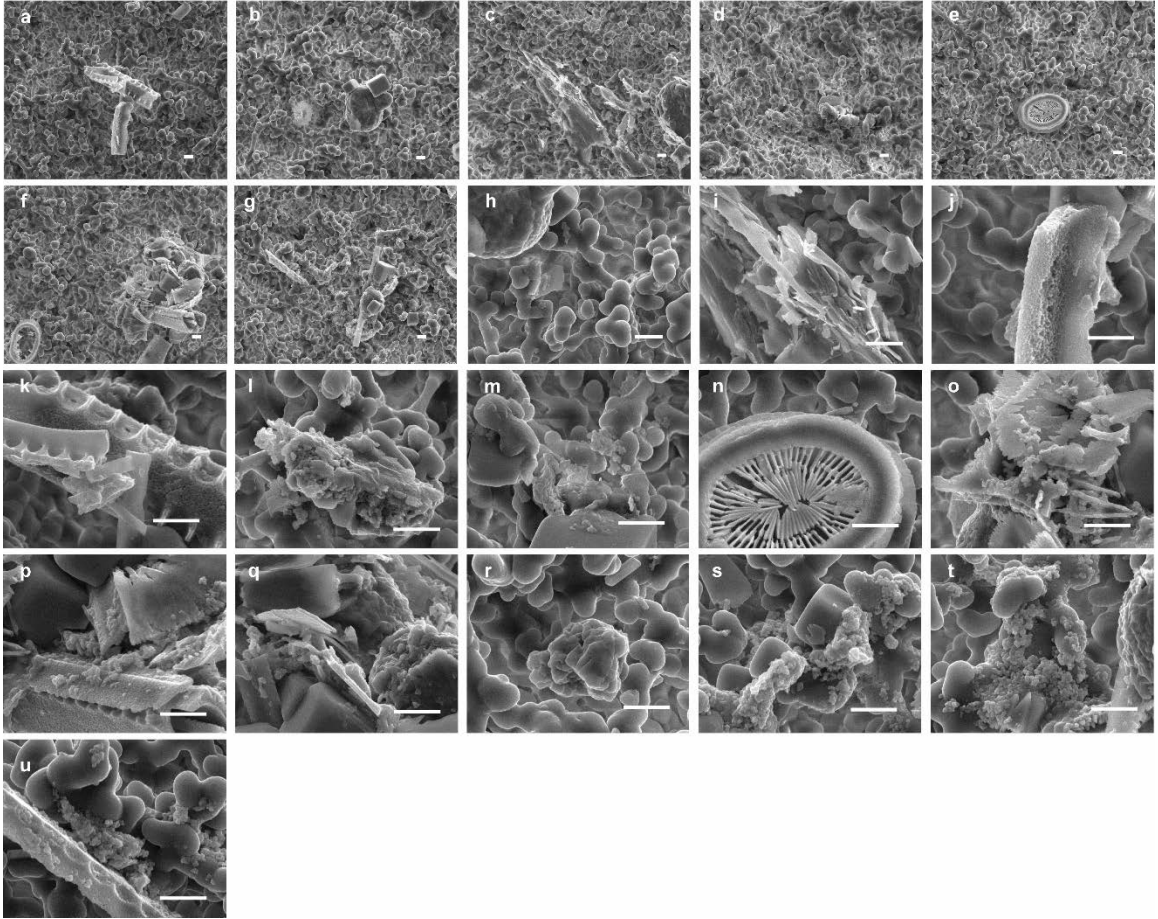
Appendix 2.1.5 SEM particle diversity at Station 25. Scale bars for images c, h, i and r are 10 μm . Scale bars for images b, d, j, k, n, p and t are 100 nm. All other scale bars are 1 μm .



Appendix 2.1.6 SEM particle diversity at Station 26. Scale bars for images m and n are 100 nm. All other scale bars are 1 μm .

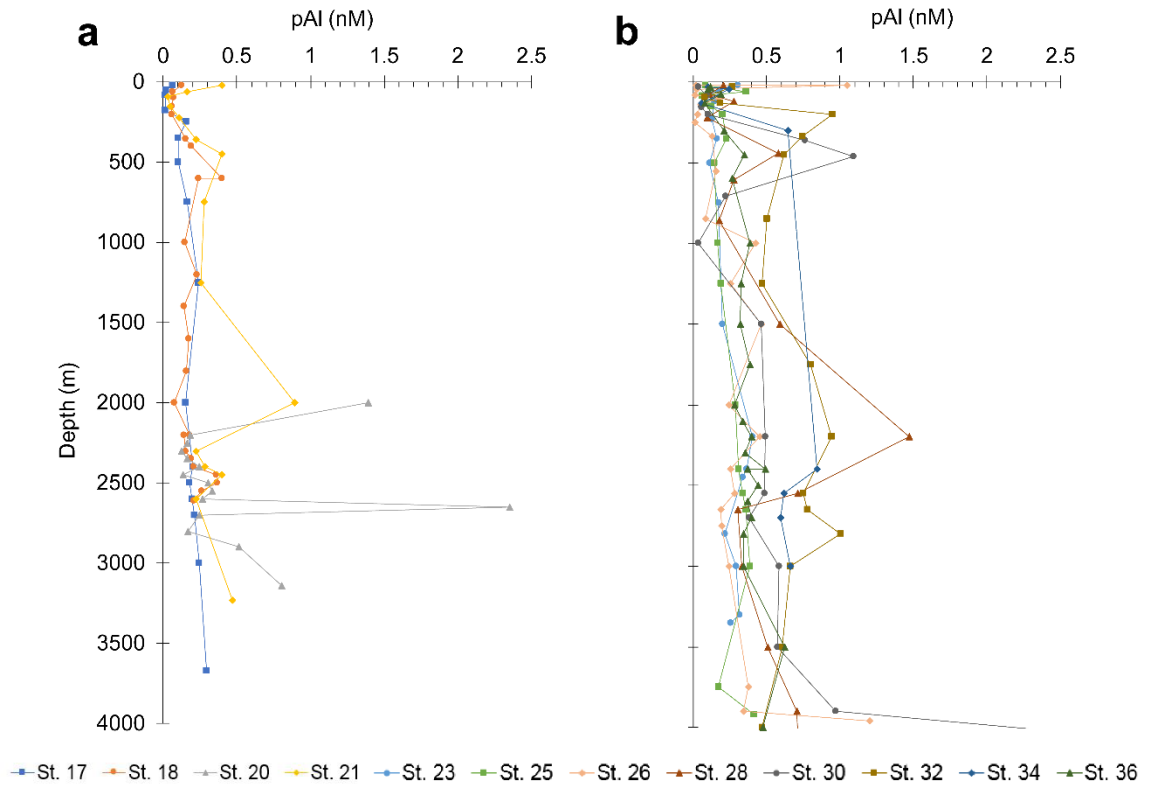


Appendix 2.1.7 SEM particle diversity at Station 28. Scale bars for all images are 1 μm .



Appendix 2.1.8 SEM particle diversity at Station 30. Scale bars for all images are 1 μm .

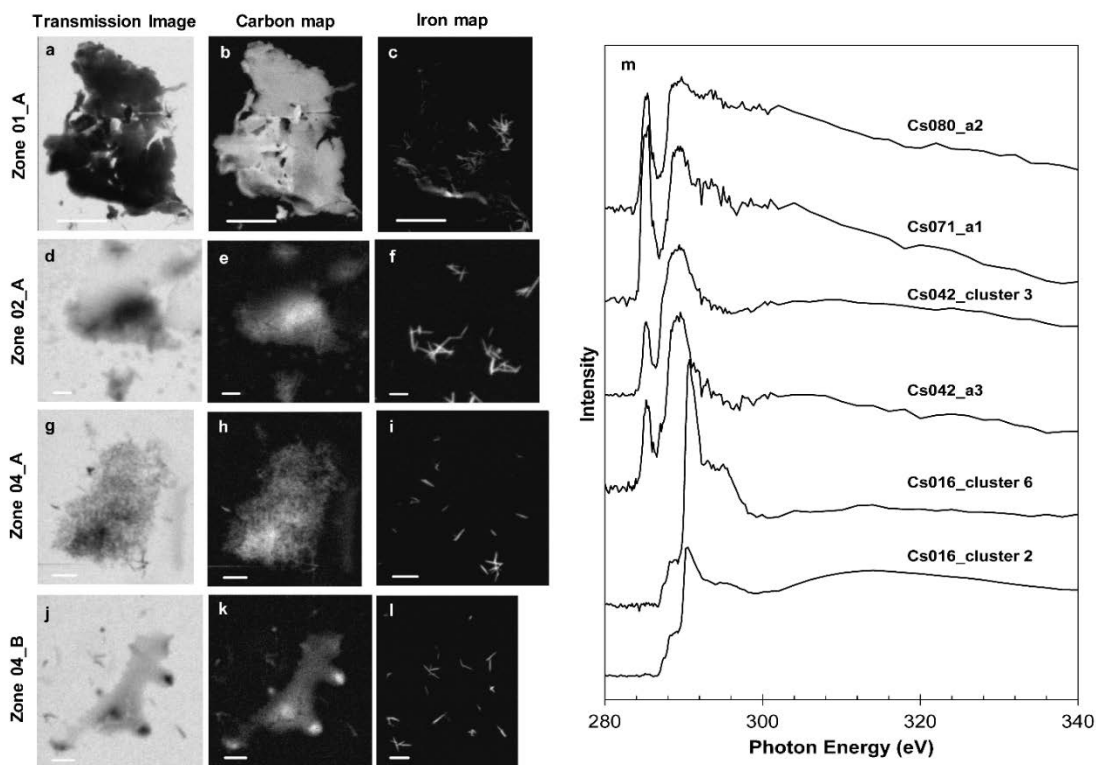
Appendix 2.2 Particulate aluminum (pAl) bulk chemistry



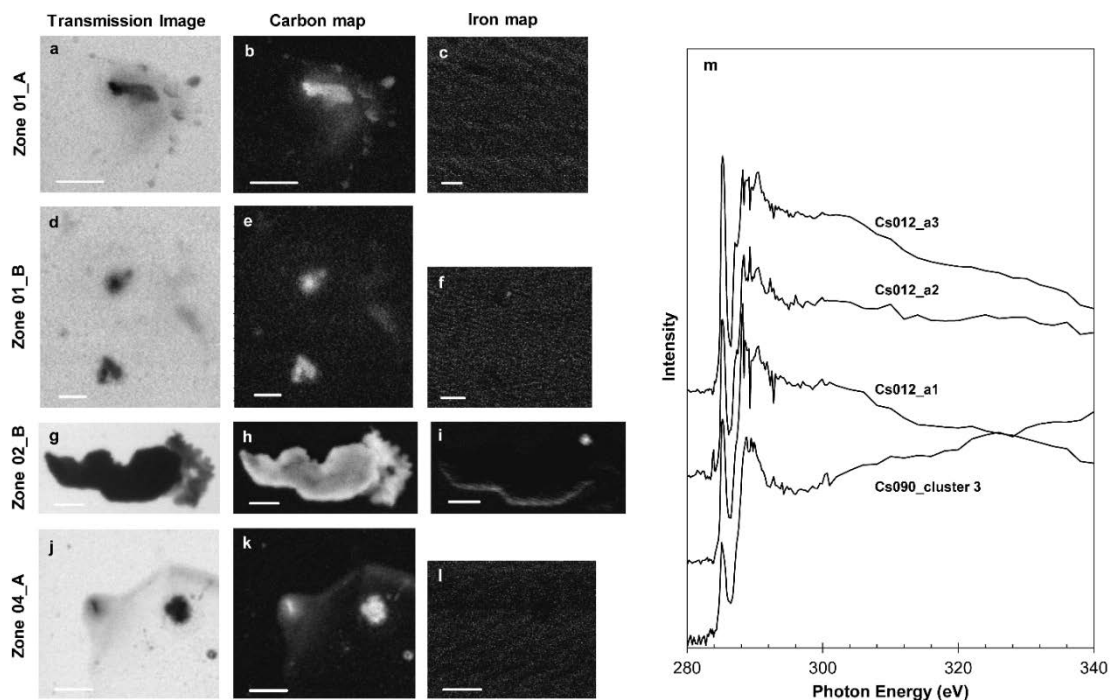
Appendix 2.2.1 Bulk pAl concentrations. (a) pAl concentration for Stations 17 (before the ridge), 18-21 and (b) pAl concentrations for Stations 23-36.

Appendix 2.3 Scanning Transmission X-ray Microscopy Images and Spectra

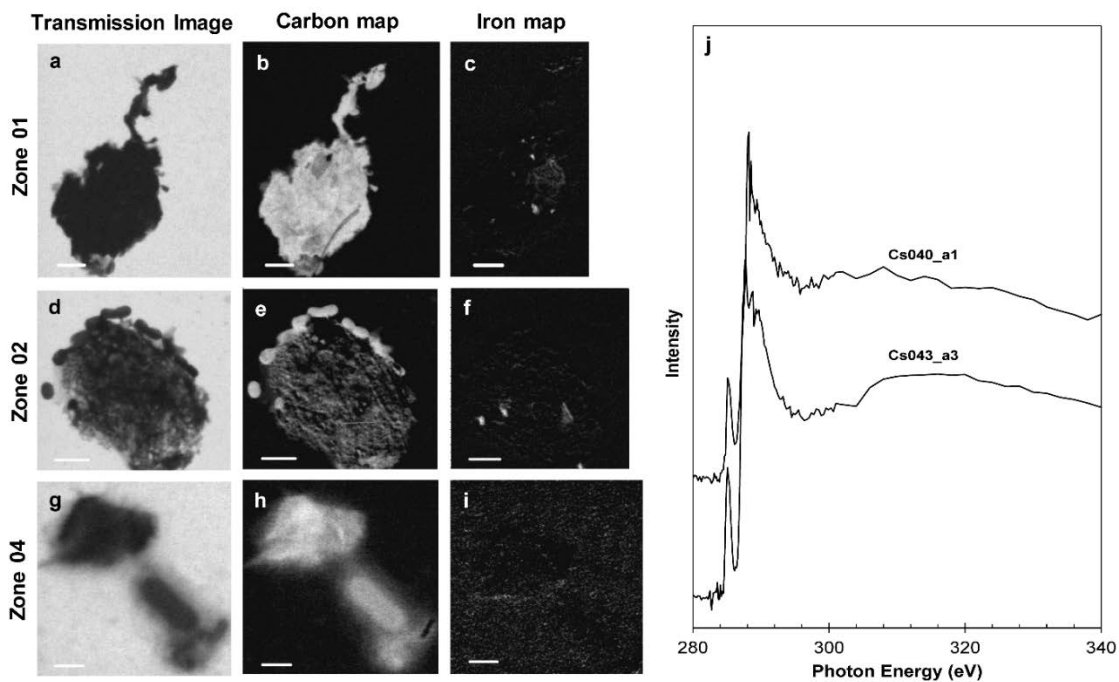
All STXM transmission images, elemental maps and C 1s XANES spectra are provided below for mid-plumes Stations 21-30 and sediment fluff Stations 20, 23, 26, and 30. The images and spectra show the particle and spectral diversity within each station.



Appendix 2.3.1 Station 21 Images and C 1s XANES. All marine particles analyzed at Station 21. Transmission images were collected at 290 eV (a, d, g, and j). Total carbon optical density ranges from 0.781 (b), 0.633 (e), 0.458 (h), and 0.365 (k). Total iron optical density ranges from 1.03 (c), 0.572 (f), 0.610 (i), and 0.609 (l). Scale bars for a-c are 5 μm , d-f are 1 μm , and g-l are 2 μm . Carbon 1s XANES spectra from Station 21 (m).

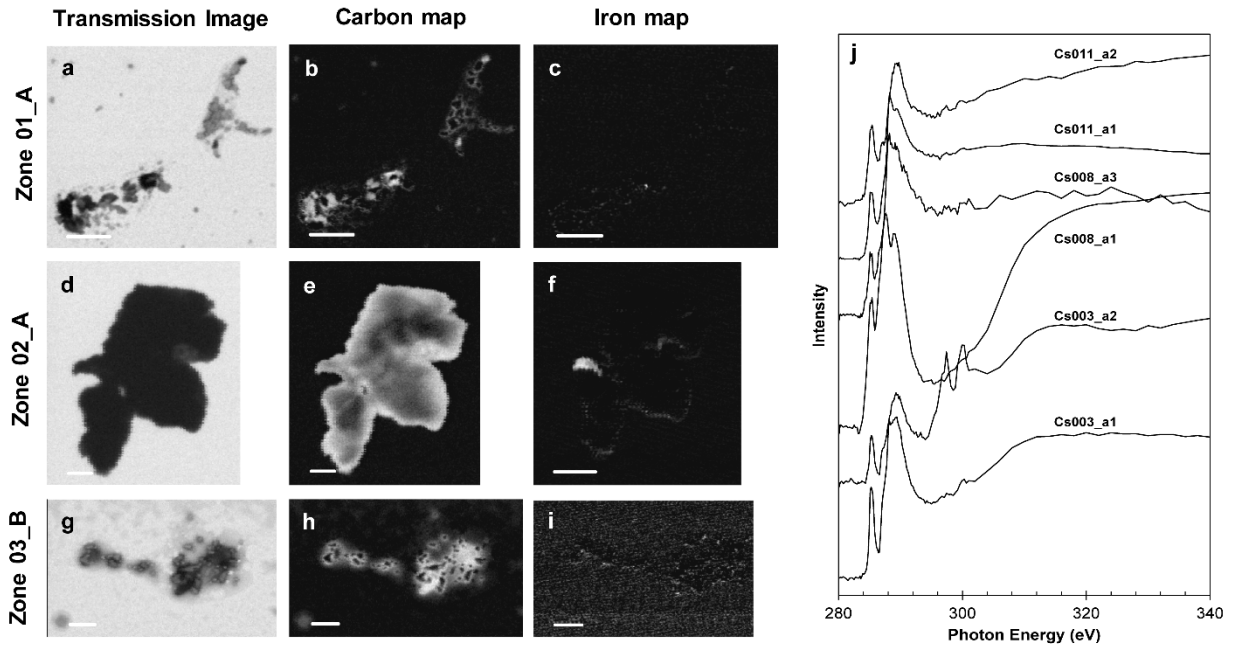


Appendix 2.3.2 Station 23 Images and C 1s XANES. All marine particles analyzed at Station 23. Transmission images were collected at 290 eV (a, d, g, and j). Total carbon optical density ranges from 0.640 (b), 0.664 (e), 0.893 (h), and 0.634 (k). Total iron optical density ranges from 0.0698 (c), 0.0717 (f), 0.379 (i), and 0.0704 (l). Scale bars for a-b, j-l are 5 μm, c-f are 2 μm, and g-i are 1 μm. Carbon 1s XANES spectra from Station 23 (m).

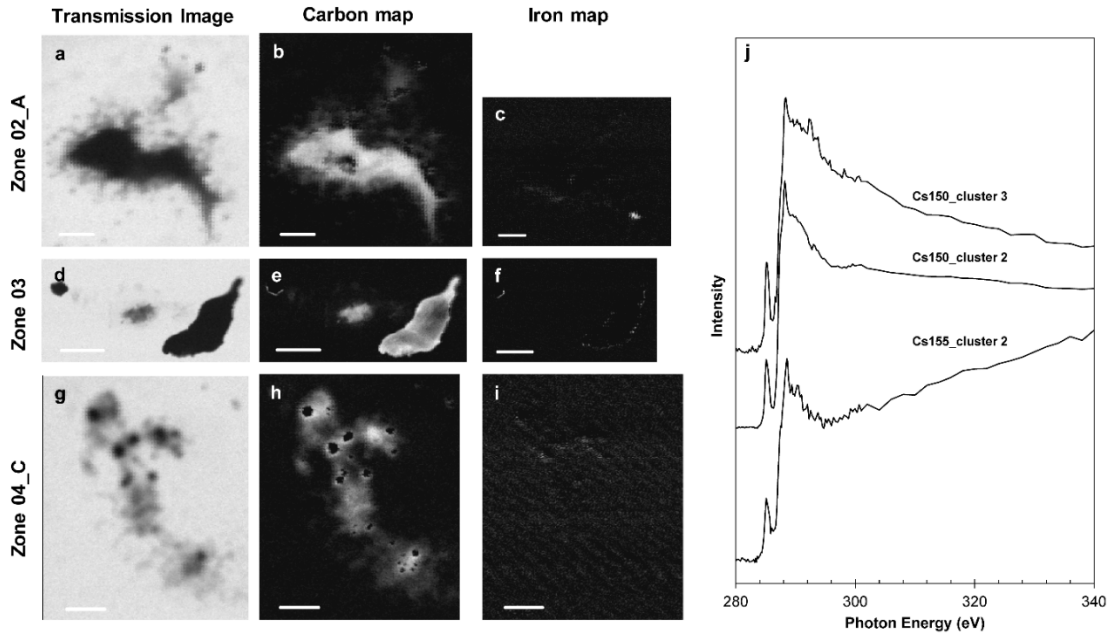


Appendix 2.3.3 Station 25 Images and C 1s XANES. All marine particles analyzed at Station 25. Transmission images were collected at 290 eV (a, d, and g). Total carbon optical density ranges from 0.849

(b), 0.725 (e), and 0.720 (h). Total iron optical density ranges from 0.317 (c), 0.364 (f), and 0.0810 (i). Scale bars for a-f are 2 μm , and g-i are 1 μm . Carbon 1s XANES spectra from Station 25 (j).

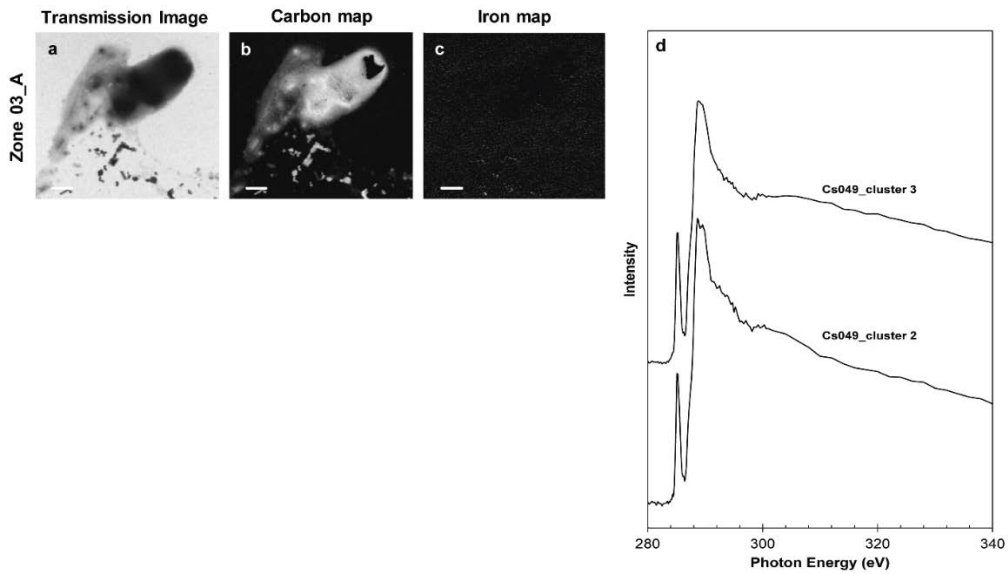


Appendix 2.3.4 Station 26 Images and C 1s XANES. All marine particles analyzed at Station 26. Transmission images were collected at 290 eV (a, d, and g). Total carbon optical density ranges from 0.722 (b), 0.717 (e), and 0.567 (h). Total iron optical density ranges from 0.478 (c), 0.644 (f), and 0.105 (i). Scale bars for a-c are 5 μm , d-e are 1 μm , and f-i are 2 μm . Carbon 1s XANES spectra from Station 26 (j).

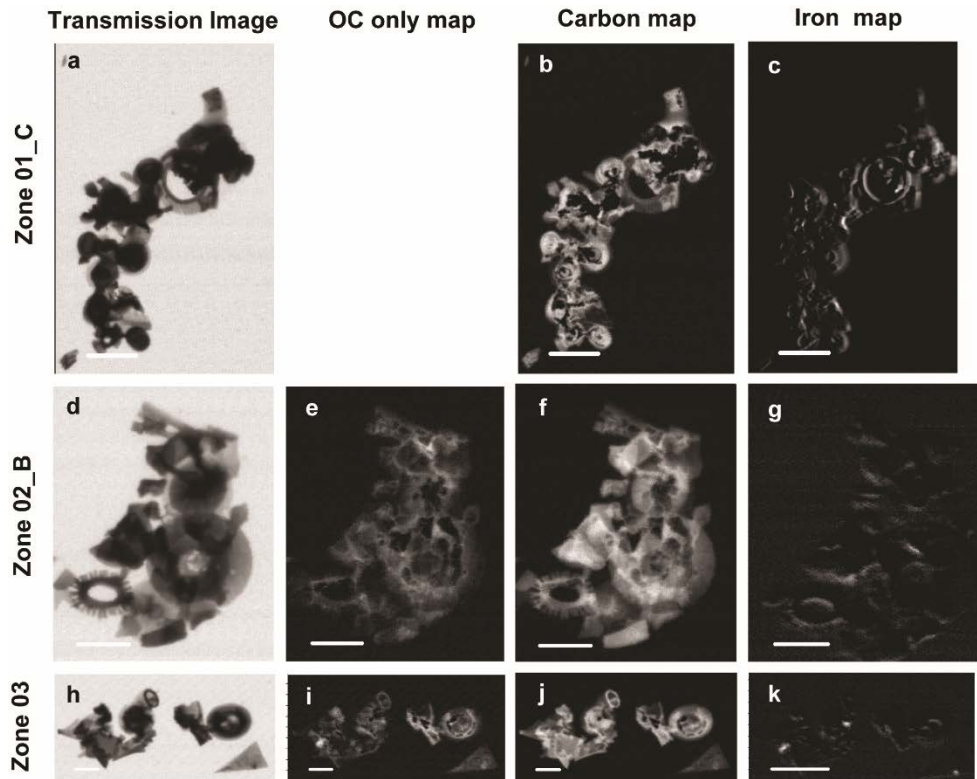


Appendix 2.3.5 Station 28 Images and C 1s XANES. All marine particles analyzed at Station 28. Transmission images were collected at 290 eV (a, d, and g). Total carbon optical density ranges from 1.50

(b), 0.701 (e), and 0.544 (h). Total iron optical density ranges from 0.321 (c), 0.389 (f), and 0.167 (i). Scale bars for a-f are 5 μm , and g-i are 2 μm . Carbon 1s XANES spectra from Station 28 (j).

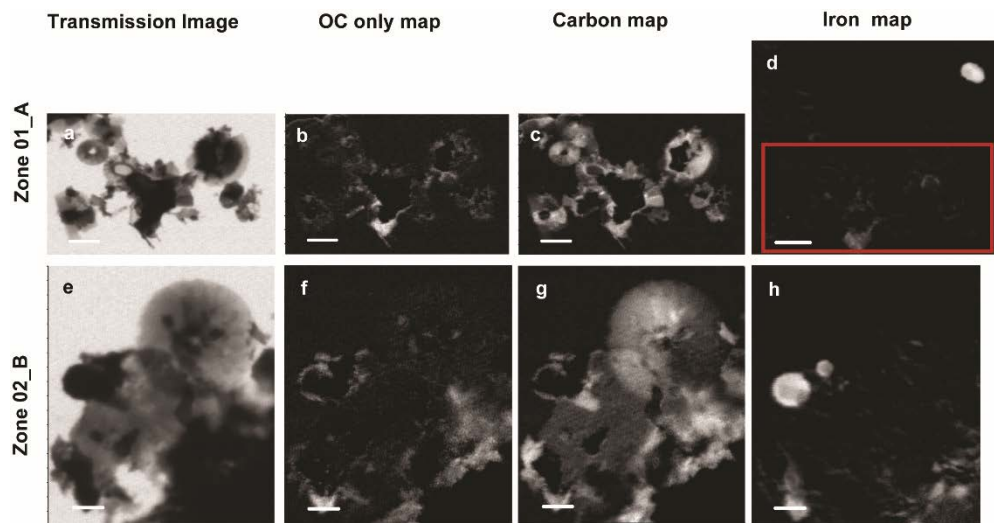


Appendix 2.3.6 Station 30 Images and C 1s XANES. All marine particles analyzed at Station 30. Transmission images were collected at 290 eV (a). Total carbon optical density is 0.778 (b). Total iron optical density is 0.164 (c). Scale bars for a-c are 5 μm . Carbon 1s XANES spectra from Station 30 (j).

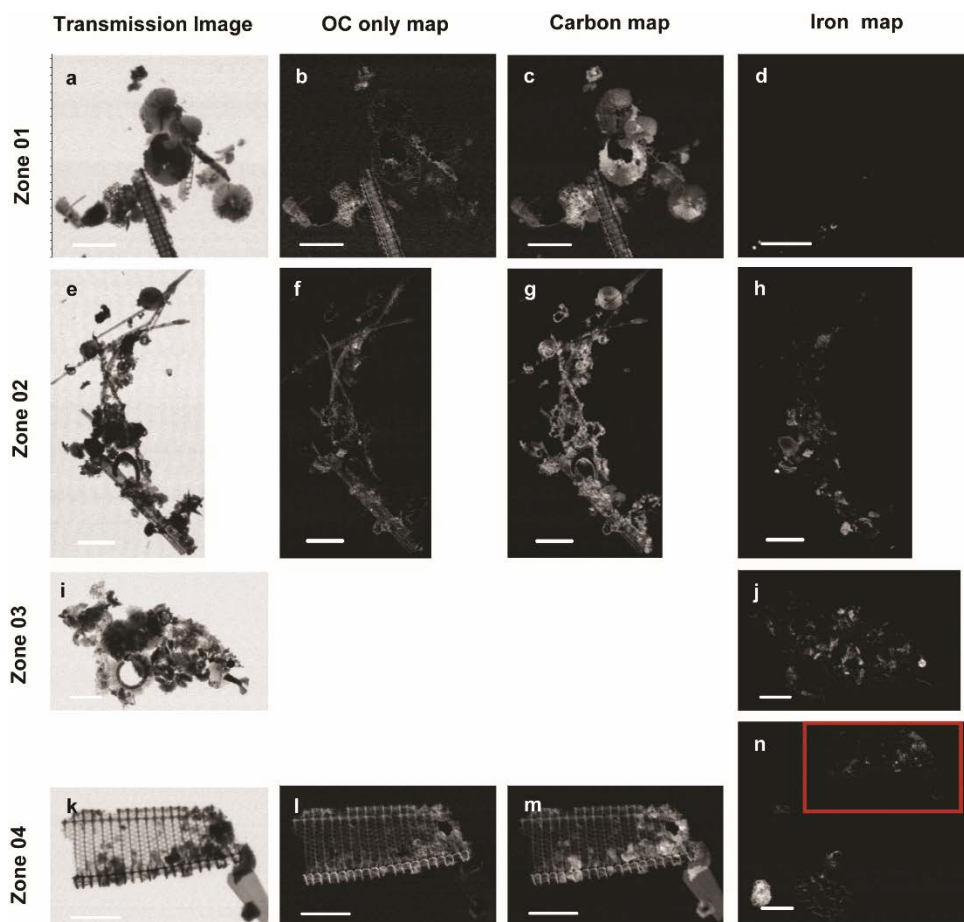


Appendix 2.3.7 Station 23 Sediment Fluff Images. All marine particles analyzed at Station 23 sediment fluff. Transmission images were collected at 290 eV (a, d, and h). Organic carbon only optical density ranges from 1.03 (e), and 0.773 (i). Total carbon optical density ranges from 1.15 (b), 1.31 (f), and 1.35 (j).

Total iron optical density ranges from 1.98 (c), 0.419 (g), and 0.514 (k). Scale bars for a-c, k are 5 μm and d-j are 2 μm .



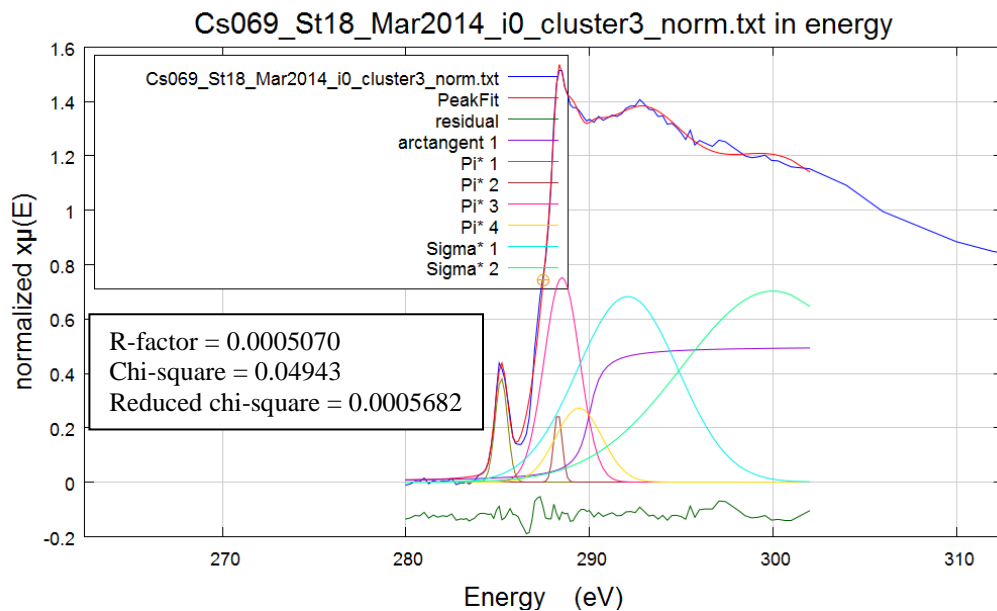
Appendix 2.3.8 Station 26 Sediment Fluff Images. All marine particles analyzed at Station 26 sediment fluff. Transmission images were collected at 290 eV (a and e). Organic carbon only optical density ranges from 0.805 (b), and 0.761 (f). Total carbon optical density ranges from 1.19 (c), and 1.07 (g). Total iron optical density ranges from 2.29 (d), and 1.19 (h). The red box in image (d) represents where the carbon maps were analyzed. Scale bars for a-c are 2 μm , and e-h are 1 μm .



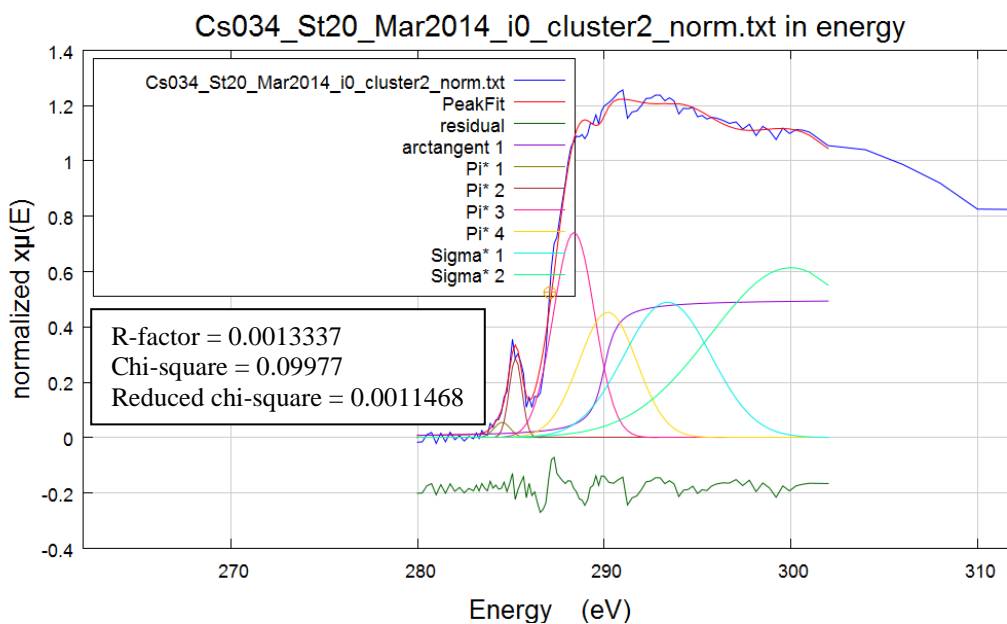
Appendix 2.3.9 Station 30 Sediment Fluff Images. All marine particles analyzed at Station 30 sediment fluff. Transmission images were collected at 290 eV (a, e, i, and k). Organic carbon only optical density ranges from 0.632 (b), 1.02 (f), 0.773 (l). Total carbon optical density ranges from 1.19 (c), 1.32 (g), and 1.27 (m). No carbon maps were collected for Zone 03. Total iron optical density ranges from 0.761 (d), 2.40 (h), 1.90 (j), and 1.86 (n). The red box in image (n) represents where the carbon maps were analyzed. Scale bars for e-h are 10 μm . All other scale bars are 5 μm .

Appendix 2.4 Carbon 1s XANES Gaussian fitting within *Athena*

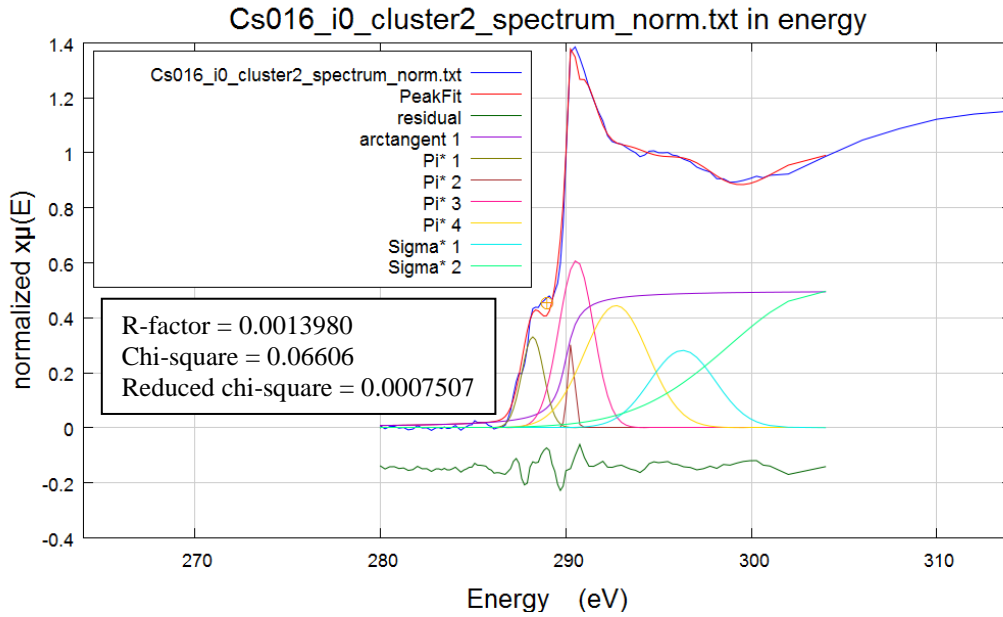
Below are the raw images from *Athena* regarding Gaussian fits for C 1s XANES from mid-plume Station 18-30 and sediment fluff Stations 20, 23, 26, and 30. All terms and peak energies are defined in Appendix Tables 2.2.1 and 2.2.2. Pi* and Sigma* peaks were chosen based off the normalize two column data. When fitting, all initial guess of Pi* heights and widths were set to 0.5. For Sigma *, all initial guesses were height of 0.5 and widths of 3. For C 1s XANES, parameters for the arctangent were always fixed at 290 eV with a height of 0.5, and width of 0.5. The model was only allowed to vary the heights and with of the Pi* and Sigma* peaks.



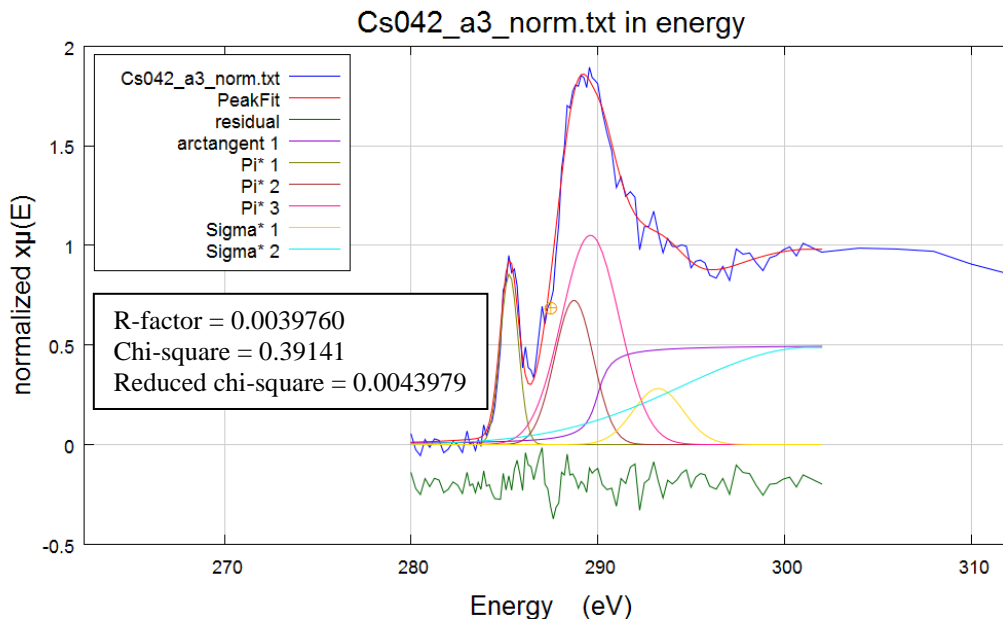
Appendix 2.4.1 C 1s XANES gaussian fitting for mid-plume Station 18



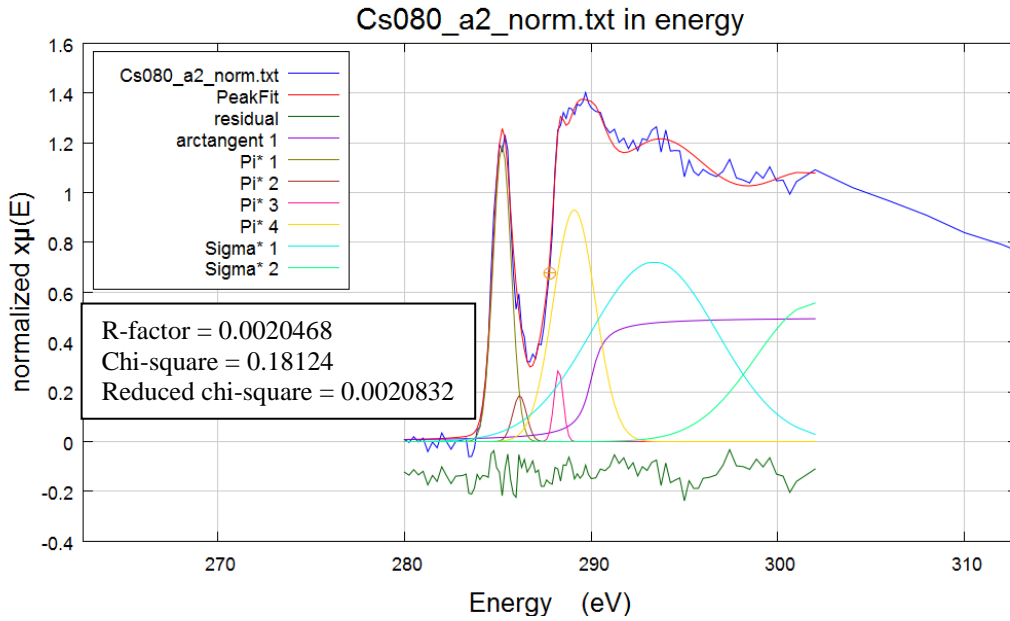
Appendix 2.4.2 C 1s XANES gaussian fitting for mid-plume Station 20



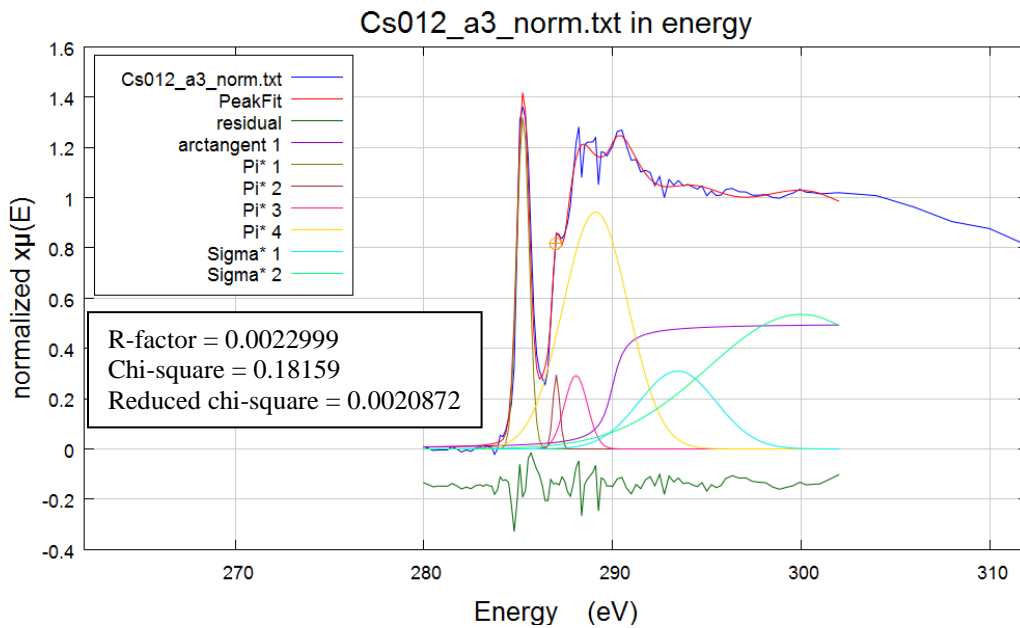
Appendix 2.4.3 C 1s XANES gaussian fitting for mid-plume Station 21



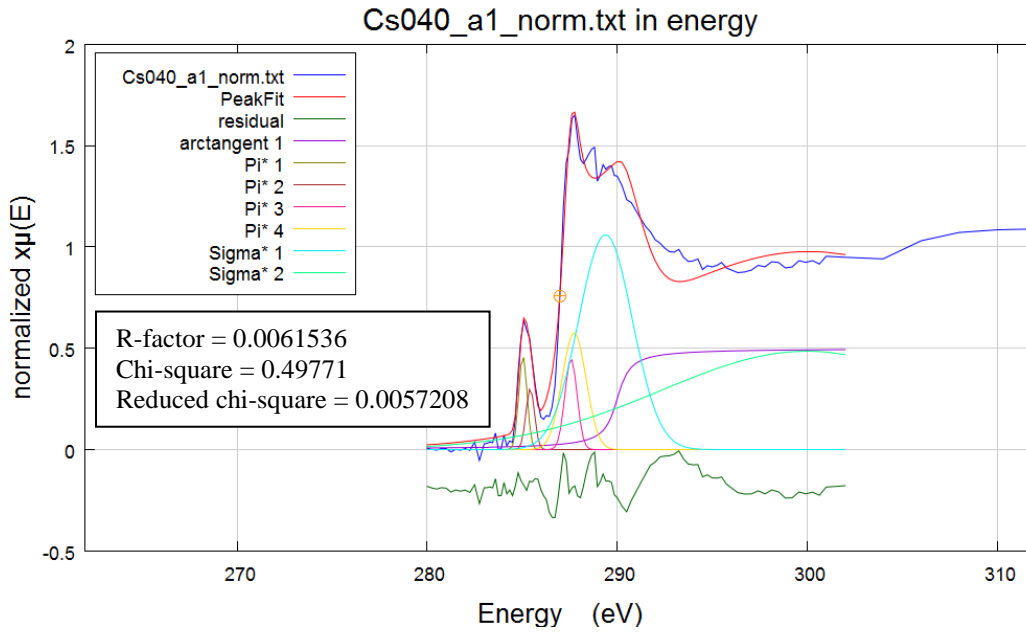
Appendix 2.4.4 C 1s XANES gaussian fitting for mid-plume Station 21



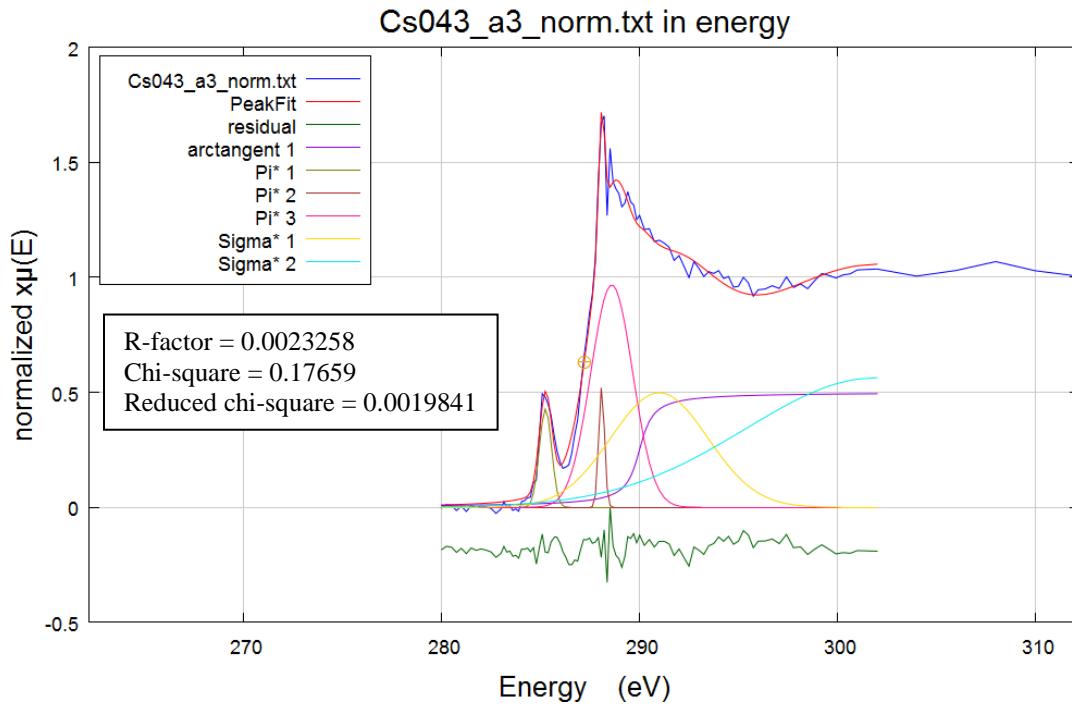
Appendix 2.4.5 C 1s XANES gaussian fitting for mid-plume Station 21



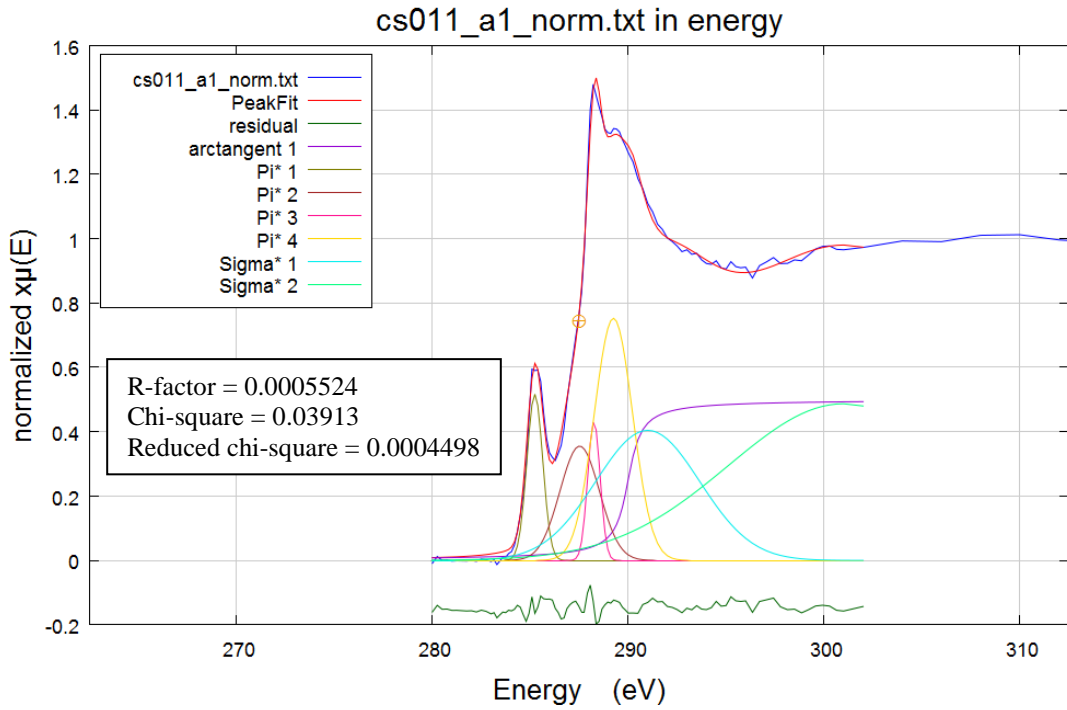
Appendix 2.4.6 C 1s XANES gaussian fitting for mid-plume Station 23



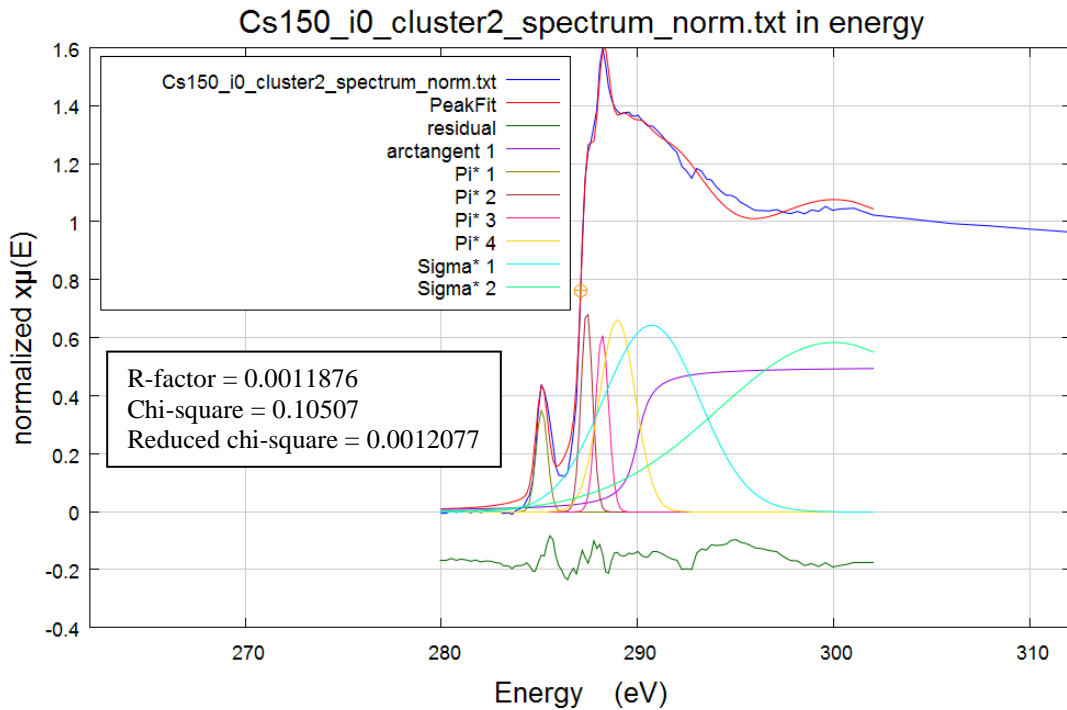
Appendix 2.4.7 C 1s XANES gaussian fitting for mid-plume Station 25



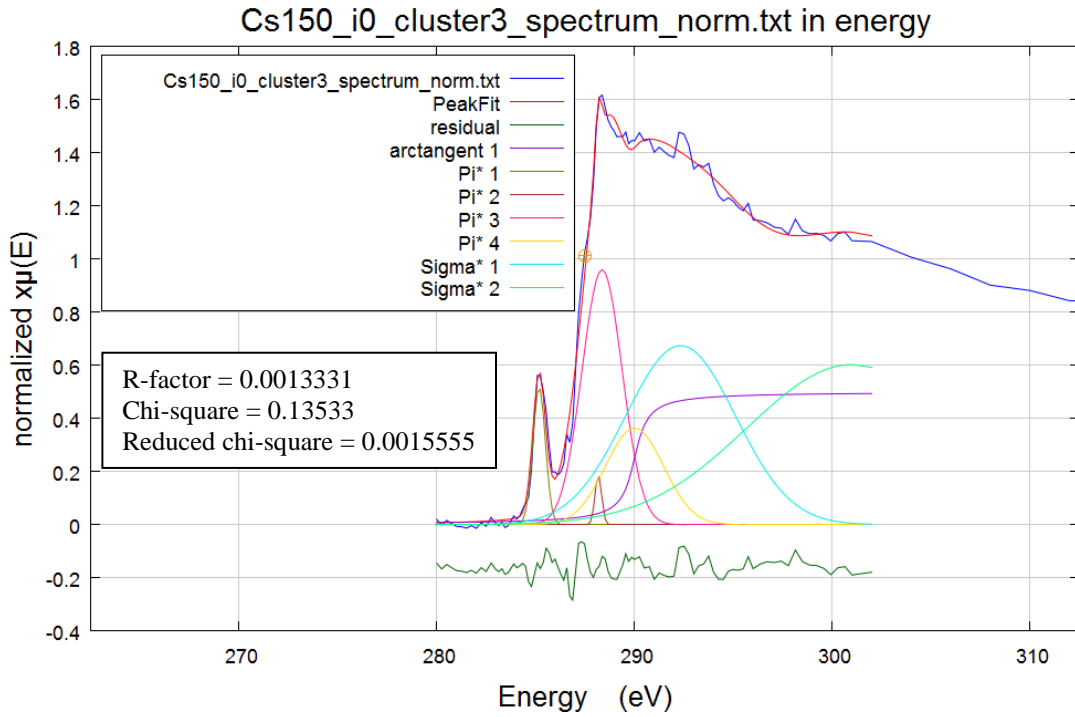
Appendix 2.4.8 C 1s XANES gaussian fitting for mid-plume Station 25



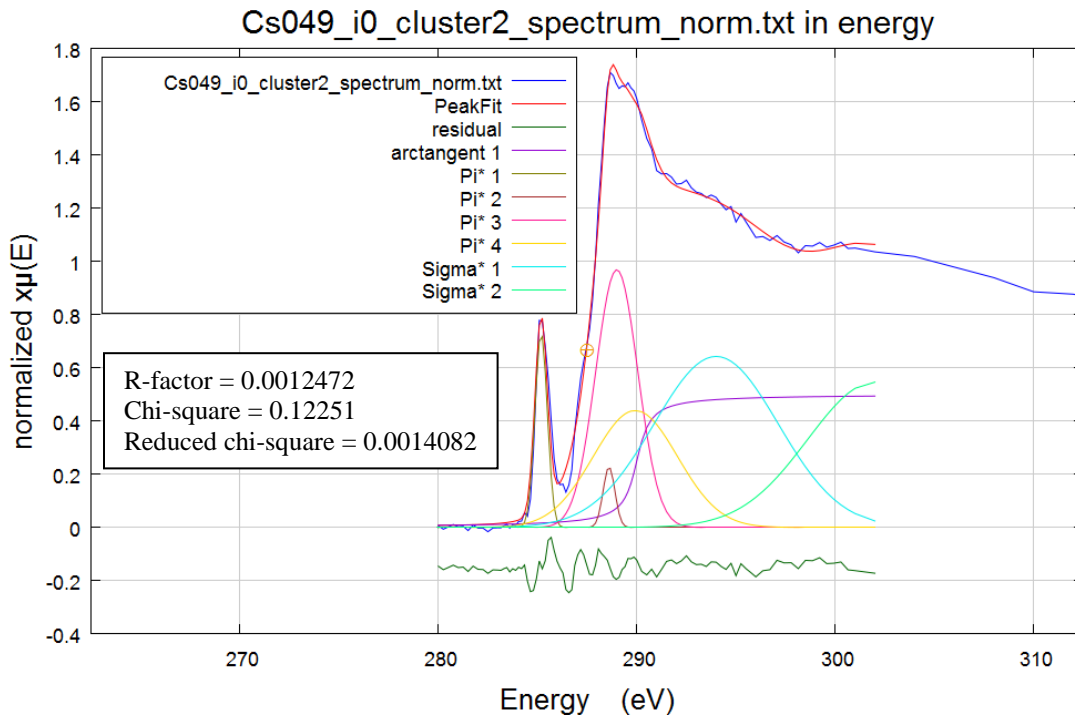
Appendix 2.4.9 C 1s XANES gaussian fitting for mid-plume Station 26



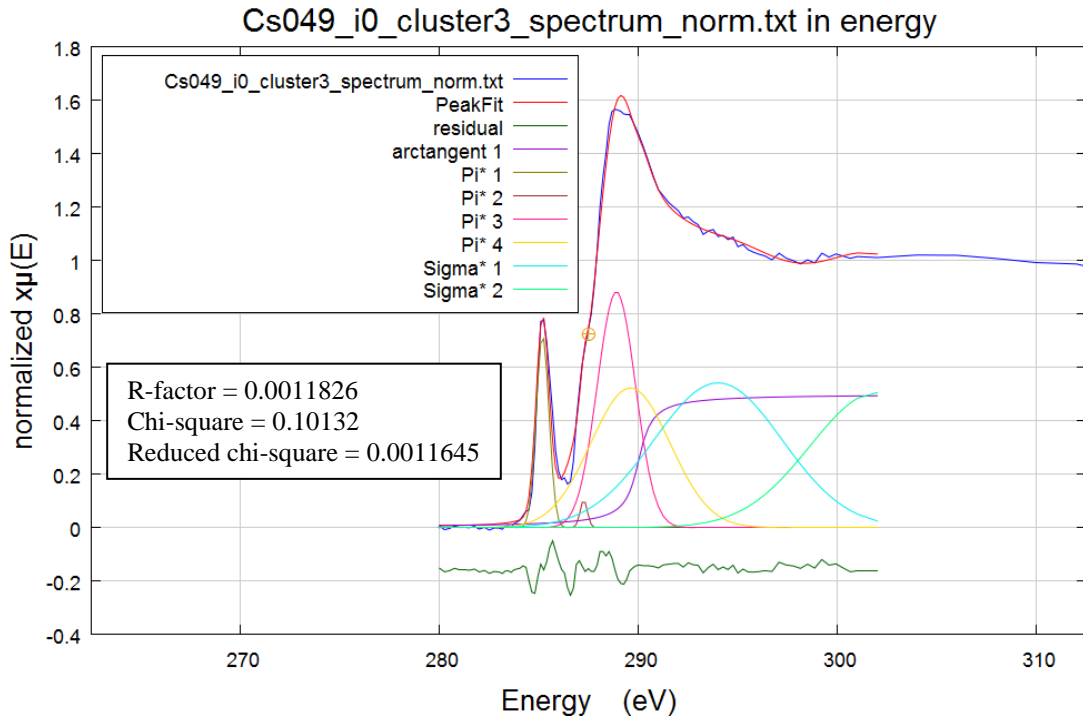
Appendix 2.4.10 C 1s XANES gaussian fitting for mid-plume Station 28



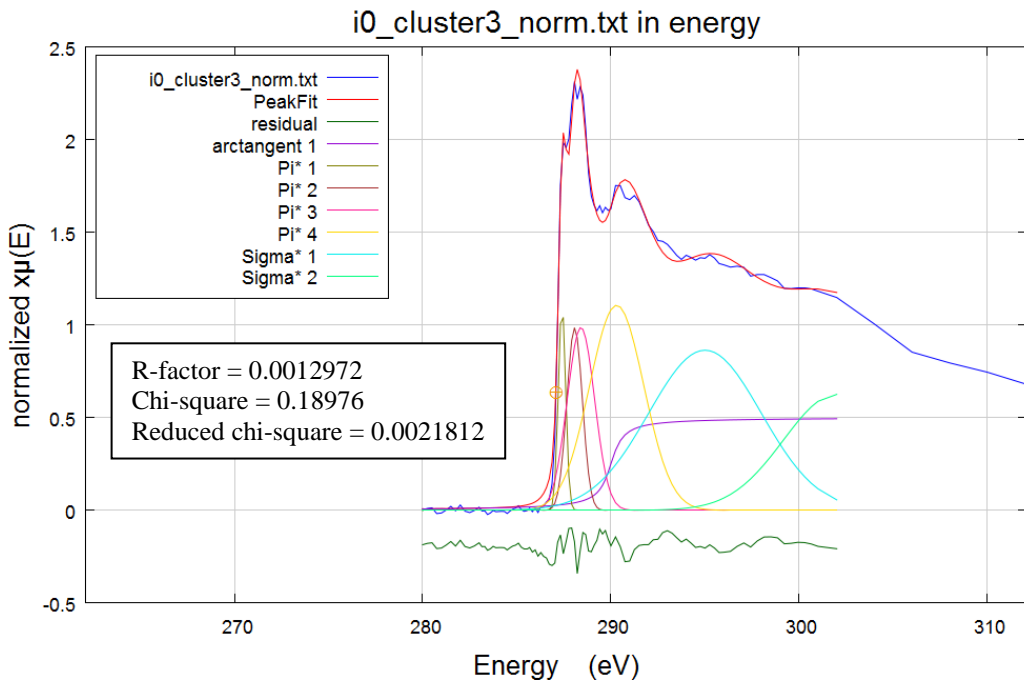
Appendix 2.4.11 C 1s XANES gaussian fitting for mid-plume Station 28



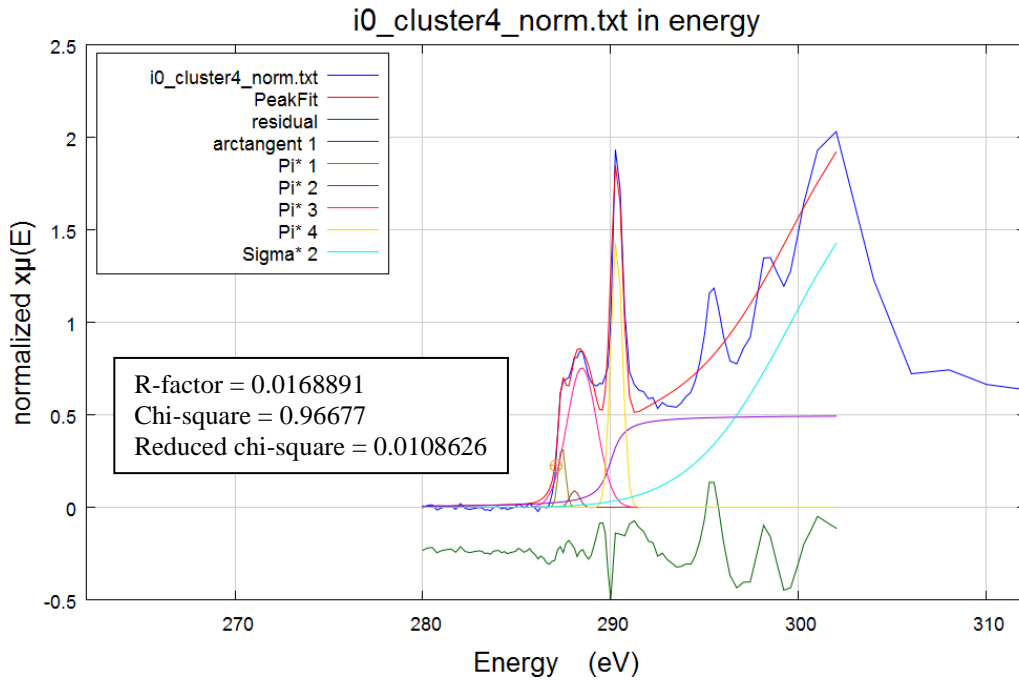
Appendix 2.4.12 C 1s XANES gaussian fitting for mid-plume Station 30



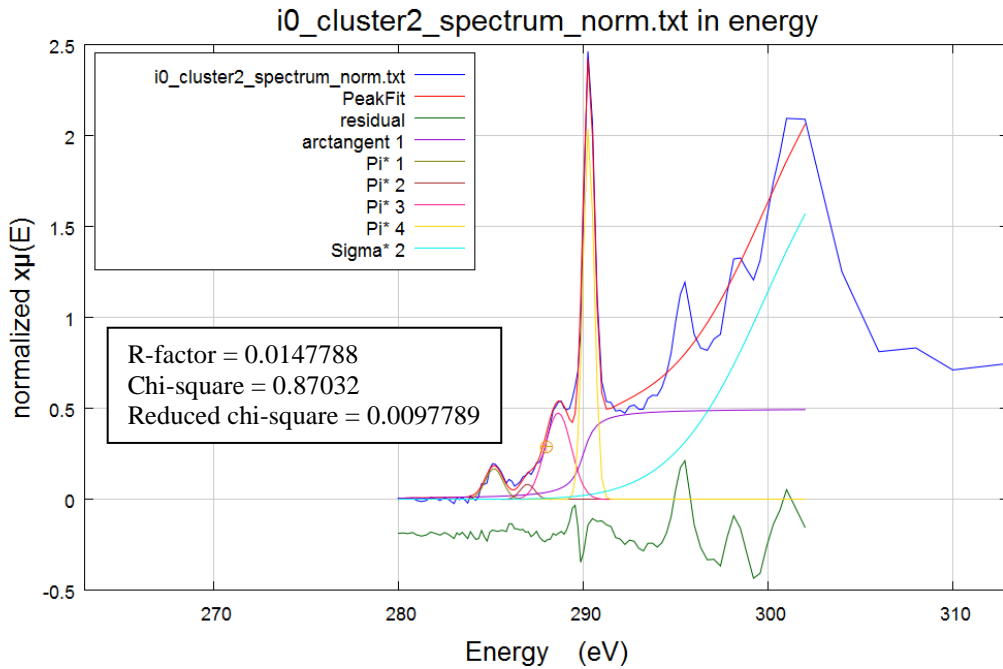
Appendix 2.4.13 C 1s XANES gaussian fitting for mid-plume Station 30



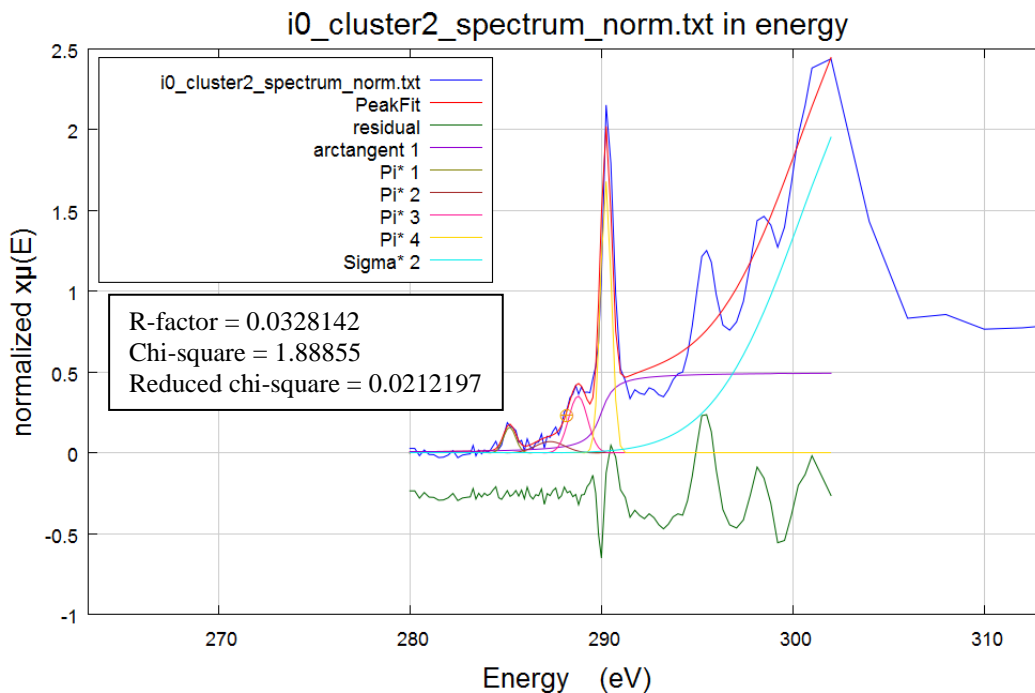
Appendix 2.4.14 C 1s XANES gaussian curve fitting for Station 20 sediment fluff layer



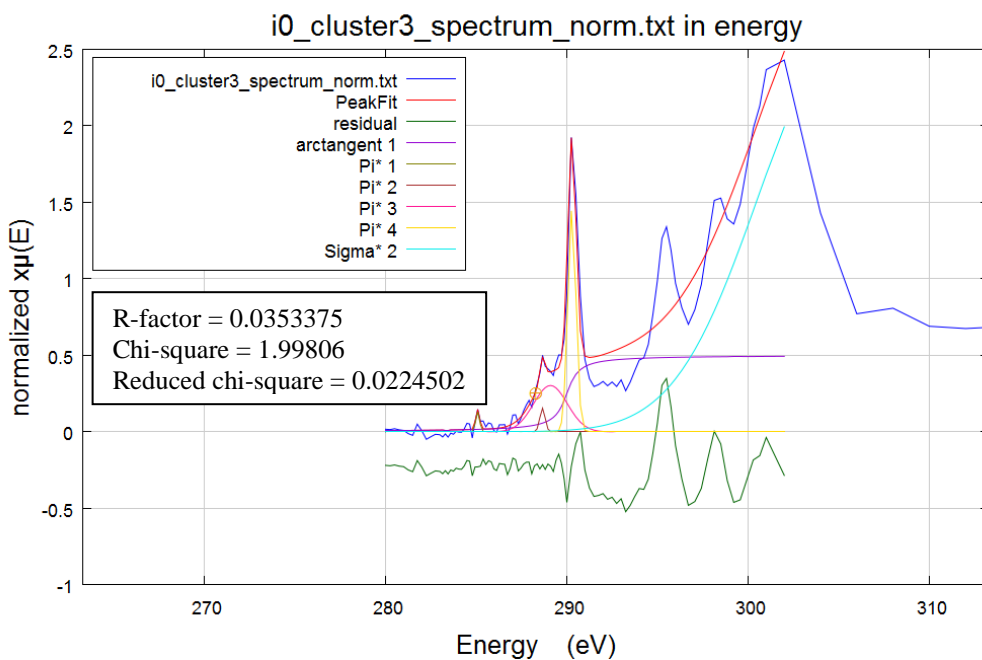
Appendix 2.4.15 C 1s XANES gaussian curve fitting for Station 20 sediment fluff layer



Appendix 2.4.16 C 1s XANES gaussian curve fitting for Station 23 sediment fluff layer



Appendix 2.4.17 C 1s XANES gaussian curve fitting for Station 26 sediment fluff layer



Appendix 2.4.18 C 1s XANES gaussian curve fitting for Station 30 sediment fluff layer

Appendix Table 2.4.1 Gaussian curve fitting parameters of mid-plume C 1s XANES.

Sample	Station	GT#	arc tangent	Pi* 1	Pi* 2	Pi* 3	Pi* 4	Sigma* 1	Sigma* 2	χ^2	reduced χ^2	R-factor
Cs069 (cluster 3)	18	8436	290	285.206	288.291	288.511	289.432	292.1	300	0.04943	0.0005682	0.0005682
Cs034 (cluster 2)	20	8705	290	284.534	285.25	288.386	290.2	293.394	300	0.09977	0.0011468	0.0013337
Cs016 (cluster 2)	21	8882	290	288.216	290.286	290.561	292.707	296.3	304	0.06606	0.0007507	0.001398
Cs042 a3	21	8882	290	285.265	288.731	289.612		293.243	301.5	0.39141	0.0043979	0.003976
Cs080 a2	21	8882	290	285.234	286.17	288.261	289.1	293.378	302	0.18124	0.0020832	0.0020468
Cs012 a3	23	9065	290	285.26	287.021	288.066	289.11	293.459	300	0.18159	0.0020872	0.0022999
Cs040 a1	25	9255	290	285.04	285.425	287.571	287.736	289.387	300	0.49771	0.0057208	0.0061536
Cs 043 a3	25	9255	290	285.25	288.086	288.6		291	302	0.17659	0.0019841	0.0023258
Cs 011 a1	26	9346	290	285.234	287.525	288.252	289.25	291	301	0.03913	0.0004498	0.0005524
Cs 150 (cluster 2)	28	9595	290	285.114	287.405	288.187	288.969	290.701	300	0.10507	0.0012077	0.0011876
Cs 150 (cluster 3)	28	9595	290	285.178	288.172	288.362	290	292.331	301	0.13533	0.0015555	0.0013331
Cs 049 (cluster 2)	30	9838	290	285.178	288.6	288.992	289.928	294	302	0.12251	0.0014082	0.0012472
Cs 049 (cluster 3)	30	9838	290	285.178	287.246	288.866	289.593	294	302	0.10132	0.0011645	0.0011826

All arc tangent, pi*, and sigma* values in eV

Appendix Table 2.4.2 Gaussian curve fitting parameters for sediment fluff C 1s XANES

Sample	Station	GT#	arc tangent	Pi* 1	Pi* 2	Pi* 3	Pi* 4	Sigma* 1	Sigma* 2	χ^2	reduced χ^2	R-factor
Cs030 (cluster 3)	20	8767	290	287.405	288.075	288.41	290.31	295	302	0.18976	0.0021812	0.0012972
Cs030 (cluster 4)	20	8767	290	287.405	288.075	288.466	290.31		305	0.96677	0.0108626	0.0168891
Cs075 (cluster 2)	23		290	285.167	286.978	288.641	290.281		305	0.87032	0.0097789	0.0147788
Cs111 (cluster 2)	26	9485	290	285.208	287.331	288.784	290.237		305	1.88855	0.0212197	0.0328142
Cs090 (cluster 3)	30	9867	290	285.084	288.66	289.1	290.281		305	1.99806	0.0224502	0.0353375

blank: no functional group identified

All arc tangent, pi*, and sigma* values in eV

Appendix 2.5 Fe 1s XANES linear least square fitting data with *Mr Fitty*

Below are the best fits for all Fe μ -XANES collected at ALS 10.3.2. Multiple spots were collected at each station to understand Fe diversity within the sample. Those spectra were then compared to our Fe standards XANES database. Using *Mr Fitty* (reference), the best fits were determined and reported below. This information was then compiled to produce the Figure 6.

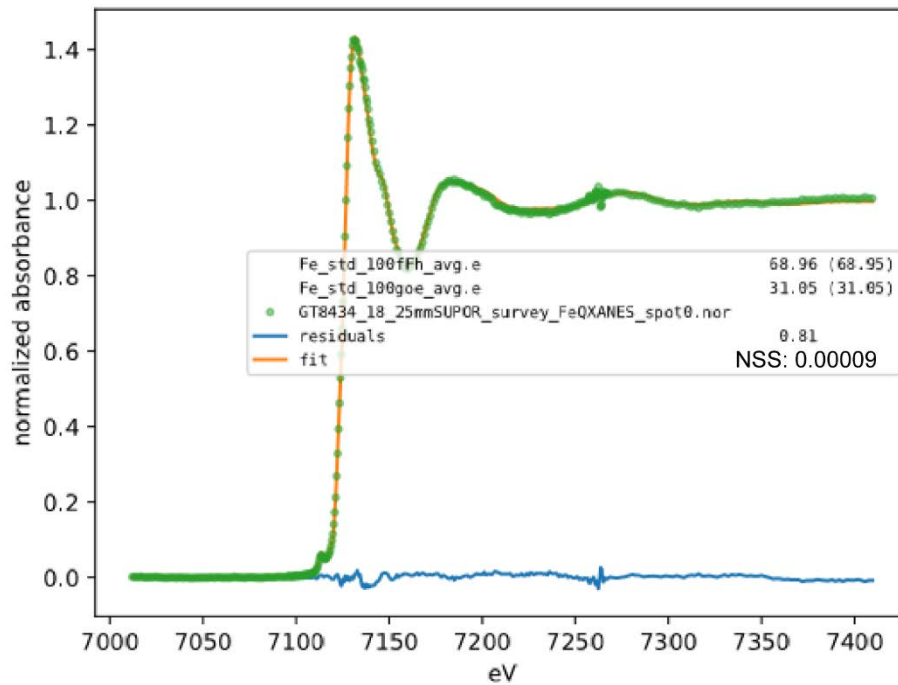


Figure 2.5.1 Fe XANES Station 18 survey spot 0

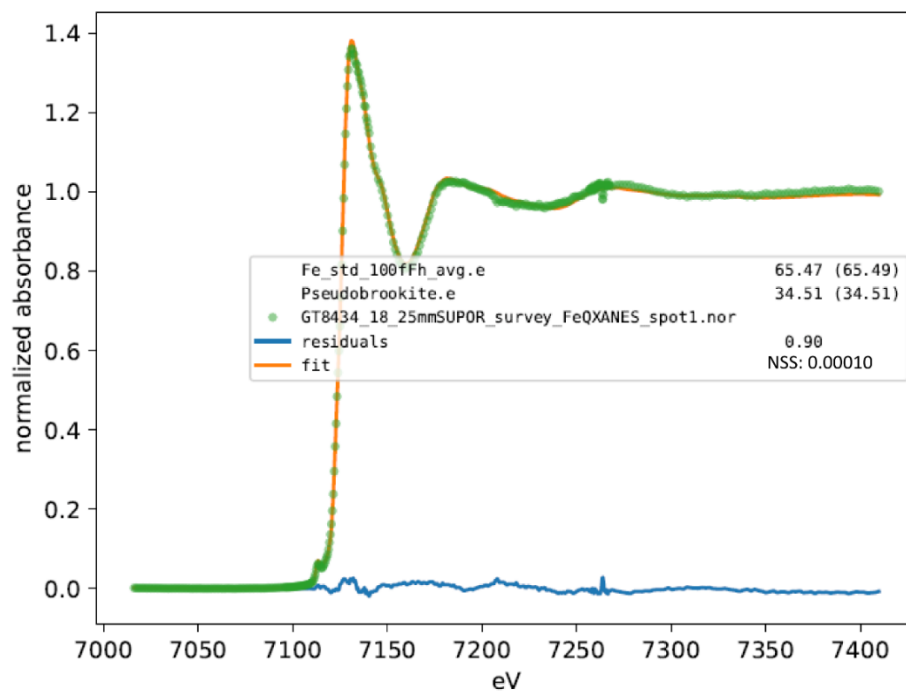


Figure 2.5.2 Fe XANES Station 18 survey spot 1

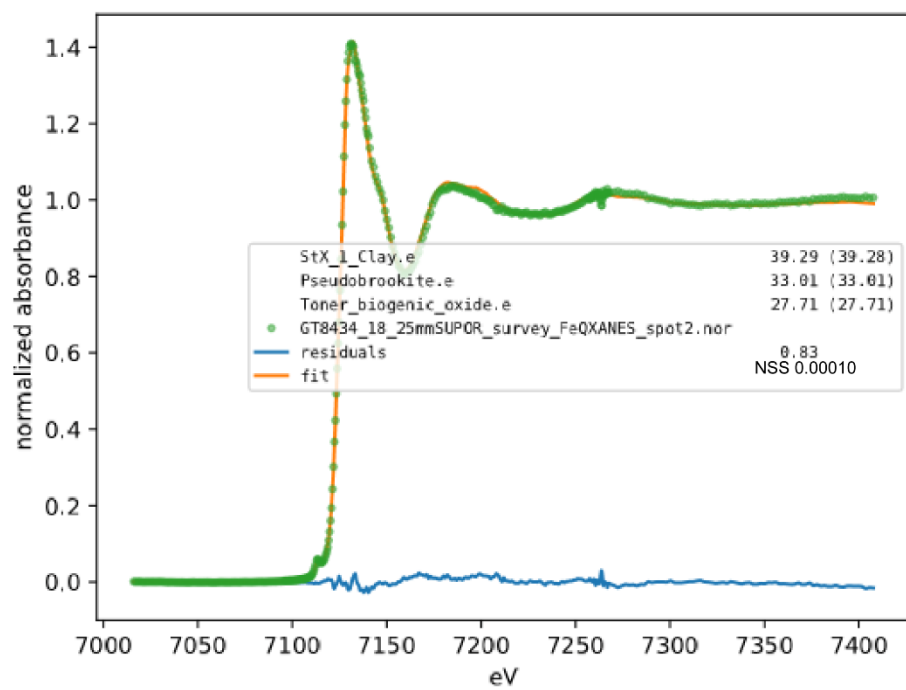


Figure 2.5.3 Fe XANES Station 18 survey spot 2

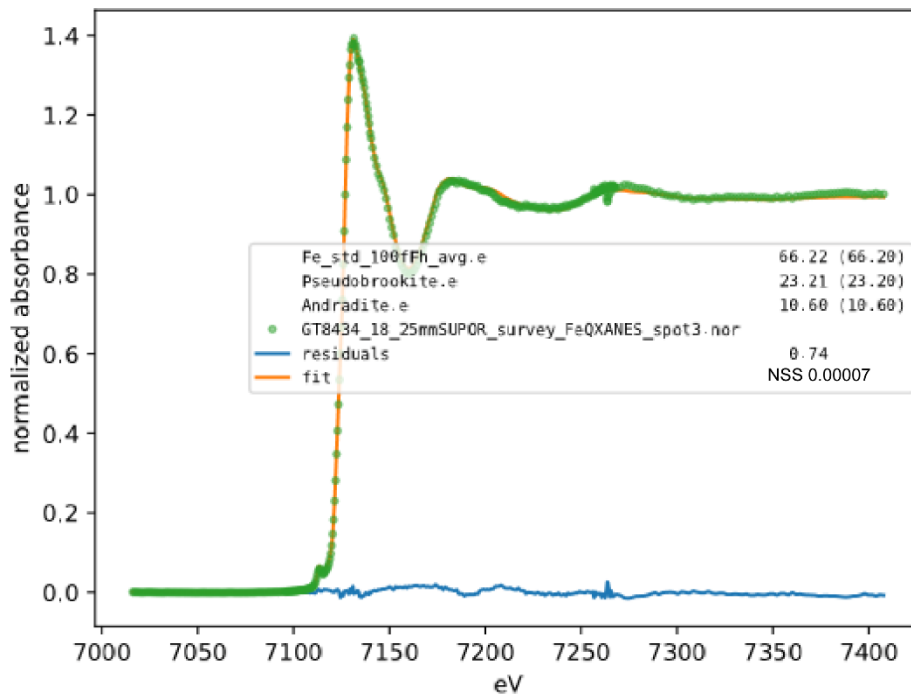


Figure 2.5.4 Fe XANES Station 18 survey spot 3

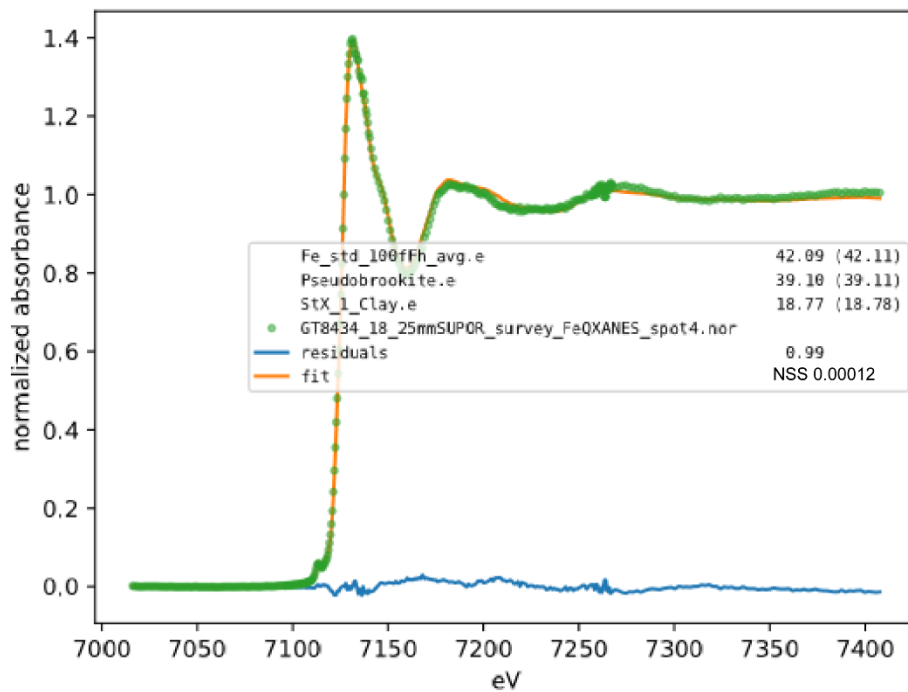


Figure 2.5.5 Fe XANES Station 18 survey spot 4

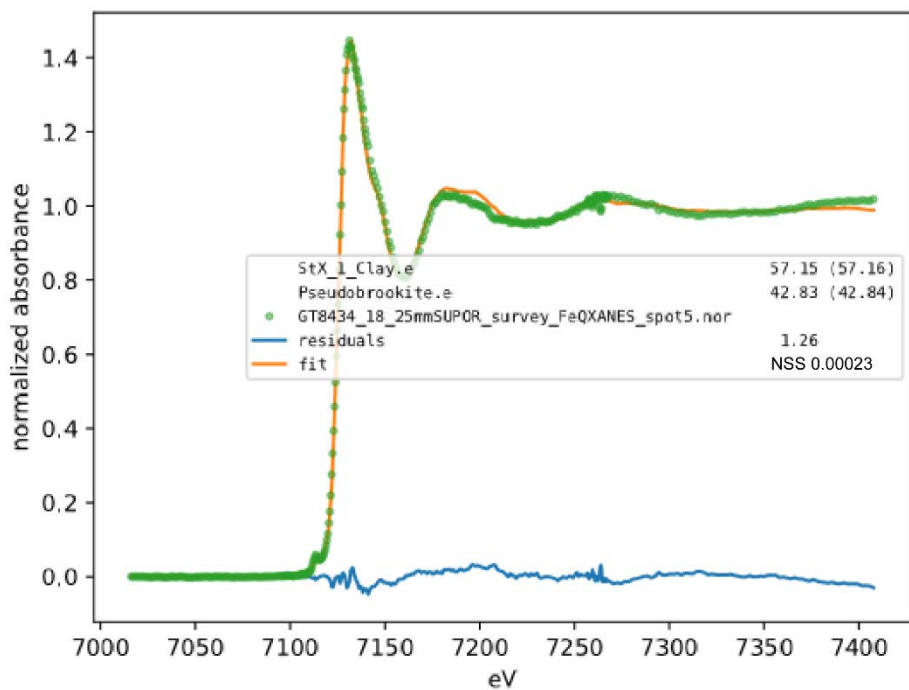


Figure 2.5.6 Fe XANES Station 18 survey spot 5

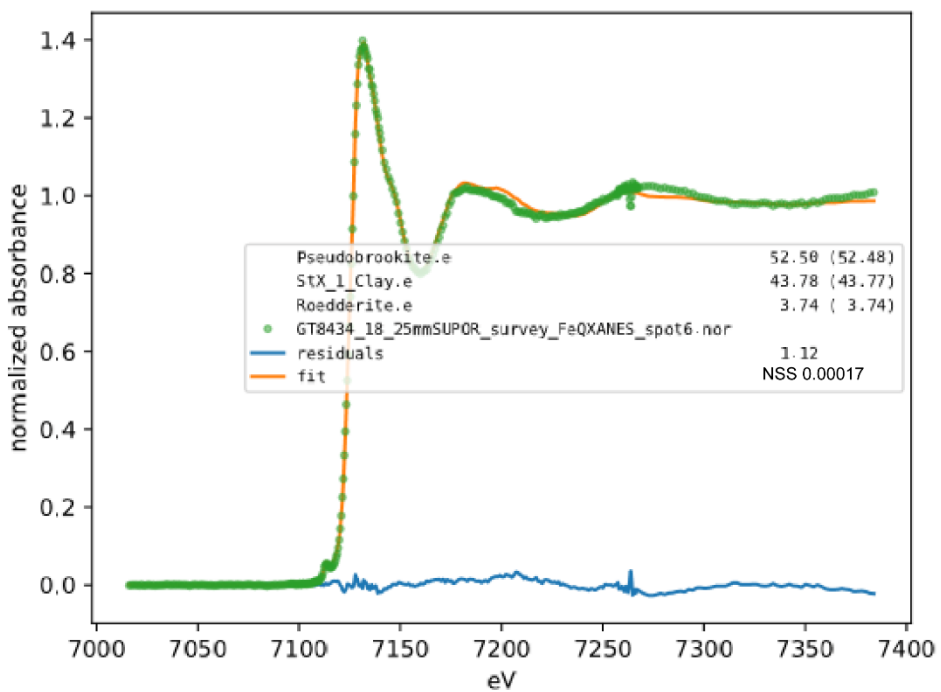


Figure 2.5.7 Fe XANES Station 18 survey spot 6

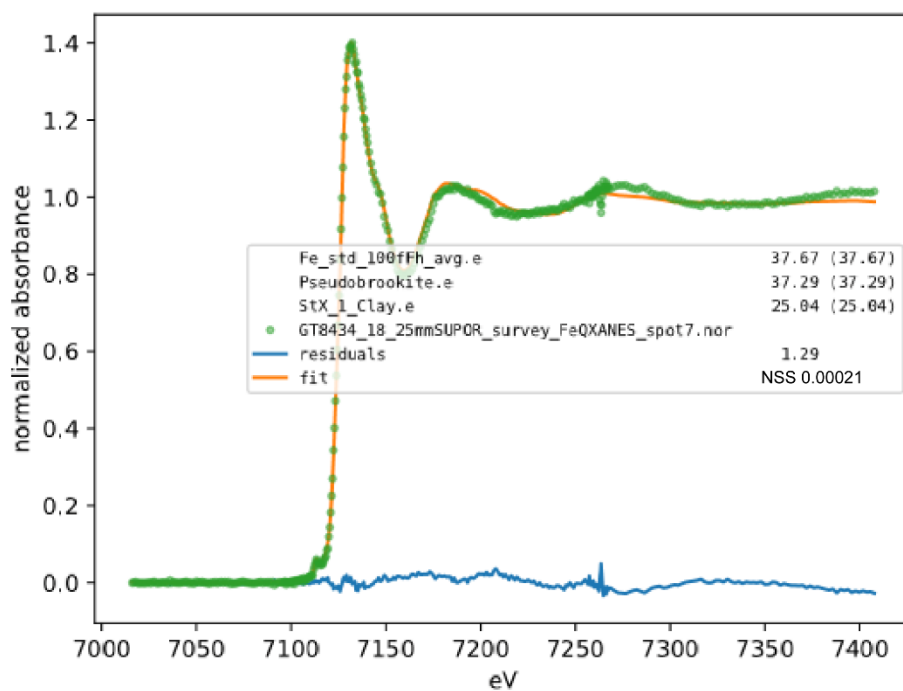


Figure 2.5.8 Fe XANES Station 18 survey spot 7

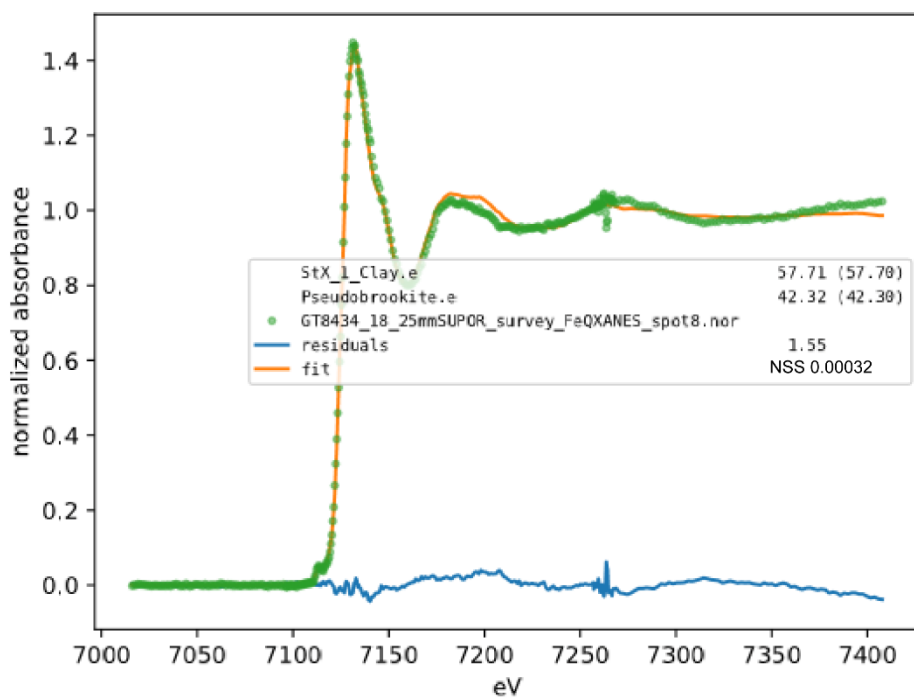


Figure 2.5.9 Fe XANES Station 18 survey

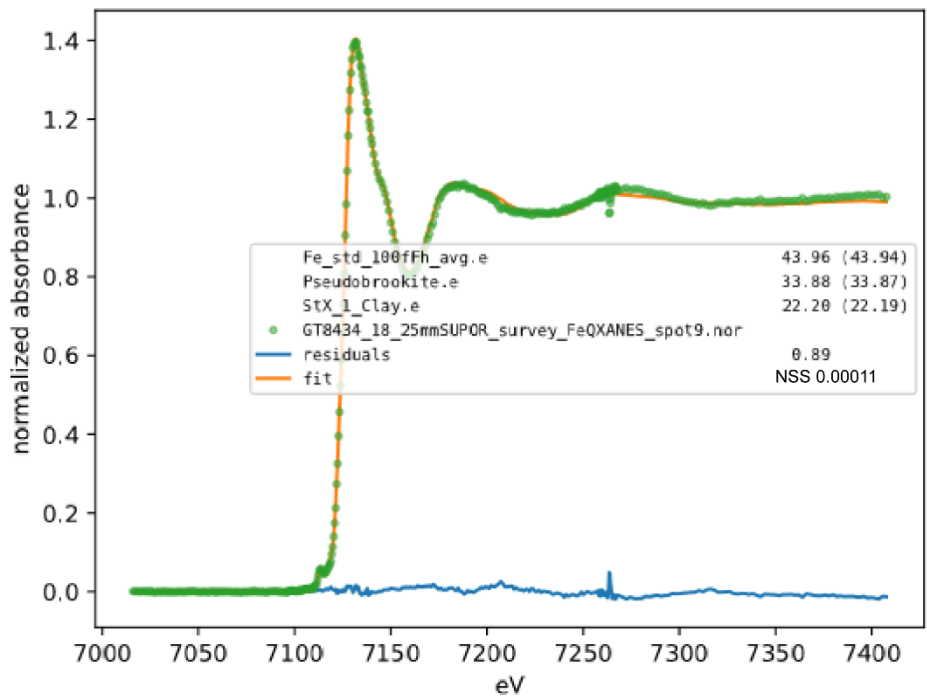


Figure 2.5.10 Fe XANES Station 18 survey spot 9

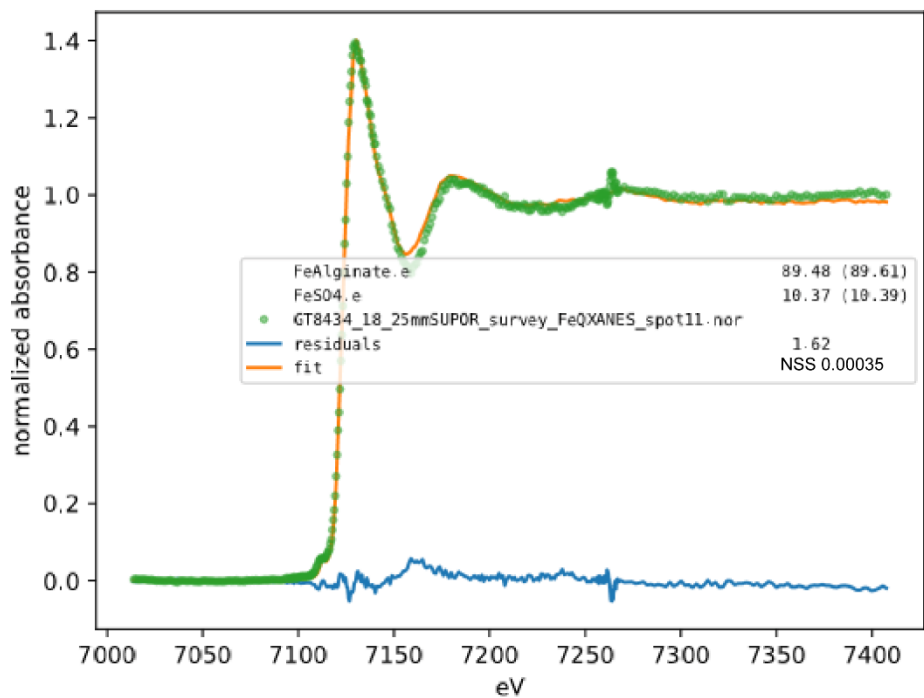


Figure 2.5.11 Fe XANES Station 18 survey spot 11

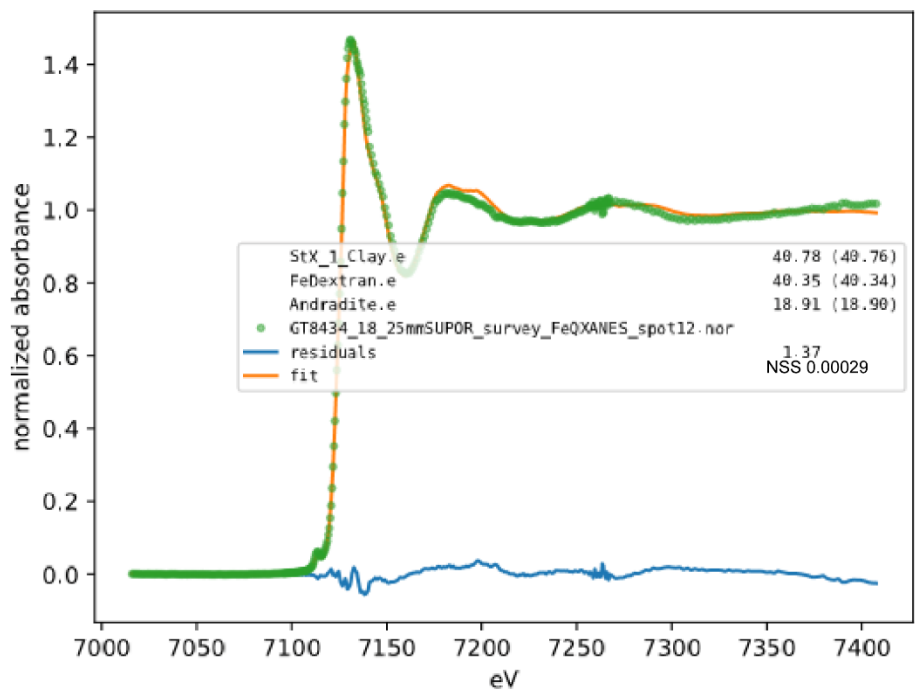


Figure 2.5.12 Fe XANES Station 18 survey spot 12

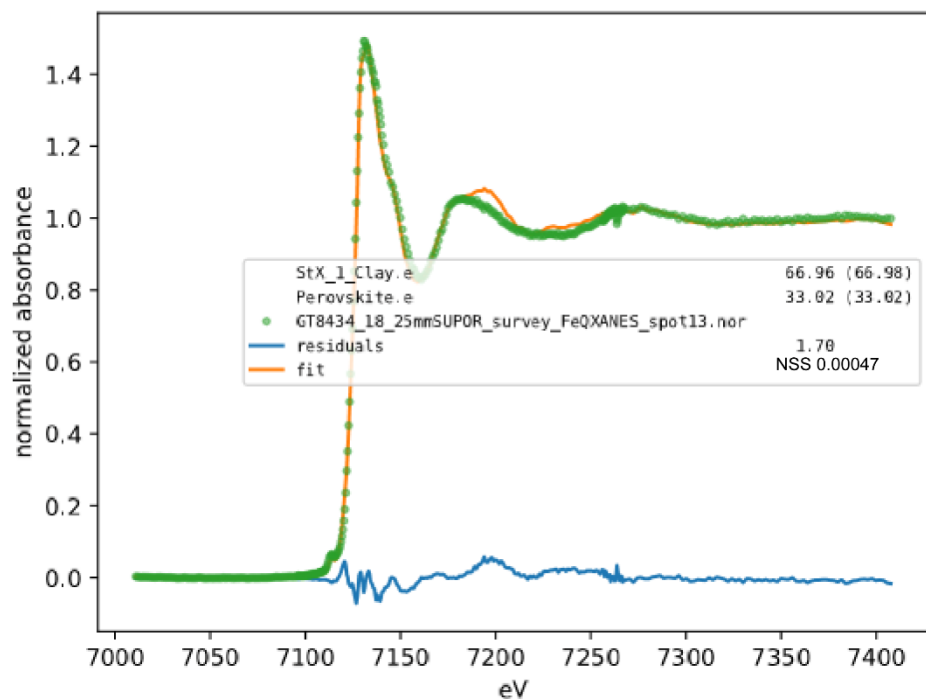


Figure 2.5.13 Fe XANES Station 18 survey spot 13

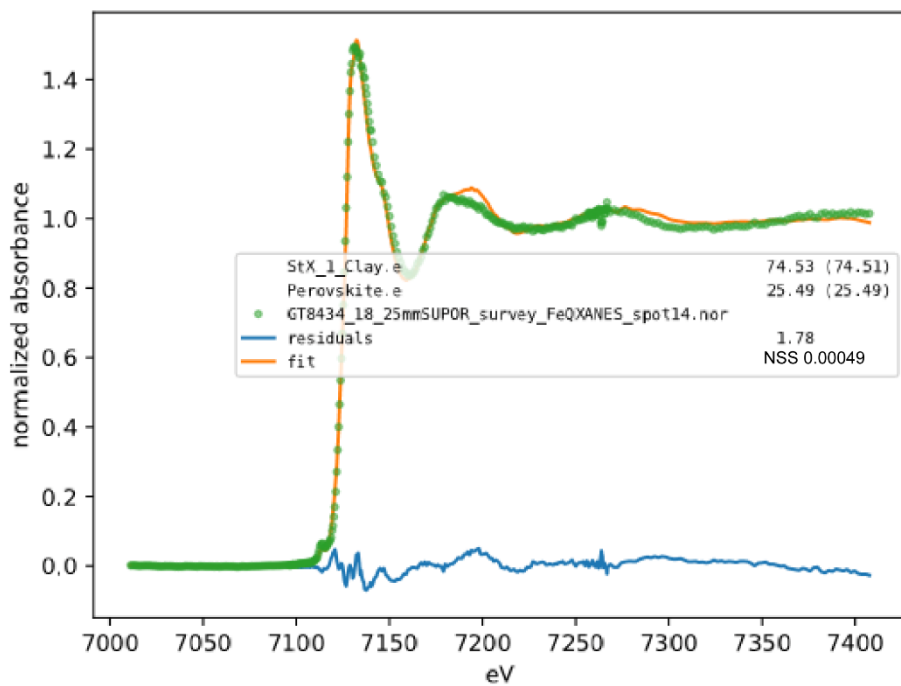


Figure 2.5.14 Fe XANES Station 18 survey spot 14

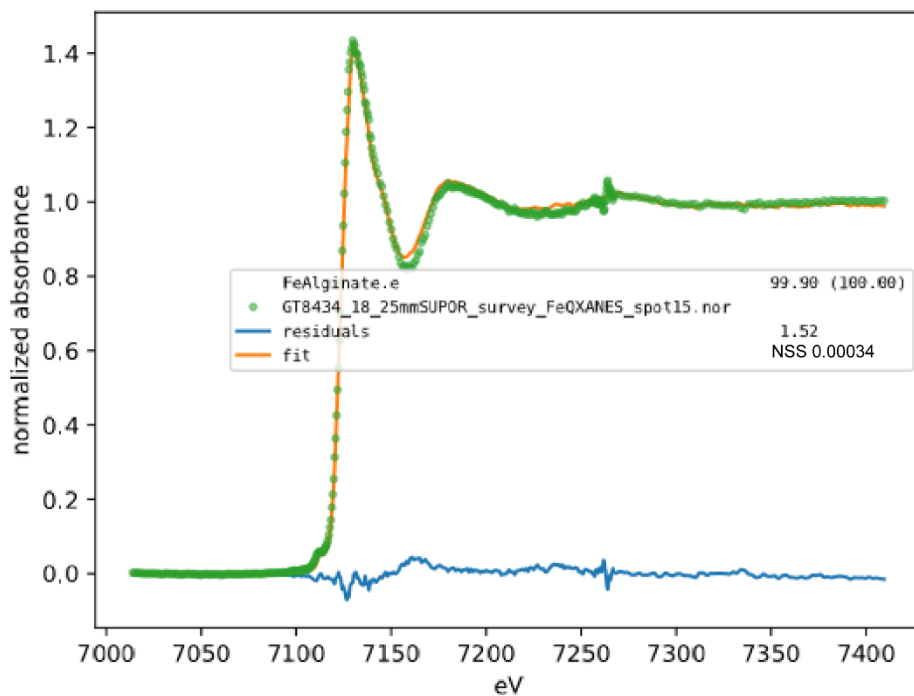


Figure 2.5.15 Fe XANES Station 18 survey spot 15

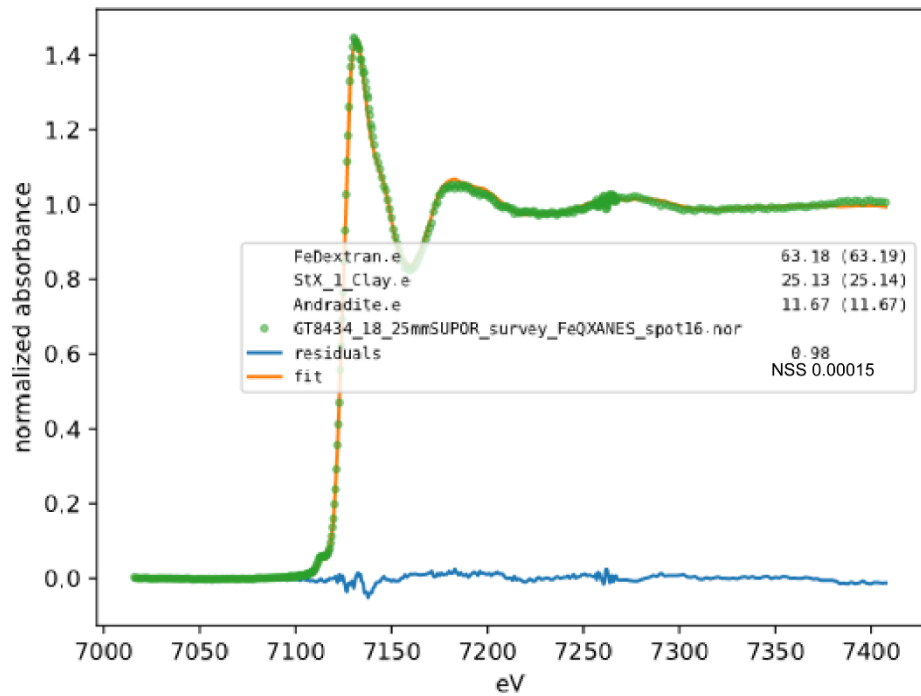


Figure 2.5.16 Fe XANES Station 18 survey spot 16

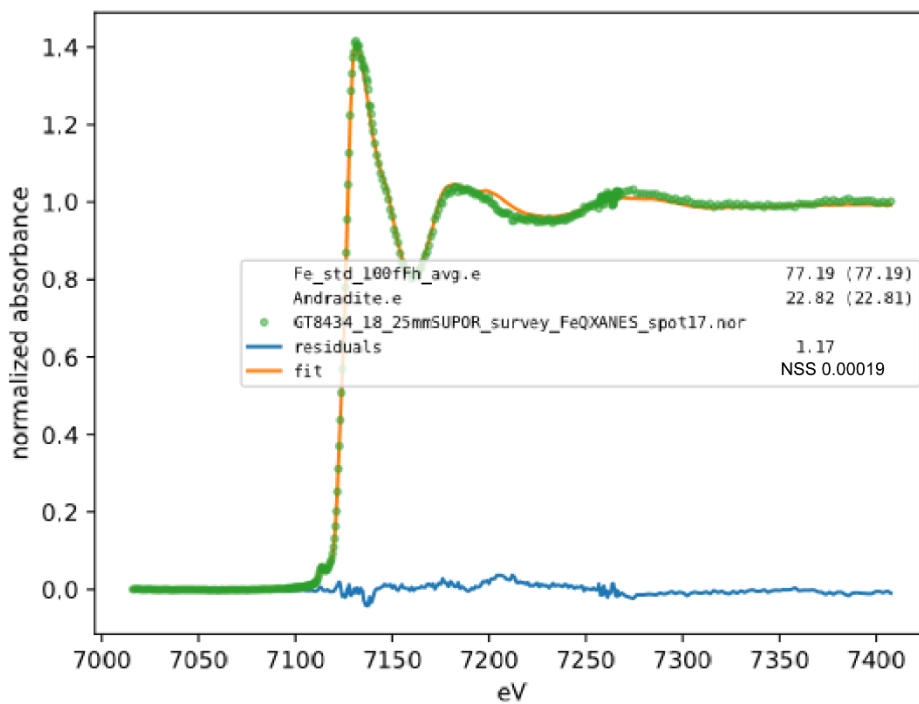


Figure 2.5.17 Fe XANES Station 18 survey spot 17

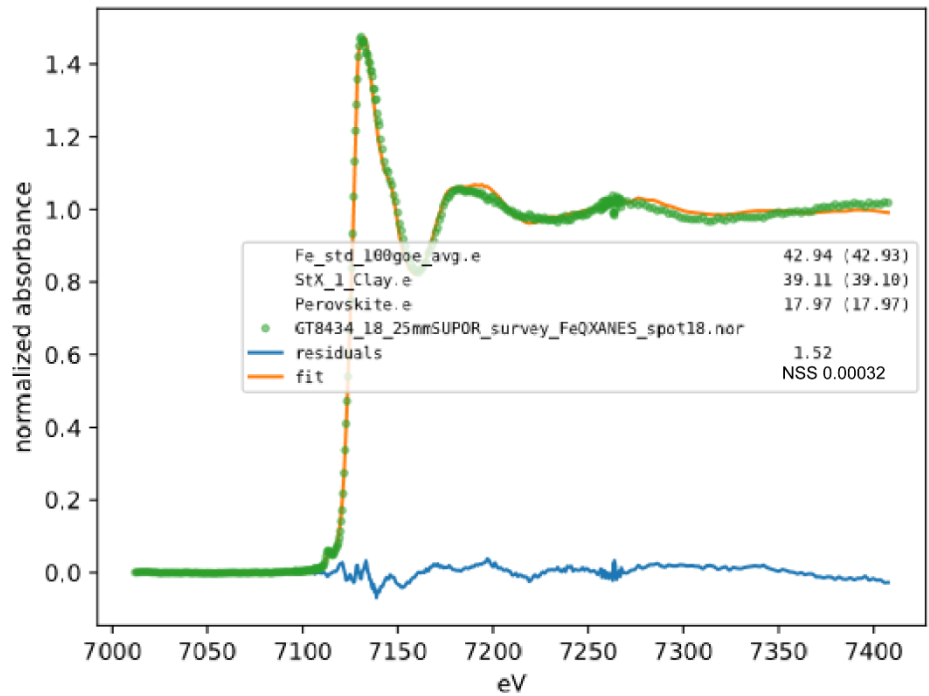


Figure 2.5.18 Fe XANES Station 18 survey spot 18

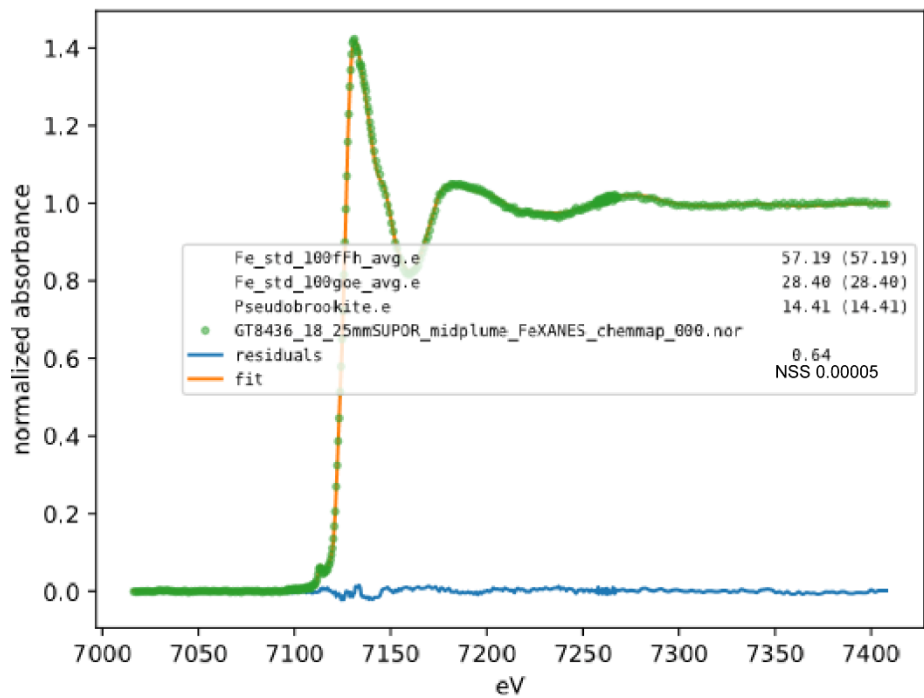


Figure 2.5.19 Fe XANES Station 18 midplume

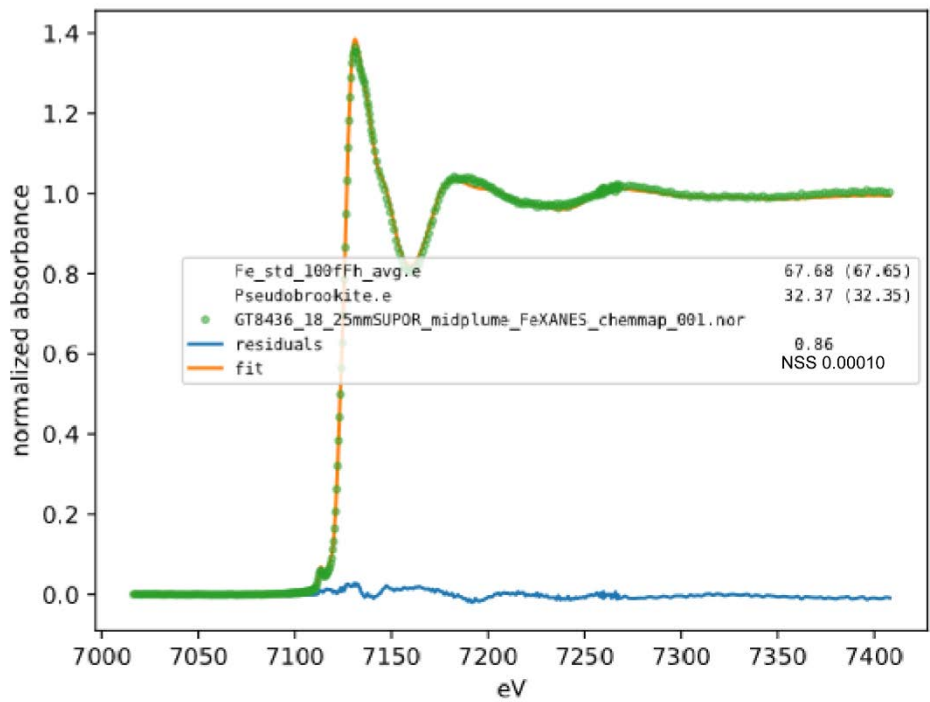


Figure 2.5.20 Fe XANES Station 18 midplume

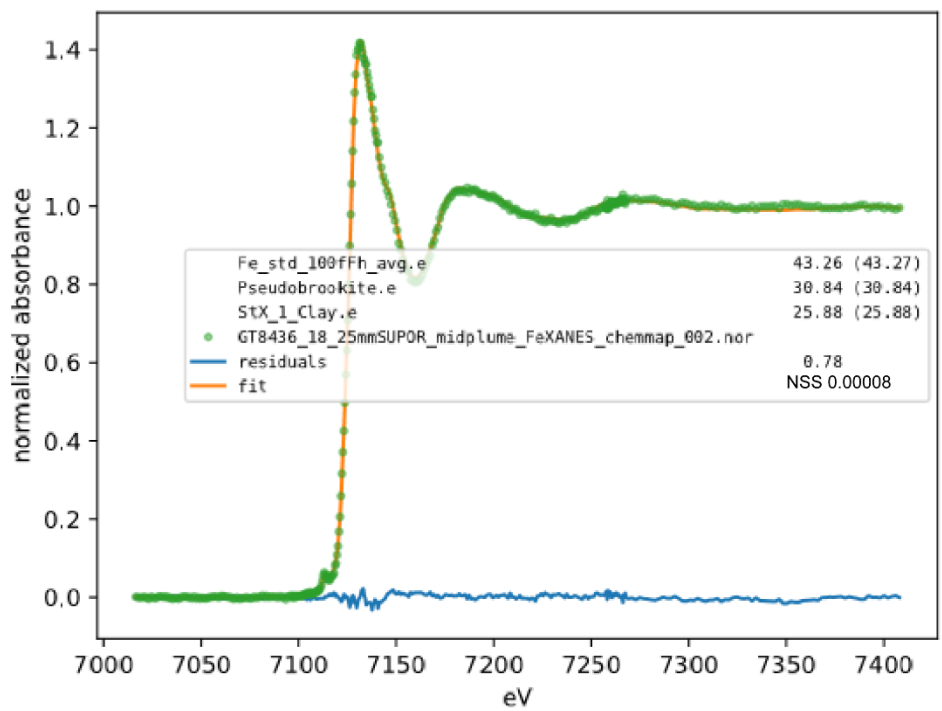


Figure 2.5.21 Fe XANES Station 18 midplume

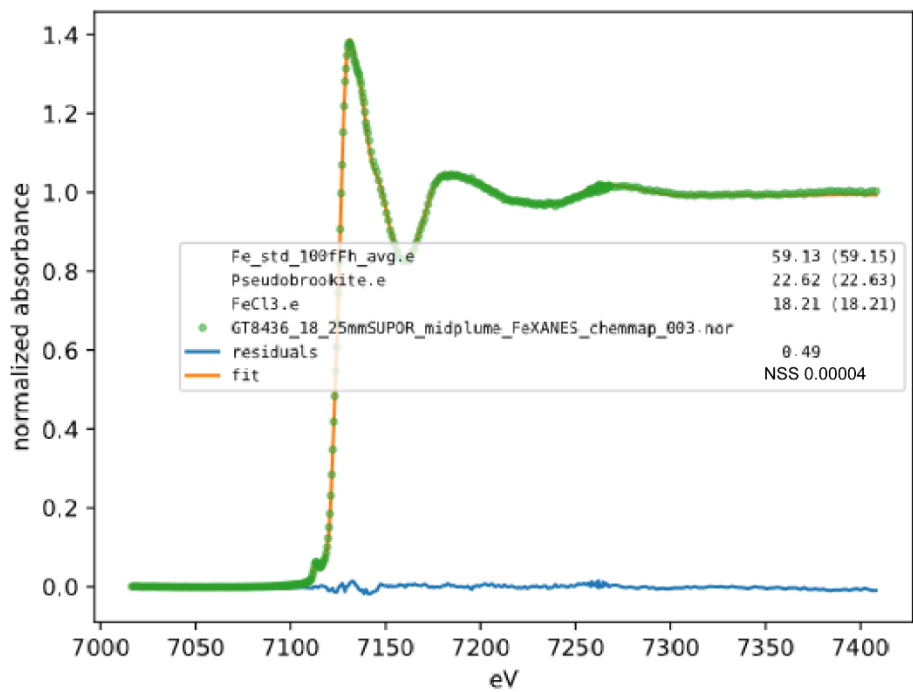


Figure 2.5.22 Fe XANES Station 18 midplume

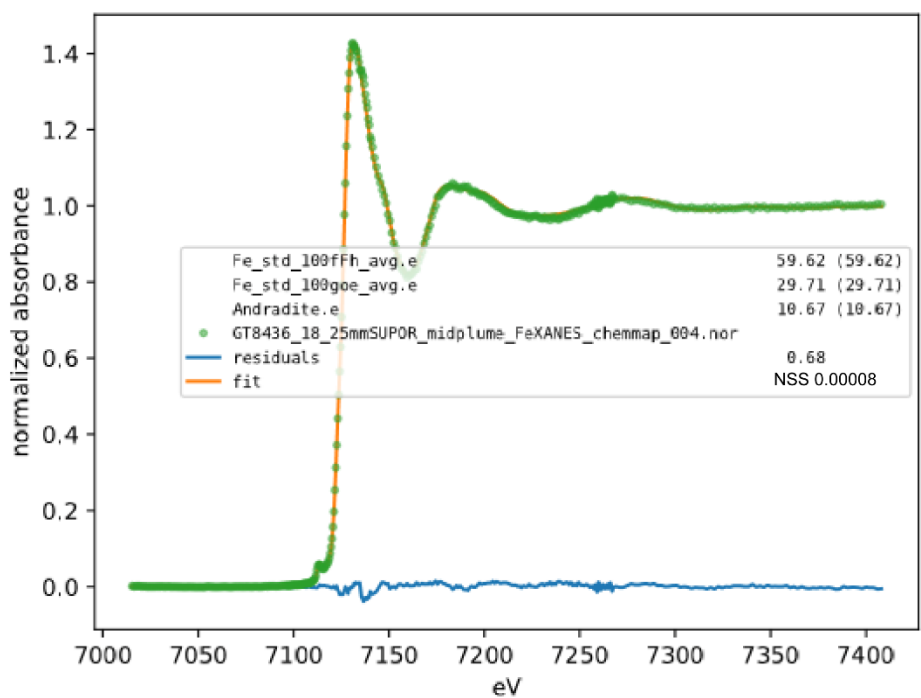


Figure 2.5.23 Fe XANES Station 18 midplume

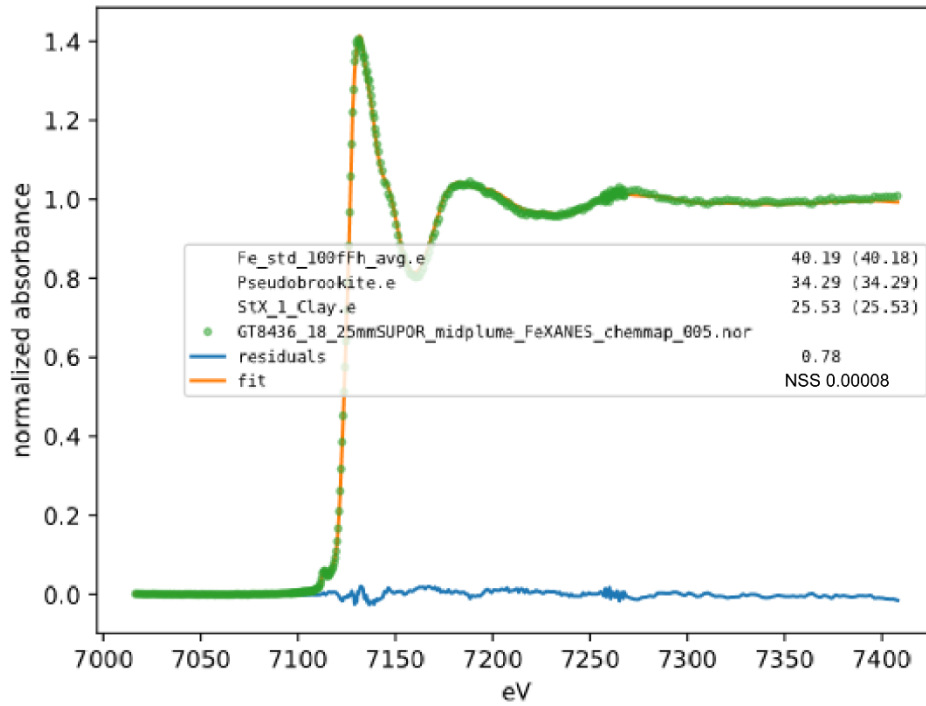


Figure 2.5.24 Fe XANES Station 18 midplume

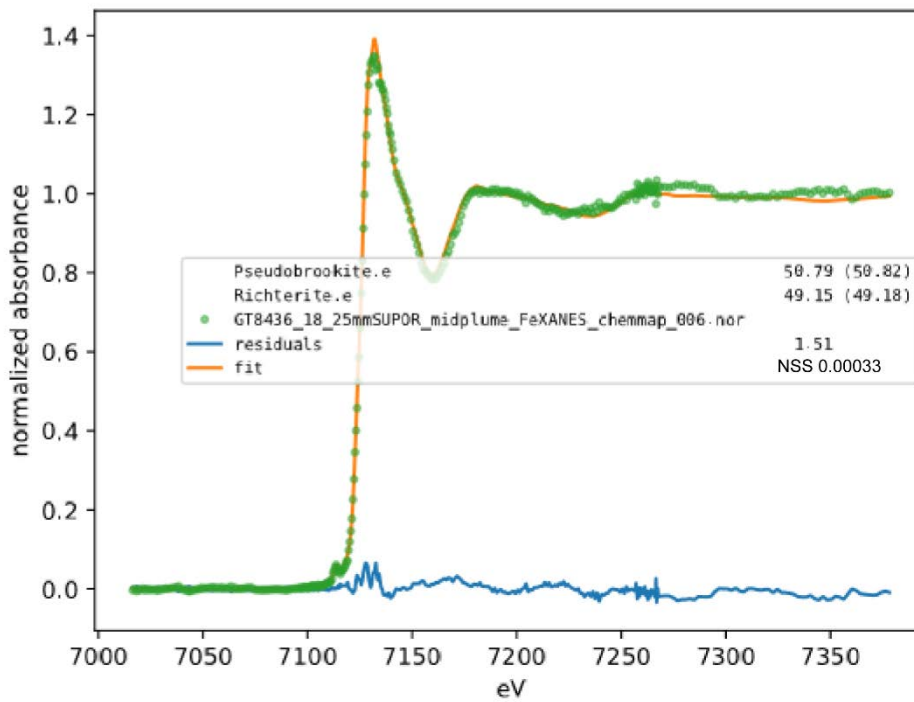


Figure 2.5.25 Fe XANES Station 18 midplume

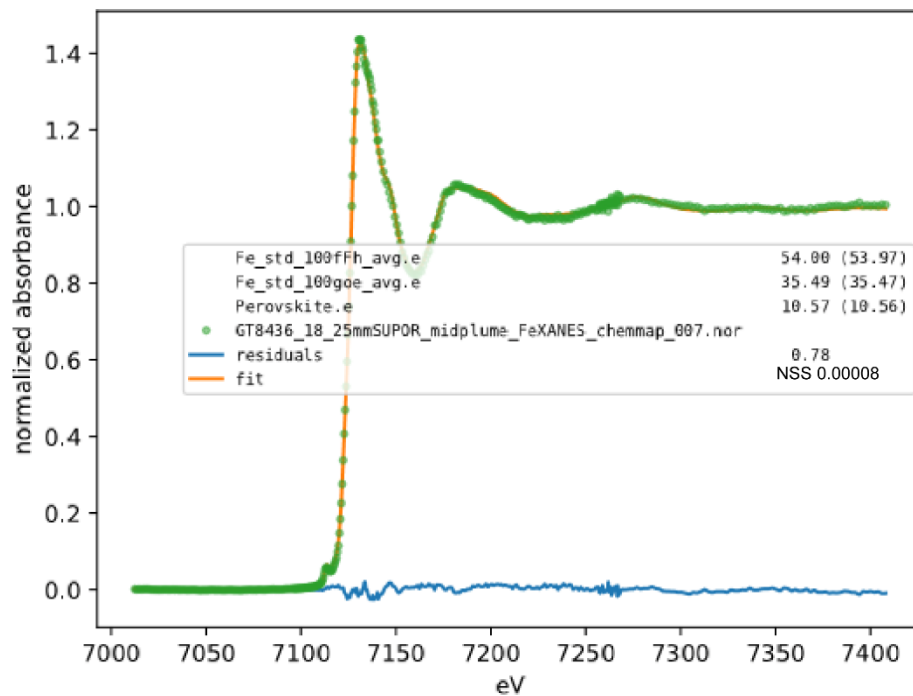


Figure 2.5.26 Fe XANES Station 18 midplume

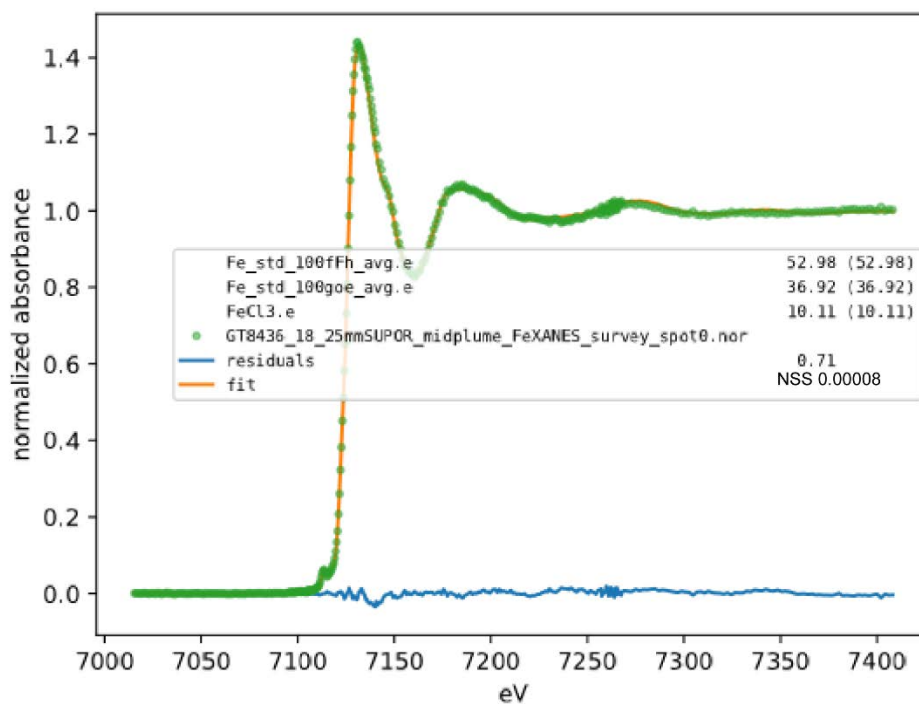


Figure 2.5.27 Fe XANES Station 18 midplume spot 0

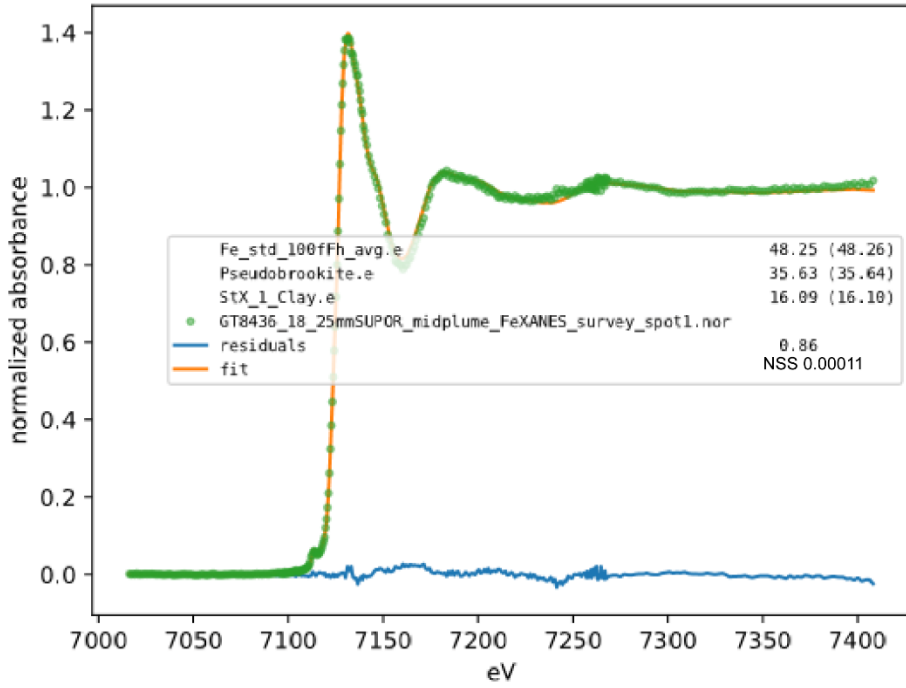


Figure 2.5.28 Fe XANES Station 18 midplume spot 1

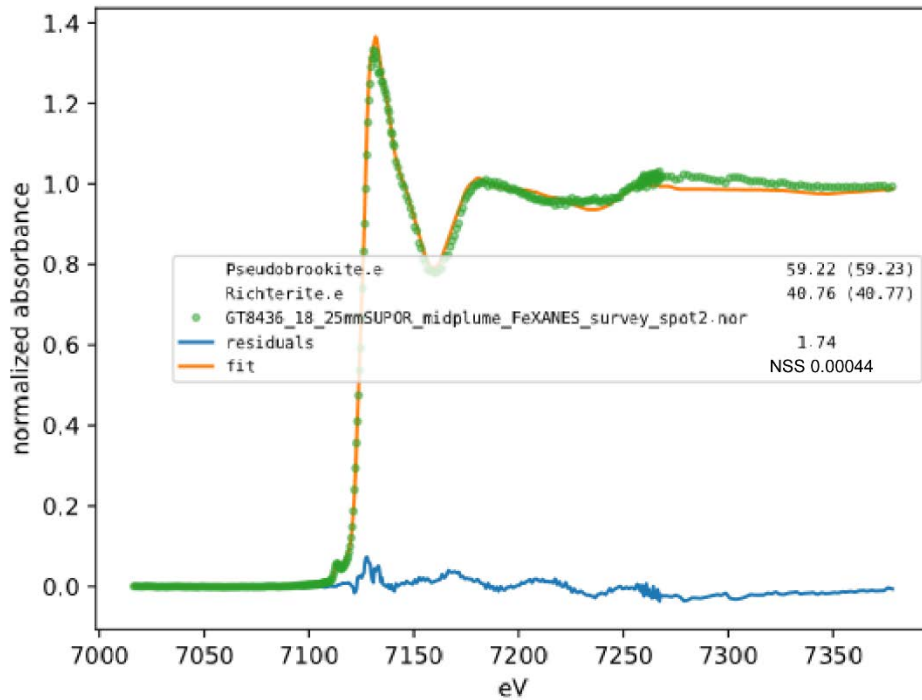


Figure 2.5.29 Fe XANES Station 18 midplume spot 2

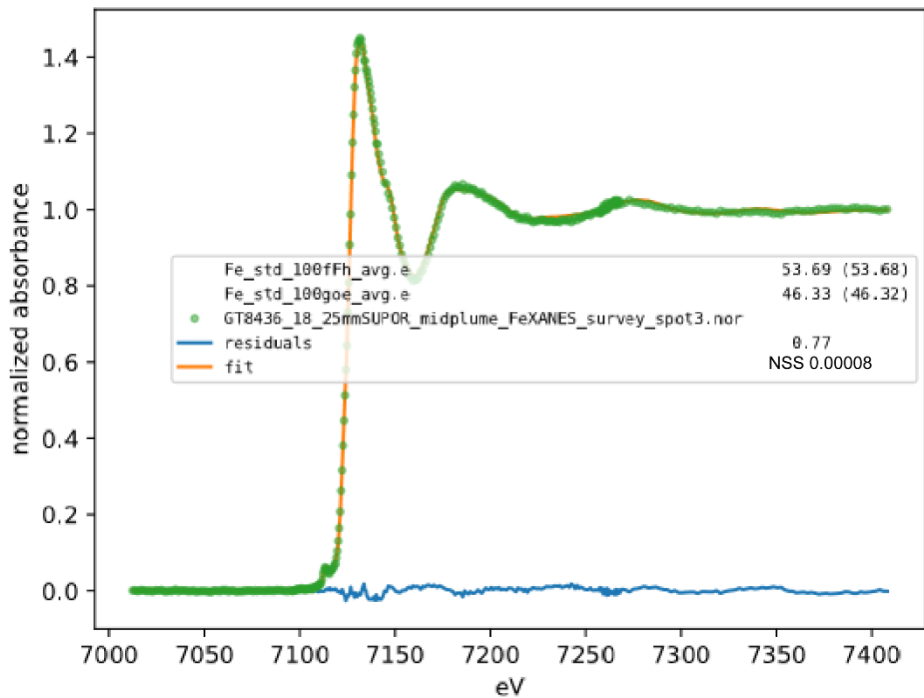


Figure 2.5.30 Fe XANES Station 18 midplume spot 3

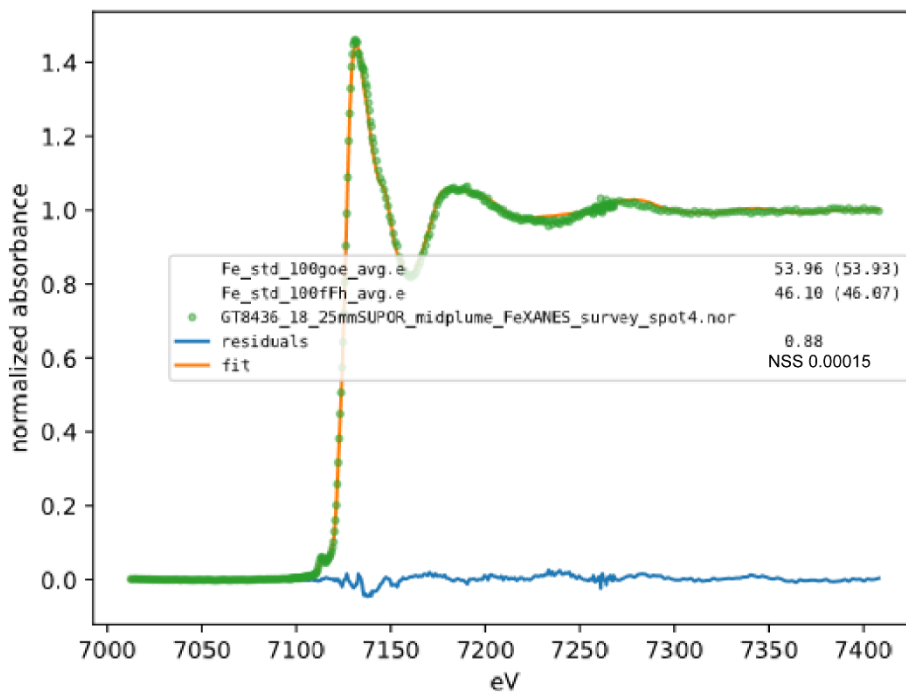


Figure 2.5.31 Fe XANES Station 18 midplume spot 4

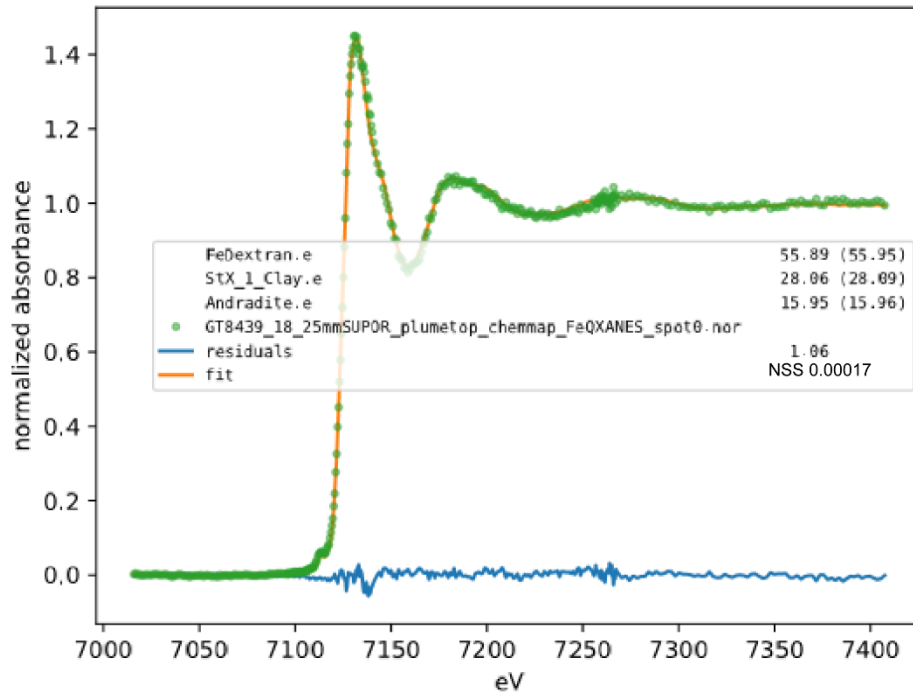


Figure 2.5.32 Fe XANES Station 18 plume top spot 0

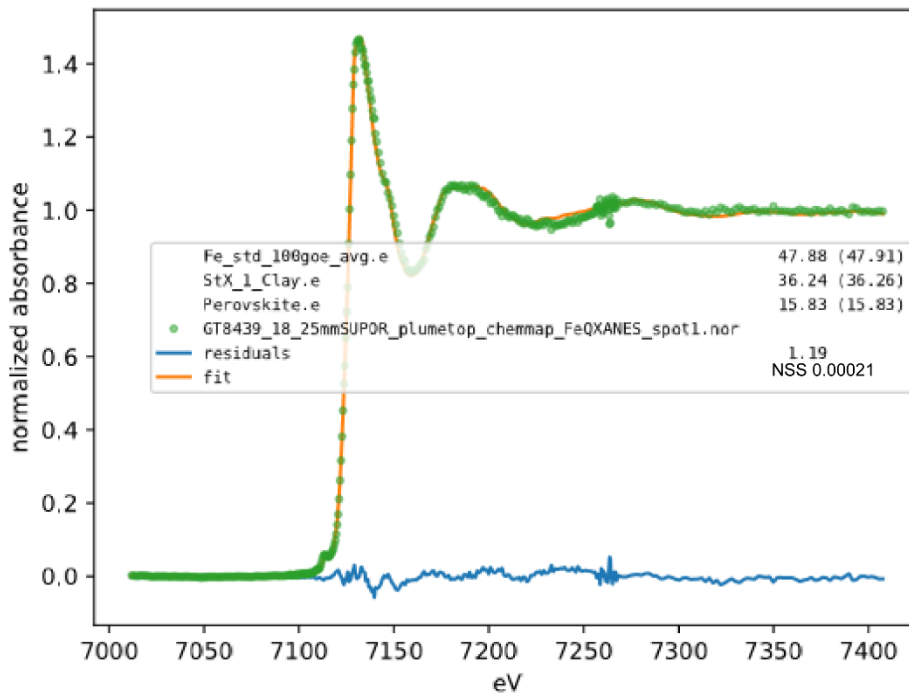


Figure 2.5.33 Fe XANES Station 18 plume top spot 1

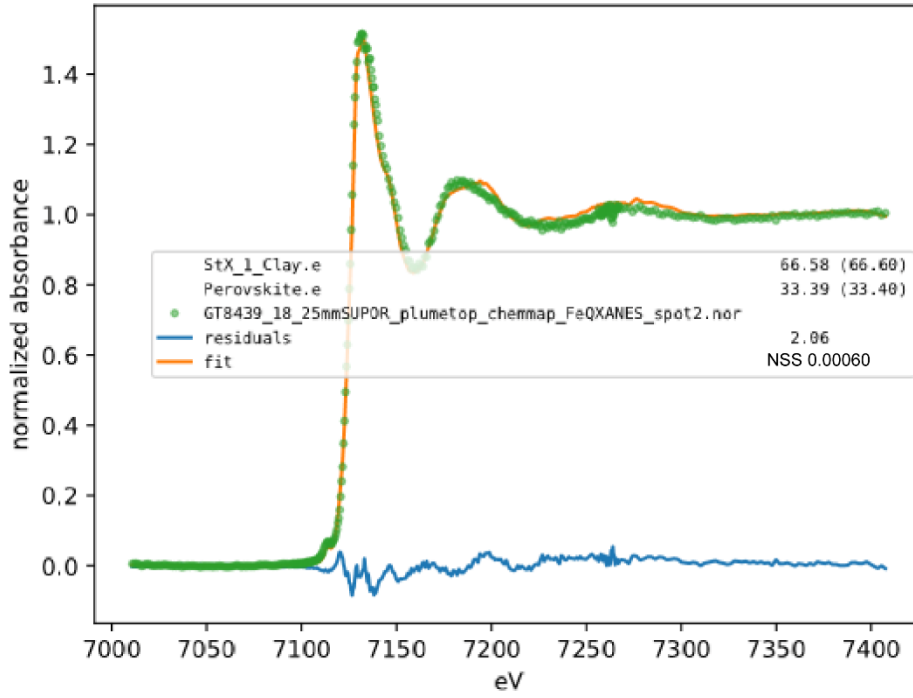


Figure 2.5.34 Fe XANES Station 18 plume top spot 2

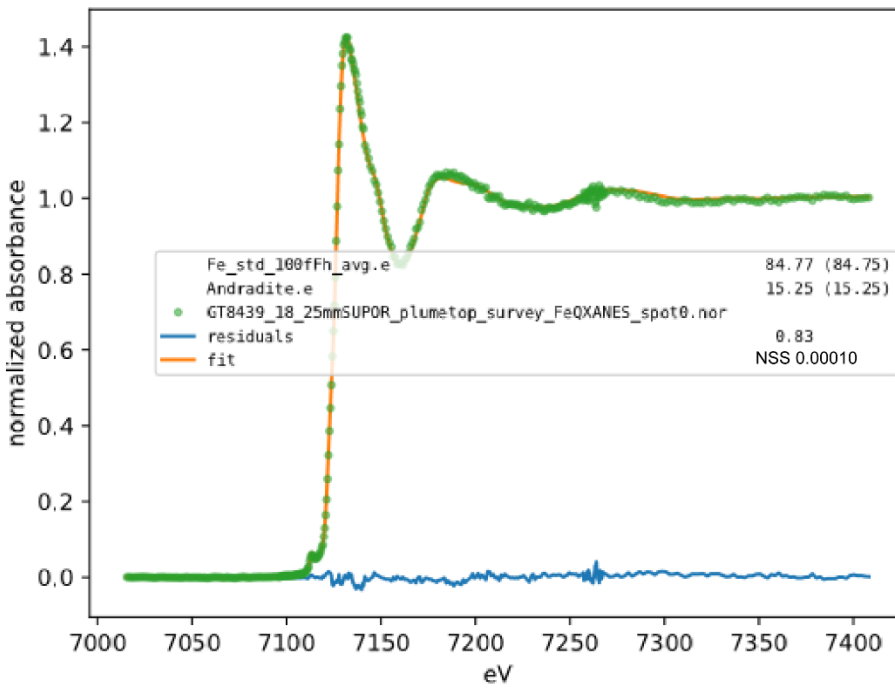


Figure 2.5.35 Fe XANES Station 18 plume top spot 0

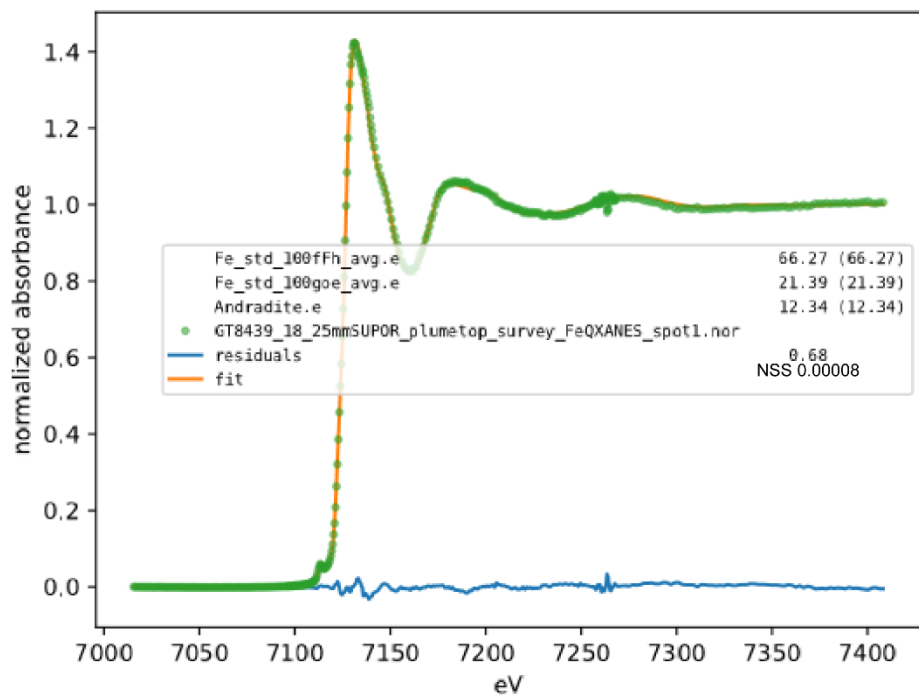


Figure 2.5.36 Fe XANES Station 18 plume top spot 1

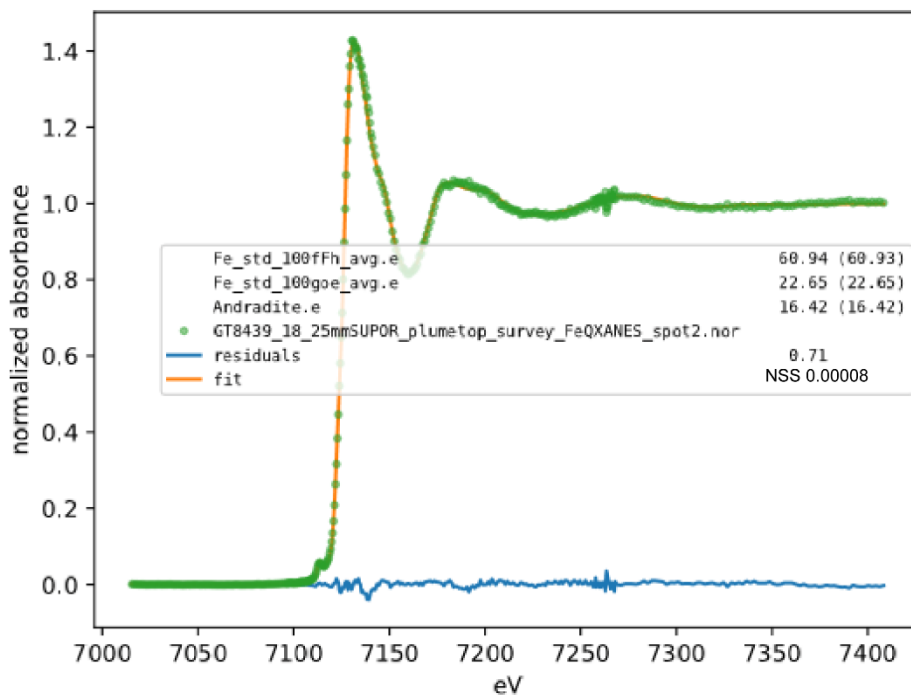


Figure 2.5.37 Fe XANES Station 18 plume top spot 2

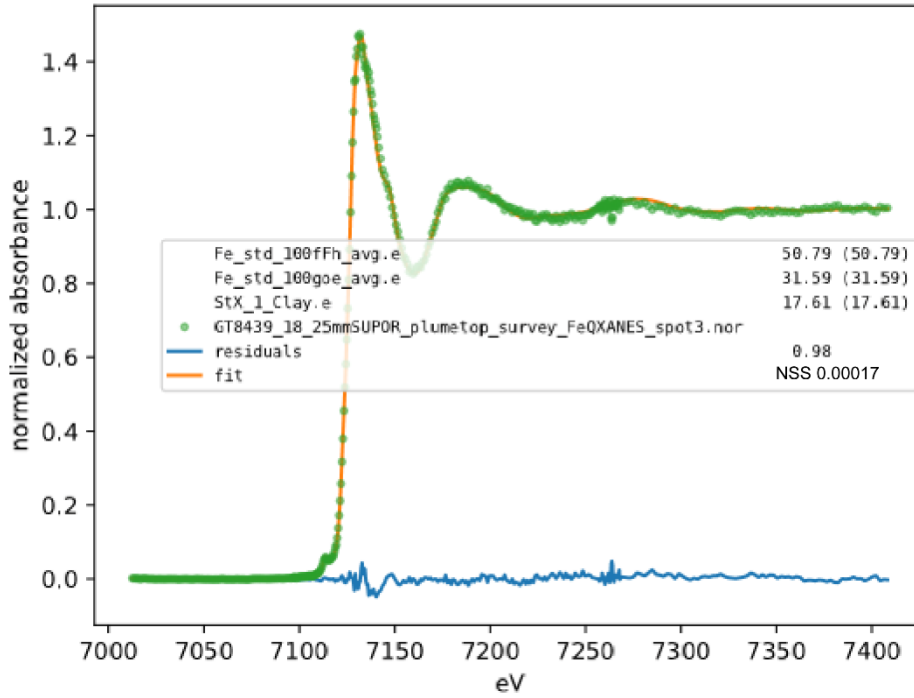


Figure 2.5.38 Fe XANES Station 18 plume top spot 3

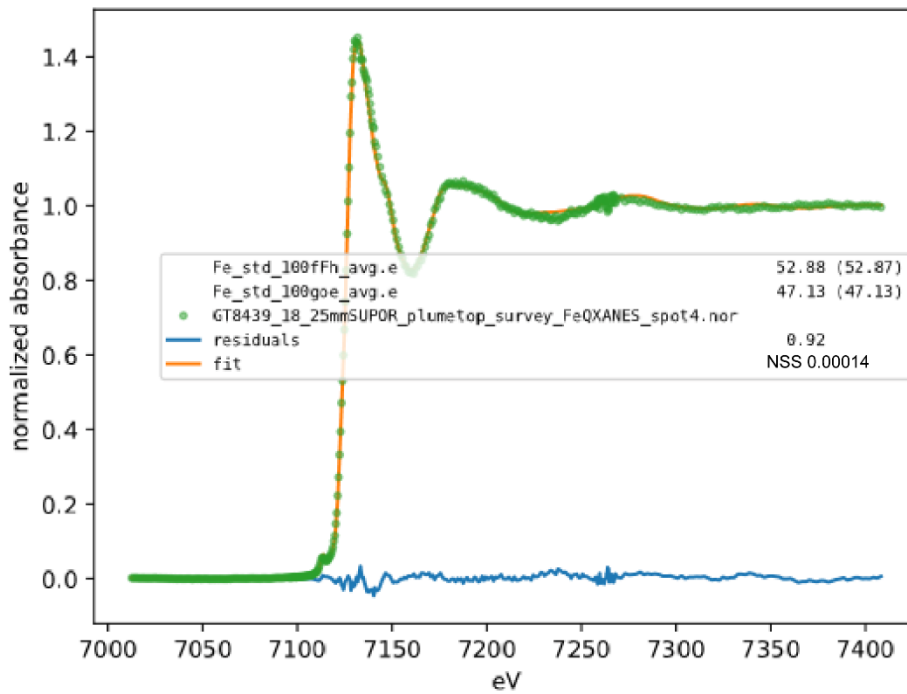


Figure 2.5.39 Fe XANES Station 18 plume top spot 4

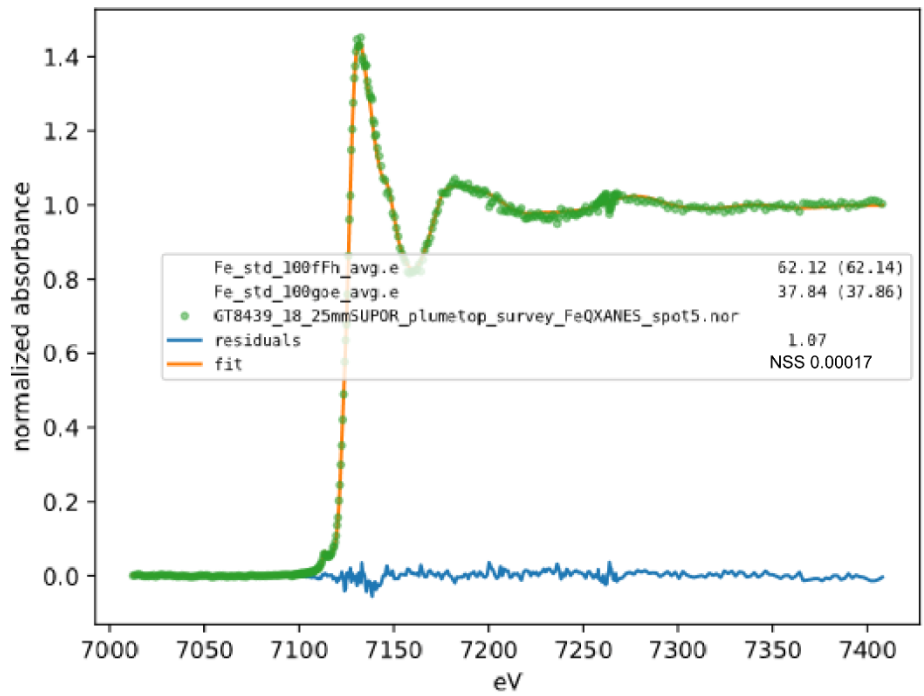


Figure 2.5.40 Fe XANES Station 18 plume top spot 5

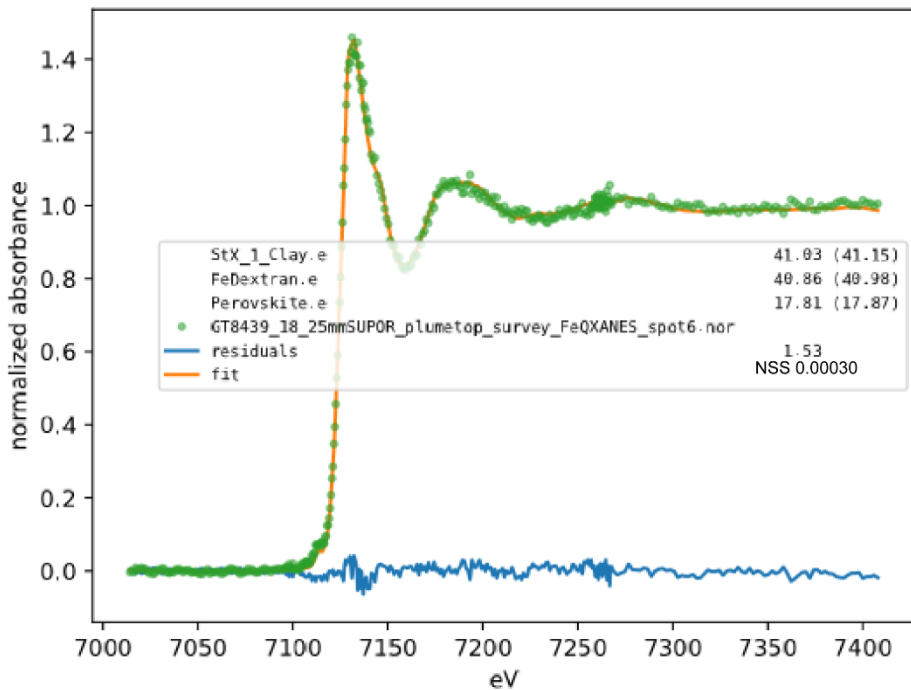


Figure 2.5.41 Fe XANES Station 18 plume top spot 6

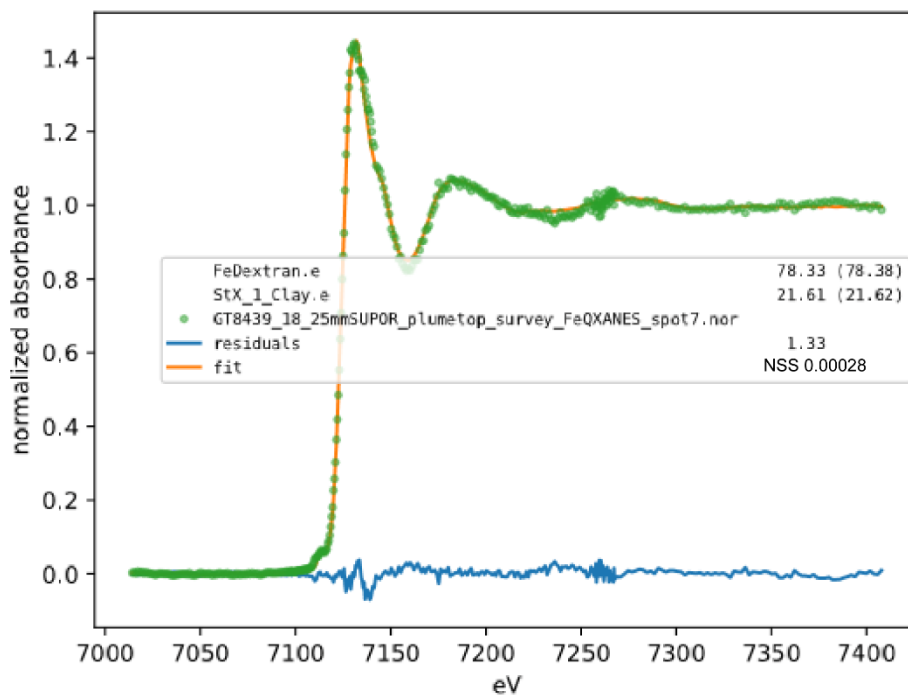


Figure 2.5.42 Fe XANES Station 18 plume top spot 7

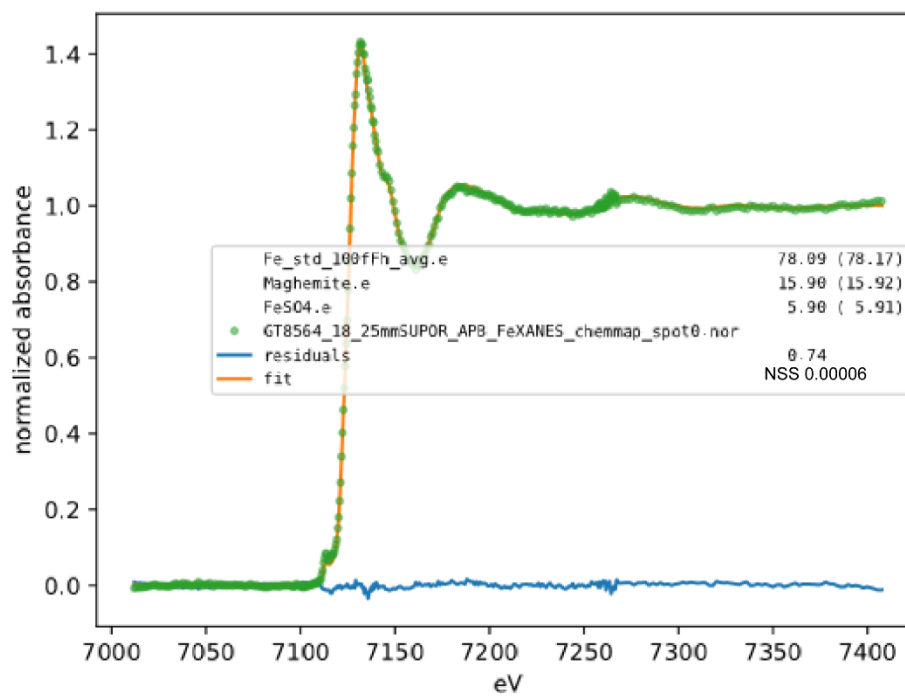


Figure 2.5.43 Fe XANES Station 18 above plume background spot 0

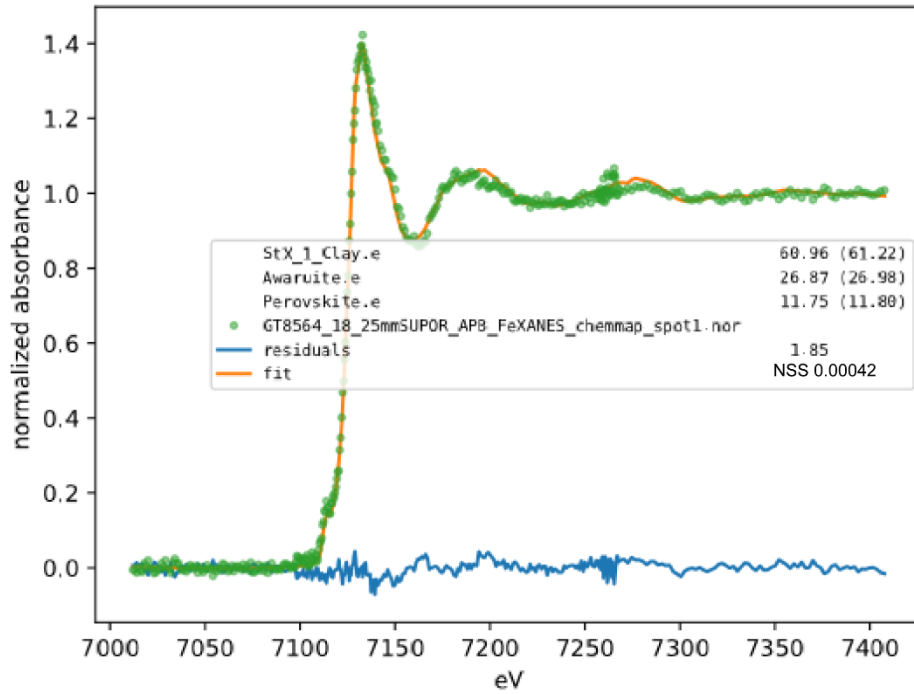


Figure 2.5.44 Fe XANES Station 18 above plume background spot 1

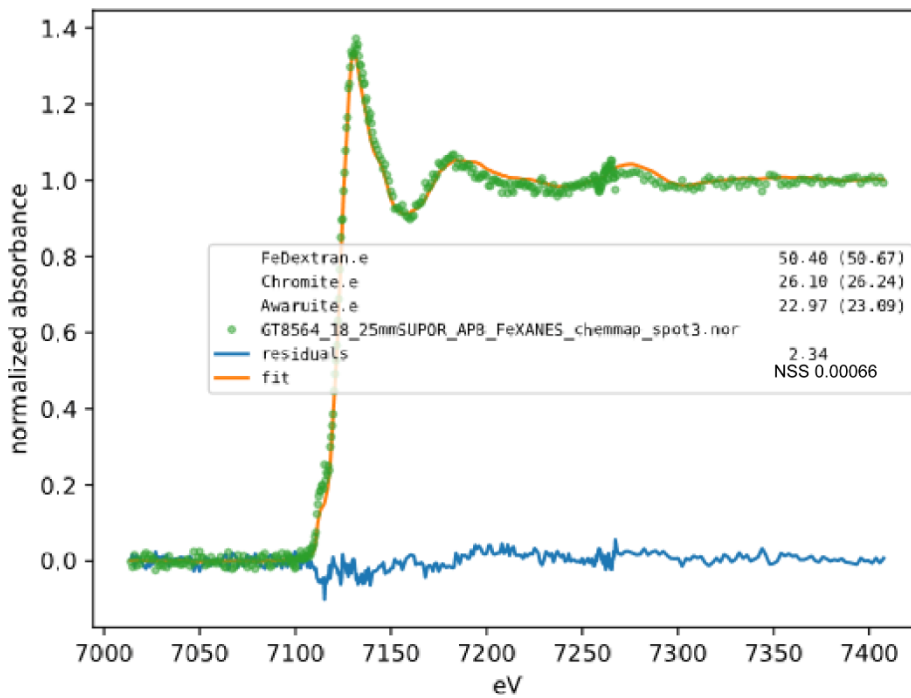


Figure 2.5.45 Fe XANES Station 18 above plume background spot 3

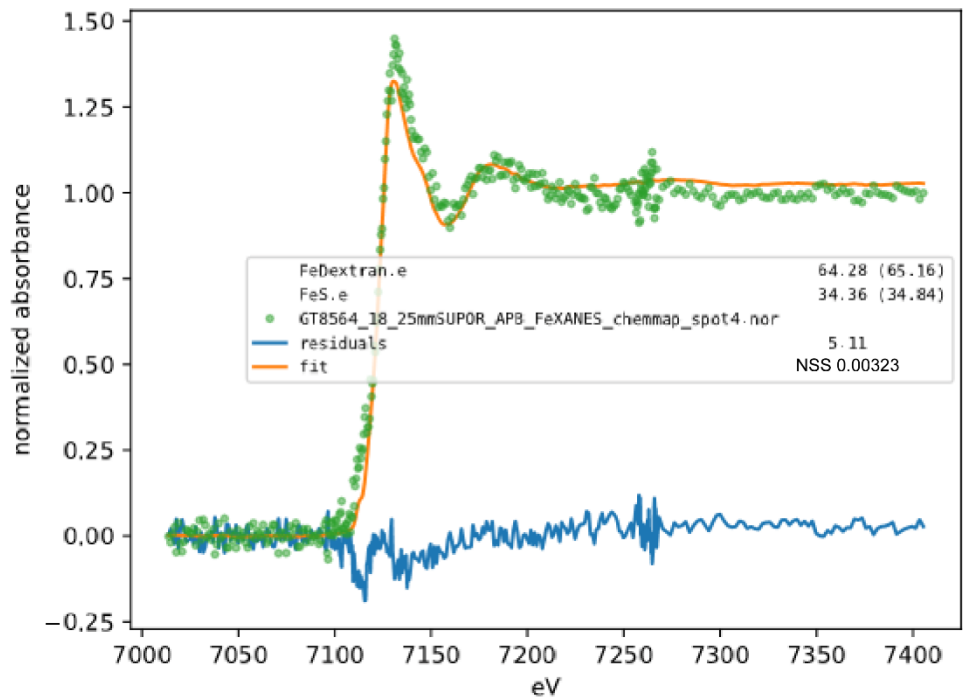


Figure 2.5.46 Fe XANES Station 18 above plume background spot 4

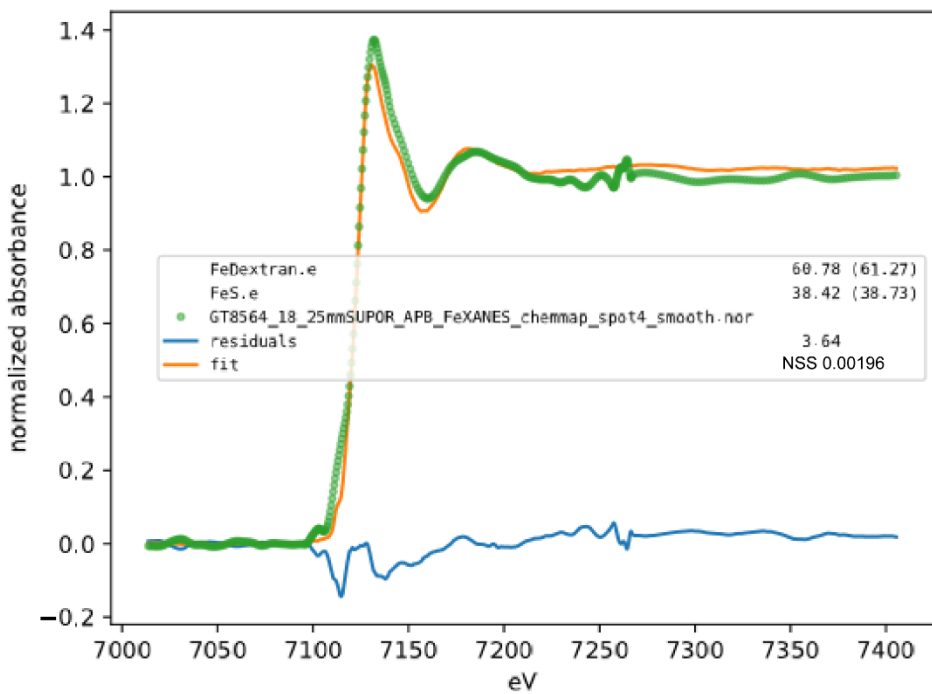


Figure 2.5.47 Fe XANES Station 18 above plume background spot 4

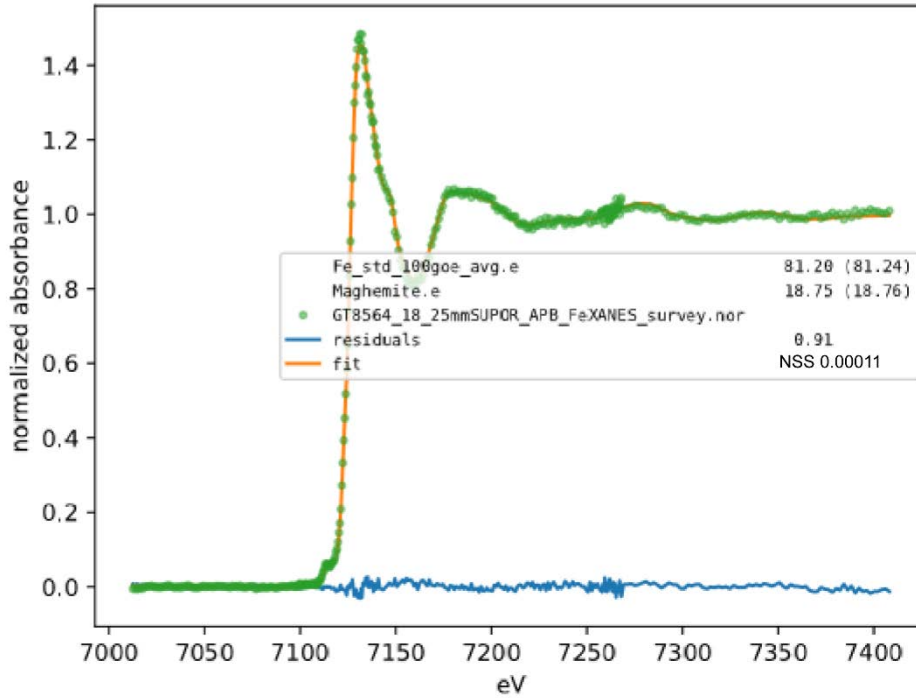


Figure 2.5.48 Fe XANES Station 18 above plume background

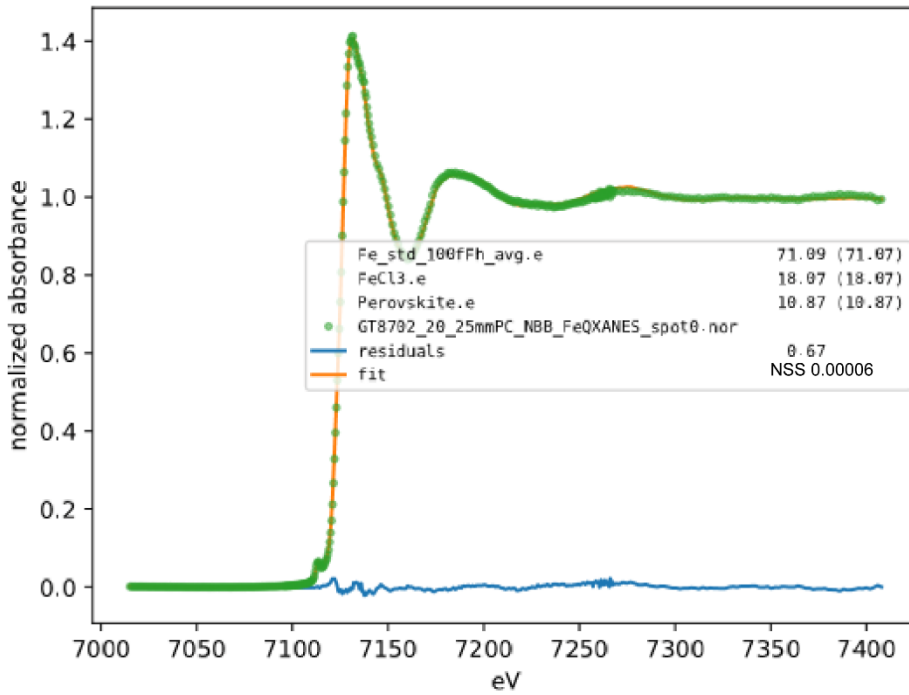


Figure 2.5.49 Fe XANES Station 20 near bottom background spot 0

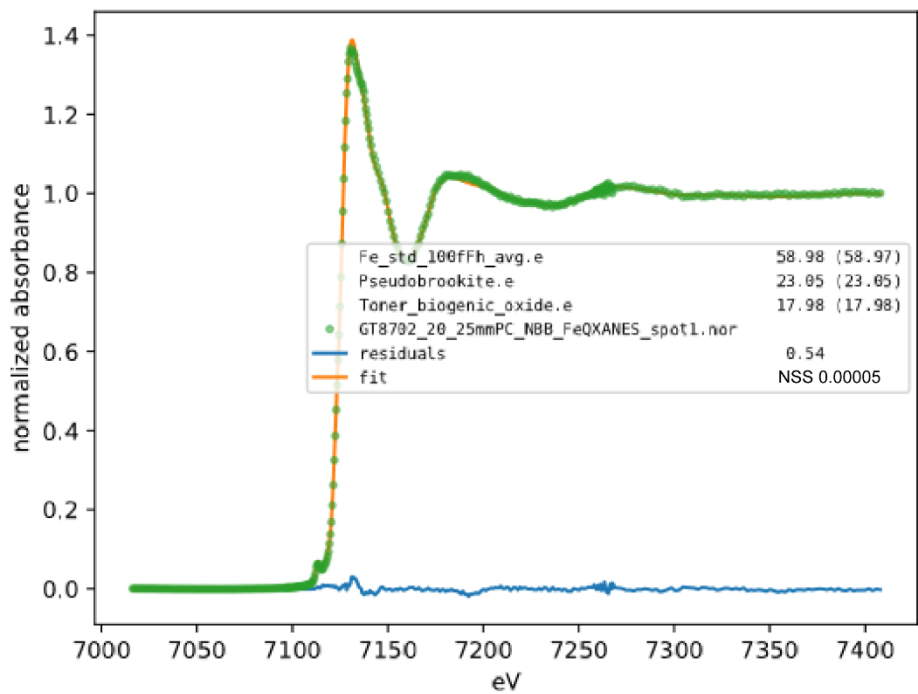


Figure 2.5.50 Fe XANES Station 20 near bottom background spot 1

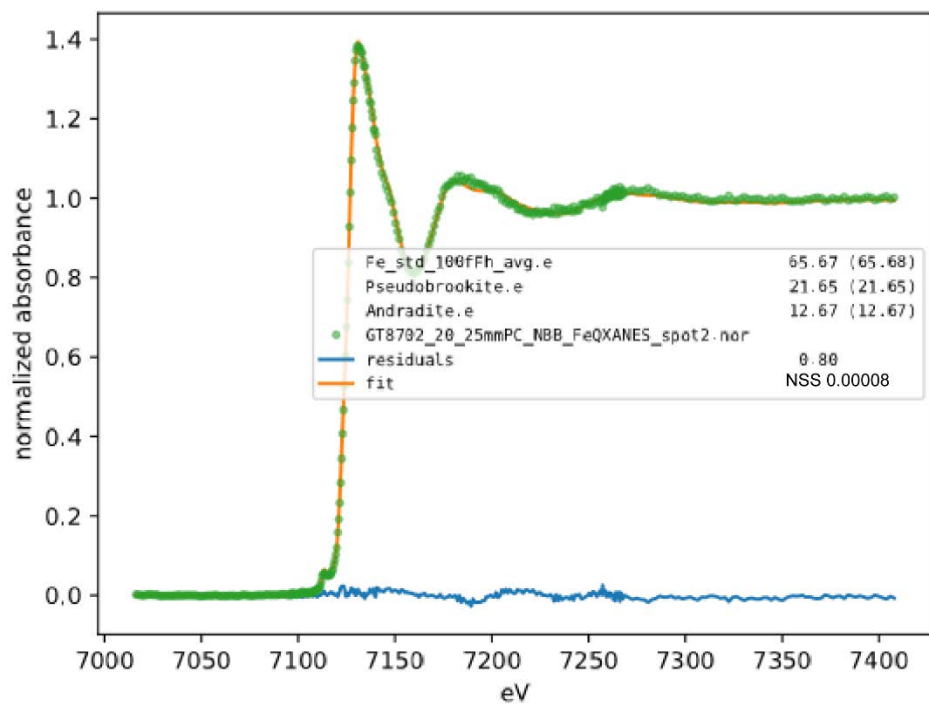


Figure 2.5.51 Fe XANES Station 20 near bottom background spot 2

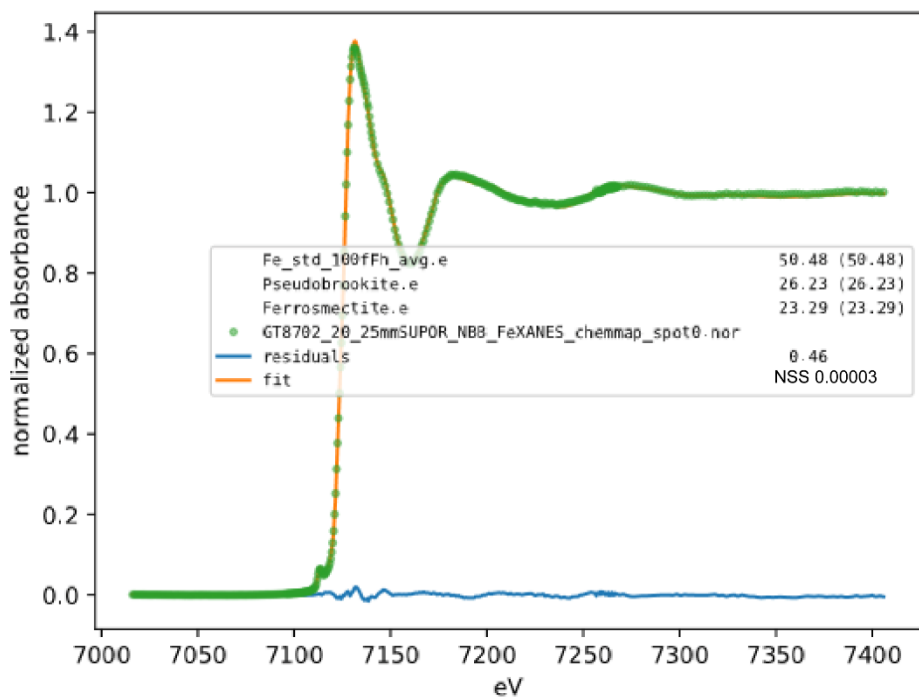


Figure 2.5.52 Fe XANES Station 20 near bottom background spot 0

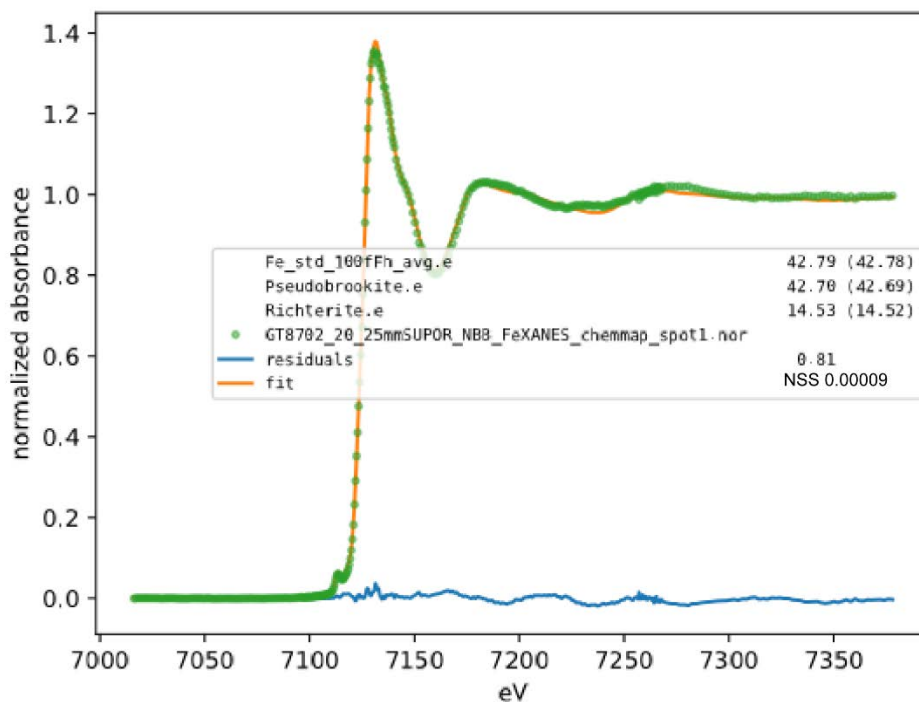


Figure 2.5.53 Fe XANES Station 20 near bottom background spot 1

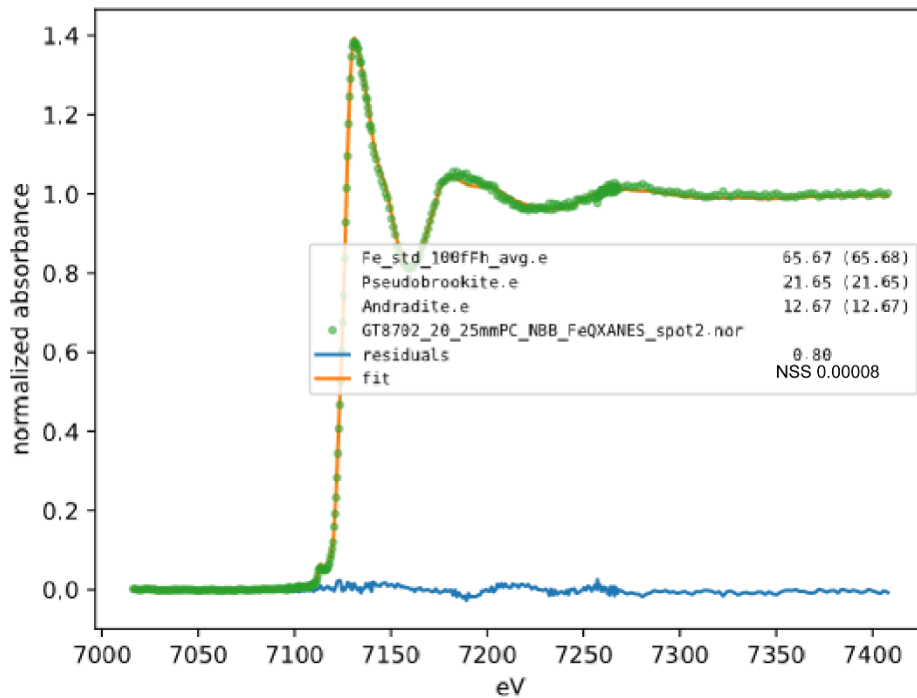


Figure 2.5.54 Fe XANES Site 20 near bottom background spot 2

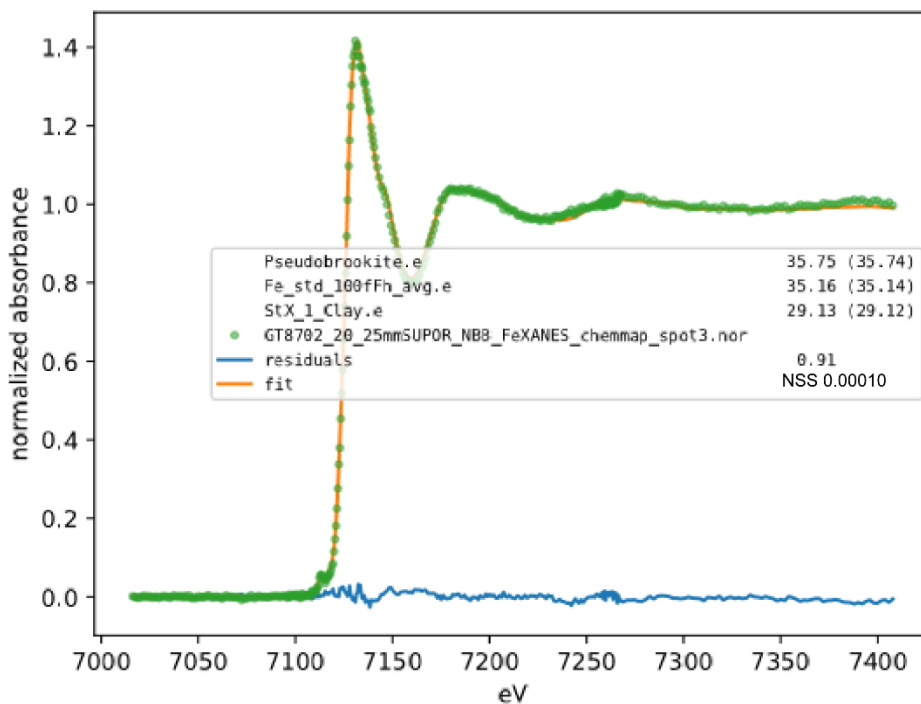


Figure 2.5.55 Fe XANES Site 20 near bottom background spot 3

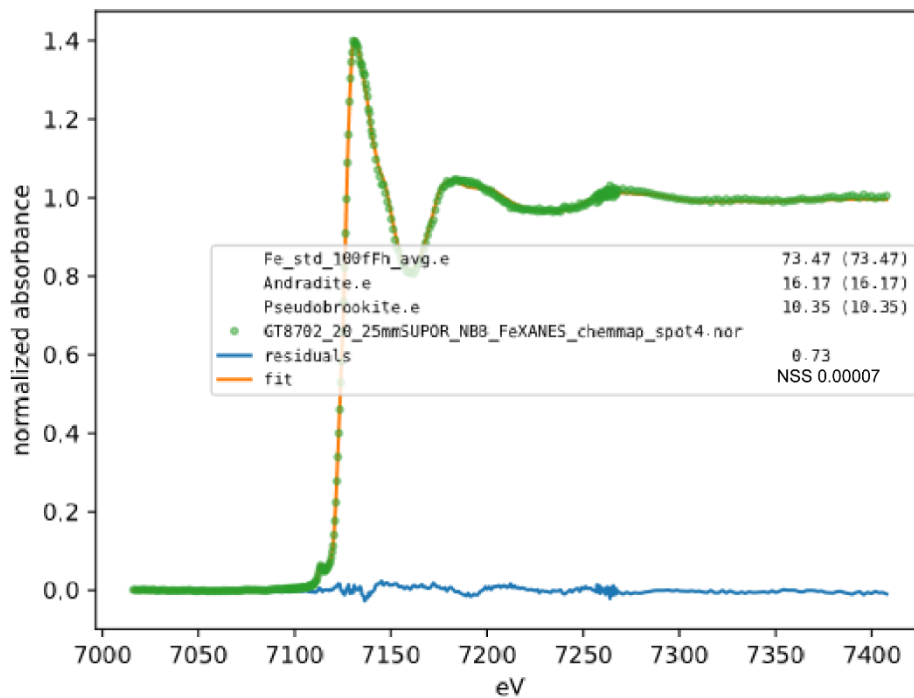


Figure 2.5.56 Fe XANES Site 20 near bottom background spot 4

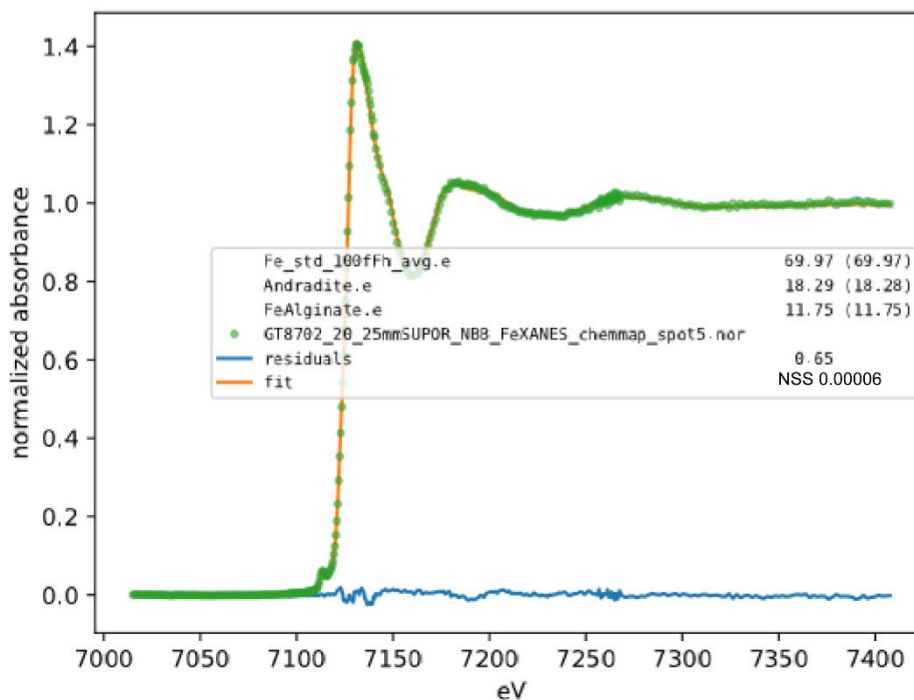


Figure 2.5.57 Fe XANES Station 20 near bottom background spot 5

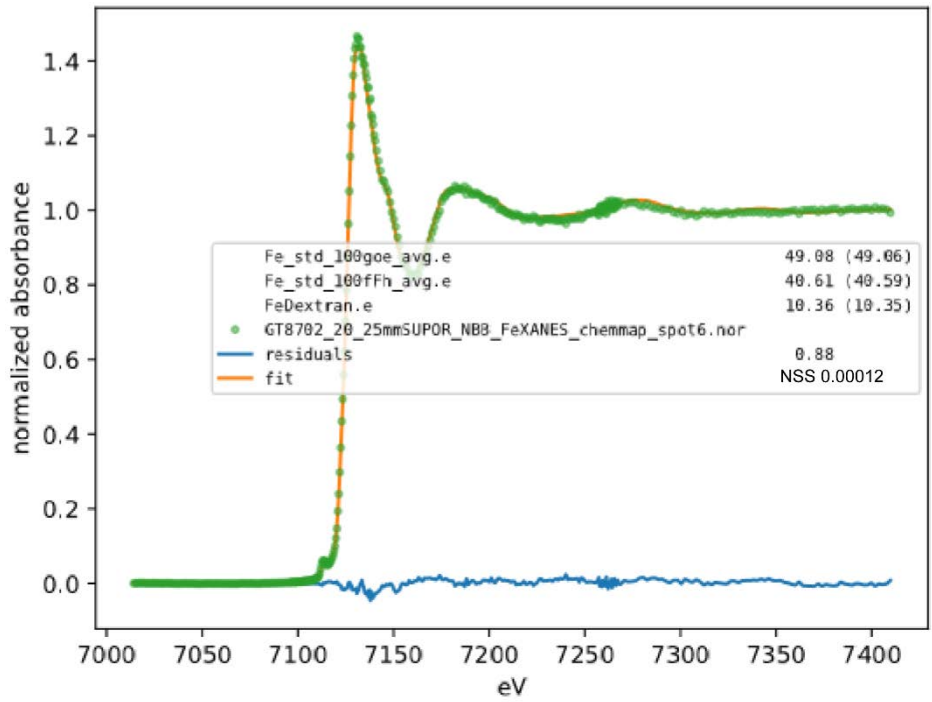


Figure 2.5.58 Fe XANES Station 20 near bottom background spot 6

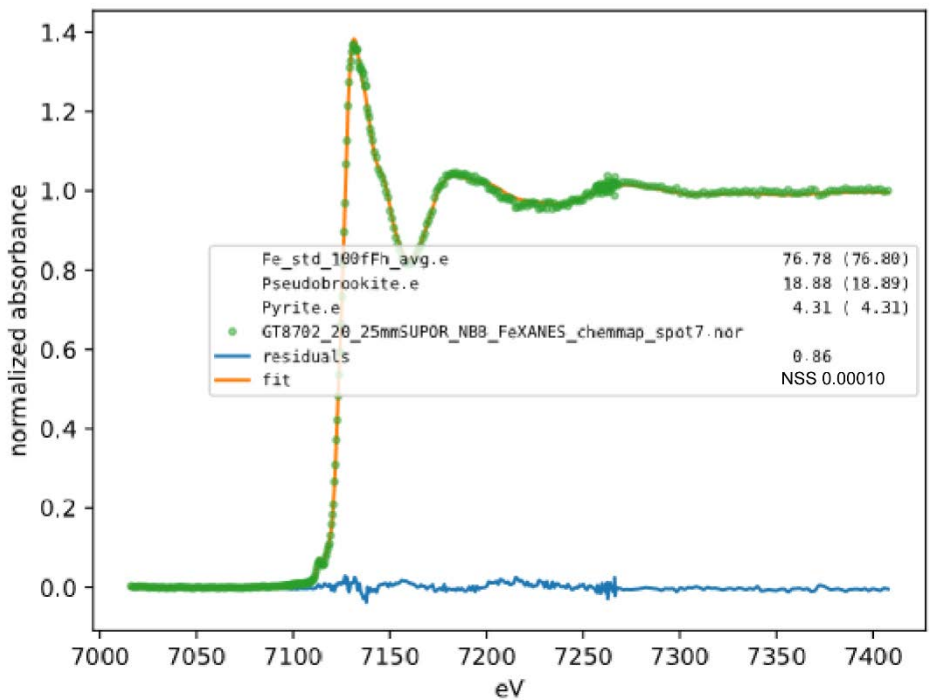


Figure 2.5.59 Fe XANES Station 20 near bottom background spot 7

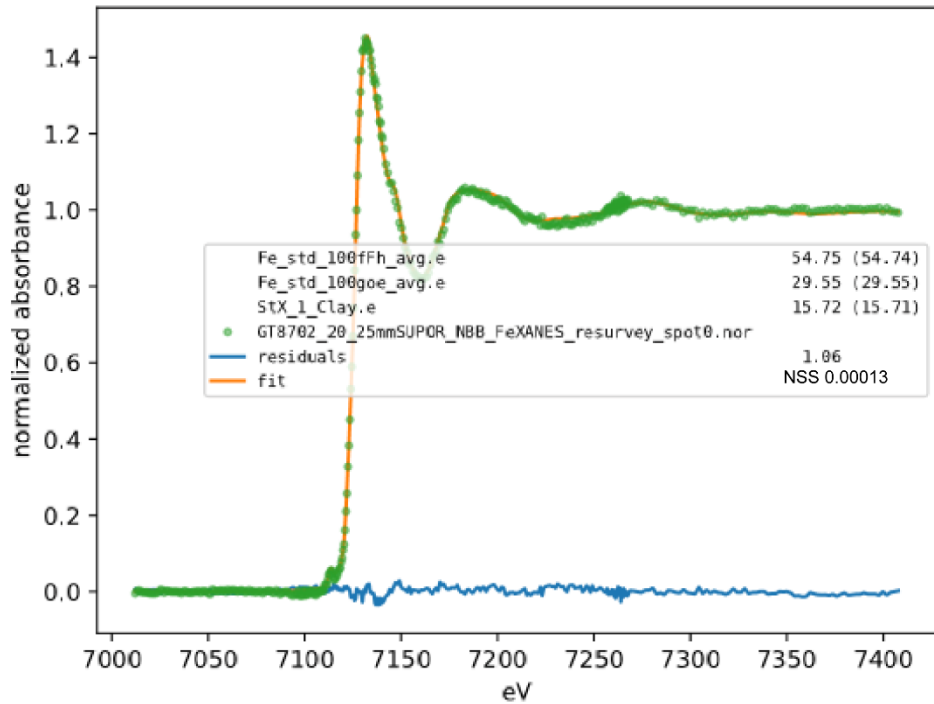


Figure 2.5.60 Fe XANES Station 20 near bottom background spot 0

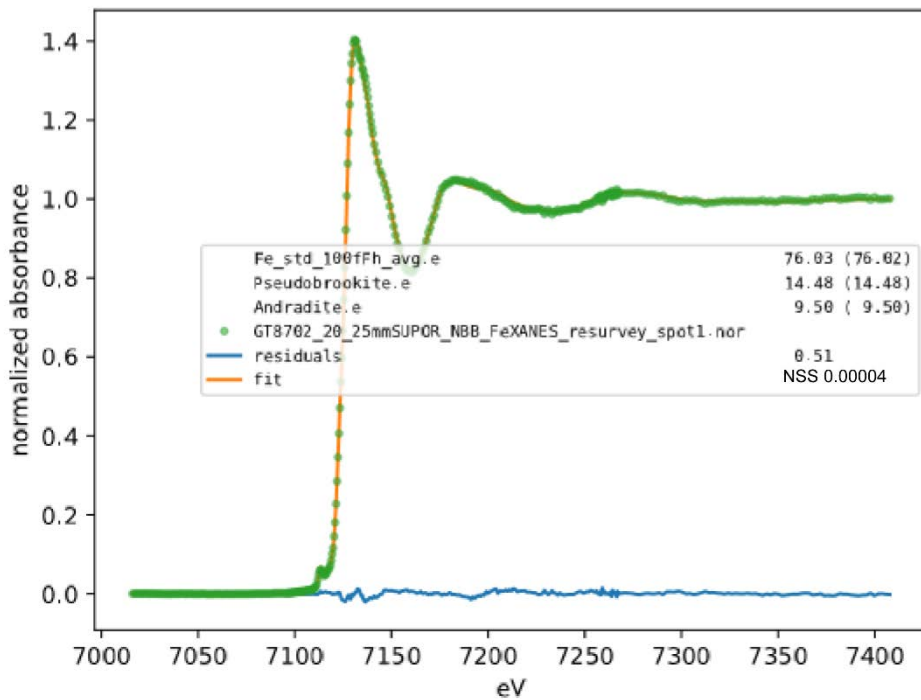


Figure 2.5.61 Fe XANES Station 20 near bottom background spot 1

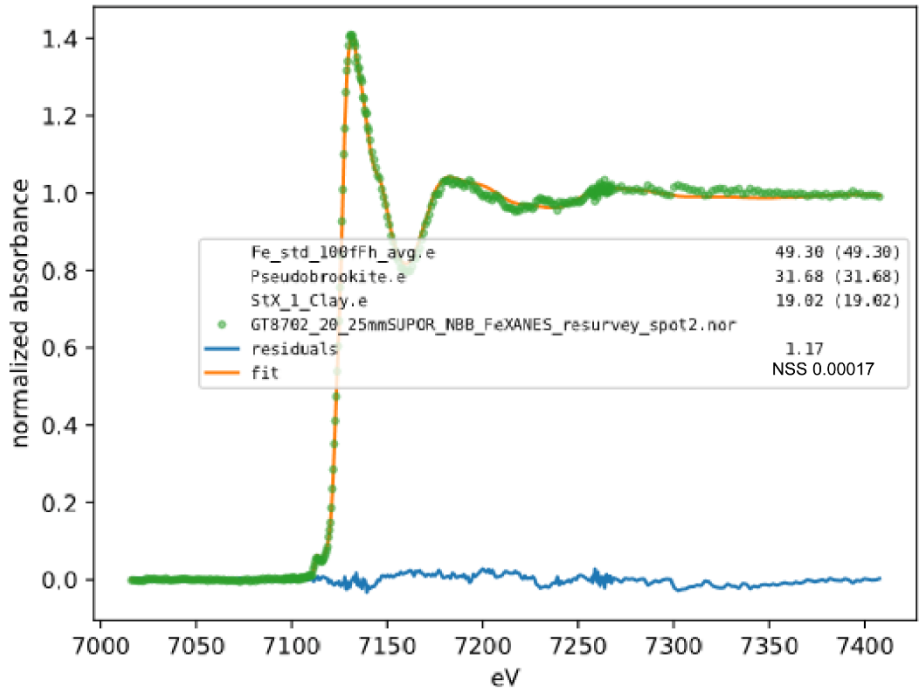


Figure 2.5.62 Fe XANES Station 20 near bottom background spot 2

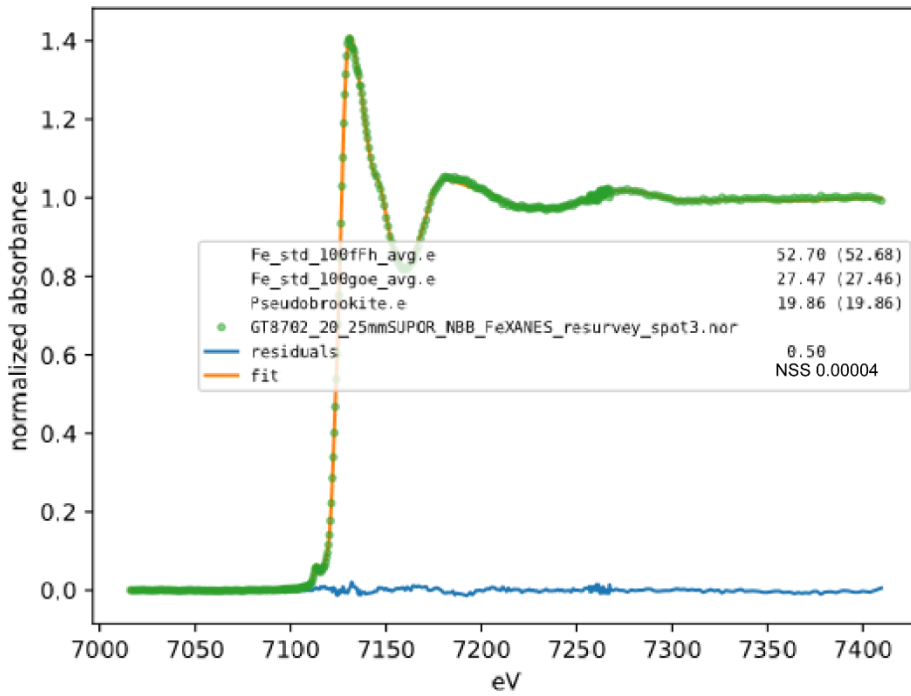


Figure 2.5.63 Fe XANES Station 20 near bottom background spot 3

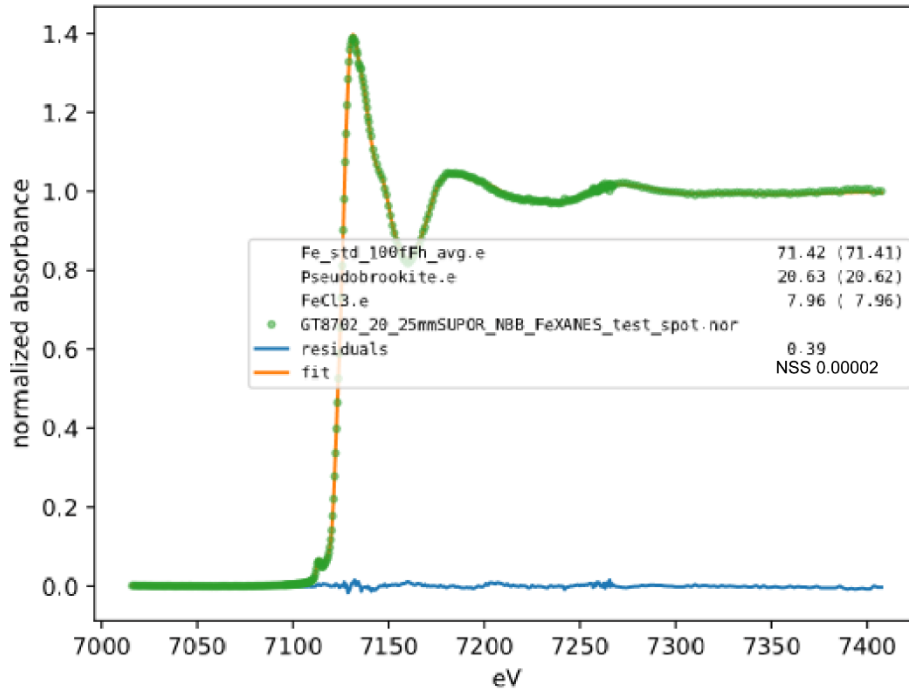


Figure 2.5.64 Fe XANES Station 20 near bottom background spot

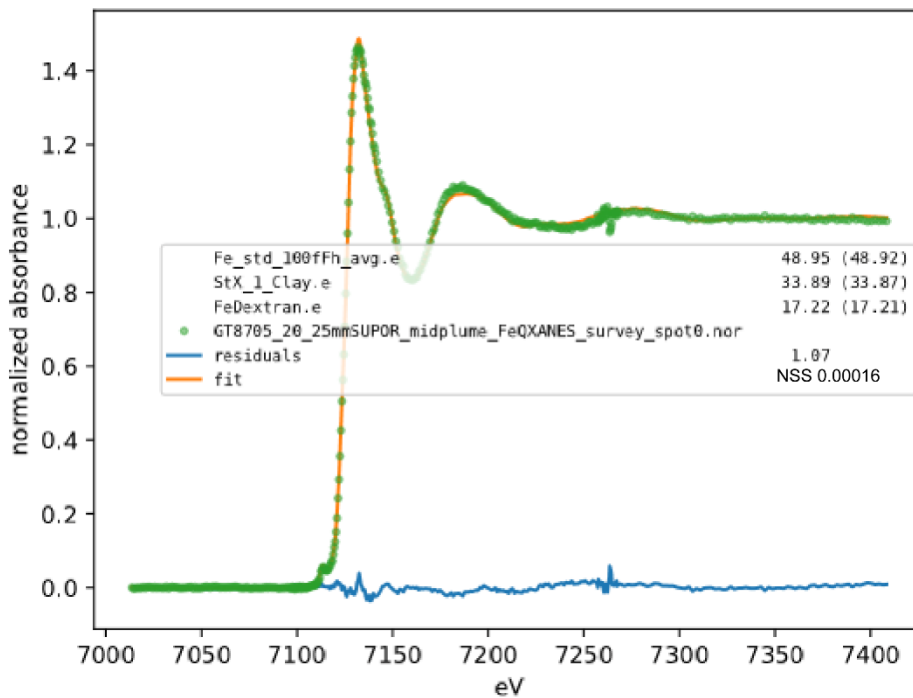


Figure 2.5.65 Fe XANES Station 20 midplume spot 0

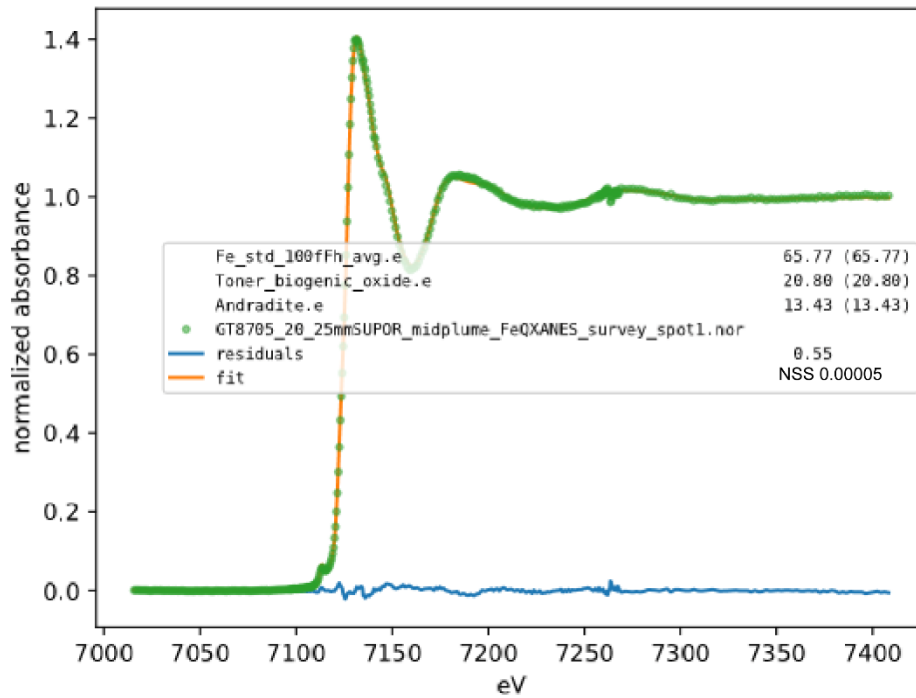


Figure 2.5.66 Fe XANES Station 20 midplume spot 1

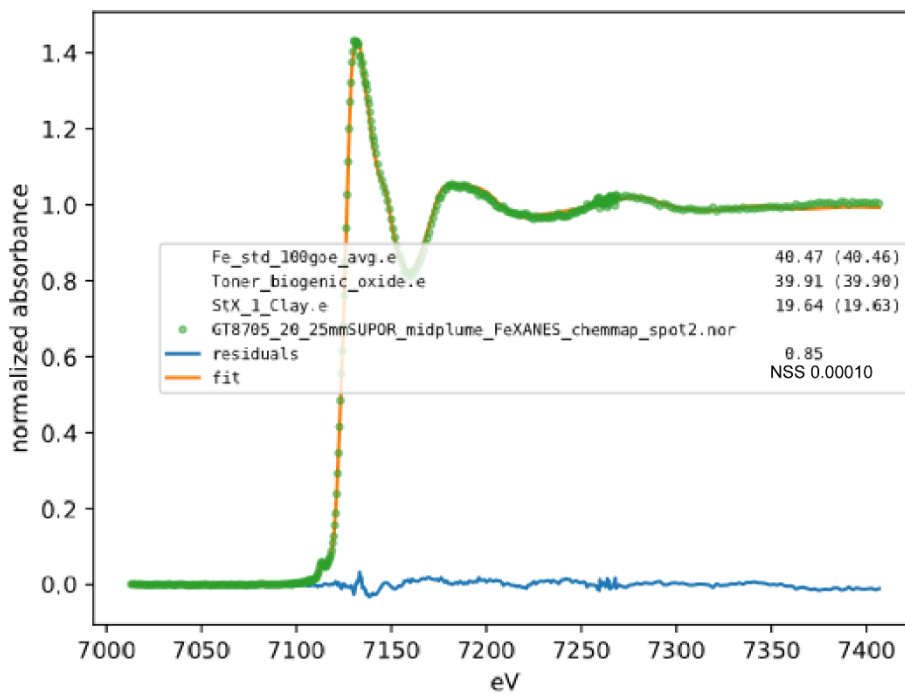


Figure 2.5.67 Fe XANES Station 20 midplume spot 2

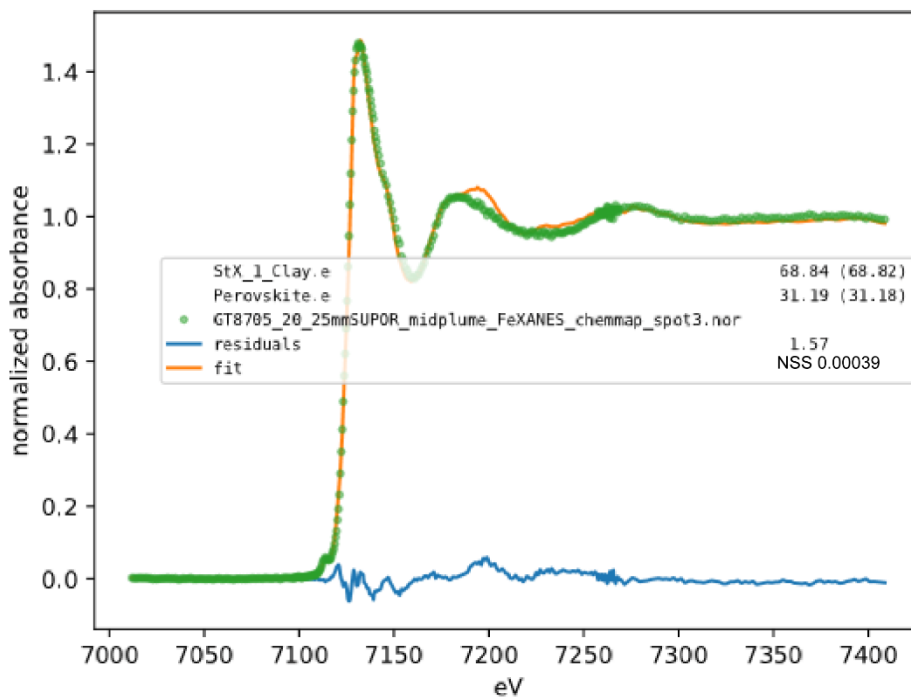


Figure 2.5.68 Fe XANES Station 20 midplume spot 3

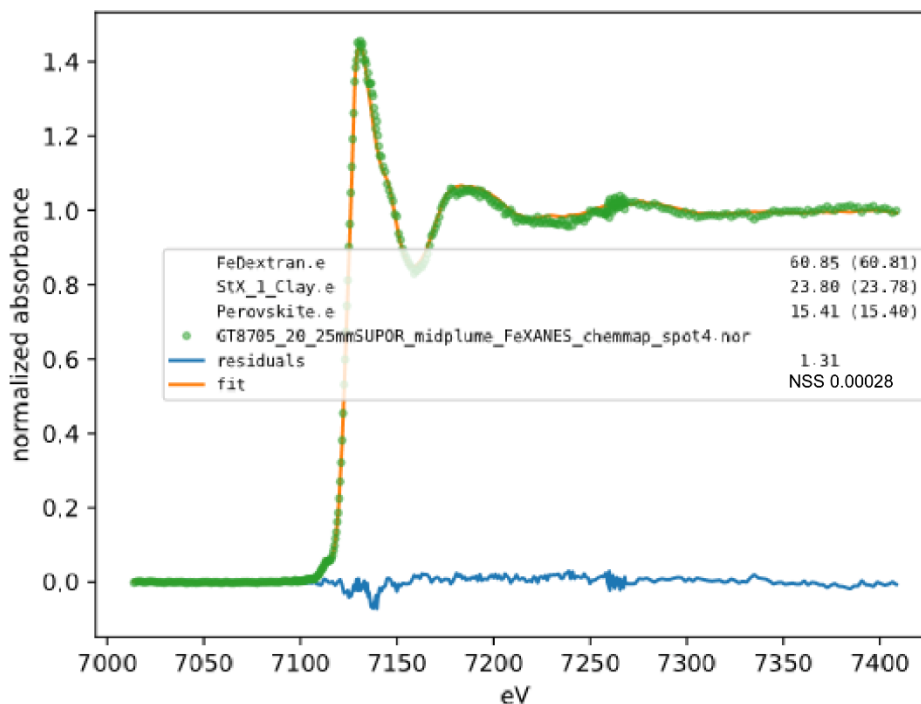


Figure 2.5.69 Fe XANES Station 20 midplume spot 4

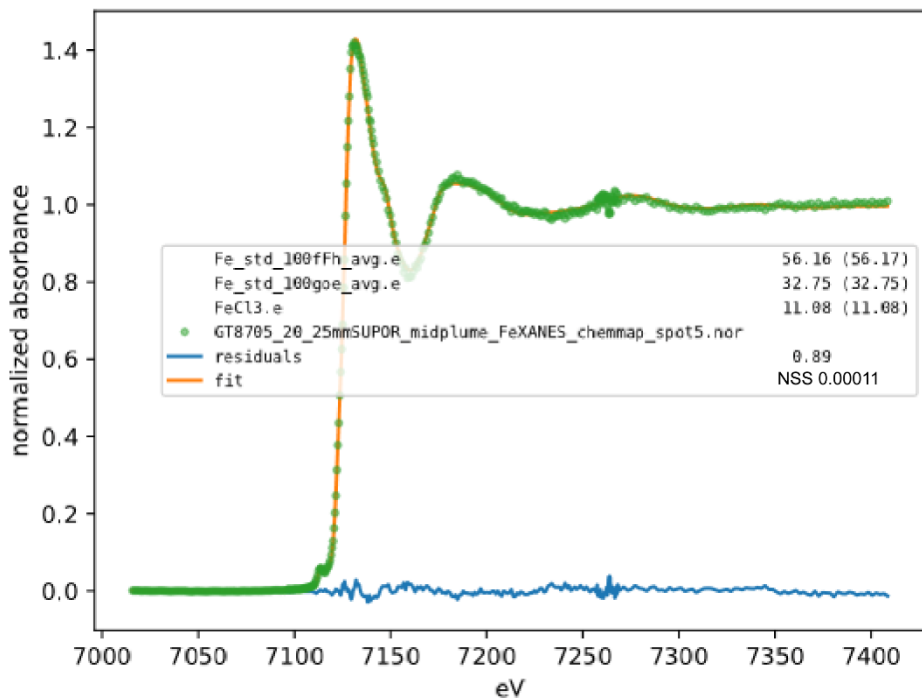


Figure 2.5.70 Fe XANES Station 20 midplume spot 5

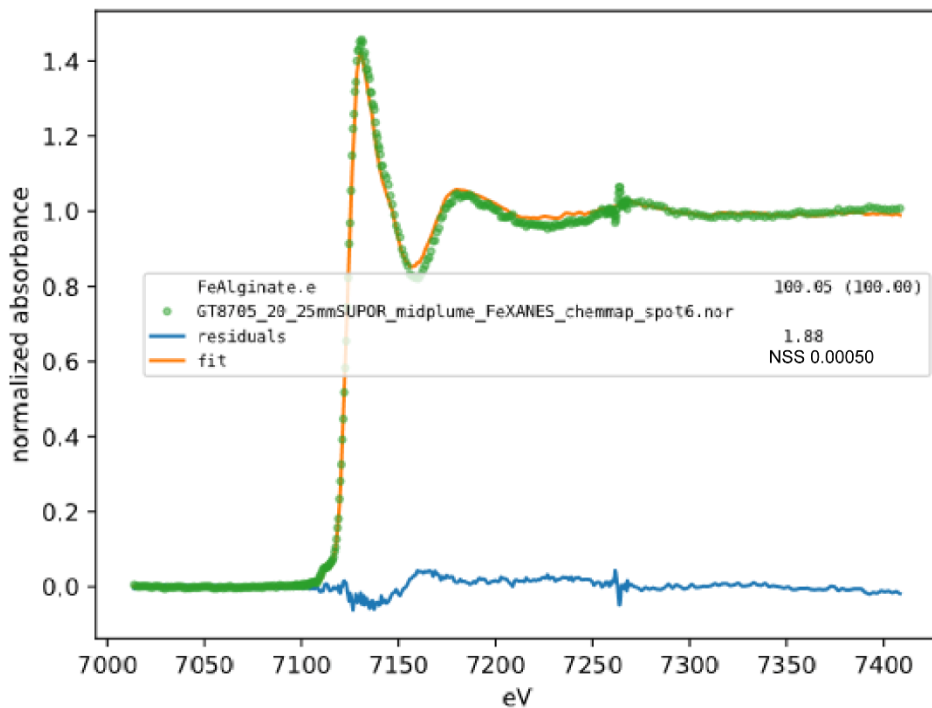


Figure 2.5.71 Fe XANES Station 20 midplume spot 6

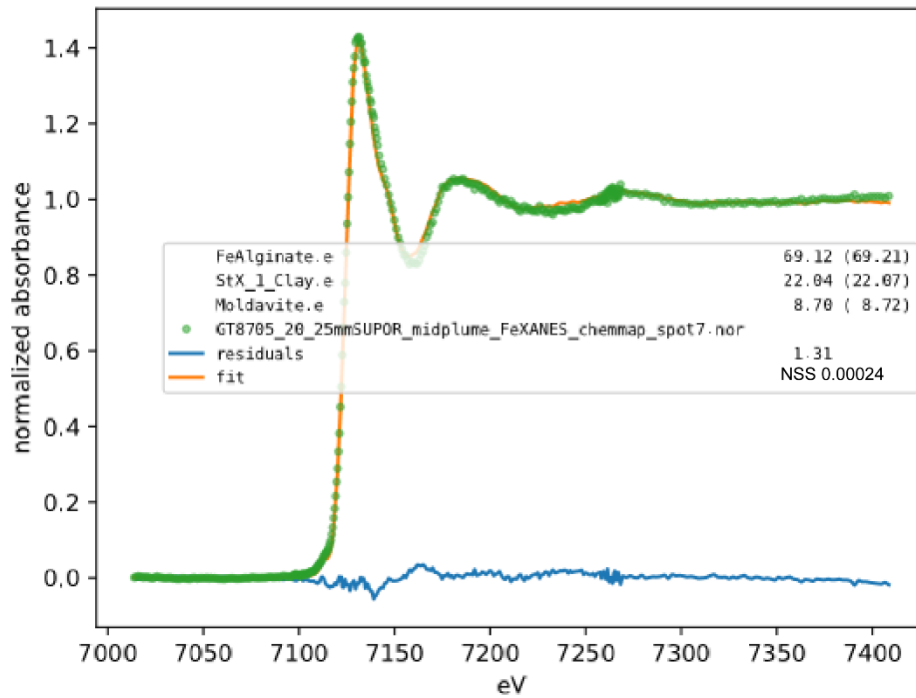


Figure 2.5.72 Fe XANES Station 20 midplume spot 7

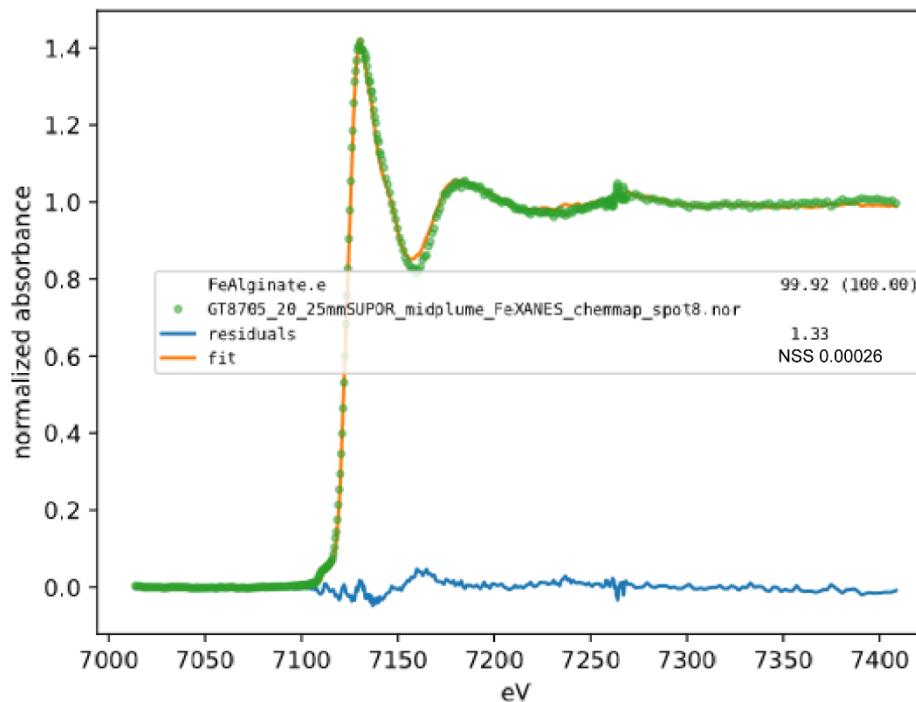


Figure 2.5.73 Fe XANES Station 20 midplume spot 8

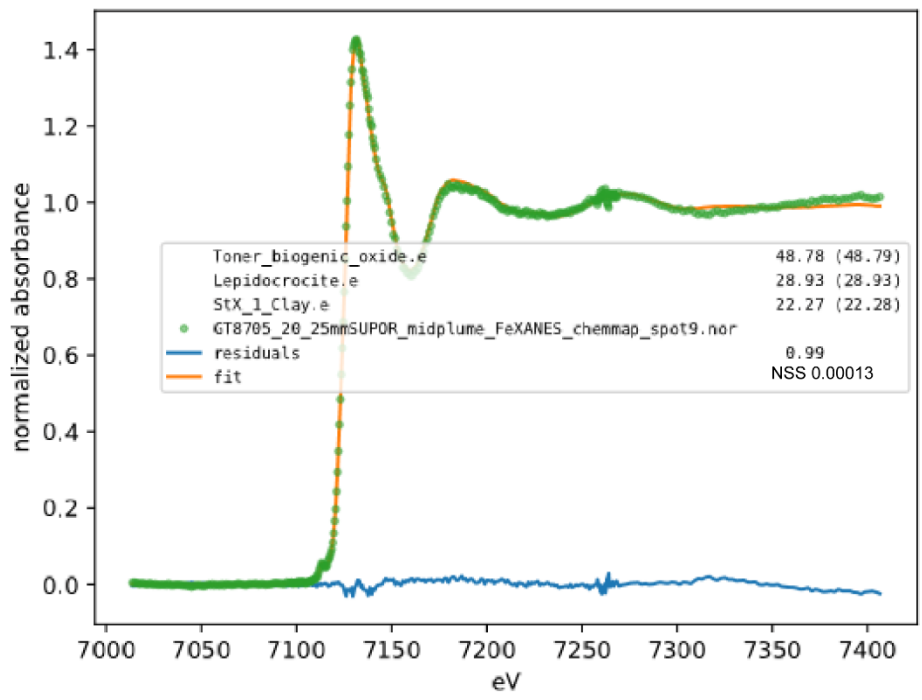


Figure 2.5.74 Fe XANES Station 20 midplume spot 9

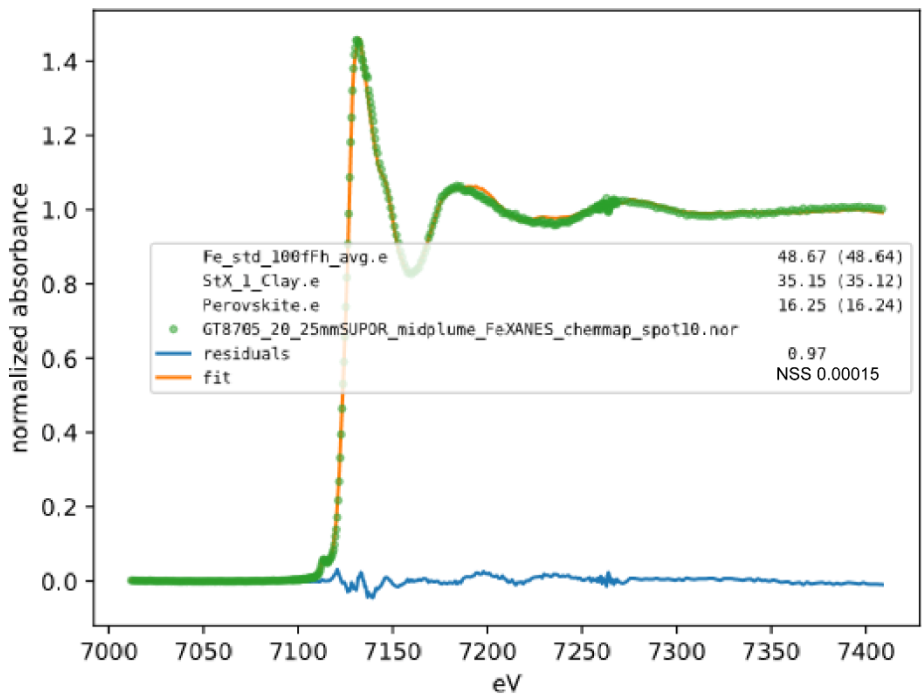


Figure 2.5.75 Fe XANES Station 20 midplume spot 10

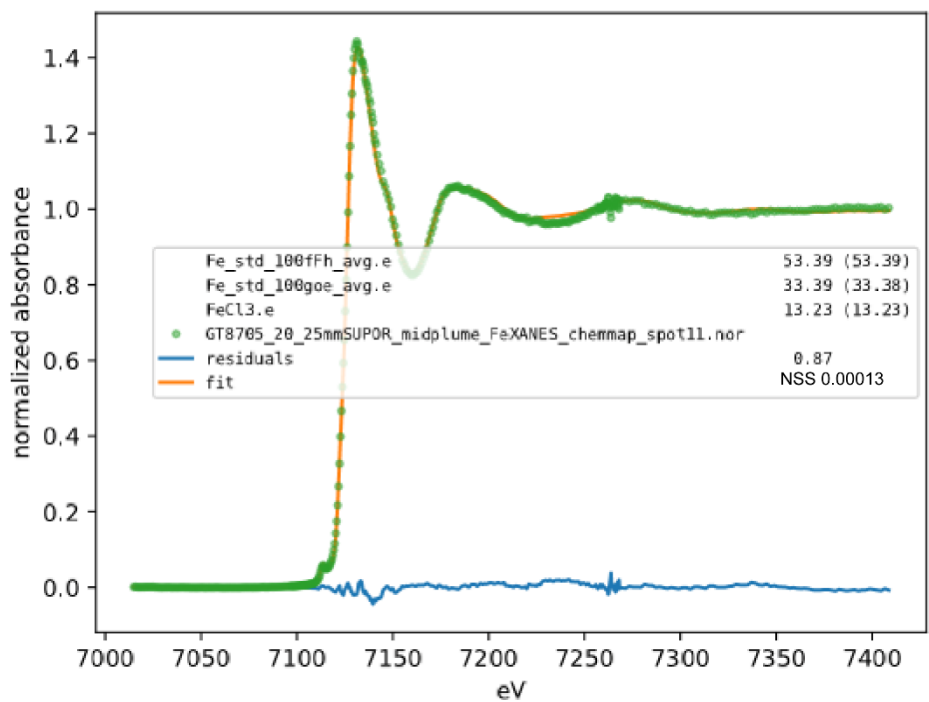


Figure 2.5.76 Fe XANES Station 20 midplume spot 11

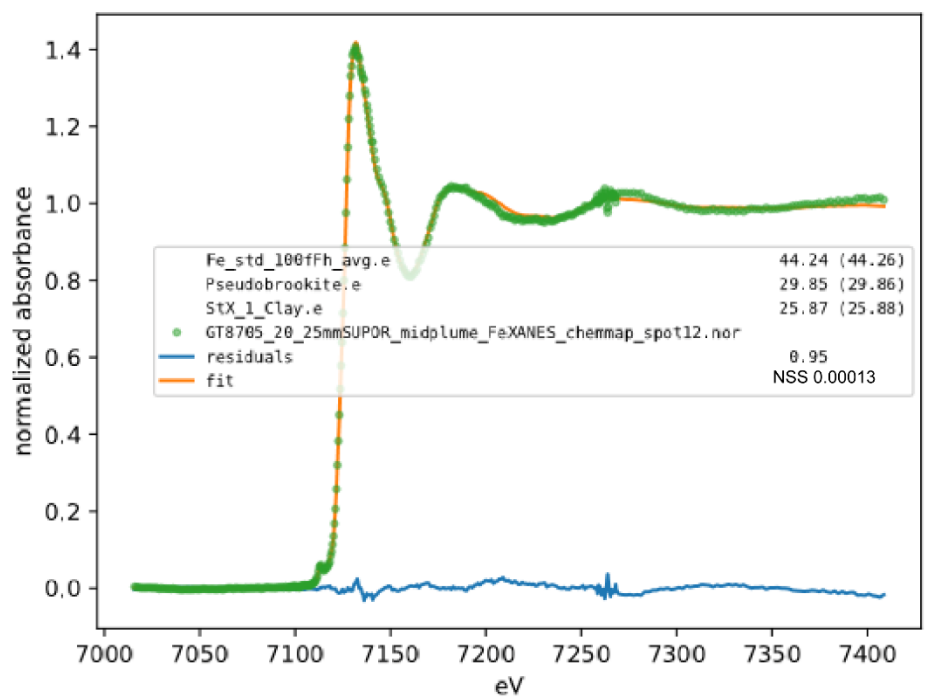


Figure 2.5.77 Fe XANES Station 20 midplume spot 12

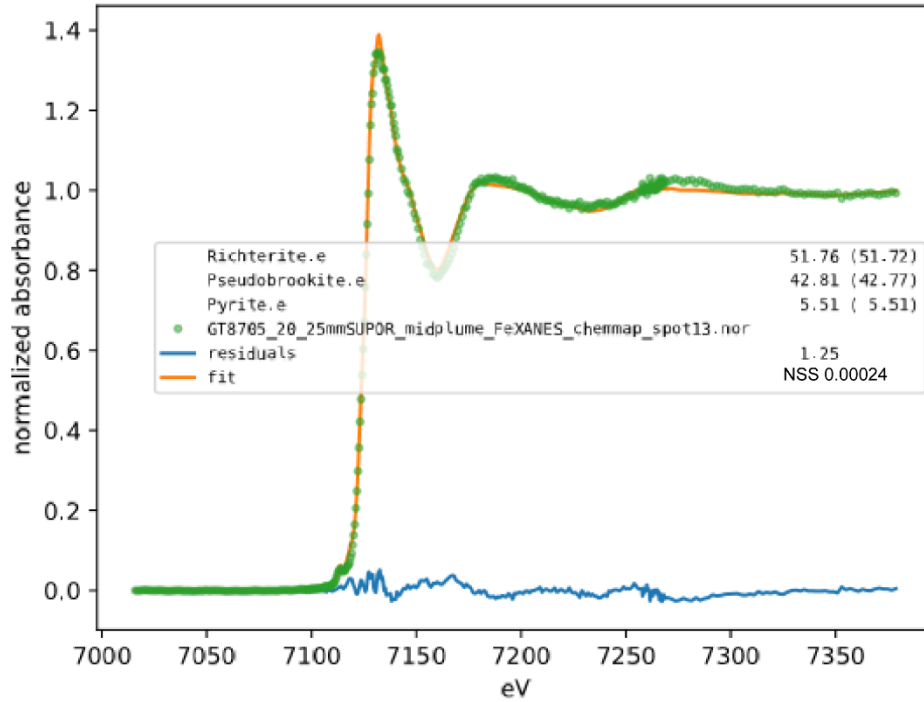


Figure 2.5.78 Fe XANES Station 20 midplume spot 13

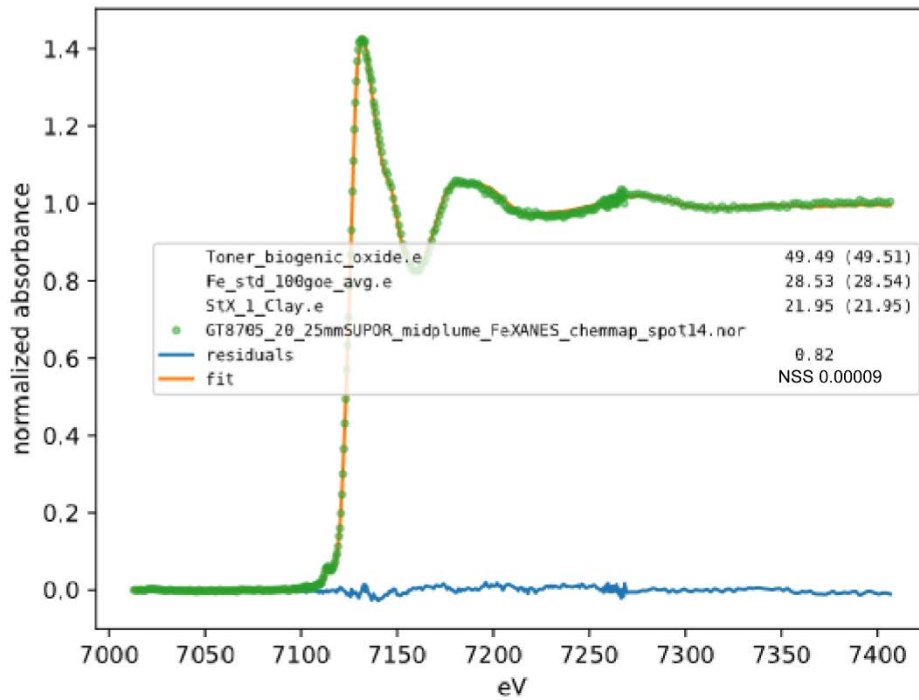


Figure 2.5.79 Fe XANES Station 20 midplume spot 14

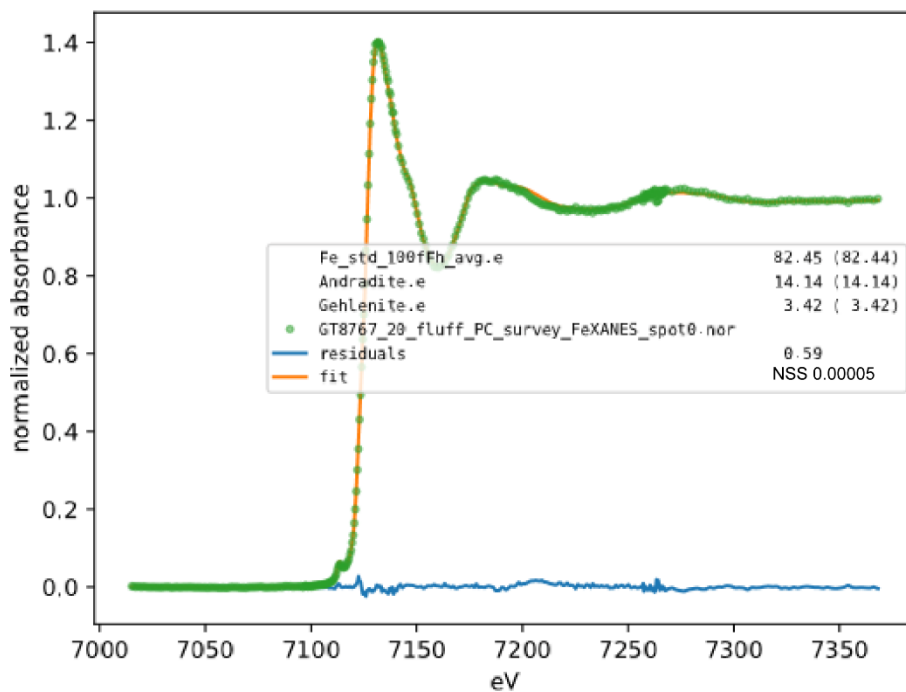


Figure 2.5.80 Fe XANES Station 20 spot 0

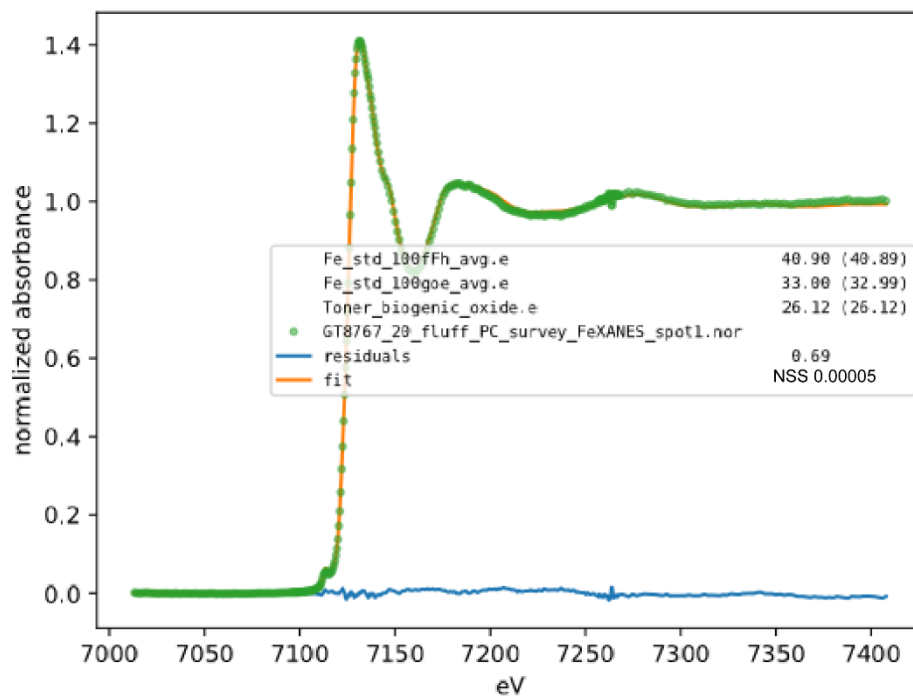


Figure 2.5.81 Fe XANES Station 20 spot 1

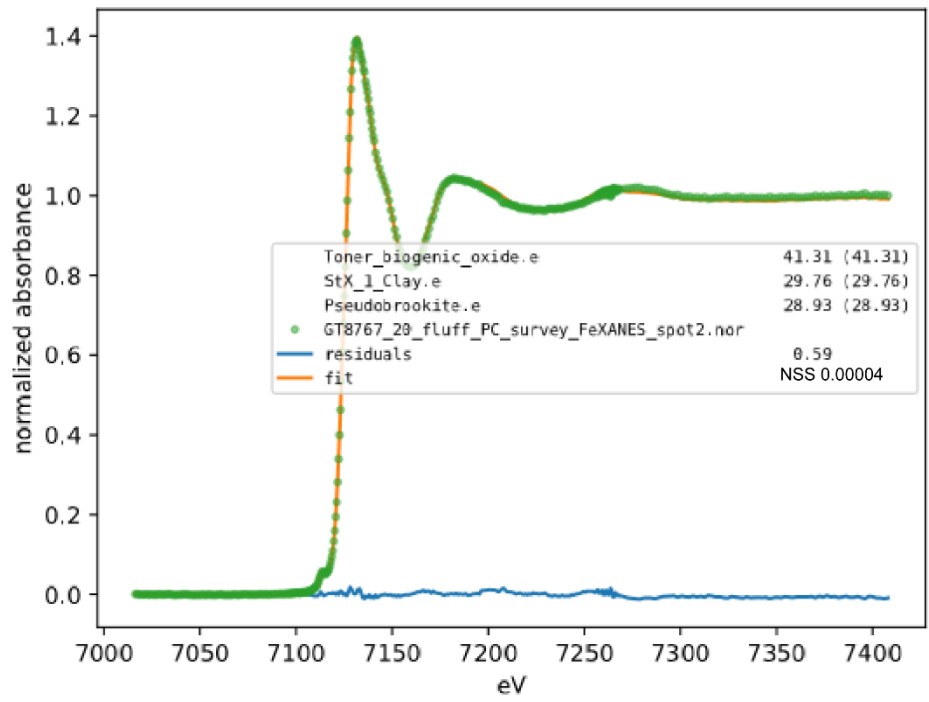


Figure 2.5.82 Fe XANES Station 20 spot 2

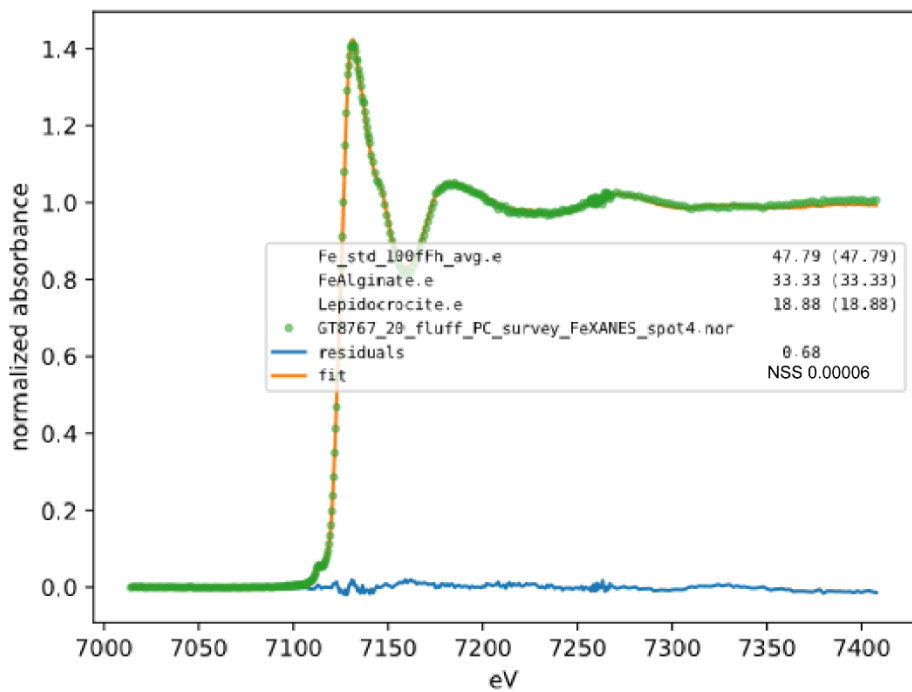


Figure 2.5.83 Fe XANES Station 20 spot 4

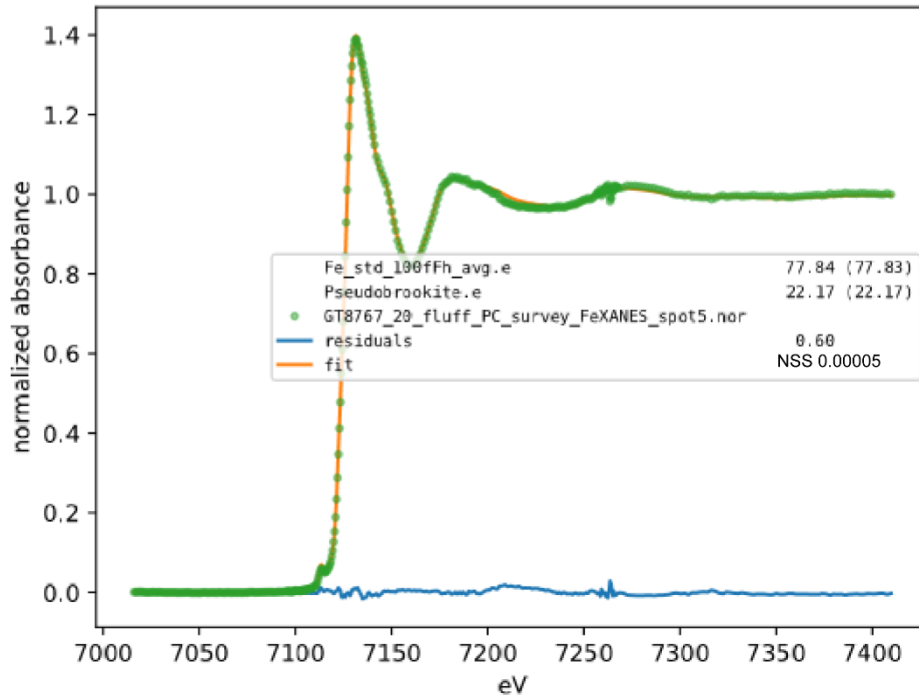


Figure 2.5.84 Fe XANES Station 20 spot 5

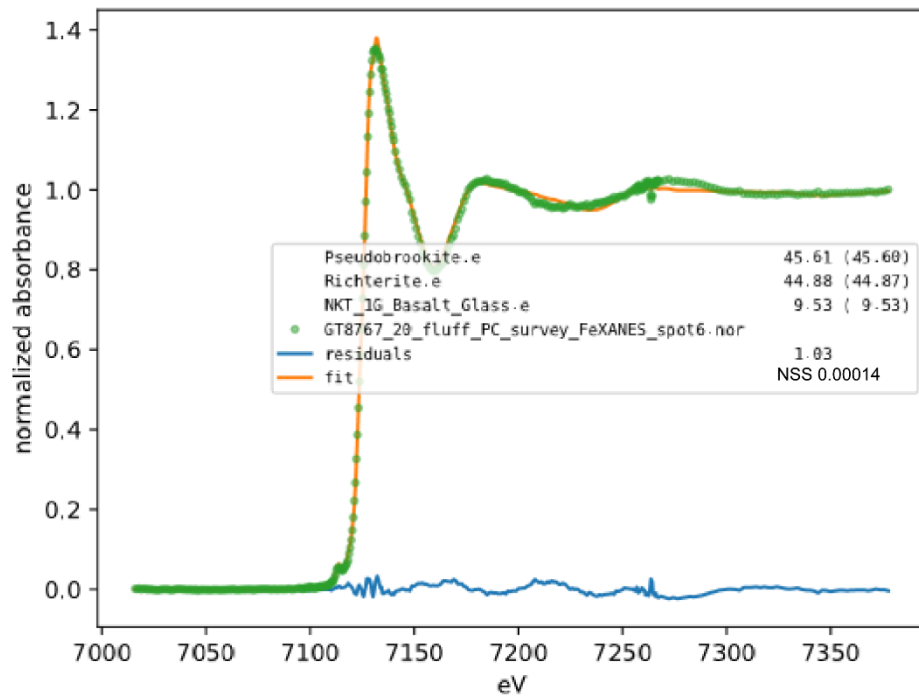


Figure 2.5.85 Fe XANES Station 20 spot 6

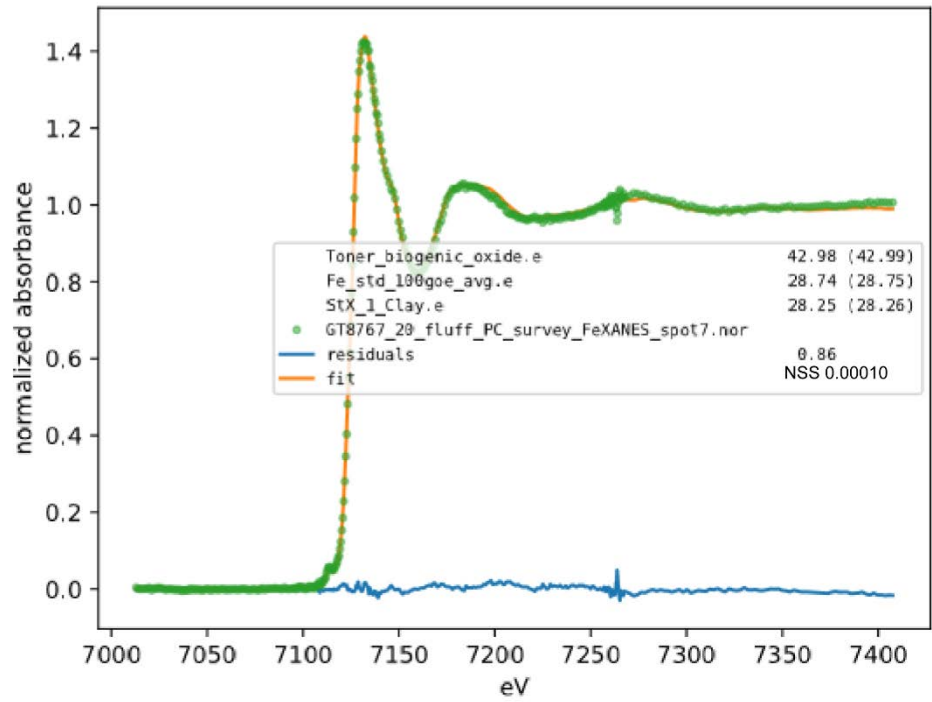


Figure 2.5.86 Fe XANES Station 20 spot 7

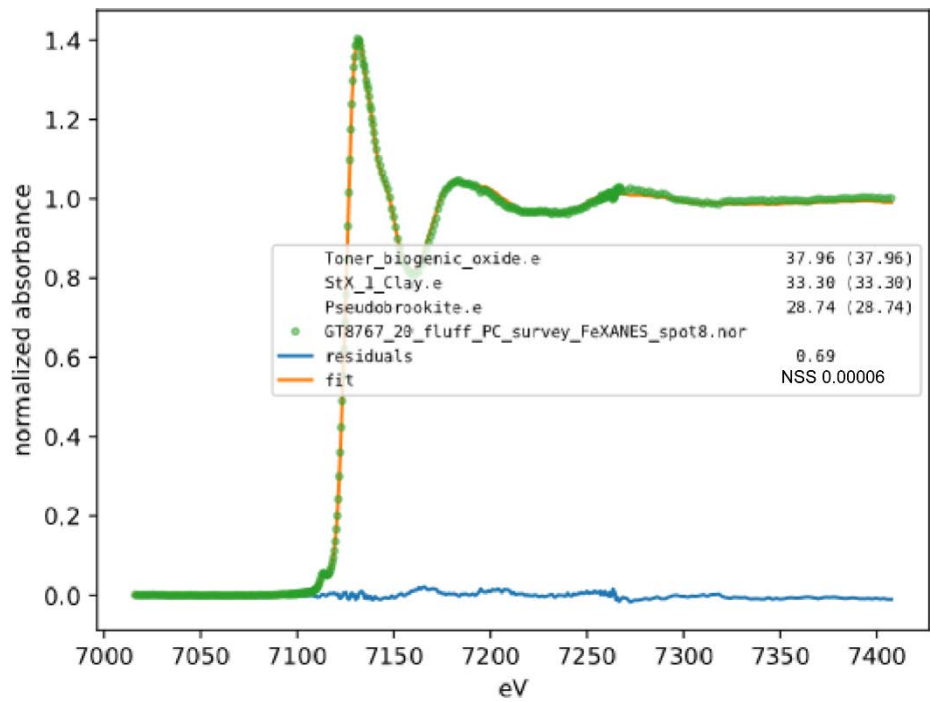


Figure 2.5.87 Fe XANES Station 20 spot 8

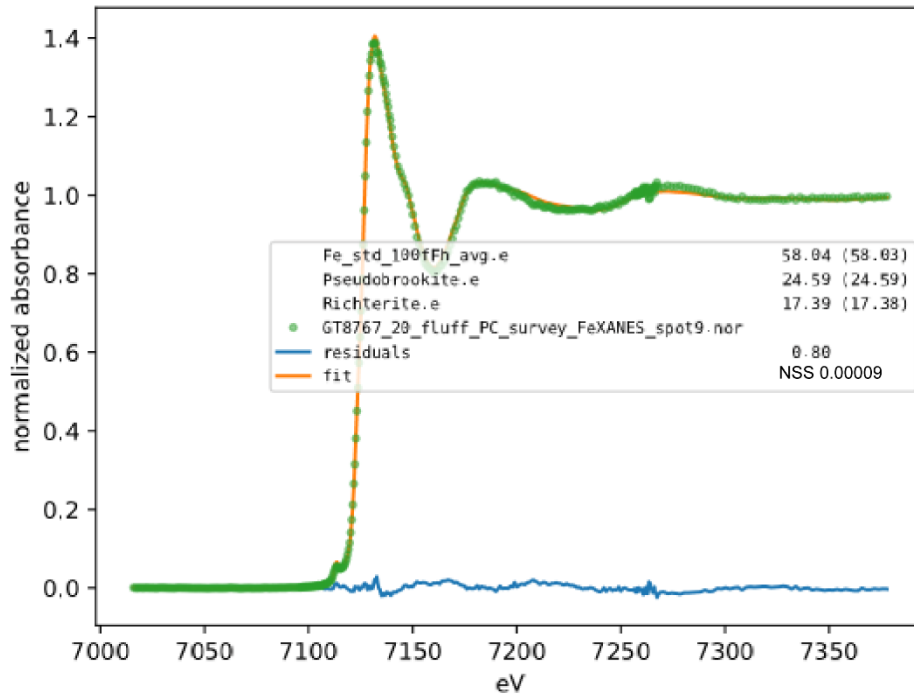


Figure 2.5.88 Fe XANES Station 20 spot 9

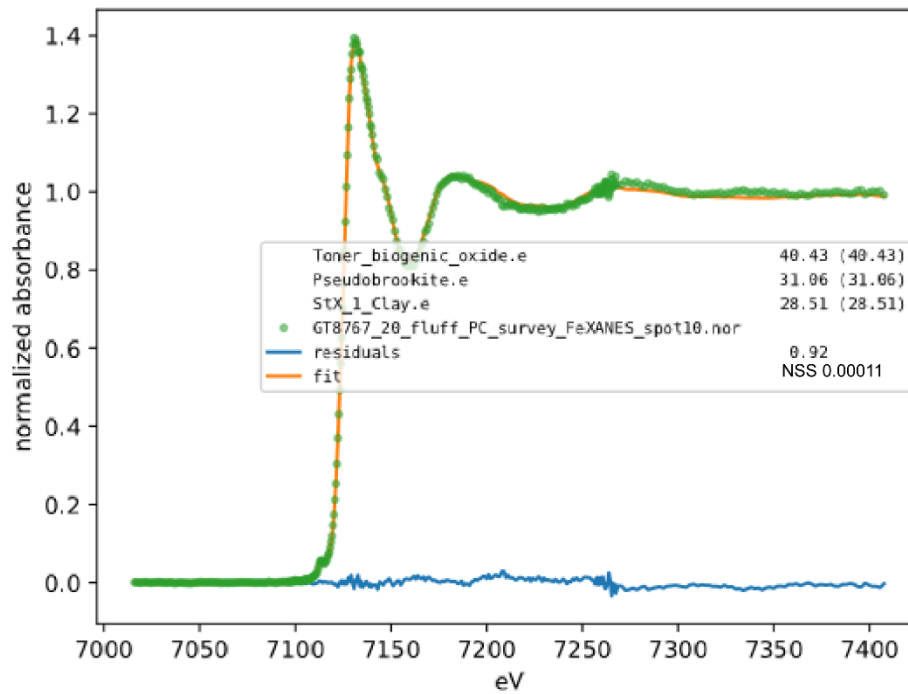


Figure 2.5.89 Fe XANES Station 20 spot 10

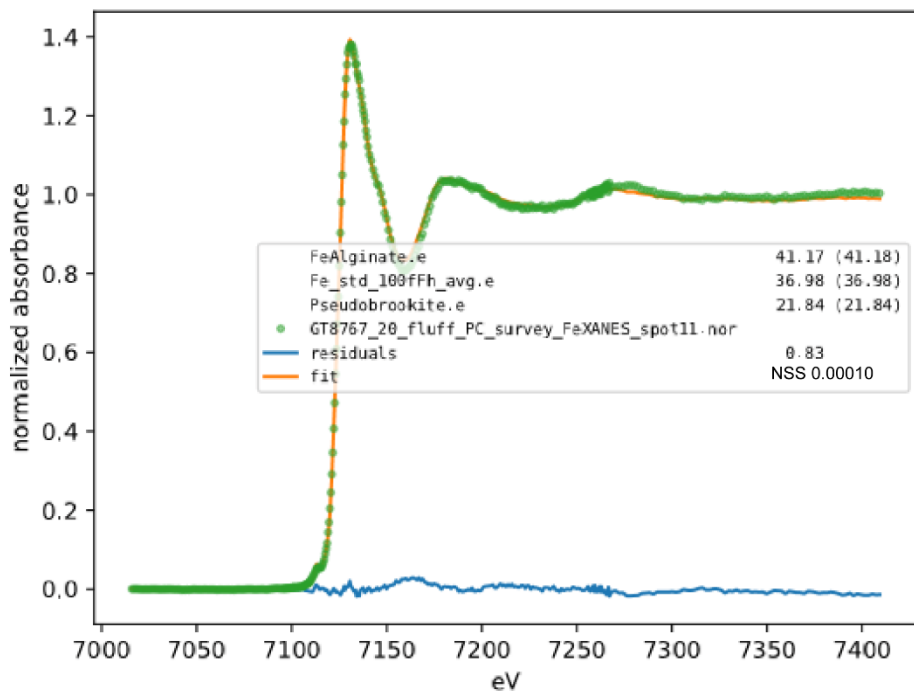


Figure 2.5.90 Fe XANES Station 20 spot 11

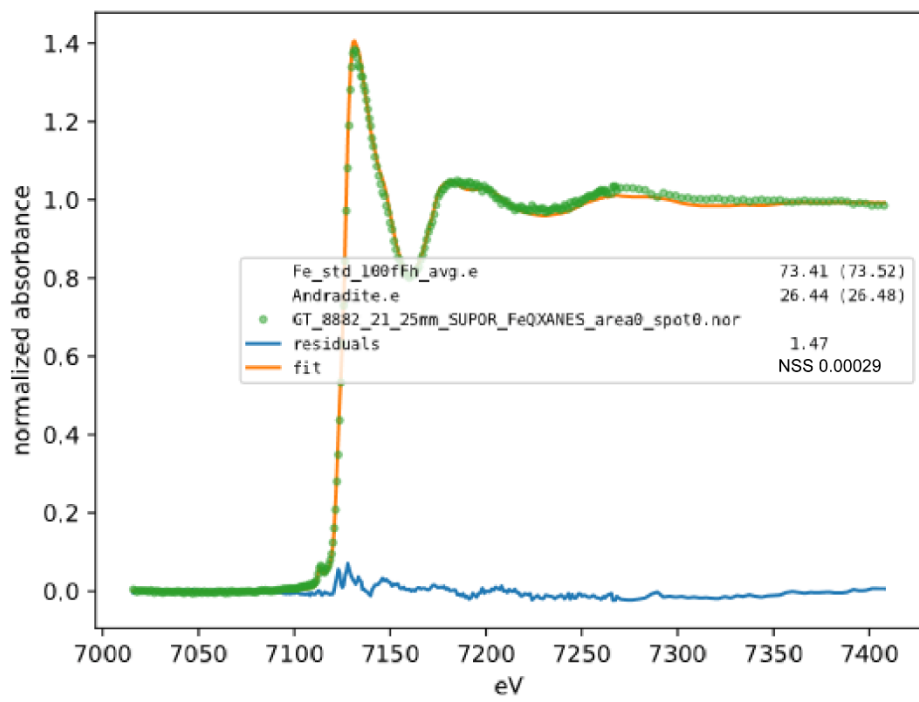


Figure 2.5.91 Fe XANES Station 21 area 0 spot 0

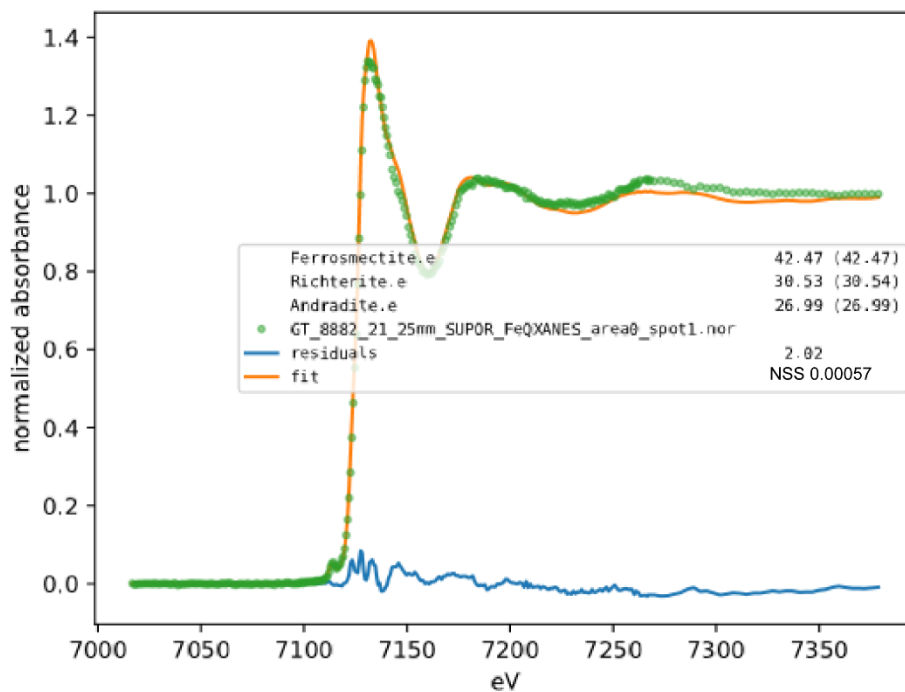


Figure 2.5.92 Fe XANES Station 21 area 0 spot 1

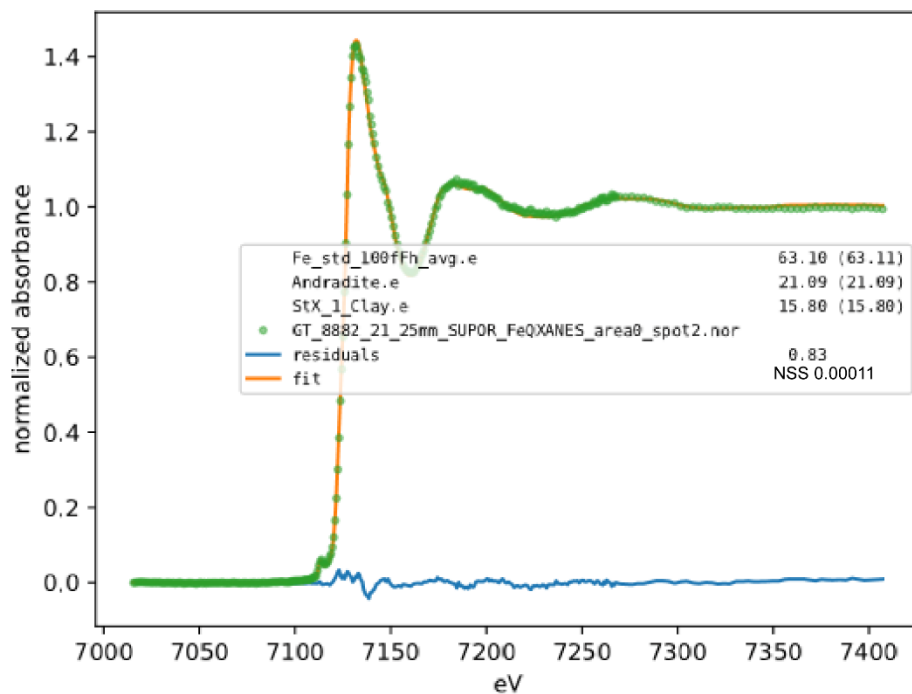


Figure 2.5.93 Fe XANES Station 21 area 0 spot 2

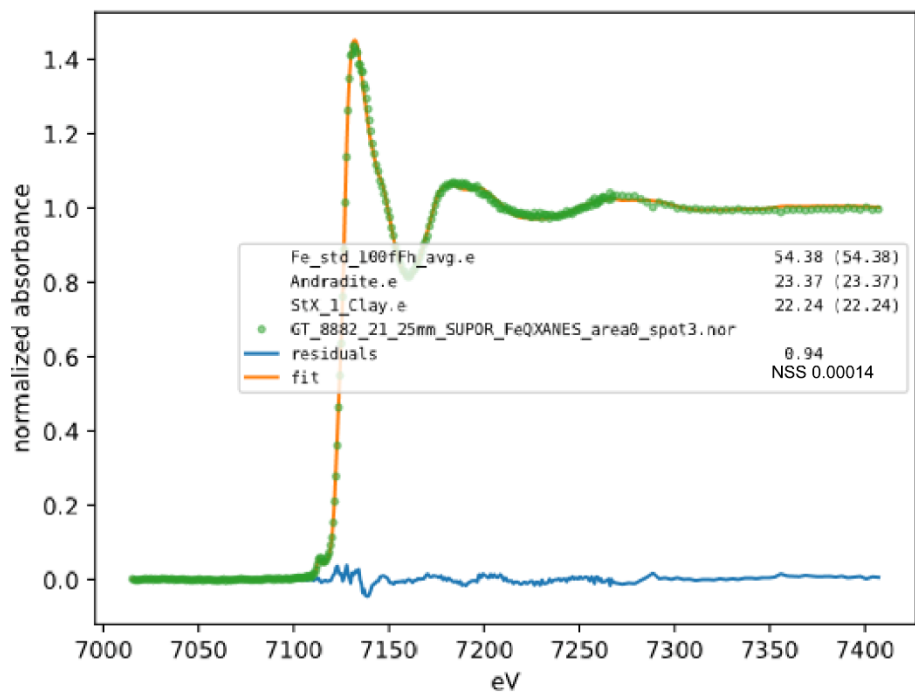


Figure 2.5.94 Fe XANES Station 21 area 0 spot 3

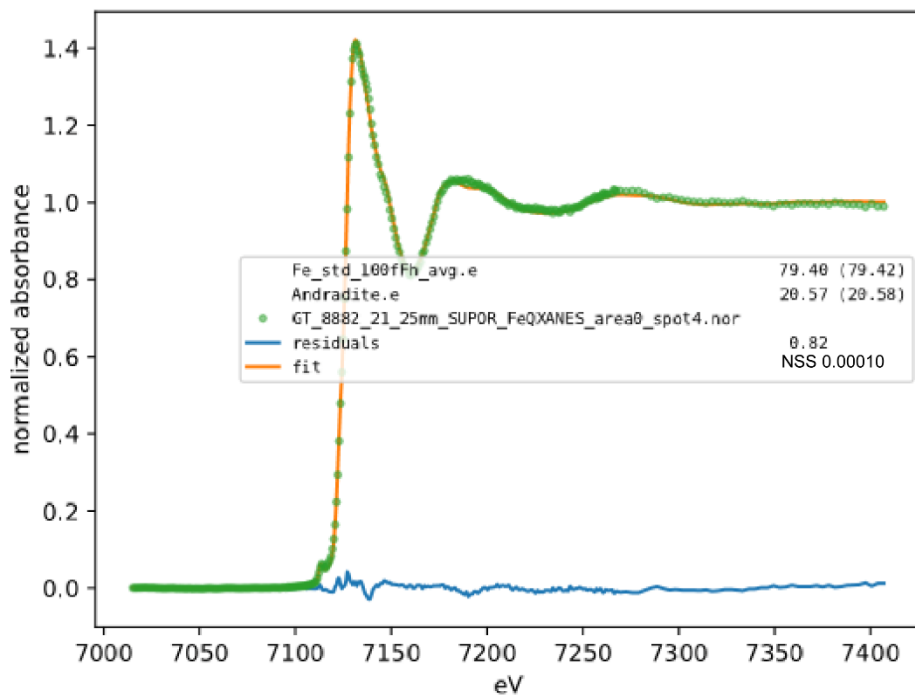


Figure 2.5.95 Fe XANES Station 21 area 0 spot 4

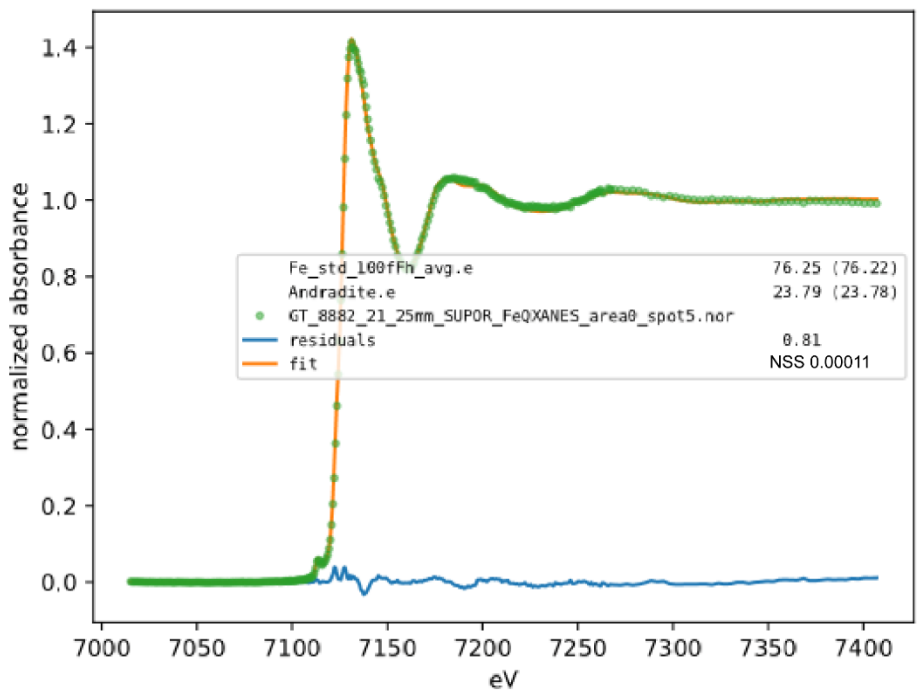


Figure 2.5.96 Fe XANES Station 21 area 0 spot 5

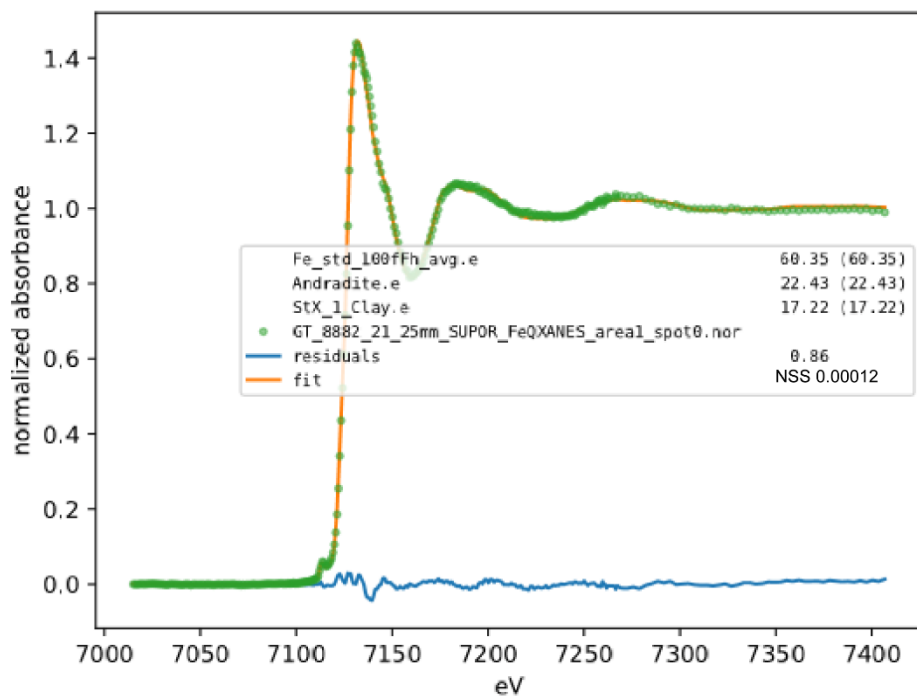


Figure 2.5.97 Fe XANES Station 21 area 1 spot 0

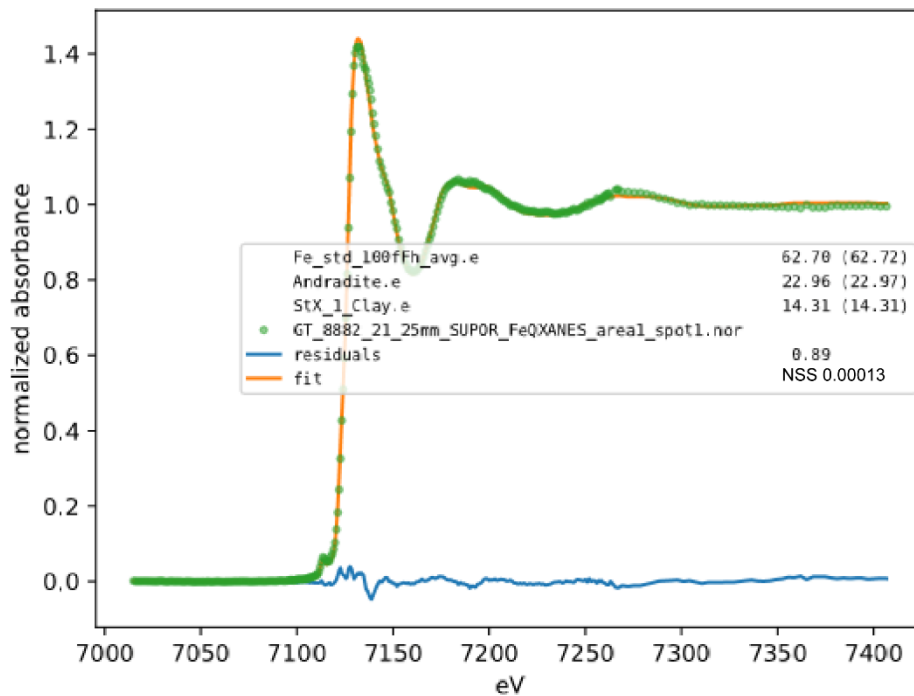


Figure 2.5.98 Fe XANES Station 21 area 1 spot 1

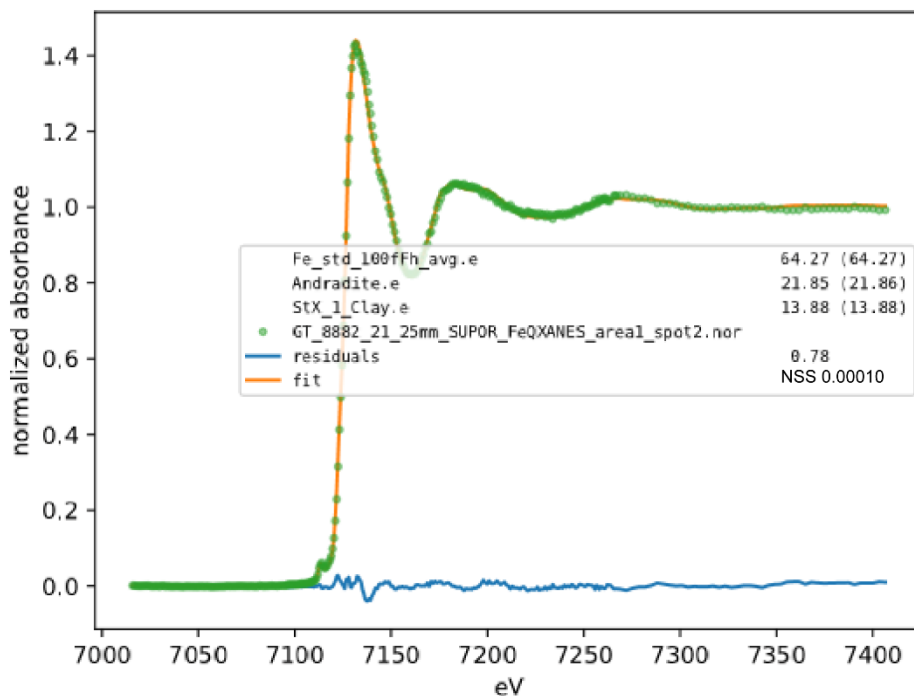


Figure 2.5.99 Fe XANES Station 21 area 1 spot 2

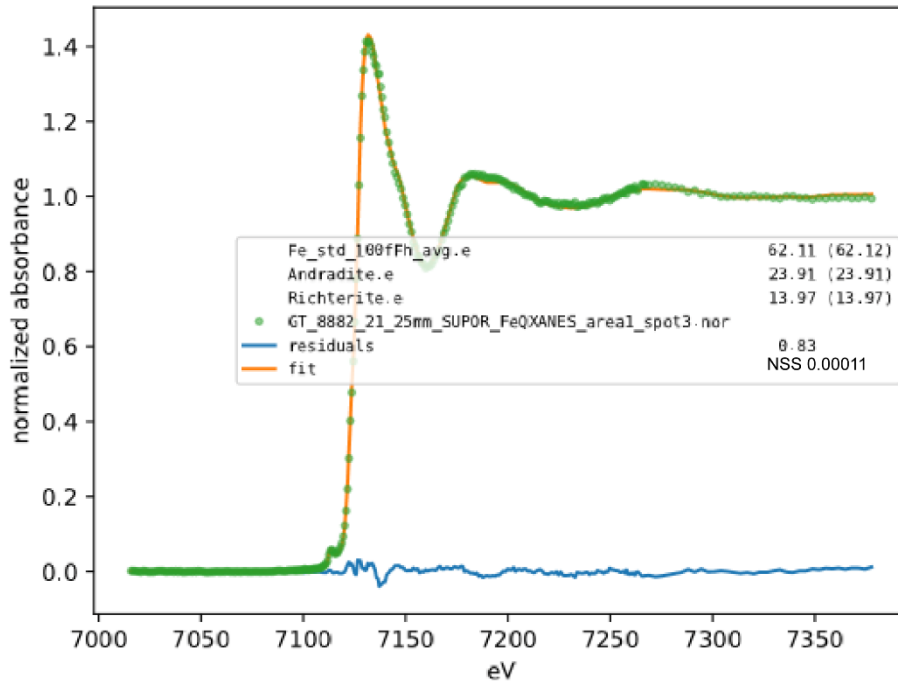


Figure 2.5.100 Fe XANES Station 21 area 1 spot 3

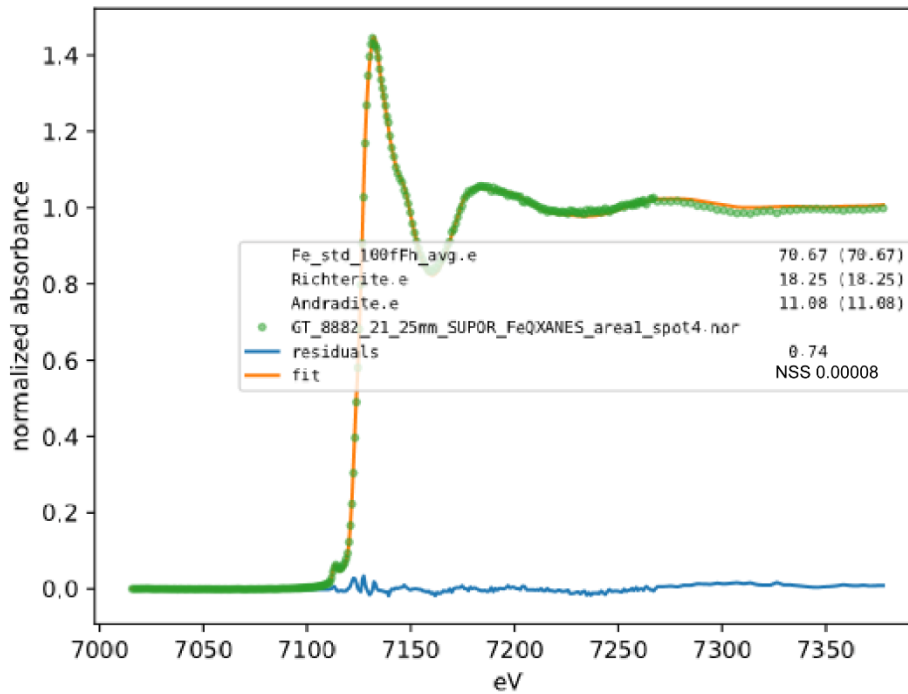


Figure 2.5.101 Fe XANES Station 21 area 1 spot 4

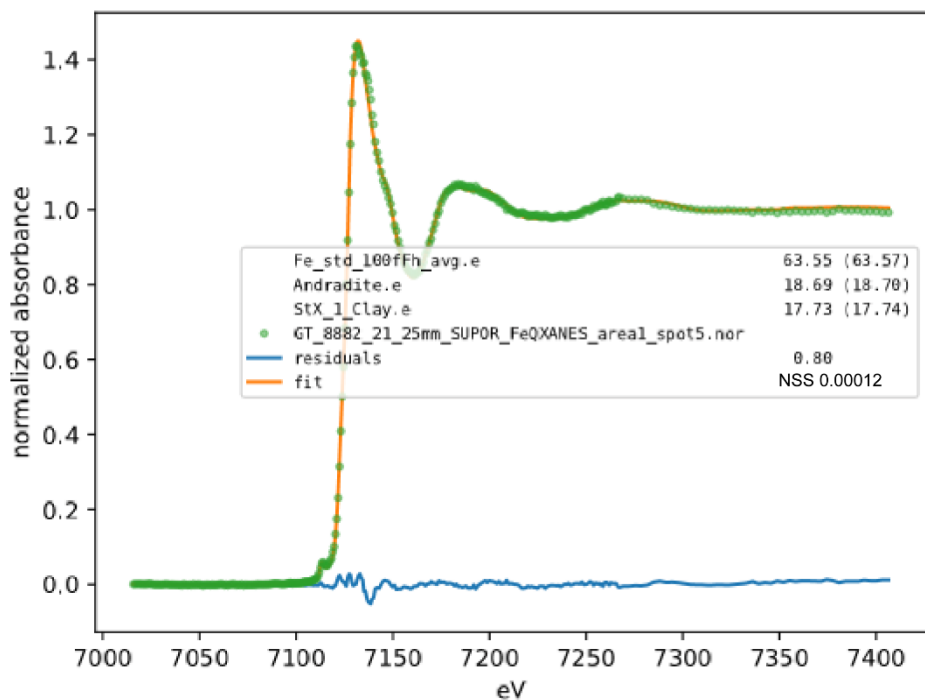


Figure 2.5.102 Fe XANES Station 21 area 1 spot 5

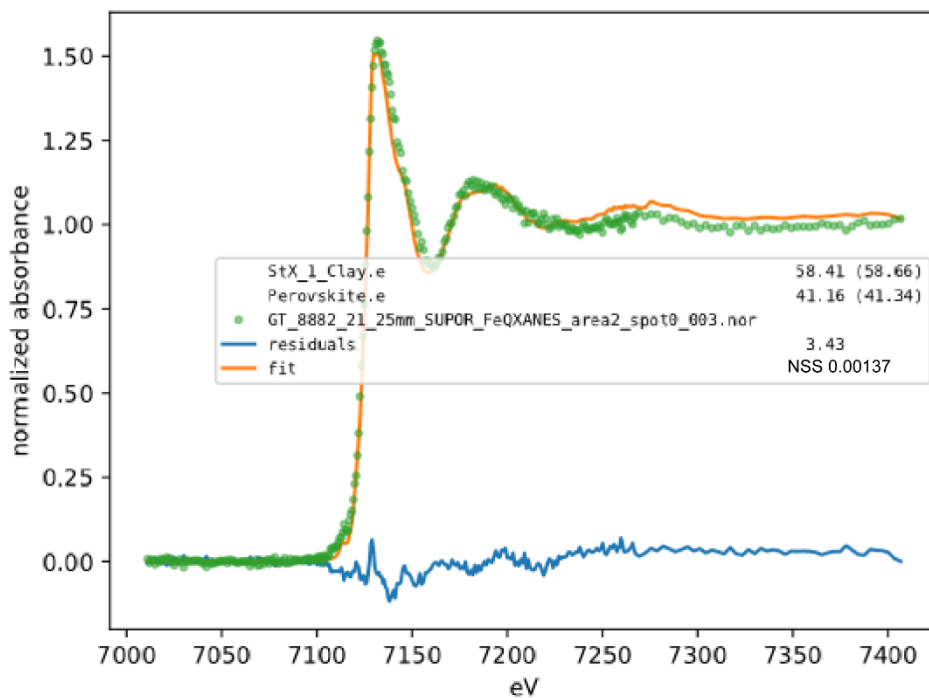


Figure 2.5.103 Fe XANES Station 21 area 2 spot 0-003

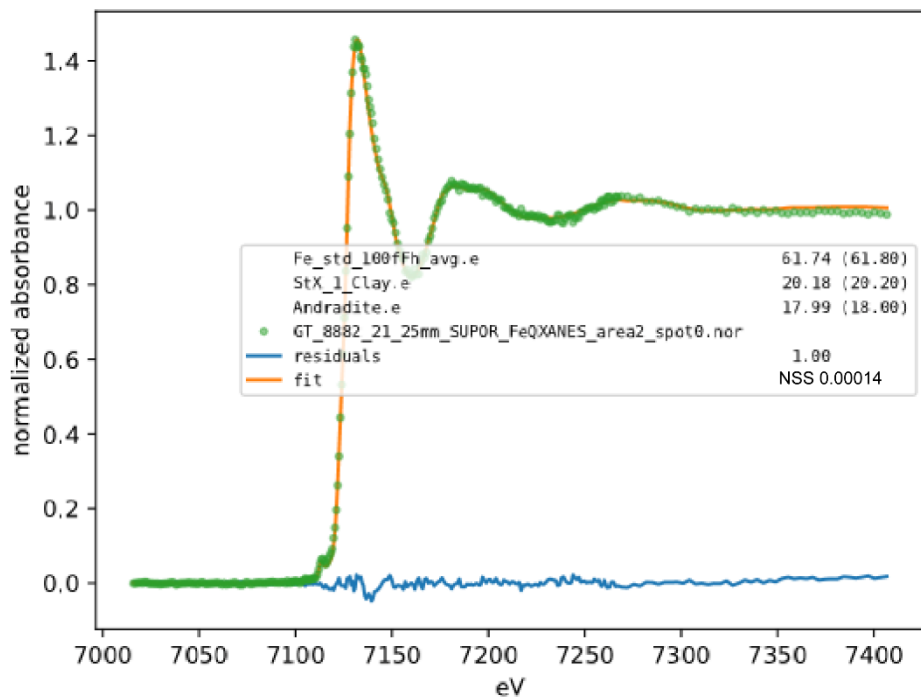


Figure 2.5.104 Fe XANES Station 21 area 2 spot 0

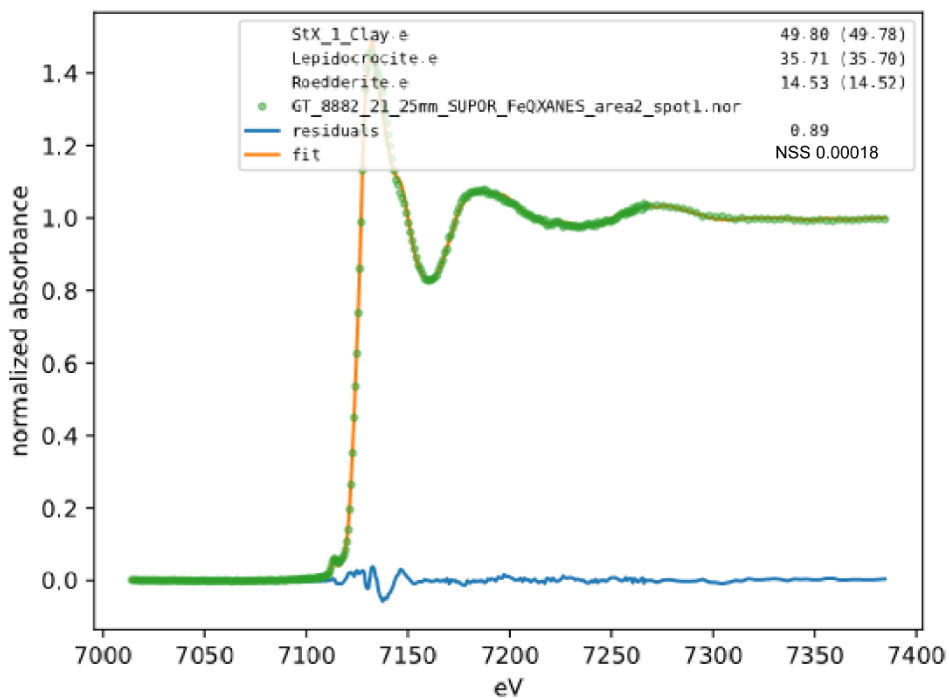


Figure 2.5.105 Fe XANES Station 21 area 2 spot 1

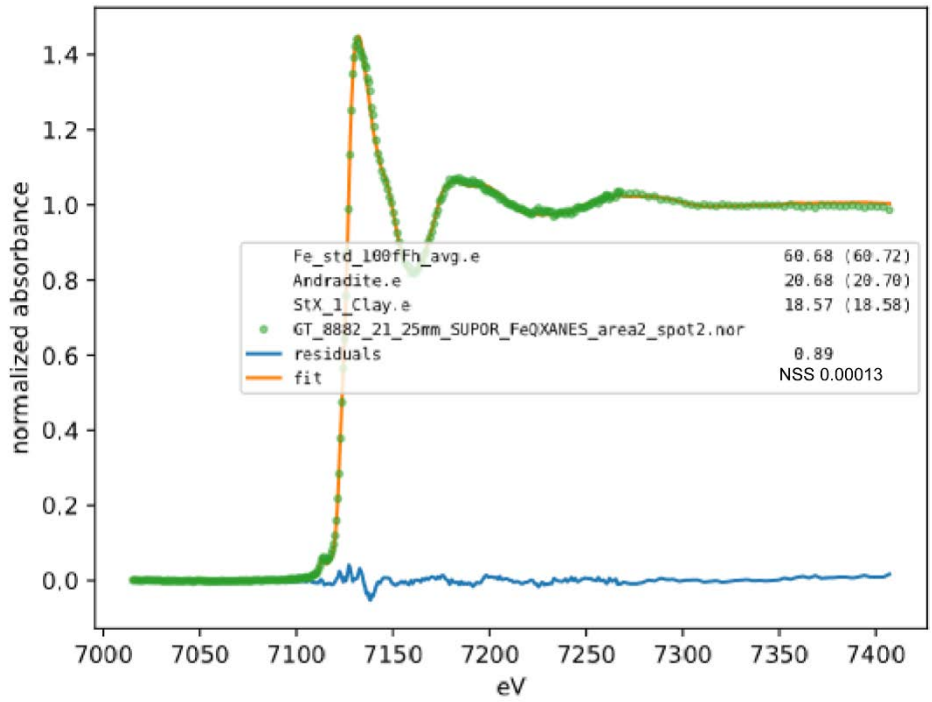


Figure 2.5.106 Fe XANES Station 21 area 2 spot 2

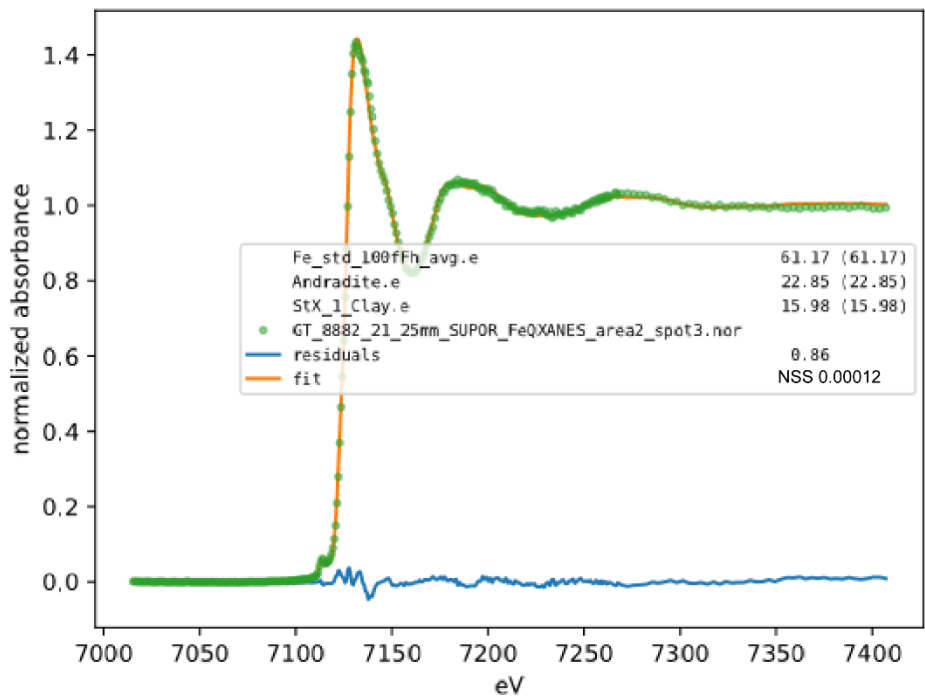


Figure 2.5.107 Fe XANES Station 21 area 2 spot 3

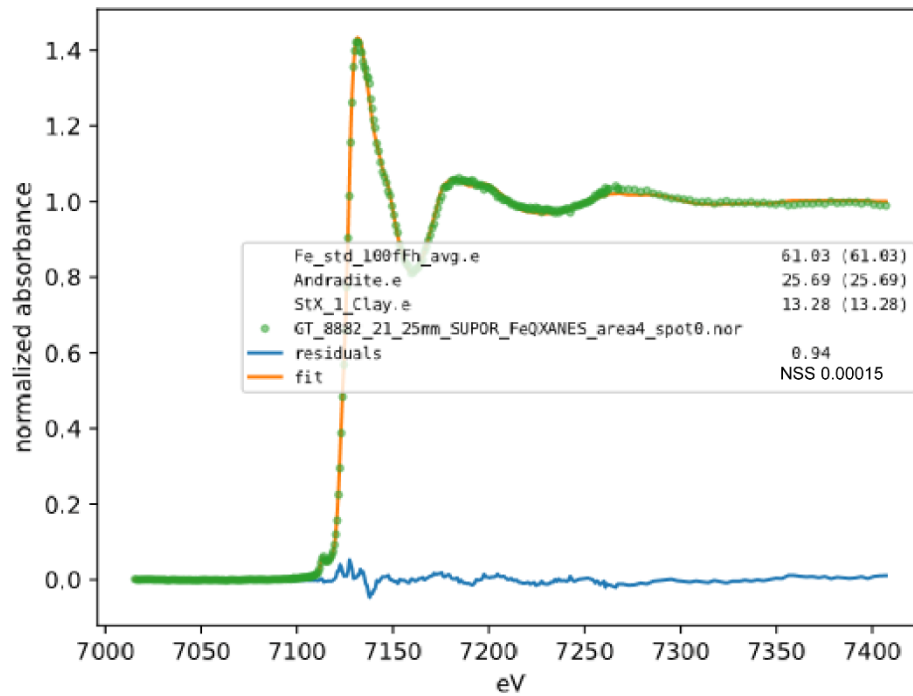


Figure 2.5.108 Fe XANES Station 21 area 4 spot 0

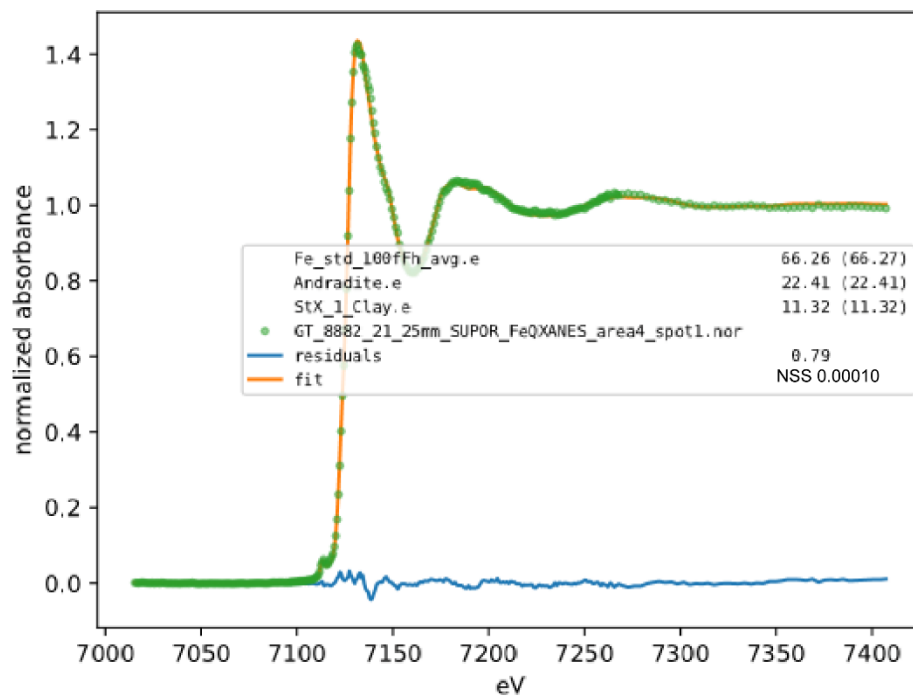


Figure 2.5.109 Fe XANES Station 21 area 4 spot 1

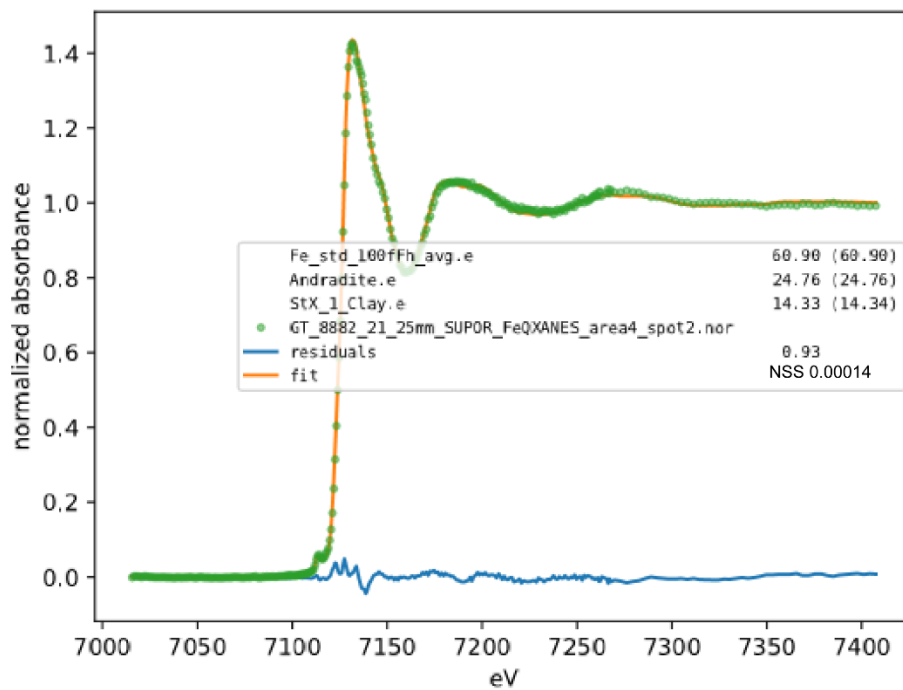


Figure 2.5.110 Fe XANES Station 21 area 4 spot 2

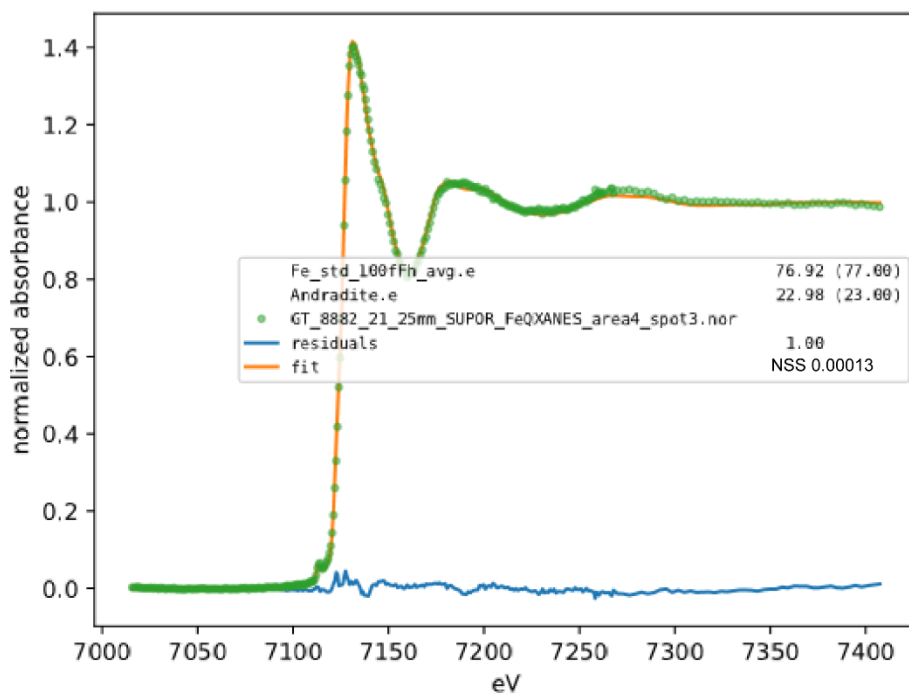


Figure 2.5.111 Fe XANES Station 21 area 4 spot 3

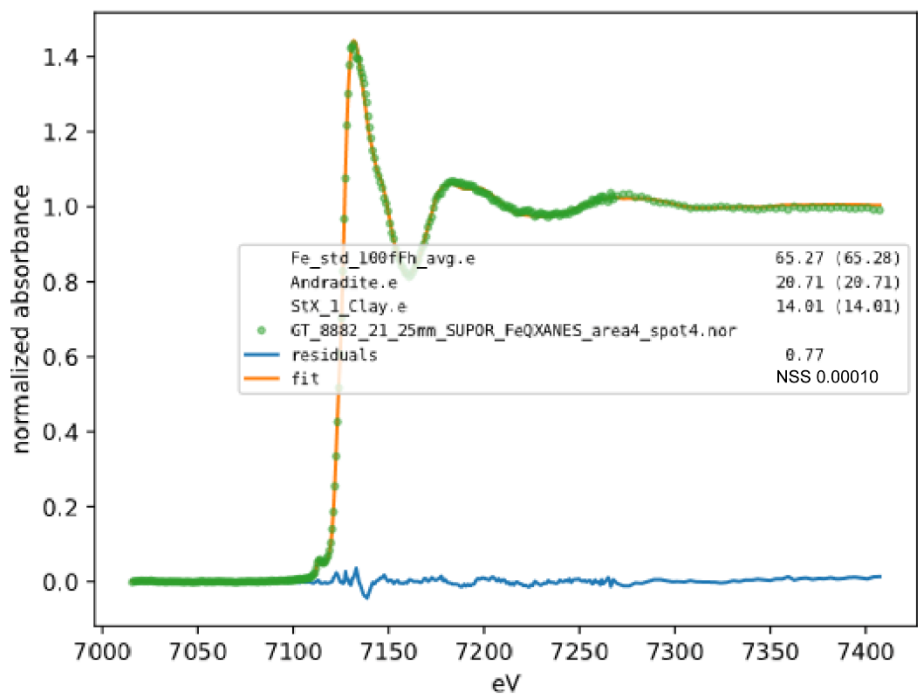


Figure 2.5.112 Fe XANES Station 21 area 4 spot 4

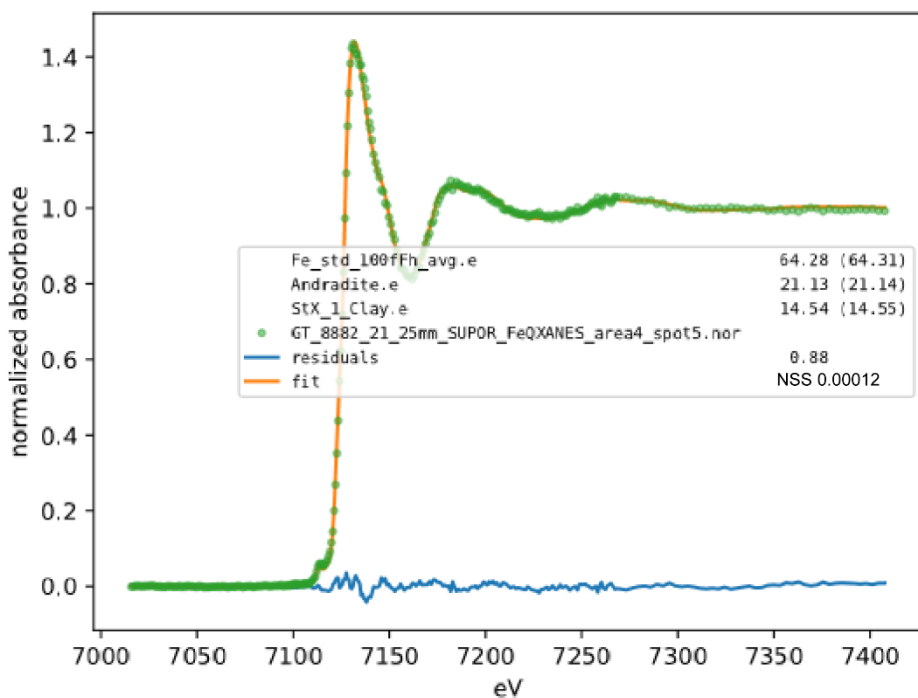


Figure 2.5.113 Fe XANES Station 21 area 4 spot 5

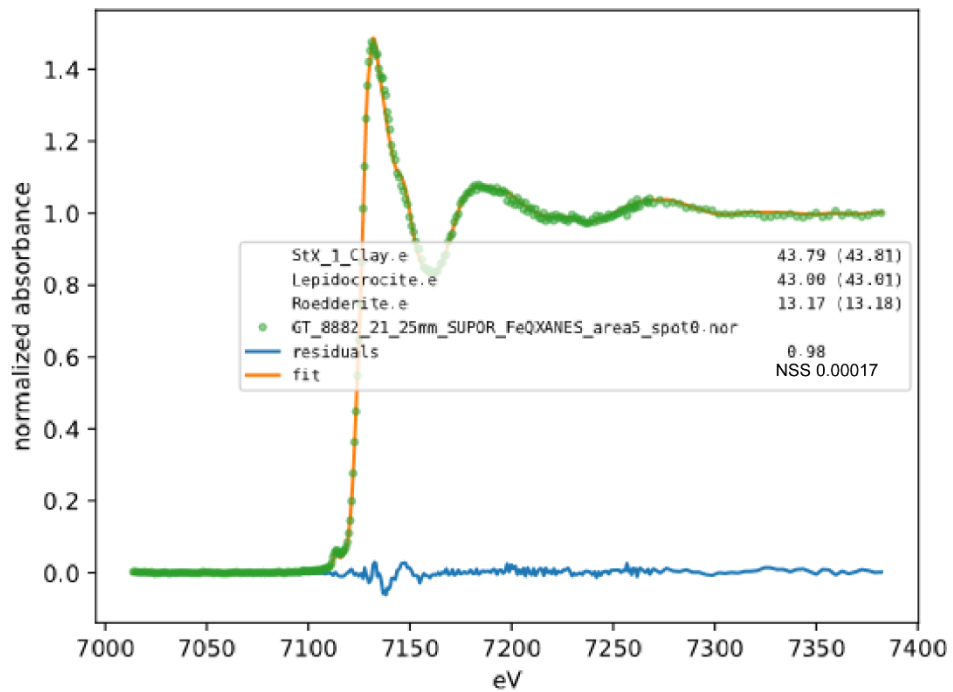


Figure 2.5.114 Fe XANES Station 21 area 5 spot 0

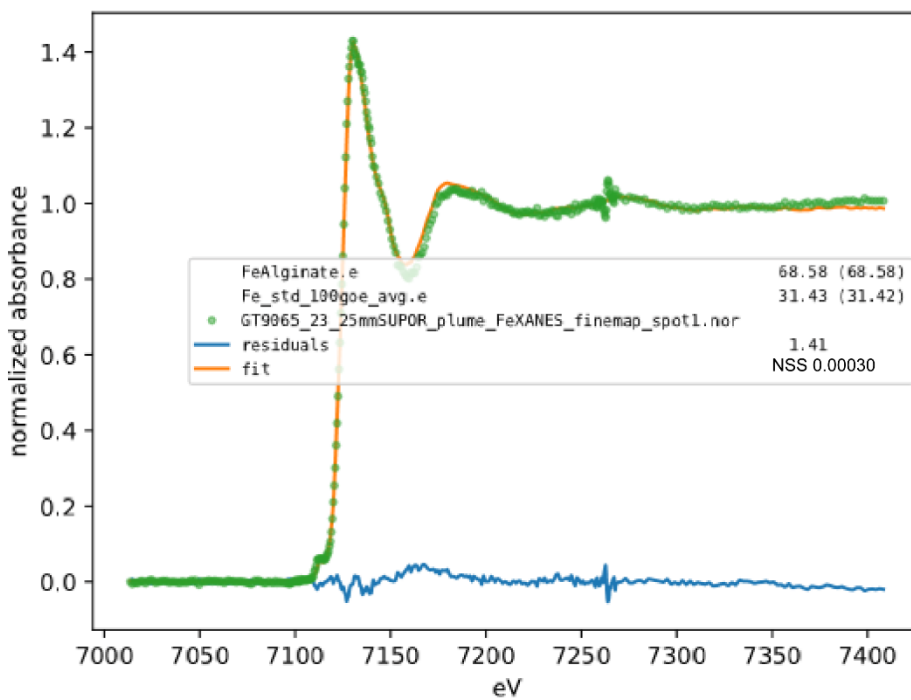


Figure 2.5.115 Fe XANES Station 23 plume spot 1

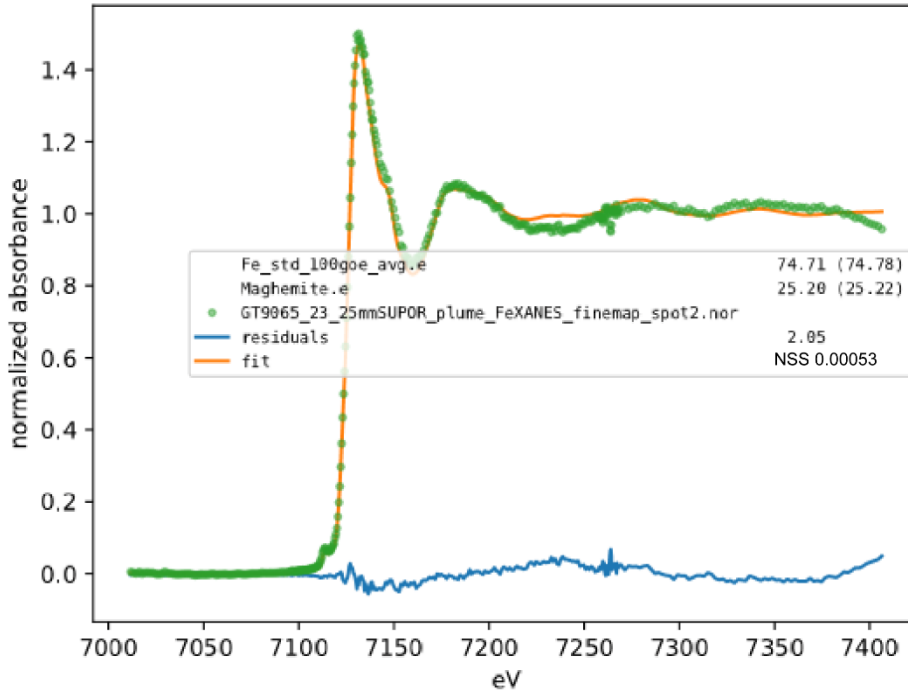


Figure 2.5.116 Fe XANES Station 23 plume spot 2

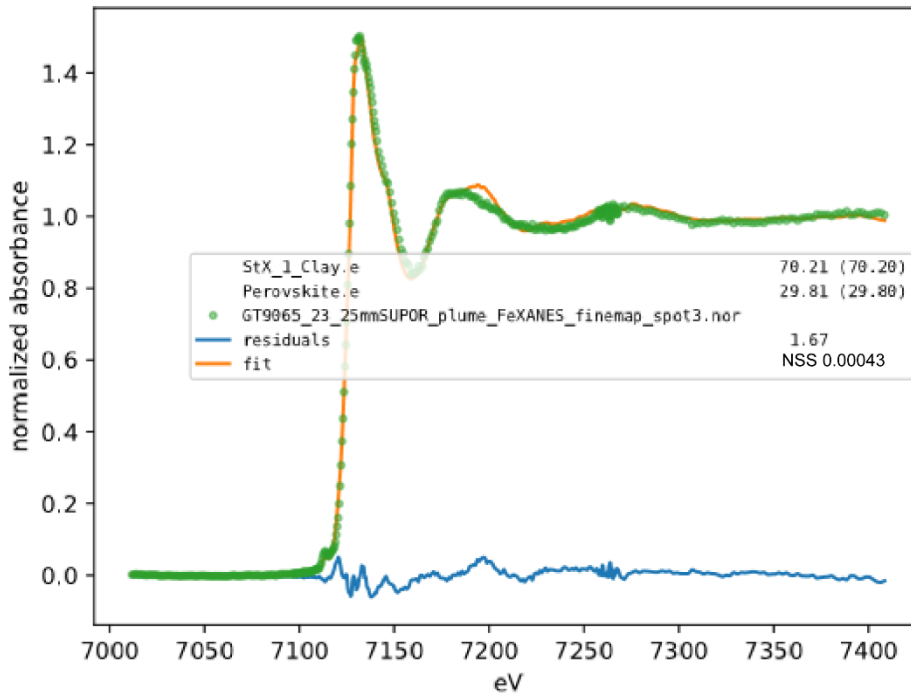


Figure 2.5.117 Fe XANES Station 23 plume spot 3

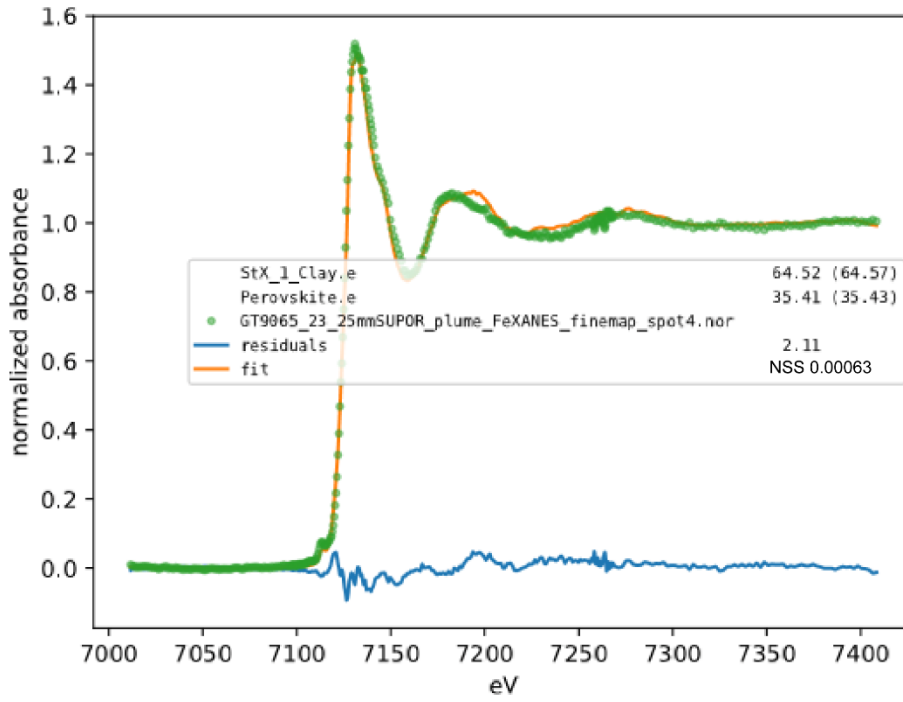


Figure 2.5.118 Fe XANES Station 23 plume spot 4

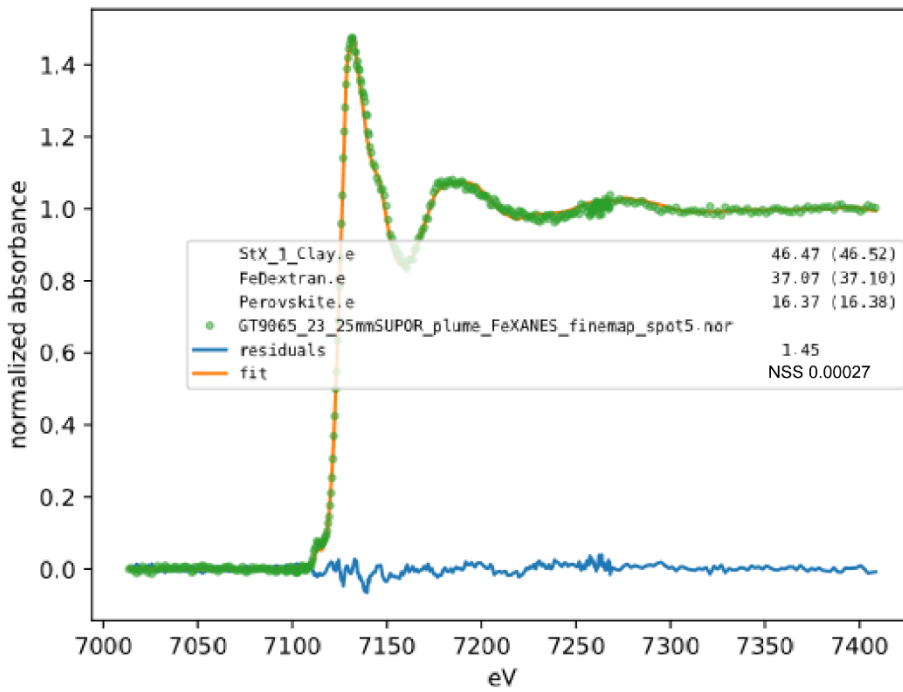


Figure 2.5.119 Fe XANES Station 23 plume spot 5

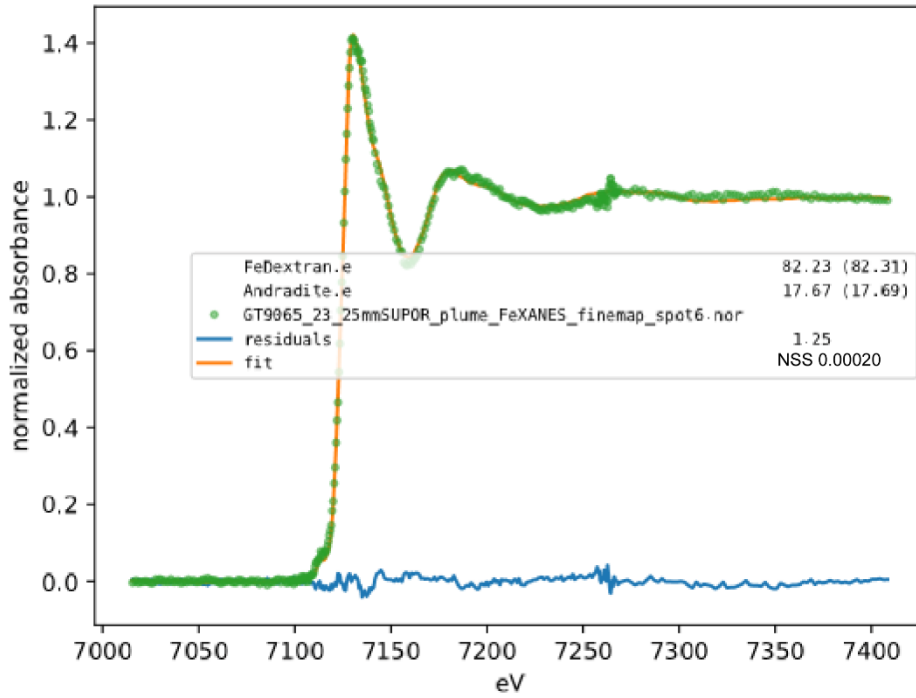


Figure 2.5.120 Fe XANES Station 23 plume spot 6

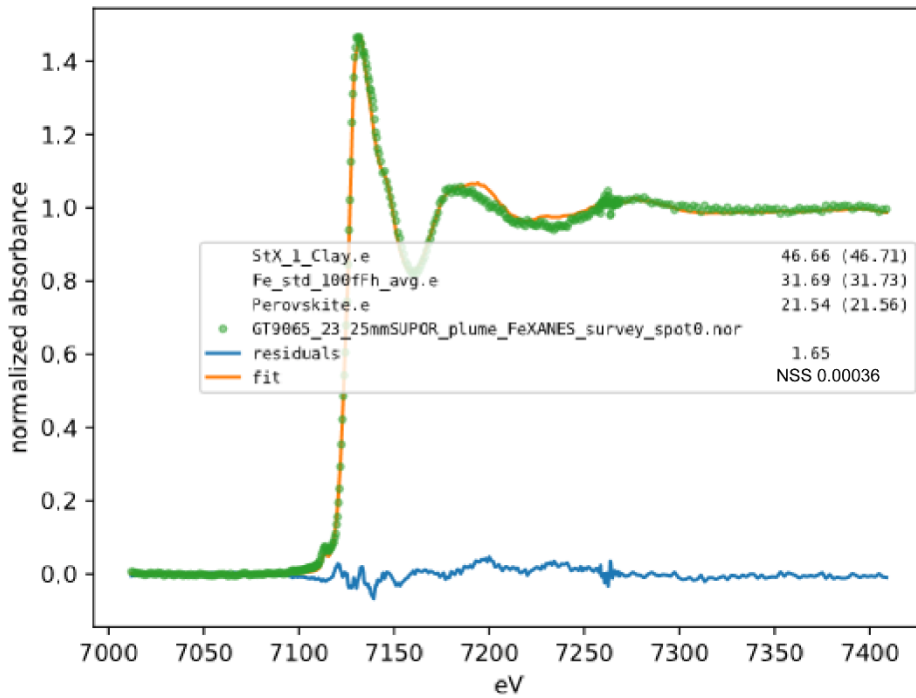


Figure 2.5.121 Fe XANES Station 23 plume spot 0

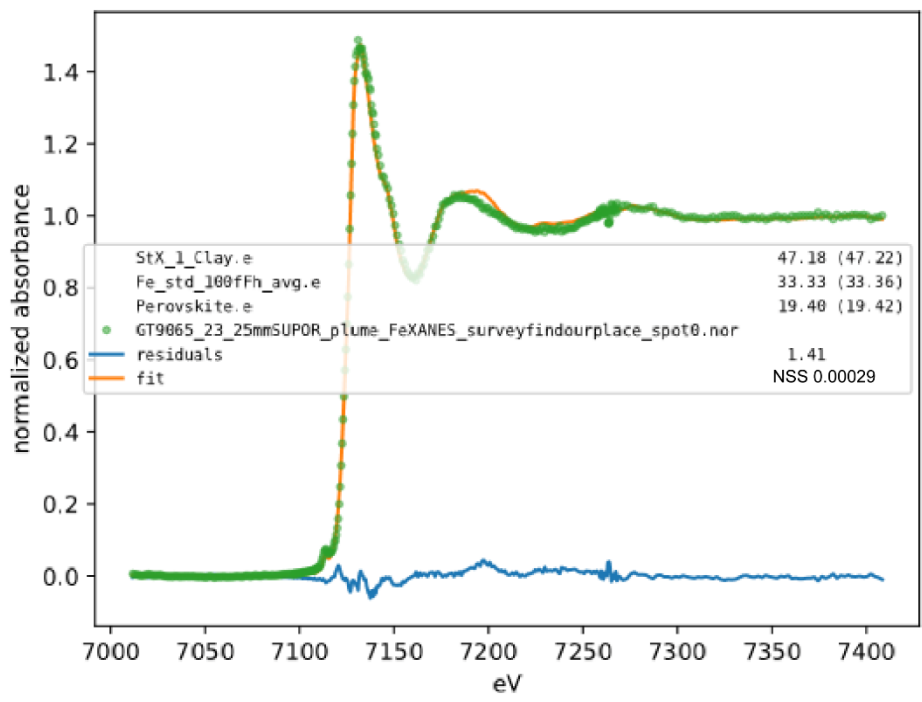


Figure 2.5.122 Fe XANES Station 23 plume spot 0

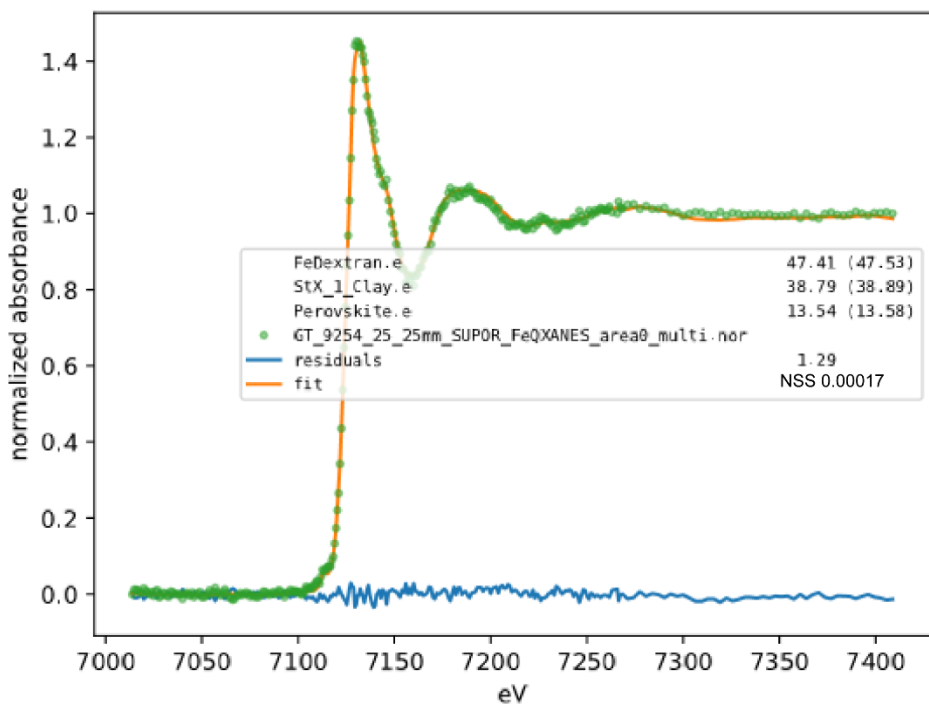


Figure 2.5.123 Fe XANES Station 25 area 0 multi

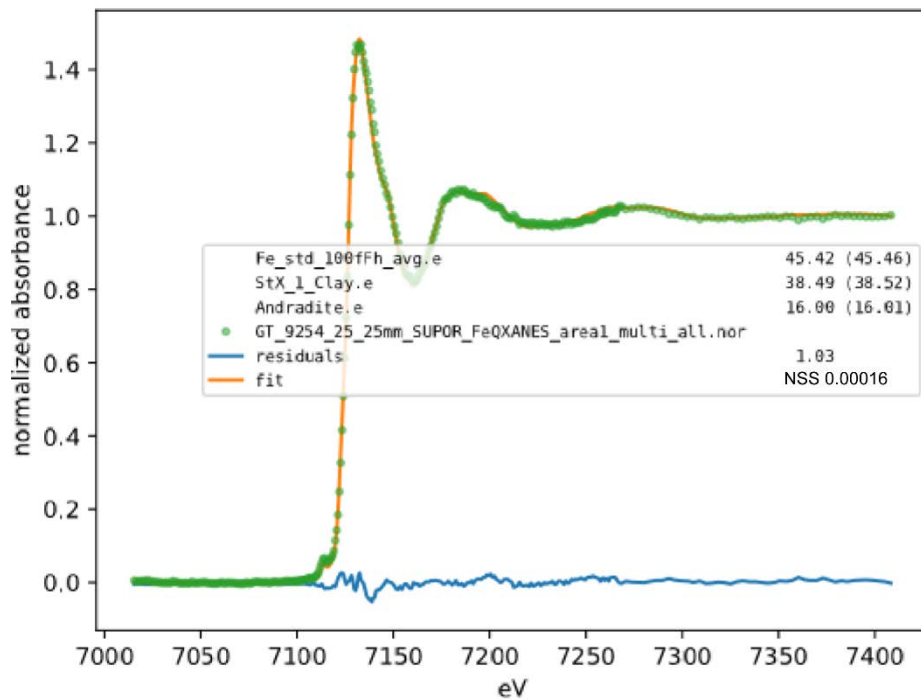


Figure 2.5.124 Fe XANES Station 25 area 1 multi

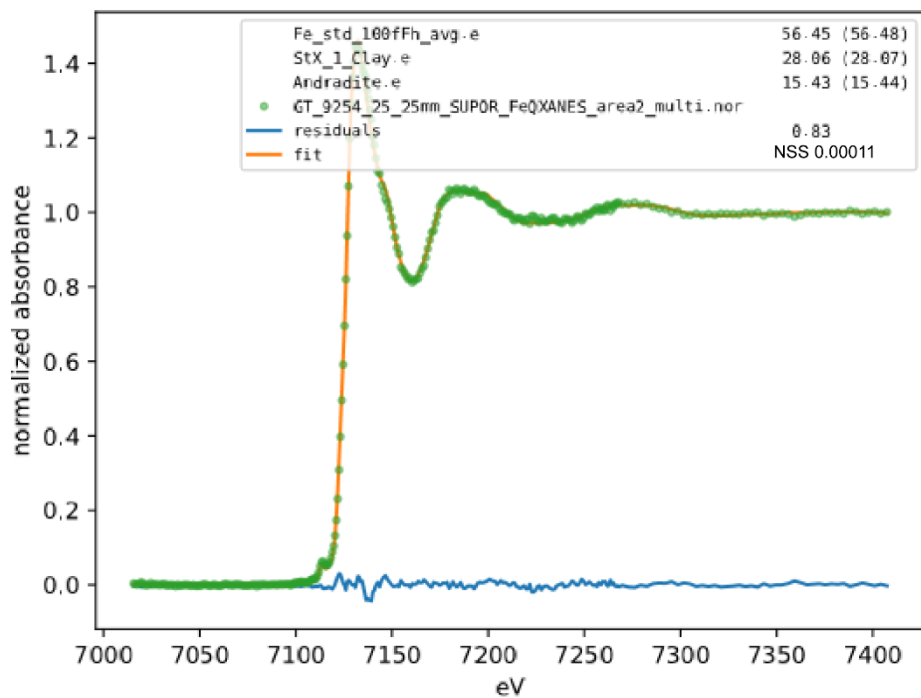


Figure 2.5.125 Fe XANES Station 25 area 2 multi

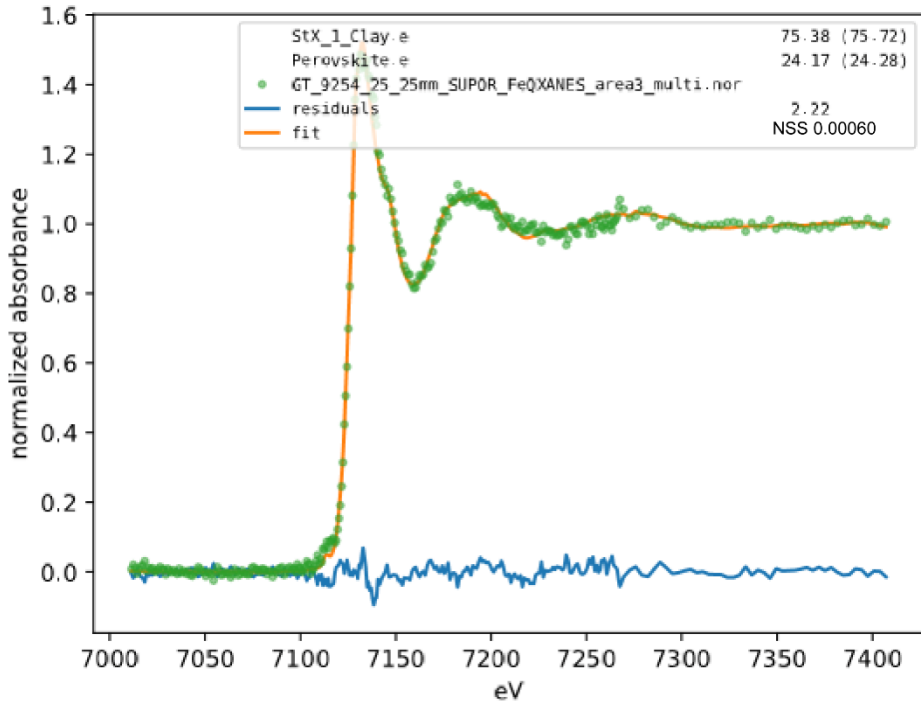


Figure 2.5.126 Fe XANES Station 25 area 3 multi

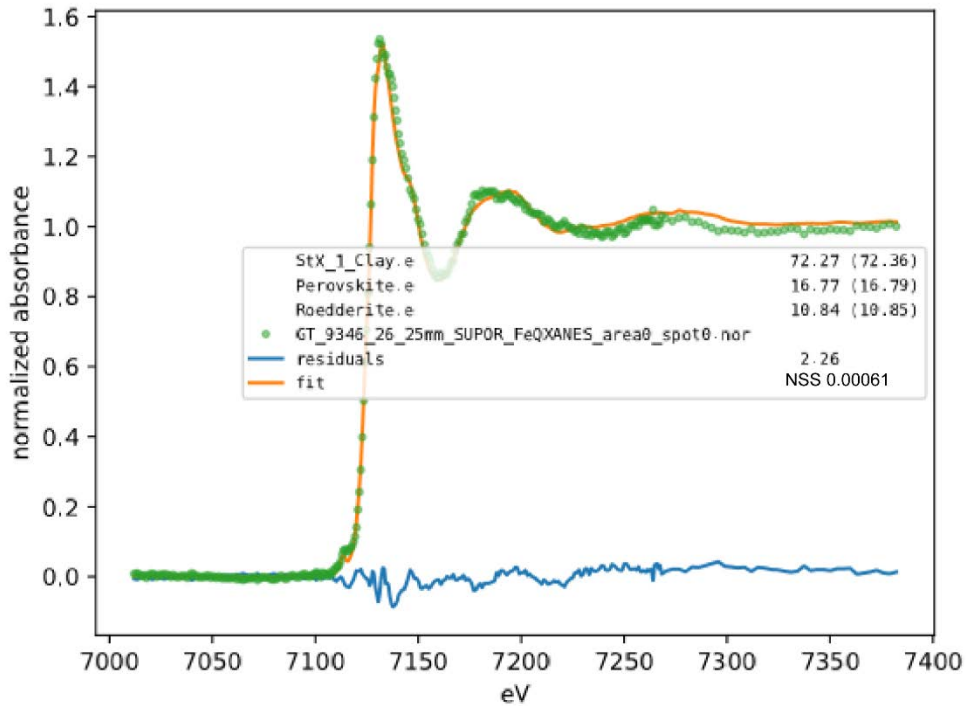


Figure 2.5.127 Fe XANES Station 26 area 0 spot 0

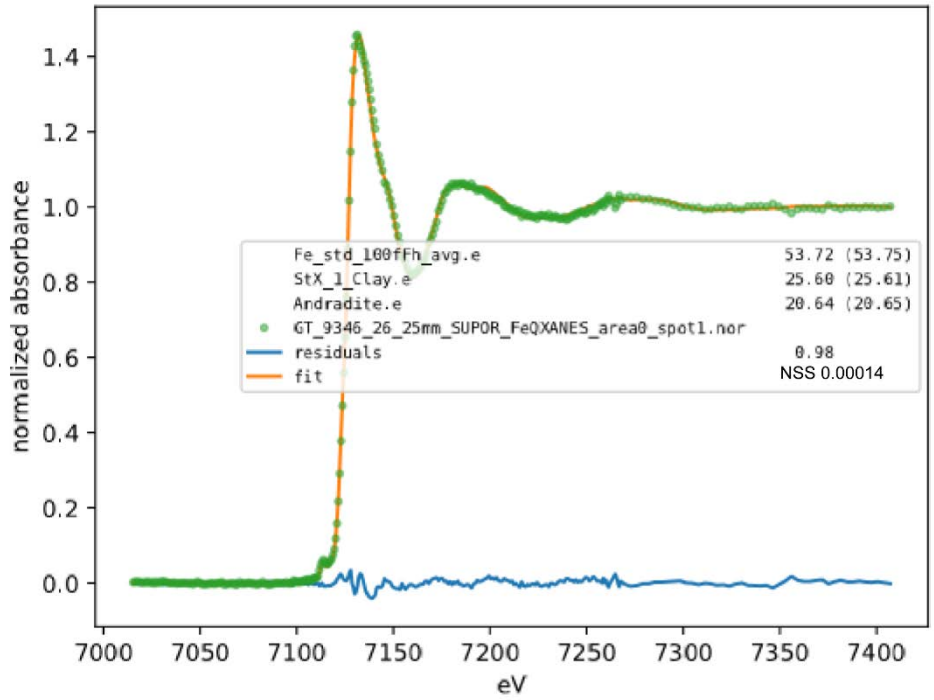


Figure 2.5.128 Fe XANES Station 26 area 0 spot 1

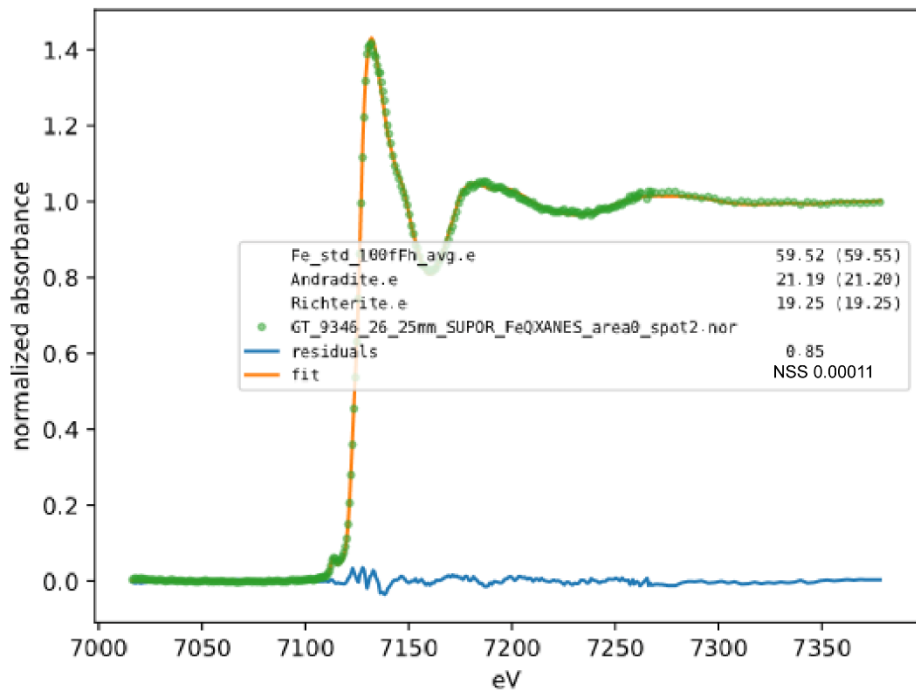


Figure 2.5.129 Fe XANES Station 26 area 0 spot 2

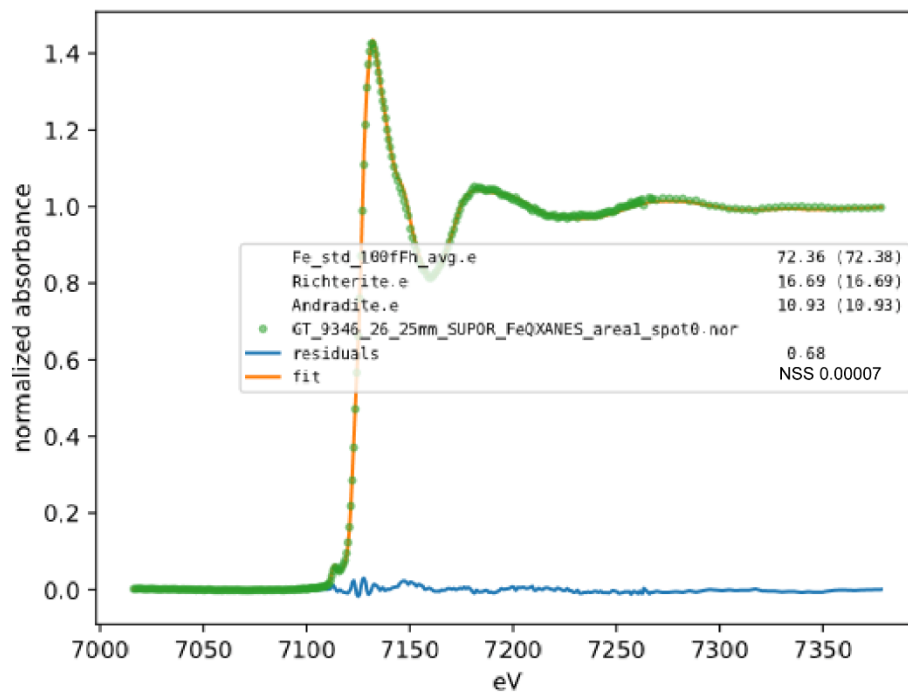


Figure 2.5.130 Fe XANES Station 26 area 1 spot 0

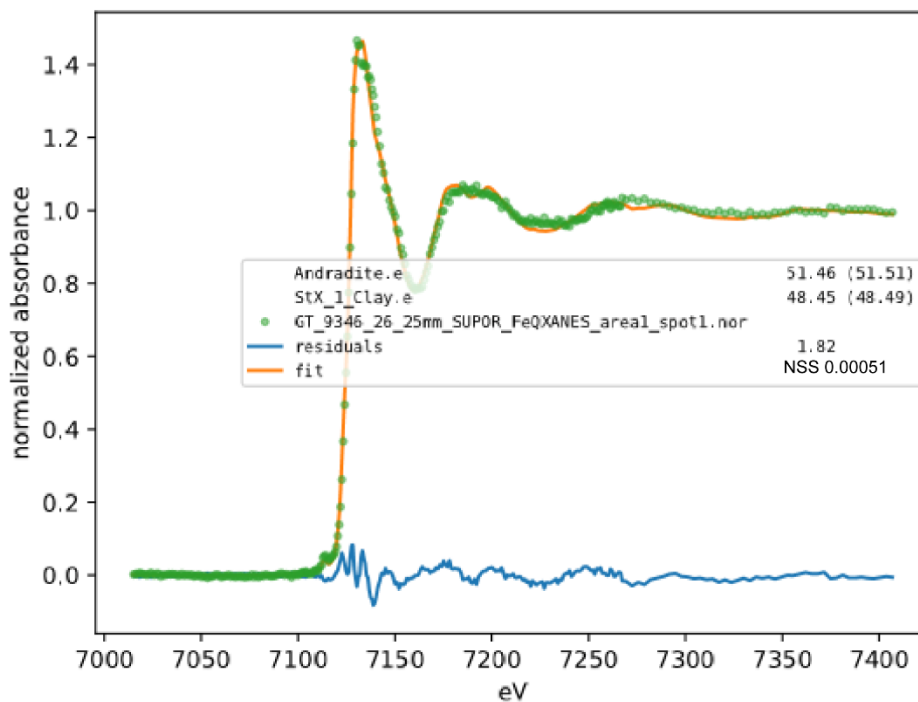


Figure 2.5.131 Fe XANES Station 26 area 1 spot 1

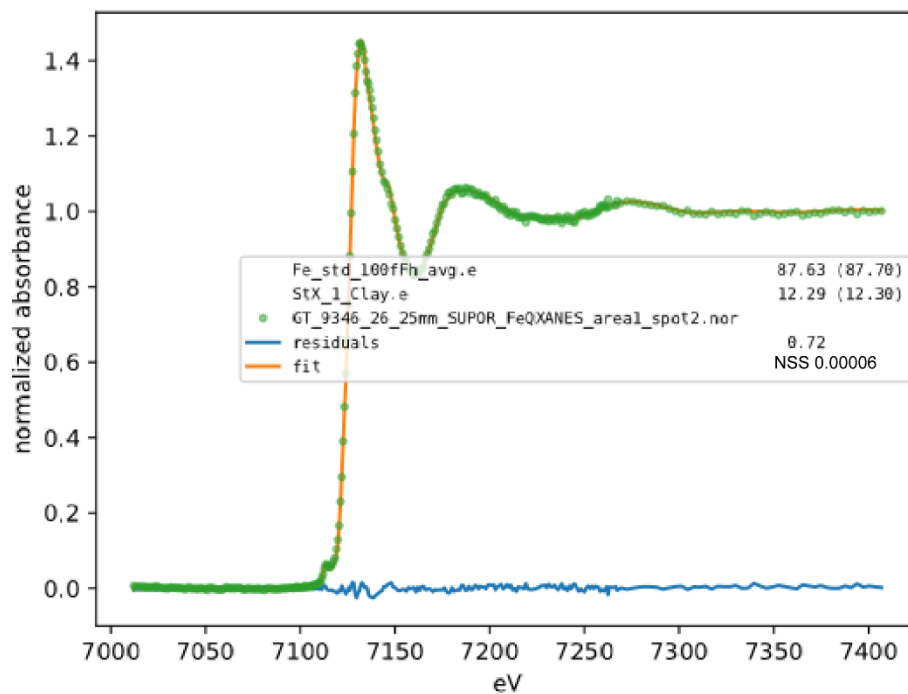


Figure 2.5.132 Fe XANES Station 26 area 1 spot 2

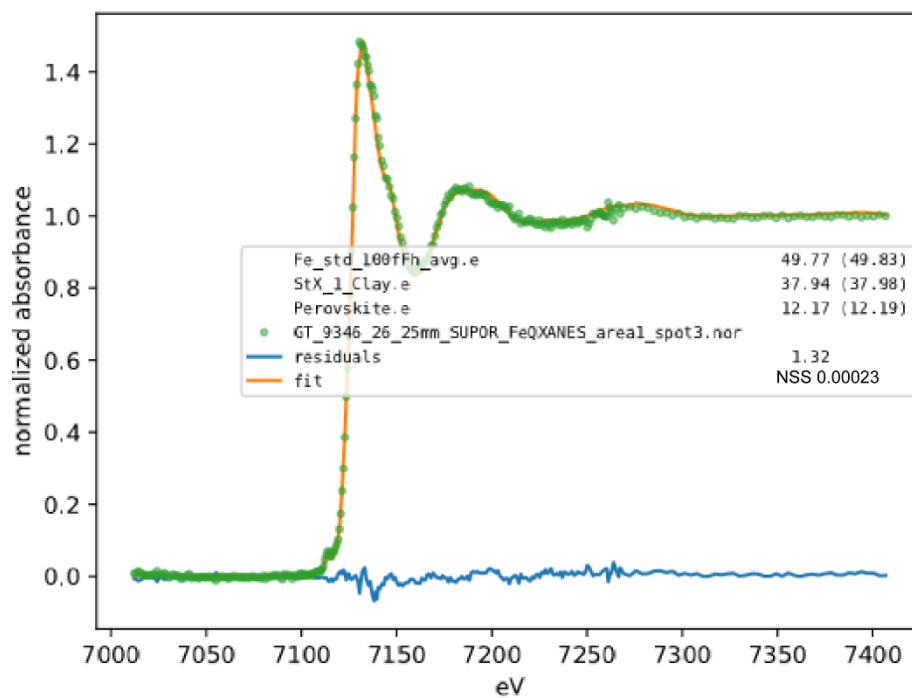


Figure 2.5.133 Fe XANES Station 26 area 1 spot 3

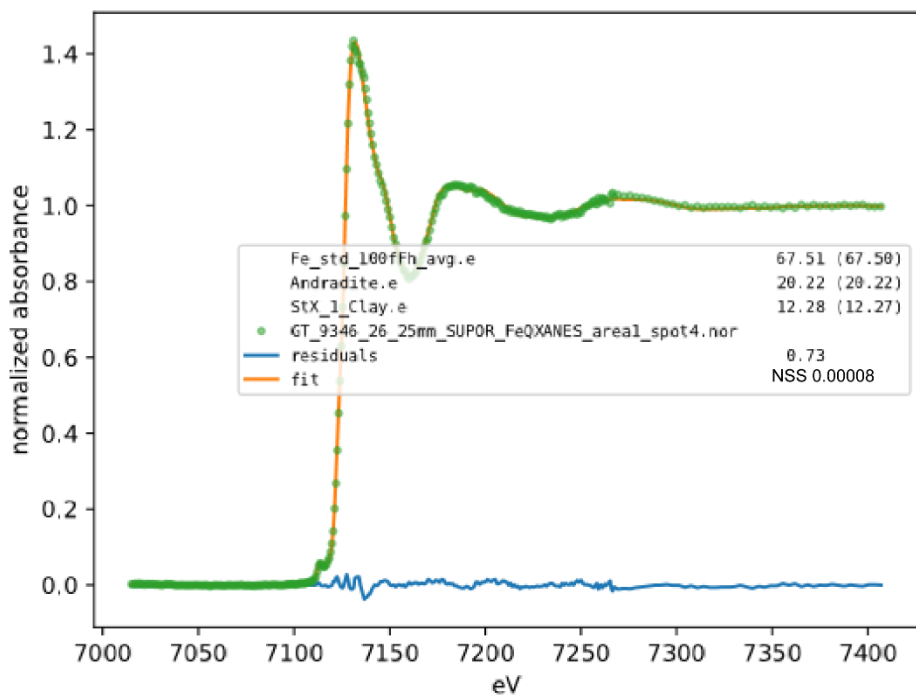


Figure 2.5.134 Fe XANES Station 26 area 1 spot 4

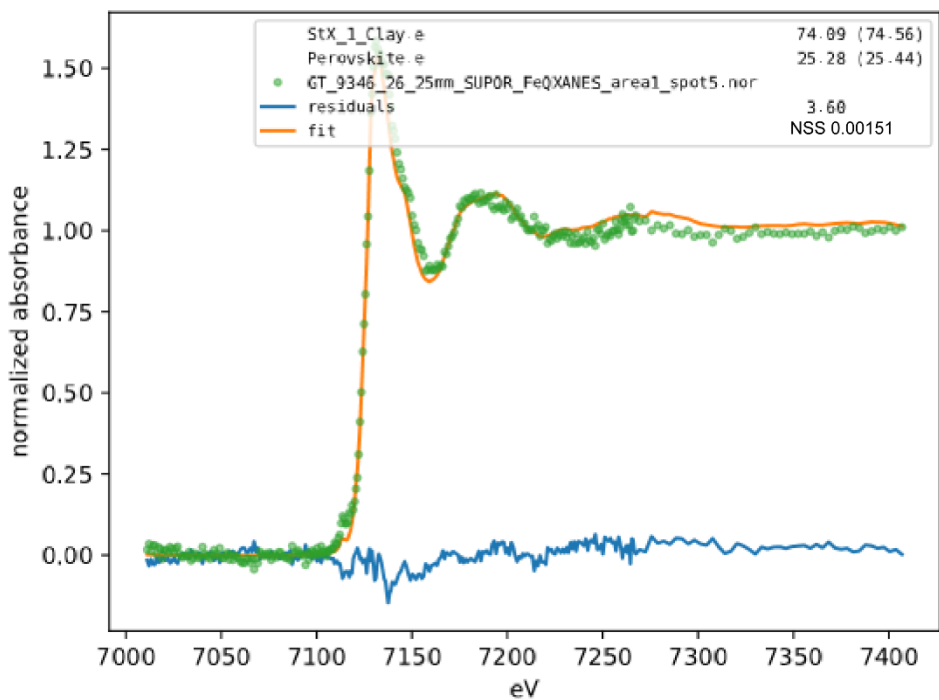


Figure 2.5.135 Fe XANES Station 26 area 1 spot 5

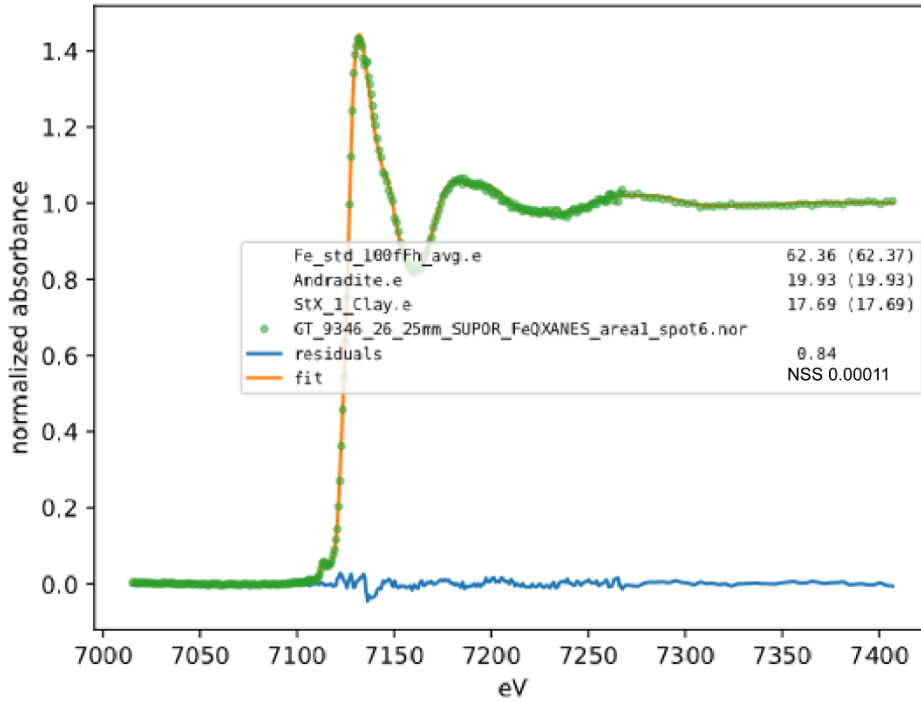


Figure 2.5.136 Fe XANES Station 26 area 1 spot 6

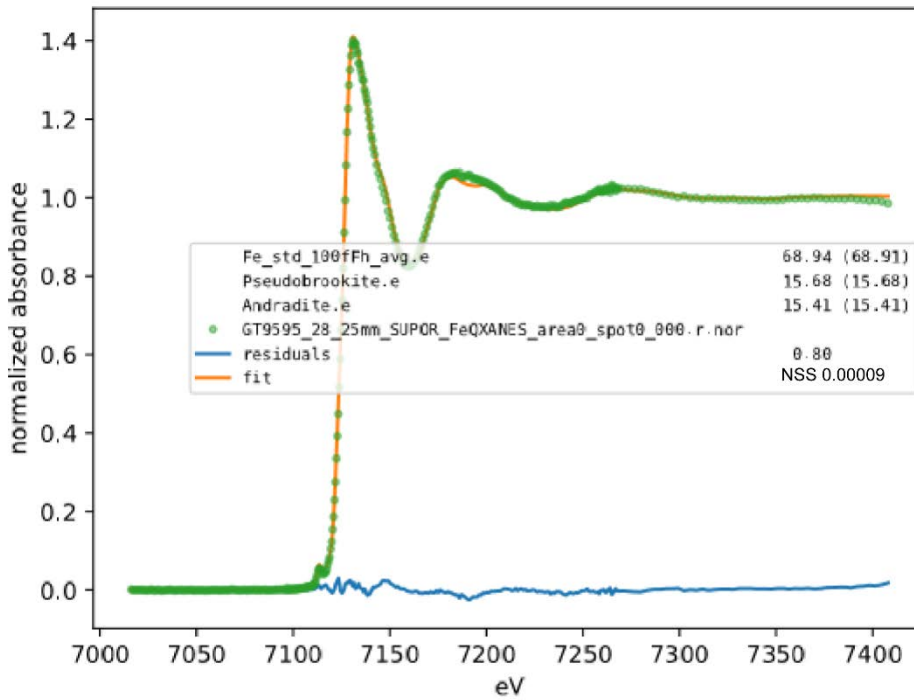


Figure 2.5.137 Fe XANES Station 28 area 0 spot 0

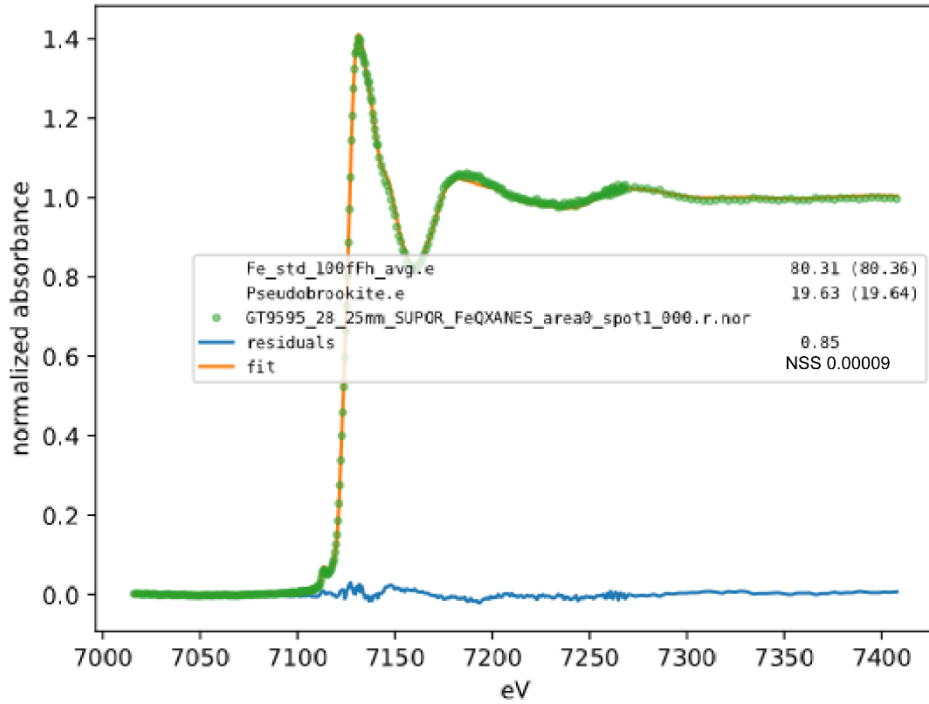


Figure 2.5.138 Fe XANES Station 28 area 0 spot 1

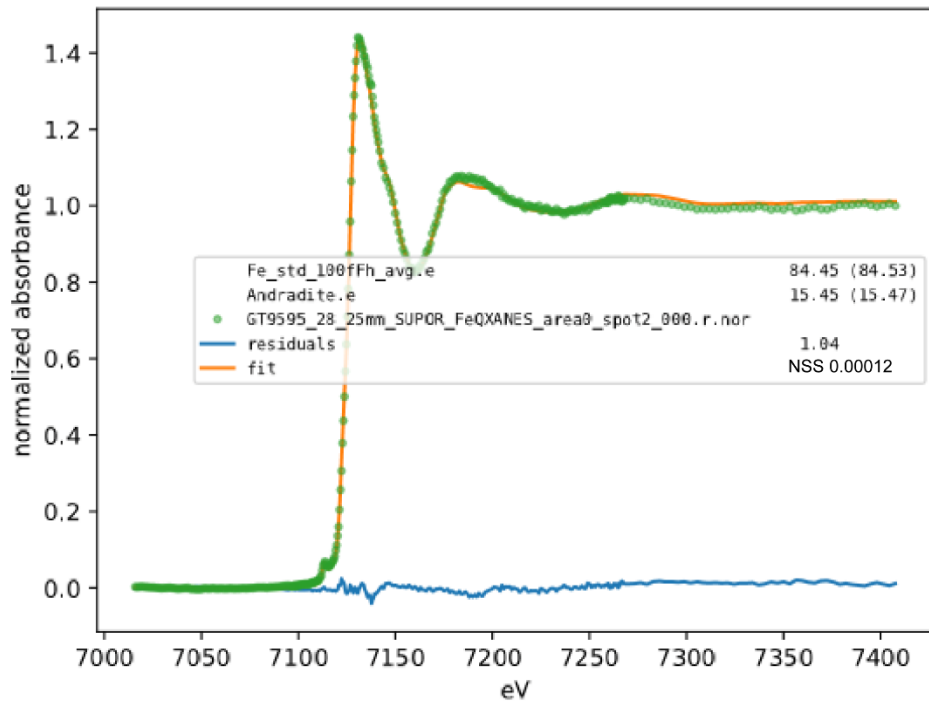


Figure 2.5.139 Fe XANES Station 28 area 0 spot 2

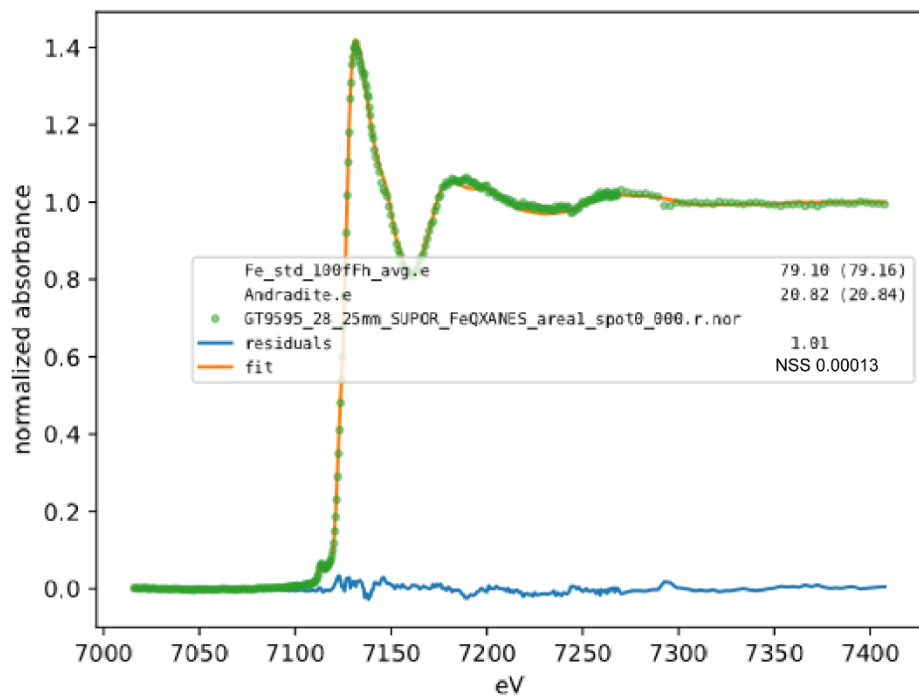


Figure 2.5.140 Fe XANES Station 28 area 1 spot 0

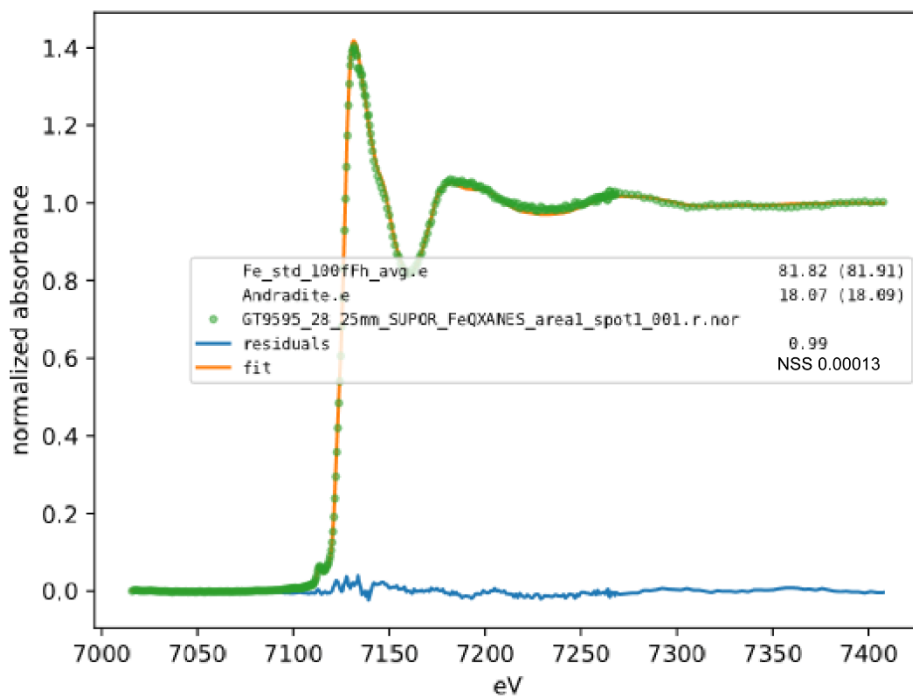


Figure 2.5.141 Fe XANES Station 28 area 1 spot 1

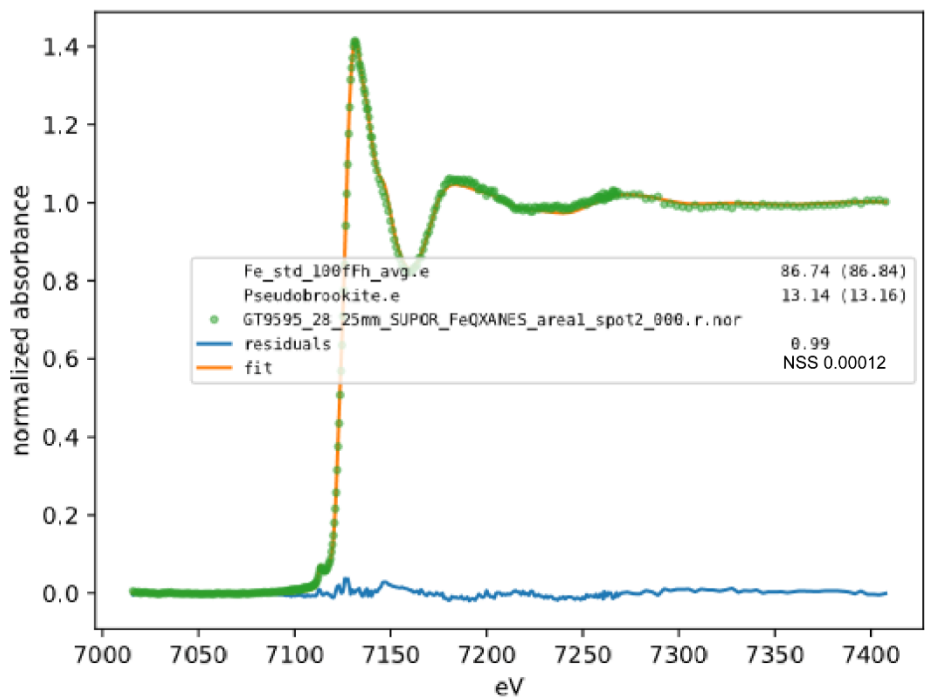


Figure 2.5.142 Fe XANES Station 28 area 1 spot 2

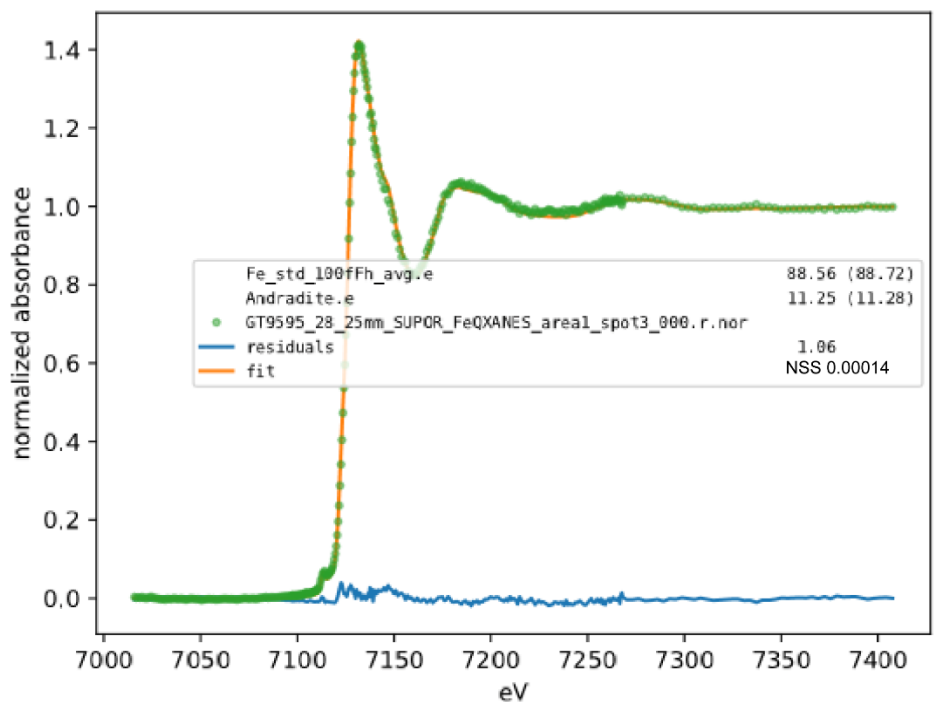


Figure 2.5.143 Fe XANES Station 28 area 1 spot 3

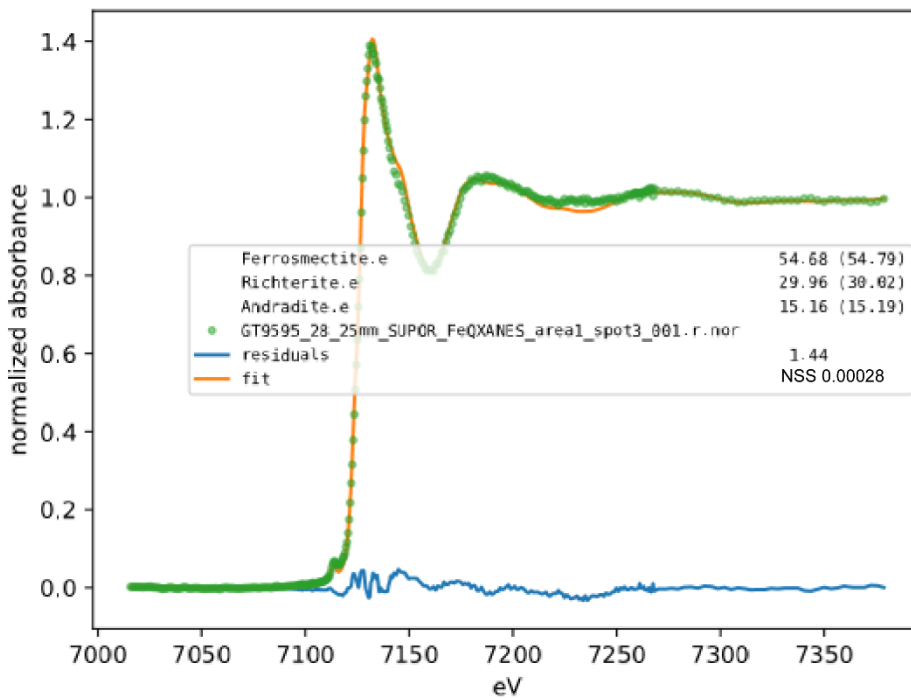


Figure 2.5.144 Fe XANES Station 28 area 1 spot 3-1

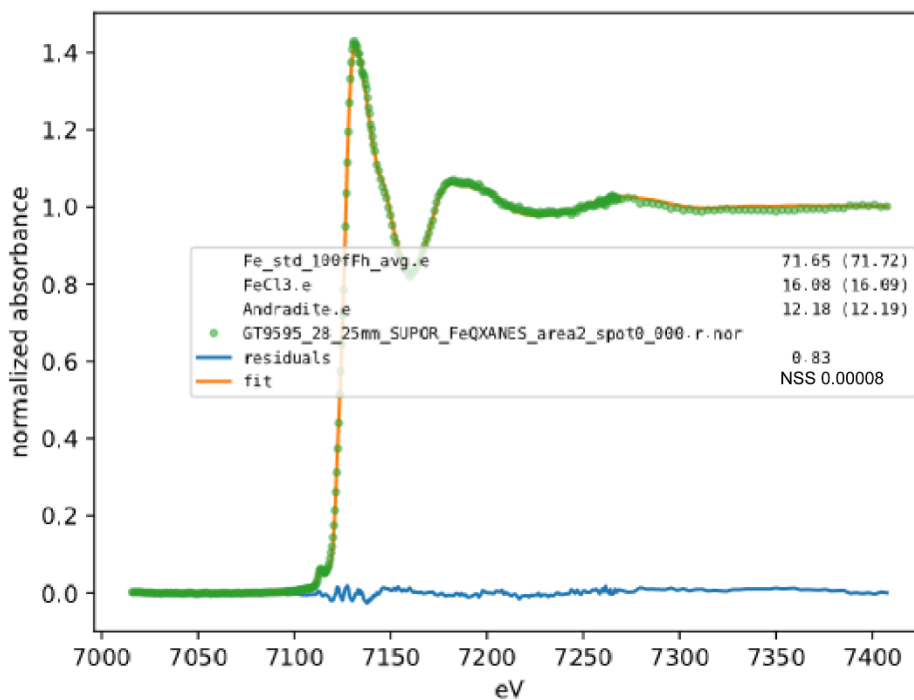


Figure 2.5.145 Fe XANES Station 28 area 2 spot 0

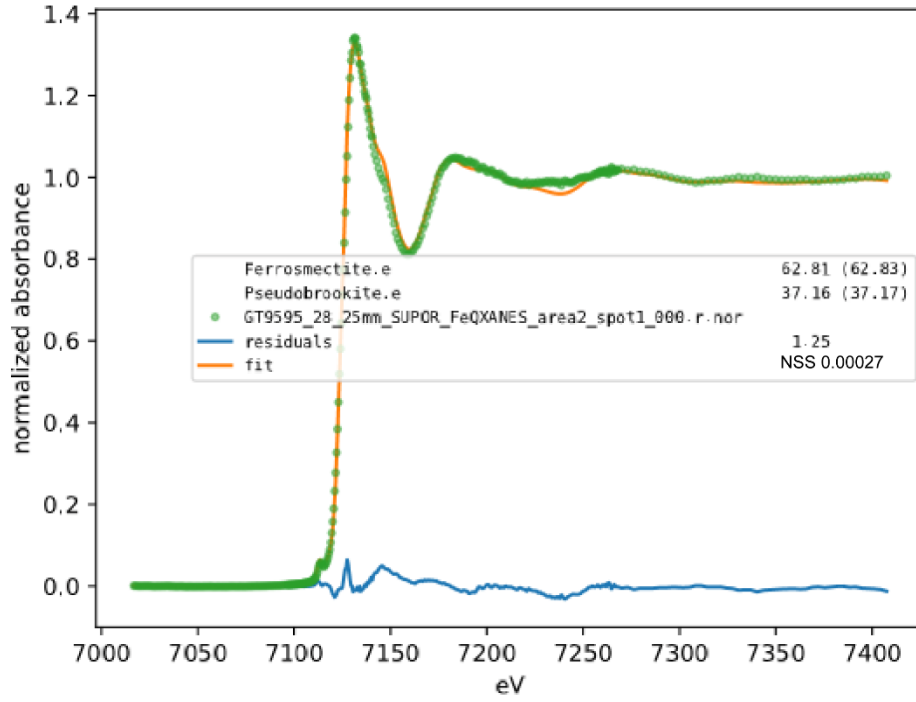


Figure 2.5.146 Fe XANES Station 28 area 2 spot 1

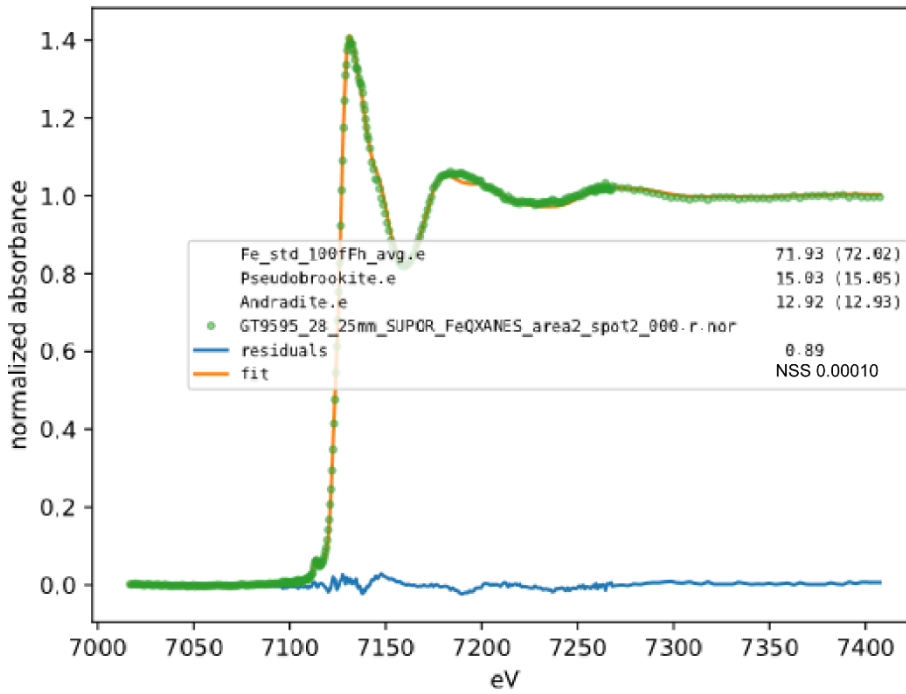


Figure 2.5.147 Fe XANES Station 28 area 2 spot 2

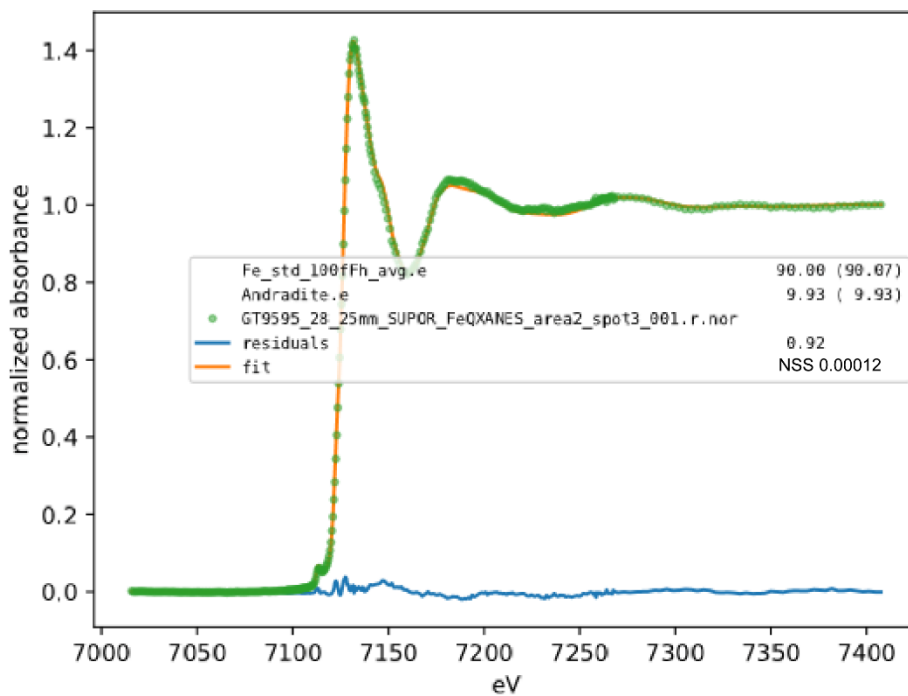


Figure 2.5.148 Fe XANES Station 28 area 2 spot 3

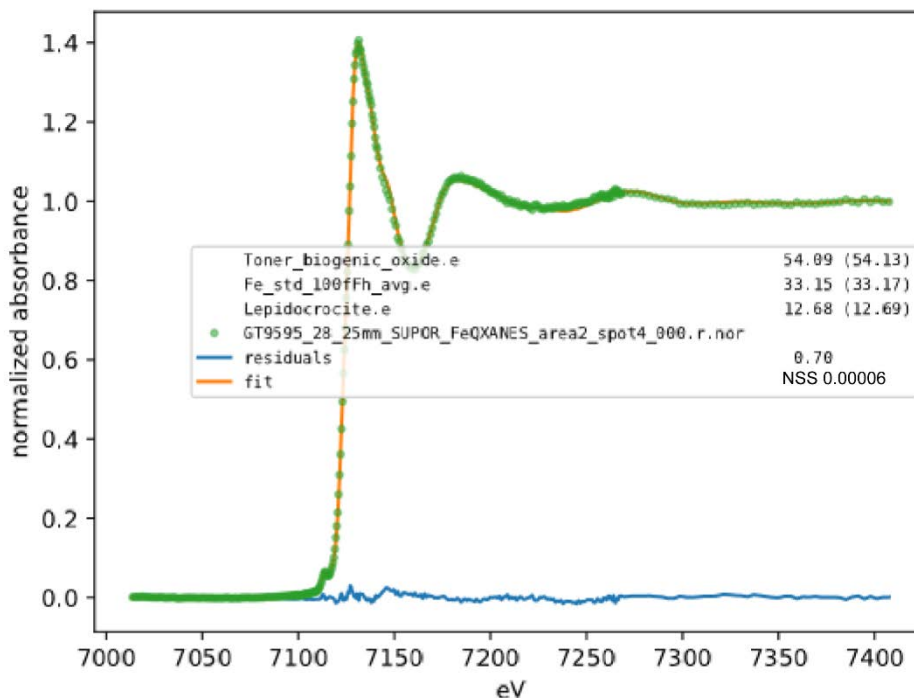


Figure 2.5.149 Fe XANES Station 28 area 2 spot 4

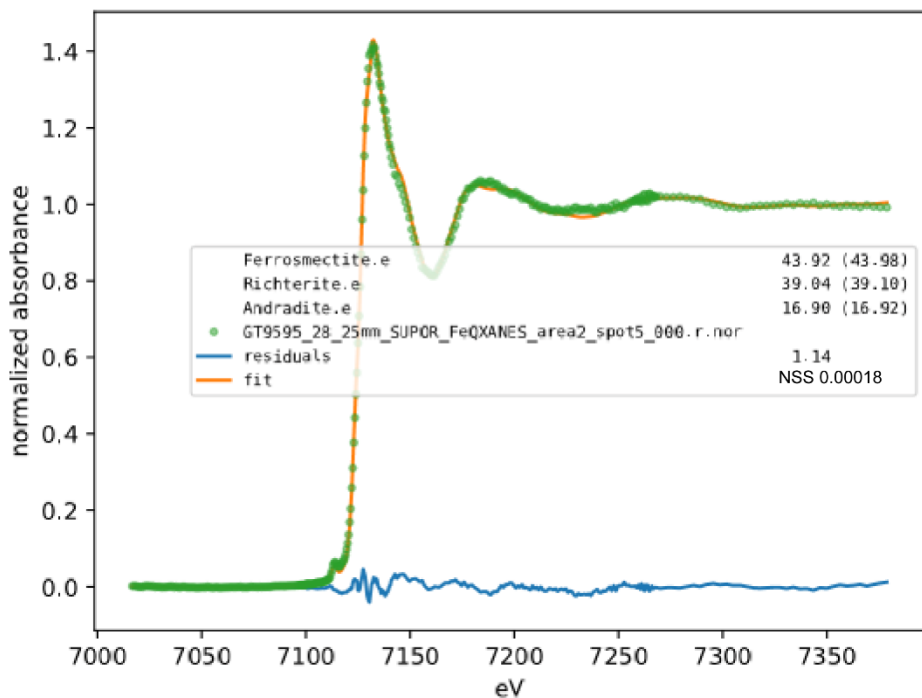


Figure 2.5.150 Fe XANES Station 28 area 2 spot 5

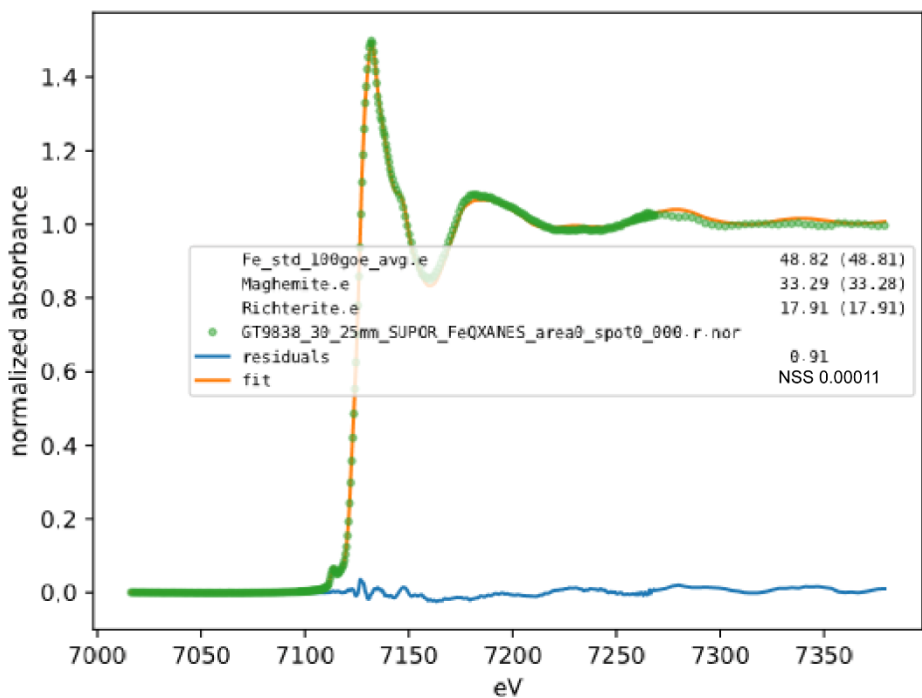


Figure 2.5.151 Fe XANES Station 30 area 0 spot 0

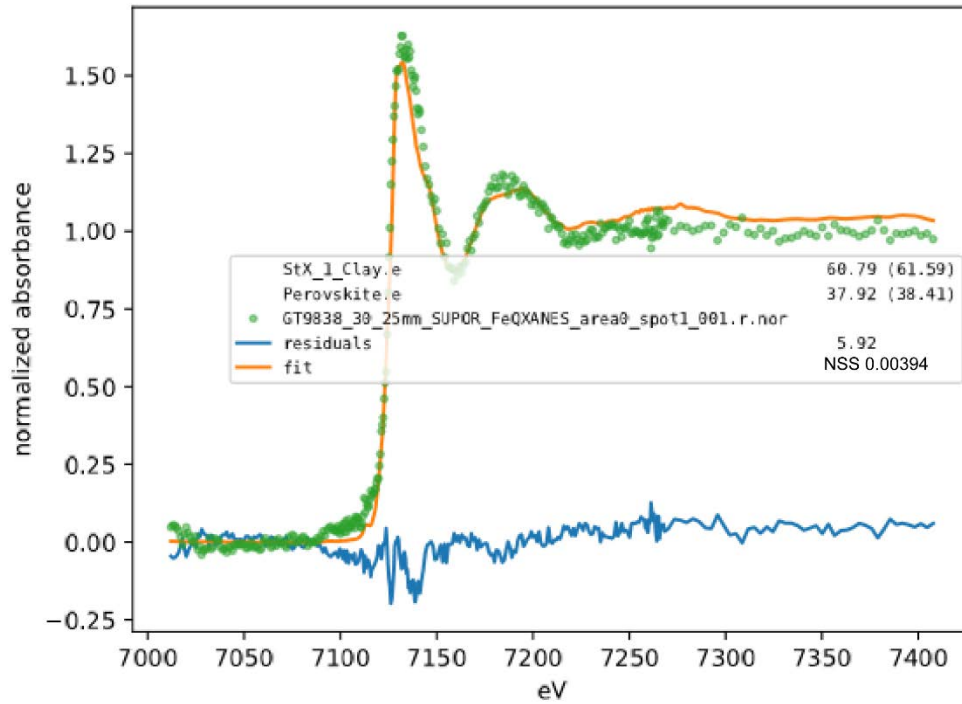


Figure 2.5.152 Fe XANES Station 30 area 0 spot 1

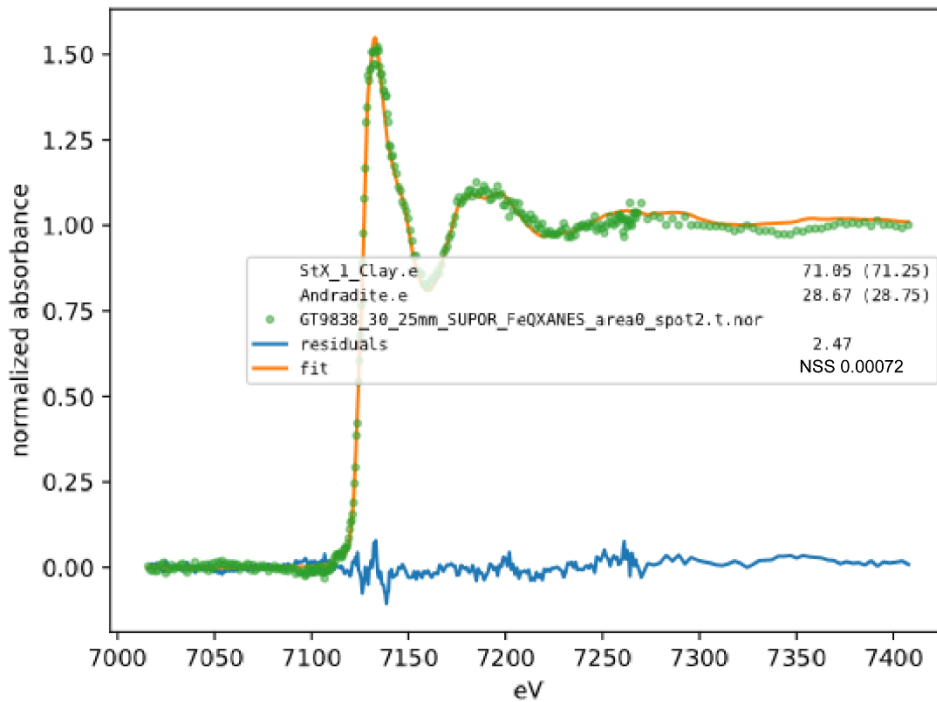


Figure 2.5.153 Fe XANES Station 30 area 0 spot 2.t

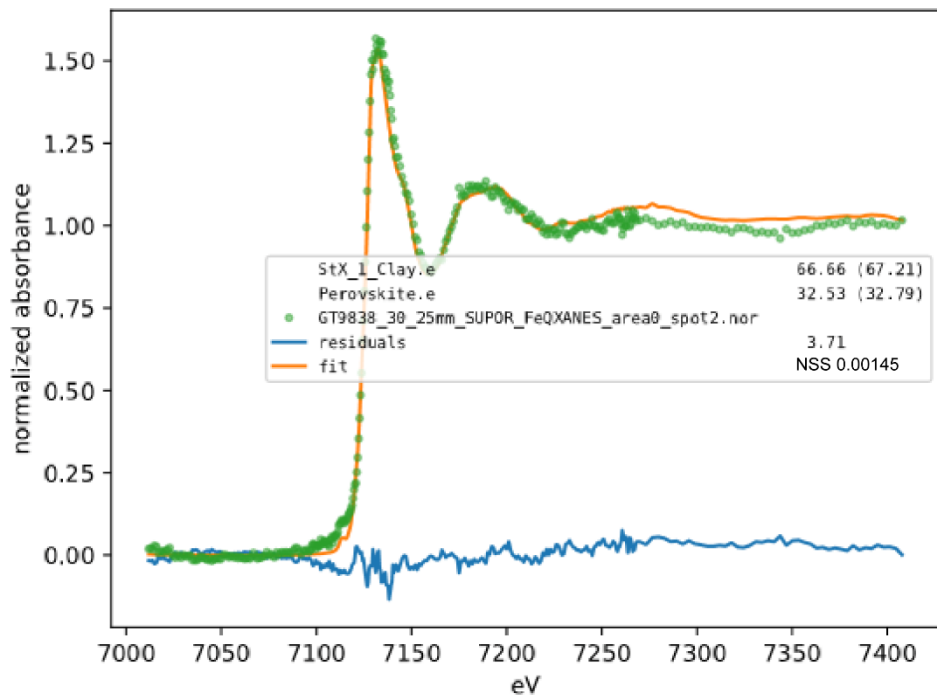


Figure 2.5.154 Fe XANES Station 30 area 0 spot 2

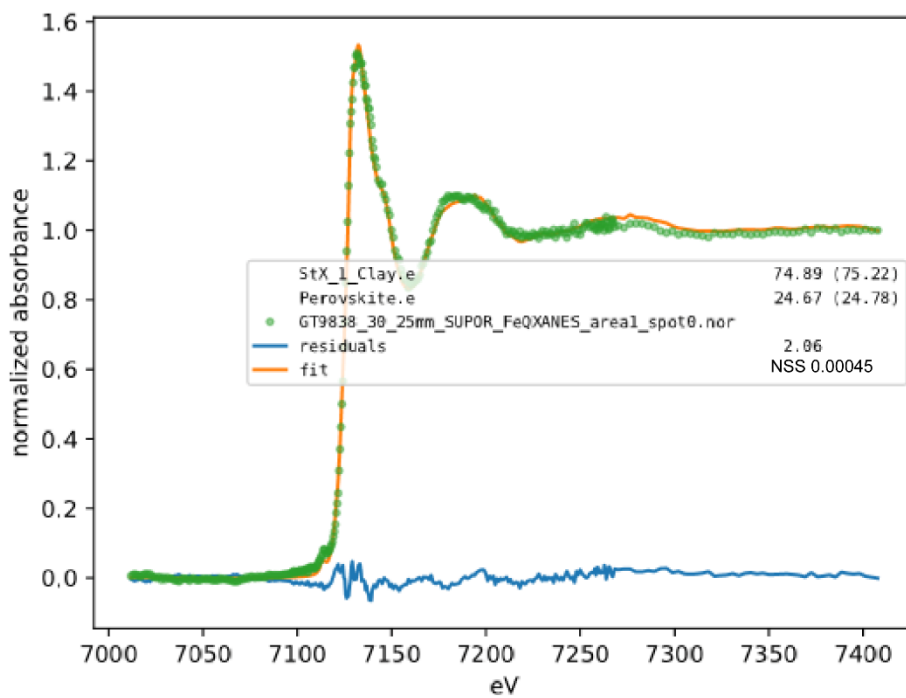


Figure 2.5.155 Fe XANES Station 30 area 1 spot 0

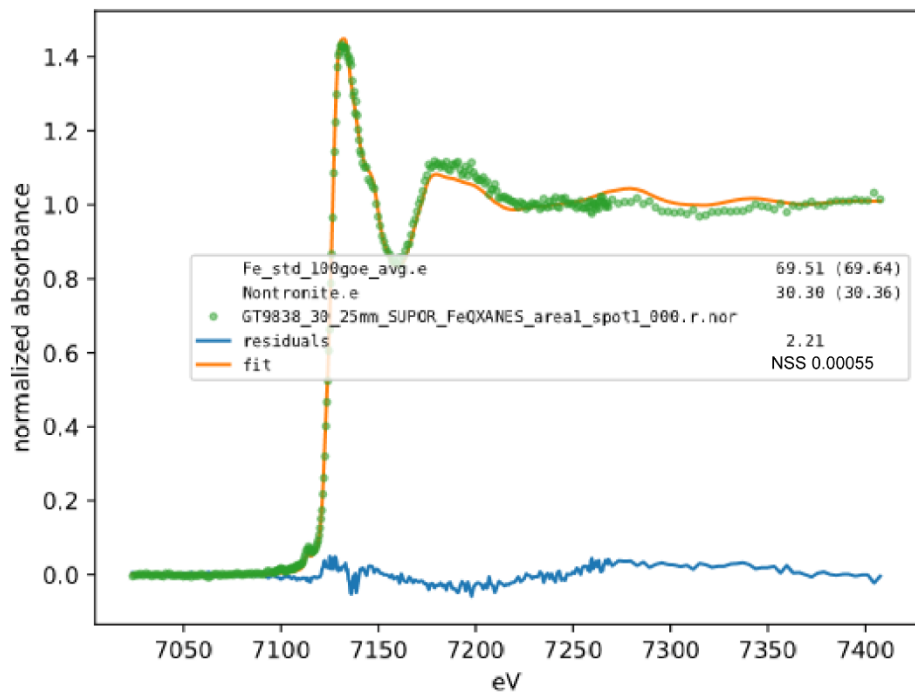


Figure 2.5.156 Fe XANES Station 30 area 1 spot 1

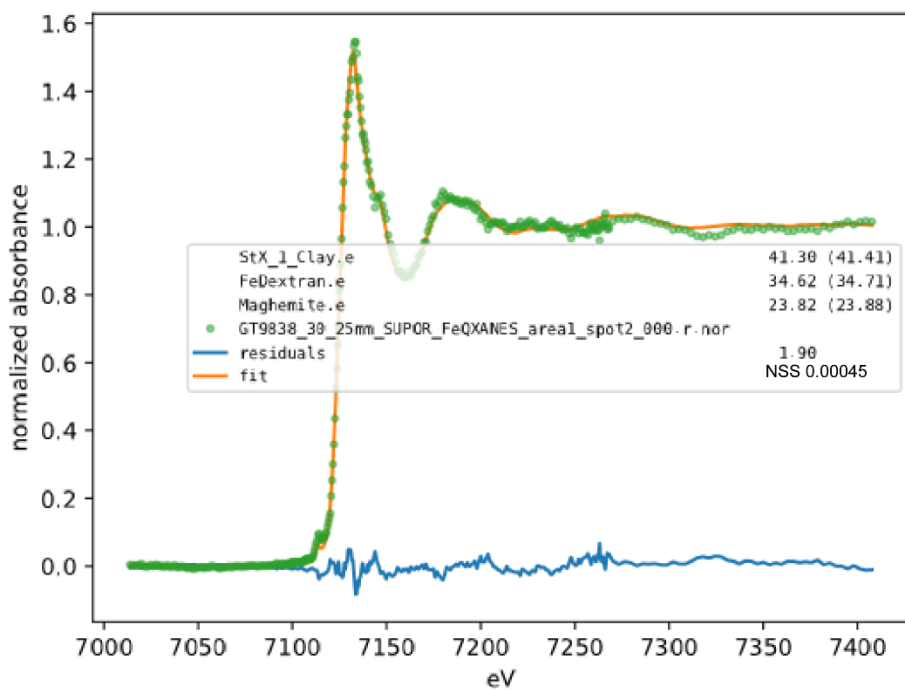


Figure 2.5.157 Fe XANES Station 30 area 1 spot 2

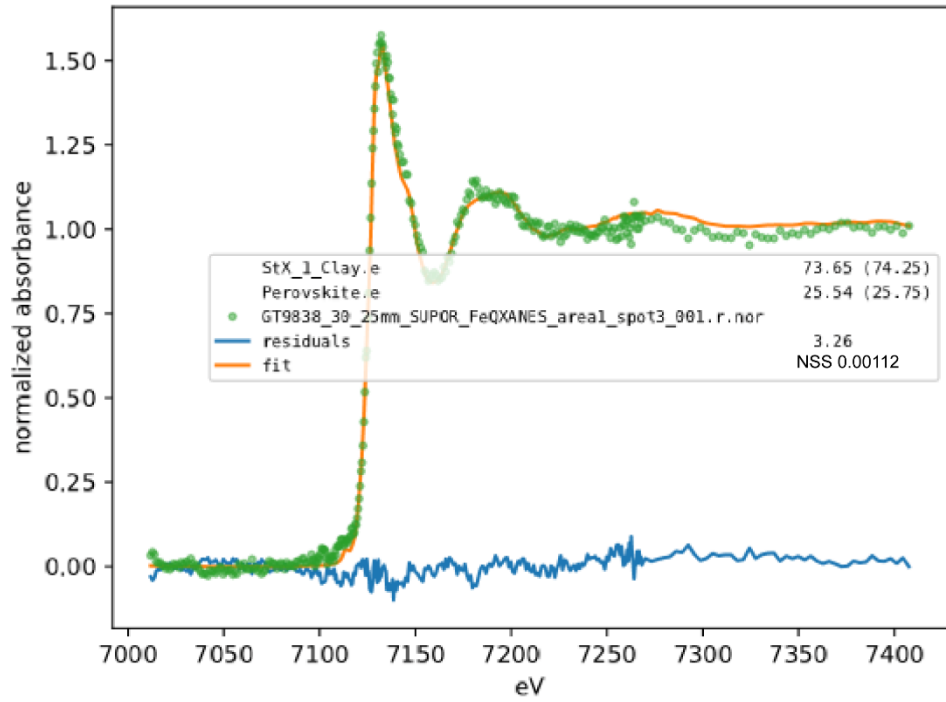


Figure 2.5.158 Fe XANES Station 30 area 1 spot 3

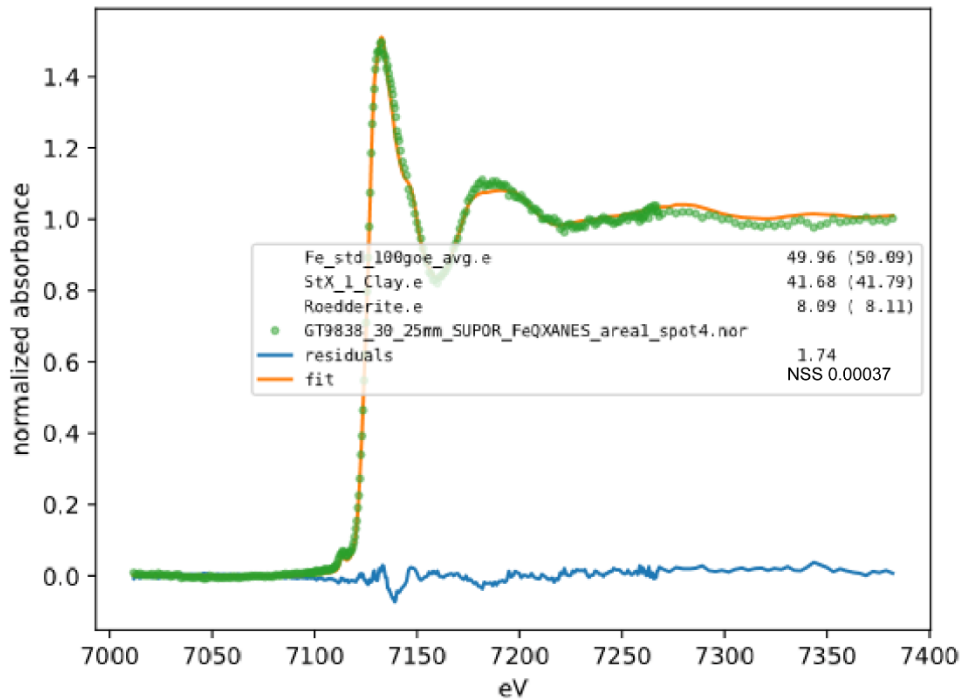


Figure 2.5.159 Fe XANES Station 30 area 1 spot 4

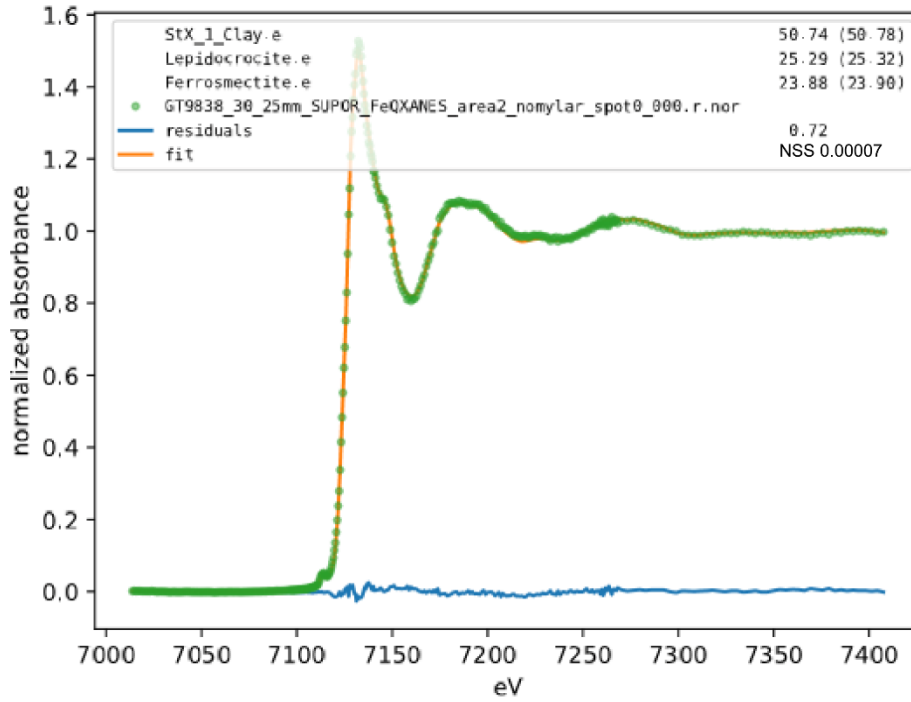


Figure 2.5.160 Fe XANES Station 30 area 2 spot 0

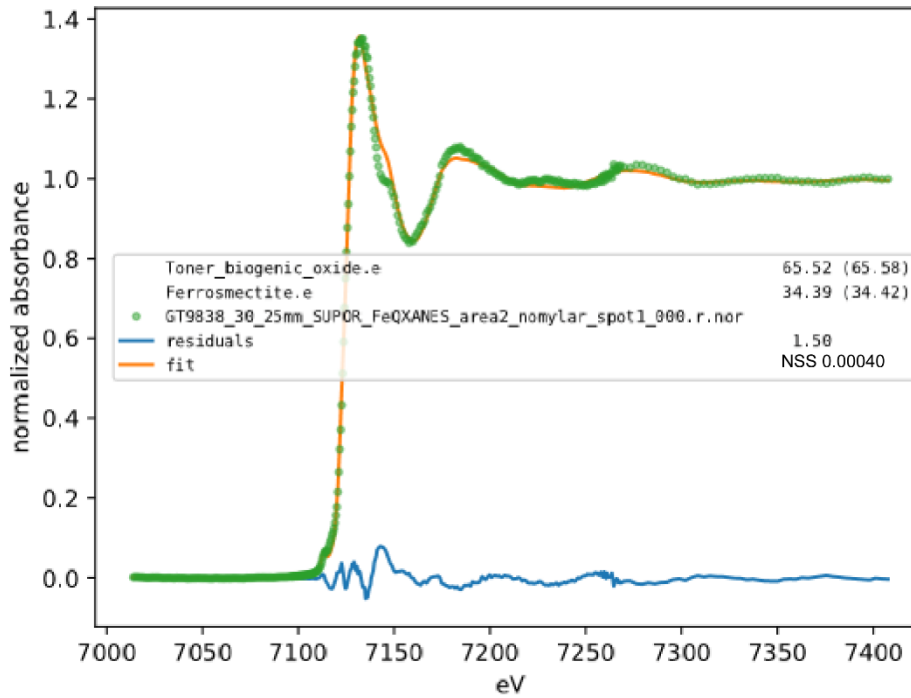


Figure 2.5.161 Fe XANES Station 30 area 2 spot 1

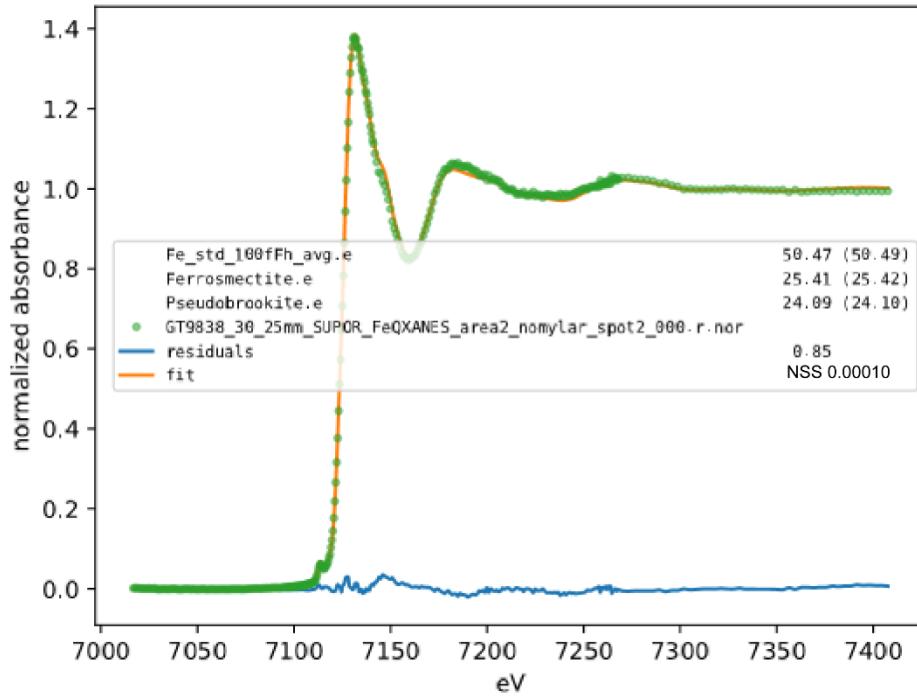


Figure 2.5.162 Fe XANES Station 30 area 2 spot 2

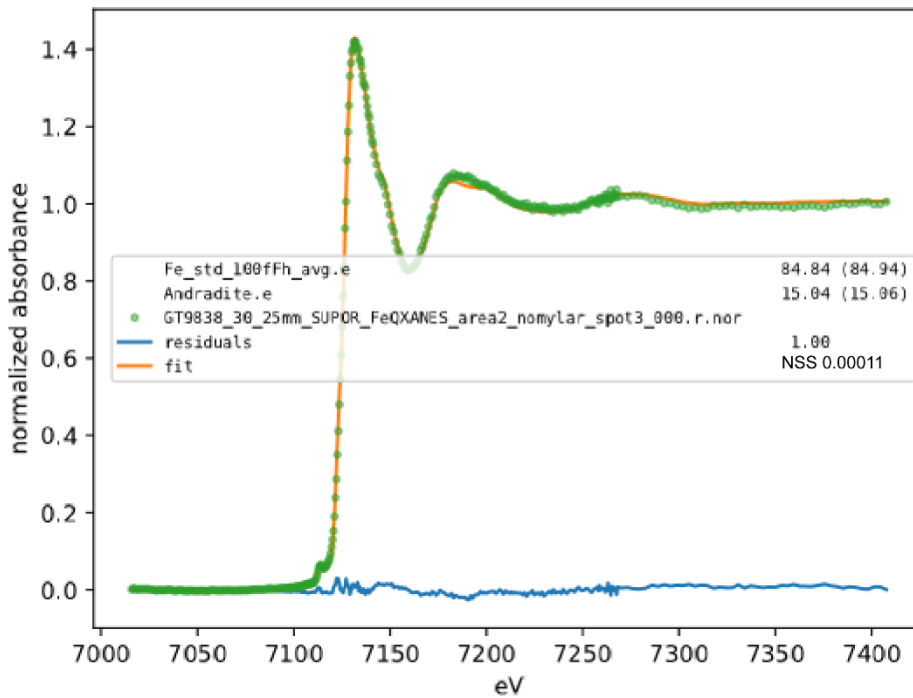


Figure 2.5.163 Fe XANES Station 30 area 2 spot 3

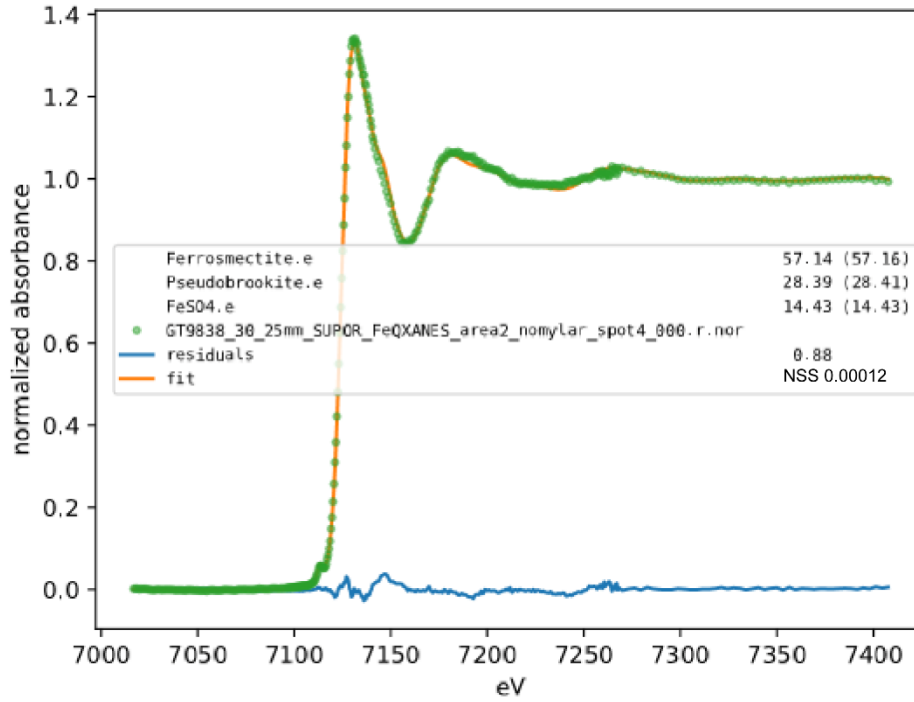


Figure 2.5.164 Fe XANES Station 30 area 2 spot 4

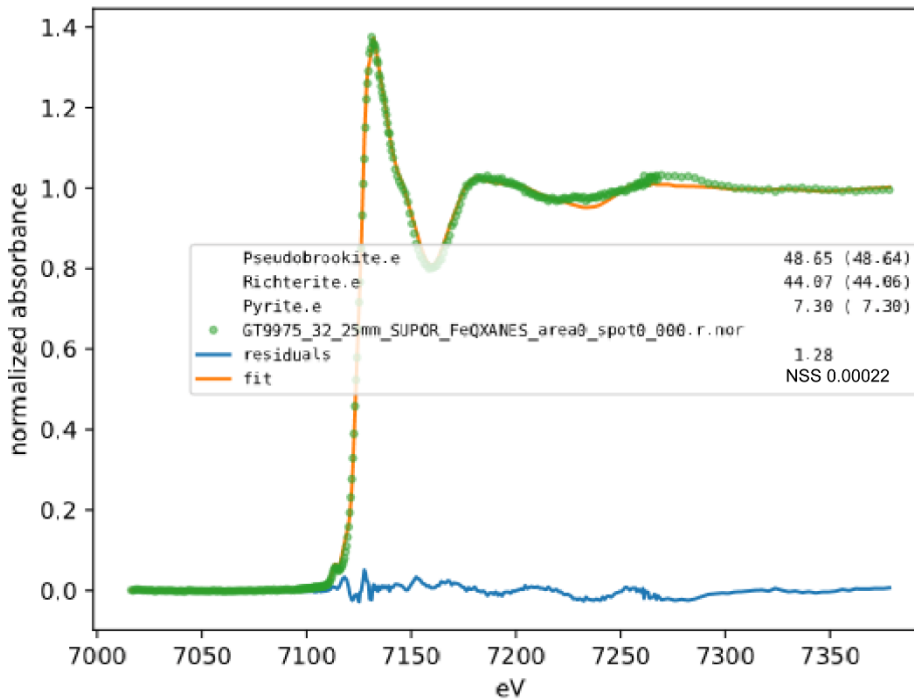


Figure 2.5.165 Fe XANES Station 32 area 0 spot 0

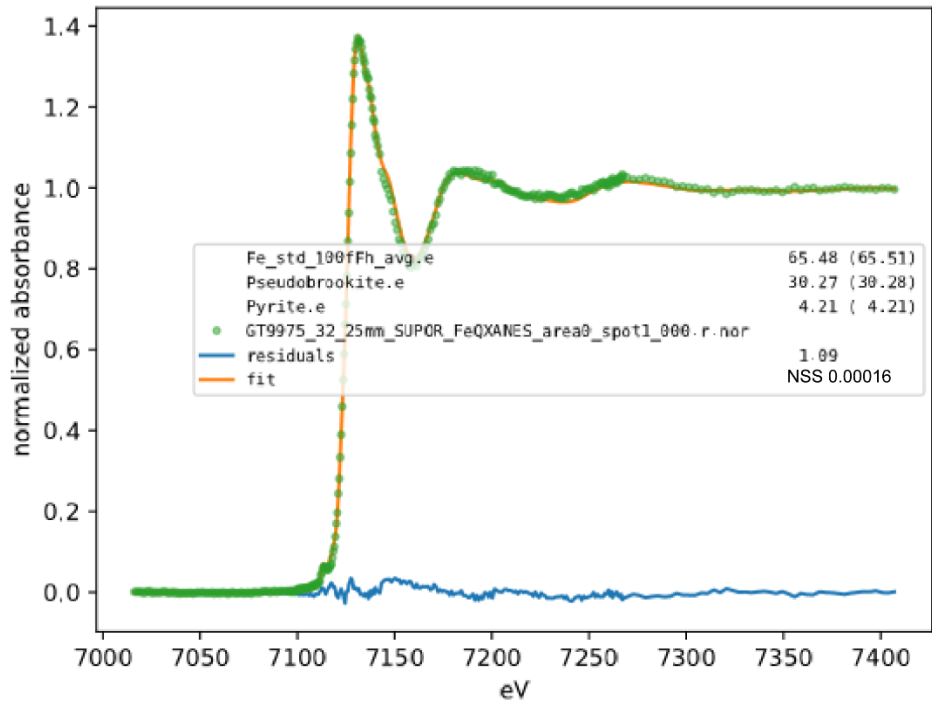


Figure 2.5.166 Fe XANES Station 32 area 0 spot 1

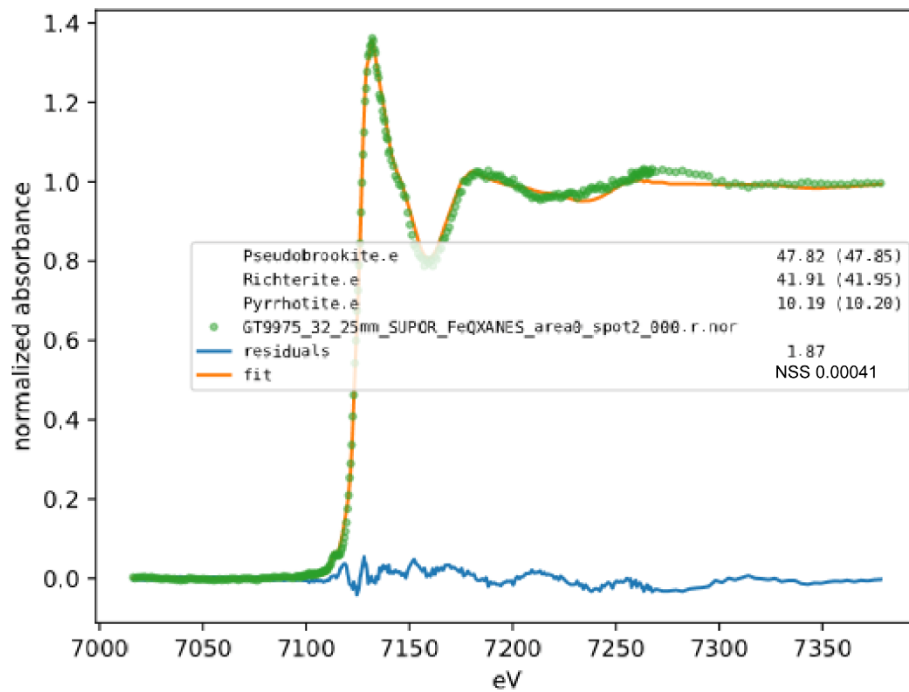


Figure 2.5.167 Fe XANES Station 32 area 0 spot 2

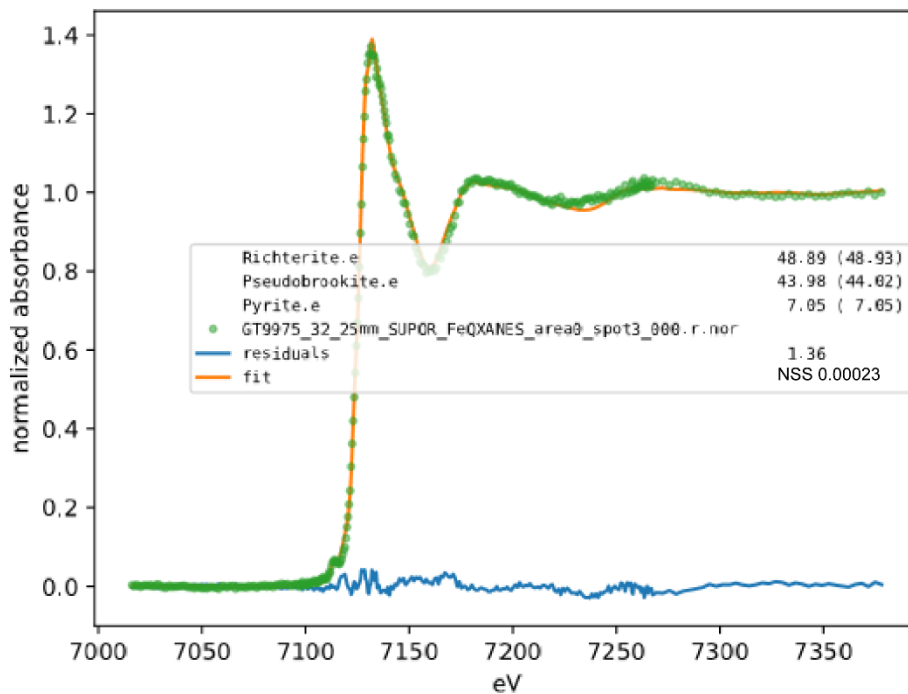


Figure 2.5.168 Fe XANES Station 32 area 0 spot 3

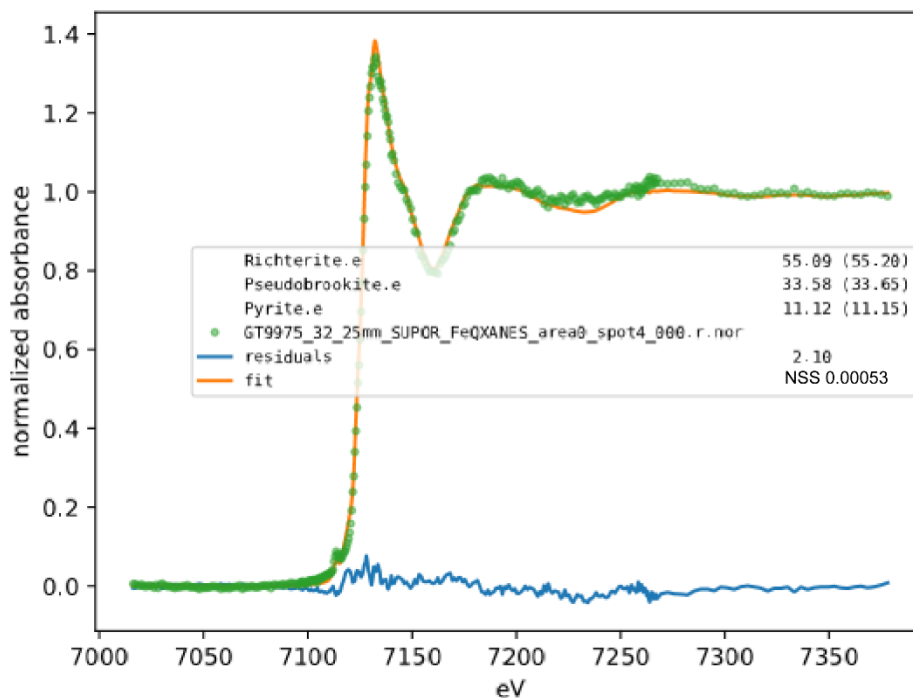


Figure 2.5.169 Fe XANES Station 32 area 0 spot 4

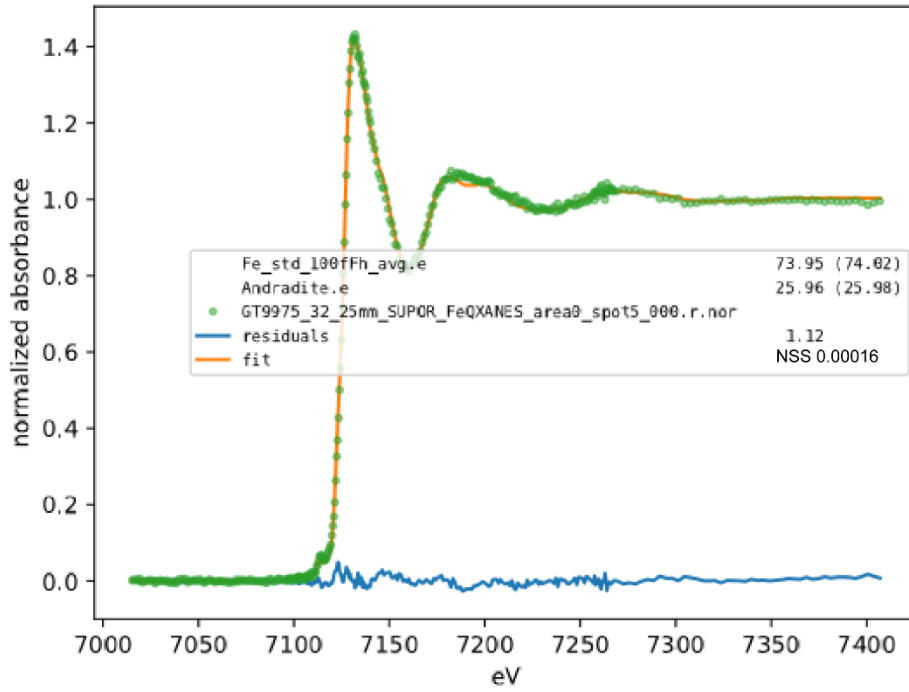


Figure 2.5.170 Fe XANES Station 32 area 0 spot 5

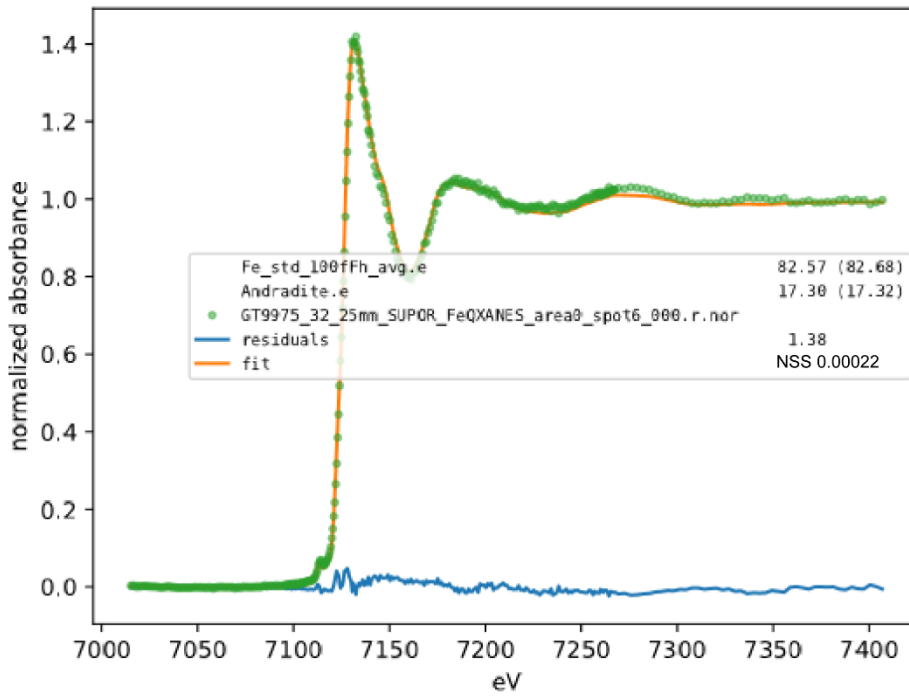


Figure 2.5.171 Fe XANES Station 32 area 0 spot 6

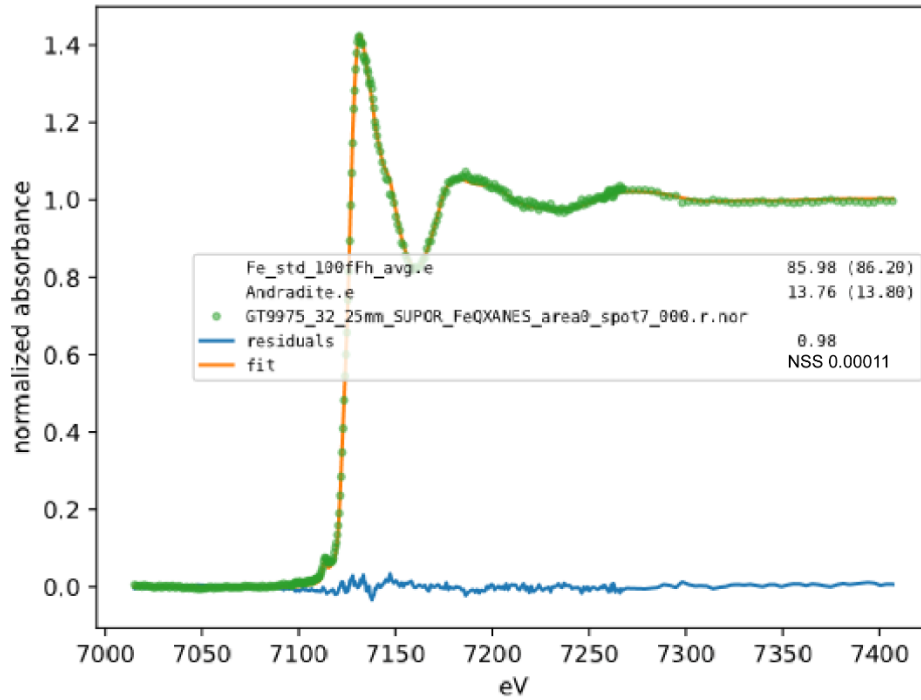


Figure 2.5.172 Fe XANES Station 32 area 0 spot 7

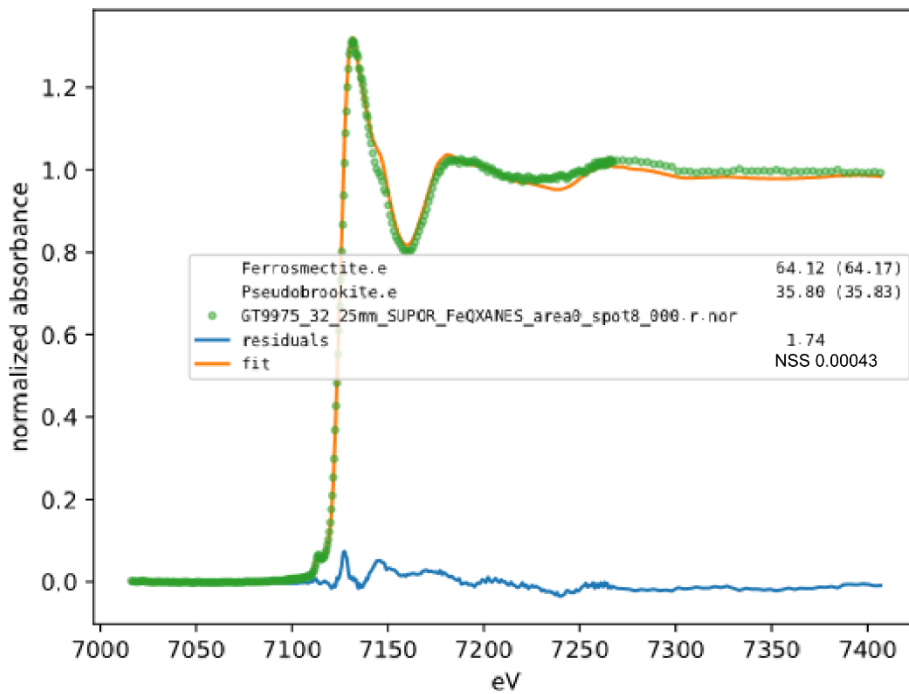


Figure 2.5.173 Fe XANES Station 32 area 0 spot 8

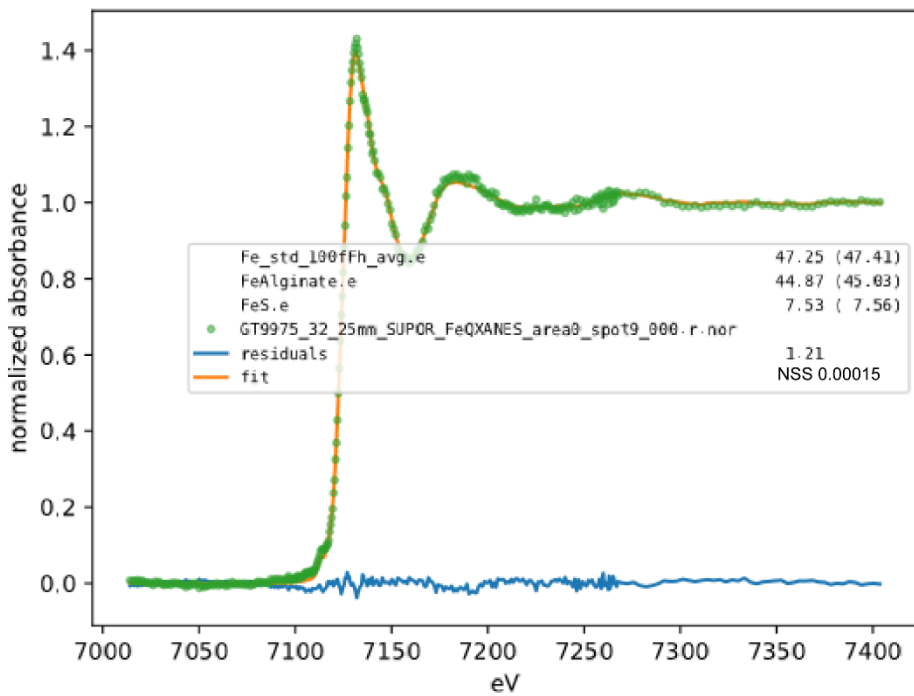


Figure 2.5.174 Fe XANES Station 32 area 0 spot 9

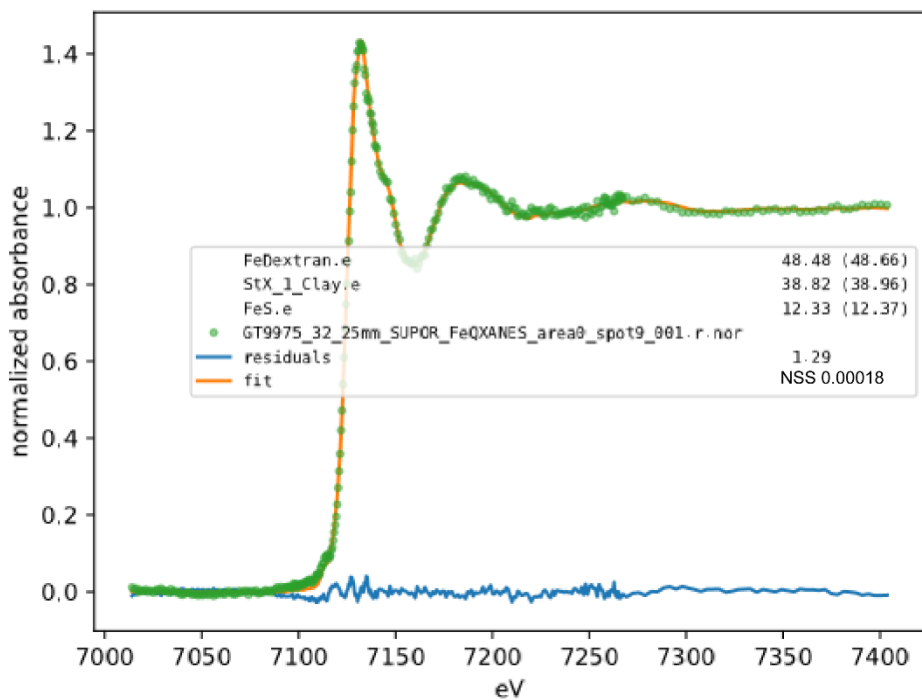


Figure 2.5.175 Fe XANES Station 32 area 0 spot 9.1

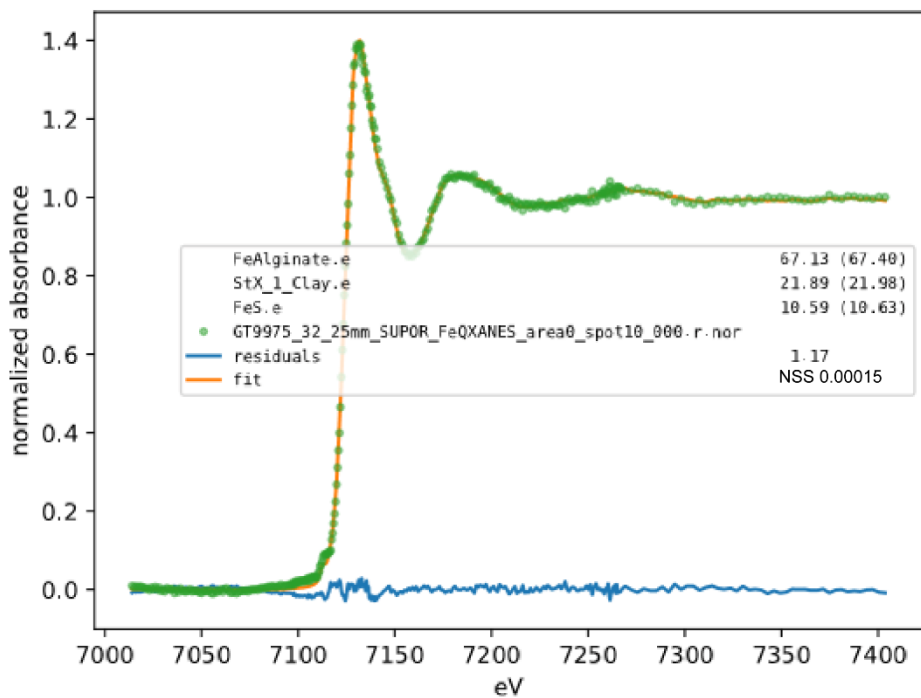


Figure 2.5.176 Fe XANES Station 32 area 0 spot 10

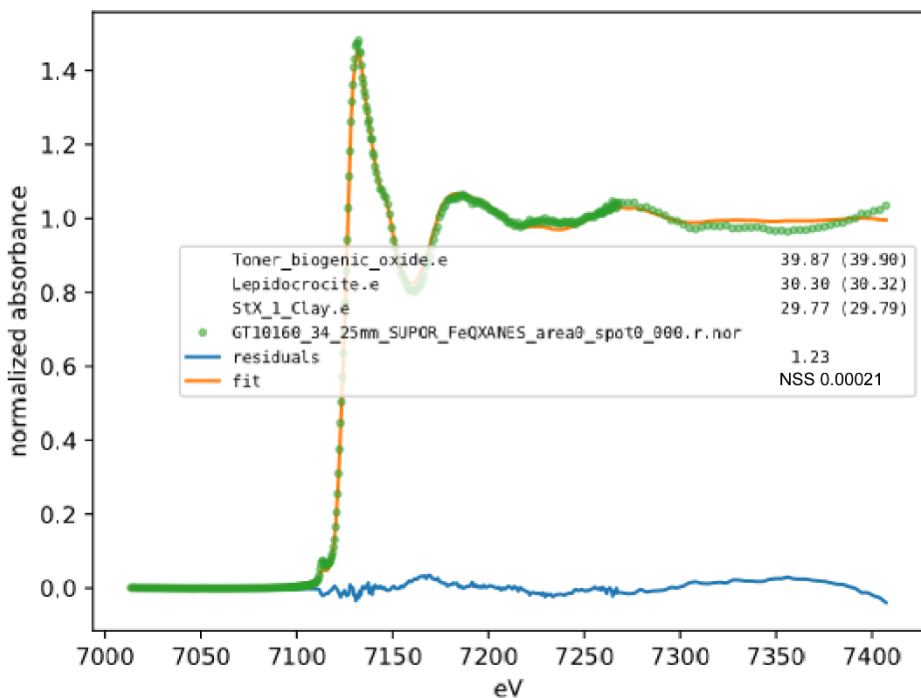


Figure 2.5.177 Fe XANES Station 34 area 0 spot 0

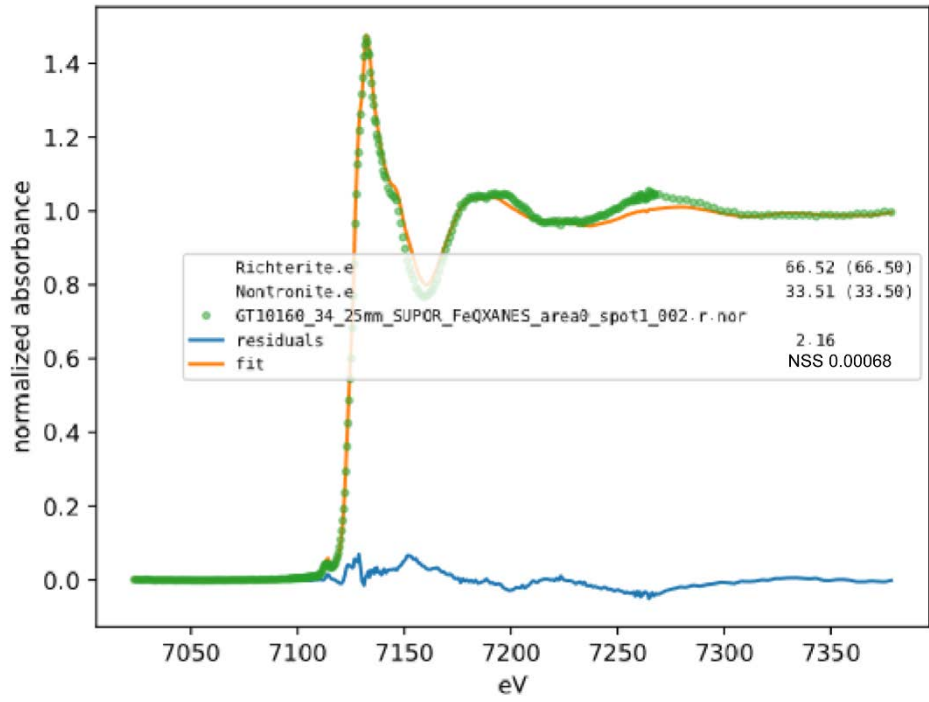


Figure 2.5.178 Fe XANES Station 34 area 0 spot 1

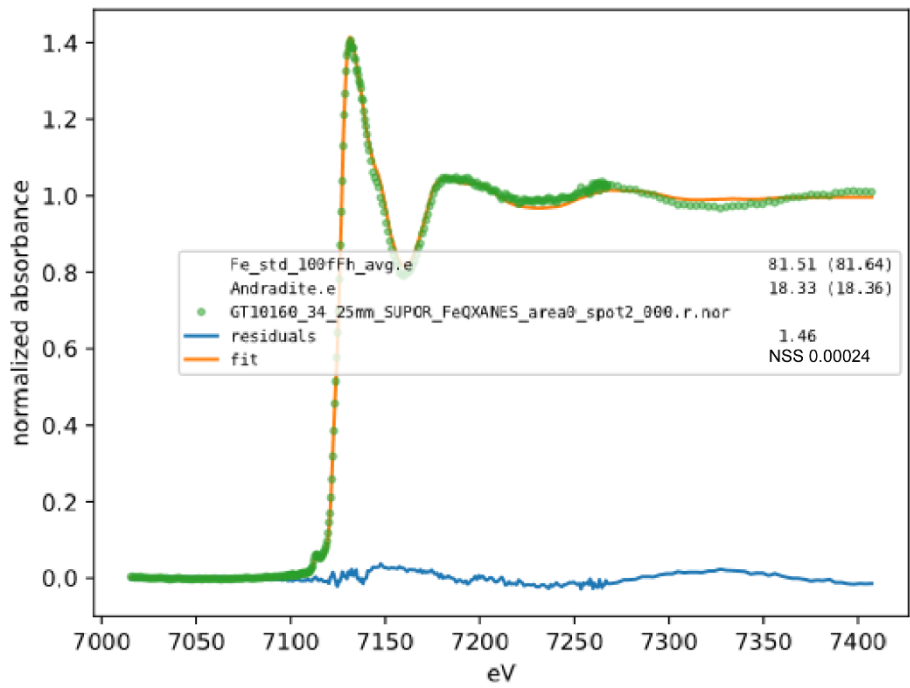


Figure 2.5.179 Fe XANES Station 34 area 0 spot 2

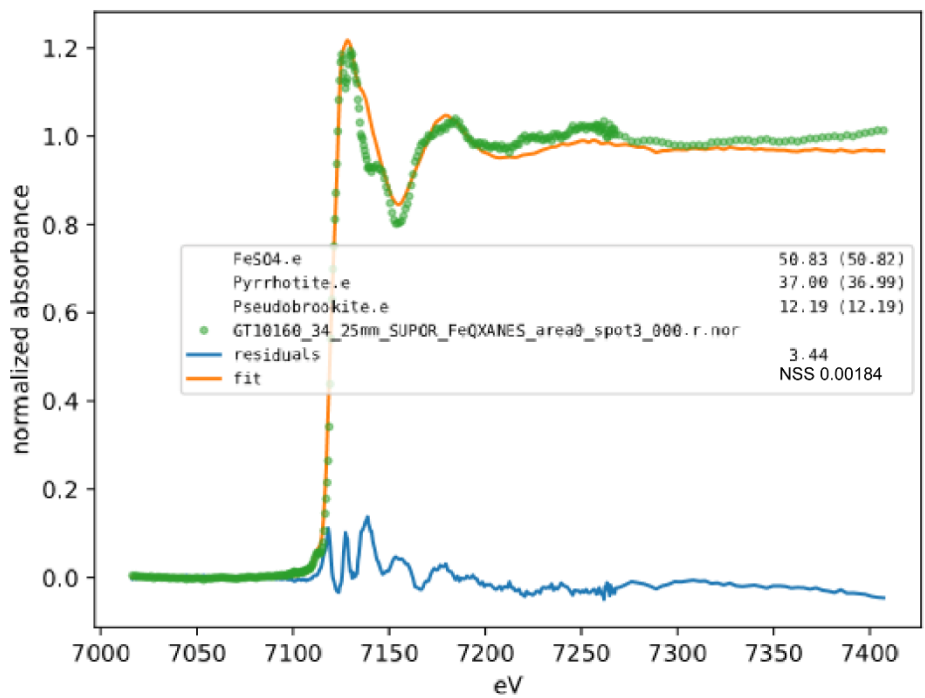


Figure 2.5.180 Fe XANES Station 34 area 0 spot 3

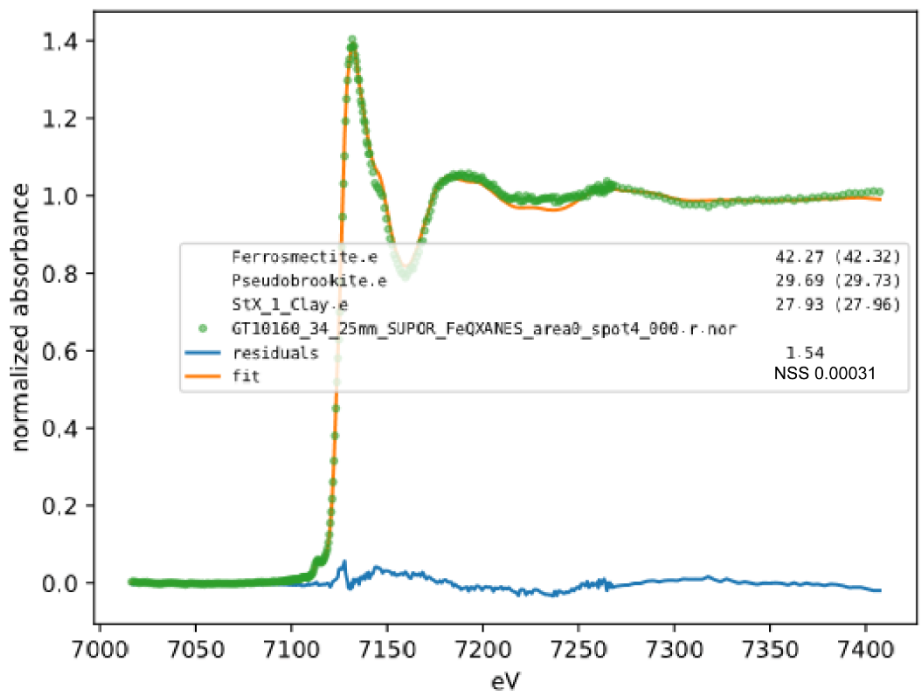


Figure 2.5.181 Fe XANES Station 34 area 0 spot 4

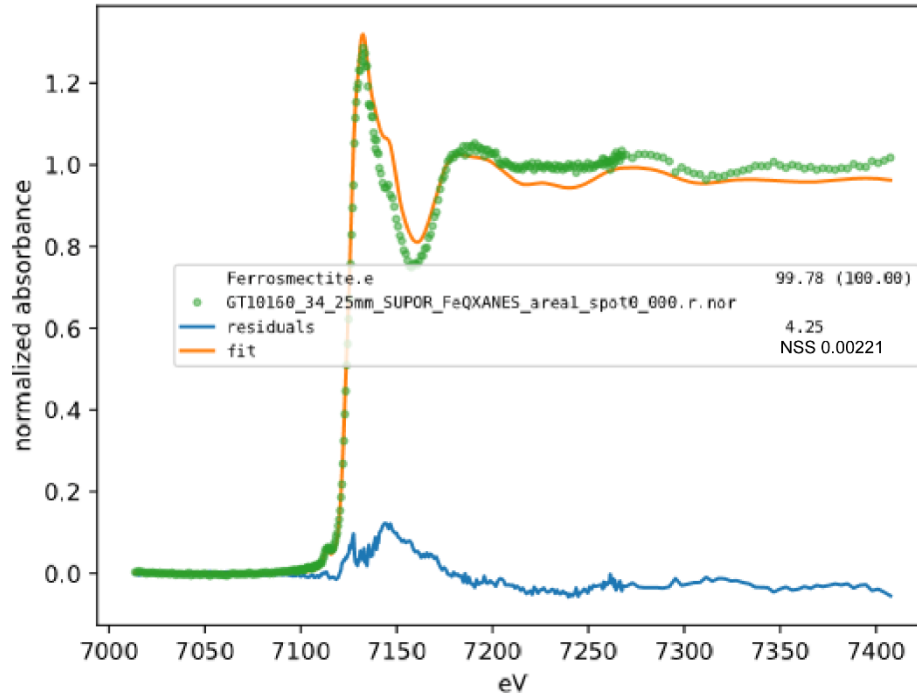


Figure 2.5.182 Fe XANES Station 34 area 1 spot 0

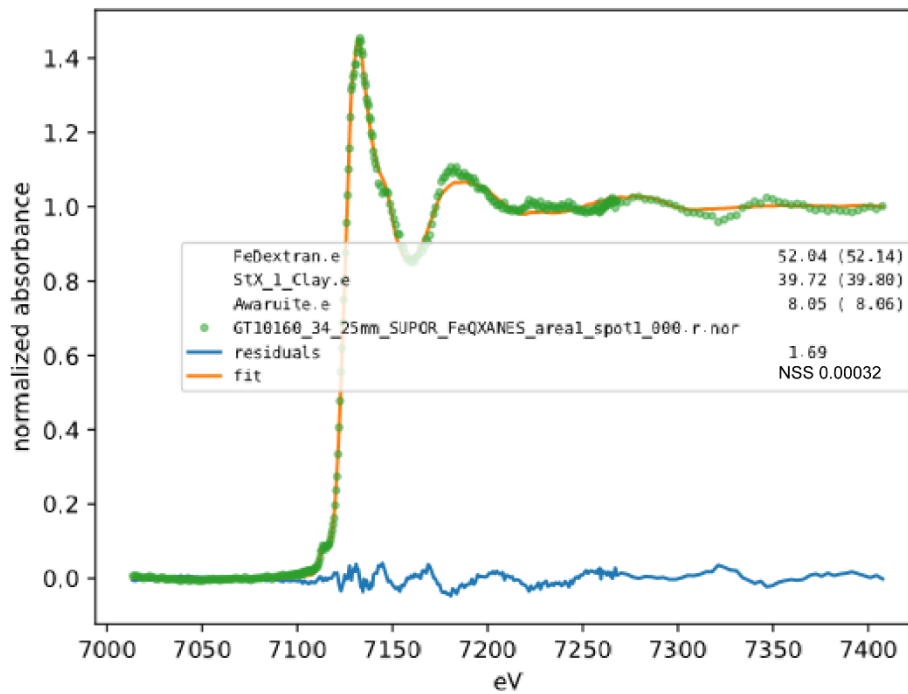


Figure 2.5.183 Fe XANES Station 34 area 1 spot 1

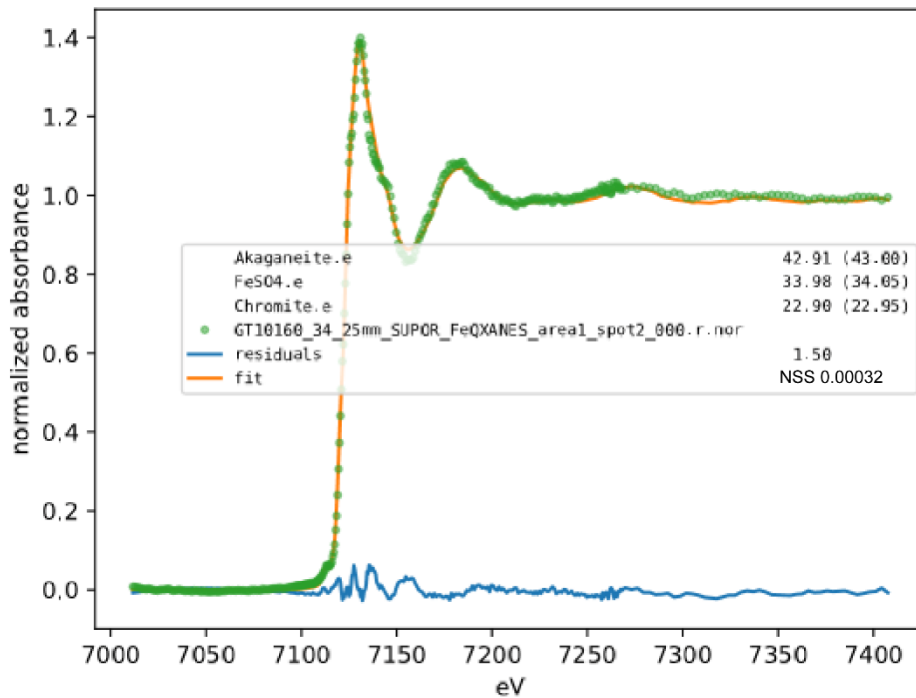


Figure 2.5.184 Fe XANES Station 34 area 1 spot 2

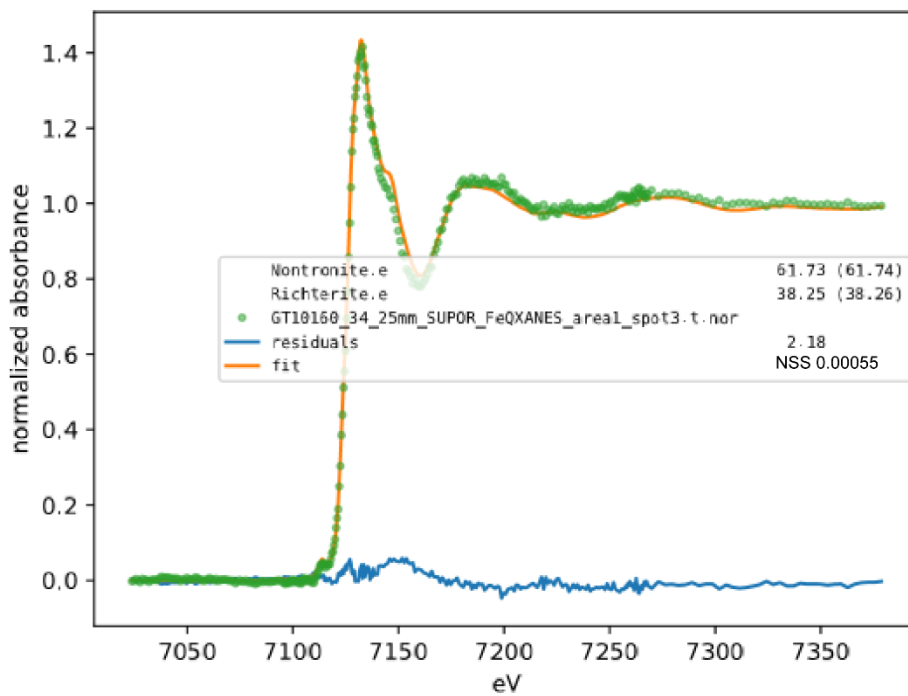


Figure 2.5.185 Fe XANES Station 34 area 1 spot 3

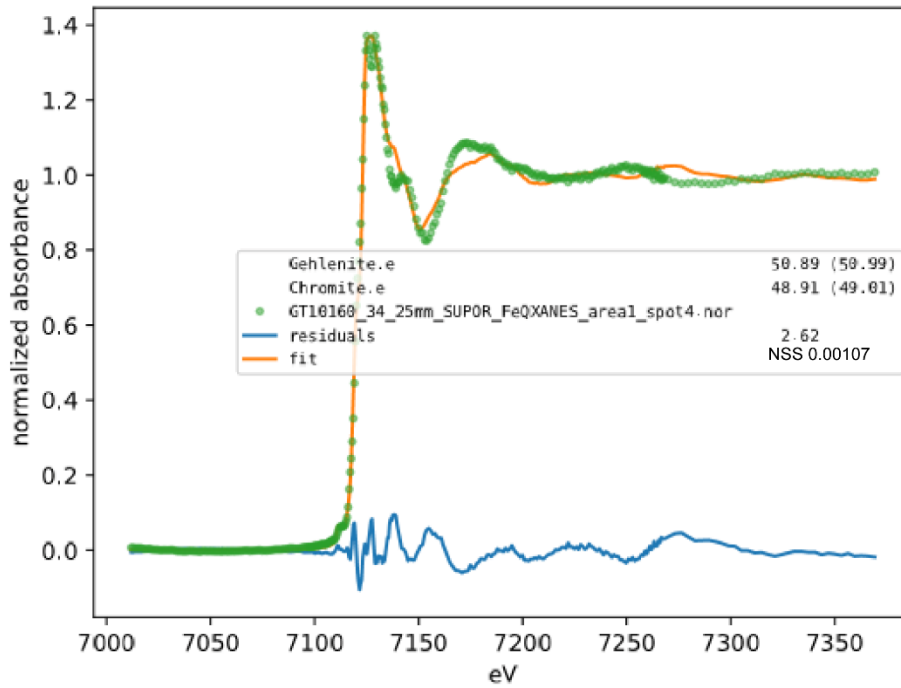


Figure 2.5.186 Fe XANES Station 34 area 1 spot 4

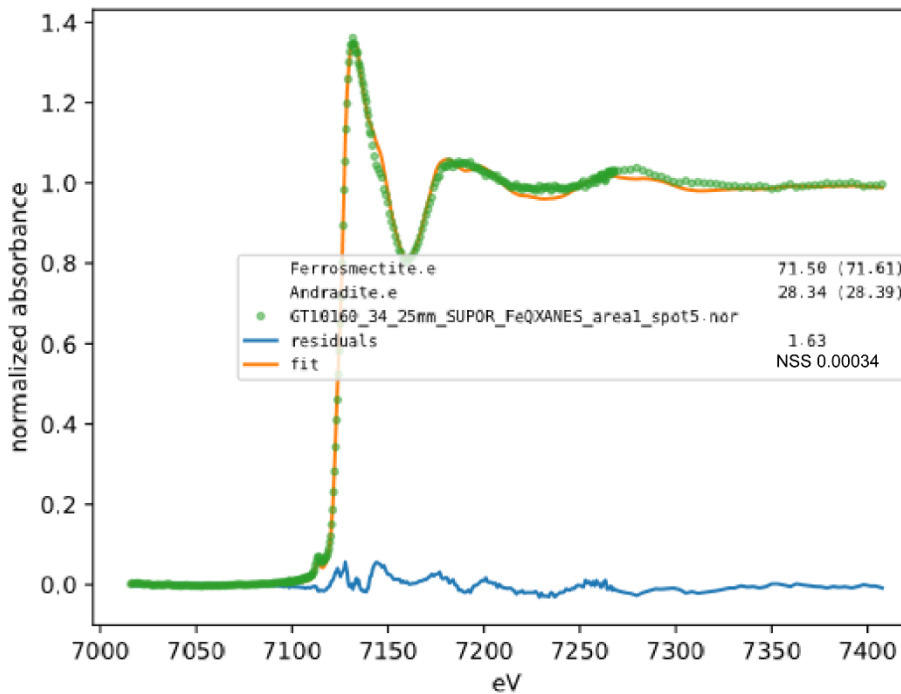


Figure 2.5.187 Fe XANES Station 34 area 1 spot 5

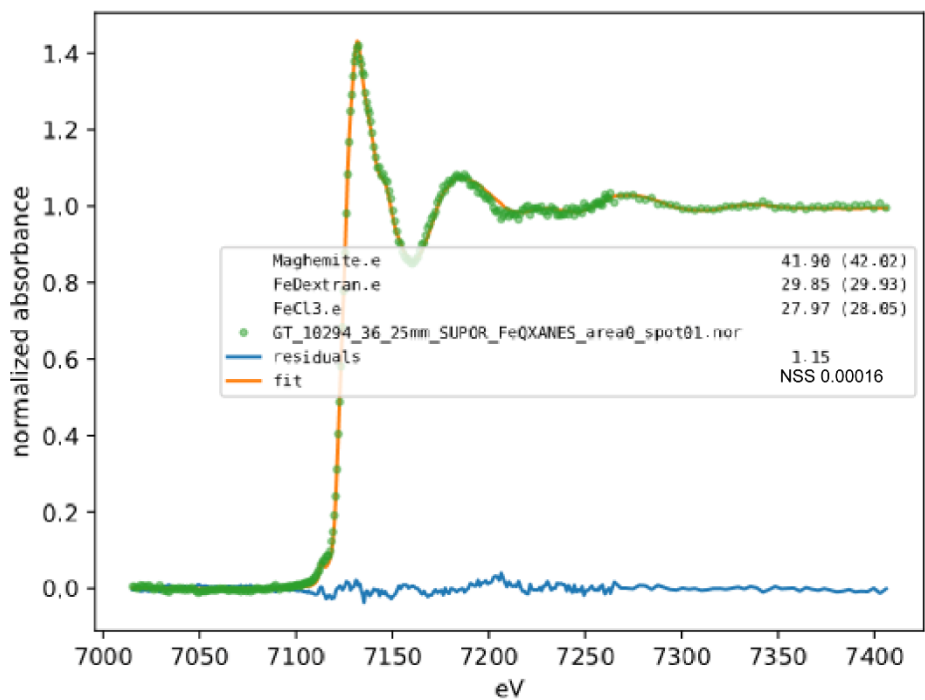


Figure 2.5.188 Fe XANES Station 36 area 0 spot 1

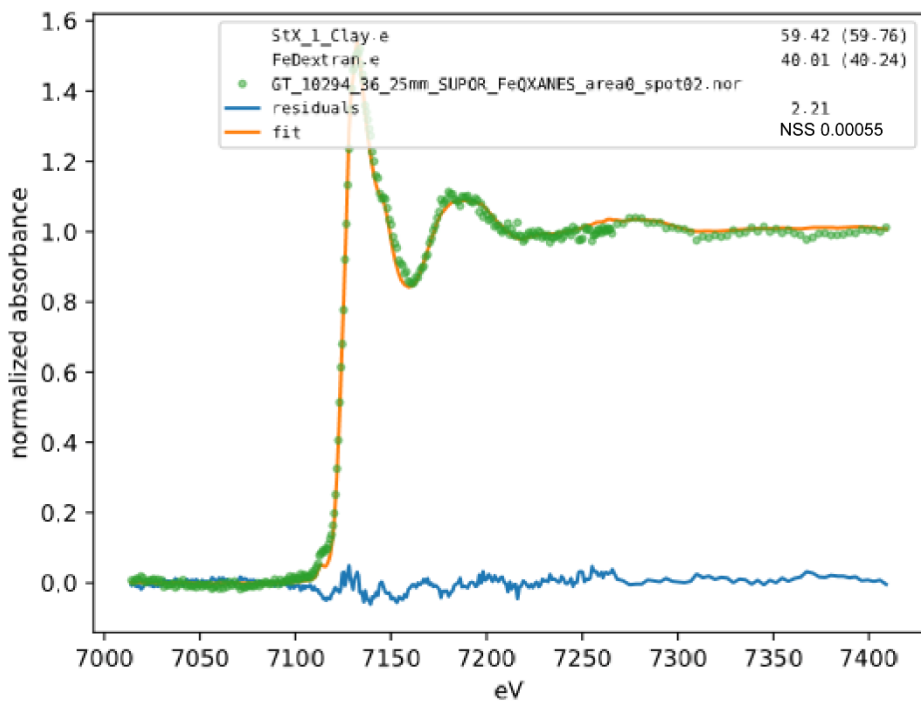


Figure 2.5.189 Fe XANES Station 36 area 0 spot 2

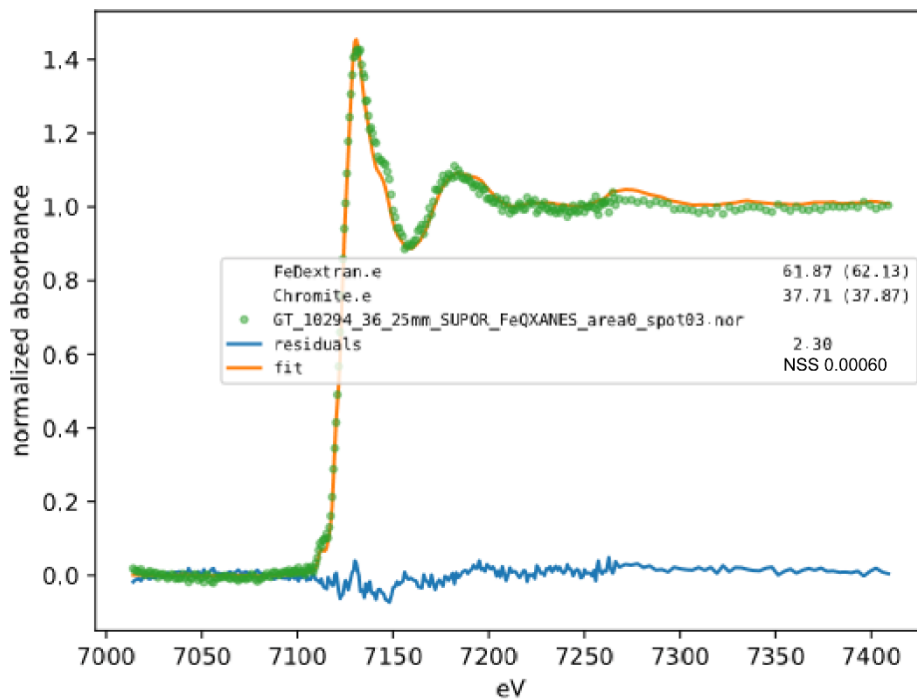


Figure 2.5.190 Fe XANES Station 36 area 0 spot 3

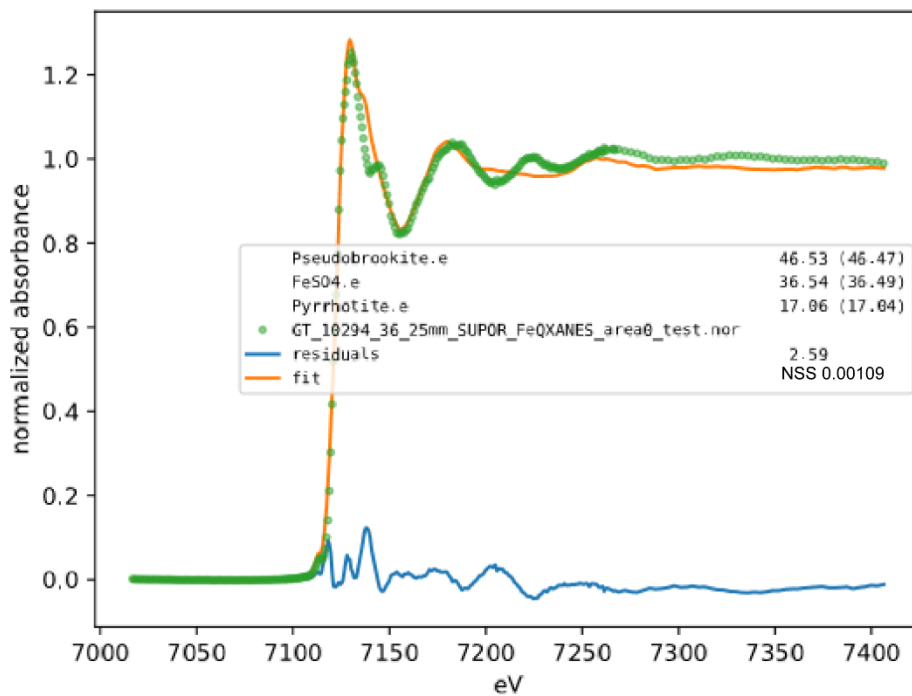


Figure 2.5.191 Fe XANES Station 36 area 0

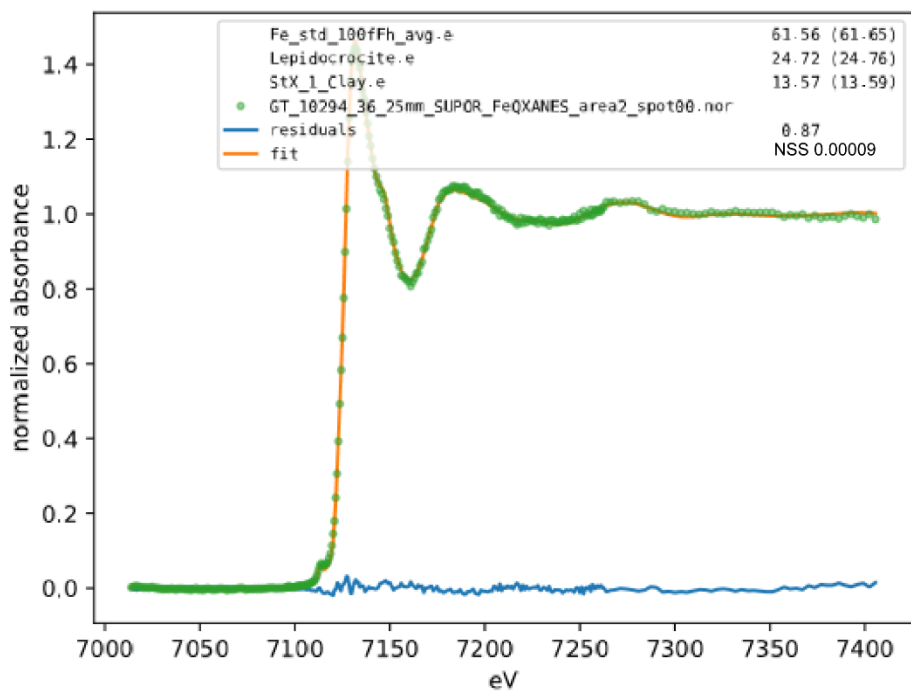


Figure 2.5.192 Fe XANES Station 36 area 2 spot 0

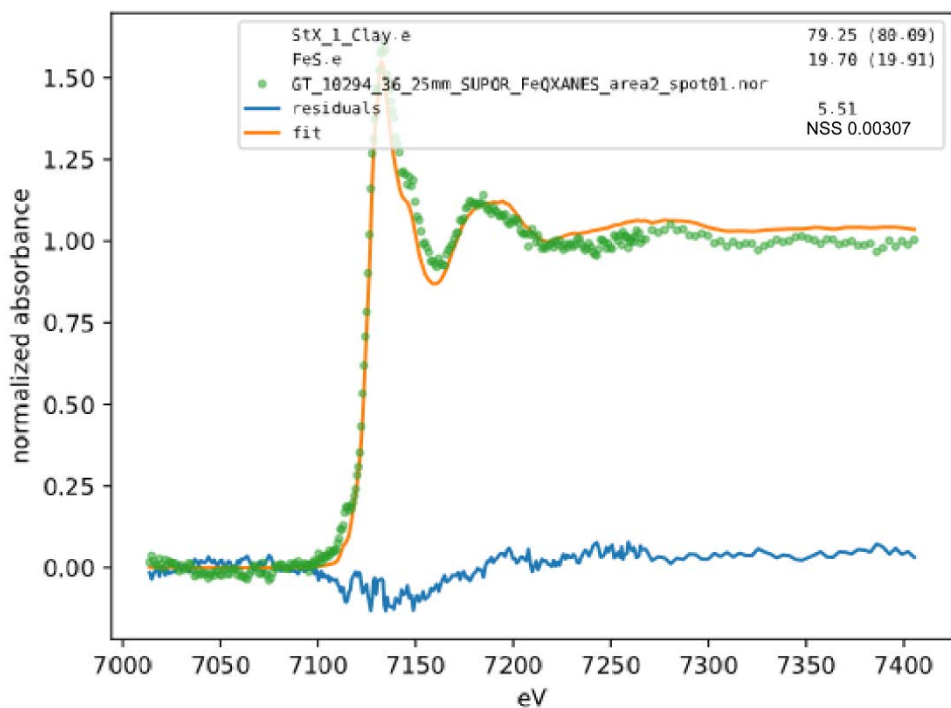


Figure 2.5.193 Fe XANES Station 36 area 2 spot 1

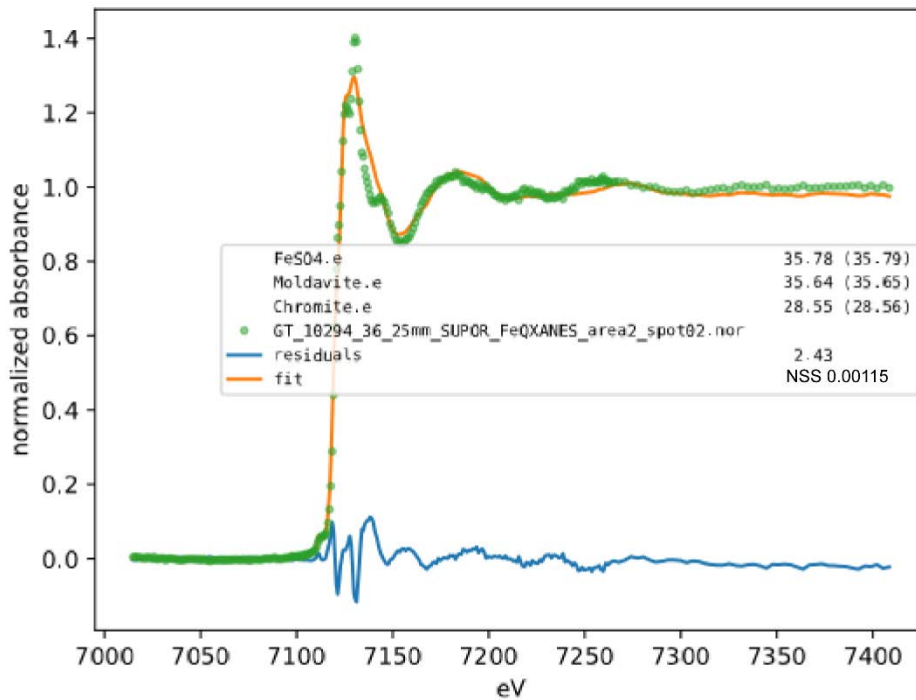


Figure 2.5.194 Fe XANES Station 36 area 2 spot 2

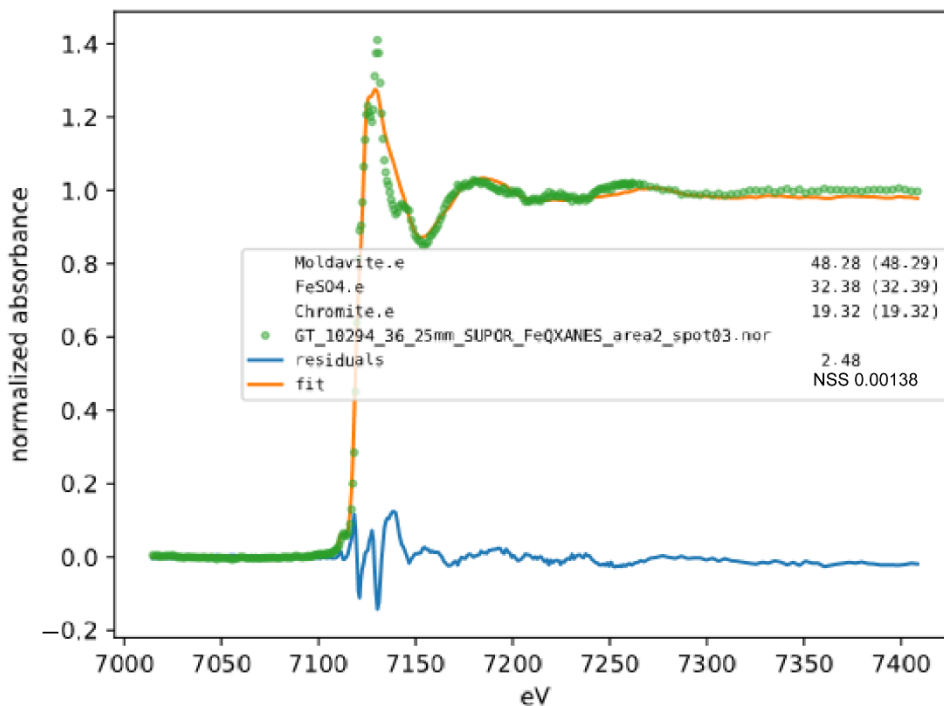


Figure 2.5.195 Fe XANES Station 36 area 2 spot 3

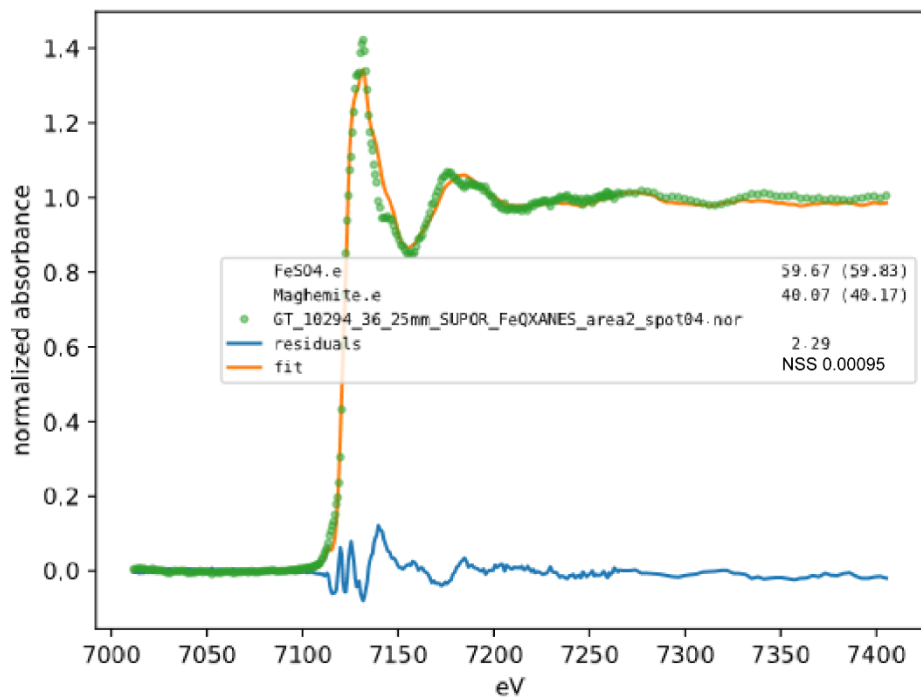


Figure 2.5.196 Fe XANES Station 36 area 2 spot 4

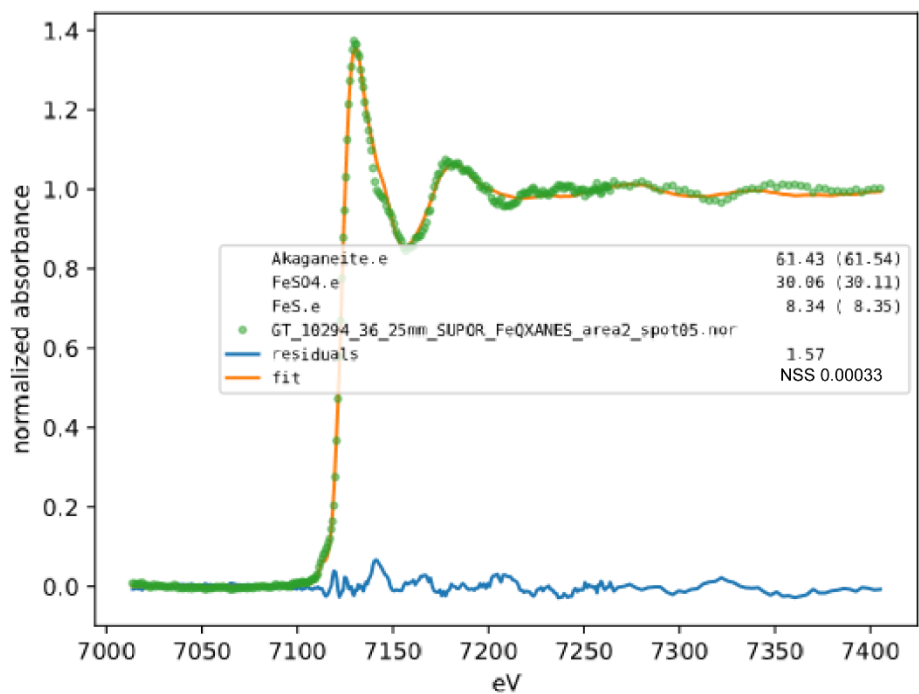


Figure 2.5.197 Fe XANES Station 36 area 2 spot 5

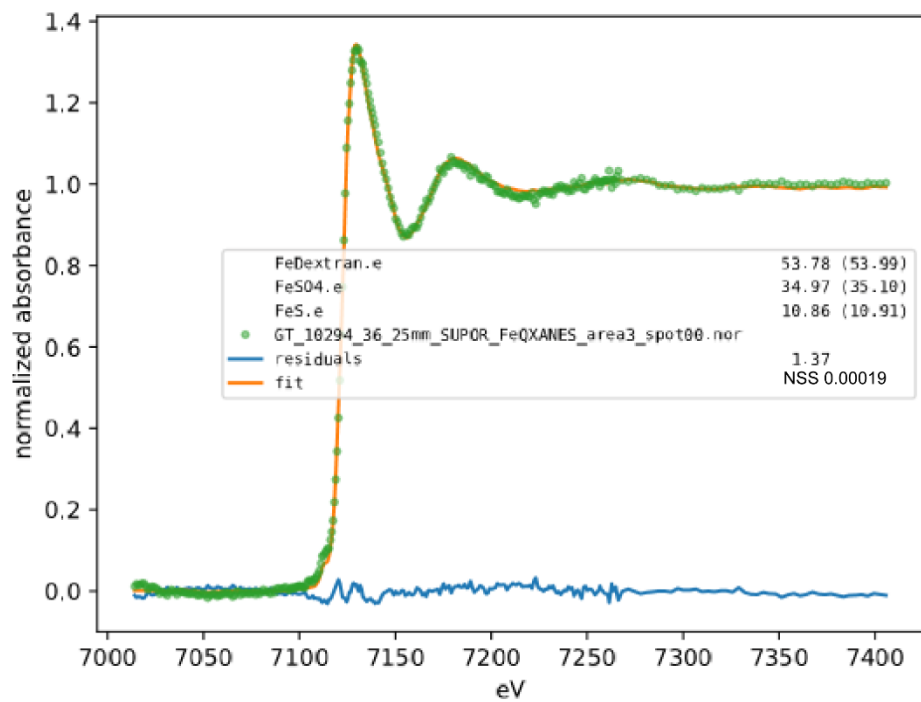


Figure 2.5.198 Fe XANES Station 36 area 3 spot 0

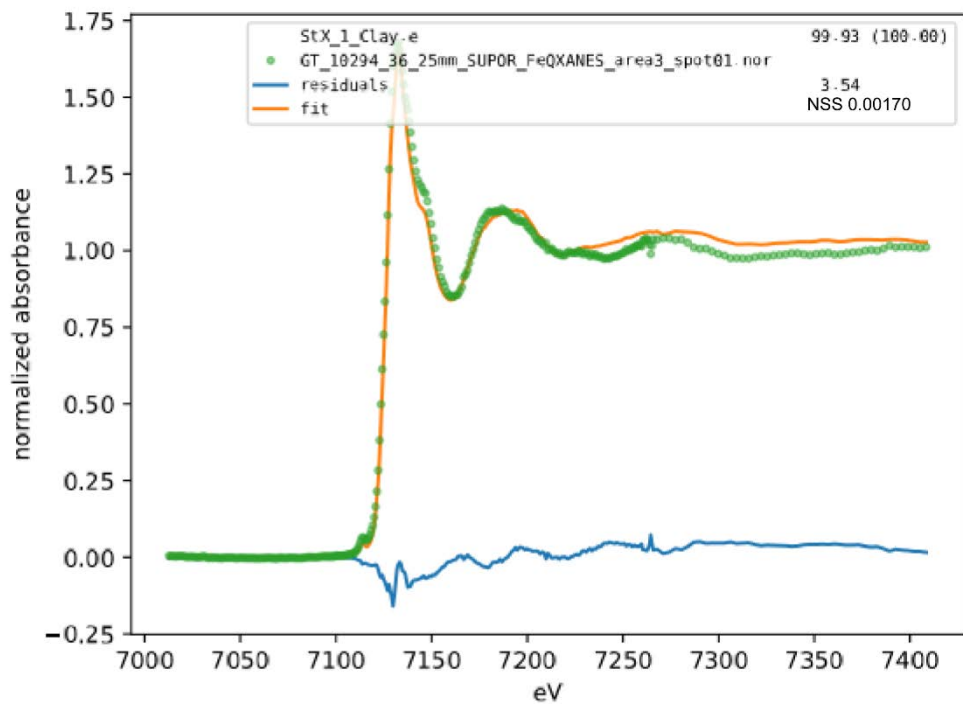


Figure 2.5.199 Fe XANES Station 36 area 3 spot 1

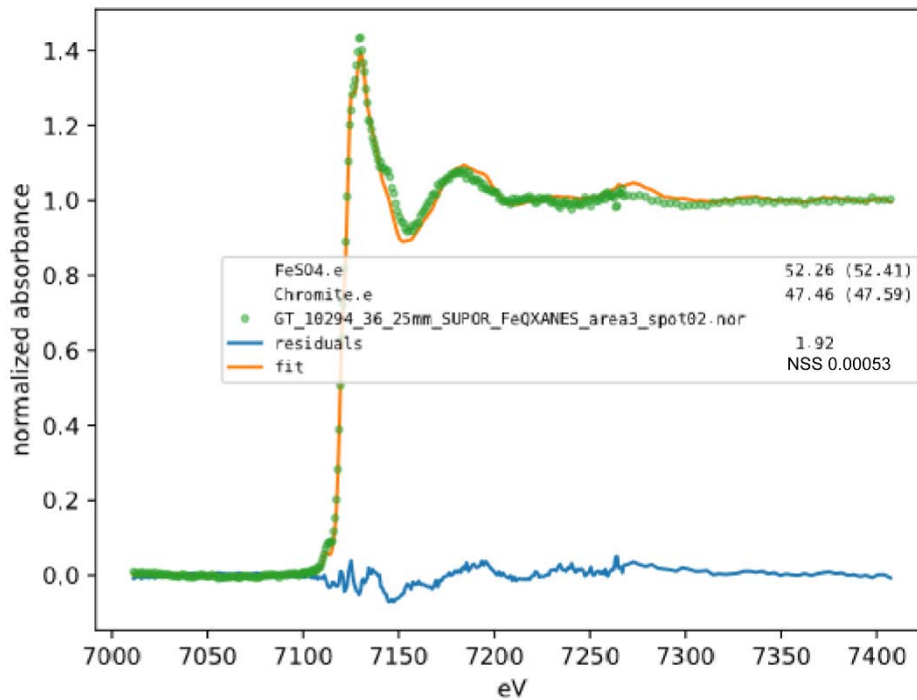


Figure 2.5.200 Fe XANES Station 36 area 3 spot 2

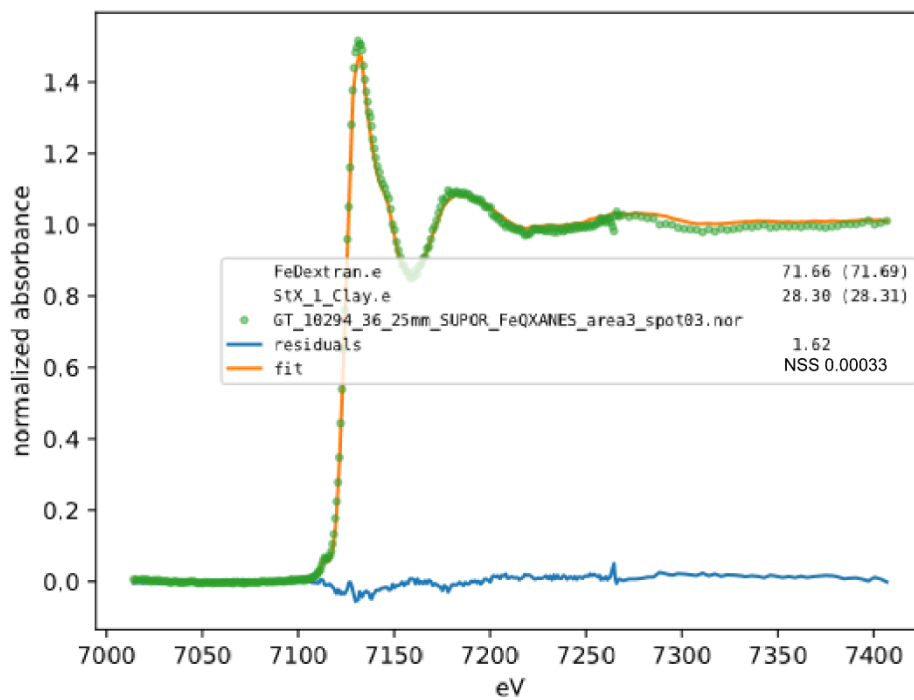


Figure 2.5.201 Fe XANES Station 36 area 3 spot 3

Appendix Table 2.5.1 Fe 1s XANES Reference material LCF Bins

Reference_Filename	Post_LCF_Bins
Akaganeite.e	Fe(III)
Andradite.e	silicate
Awaruite.e	native Fe
Chromite.e	Fe(II)
Fe_std_100fFh_avg.e	Fe(III)
Fe_std_100goe_avg.e	Fe(III)
FeAlginate.e	Fe(III)
FeCl3.e	Fe(III)
FeDextran.e	Fe(III)
Ferrosmeectite.e	Fe(III)
FeS.e	Fe sulfide
FeSO4.e	Fe(II)
Gehlenite.e	silicate
Lepidocrocite.e	Fe(III)
Mackinawite.e	Fe sulfide
Maghemite.e	Fe(III)
Moldavite.e	Fe(II)
NKT_1G_Basalt_Glass.e	Fe(II)
Nontronite.e	Fe(III)
Perovskite.e	Fe(II)
Pseudobrookite.e	Fe(III)
Pyrite.e	Fe sulfide
Pyrrhotite.e	Fe sulfide
Richterite.e	silicate
Roedderite.e	silicate
StX_1_Clay.e	Fe(III)
Toner_biogenic_oxide.e	Fe(III)
Troilite.e	Fe sulfide

Appendix Table 2.5.2 Iron 1s μ XANES

GT #	St.	Average %pFe species (per an atom)				
		Fe sulfide	Fe(II)	native Fe	silicate	Fe(III)
8436	18	0.0	0.8	0.0	7.7	91.5
8705	20	0.4	4.8	0.0	4.3	90.5
8882	21	0.0	1.7	0.0	23.0	75.2
9065	23	0.0	15.3	0.0	2.2	82.4
9254	25	0.0	9.4	0.0	7.9	82.5
9346	26	0.0	5.4	0.0	19.1	75.3
9595	28	0.0	0.0	0.0	15.5	84.4
9838	30	0.0	9.6	0.0	5.0	85.0
9975	32	5.9	0.0	0.0	20.6	73.4

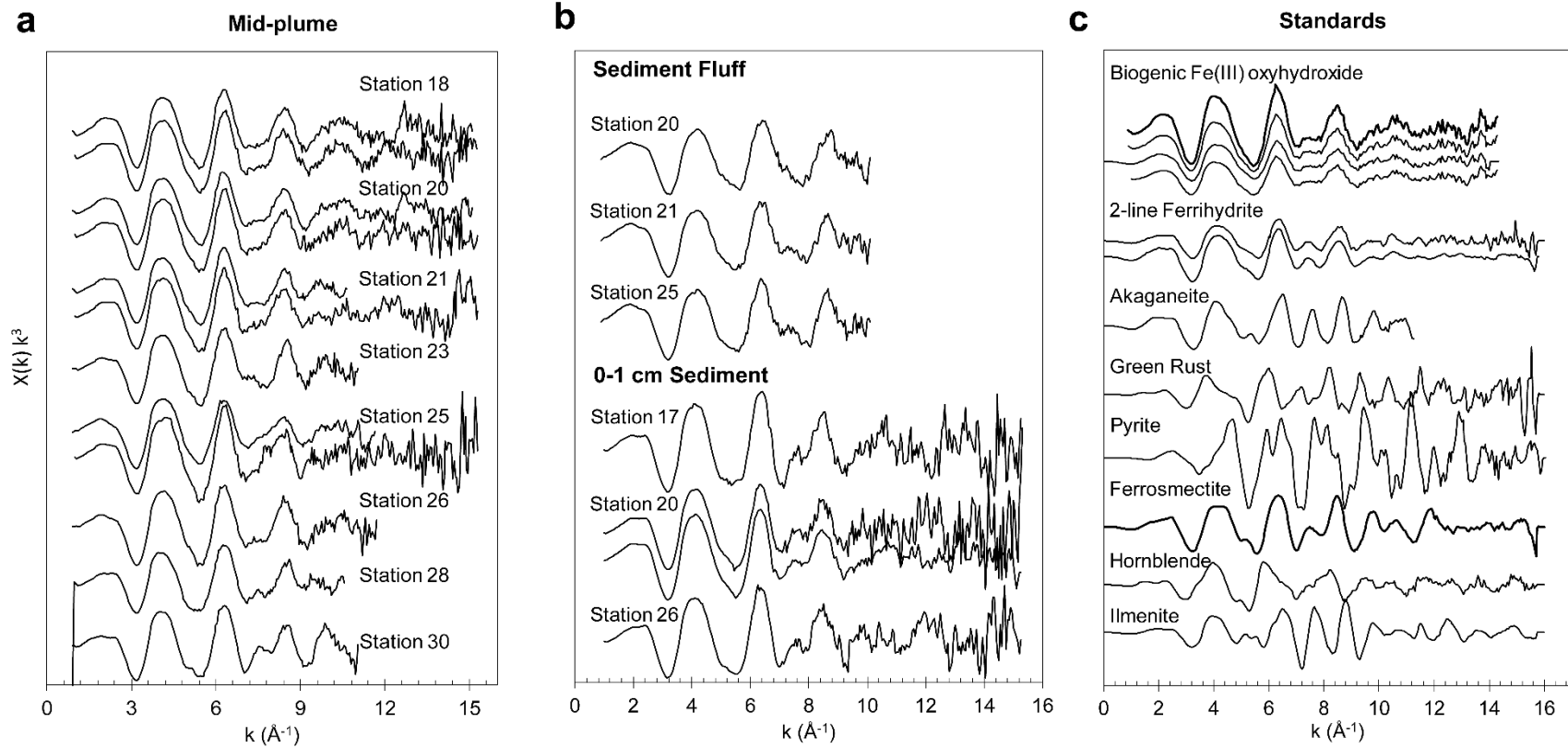
10160	34	3.4	14.2	0.7	18.4	63.2
10294	36	4.0	35.6	0.0	0.0	60.1

Appendix 2.6 Fe 1s EXAFS linear combinations fitting results and unaltered spectra

Below are the tables with reference material for all Fe EXAFS processed at ALS 10.3.2., CLS STXMB, and APS 20 BM-B. All spectra that were collected are provided below. Multiple spots were collected at each station to understand Fe diversity within the sample. This information was then compiled to produce Figure 7.

Appendix Table 2.6.1 Fe 1s EXAFS Reference material LCF bins

Reference_Filename	Post_LCF_Bins
Akaganeite.chi3	Fe(III) oxyhydroxide
Biogenic_oxyhydroxide_Toner.chi3	Fe(III) oxyhydroxide
Biogenic_oxyhydroxide_Toner_SAC_00.chi3	Fe(III) oxyhydroxide
Biogenic_oxyhydroxide_Toner_SAC_02.chi3	Fe(III) oxyhydroxide
Biogenic_oxyhydroxide_Toner_SAC_05.chi3	Fe(III) oxyhydroxide
Biogenic_oxyhydroxide_Toner_SAC_10.chi3	Fe(III) oxyhydroxide
Biotite_Fendorf.chi3	mica
Ferrihydrite_2L_Fendorf.chi3	Fe(III) oxyhydroxide
Ferrihydrite_2L_Toner.chi3	Fe(III) oxyhydroxide
Ferrihydrite_sorbed_to_sand_Fendorf.chi3	Fe(III) oxyhydroxide
Ferrihydrite_t48hr_wet_Toner.chi3	Fe(III) oxyhydroxide
Ferrosmeectite_Fendorf.chi3	Fe(III) phyllosilicate
fFh_10_Goe_90_Toner.chi3	Fe(III) oxyhydroxide
fFh_25_Goe_75_Toner.chi3	Fe(III) oxyhydroxide
fFh_50_Goe_50_Toner.chi3	Fe(III) oxyhydroxide
fFh_75_Goe_25_Toner.chi3	Fe(III) oxyhydroxide
fFh_90_Goe_10_Toner.chi3	Fe(III) oxyhydroxide
Goethite_Toner.chi3	Fe(III) oxyhydroxide
Goethite_Fendorf.chi3	Fe(III) oxyhydroxide
GreenRust_Cl_Fendorf.chi3	Fe(II,III) hydroxide
GreenRust_CO3_Fendorf.chi3	Fe(II,III) hydroxide
GreenRust_SO4_Fendorf.chi3	Fe(II,III) hydroxide
Hematite_Fendorf.chi3	Fe(III) oxide
Hornblende_Fendorf.chi3	amphibole
Ilmenite_Fendorf.chi3	Ti Fe oxide
Lepidocrocite_Fendorf.chi3	Fe(III) oxyhydroxide
Magnetite_n_Fendorf.chi3	Fe(II,III) oxide
Magnetite_s_Fendorf.chi3	Fe(II,III) oxide
Nontronite_Fendorf.chi3	Fe(III) phyllosilicate
Pyrite_Fendorf.chi3	Fe(II) sulfide
Pyrrhotite_Fendorf.chi3	Fe(II) sulfide
Siderite_n_Fendorf.chi3	Fe(II) carbonate
Vivianite_Fendorf.chi3	Fe(II) phosphate



Appendix 2.6.1 Full length Fe EXAFS spectra from the GP16 transect and standards. Full length Fe EXAFS spectra for (a) the mid-plume, (b) fluff layer and 0-1 cm sediments along the GP16 transect, and (c) standards used for linear combination fitting (Toner et al. 2009b). Station 25 spectra was removed from the main text due to the feature at 7.5 k. This feature was most likely caused by the low over all fluorescence of our sample or instrument, not representative of the Fe mineralogy in our sample.

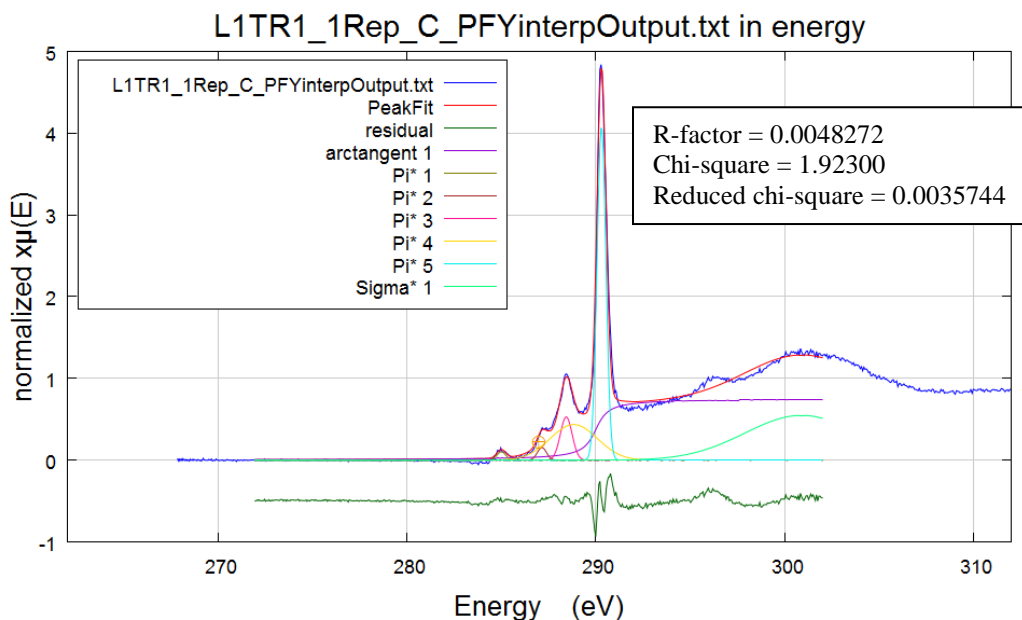
APPENDIX 3 - Chapter 4

Supplemental Information

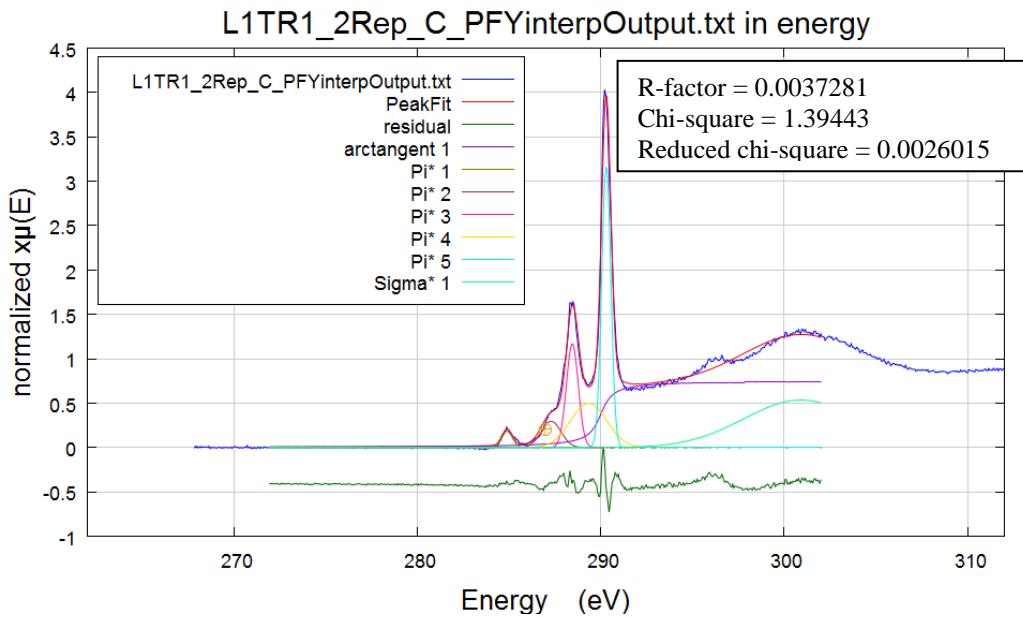
The figures and tables below correspond to supplement materials for Chapter 3 “Carbon, nitrogen, and oxygen speciation of hydrothermal plume particles at East Pacific Rise 9°50’N”. Please refer below and within Chapter 4 for further explanations and significance.

Appendix 3.1 Carbon 1s XANES Gaussian fitting within *Athena*

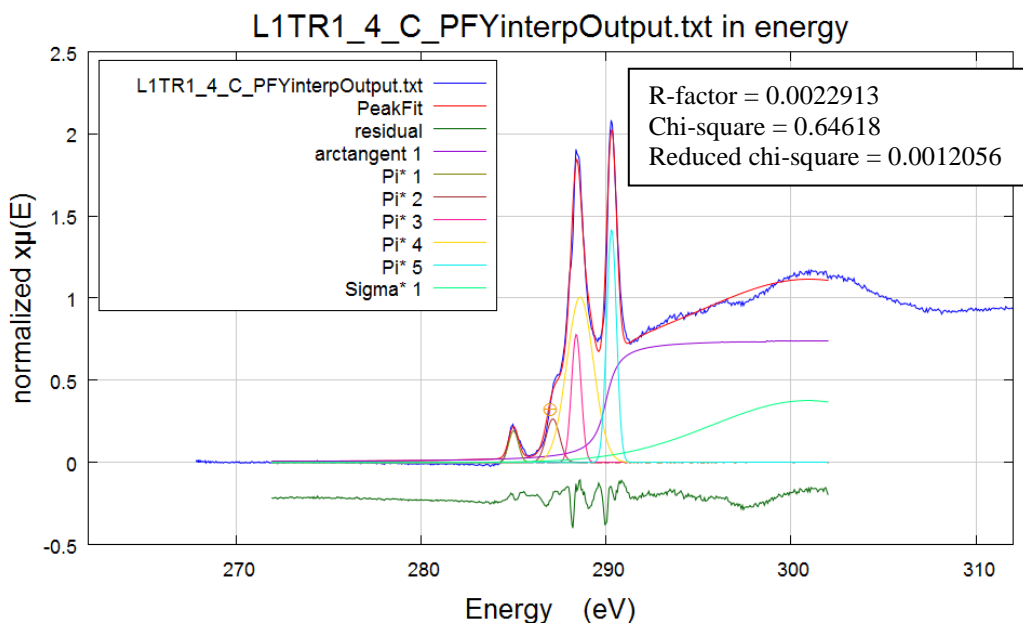
Below are the raw images from *Athena* regarding Gaussian fits for R1 and R2 C 1s XANES. All terms and peak energies are defined in Appendix Table 3.1.1. Pi* and Sigma* peaks were chosen based off the normalize two column data. When fitting, all initial guess of Pi* heights and widths were set to 0.5. For Sigma *, all initial guesses were height of 0.5 and widths of 3. For C 1s XANES, parameters for the arctangent were always fixed at 290 eV with a height of 0.75, and width of 0.5. The model was only allowed to vary the heights and with of the Pi* and Sigma* peaks.



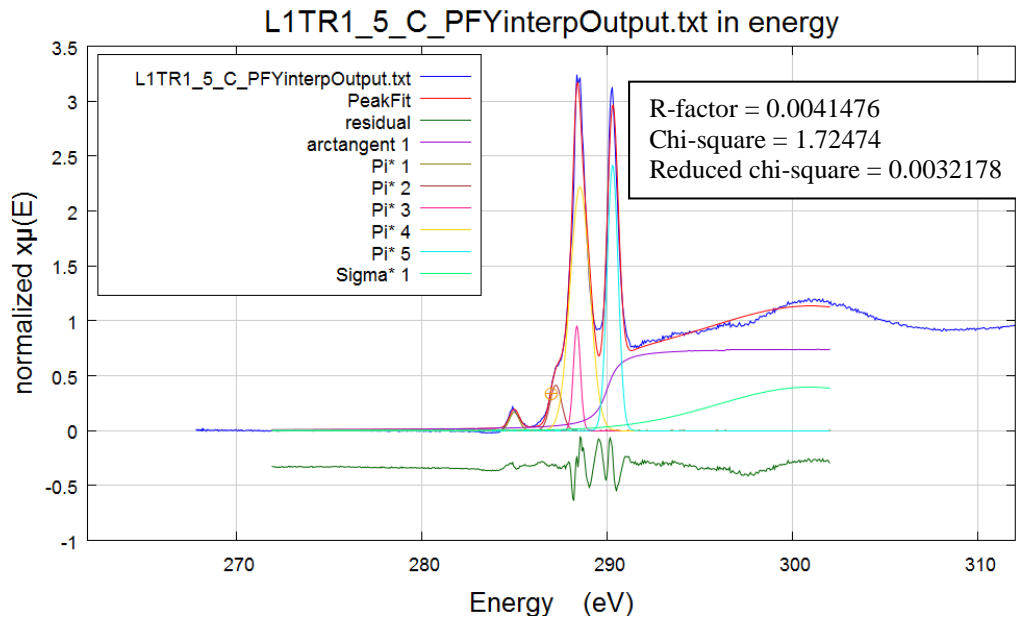
Appendix 3.1.1 C 1s XANES gaussian fitting for R1-1



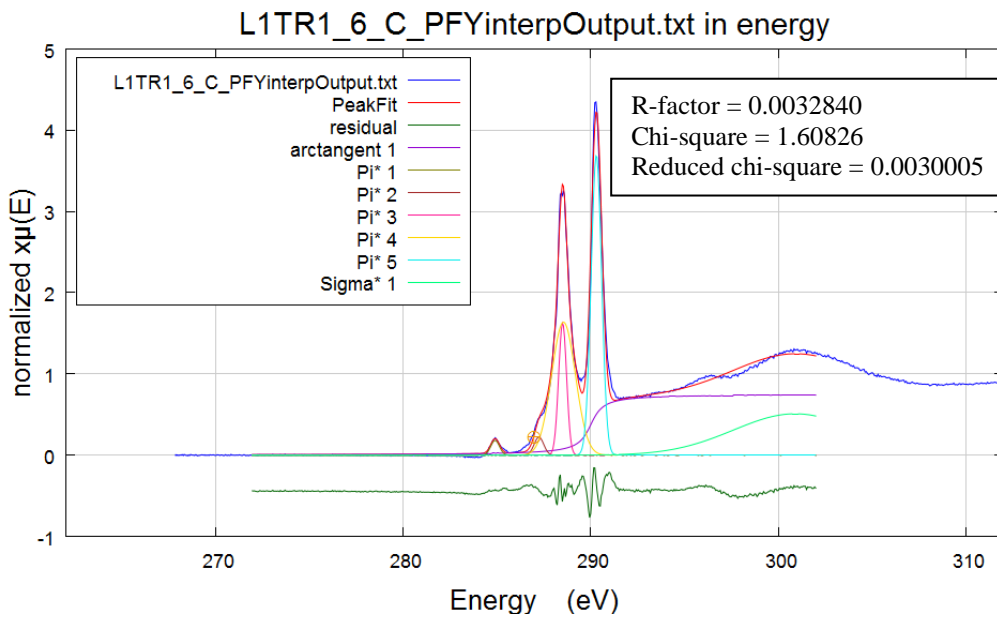
Appendix 3.1.2 C 1s XANES gaussian fitting for R1-2



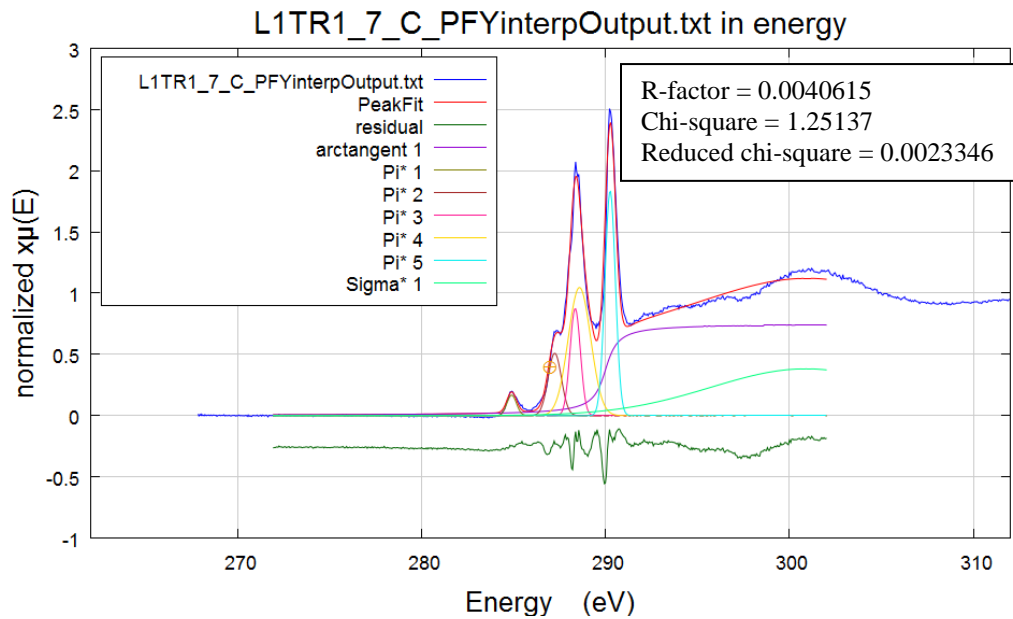
Appendix 3.1.3 C 1s XANES gaussian fitting for R1-3



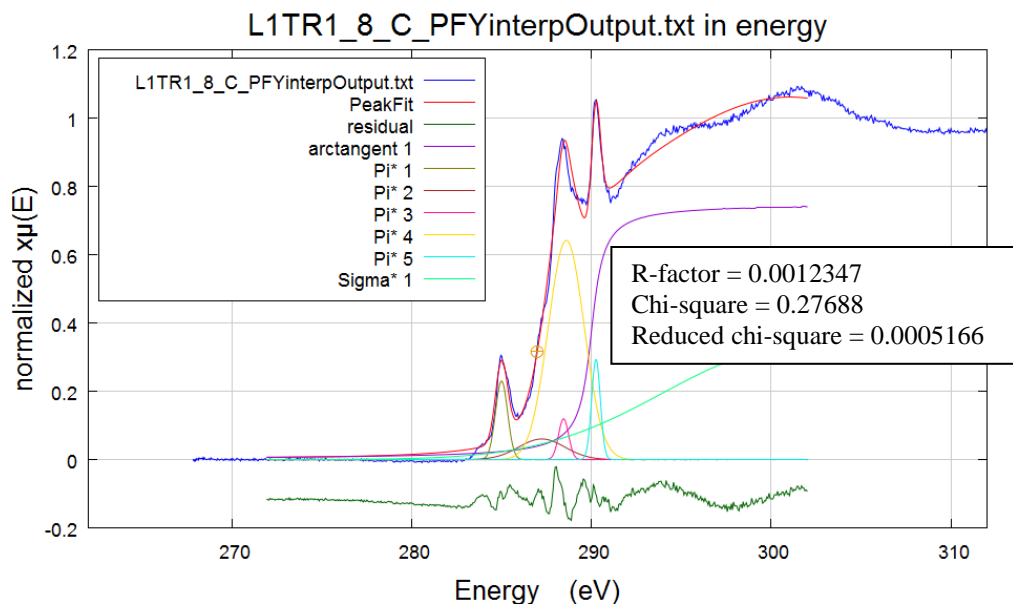
Appendix 3.1.4 C 1s XANES gaussian fitting for R1-5



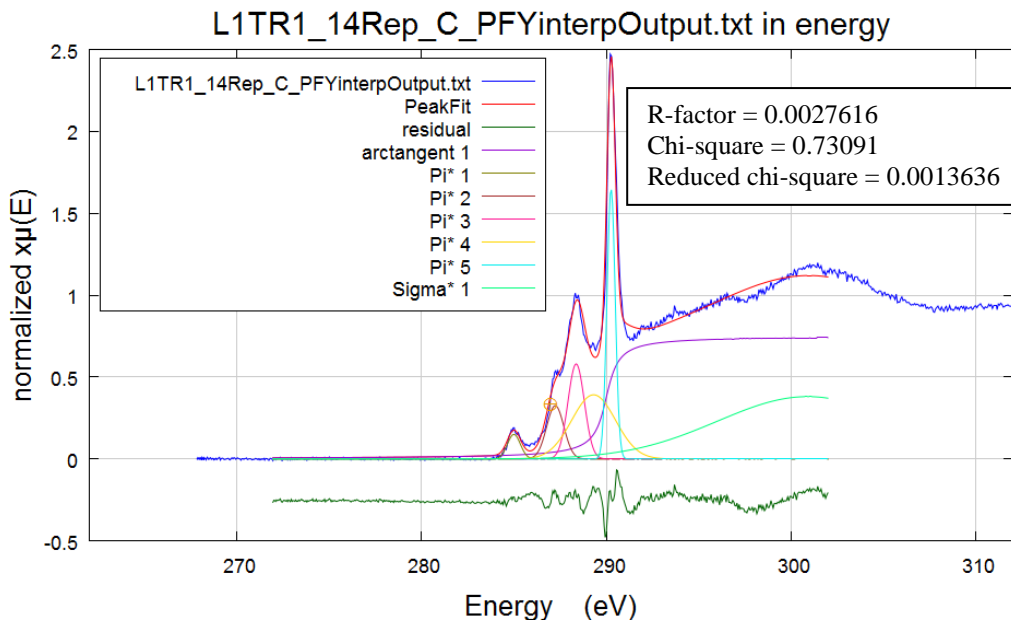
Appendix 3.1.5 C 1s XANES gaussian fitting for R1-6



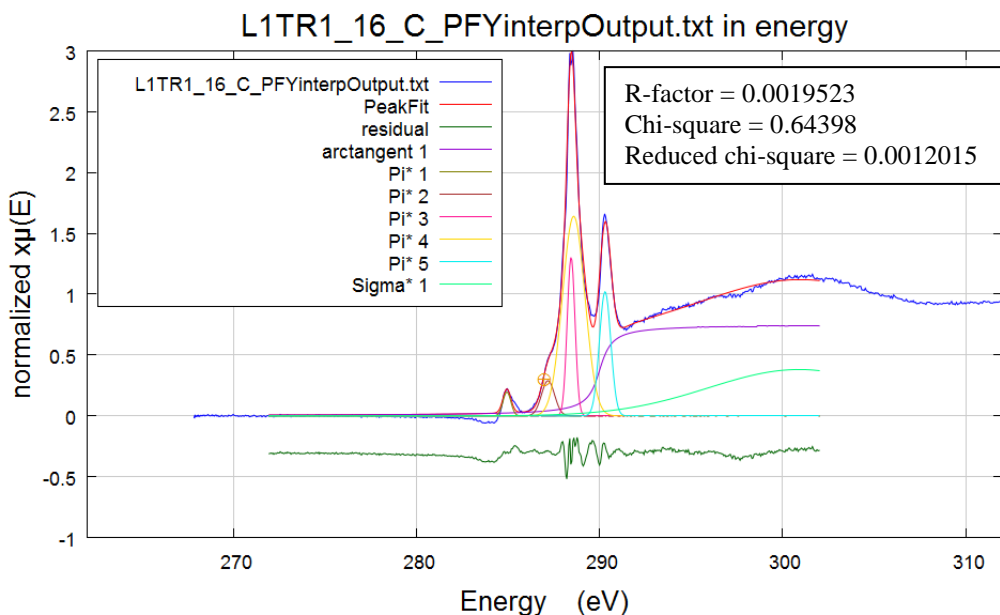
Appendix 3.1.6 C 1s XANES gaussian fitting for R1-7



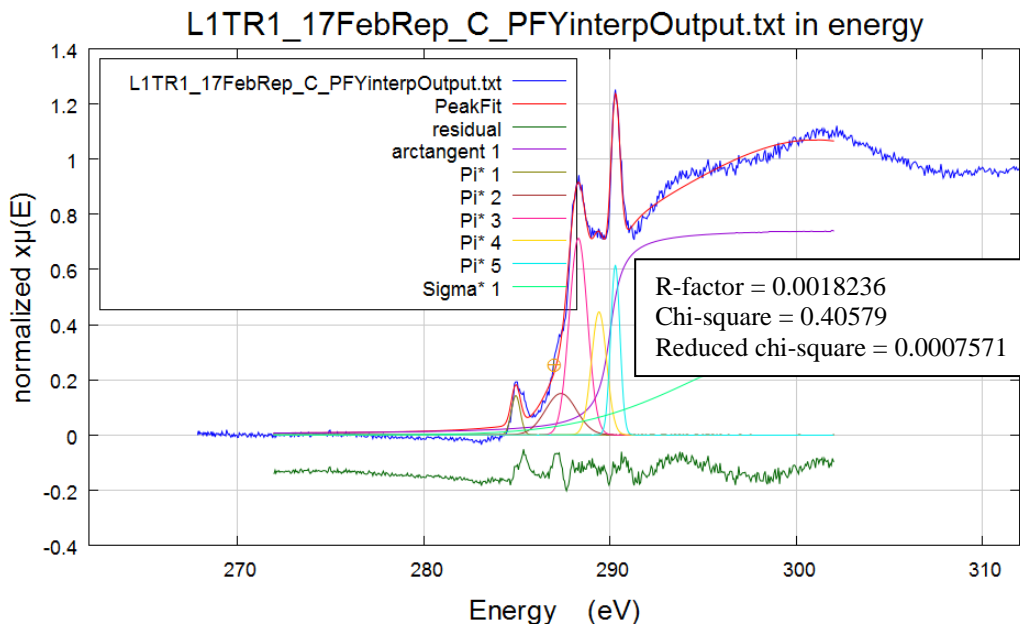
Appendix 3.1.7 C 1s XANES gaussian fitting for R1-8



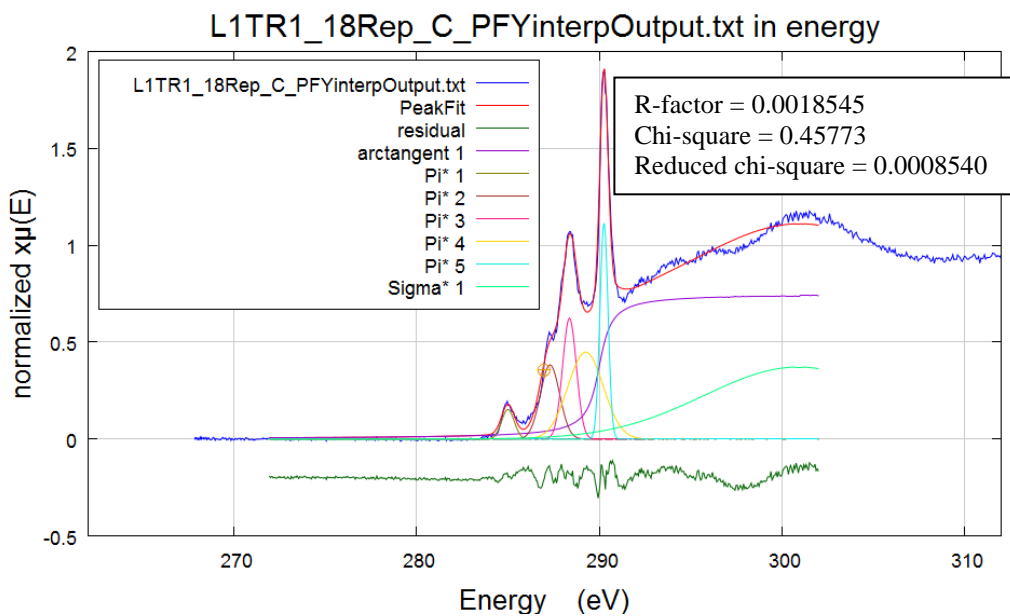
Appendix 3.1.8 C 1s XANES gaussian fitting for R1-14



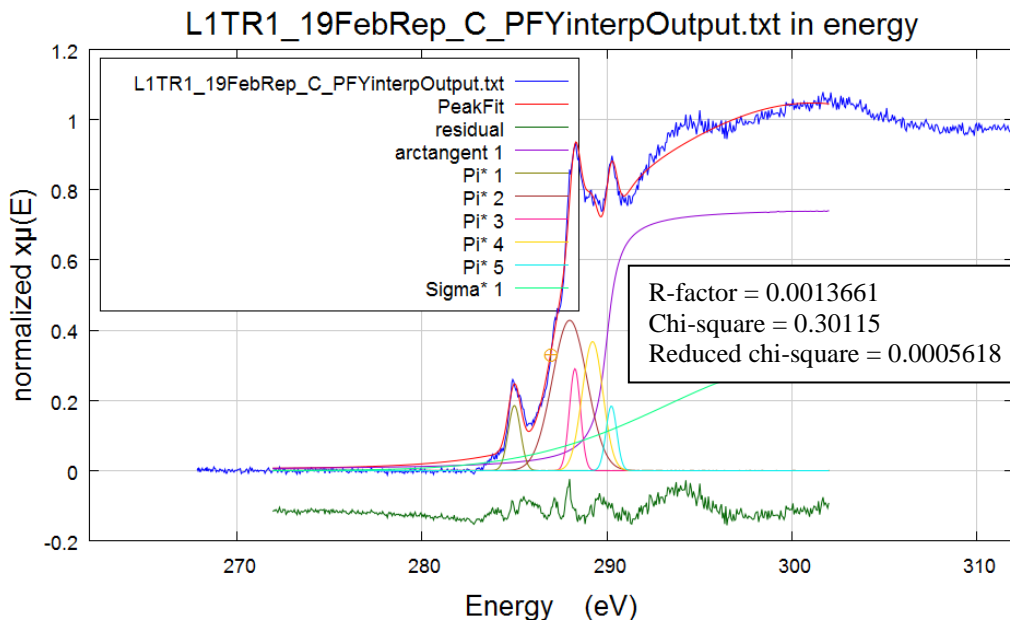
Appendix 3.1.9 C 1s XANES gaussian fitting for R1-16



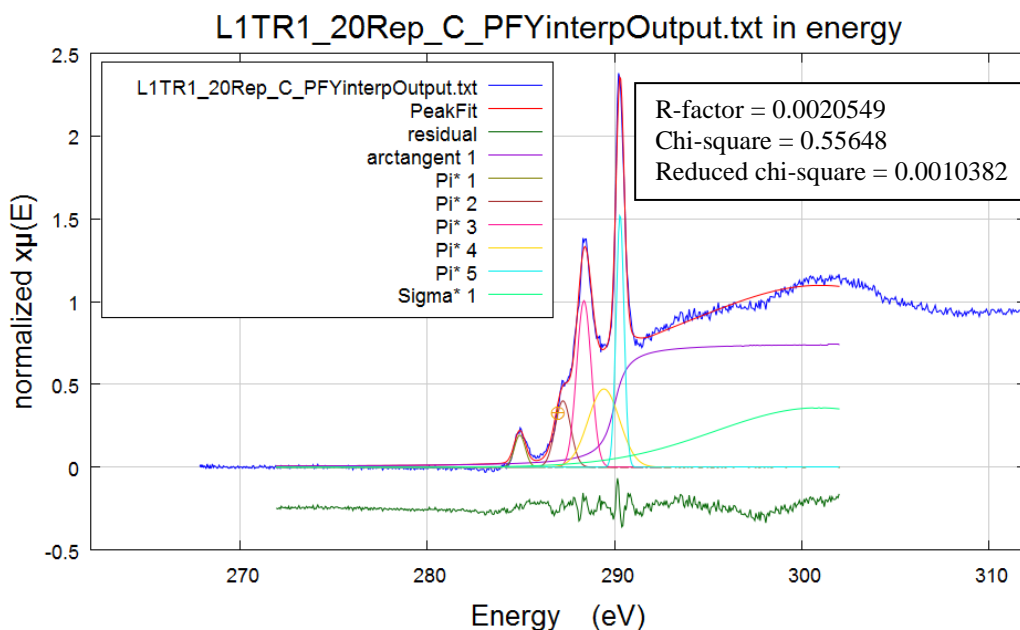
Appendix 3.1.10 C 1s XANES gaussian fitting for R1-17



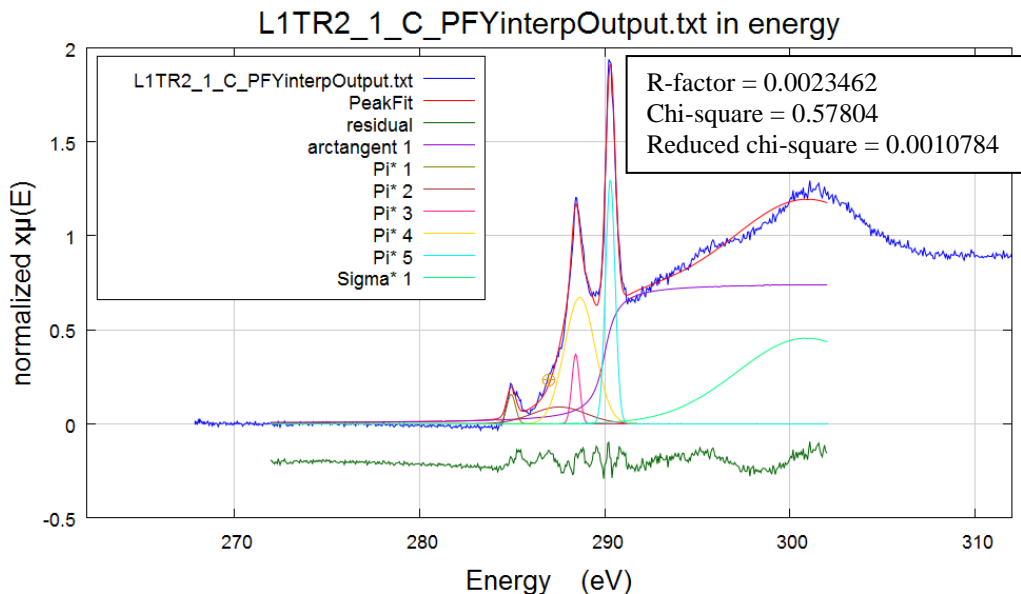
Appendix 3.1.11 C 1s XANES gaussian fitting for R1-18



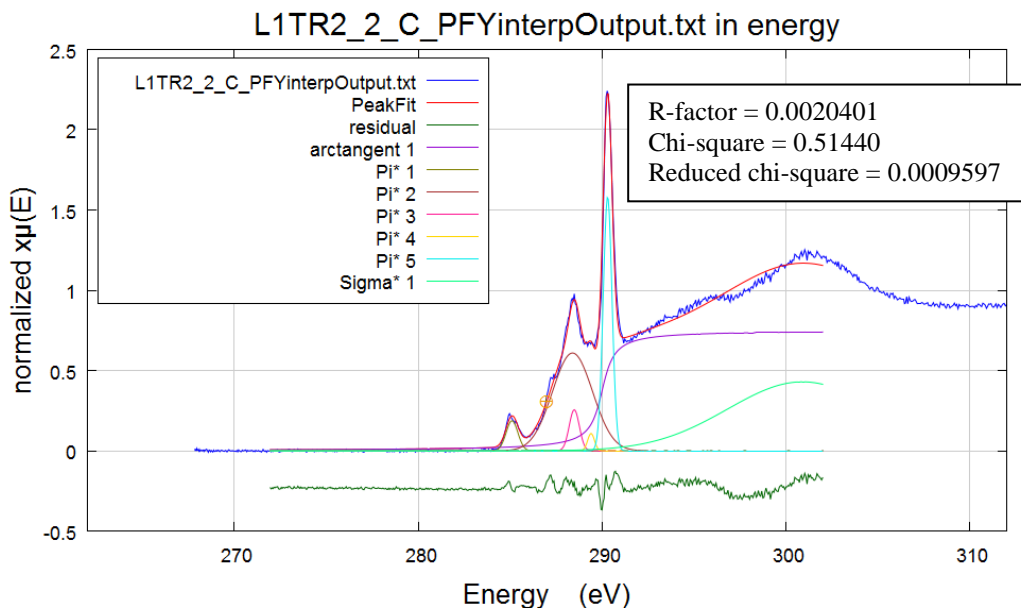
Appendix 3.1.12 C 1s XANES gaussian fitting for R1-19



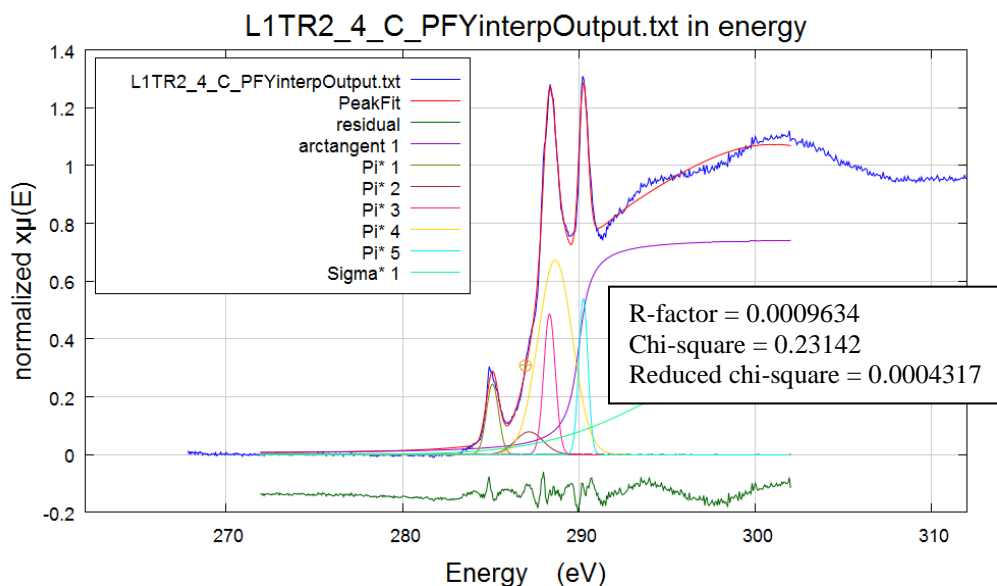
Appendix 3.1.13 C 1s XANES gaussian fitting for R1-20



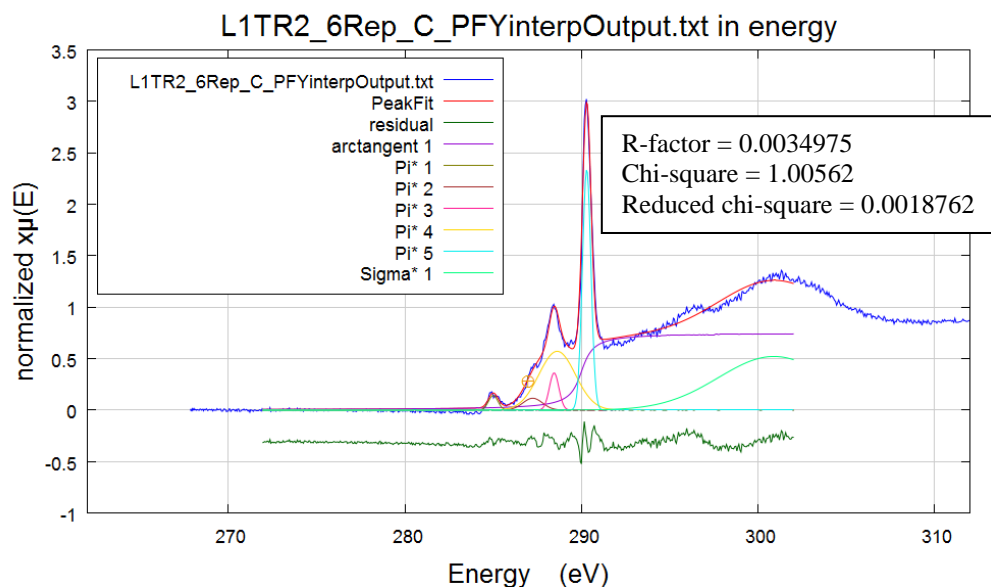
Appendix 3.1.14 C 1s XANES gaussian fitting for R1-21



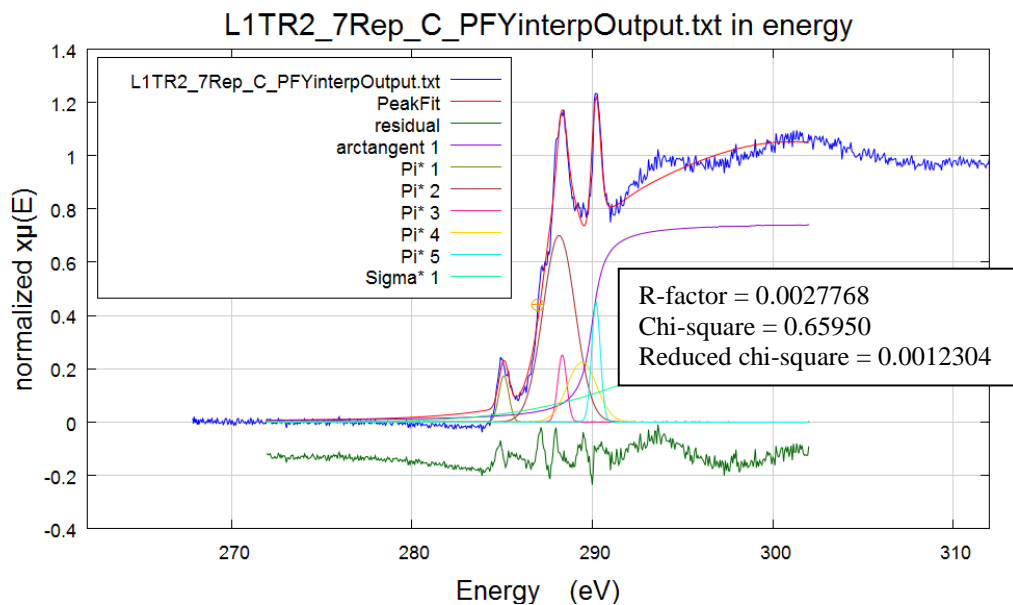
Appendix 3.1.15 C 1s XANES gaussian fitting for R2-2



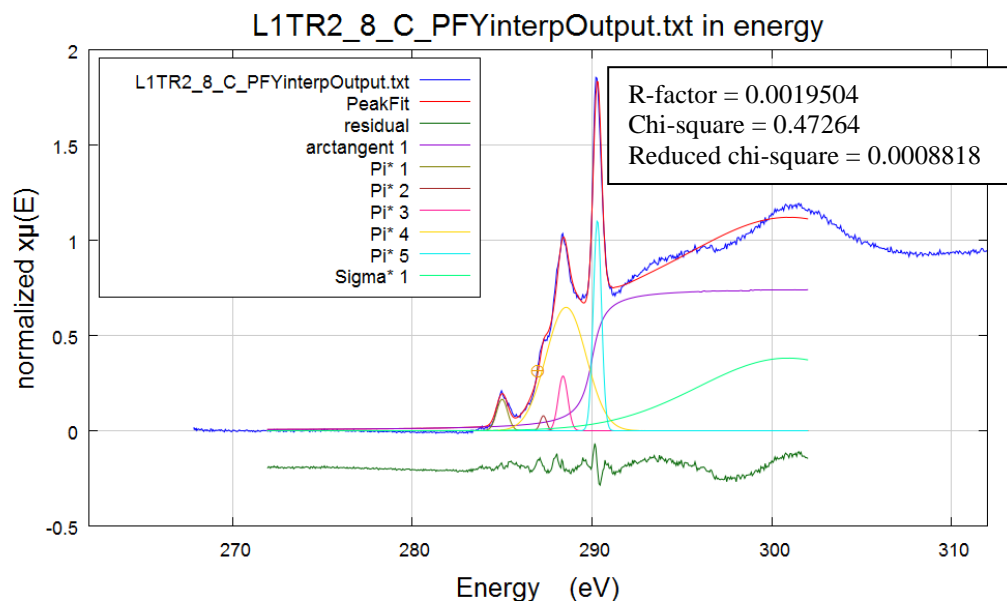
Appendix 3.1.16 C 1s XANES gaussian fitting for R2-4



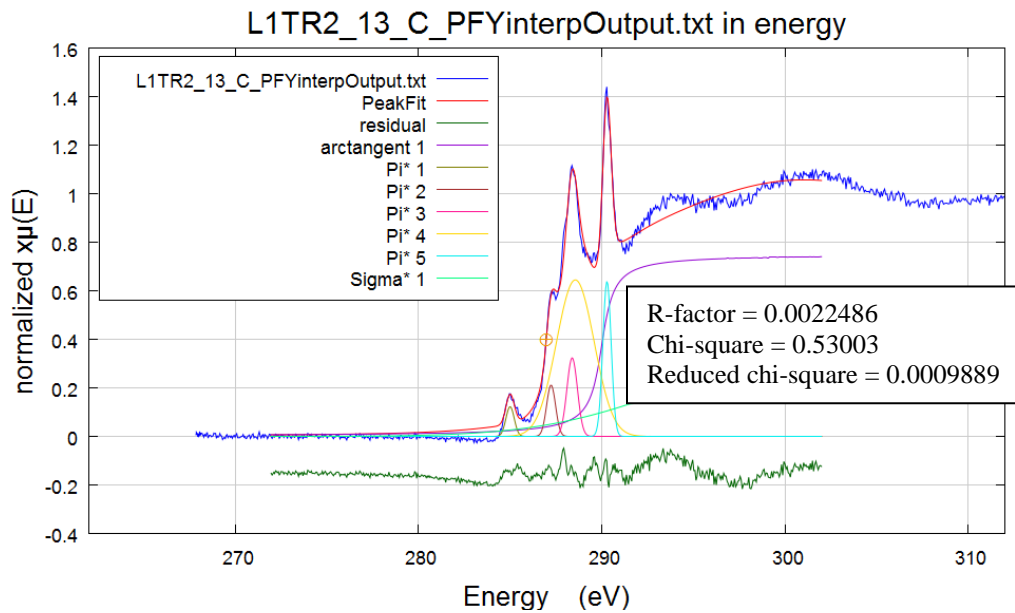
Appendix 3.1.17 C 1s XANES gaussian fitting for R2-6



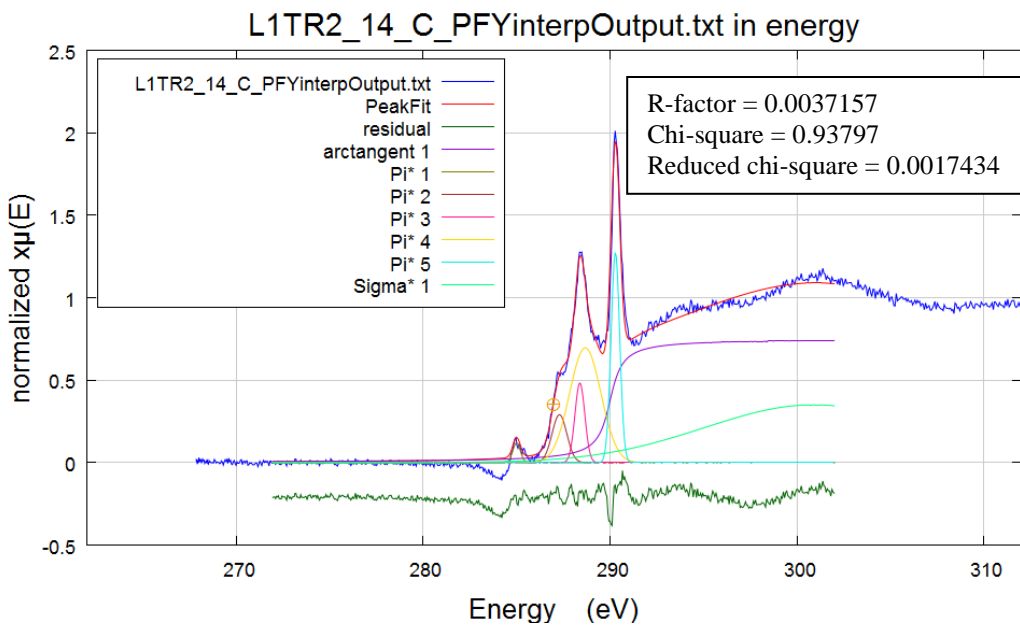
Appendix 3.1.18 C 1s XANES gaussian fitting for R2-7



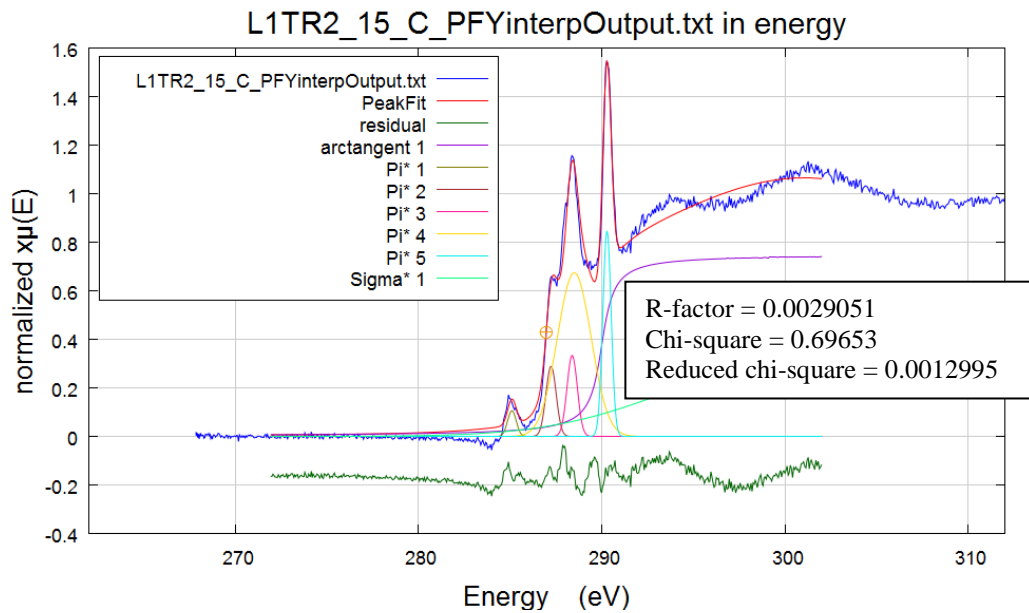
Appendix 3.1.19 C 1s XANES gaussian fitting for R2-8



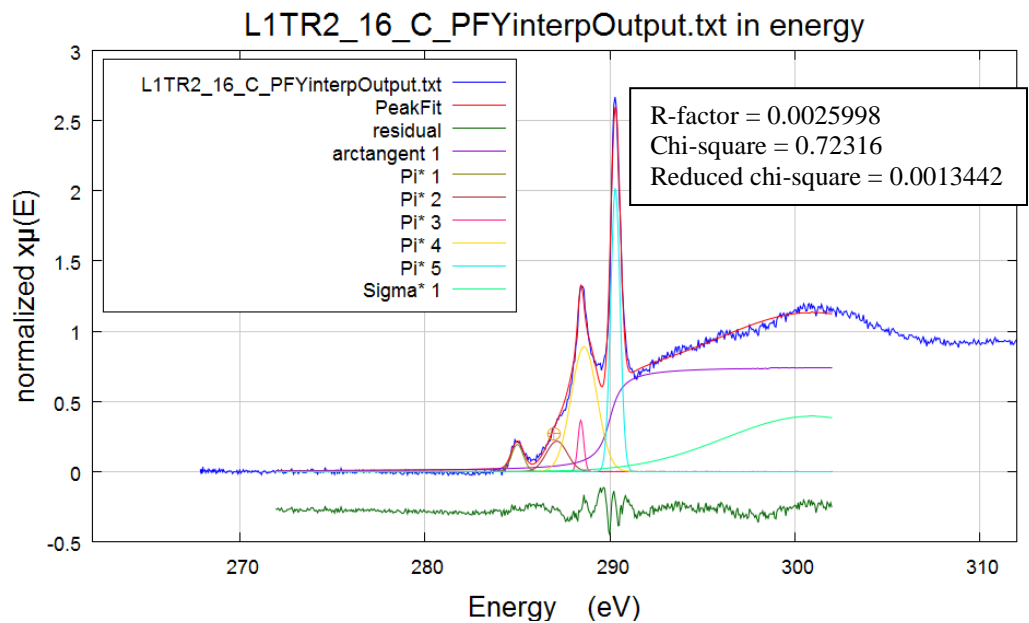
Appendix 3.1.20 C 1s XANES gaussian fitting for R2-13



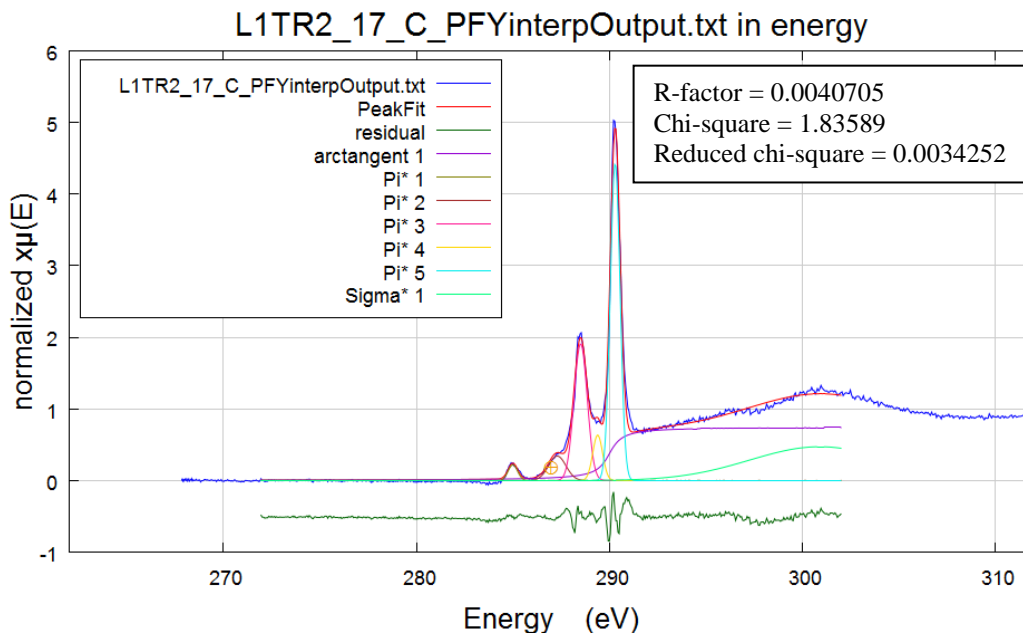
Appendix 3.1.21 C 1s XANES gaussian fitting for R2-14



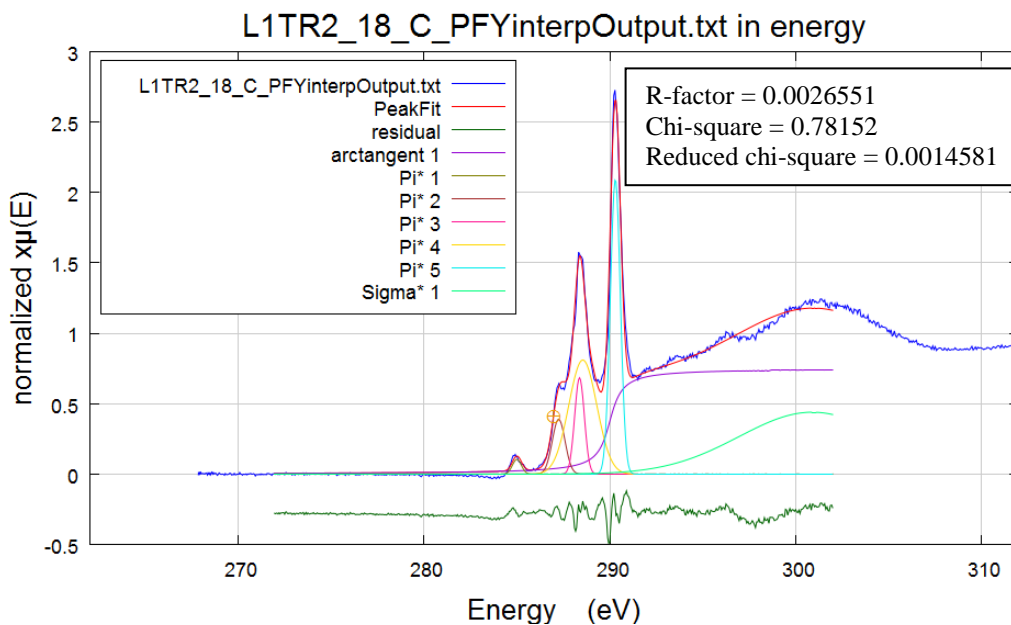
Appendix 3.1.22 C 1s XANES gaussian fitting for R2-15



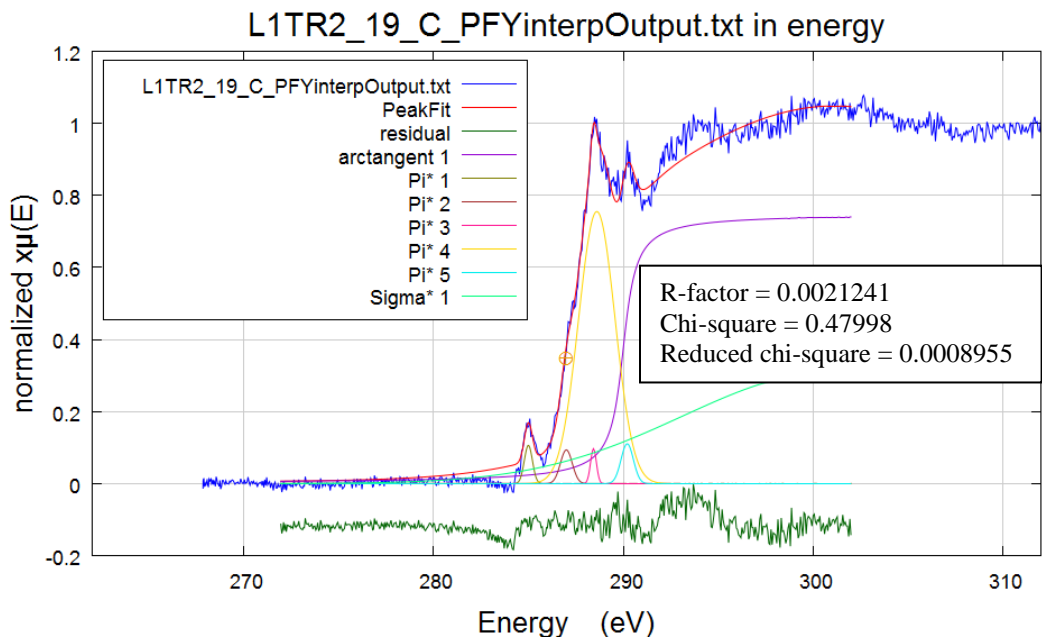
Appendix 3.1.23 C 1s XANES gaussian fitting for R2-16



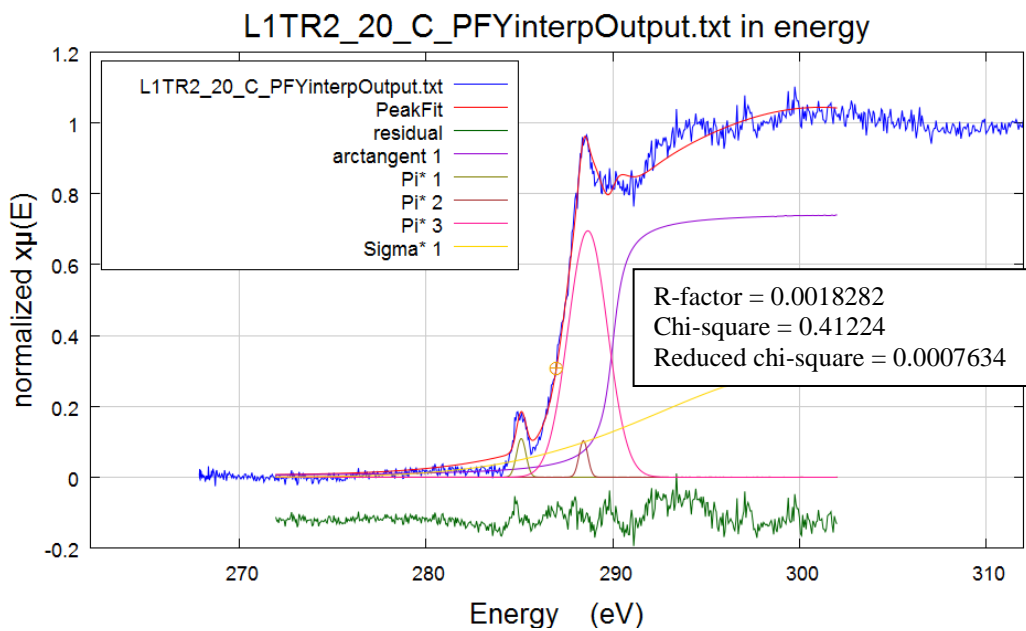
Appendix 3.1.24 C 1s XANES gaussian fitting for R2-17



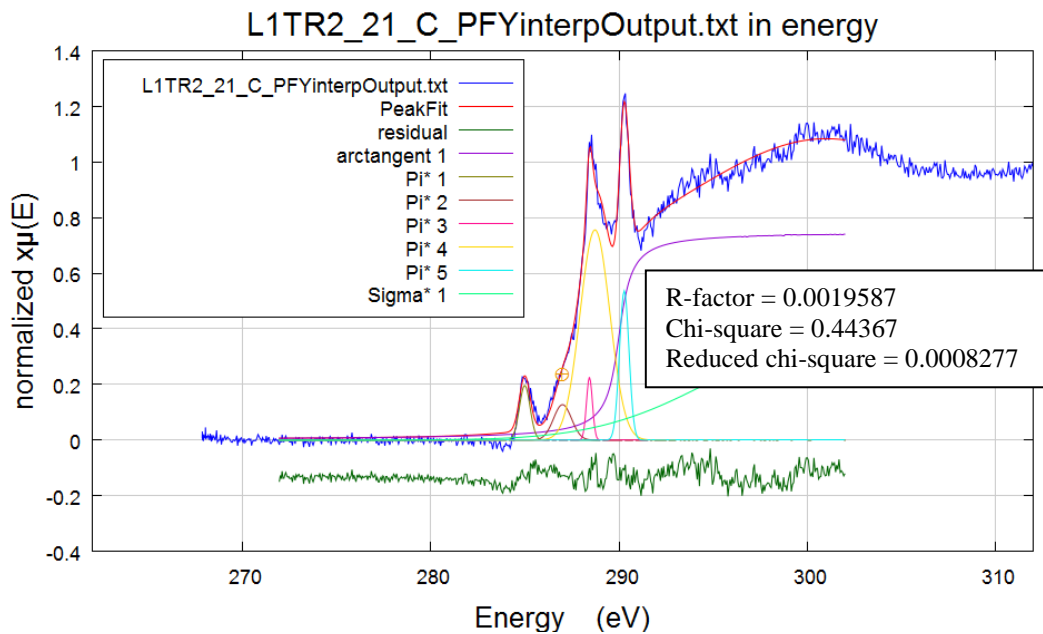
Appendix 3.1.25 C 1s XANES gaussian fitting for R2-18



Appendix 3.1.26 C 1s XANES gaussian fitting for R2-19



Appendix 3.1.27 C 1s XANES gaussian fitting for R2-20



Appendix 3.1.28 C 1s XANES gaussian fitting for R2-21

Appendix Table 3.1.1 Gaussian curve fitting parameters for C 1s XANES

Sample	Station	Arc					Sigma* 1	χ^2	reduced χ^2	R-factor	
		Tangent	Pi* 1	Pi* 2	Pi* 3	Pi* 4					
R1_1	Bio 9	290	285	287.147	288.44	288.83	290.3	300.9	1.923	0.0035744	0.0048272
R1_2	Bio 9	290	284.9	287.29	288.45	289.34	290.3	300.9	1.39443	0.0026015	0.0037281
R1_4	Bio 9	290	285	287.126	288.391	288.601	290.3	300.9	0.64618	0.0012056	0.0022913
R1_5	Bio 9	290	285	287.24	288.374	288.542	290.3	300.9	1.72474	0.0032178	0.0041476
R1_6	Bio 9	290	284.9	287.237	288.5	288.549	290.3	300.9	1.60826	0.0030005	0.003284
R1_7	Bio 9	290	284.9	287.24	288.352	288.585	290.253	300.9	1.25137	0.0023346	0.0040615
R1_8	Bio 9	290	285	287.24	288.45	288.601	290.253	300.9	0.27688	0.0005166	0.0012347
R1_14	Bio 9	290	285	287.248	288.371	289.316	290.261	300.9	0.73091	0.0013636	0.0027616
R1_16	Bio 9	290	284.939	287.184	288.445	288.585	290.3	300.9	0.64398	0.0012015	0.0019523
R1_17	Bio 9	290	284.965	287.359	288.294	289.403	290.279	300.9	0.40579	0.0007571	0.0018236
R1_18	Bio 9	290	285	287.307	288.371	289.257	290.261	300.9	0.45773	0.000854	0.0018545
R1_19	Bio 9	290	285	287.989	288.273	289.228	290.244	300.9	0.30115	0.0005618	0.0013661
R1_20	Bio 9	290	284.944	287.248	288.371	288.489	290.2	300.9	0.55648	0.0010382	0.0020549
R2_1	Ty-Io	290	284.944	287.544	288.43	289.434	290.261	300.9	0.57804	0.0010784	0.0023462
R2_2	Ty-Io	290	285.1	288.391	288.486	289.4	290.3	300.9	0.5144	0.0009597	0.0020401
R2_4	Ty-Io	290	284.95	287.179	288.334	288.66	290.239	300.9	0.23142	0.0004317	0.0009634
R2_6	Ty-Io	290	285	287.352	288.449	288.622	290.296	300.9	1.00562	0.0018762	0.0034975
R2_7	Ty-Io	290	285.1	288.16	288.33	289.425	290.2	300.9	0.6595	0.0012304	0.0027768
R2_8	Ty-Io	290	285	287.294	288.388	288.561	290.3	300.9	0.47264	0.0008818	0.0019504
R2_13	Ty-Io	290	285	287.236	288.388	288.561	290.289	300.9	0.53003	0.0009889	0.0022486
R2_14	Ty-Io	290	285	287.294	288.388	288.676	290.289	300.9	0.93797	0.0017434	0.0037157
R2_15	Ty-Io	290	285.1	287.236	288.388	288.503	290.289	300.9	0.69653	0.0012995	0.0029051
R2_16	Ty-Io	290	285	287.13	288.43	288.607	290.3	300.9	0.72316	0.0013442	0.0025998
R2_17	Ty-Io	290	285	287.3	288.512	289.395	290.3	300.9	1.83589	0.0034252	0.0040705
R2_18	Ty-Io	290	285	287.248	288.371	288.548	290.3	300.9	0.78152	0.0014581	0.0026551

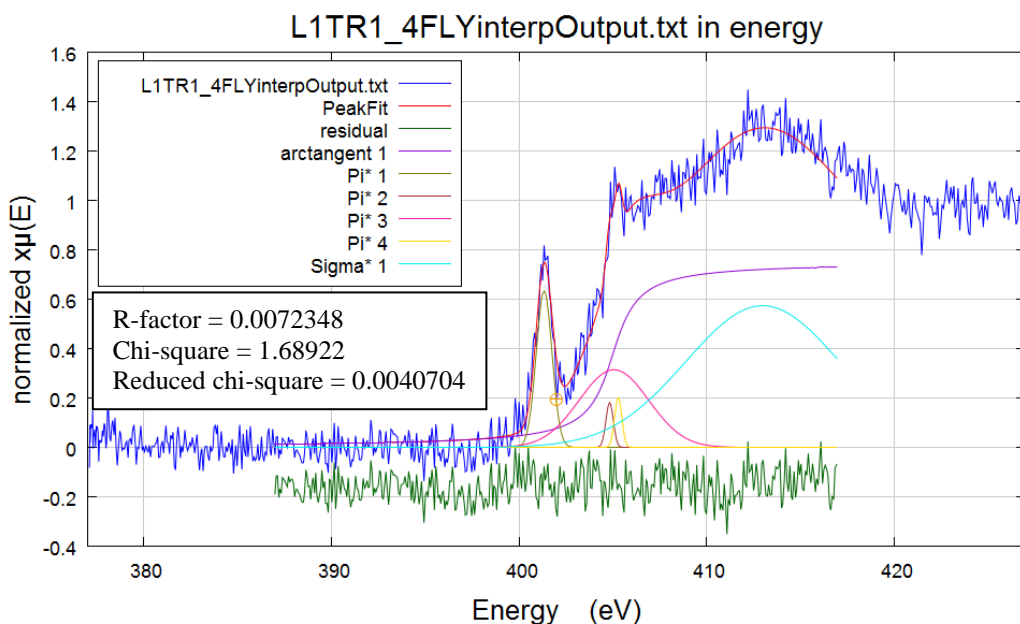
R2_19	Ty-Io	290	285	287	288.43	288.607	290.208	300.9	0.47998	0.0008955	0.0021241
R2_20	Ty-Io	290	285.1	288.43	288.666			300.9	0.41224	0.0007634	0.0018282
R2_21	Ty-Io	290	284.994	287	288.43	288.725	290.279	300.9	0.44367	0.0008277	0.0019587

blank: no functional group identified

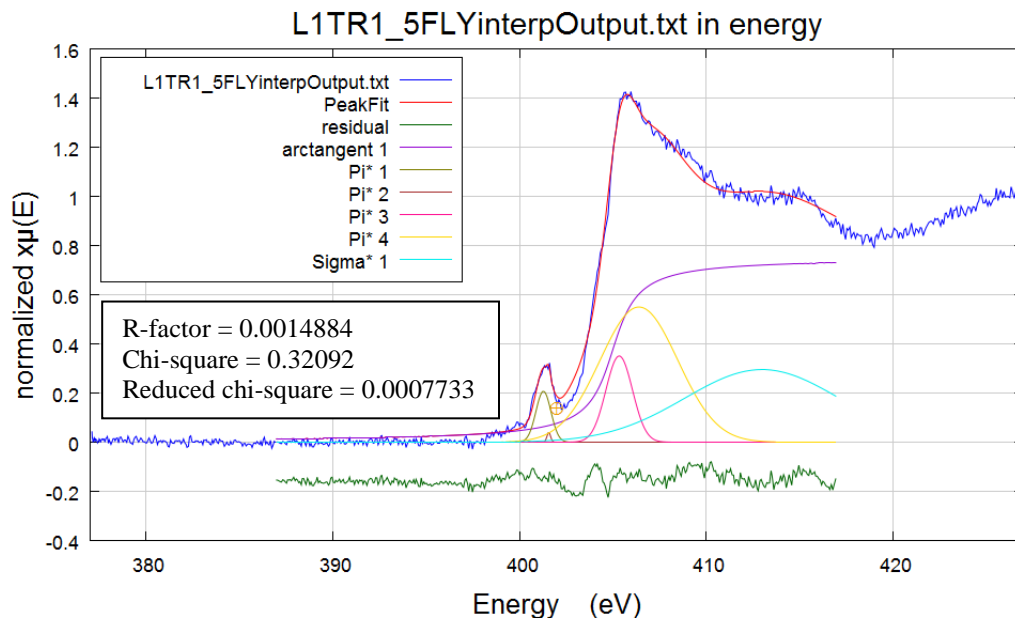
All arc tangent, pi*, and sigma* values in eV

Appendix 3.2 Nitrogen 1s XANES Gaussian fits within Athena

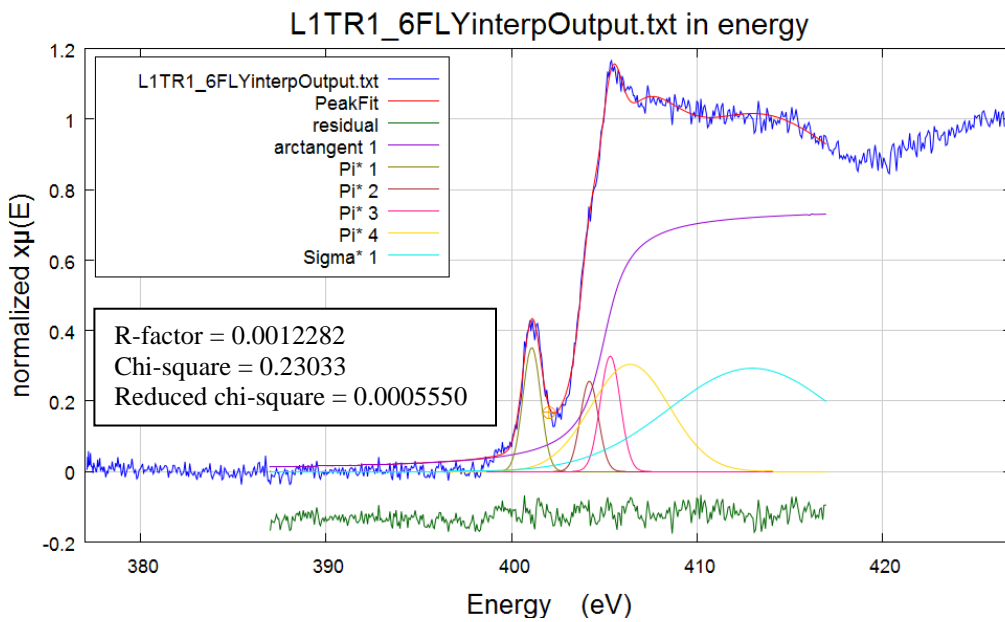
Below are the raw images from *Athena* regarding Gaussian fits for R1 and R2 N 1s XANES. All terms and peak energies are defined in Appendix Table 3.2.1. Pi* and Sigma* peaks were chosen based off the normalized two column data. When fitting, all initial guess of Pi* heights and widths were set to 0.5. For Sigma *, all initial guesses were height of 0.5 and widths of 3. For N 1s XANES, parameters for the arctangent were always fixed at 405 eV with a height of 0.75, and width of 1.0. The model was only allowed to vary the heights and with of the Pi* and Sigma* peaks.



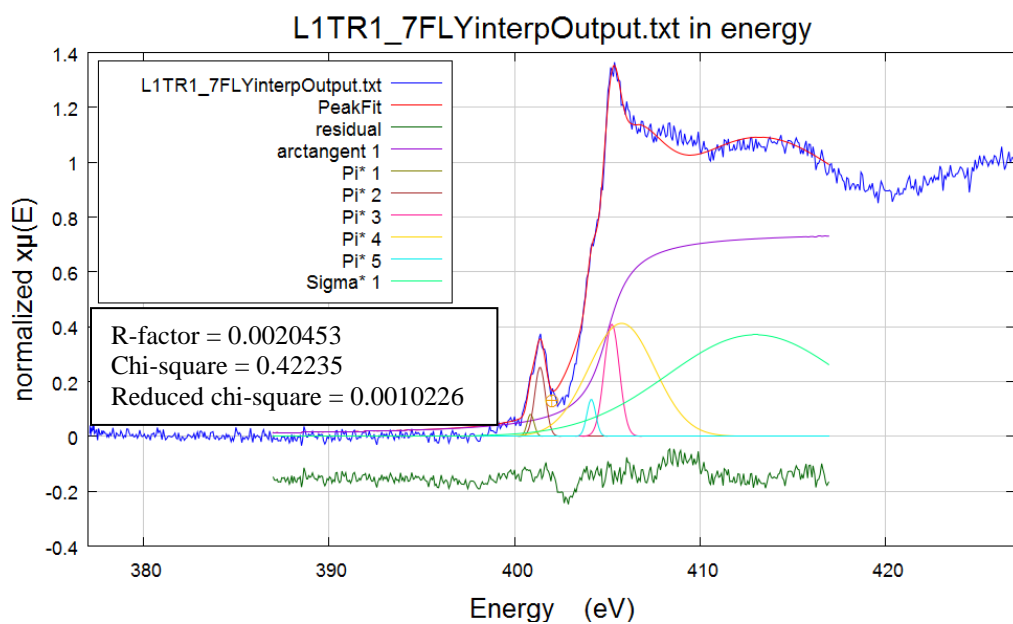
Appendix 3.2.1 N 1s XANES gaussian fitting for R1-4



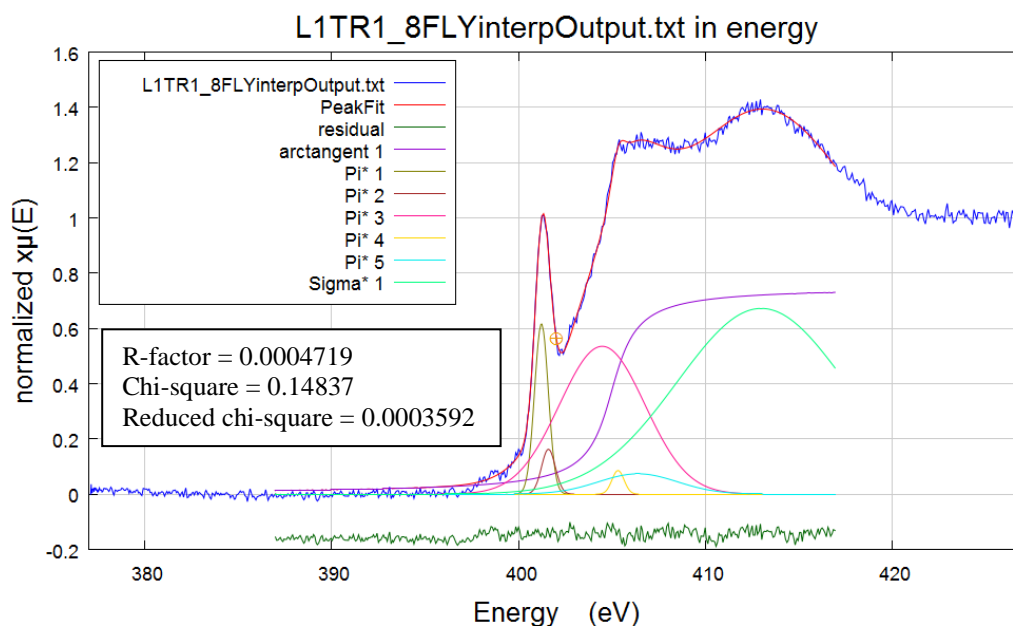
Appendix 3.2.2 N 1s XANES gaussian fitting for R1-5



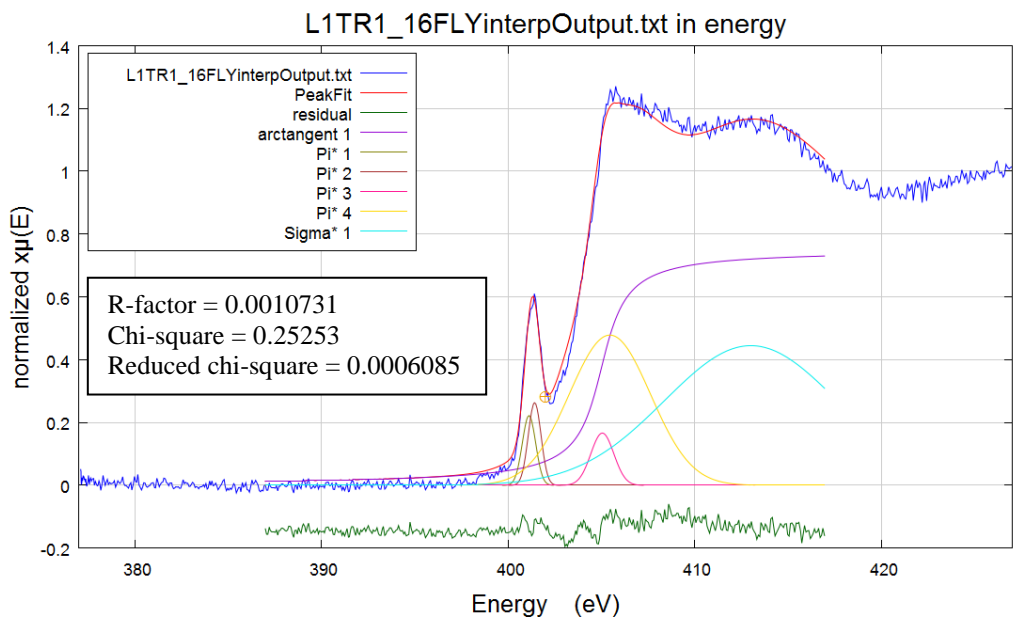
Appendix 3.2.3 N 1s XANES gaussian fitting for R1-6



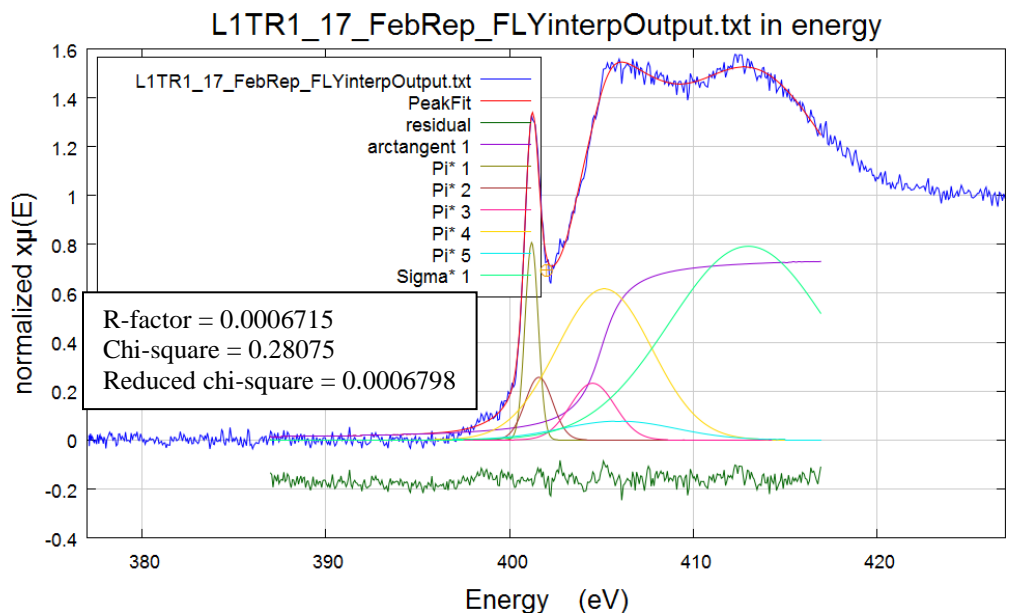
Appendix 3.2.4 N 1s XANES gaussian fitting for R1-7



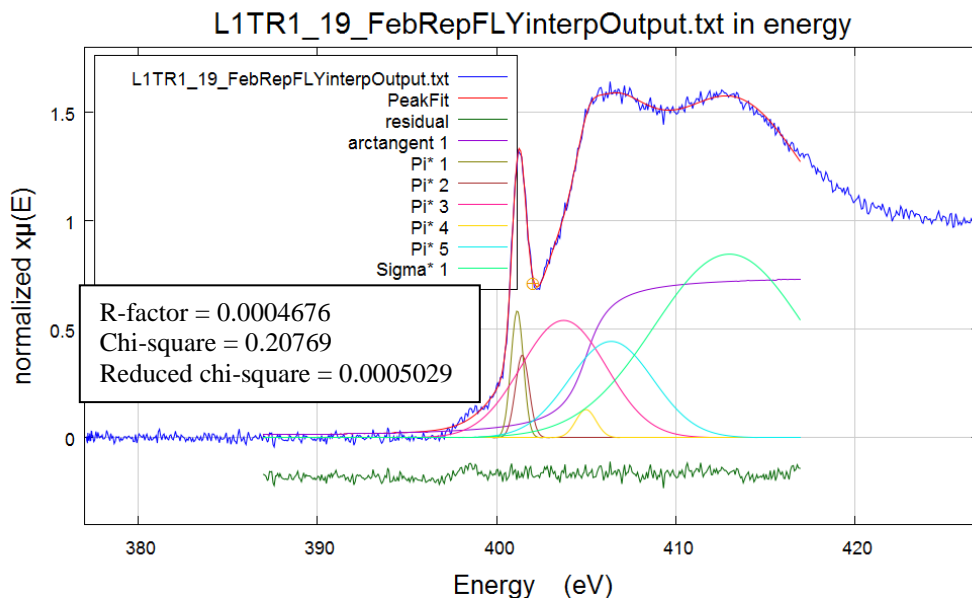
Appendix 3.2.5 N 1s XANES gaussian fitting for R1-8



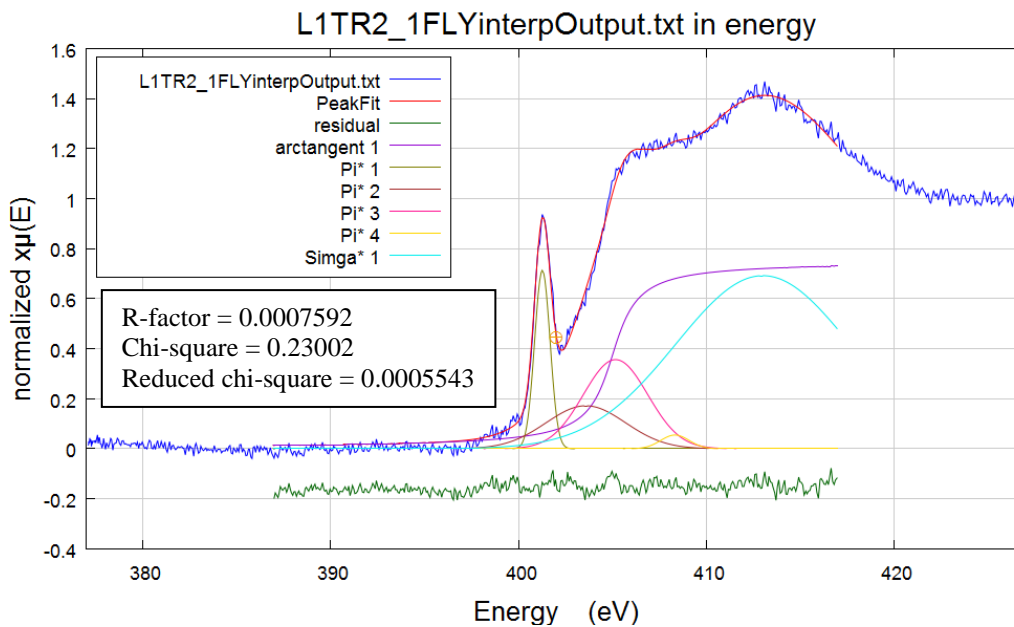
Appendix 3.2.6 N 1s XANES gaussian fitting for R1-16



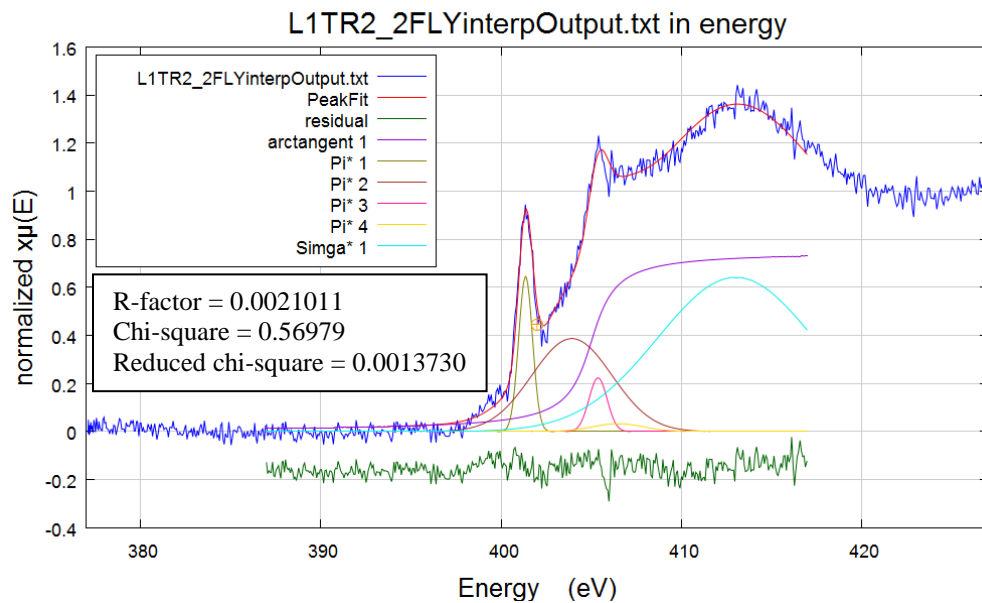
Appendix 3.2.7 N 1s XANES gaussian fitting for R1-17



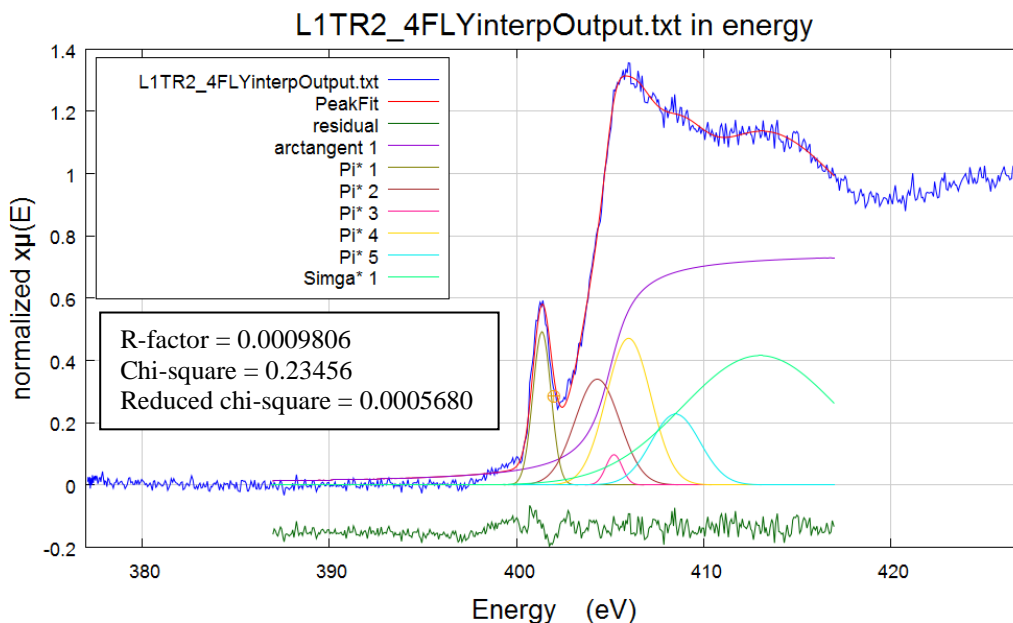
Appendix 3.2.8 N 1s XANES gaussian fitting for R1-19



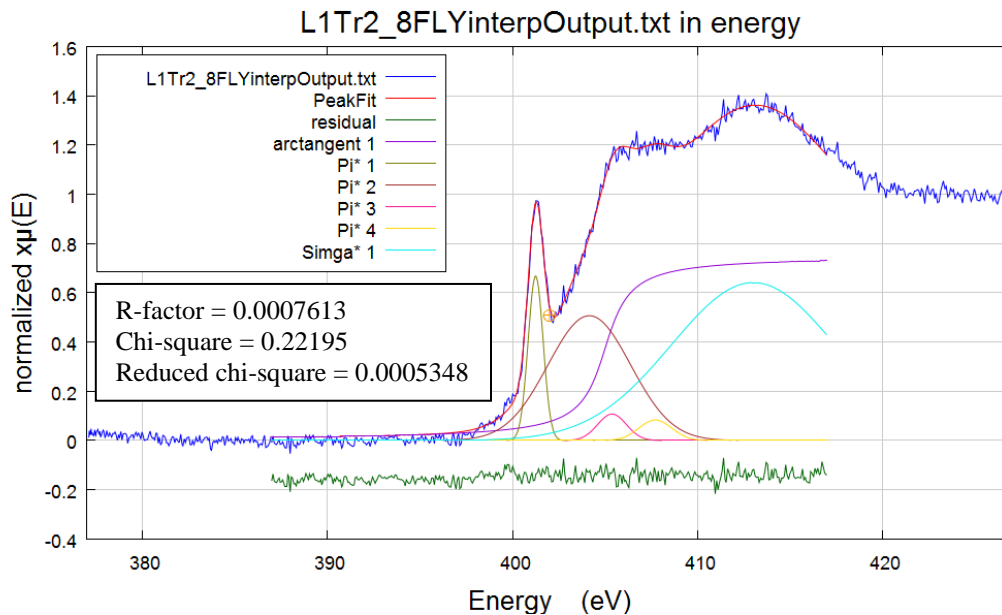
Appendix 3.2.9 N 1s XANES gaussian fitting for R2-1



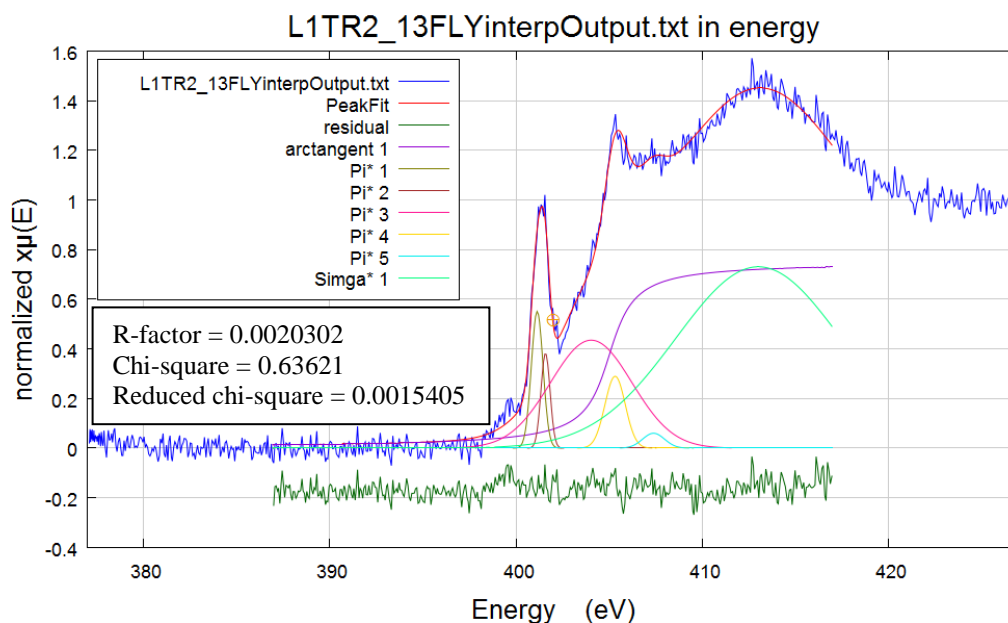
Appendix 3.2.10 N 1s XANES gaussian fitting for R2-2



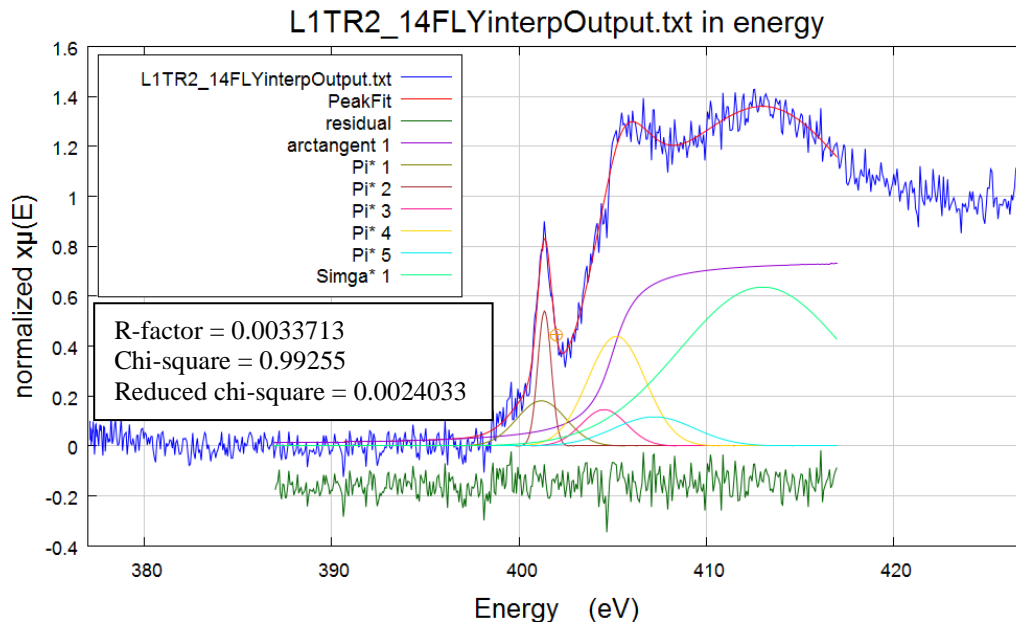
Appendix 3.2.11 N 1s XANES gaussian fitting for R2-2



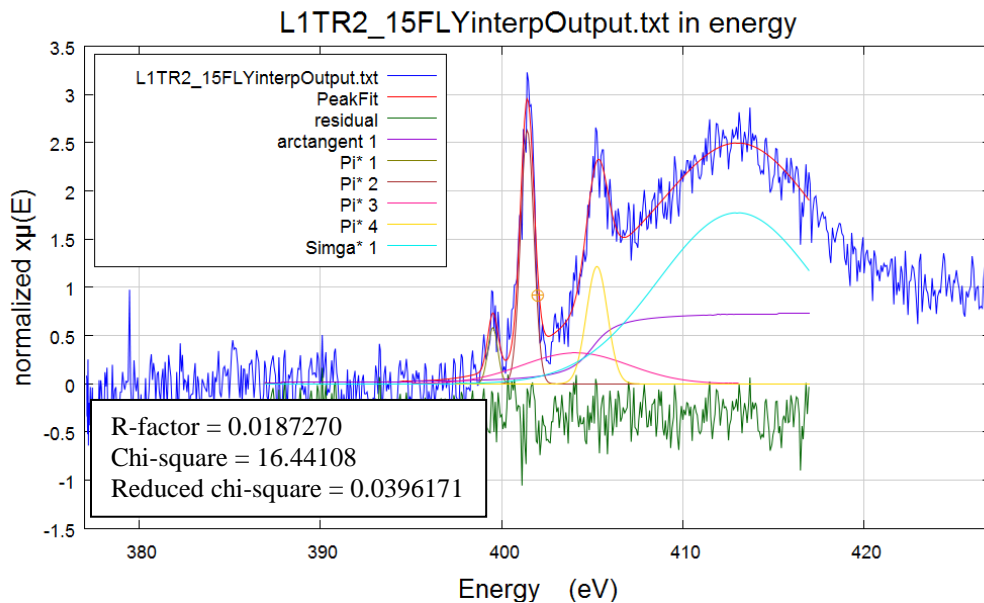
Appendix 3.2.12 N 1s XANES gaussian fitting for R2-8



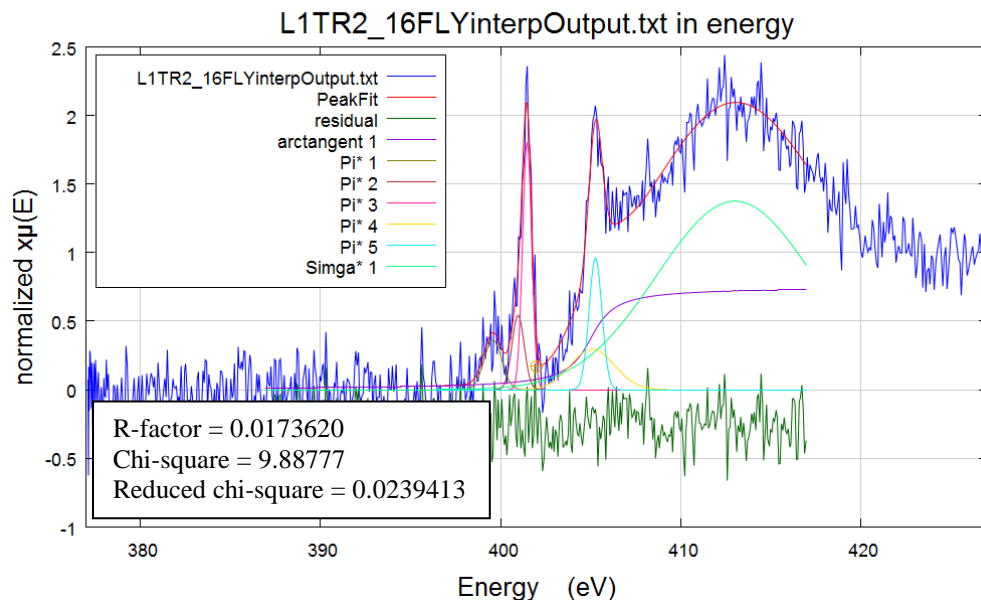
Appendix 3.2.13 N 1s XANES gaussian fitting for R2-13



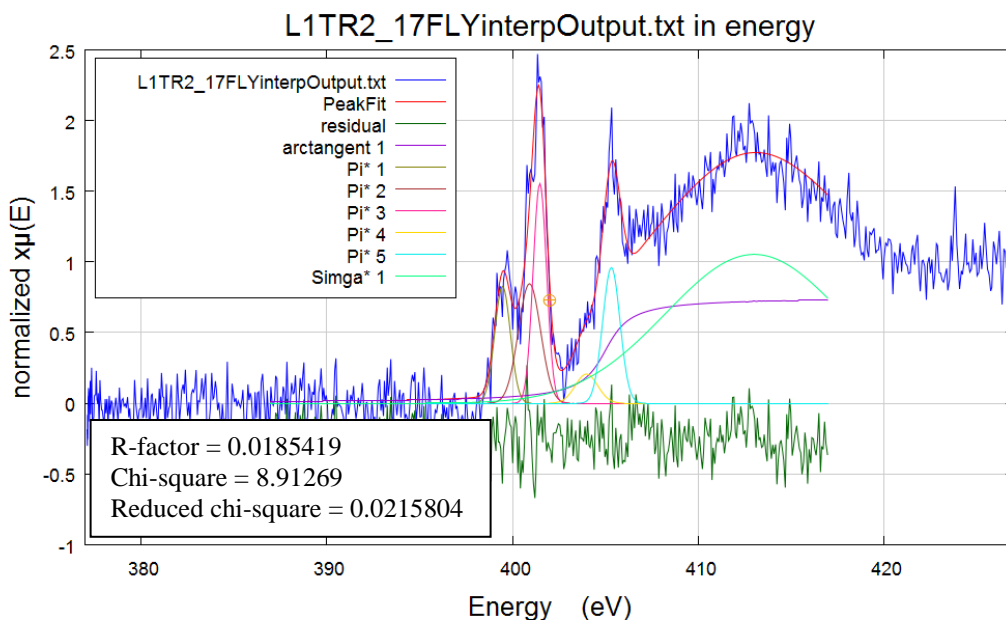
Appendix 3.2.14 N 1s XANES gaussian fitting for R2-14



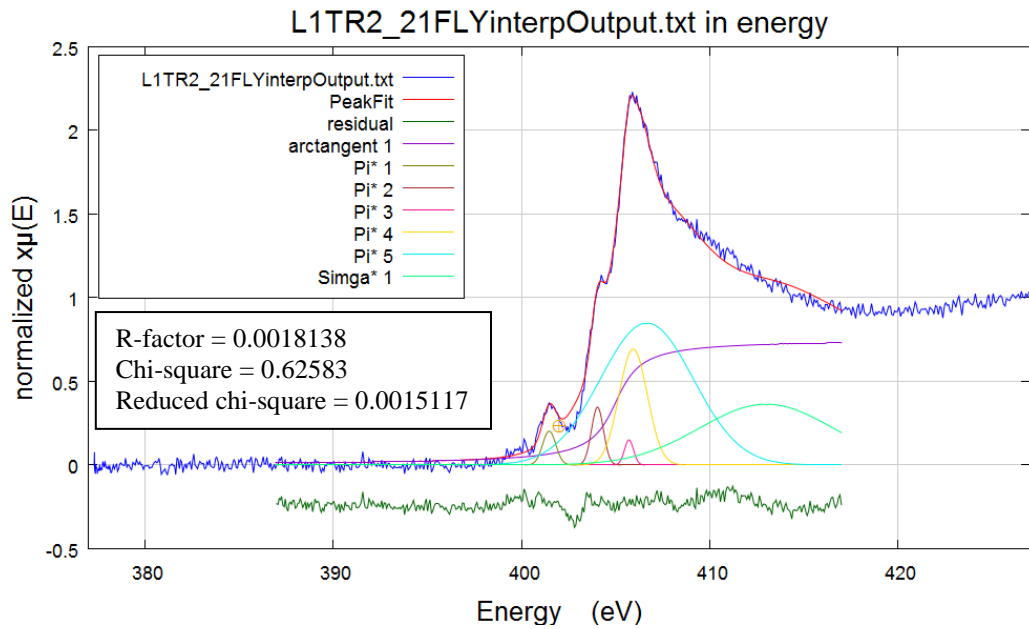
Appendix 3.2.15 N 1s XANES gaussian fitting for R2-15



Appendix 3.2.16 N 1s XANES gaussian fitting for R2-16



Appendix 3.2.17 N 1s XANES gaussian fitting for R2-17



Appendix 3.2.18 N 1s XANES gaussian fitting for R2-21

Appendix Table 3.2.1 Gaussian curve fitting parameters for N 1s XANES

Sample	Station	Arc					Sigma* 1	χ^2	reduced χ^2	R-factor	
		Tangent	Pi* 1	Pi* 2	Pi* 3	Pi* 4					
R1_1	Bio 9	-	-	-	-	-	-	-	-	-	
R1_2	Bio 9	-	-	-	-	-	-	-	-	-	
R1_4	Bio 9	405	401.346	404.839	405.068	405.287	413	1.68922	0.0040704	0.0072348	
R1_5	Bio 9	405	401.288	401.575	405.347	406.404	413	0.32092	0.0007733	0.0014884	
R1_6	Bio 9	405	401.097	404.201	405.33	406.402	413	0.23033	0.000555	0.0012282	
R1_7	Bio 9	405	400.871	401.379	405.25	405.781	404.145	413	0.42235	0.0010226	0.0020453
R1_8	Bio 9	405	401.232	401.605	404.483	405.33	406.4	413	0.14837	0.0003592	0.0004719
R1_14	Bio 9	-	-	-	-	-	-	-	-	-	
R1_16	Bio 9	405	401.116	401.418	405.044	405.447	413	0.24253	0.0006085	0.0010731	
R1_17	Bio 9	405	401.207	401.602	404.526	405.316	406.58	413	0.28075	0.0006798	0.0006715
R1_18	Bio 9	-	-	-	-	-	-	-	-	-	
R1_19	Bio 9	405	401.153	401.436	403.75	404.991	406.402	413	0.20769	0.0005029	0.0004676
R1_20	Bio 9	-	-	-	-	-	-	-	-	-	
R2_1	Ty-Io	405	401.266	403.58	405.161	408.321	413	0.23002	0.0005543	0.0007592	
R2_2	Ty-Io	405	401.356	403.921	405.37	406.485	413	0.56979	0.001373	0.0021011	
R2_4	Ty-Io	405	401.356	404.311	405.203	405.984	408.493	413	0.23456	0.000568	0.0009806
R2_6	Ty-Io	-	-	-	-	-	-	-	-	-	
R2_7	Ty-Io	-	-	-	-	-	-	-	-	-	
R2_8	Ty-Io	405	401.245	404.144	405.37	407.712	413	0.22195	0.0005348	0.0007613	
R2_13	Ty-Io	405	401.133	401.579	404.032	405.315	407.377	413	0.63621	0.0015405	0.0020302
R2_14	Ty-Io	405	401.189	401.356	404.534	405.203	407.21	413	0.99255	0.0024033	0.0033713
R2_15	Ty-Io	405	399.516	401.412	404.088	405.259	413	16.44108	0.0396171	0.018727	
R2_16	Ty-Io	405	399.572	400.966	401.468	405.259	405.203	413	9.88777	0.0239413	0.017362
R2_17	Ty-Io	405	399.46	400.91	401.468	403.976	405.315	413	8.91269	0.0215804	0.0185419
R2_18	Ty-Io	-	-	-	-	-	-	-	-	-	
R2_19	Ty-Io	-	-	-	-	-	-	-	-	-	

R2_20	Ty-Io	-	-	-	-	-	-	-	-	-	-
R2_21	Ty-Io	405	401.468	404.032	405.705	405.928	406.653	413	0.62583	0.0015117	0.0018138

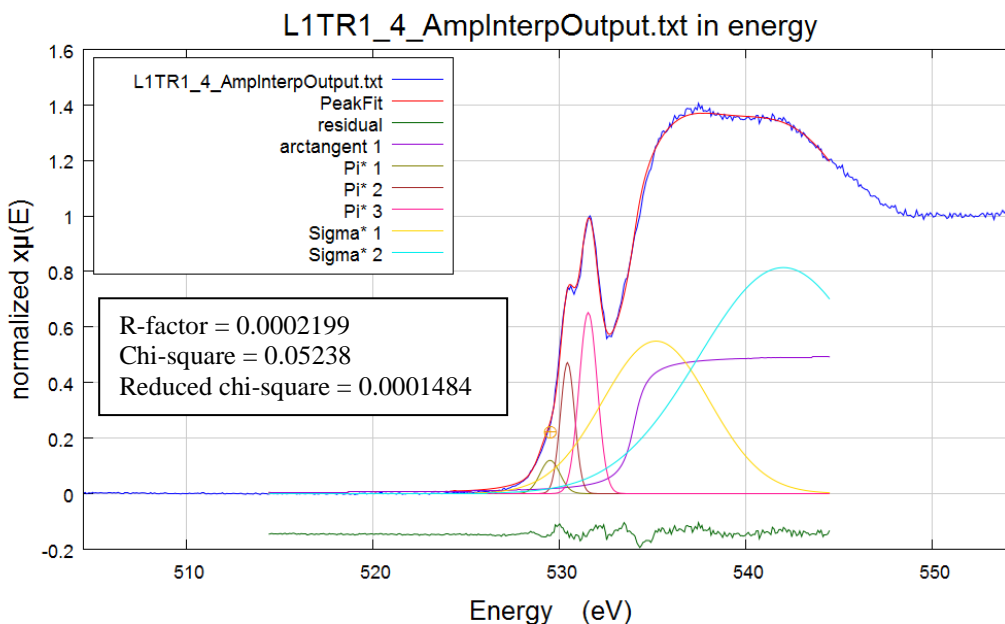
- : no XANES data

blank: no functional group identified

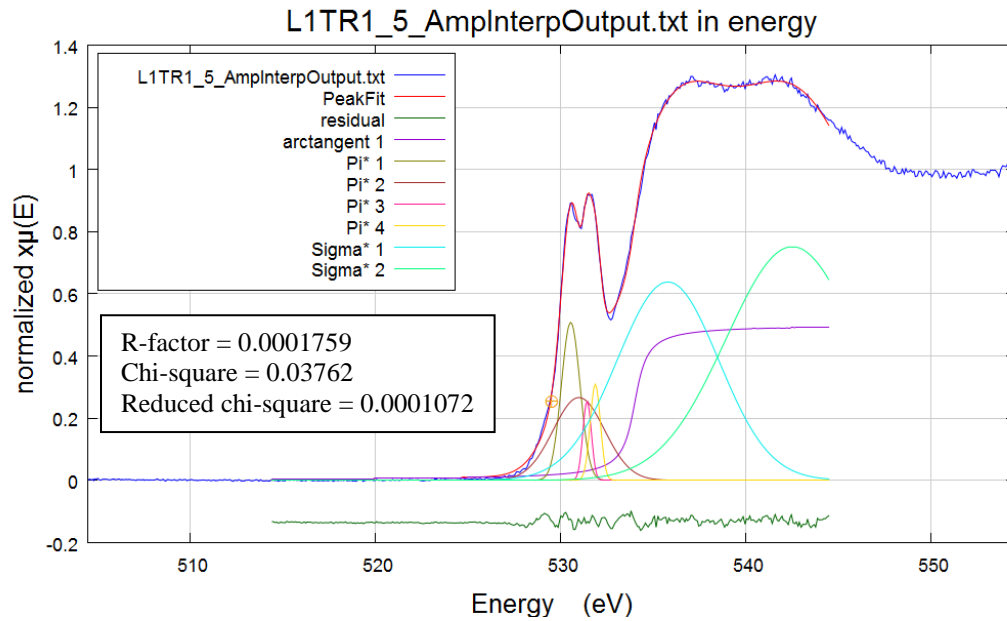
All arc tangent, pi*, and sigma* values in eV

Appendix 3.3 Oxygen 1s XANES Gaussian fitting in Athena

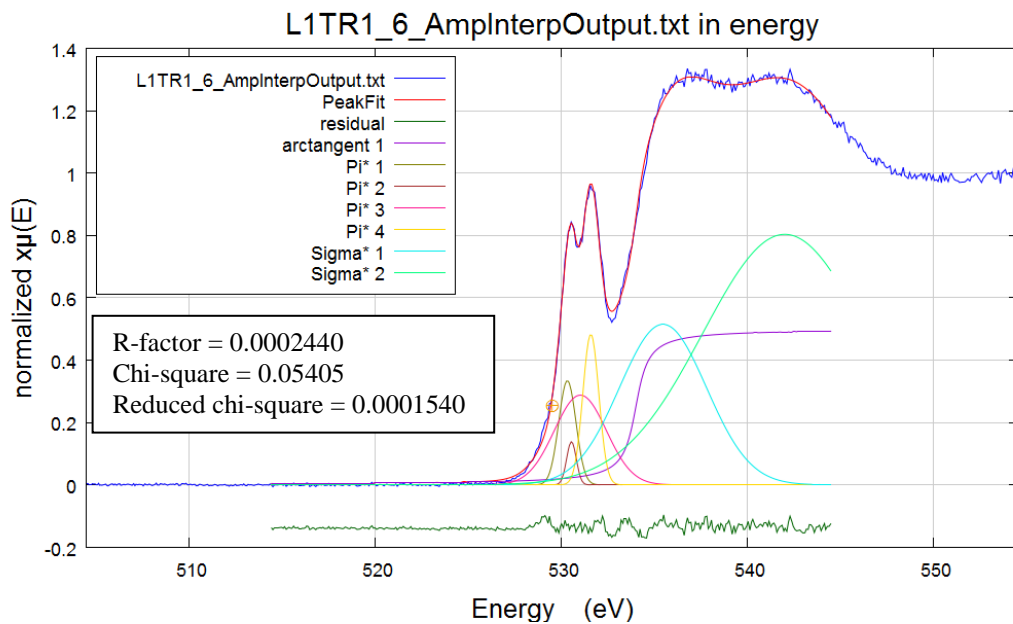
Below are the raw images from *Athena* regarding Gaussian fits for R1 and R2 O 1s XANES. All terms and peak energies are defined in Appendix Table 3.3.1. Pi* and Sigma* peaks were chosen based off the normalized two column data. When fitting, all initial guess of Pi* heights and widths were set to 0.5. For Sigma *, all initial guesses were height of 0.5 and widths of 3. For O 1s XANES, parameters for the arctangent were always fixed at 534.0 eV with a height of 0.5, and width of 0.5. The model was only allowed to vary the heights and with of the Pi* and Sigma* peaks.



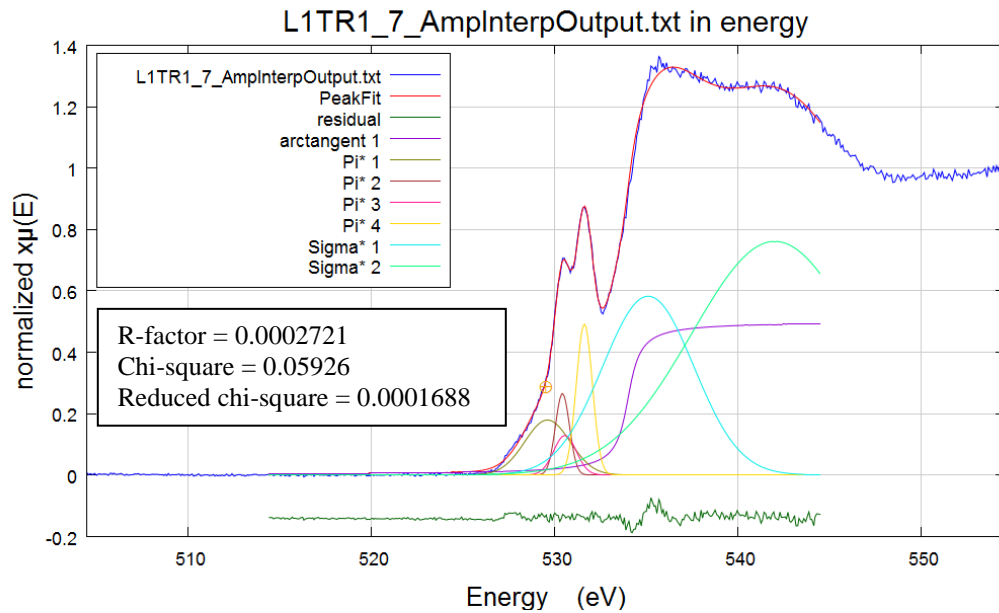
Appendix 3.3.1 O 1s XANES gaussian fitting for R1-4



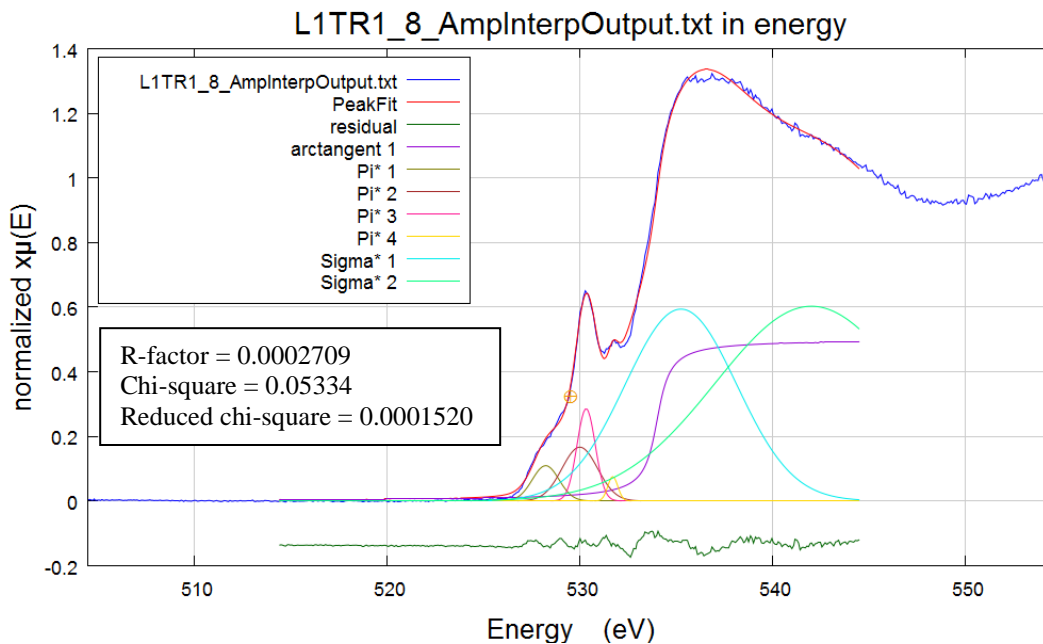
Appendix 3.3.2 O 1s XANES gaussian fitting for R1-5



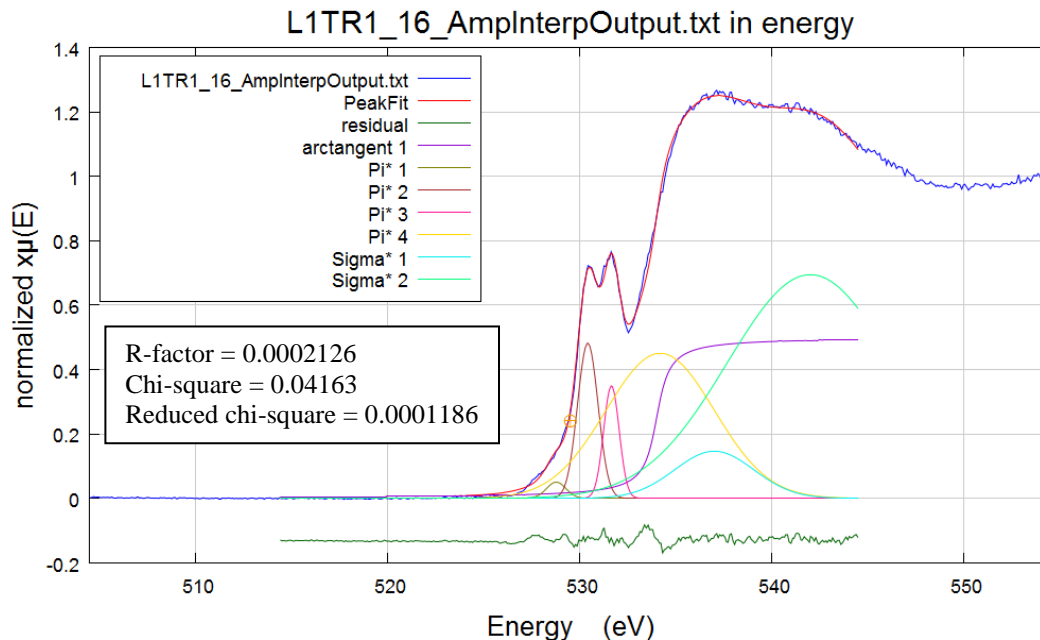
Appendix 3.3.3 O 1s XANES gaussian fitting for R1-6



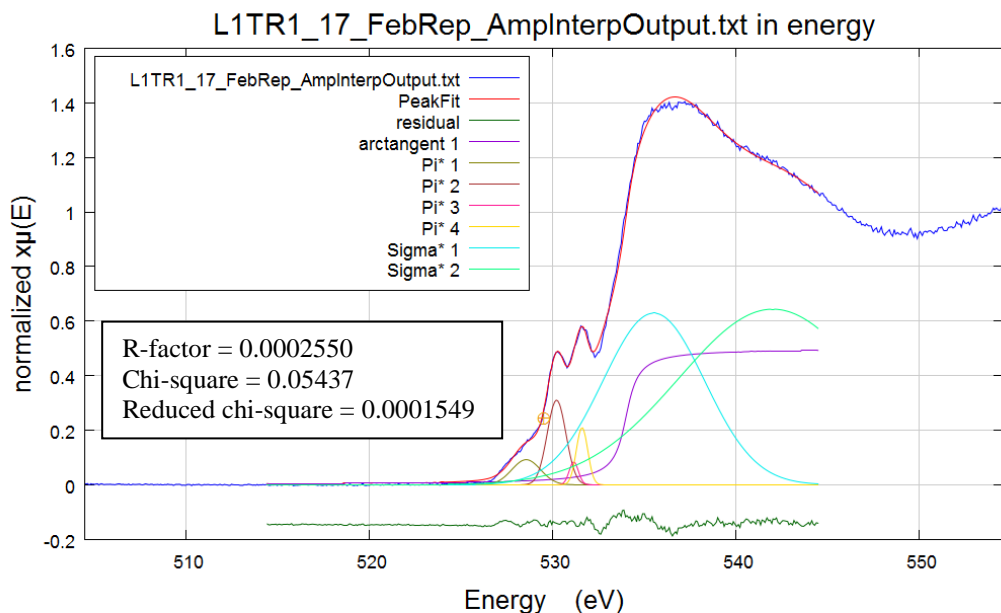
Appendix 3.3.4 O 1s XANES gaussian fitting for R1-7



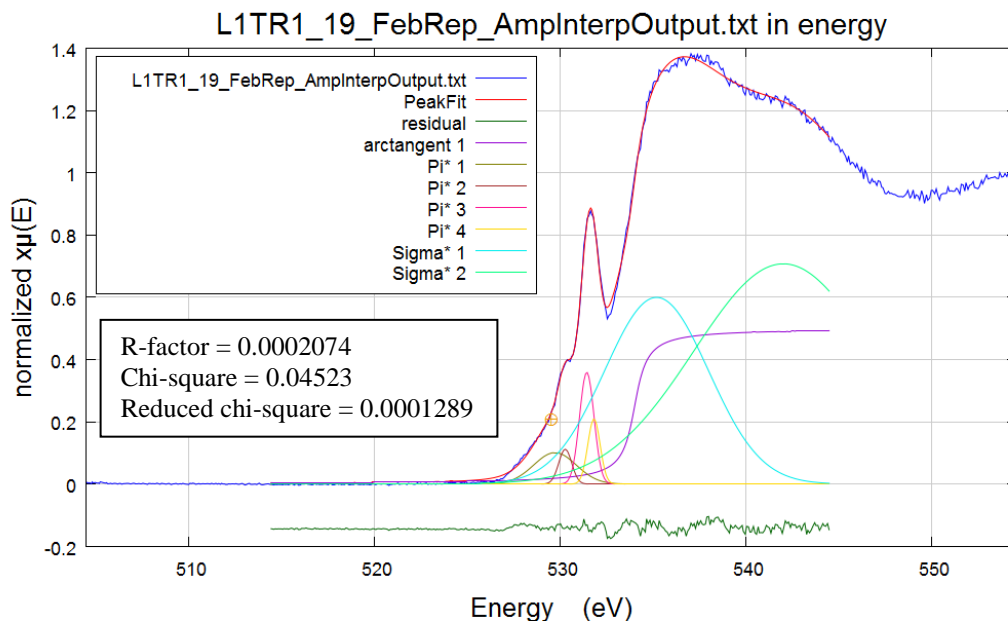
Appendix 3.3.5 O 1s XANES gaussian fitting for R1-8



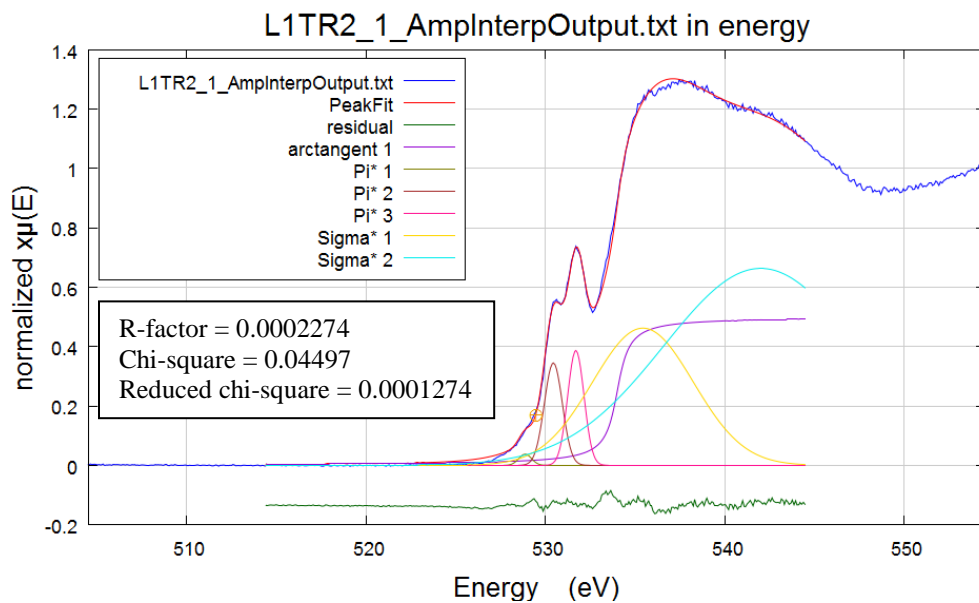
Appendix 3.3.6 O 1s XANES gaussian fitting for R1-16



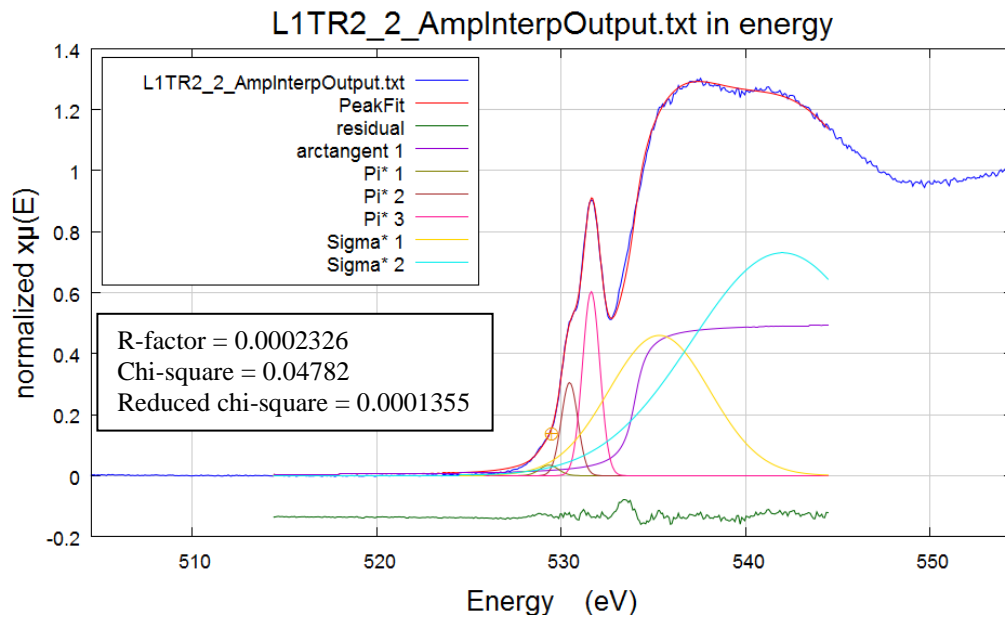
Appendix 3.3.7 O 1s XANES gaussian fitting for R1-17



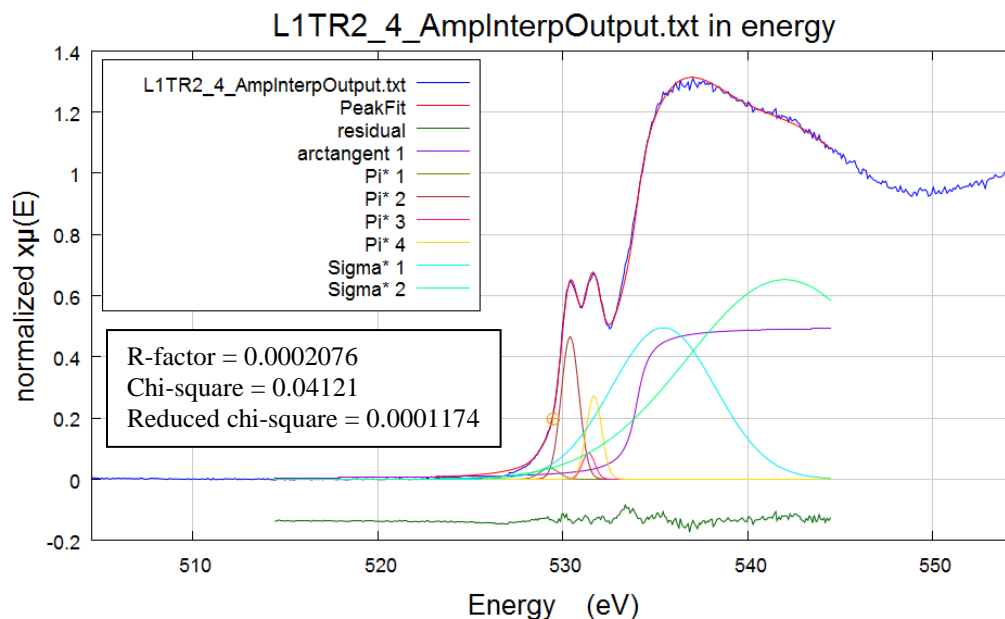
Appendix 3.3.8 O 1s XANES gaussian fitting for R1-19



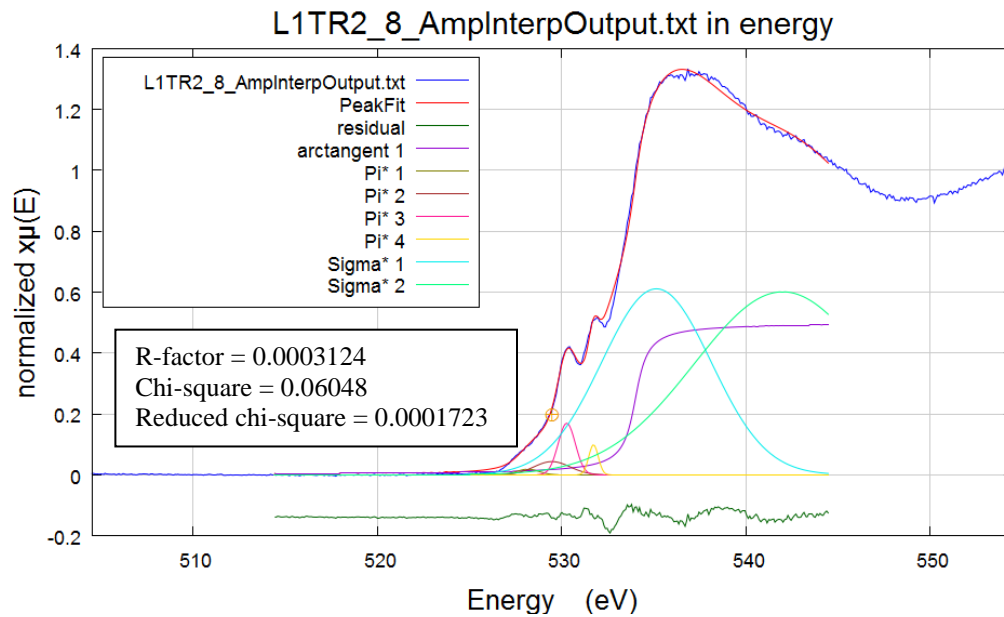
Appendix 3.3.9 O 1s XANES gaussian fitting for R2-1



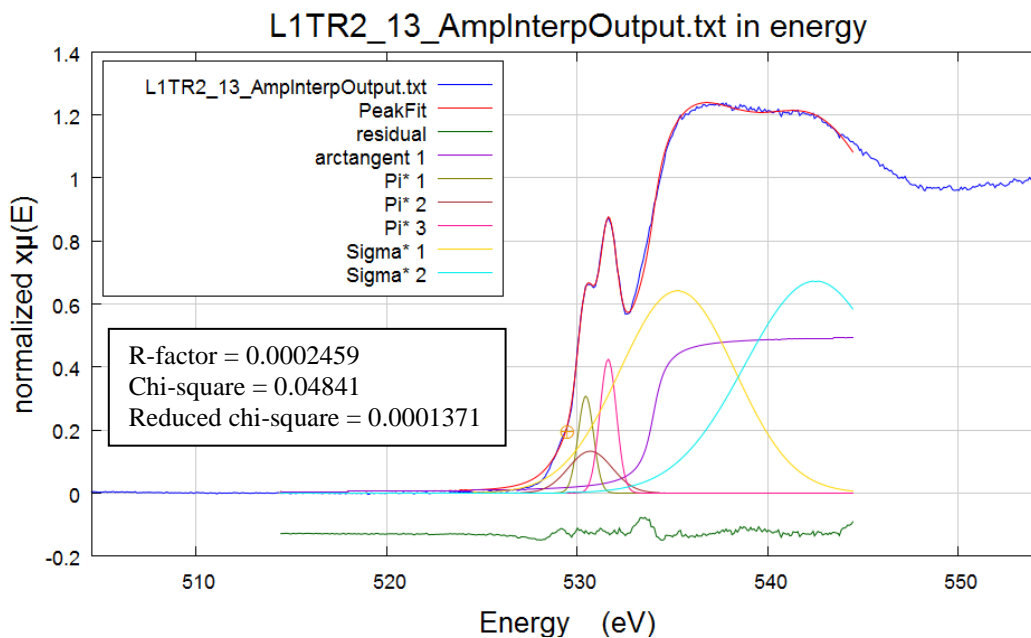
Appendix 3.3.10 O 1s XANES gaussian fitting for R2-2



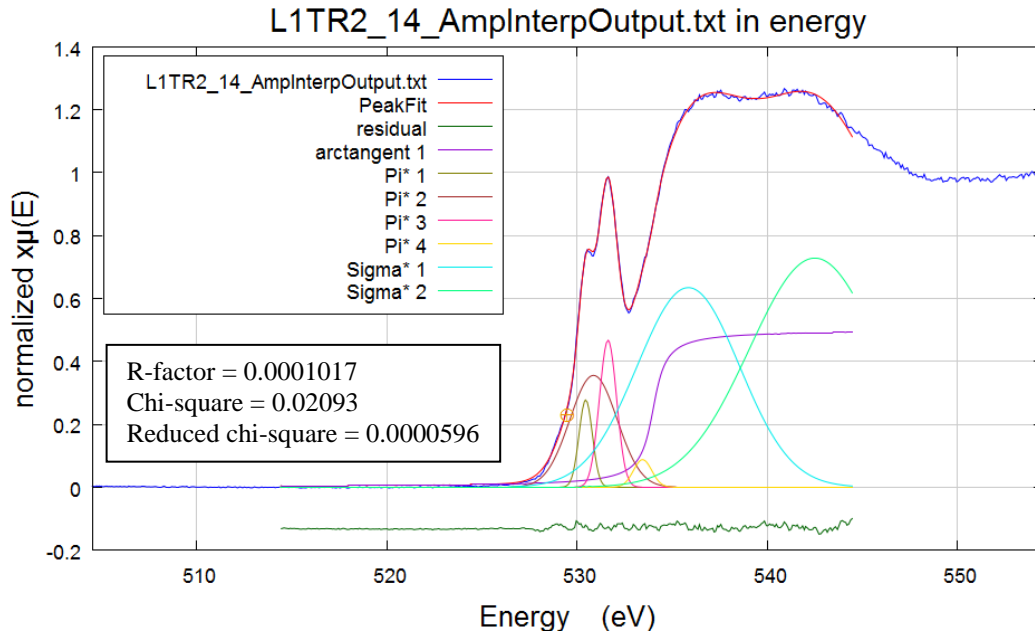
Appendix 3.3.11 O 1s XANES gaussian fitting for R2-4



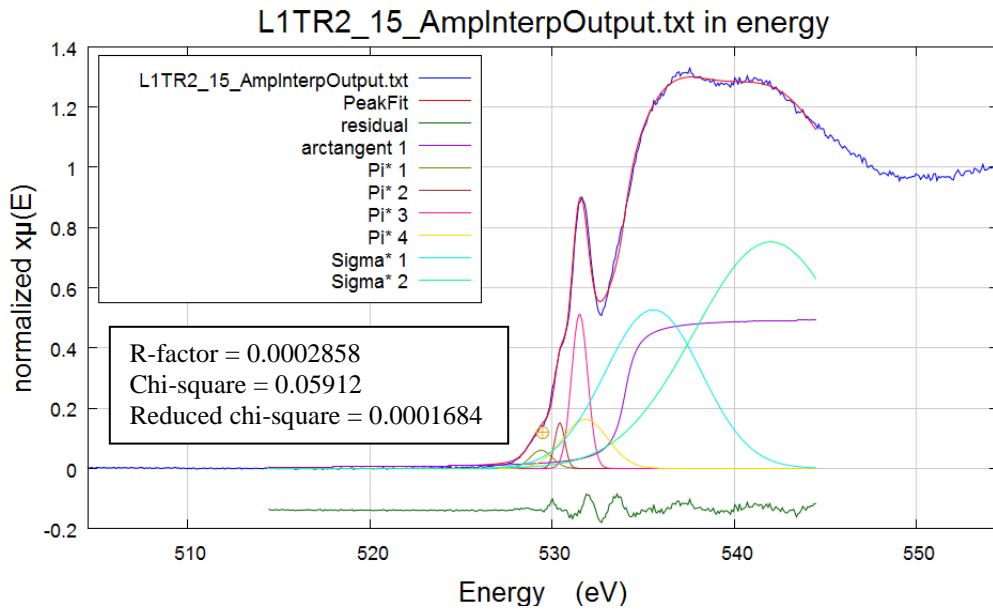
Appendix 3.3.12 O 1s XANES gaussian fitting for R2-8



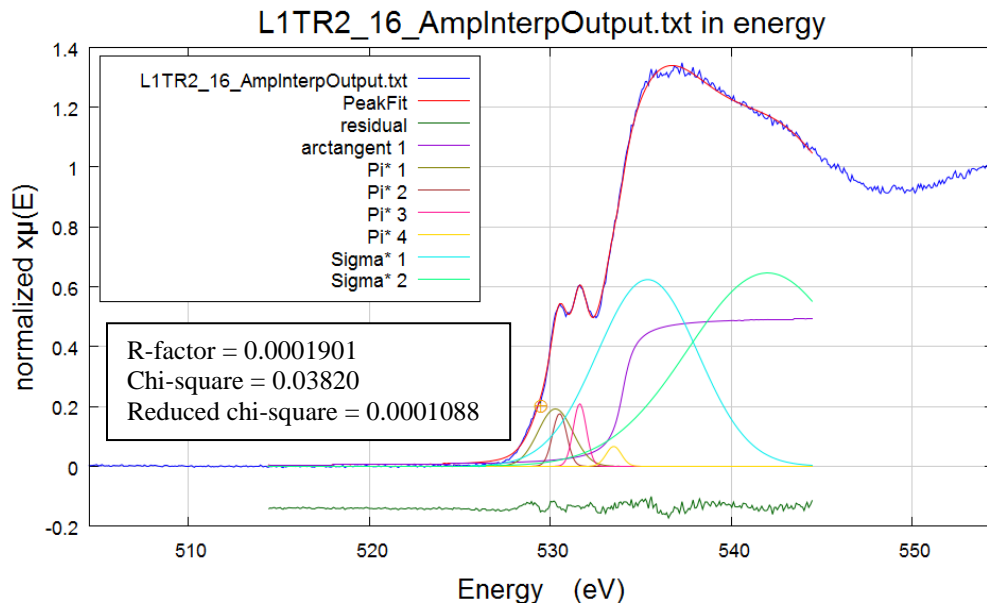
Appendix 3.3.13 O 1s XANES gaussian fitting for R2-13



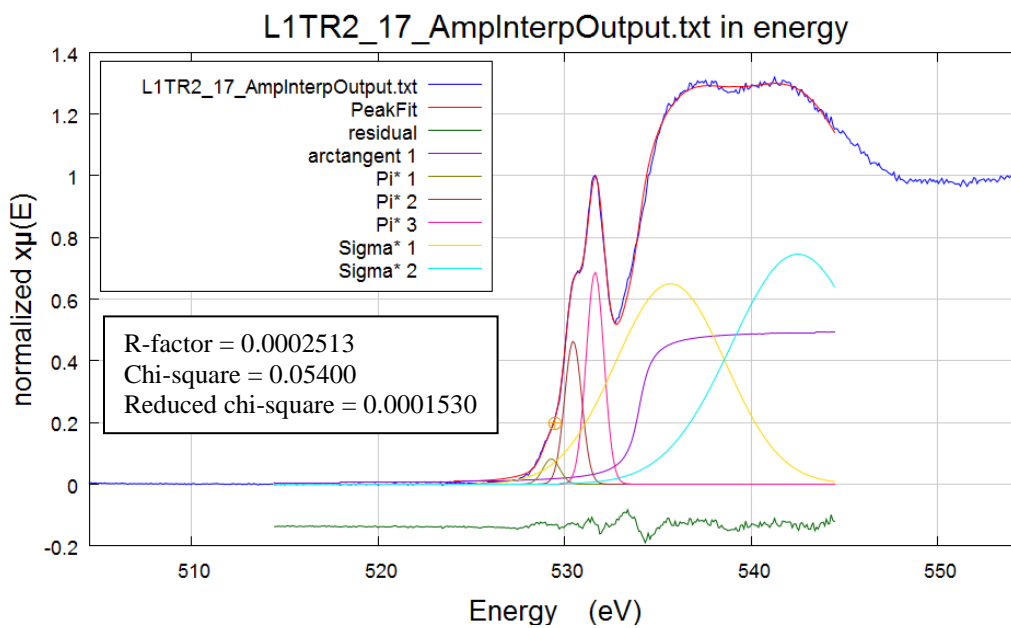
Appendix 3.3.14 O 1s XANES gaussian fitting for R2-14



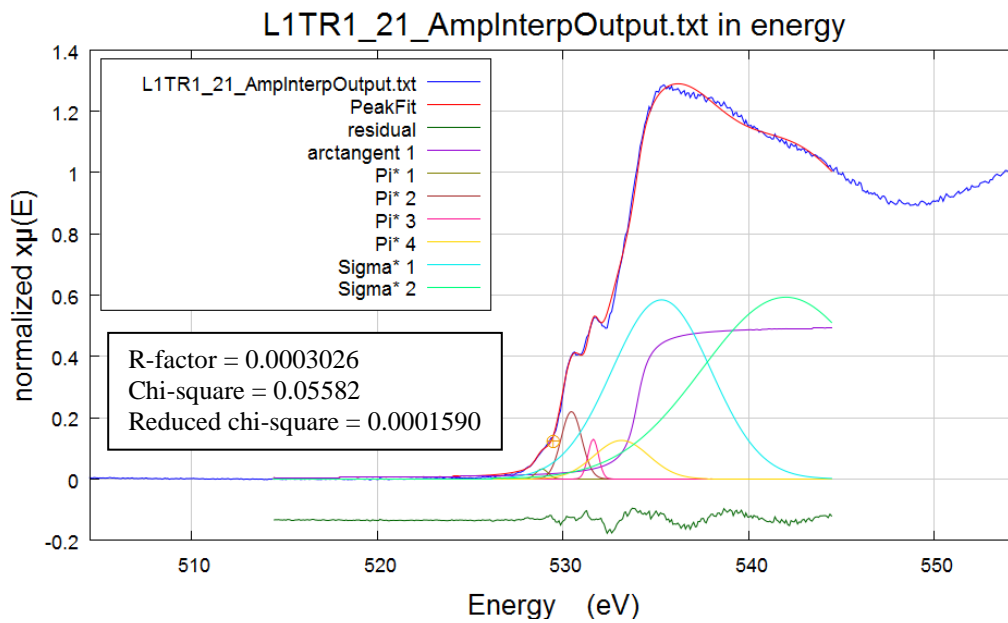
Appendix 3.3.15 O 1s XANES gaussian fitting for R2-15



Appendix 3.3.16 O 1s XANES gaussian fitting for R2-16



Appendix 3.3.17 O 1s XANES gaussian fitting for R2-17



Appendix 3.3.18 O 1s XANES gaussian fitting for R2-21

Appendix Table 3.3.1 Gaussian curve fitting parameters for O 1s XANES

Sample	Station	Arc				Sigma* 1	Sigma* 2	χ^2	reduced χ^2	R-factor	
		Tangent	Pi* 1	Pi* 2	Pi* 3						
R1_1	Bio 9	-	-	-	-	-	-	-	-	-	
R1_2	Bio 9	-	-	-	-	-	-	-	-	-	
R1_4	Bio 9	534	529.494	530.433	531.542	535.181	542	0.05238	0.0001484	0.0002199	
R1_5	Bio 9	534	530.543	530.985	531.427	531.868	535.788	542.5	0.03762	0.0001072	0.0001759
R1_6	Bio 9	534	530.323	530.543	531.202	531.583	535.457	542	0.05405	0.000154	0.000244
R1_7	Bio 9	534	529.605	530.424	530.557	531.617	535.1	542	0.05929	0.0001688	0.0002721
R1_8	Bio 9	534	528.225	529.994	530.323	531.704	535.236	542	0.05334	0.000152	0.0002709
R1_14	Bio 9	-	-	-	-	-	-	-	-	-	-
R1_16	Bio 9	534	528.77	530.418	531.648	534.187	537	542	0.04163	0.0001186	0.0002126
R1_17	Bio 9	534	528.556	530.212	531.151	531.6	535.512	542	0.05437	0.0001549	0.000255
R1_18	Bio 9	-	-	-	-	-	-	-	-	-	-
R1_19	Bio 9	534	529.715	530.267	531.427	531.813	535.181	542	0.04523	0.0001289	0.0002074
R1_20	Bio 9	-	-	-	-	-	-	-	-	-	-
R2_1	Ty-Io	534	528.865	530.437	531.691	535.432	542	0.04497	0.0001274	0.0002274	
R2_2	Ty-Io	534	529.334	530.449	531.622	535.318	542	0.04782	0.0001355	0.0002326	
R2_4	Ty-Io	534	529.276	530.39	531.388	531.681	535.436	542	0.04121	0.0001174	0.0002076
R2_6	Ty-Io	-	-	-	-	-	-	-	-	-	-
R2_7	Ty-Io	-	-	-	-	-	-	-	-	-	-
R2_8	Ty-Io	534	528.158	529.472	530.273	531.725	535.143	542	0.06048	0.0001723	0.0003124
R2_13	Ty-Io	534	530.449	530.684	531.622	535.26	542.5	0.04841	0.0001371	0.0002459	
R2_14	Ty-Io	534	530.449	530.86	531.622	533.441	535.846	542.5	0.020293	0.0000596	0.0001017
R2_15	Ty-Io	534	529.393	530.416	531.505	531.813	535.553	542	0.05912	0.0001684	0.0002858
R2_16	Ty-Io	534	530.273	530.508	531.622	533.5	535.377	542	0.0382	0.0001088	0.0001901
R2_17	Ty-Io	534	529.276	530.449	531.625	535.67	542.5	0.054	0.000153	0.0002513	
R2_18	Ty-Io	-	-	-	-	-	-	-	-	-	-
R2_19	Ty-Io	-	-	-	-	-	-	-	-	-	-

R2_20	Ty-Io	-	-	-	-	-	-	-	-	-	-
R2_21	Ty-Io	534	528.865	530.449	531.625	533.148	535.304	542	0.05582	0.000159	0.0003026

- : no XANES data

blank: no functional group identified

All arc tangent, pi*, and sigma* values in eV

